



HAL
open science

Investigation of silver nanowire networks : physical properties, stability and integration into devices

Theodora Papanastasiou

► **To cite this version:**

Theodora Papanastasiou. Investigation of silver nanowire networks : physical properties, stability and integration into devices. Materials Science [cond-mat.mtrl-sci]. Université Grenoble Alpes [2020-..], 2020. English. NNT : 2020GRALI083 . tel-03332613

HAL Id: tel-03332613

<https://theses.hal.science/tel-03332613v1>

Submitted on 3 Sep 2021

HAL is a multi-disciplinary open access archive for the deposit and dissemination of scientific research documents, whether they are published or not. The documents may come from teaching and research institutions in France or abroad, or from public or private research centers.

L'archive ouverte pluridisciplinaire **HAL**, est destinée au dépôt et à la diffusion de documents scientifiques de niveau recherche, publiés ou non, émanant des établissements d'enseignement et de recherche français ou étrangers, des laboratoires publics ou privés.

THÈSE

Pour obtenir le grade de

DOCTEUR DE L'UNIVERSITÉ GRENOBLE ALPES

Spécialité : **Matériaux, Mécanique, Génie Civil, Electrochimie**

Arrêté ministériel : 25 mai 2016

Présentée par

Theodora PAPANASTASIOU

Thèse dirigée par **Daniel BELLET**, Professeur des universités,
Grenoble INP et

codirigée par **David MUNOZ-ROJAS**, Directeur de Recherche,
CNRS

préparée au sein du **Laboratoire des Matériaux et du Génie
Physique**

dans l'École Doctorale IMEP-2

Investigation of silver nanowire networks: physical properties, stability and integration into devices

Thèse soutenue publiquement le **18 Décembre 2020**,
devant le jury composé de :

Monsieur Alain SYLVESTRE

Professeur, G2ELAB, Université Grenoble Alpes, Président du Jury

Madame Laurence RESSIER

Professeur, LPCNO, INSA de Toulouse, Rapporteuse

Monsieur Philippe POULIN

Directeur de Recherche, CNRS, Université of Bordeaux, Rapporteur

Madame Irene GOLDTHORPE

Professeure associée, University of Waterloo, Examinatrice

Monsieur Matthias PAULY

Maitre de Conférences, Université de Strasbourg, Examineur

Monsieur Jean-Pierre SIMONATO

Directeur de Recherche, CEA LITEN Grenoble, Examineur

Monsieur Daniel BELLET

Professeur, Grenoble INP, Directeur de thèse

Monsieur David Muñoz-Rojas

Directeur de Recherche, CNRS, Co-directeur de thèse



Στη μνήμη του μπαμπά μου
In the memory of my dad

Acknowledgments

The last three years of the PhD journey in Grenoble, have been the best years in my life so far. I had never imagined that a day like this would come for me that my mind is full of precious knowledge and skills, my heart is full of happiness thanks to all these people I have met in a scientific and personal level. As I look back I realize how beautifully and unexpectedly everything flew. But always mindfully. The right things, the right moment. The appropriate decisions, but of course with a good dose of luck. I didn't have a plan to make a PhD when I came in Grenoble for my master. But it felt already like a destiny; I came back actually, since I had done my Erasmus in 2012 in Grenoble too. And the real destiny is when I passed the door of LMGP in February 2017, to start my internship in silver nanowire networks. Then, everything began. In the house of "LMGP Family", as I like to call it. In this special team; noble, rare and shiny like silver. Nothing would have been like this without the support of the Family, especially during the last months of my thesis that were totally marked by the coronavirus pandemics.

First of all, I would like to thank from the bottom of my heart my PhD supervisor Prof. Daniel Bellet for all his support, his kindness and all the opportunities he gave me to explore more and deeper the science during this exceptional journey of my doctoral thesis. Thank you for your love for Physics and the inspiration you give to the younger physicists, your scientific ideas and your personal actions for a better world. I will always feel so lucky to have been your student. I would like to express my sincere gratitude to my co-supervisor Dr. David Muñoz-Rojas for his support, his encouragement and his generosity. Your passion and tireless devotion to science, and your knowledge in so many cultural and other domains are always a remarkable example for me. Thank you for the opportunity you gave me to explore more the world of oxides and be also part of the SALD team during my current post-doc.

My immense gratitude to Dr. João Resende for all these that he signifies for my scientific and personal life. Without you my PhD wouldn't have been like this at all. Thank you for your constant presence, inspiration and advice. The day you finished your post-doc I felt empty. But I had and I will always have the best memories of working together and also sharing life's adventures with you; and like this, I get the strength to carry on joyfully. Para sempre obrigada.

I would like to thank all the people that we have worked together in AgNW team, starting from Dr. Thomas Sannicolo that co-supervised my master internship and made me love the topic since the very beginning. His exceptional PhD thesis and his hard work was always a source of inspiration for me. I would like to deeply thank all the interns that have worked in AgNW team during these years. Silas Kraus, Martin Bordas, Nil Fontanals, Dominik Moritz, Tomy Chatin, Vladimir Tsukanov, Stefano Saroglia, I will never forget your catalytic contribution, hard-working and dynamic spirit. I would like to thank all the highly motivated, bright students of Phelma that we have worked together in projects of 1st year and the instrumentation projects of the biomed parcours, as well.

My warmest thank you to Laetitia Bardet, this silver girl, for her love and support. My lab little sister, I wish you the best for your PhD, I know it is going to be awesome as you. I will always be gladly by your side. I would like to thank the colleagues from the SALD team and especially Dr. Viet Huong Nguyen and Abderrahime Sekkat for their amazing collaboration, significant expertise and unstoppable work. Along with Chiara, Fidel, Octavio and Masoud, you are all an example of hard-working and creativity. Viet we miss you so much in the lab. Abdou I deeply thank you for your valuable advices and the fruitful conversations we share the last months in our office.

I would like to express my sincere gratitude to the direction of LMGP, Dr. Carmen Jimenez and Prof. Franz Bruckert. Without their outstanding professional and personal investment to the lab, LMGP wouldn't have been at this level of scientific production, expertise and a unique example of organization and working conditions. I'm very lucky that I had the great opportunity to work with Prof. Franz and get a small taste of the world of biology. I will always be profoundly thankful for having Carmen by our side, being for real the mother of the lab. Without you next to me in the hardest not only working but also personal issues, I certainly wouldn't have made it till the end.

My warmest thank you to all the researchers and professors of LMGP. With their significant scientific work and their human qualities, show the way to the younger people to love and continue in the academic field. I'm deeply grateful for the tireless and warm support of the HR, Michele San-Martin, Annie Ducher and Josiane Viboud; the informatics excellence and joyful spirit of Nadjib Medjaldi; the expertise and willingness of all engineering staff, especially Isabelle Gerald, Laetitia Rapenne, Micha Anikin, Matthieu Jouvert and Serge Quessada; the kindness of all Phelma staff, especially George Capone for his smile at the evenings of working late in the lab, and the lovely ladies of the reception.

During my PhD I had the great chance to contribute in several regional and national projects of the AgNW-SALD team and collaborate in local and international level as well. I am so grateful to have been interacting with amazing people from laboratory and industrial partnership, and have learnt so much in a theoretical and technical level. The researchers, engineers, post-docs, PhD students and interns that have worked in projects such as ANR-PANASSE, ANR-MEANING, Campus France-Pessoa. A warm thank you to the amazing collaboration with the scientific team of Dr. Lavinia Balan in Mulhouse and congratulations to Marine Dabert for her PhD. A big thank you to Prof. Mona Tréguer-Delapierre, Prof. Irene Goldthorpe and Dr. Alexandra Madeira for the exceptional collaboration. Thank you to the scientific team of Prof. Christophe Vallée and Prof. Marceline Bonvalot in CEA-LTM.

I would like to express my gratitude to the scientific team of Dr. Jean-Pierre Simonato in CEA-LITEN, Dr. Caroline Celle, Dr. Alexandre Carella and Dr. Amélie Schultheiss (Congratulations for your PhD Amélie) for the outstanding collaboration and this beautiful review-article we made all together; my first article as first-author, I will never forget it. My warmest thank you to Prof. Lionel Flandin and the engineer Nicolas Charvin in LEPMI-Bourget du Lac, for their unforgettable collaboration and the remarkable scientific results we obtained together. I also would like to thank Dr. Simonato and Prof. Flandin for their important advice and support as members of my PhD-CSI committee.

At this point, I would like to express my thankfulness to the researchers that participated in my PhD jury, for giving their precious time to review my manuscript and for all the pertinent remarks, questions and suggestions during my defense as well. The reviewers Prof. Laurence Ressler from LPCNO-INSA of Toulouse and Dr. Philippe Poulin from University of Bordeaux; the examiners Prof. Irene Goldthorpe from University of Waterloo, Dr. Mattias Pauly from University of Strasbourg and Dr. Jean-Pierre Simonato; the President of the Jury Prof. Alain Sylvestre from G2Elab. Our fruitful dialogue and their significant feedback definitely contributes to the continuity of our studies in the field of transparent conductive materials. I'm glad I had the chance to interact with scientists of such high level.

I would like to address a special thank you to the people of project Carnot-FREE, Prof. Skandar Basrour from TIMA and Prof. Alain Sylvestre from G2Elab, not only for sharing their expertise and an unforgettable collaboration, but also for their significant support and kindness. Prof. Alain Sylvestre I also thank you for kindly giving me the opportunity to teach in practical sessions in Polytech. Marwa Gassab thank you for the recently started cool collaboration and good luck with your PhD thesis.

I would like also to express my gratitude to Prof. David Riassetto and Prof. Etienne Pernot that encouraged me to participate in several scientific ateliers and fêtes de science, and also gave me the opportunity to teach in practical sessions in Phelma. I am profoundly happy for the TP that I have given. I will remember in a significant way the Nano@school sessions addressed to high school students; an immense thank you to all the people of CIME-Nanotech for their willingness, especially to the direction of CIME, to Lorraine Chagowa and to Valentine Bolcato for their constant support. A big, warm thank you to Prof. Gilles Baudrant for being an extraordinary example of teaching and creativity, for his valuable help in the ateliers Nanomonde and his bright and inspiring spirit in life. I'm very grateful for all the people that I have interacted with during my teaching activities. I would like also to express my gratitude to Prof. Céline Ternon and all the amazing women of the association "Parité Science", for the example that they represent; their passionate fight for women's rights, along with their remarkable scientific oeuvre.

My PhD life is deeply marked by the presence of unique, brilliant, lovely people of our LMGP Family. Exceptional people from all over the world. From France, Italy, Spain, Portugal, Germany, Ireland, Russia, Austria, Iceland, Ukraine, Greece, Morocco, Algeria, Tunisia, Ethiopia, Egypt, Lebanon, Iran, Uzbekistan, Kazakhstan, India, Pakistan, Vietnam, China, South Korea, Japan, Mexico, Guatemala, Colombia, Brazil, Argentina, USA. I will be forever thankful to the PhD students, the post-docs, the interns that made these years so exceptional, so unforgettable. I am profoundly honored to have been the representative of non-permanent staff, together with Dr. Pierre Gaffuri (congratulations for your PhD Pierre and a big thank you), honored and lucky to have shared so many activities, like our traditional Friday pastry duels, so much laughter and even tears, the joys and the stress of the PhD, the psychological support, the practical assistance and scientific advice, the hugs, the beers, the picnics, the randonnées, the parties, the music and the food from around the world, the love. You will always be tattooed in my heart.

All these unforgettable people I have met in Grenoble will always be tattooed in my heart. I am sorry I may forget to mention here now a lot of names; the important is that my soul will never forget you. A big, warm thank you to "The Louvre" and our "Sunday brunches", Nikolas, Ioanna, Theano, Christoforos, Christina, Samira, Dimitris, Nikos Kekatos, Hosein, Myrto, Aliko, Sofia, Kyprianos, Julius, Yorgos, Andrea, Roza, Baptiste, Maria, Nikos Andrikos, Tzoulia, Andréa, Can, Anna, Stefanos; the nights shared with the people at "Coq-tail", our never-ending stories, our never-ending love; all the amazing volunteers, bartenders, cultural and technical staff of the association "La Bobine"; the band and family of "Black Loucoum", the non-stop music and the friends in "Café Bayard"; the punk-rock evenings "A l'Ouest"; the entire greek team of theatre and our unforgettable Ionesco's play "La Cantatrice Chauve"; the yoga and dance teachers; my friends in Greece always there, no matter the distance, Vaggelis, Aris, Nikolas, the super girls from Patissia-Galatsi.

I will always be grateful to my family, for their infinite love and support. My mother Vivi and my sister Aphrodite. These extraordinary, strong, inspiring, talented women. Forever thankful to all the remarkable family friends that stand always by our side.

I dedicate my PhD thesis in the memory of my dad. I will always keep deep in my heart his love and his encouragement to enjoy the science and never give up. Before he left us, he learnt that I got the grant to start the PhD. Today he would be the happiest person in the world.

*la vie est belle
l'amour intemporel*

Abstract. Transparent electrodes are essential components in a huge variety of energy, lighting and heating devices with indium tin oxide being the most efficient and widely used so far. However, due to the brittleness and scarcity of indium, an intensive research interest has emerged the last decade towards alternative transparent conductive materials (TCM). Metallic nanowire networks and especially silver nanowire (AgNW) networks appear to be one of the most promising among them, thanks to their excellent electrical and optical properties combined with their excellent mechanical performance and low cost fabrication. Despite the optimization of AgNW network fabrication methods and properties, there are still challenges to be tackled, in order to build a mature technology that can be successfully integrated into devices. The present PhD thesis focuses on the fundamental understanding of the physical phenomena that take place at both scales of nanowires and networks. Combining both experimental and modelling approaches, one of the main goals focuses on the origin of failure in AgNW networks during electrical stress. *In situ* measurements of the electrical resistance with a parallel recording of the spatial surface temperature by IR imaging are techniques that provide valuable information for the degradation mechanisms in a AgNW network. The simulation of the electrical distribution and power-induced heating offer a deeper understanding of the underlying physics and can be used to predict the networks electrical and heating performances. Moreover, an experimental study, conducted under simultaneous electrical and thermal stress, was useful for the successful integration of AgNW into devices. Based on these data, a physical model was proposed for the prediction of the time of failure, with its dependence with temperature, electrical current and AgNW network density (i.e. electrical resistance). Another crucial parameter that is investigated during this PhD thesis, is the presence of defects and the impact of networks non-homogeneity on the electrical distribution, the dynamics of failure and the surface temperature induced by Joule heating. Furthermore, the enhancement of the AgNW networks stability was successful with the network encapsulation by transparent, protective oxides developed in LMGP by Atmospheric Pressure Spatial Atomic Layer Deposition (AP-SALD). The AP-SALD is now an emerging open air, low-cost and scalable deposition method and the resulting AgNW-oxide composites retain an excellent flexibility. Finally, during the present PhD thesis, the integration of AgNW networks in devices was studied in the framework of several collaborations and projects with scientific teams of laboratories in Grenoble and elsewhere. Transparent heaters (TH) are in the core of our research and biomedical lab-on-a-chip devices were thoroughly studied. In addition, the increasing interest of the TCM community to the TH, lead our team to write and publish recently a review-article on the topic, including all different technologies and the physics related to Joule heating and the associated applications. Another example of studied integration is the use of the AgNW embedded in polymer substrates, as stretchable electrodes for electrostatic or piezoelectric generators in energy harvesting devices. In the framework of ANR projects with laboratory and industrial partners, we studied the use of AgNWs in cold field emission for miniaturized X-ray sources and as transparent, flexible electrodes in organic photovoltaic. To conclude, the AgNW networks optimized electrical, optical and mechanical properties and their combination with other transparent thin films or 2D materials are highly promising, as well as the growing industrial interest for their implementation. During this PhD Thesis, potential pathways for the stability enhancement and the improvement of the integration into devices have been traced, by means of both experimental and modelling approaches.

Résumé. Les électrodes transparentes sont des composants essentiels au sein d'une grande variété de dispositifs, par exemple, chauffants ou liés à l'énergie et l'éclairage. L'oxyde d'indium et d'étain est le matériau le plus utilisé jusqu'à présent. Cependant, en raison de la fragilité et de la rareté de l'indium, un intérêt de recherche intensif a émergé au cours de la dernière décennie pour des matériaux conducteurs transparents (TCM) alternatifs. Les réseaux de nanofils métalliques, et surtout les réseaux de nanofils d'argent (AgNW), semblent être parmi les plus prometteurs, grâce à leurs très bonnes propriétés électriques et optiques, combinées à leurs excellentes performances mécaniques et à leur faible coût de fabrication. Malgré l'optimisation des réseaux AgNW, il reste des défis à relever pour mettre au point une technologie plus mature qui puisse être intégrée avec succès dans les dispositifs. La présente thèse de doctorat se concentre sur la compréhension fondamentale des phénomènes physiques qui ont lieu à l'échelle des nanofils et des réseaux. En combinant les approches expérimentales et de modélisation, l'un des principaux objectifs est de déterminer l'origine de l'instabilité des réseaux AgNW lors de contraintes électriques. Les mesures in situ de la résistance électrique avec une mesure parallèle de la température de surface spatiale par imagerie IR fournissent des informations précieuses pour les mécanismes de dégradation. La simulation de la distribution électrique et du chauffage induit par la puissance permet de mieux comprendre la physique sous-jacente et peut être utilisée pour prédire les performances électriques et de chauffage des réseaux. Sur la base de ces données, un modèle physique a été proposé estimant la durée de vie du réseau, et sa dépendance à la température, au courant électrique et à la densité du réseau AgNW. Un autre paramètre crucial qui est étudié est la présence de défauts et l'impact de la non-homogénéité des réseaux sur la distribution électrique, la dynamique de l'instabilité et la température de surface induite par le chauffage par effet Joule. De plus, la stabilité des réseaux AgNW a été grandement améliorée grâce à l'encapsulation des réseaux par des oxydes transparents et protecteurs développés au LMGP pour le dépôt de couches minces à pression atmosphérique grâce à l'ALD spatiale (AP-SALD). L'AP-SALD est désormais une méthode de dépôt à l'air, peu coûteuse et évolutive, et les composites d'oxydes AgNW qui en résultent conservent une excellente flexibilité. Enfin, l'intégration des réseaux AgNW dans les dispositifs a été étudiée grâce à plusieurs collaborations et projets avec des équipes scientifiques. Les films chauffants transparents (TH) ont été étudiés et intégrés à des dispositifs de laboratoire biomédical sur puce. De plus, nous avons récemment publié un article de synthèse sur les TH, incluant les différentes technologies et la physique liées au chauffage par effet Joule et aux applications associées. Un autre exemple d'intégration étudiée est l'utilisation des AgNW intégrés dans des substrats polymères, comme électrodes étirables pour les générateurs électrostatiques ou piézoélectriques dans les dispositifs de collecte d'énergie. Dans le cadre de projets ANR avec des partenaires de laboratoire et industriels, nous avons étudié l'utilisation des AgNW en émission de champ froide pour des sources de rayons X miniaturisées et comme électrodes transparentes et flexibles pour le photovoltaïque organique. En conclusion, les réseaux AgNW optimisés en termes de propriétés électriques, optiques et mécaniques et leur combinaison avec d'autres films minces transparents ou des matériaux 2D sont très prometteurs, ainsi que l'intérêt industriel croissant pour leur mise en œuvre. Au cours de cette thèse de doctorat, des pistes potentielles pour l'amélioration de la stabilité et de l'intégration dans les dispositifs ont été étudiées, au moyen d'approches expérimentales et de modélisation.

Table of Contents

Main Abbreviations	2
0. Brief Introduction.	4
1. Introduction to Transparent Electrodes based on Silver Nanowire Networks	14
1.1. Transparent Electrodes: traditional and emerging technologies	15
1.2. Silver Nanowire Networks	18
1.2.1. Synthesis of Silver Nanowires: the polyol process and the key role of PVP in the growth	18
1.2.2. Fabrication of Silver Nanowire Networks	20
1.2.3. Electrical and optical properties and Figure of Merit trade-off	22
1.2.4. Optimization of the network properties. The case of thermal annealing	25
1.2.5. Mechanical Properties	27
1.2.6. Stability issues and the case of electrical stress	30
1.3. Stability enhancement by oxide coatings	33
1.4. Conclusion	38
2. A review on Transparent Heaters	40
2.1. Introduction	41
Transparent Heaters: a Review	43
2.2. Recent advances and prospects	95
3. Experimental techniques and simulation methods: generalities and few preliminary results	98
3.1. Fabrication of MNW networks by spray coating and comparison with other methods	99
3.2. Experimental characterization techniques	106
3.3. Simulation models	110
4. Exploring the degradation of AgNW networks under electrical and thermal stress	116
4.1. Degradation of AgNW networks under electrical stress investigated by experiments and simulations	118
4.2. Time to Failure of AgNW networks under thermal and/or electrical stress: The so-called “T-I experiments”	124
4.3. Conclusions and prospects	140

5. Non-homogeneity on silver nanowire networks: investigation of their effects thanks to experiments and simulations. Stability enhancement by oxide coatings	144
5.1. Materials fabrication and experimental characterization	146
5.2. Bare AgNW network and non-homogeneity	149
5.3. Simulations of electrical and thermal distribution	155
5.4. ZnO coated AgNW networks and its effect on the electrical distribution and the degradation of the networks	159
5.5. Additional examples, conclusions and prospects	163
6. Integration of Ag-based nano-objects into devices.	168
6.1. Transparent Heaters (TH) for lab-on-a-chip applications	172
6.2. Stretchable transparent electrodes for energy harvesters	188
6.3. Industrial collaborations on medical and energy applications	203
6.4. Thermal annealing effects on Ag@polymer reflective conductive coatings	209
7. Conclusions and prospects	222
References	232
Annexes	259
List of publications	274
Résumé en français	275

Main Abbreviations

Transparent Conductive Materials (TCM)
Silver Nanowire (AgNW)
Atmospheric Pressure Spatial Atomic Layer Deposition (AP-SALD)
Transparent Electrodes (TE)
Transparent Heaters (TH)
Transparent Conductive Oxides (TCOs)
Indium Tin Oxide (ITO)
Carbon Nanotube (CNT)
Organic photovoltaic (OPV)
One-probe (1P)
Zinc Oxide (ZnO)
Real-Time quantitative Polymerase Chain Reaction (RT-qPCR)
Internet of things (IoT)
Polydimethylsiloxane (PDMS)
Liquid Crystal Displays (LCDs)
Organic Light-Emitting Diodes (OLEDs)
Dye Sensitized Solar Cells (DSSC)
Fluorine doped Tin Oxide (FTO)
Aluminium doped Zinc Oxide ZnO:Al (AZO)
Metallic Nanowire (MNW)
Ethylene Glycol (EG)
Silver Nitrate (AgNO₃)
Polyvinylpyrrolidone (PVP)
X-Ray Diffraction (XRD)
Transmission Electron Microscopy (TEM)
Mercaptoundecanoic Acid (MUA)
Scanning Electron Microscopy (SEM)
Figure of Merit (FoM)
Roll-to-Roll (R2R)
Aluminium Oxide (Al₂O₃)
Graphene Oxide (GO)
Atomic Layer Deposition (ALD)
Chemical Vapour Deposition (CVD)
Technological Readiness Level (TRL)
Programmable Automation Controller (PAC)
Polyethylene Naphthalate (PEN)
Polyethylene Terephthalate (PET)
Polyimide (PI)
Eutectic Gallium-Indium (EGaIn)
Fine Element Method (FEM)
Time of Failure (ToF)
Homogenous networks (Hom)
Empty Triangles (ET)
Denser Triangles (DT)
Silver nanoparticles (AgNPs)

σοφόν τοι τὸ σαφές

Εὐριπίδης

« Wise is the clear »

Euripides (480-406 BC)

Chapter 0

0. Brief Introduction.

Transparent Conductive Materials (TCM) are crucial for a large variety and diversity of emerging applications such as photovoltaic, lighting, sensing and heating devices.^{1,2} The digital and energy transition of the 21st century, together with geostrategic issues related to critical materials, have urged the search for new materials in order to replace the traditional Transparent Conductive Oxides (TCO) used currently.³ In particular, indium tin oxide (ITO) has single-handedly dominated the field of transparent electrodes (TE) in devices for almost four decades thanks to its very good physical properties, namely a good optical transparency and electrical conductivity, and its high stability. But despite these assets, ITO suffers from serious limitations related to fabrication cost, brittleness and In scarcity.^{4,5} Due to the necessity of saving raw materials and the increasing demand for flexible, light-weighted and smart devices, alternative TE are thus needed.^{6,7} This is why a variety of other TCM have been intensively investigated for more than a decade. The vast development of nanoscience worldwide has resulted catalytic to the advancement in this field, where many different nanomaterials have been proposed as alternative TCM; In particular, significant advances have been reported in the physics and processability of carbon nanotube (CNT) networks,⁸ graphene thin films,^{9,10} conducting polymers,^{11,12} metallic grids,^{13,14} and metal nanowire networks.^{15,16} The electrical, optical and mechanical properties, the sustainable and low cost fabrication, the available raw materials and their recyclability, the stability and the compatibility with other materials are key features to select the appropriate technology for each application.¹⁷

Silver nanowire (AgNW) networks appear to be one of the most promising candidate in the race to replace ITO since: i/ they exhibit very promising optical and electrical properties, ii/ unlike ITO and many other TCM, they have proven to be very flexible, and iii/ they can be fabricated by low-cost, solution-based techniques suitable for large scale, industrial production.^{16,18,19} Another advantage is that due to the very high aspect ratio of the nanowires, the amount of raw materials can be drastically decreased in comparison with the amount of Indium in an ITO-based electrode.² Thanks to their properties, AgNW networks have been already integrated in many devices that cover a broad spectrum from transparent heaters, solar cells, radio frequency antennas, touch screens, lighting to energy harvesting.²³ AgNW networks allow to combine flexibility, transparency and high heating performances at low voltages, which constitutes a clear asset for integration in transparent heaters (TH).²⁴ These applications have attracted intense attention from both scientific and industrial actors due to the key role they play in many

technologies, including smart windows, deicers, defoggers, displays, actuators and sensors.¹ In addition, AgNW based TE can be essential components of soft, wearable electronic skin devices for detecting motion and health monitoring.²⁵⁻²⁷

Significant progress has been done in the study of AgNW networks as TE and TH for almost a decade now by the AgNW team in LMGP, led by Prof Daniel Bellet. The research is focused on the fundamental understanding of the physical phenomena taking place at the scales of both the network (macroscale) and the nanowires (nanoscale). One principal goal concerns the study of failure under applied electrical and/or thermal stress and the stability enhancement, which is crucial for the performance of AgNW networks. In the framework of several collaborations and projects with laboratory and industrial partners, the combination of AgNW networks with other technologies and the implementation into devices is an important aspect of the team research.

In particular, starting with the PhD thesis of Dr Daniel Langley (2011-14) and Dr Mélanie Lagrange (2012-15), the team investigated the electrical percolation and the relationship between the morphology of AgNWs and network density, combining Monte Carlo simulations and experiments.^{28,29} The effect of thermal annealing and the optimization of the physical properties have been studied thoroughly by *in situ* experiments and nanocharacterization tools, such as, SEM, TEM or AFM among other.³⁰ Following this work, Dr Thomas Sannicolo, (PhD thesis 2014-17, lauréat du prix de thèse 2018 Univ. Grenoble Alpes) studied the electrical distribution and the degradation of AgNW networks by several techniques, i.e. lock-in thermography and electrical mapping.^{31,32} He explored the integration into applications like electromagnetic shielding and extended the modelling tools with Comsol Multiphysics. He started investigating the mechanical properties of AgNW/elastomer composites, in which I worked too during my internship in the lab (Master2, 2017). The fundamental study of the mechanisms of failure under electrical and thermal stress, as well as the integration of AgNW networks in organic photovoltaic (OPV) and resistive switching devices were some of the axis of the post-doc of Dr João Resende (2018-19).

Furthermore, the AgNW team always works closely with the SALD (Spatial Atomic Layer Deposition) team, led by Dr David Muñoz-Rojas, towards the enhancement of the AgNW network stability. This is achieved by the encapsulation with thin oxide layers, performed by the Atmospheric Pressure SALD (AP-SALD) method developed in the lab.³³ While maintaining the advantages of ALD (low-temperature deposition, thickness control, high-quality materials, and conformality), AP-SALD can be up to 2 orders of magnitude faster than ALD and it is compatible with roll-to-roll (R2R) and open-air processing.³⁴ Lately, during the

PhD thesis and post-doc of Dr Viet H. Nguyen (2015-18), Abderrahime Sekkat (on-going PhD thesis since 2018) and Sara Aghazadehchors (since 2015), the teams have been elaborating transparent electrodes based on nanocomposites of AgNW networks protected by thin films like ZnO, Al₂O₃ and ZnO:Al.³⁵⁻³⁷

It is also worth noting that the activities of LMGP related to AgNWs have often been tackled with several collaborations, including the one with Dr Jean-Pierre Simonato from CEA LITEN from the beginning. The interaction between chemists and engineers in charge of integration within devices (CEA LITEN) and physicists dealing with both experimental and modeling aspects is of clear interest, which has led to the joint publication of several articles.^{1,2,31,32}

Although the properties of these transparent electrodes are already remarkable, there are still crucial challenges to tackle so that this technology can be mature and perfectly mastered for future device implementation. Continuing the previous work in LMGP, the main objectives of the present PhD Thesis were: i/ the fundamental investigation of the physical phenomena that take place at both scales of nanowires and networks, ii/ the enhancement of their stability and iii/ the integration in devices. The association of different characterization techniques, like *in situ* electrical measurements, IR and SEM imaging, revealed important information for the non-homogeneities and instabilities of AgNW networks. Moreover, the combination of both experimental and simulation approaches was proven prominent to better understand the mechanisms of failure and predict the AgNW based TE and TH performance. Finally, during this PhD Thesis, potential pathways for the stability enhancement and the improvement of the integration into devices have been traced, in the framework of several projects and collaborations with laboratories and industrial partners in Grenoble and elsewhere.

The present PhD Thesis consists of 6 chapters. **Chapter 1** starts with a general information about the need for emerging TCM and the wide range of applications, and then presents an overview of TE based on AgNW networks. The main techniques for the synthesis of AgNWs and the fabrication of TE are presented in section 1.2, followed by a description of the physical properties of the networks and their optimization (i.e. electrical, optical and mechanical properties), their advantages and the instability issues. Finally, the enhancement of their performance thanks to protective coatings deposited by AP-SALD are discussed in detail in section 1.3. **Chapter 2** focuses more specifically on the physics and applications of TH. It includes the review-article entitled “*Transparent Heaters: a Review*”, published in *Advanced Functional Materials* in March 2020 by D. T. Papanastasiou, A. Schultheiss, D. Muñoz-Rojas,

C. Celle, A. Carella, J.-P. Simonato, and D. Bellet.¹ The most recent developments and strategies to improve the properties, stability, and integration of the emerging THs are reviewed. Prior to the deep analysis of the experimental and simulation results obtained within this Thesis (chapters 4 to 6), important basics regarding the fabrication steps of AgNW networks by spray coating, the characterization of their electrical, optical and mechanical properties, the morphological characterization by electronic microscopy, and the temperature measurements are presented in **chapter 3**. In addition, the comparison between spray, rod and spin coating for the deposition of ultra-long AgNWs is presented in section 3.2, based on the research article entitled “*Rapid synthesis of ultra-long silver nanowires for high performance transparent electrodes*”, published recently on *Nanoscale Advances* by A. Madeira, D.T. Papanastasiou, T. Toupance, L. Servant, M. Tréguer-Delapierre, D. Bellet, I.A. Goldthorpe, a work performed in collaboration with two scientific teams of ICMCB in Bordeaux and the University of Waterloo in Canada.³⁸ In the last section 3.3, the simulation methods used and developed during this PhD Thesis are introduced and preliminary results such as the effect of nanowire lengths and diameters on the electrical performances are presented. The results of such simulations are compared with the experimental ones from the deposition of AgNW networks of different nanowire dimensions. The AgNWs suspensions were kindly provided by the team of J.-P. Simonato at CEA-Liten (Grenoble, France), as well as for the majority the AgNWs that I have used for the fabrication and study of TE during my Thesis.

Chapter 4 deals with the degradation of silver nanowire networks under electrical and thermal stress, starting from the failure of the networks triggered by the Joule heating effect, when an electrical bias is applied to the network. The local current density inhomogeneities can lead to an elevated Joule heating in highly localized points on the network, with further damaging effects. In section 4.1, the main results from a deeper study of the origin of and propagation of hotspots in a AgNW network are presented, focusing on the electrical and thermal simulations of a local defect, and their correlation with other electrical simulations and experimental data. This study was conducted in the framework of the project EARTH, between LMGP and LEPMI-Bourget-du-Lac, funded by the labex CEMAM and is presented in detail in the article entitled “*Dynamic degradation of metallic nanowire networks under electrical stress: a comparison between experiments and simulations*” recently submitted by N. Charvin, J. Resende, D. T. Papanastasiou, D. Muñoz-Rojas, C. Jiménez, A. Nourdine, D. Bellet, and L. Flandin. The second part of chapter 4 is related to the main results of $T-I$, i.e. temperature-current experiments, that was conducted in order to explore the time of failure of AgNW

networks. Section 4.2 is highly inspired by the article entitled “*Endurance tests on silver nanowire networks under constant thermal and electrical stress*” to be submitted, by J. Resende, D. T. Papanastasiou, D. Moritz, N. Fontanals, C. Jiménez, and D. Bellet. To date, the majority of the related studies deal with the thermal and electrical stress separately, but both of them affect simultaneously the performance of AgNW based transparent electrodes. Therefore, our objective was to better explain these mechanisms of failure, by studying the *in situ* evolution of electrical resistance, when the stress is associated to a given applied temperature and to a given applied electrical current. In addition, as discussed in the last part of chapter 4, it would be useful for an efficient integration into devices, to build a model that predicts the time of failure, for given conditions of temperature and/or applied electrical current, and if possible, AgNW network densities (associated to a given electrical resistance).

The failure of AgNW networks is still the main challenge to tackle for their successful integration into devices, with the electrical stability being crucial. **Chapter 5** reports on the impact of non-homogeneous AgNW networks, thanks to experiments and simulations, and the stability enhancement by zinc oxide (ZnO) coatings. The simulations, presented in section 4.1, confirm the correlation of initial defects with the origin of failure, which is observed experimentally as well. The huge local increase of the current density, followed by a locally elevated power-induced Joule heating, is the key parameter for these instabilities. Therefore, we decided to go a step further and investigate the effect of non-homogeneity in a more macroscopic way, always combining experimental and simulation approaches. In section 5.2, different patterns of AgNW networks are investigated by one-probe (1P) electrical mapping and IR imaging. The results are compared in section 5.3 with simulations of electrical and thermal distribution by physical modelling using COMSOL Multiphysics®. Finally, section 5.4 focuses on the study of the influence of zinc oxide (ZnO) coatings on the electrical distribution and the performance enhancement of non-homogeneous specimens. The ZnO increases significantly the stability with a 50 % higher failure voltage, while maintaining the high optical transparency of the electrodes. Furthermore, the presence of a thin oxide layer allows the electrodes to reach higher temperatures above 300 °C generated by Joule heating. This study was also conducted in the framework of project EARTH. This chapter 5 is highly inspired by the article entitled “*Effects of non-homogeneity and oxide coating on silver nanowire networks under electrical stress: comparison between experimental and modelling approaches*” which is to be submitted by the following authors: D.T. Papanastasiou, N. Charvin, J. Résende, V. H. Nguyen, A. Sekkat, D. Muñoz-Rojas, C. Jiménez, L. Flandin and D. Bellet.

The last chapter is related to the integration of AgNW networks and other Ag-based nanomaterials into devices, through several projects and collaborations that I had the great chance to work on and expand my knowledge on diverse topics. The 4 sections of **chapter 6** are the following:

- TH are in the core of our research on AgNW. We have applied this technology on biomedical lab-on-a-chip devices, thanks to a collaboration with the Director of LMGP, Prof Franz Bruckert. We investigated these TH on such devices and thoroughly studied them during the present PhD Thesis. As presented in section 6.1, the goal is to develop *in situ* quantitative PCR (qPCR) for DNA amplification in a microfluidic chip with direct monitoring of the fluorescence by a microscope. PCR has routinely been used for the detection of infectious diseases, including those by bacteria or viruses, like the pandemic of coronavirus disease that we are facing since March 2020.³⁹⁻⁴¹ The quantitative reverse transcription-PCR (RT-qPCR) assay for SARS-CoV-2 using upper and lower respiratory tract specimens is the gold standard for diagnosing COVID-19.⁴² As discussed in section 6.1, we embed the AgNW networks on the chip and apply voltage steps in order to induce the heating and cooling cycles and obtain the temperatures needed for the PCR assay. Thanks to the optical transparency of the AgNW-based TH, the fluorescent signal is not affected and thus we can study its variance *in situ*, during successive, power-induced thermal cycles.

- In section 6.2, the integration of AgNW networks on flexible energy harvesters will be presented. In the framework of the Institut Carnot Energies du Futur project *FREE* in collaboration with Prof Alain Sylvestre from G2Elab and Prof Skandar Basrour from TIMA in Grenoble, we aim to elaborate electrostatic generators with superior mechanical properties (i.e. stretchability) to fit in Internet of things (IoT) applications, including smart clothes and hybrid vehicles.^{26,43} TE based on AgNW networks are promising candidates for such applications.⁴⁴⁻⁴⁶ Our goal is to develop flexible energy generators designed from electro-active elastomers, based on the deformation of materials incorporated between two deformable electrodes and operating in an electrostatic mode. As discussed in 6.2, during my Thesis we optimized the mechanical properties of AgNW-based stretchable electrodes and improve their integration into elastomers, in order to replace other commonly used electrodes with conductive pastes that are fragile to mechanical stress.

- Section 6.3 includes a brief presentation and selected results of the two ANR projects, in which our team is participating, in collaboration with laboratories and industrial partners. The first one, named *PANASSE*, concerns the fabrication of AgNW-based cold cathodes for

compact X-ray sources for integration in future generation of medical scanners. PANASSE is in collaboration with Thalès in Palaiseau and IEMN in Lille that have great expertise in the development of CNT cathodes and in nanocharacterization, respectively. The second project, *MEANING*, is related to the integration of AgNW networks in emerging OPV, in collaboration with nanochemistry researchers from ICMCB in Bordeaux and the industrial partner ARMOR in Nantes. Some results of the electrical characterization performed in LMGP to AgNW networks deposited in large plastic substrates by ARMOR, will be presented in section 6.3.2.

- The last part of chapter 6 is related to the study of a different material than AgNW networks. It concerns the characterization of nanocomposites consisting of silver nanoparticles (AgNPs) on polymer coatings, which are elaborated by Dr. Lavinia Balan and Marine Dabert (PhD thesis 2017-20) in IS2M and CEMHTI. The Ag@polymer coatings demonstrate promising electrical and optical properties, such as high reflectivity in NIR, which is interesting for their integration to a wide variety of energy-saving applications. In the framework of our collaboration, the electrical characterization of these hybrid materials was performed in LMGP, focusing on the effect of thermal annealing. The main results are presented in the section 6.4, which are highly inspired by the article entitled “*Exploring the Effects of Thermal Annealing on the Optical and Electrical Properties of a Photo-generated Ag@polymer Metallized Coating*” recently submitted in by M. Dabert, D. T. Papanastasiou, L. Vidal, S. Hajjar-Garreau, D. Bellet, L. Balan.

The general conclusions and prospects will end the present manuscript.

ἀρχὴ [...] ἡμισυ παντὸς

Πλάτων

« The beginning is the half of the whole »

Plato (427-347 BC)

Chapter 1

1. Introduction to Transparent Electrodes based on Silver Nanowire Networks

The present chapter presents an overview on transparent electrodes based on random silver nanowire (AgNW) networks, starting from a brief presentation of the related applications and a general comparison between traditional and emerging materials. Then, focusing on silver nanowire networks, the most common techniques for their synthesis and the fabrication of the electrodes are presented, followed by a description of the physical properties of the networks, namely, electrical, optical and mechanical. Furthermore, electrode stability issues linked with the degradation of individual nanowires under electrical stress are demonstrated. Finally, the enhancement of the stability of electrodes based on AgNWs thanks to protective coatings of transparent oxides is discussed in detail.

1.1. Transparent Electrodes: traditional and emerging technologies

Transparent electrodes (TE) are essential for a large variety of energy, lighting and heating devices, such as liquid crystal displays (LCDs), organic light-emitting diodes (OLEDs), touch panels, gas sensors, heat reflective coatings, energy efficient/smart windows, electrochromics, medical devices, smart clothing or emerging photovoltaic applications.^{2,15,47} **Figure 1-1** shows examples of such applications, which are now part of our daily life and whose performances have shown a tremendous progress in the last decades. Nowadays, the constantly increasing use of displays (laptop, TV, smartphone, digital gadgets) has made the materials with both optical transparency and electrical conductivity indispensable. The electronic industry, mostly based in East Asia-Pacific countries, is searching for raw materials allowing the advent of new advanced devices, in order to fulfil the needs of 21st century devices: transparent OLED displays (Figure 1-1a), flexible smartphones (Figure 1-1b) and transparent antennas (Figure 1-1c) with superior mechanical properties (flexible, foldable, stretchable). Another sector that comes after electronics in terms of TE materials consumption, is nowadays energy, and especially the emerging photovoltaic (PV) fabrication and energy efficient buildings construction. (Semi)transparent thin films and organic PV present reduced costs and larger surface area for light absorption, compared to traditional solar cells based on crystalline silicon, and TE are mandatory to allow light pass through the solar cell and collect efficiently the photo-generated charge carriers.⁴⁸ Emerging PV technologies have versatile use like the colorful solar cell panels integrated in a building in Lausanne, city of origin of these dye sensitized solar cells

(DSSC) or Grätzel cells (Figure 1-1d);⁴⁹ In addition, thermochromic or electrochromic films integrated in windows or glass rooftops, can be a smart response for heating and cooling the houses (Figure 1-1e). Finally, there are plenty of smart applications such as wearable electronics for detecting motion and health monitoring, or other devices that need transparent and flexible electrodes. A significant applicative domain concerns airplane windscreens and car or motorcycle visors, which need defrosting and/or defogging achieved through the heat produced by conductive materials that are also optically transparent to ensure the light transmission (Figure 1-1f). Such transparent heaters have a large variety of applications, which are thoroughly presented in Chapter 2 of the present manuscript.

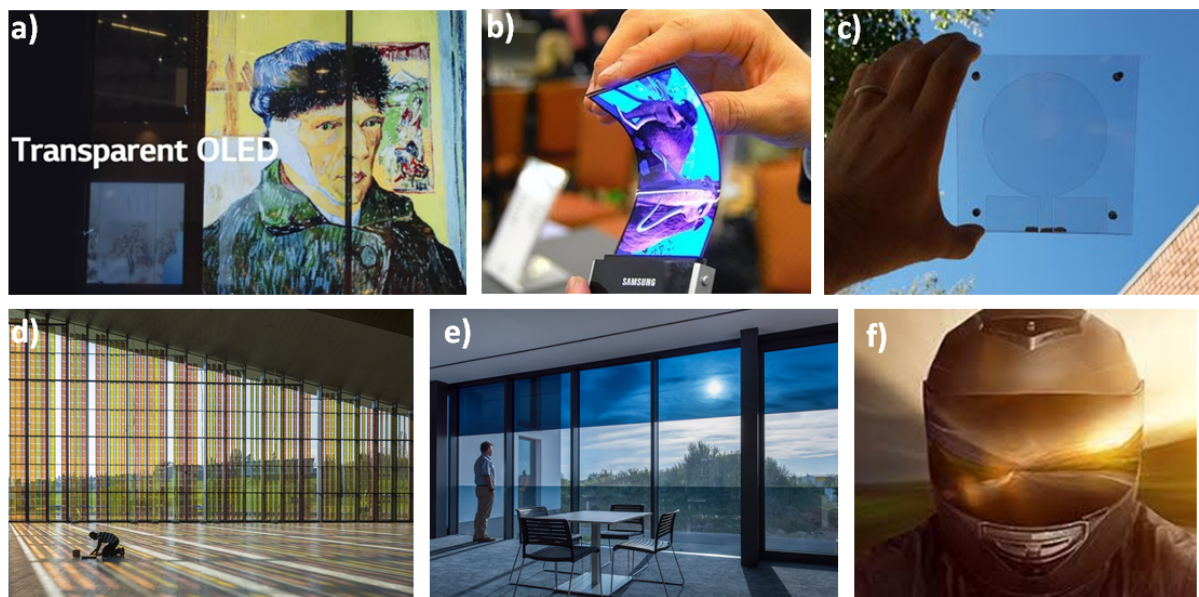


Figure 1-1: Examples of applications using transparent electrodes. a) Transparent OLED TV Display by LG.⁵⁰ b) Flexible OLED smartphone display by Samsung.⁵¹ c) Transparent antenna by Metamaterials.⁵² d) Dye Sensitised Solar Cell façade by Solaronix, in SwissTech convention center at EPFL campus in Lausanne.⁵³ e) Smart window with electrochromic film by Sage Electrochromics.⁵⁴ f) A motorcycle-visor prototype by CEA Tech, with defrosting-defogging device.⁵⁵

Traditionally, transparent conductive oxides (TCOs), like indium tin oxide (ITO) and, to a less extent, fluorine doped tin oxide (FTO) or aluminium doped thin oxide (AZO), are currently the most widely used transparent conductive materials (TCMs). The high transparency is achieved if the material has a wide band gap above 3 eV, while the large carrier concentration necessary for high electrical conductivity is provided by intrinsic defects and extrinsic doping.⁵⁶ For four decades, ITO, associated usually to a composition of 90% of indium oxide and 10% of tin oxide, has been the leading transparent conductive anode in the devices briefly described above, thanks to its very good physical properties and the precise control of its deposition.⁴ This n-type semiconductor with a large band gap around 4 eV, shows a high optical transparency above

80% in the visible region and a nearly metallic electrical resistivity of $2.0 \times 10^{-4} \Omega \text{ cm}$.⁵⁶ Despite its high efficiency and good adaptation to some traditional applications, it suffers from serious limitations, namely, fabrication cost, brittleness and scarcity. ITO is a thin ceramic film that can crack even under very low tensile strains, which can result in a drastic decrease of the electrical conductivity.⁵⁷ Furthermore, as also presented in a study carried out by NREL-Colorado School of Mines, indium (In) is one of the scarcer elements in terms of average abundance in the Earth's crust, which leads to high prices.⁵⁸ In addition, indium availability at present is estimated to be for more than two thirds in China and with a broader estimation around 50%, including reserves and resources. The indium production almost completely depends on the zinc industry because at the moment there is no direct production of indium from primary ores. In contrast, the production routes of silver are numerous: its main sources derive from the lead, copper, and gold industry from the production facilities all over the world.⁵⁹ Last but not least, another crucial parameter, related to the energy and digital transition of our time is the recycling rates: for silver the end-of-life functional recycling and old scrap ratio are estimated at around 80% and above 50%, respectively, while for indium these values are below 1%.⁶⁰ The main limitation to indium recycling is the high dissipation rate (90 %) due to technological and economical barriers of recycling, such as lack of suitable technologies of dismantling and purification and economic profitability for recycling of very low concentrations.^{61,62} However, there is more and more research and industrial interest in developing eco-friendly ways to recycle indium from LCDs, which consume the 70 % of this rare earth worldwide.^{63,64}

For the above geostrategic reasons and materials performances, for more than a decade new technologies have been under investigation as alternatives to ITO.⁶⁵ As it was very well stated ten years ago by Kumar and Zhou, the next generation of electronic devices requires transparent electrodes to be lightweight, flexible, cheap, and compatible with large-scale manufacturing methods.⁴ This is why a variety of other transparent conductive materials have been intensively investigated during the last years. For example many advances in the physics and processability of carbon nanotube networks (CNTs),^{8,66} graphene thin films,^{65,67-69} conducting polymers,^{11,70,71} metallic grids or meshes⁷²⁻⁷⁴ and metallic nanowire (MNW) networks^{2,15,16,75} have been reported. The electrical, optical, thermal and mechanical properties, the fabrication methods and costs, the stability and the compatibility with other materials are the key parameters to select the appropriate material for a given application. An interesting approach is the combination of materials in order to build a robust technology that serves the superior demands of modern transparent electrodes. Core-shell nanomaterials,^{76,77} encapsulated

networks with oxide protective thin films,^{35–37,78–80} nanowires or grids embedded in conductive polymers or grown in cellulose nanofibrils,^{81–83} hybrids combining two or more materials,^{84–88} are all composites that take advantage of each material properties and features leading eventually to enhanced and stable performances.

Alone or combined with other technologies, AgNW networks appear to be one of the most promising candidates to replace ITO because, firstly, they exhibit high optical and electrical properties. Secondly, they are proved to be very flexible and, finally, they can be fabricated by low-cost solution-based methods.¹⁶ Another advantage is that due to the very high aspect ratio of the nanowires, the amount of raw materials can be much smaller in comparison with the amount of indium in an ITO-based electrode; for ITO 0.75 – 1.05 g/m² of indium while for AgNWs 0.15 – 0.20 g/m² of silver are needed to fabricate an electrode of similar electrical and optical properties.² The following sections describe in detail the physical properties of AgNW networks, from the synthesis and TE fabrication to their performance and stability issues.

1.2. Silver Nanowire Networks

1.2.1. Synthesis of Silver Nanowires: the polyol process and the key role of PVP in the growth

Firstly introduced by Fievet and co-workers for the synthesis of colloidal particles of metals and alloys such as Ag, Au, Cu, etc.⁸⁹ the polyol process seems to be the most promising among several methods for the synthesis of AgNWs. The polyol process is based on the reduction of an inorganic salt by a polyol. A surfactant is used to prevent agglomeration of the colloidal particles. Later on, Xia and co-workers developed a suitable process for the shape-controlled synthesis of silver nanostructures.⁹⁰ Thus the used polyol process is mainly based on ethylene glycol (EG), which serves as a good solvent for both silver nitrate (AgNO₃) and Polyvinylpyrrolidone (PVP), because of its relatively high dielectric constant. AgNO₃ is reduced in EG solvent leading to the nucleation of silver nanoparticles (AgNPs). PVP is then introduced as capping agent to ensure the unidimensional growth of the Ag-based nano-objects. As it is illustrated in **Figure 1-2** by Sun et al.,⁹¹ using the PVP helps passivating the {100} crystallographic facets, so that growth solely occurs along the {111} facets leading to uniaxial growth from a decahedra into a pentagonal rod. As the addition of Ag⁺ ions continues, the nanorod can readily grow into a longer five-fold twinned wire with straight and flat edges (a), which can reach length of hundreds of micrometres (b). X-Ray Diffraction (XRD) confirms the face centre cubic (fcc) structure of silver crystal for AgNWs grown by the polyol process, as

seen in Figure 1-2c from Nengduo et al.⁹² According to the XRD patterns, the distinctive peaks can be indexed to the (111), (200) and (220) planes of fcc silver (JCPDS card file no. 04–0783). From the pattern obtained, lattice constant of the grown AgNW is calculated to be 0.4089 nm, a value very close to the standard bulk Ag value (0.4086 nm). This confirms the fcc structure of silver crystal. In addition, Figure 1-2d depicts the Selected Area Electron Diffraction (SAED) of a few AgNWs, technique similar to XRD in which the electrons in a Transmission Electron Microscopy (TEM) are the ones diffracted, proving the crystalline nature of AgNWs. High-resolution TEM (HRTEM) was carried out by the same authors and, as shown in Figure 1-2e, a fringe spacing of 2.36 Å is measured, which is consistent with the spacing of the fcc Ag (111) planes.⁹²

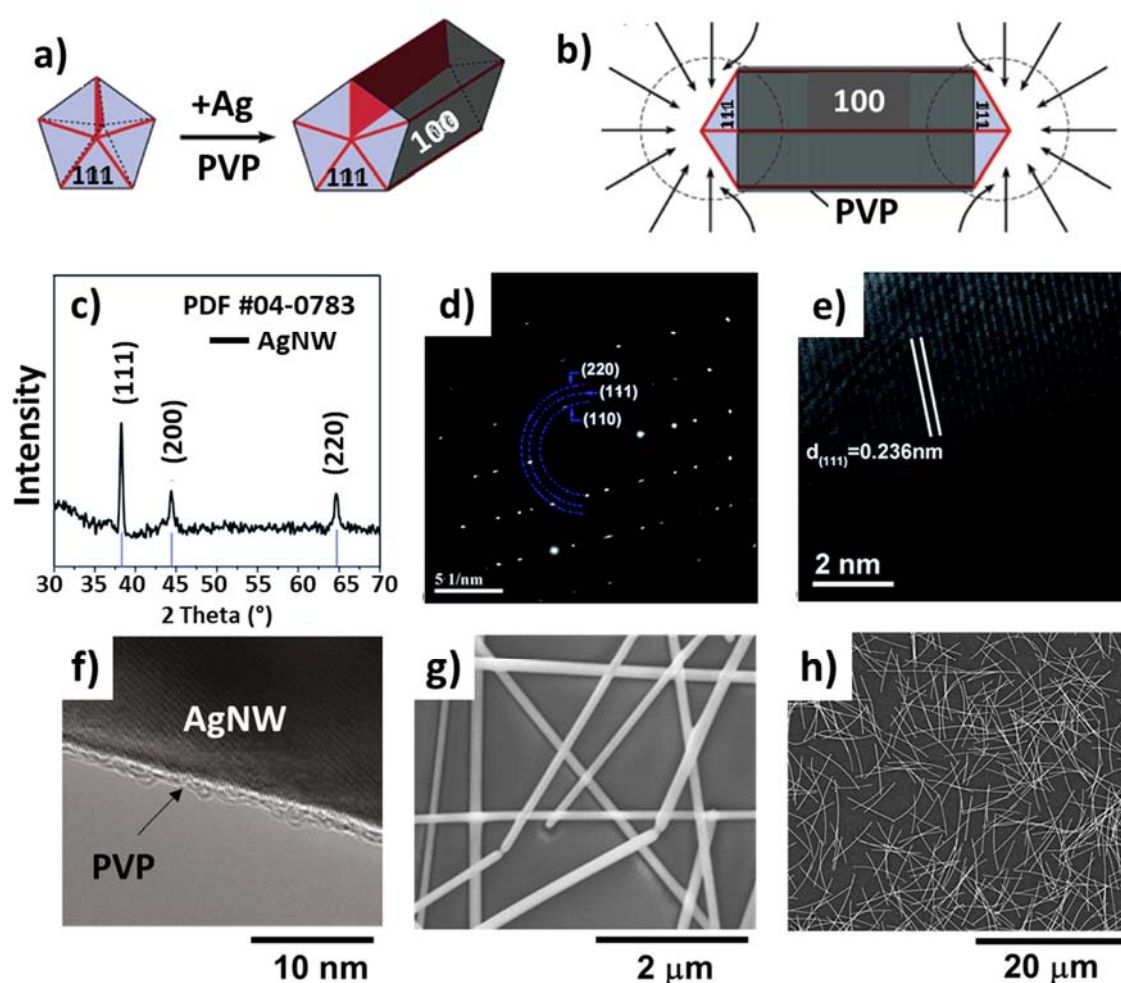


Figure 1-2: a-b) Schematic illustration of the growth mechanism by the polyol process of AgNWs. The {100} facets are passivated by the PVP and the nanowires grow on {111} facets having a pentagonal cross-section.⁹¹ c) X-Ray diffraction (XRD) pattern of the silver nanowires showing the distinctive peaks of (111), (200) and (220) planes of the fcc silver.⁹² d) Selected Area Electron Diffraction (SAED) of a few nanowires, proving the crystalline nature of AgNWs.⁹² e) High-resolution Transmission Electron Microscopy (HRTEM) of AgNW, whose observed fringe spacing is measured as 2.36 Å, thus consistent with the spacing of Ag(111) plane.⁹² f) TEM of AgNW revealing the PVP layer in its surface.⁹³ g-h) AgNW random networks deposited by spray method on glass substrates observed by Scanning Electron Microscopy (SEM) at two different scales.²³

As presented in Figure 1-2f, the observation by TEM reveals the presence of a thin amorphous organic layer of PVP surrounding the {100} AgNW surfaces, synthesized by Coskun et al.⁹³ The PVP as an insulating capping agent influences the network's electrical performances because it forms a metal–insulator–metal contact at the AgNW junction and increases the contact resistance between the nanowires and therefore the overall resistance of the network.⁹⁴ Several theoretical and experimental studies have shown that the reduction of PVP thickness by pre-deposition techniques and the optimisation of the junctions after deposition, can lead to the enhancement of the electrical performances.^{28,30,94,95} This issue will be discussed in more detail in section 1.2.4. Concerning the improvements of the AgNWs synthesis, recent works have shown progress by developing nanowires with other types of passivating agents, such as 11-mercaptoundecanoic acid (MUA).⁹⁶ Also, chemists can tune the growth in order to obtain nanowires with different diameters and lengths, even ultra-long nanowires with facile, one-step procedures.^{97,98} Examples of such nanowires are presented in Chapter 3.

1.2.2. Fabrication of Silver Nanowire Networks

Various deposition techniques using solutions have been tested, like spin-coating,^{99,100} drop-casting^{101,102} or rod-casting.^{103,104} The random distribution of NWs, as well as their structural integrity during the deposition process, and finally the optimal physical properties of the resulting networks are the necessary parameters to ensure. Besides, the use of up-scalable and cost-efficient production techniques is an important factor to consider for industrial integration. Each technique has its advantages and its pitfalls. Among the deposition techniques, spin coating, is a rapid and low-cost method to deposit thin films onto flat substrates by centrifugal force. Apart from its limitation to small laboratory-scale samples, another drawback is the undesirable radial orientation of the nanowires. To avoid these two drawbacks, spray coating is often used and appears as a suitable procedure which remains cheap and easy to handle. Many recent studies have been conducted on AgNW samples fabricated by spray coating. The latter method uses small droplets which are deposited via an ultrasonic nozzle, whose vibration is produced by piezoelectric transducers. However, it has been demonstrated by Ko et al. that ultrasonic spraying provokes a significant decrease in the length of AgNWs and increase of sheet resistance, while no such effect is exhibited by the pneumatic air-sprayed AgNWs.¹⁰⁵ In a recent study of our team in collaboration with other laboratories, Sannicolo et al.³² have shown experimentally the difference between spin and spray coating using an one-probe(1P) mapping technique to measure the electrical homogeneity of the deposited networks. The electrical

homogeneity is an important parameter for the reliable and uniform performance of transparent electrodes when integrated into the devices. As shown in **Figure 1-3**, the spray-coated sample exhibits linear, smooth and vertically aligned equipotential lines, which corresponds to a homogeneous distribution in electrical voltages and currents. On the contrary, the 1P-map associated with the spin-coated network exhibits nonparallel equipotential lines. The non-isotropic and centripetal orientation of the equipotential lines originates from the spin-coating procedure, which involves a preferential orientation of the AgNWs along the centrifugal force during the deposition process.³²

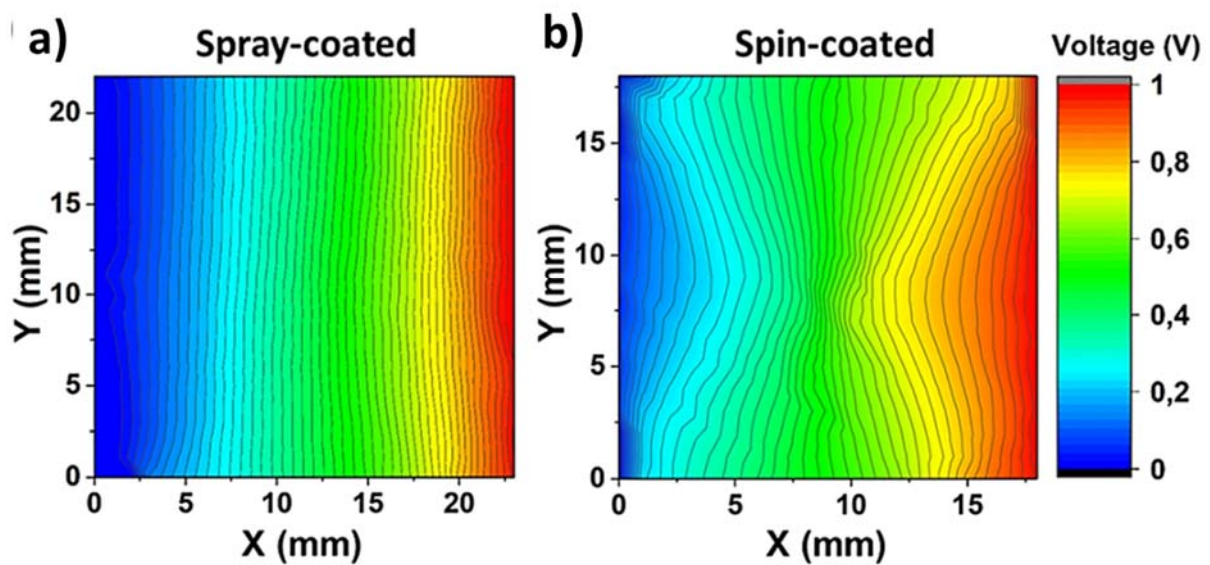


Figure 1-3: One probe-maps corresponding to AgNW networks deposited by spray-coating (a) and spin-coating (b). The spray-coated sample (a) exhibits parallel equipotential lines due to the random orientation of the nanowires during the deposition process. On the contrary, the spin-coated sample (b) exhibits nonparallel equipotential lines (radial distribution) resulting from the preferential orientation of the nanowires during the deposition process. Both electrical resistances are low, for the spray coated sample is 55 Ohm and for the spin 16 Ohm.³² The two opposite electrodes are vertical.

Spray coating is suitable for the majority of synthesized AgNWs but it might induce some breakages of the long NWs (roughly longer than 40 μ m) due to the ultrasonic nozzle. In order to take advantage of spray coating's large area coverage and also prevent the long NWs from being damaged, another deposition set-up is used in LMGP by replacing the ultrasonic nozzle spray with an air brush. Scanning Electron Microscopy (SEM) images of the obtained randomly deposited AgNW networks are displayed in Figure 1-2g and h.²³ More details about this simple but promising technique, specifically for industrial upscaling, are discussed in Chapter 2, as well as the comparison study between spin, spray and rod coating.

Furthermore, the waste management and material reuse during the fabrication steps is very important regarding the costs and the environmental impact. There are few studies on this issue until present; concerning the synthesis, Wang et al. recycled Ag from the waste generated in

diverse nanotemplate reactions and resynthesized AgNWs with similar properties to the pristine ones.¹⁰⁶ Yoo et al. developed a procedure to recycle AgNWs during the patterning on polymer substrates that, when re-deposited, show comparable performance with the initial ones and still higher compared to commercial ITO.¹⁰⁷ Finally, concerning a possible metal release from the transparent electrodes to the environment, Omaña-Sanz et al. demonstrated recently a fast approach to diagnose this risk.¹⁰⁸

1.2.3. Electrical and optical properties and Figure of Merit trade-off

Starting with the electrical properties and the size effects at the nanoscale, the diameter of an individual nanowire has an impact on its electrical resistivity. Bid et al.¹⁰⁹ found that the resistivity of single AgNWs is larger than the one of bulk silver due to the enhancement of electron surface scattering. This occurs when the mean free path of electrons ($\lambda \approx 53$ nm)¹¹⁰ is of the order of the nanowire diameter. Thus the bulk assumption is no longer valid and the electrons are scattered additionally by the external surface of the nanowires. The smaller the NW diameter the larger the electrical resistivity, as shown in **Figure 1-4a**, and this will also increase the whole AgNW network electrical resistance.²⁸ Bid et al. analysed the resistivity data of the model proposed by Dingle and Chambers and after experimental measurements proposed the equation (1-1) for the resistivity of individual AgNWs, ρ_{NW} :

$$\rho_{NW} = \rho_{bulk} \left(1 + \frac{\lambda}{2D_{NW}}\right) \quad (1-1)$$

where ρ_{bulk} is the resistivity of bulk silver, $1.59 \times 10^{-8} \Omega\text{m}$,¹¹¹ λ is the bulk mean free path of bulk silver and D_{NW} is the nanowires diameter. At the scale of the network, the key parameter that drastically influences the electrical performances of the resulting electrodes is the network density which refers to the number of nanowires per unit area. According to the percolation theory,¹¹² the conductivity σ of the resulting percolating electrodes is intimately linked to the NW density as follows:

$$\sigma \propto (n - n_c)^m \quad (1-2)$$

with n being the network density and n_c the percolation density or percolation threshold, which is the number of nanowires per unit area at which the network has a percolation probability of $1/2$, and m the percolation exponent. Equation (1-2) is supposed to be valid only when n is slightly larger than n_c . For convenience, the community often prefers to work with the areal mass density (amd), which expresses the mass of silver per unit area (mg/m^2), instead of the classical network density n . Monte Carlo simulations from the same authors show that for an

infinite 2D system of percolating objects, the percolation exponent is approximately equal to 4/3. In addition Monte Carlo simulations by Li and Zhang determine the critical density dependence on the nanowire length¹¹³ as follows:

$$n_c L_{NW}^2 = 5.63726 \pm 0.00002 \quad (1-3)$$

This means that the longer the nanowires, the fewest are needed to reach the electrical percolation. Moreover, Figure 1-4b illustrates the influence of the *amd* value on the electrical resistance. Experiments performed on AgNW networks having different network *amd* values confirmed the existence of a critical value of *amd*, *amd_c*, below which no finite resistance can be measured. Above *amd_c* the measured electrical resistance rapidly decreases following a power law, as shown by Figure 1-4b; there is a rather good agreement observed between the experimental data (symbols) and the percolation theory (line) demonstrated above, as shown by Lagrange et al.²⁸ For even higher *amd* values, another transition, less known and studied, exists between the percolative regime and the bulk regime; for the latter the electrical resistivity does not depend anymore on the network density, as reported by Sorel et al.¹¹⁴

Another critical feature of AgNW-based electrodes is their optical transparency. Figure 1-4c shows different optical transmittance spectrum of different transparent conductors in the visible/near infra-red range. Transparent conductive oxides, like ITO and FTO, are transparent in the visible but due to plasma frequency falling in the near infra-red (NIR) the optical transmittance decreases dramatically in that fraction of the spectrum. Transparency in NIR region can be a very important asset, especially for photovoltaic applications. On the contrary, in AgNW networks the incident light is transmitted through the empty spaces between neighbouring NWs, thus they demonstrate similar transmittance in the whole spectral range. In addition, this means that the transmittance of AgNW networks is also intimately linked to the NW density. As already mentioned above concerning the electrical properties, the denser the network, the larger the number of percolating pathways available for the electrical conduction, and the higher the conduction level of the resulting networks. But on the other hand, as the density increases, the number of empty spaces through which incident light is likely to be transmitted is significantly decreased, leading to a lower level of transmittance of the resulting electrodes. This shadowing effect shows a linear relationship between transmittance and areal mass density.^{28,115} Finally, another important parameter of a TCM optical performance is the light scattering, which is associated to the amount of transmitted light that is scattered by the material. The physical parameter used to assess the light scattering phenomenon is the haze factor, defined as the ratio between diffused and total transmittance:

$$\text{Haze Factor} = \frac{\text{Diffuse Transmittance}}{\text{Total Transmittance}} \quad (1-4)$$

Each application is associated with different requirements in terms of haze factor according to its operation. For example, solar cells require high haze factor because scattering light enhances the optical path length of photons, thus increasing their probability of being absorbed, and boosting the photo-generated carrier current as well as the photo-conversion efficiency.¹¹⁶ On the other hand, touch panels and some transparent heaters need a low haze factor in order to ensure comfort for the human eye.²

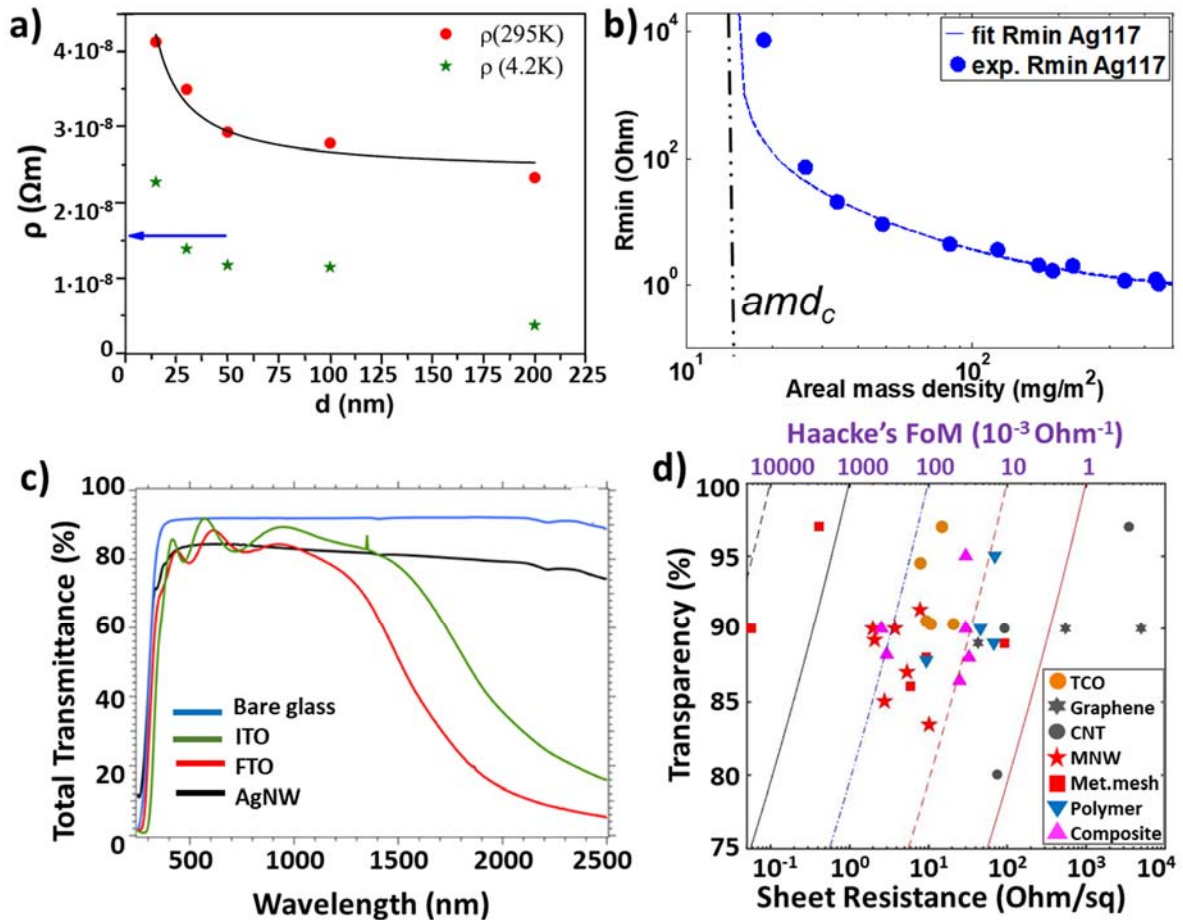


Figure 1-4: a) Electrical resistivity of AgNW versus their diameter at room temperature and at 4.2 K showing that when AgNW diameter is close or lower to the mean free path of electrons in bulk Ag the electrical resistivity increases.¹⁰⁹ Let note that the blue arrow corresponds to silver bulk resistivity at room temperature. b) Minimum electrical resistance versus the thermally optimized network areal mass density.³⁰ Below a critical value, amd_c , no finite electrical resistance can be measured. Just above this, very large resistance values are measured, while the resistance decreases as a power law for larger amd values; the onset correspond to the stick percolation. c) Optical total transmittance (substrate contribution non-subtracted) of a bare substrate (in blue) and three types of transparent conductive materials in the UV-VIS-NIR region: ITO (green), FTO (red), and AgNW network (black) depicted with similar sheet resistance around 15 ohms/square.¹⁶ d) Optical transparency versus sheet resistance diagram for different transparent heater (TH) technologies based on: TCO, CNT, graphene, MNW networks, metallic grids-meshes, conductive polymers, and nanocomposites. The dashed lines correspond to different values of Haacke's FoM: 10000, 1000, 100, 10, 1 times 10^{-3} (Ω/sq^{-1}).⁴⁷

Experimental data by Lagrange et al.²⁸ show that haze factor increases linearly with the areal mass density. In addition, there is a clear influence of the AgNW diameter on the optical properties; higher diameters increase the shadowing effects, thus decreasing the transmittance and increasing the diffuse scattering leading to high haze factor values.^{117,118} The optical and electrical properties can be controlled by the NW density and the NW dimensions, as demonstrated above, but also by the optimisation of the electrical resistance associated to AgNW junctions (more details to be discussed below in the thermal annealing). Finally, an adequate trade-off has to be found since the electrical resistance and the optical transmittance are intimately competing properties for the AgNW networks. An interesting manner for finding the appropriate trade-off between optical and electrical performances is the calculation of the Figure of Merit (*FoM*) introduced by Haacke¹¹⁹ in 1976 for transparent conductors:

$$FoM = \frac{T^{10}}{R_{sh}} \quad (1-5)$$

Figure 1-4d presents a comparative figure in which the transmittance T versus the sheet resistance R_{sh} is plotted for different TCMs, in series of samples with varying film thickness or network density.⁴⁷ The region at the top left corner is the goal for these technologies. This figure shows that AgNW can compete with ITO and other emerging materials such as metallic grids. Typically for devices that require an electrode that ensures the optical transparency, it is often required to integrate transparent electrodes with T higher than 90% at 550 nm and R_{sh} below 100 Ohm/sq. The sheet resistance is used to evaluate the resistance of thin films that are uniform in thickness and thus a common parameter for characterizing the electrical performances of TCMs. Details about the measurement techniques are presented in Chapter 3. Another commonly used *FoM*, proposed by the scientific team of J. N. Coleman, is the ratio between DC conductivity, σ_{DC} , and optical conductivity, α_{opt} , the latter being proportional to the optical absorption coefficient.¹²⁰

1.2.4. Optimization of the network properties. The case of thermal annealing

After deposition, AgNW networks might still show an elevated sheet resistance, even when their density is much larger than the percolation threshold. This is due to the presence of the resistive organic PVP layer that is surrounding the NWs (as already mentioned in section 1.1), but as well to the very local contacts between adjacent AgNWs. Several post-deposition treatments suitable for reducing the electrical resistance of AgNW networks have been reported in the literature, such as mechanical pressing,¹²¹ laser annealing,¹²² chemical treatment,¹²³

plasmonic nano-welding,¹²⁴ as well as capillary-force-induced cold welding^{125–128} or thermal treatment.^{30,129} Such treatments are helpful for having an improved contact between the NWs. The use of a thermal annealing is very appealing due to its simplicity. More specifically, thermal annealing has been extensively investigated at LMGP with very promising optimization impact.

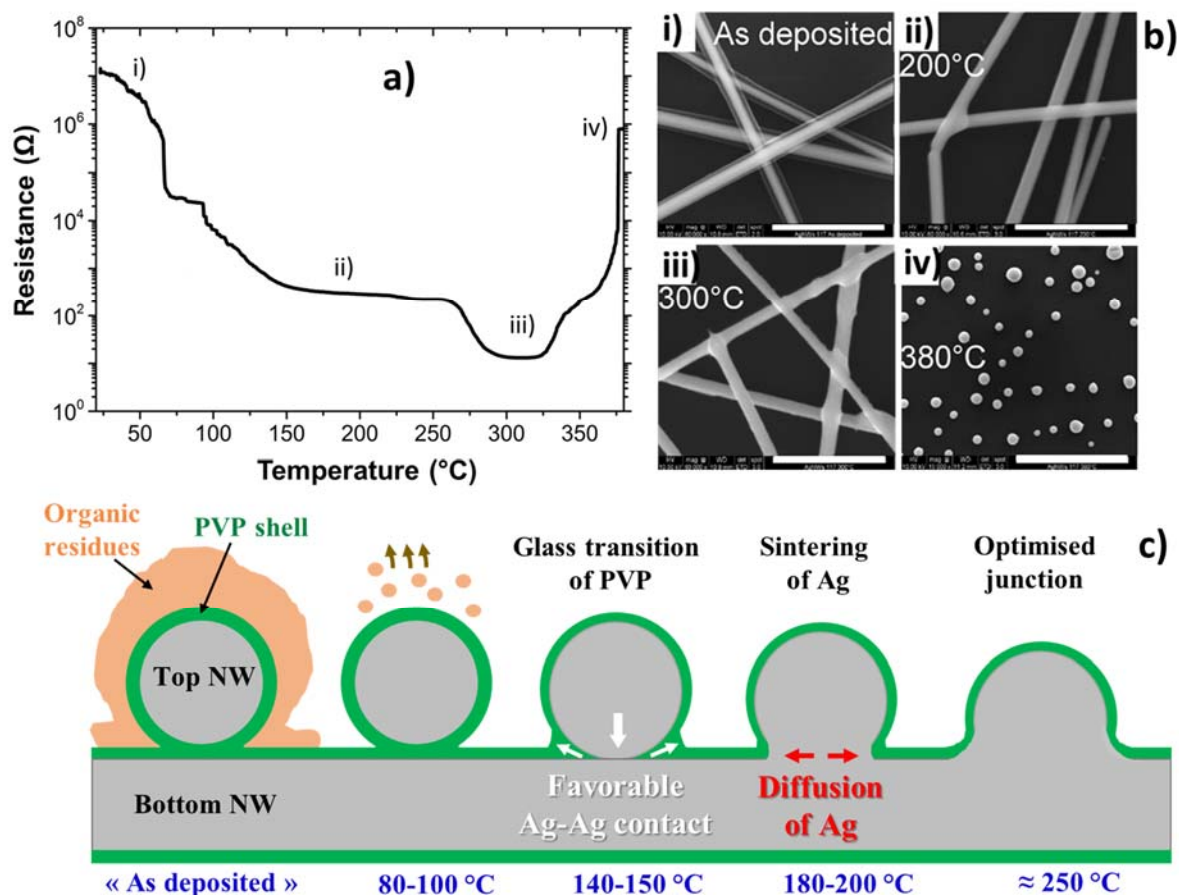


Figure 1-5: a-b) Thermal annealing effect on electrical resistance; evolution of electrical resistance of a AgNW network during a continuous thermal ramp of 15°C/min and SEM images of i) as-deposited sample, and to a sample annealed for 10 minutes at different temperatures ii) 200°C with first occurrence of observable sintering occurs, iii) 300°C all junctions are sintered, iv) 380°C complete spheroidization of the network. Scales for (i), (ii), (iii) 1 μm and for (iv) 4 μm.³⁰ c) Schematic representation of the successive mechanisms involved in the reduction of junction electrical resistance by thermal annealing. Temperature values depicted are given as indications due to a high dependence of the kinetics on both temperature of the annealing and AgNW dimensions.²³

The entire evolution of the electrical resistance as a function of the temperature during a continuous thermal ramp can be observed in **Figure 1-5a**³⁰. The reduction of electrical resistance of AgNW networks via thermal annealing is dominated by desorption of organic residues such as solvents from the AgNW suspensions and by the local sintering at the NWs junctions.³⁰ Annealing tests performed at several temperatures (either constant or performing a ramp) have been done along with SEM observations in order to describe the mechanisms that lie behind the

thermal annealing (Figure 1-5b). According to Langley et al.³⁰ at the beginning of a temperature ramp (30-140 °C), organic molecules which were adsorbed on the surface of the NWs start desorbing. At higher temperatures (150-250 °C) the PVP might undergo thermal degradation, which leads to a reduced sheet resistance. At slightly higher temperatures (200-250°C and at 275°-300°C for ramped annealing) the resistance drops even more due to local sintering. Sintering, a term also used in powder metallurgy, refers to the increase in mechanical strength and decrease in porosity of powder particle networks when heated at temperatures approaching the melting point. The associated driving force is the reduction of surface energy as schematically shown in Figure 1-5c. The same driving force is in fact responsible for the transformation of nanowires into spheres observed when annealing temperatures become too high (SEM image (iv) in the example above). This spheroidization phenomenon is a good illustration of the so-called Plateau-Rayleigh instability. And its dependence on the surface atomic diffusion implies that NWs diameter plays an important role on the process; the lower the diameter, the lower the temperature at which spheroidization takes place, by analogy to the Gibbs-Thomson model for cluster physics.¹³⁰

1.2.5. Mechanical Properties

Electrically conductive materials that are also both optically transparent and mechanically robust have been one of the major challenges for contemporary electronic devices such as foldable smartphones, flexible solar cells, wearable devices, e-skin, supercapacitors, sensors and elastomeric actuators.¹³¹⁻¹⁴⁰ AgNW and other MNW networks embedded in plastic substrates like PET and PEN show excellent flexibility with negligible increase in the sheet resistance, property that has been already demonstrated in several articles.^{19,141,142} This is one of their main assets as compared with traditional brittle TCOs. The flexibility of AgNW networks has already been confirmed by our team with a series of tests, using a bending apparatus as the one shown in **Figure 1-6a-c**. As presented in Figure 1-6d, when subjected to continuous mechanical bending with a radius of curvature of 5 mm, AgNW network remains electrically stable while the electrical resistance of ITO and ZnO:Al (AZO) increases drastically.³⁷ Another example from the literature was provided by Kim et al.¹⁴³ that reported no resistance change after 10,000 cycles of outer and inner bending of slot-die coated AgNW network. in contrast to ITO films that suffered a marked increase in resistance when subjected to the same test. The flexibility of MNW networks is important even if the final application does not require bendable components but when the fabrication of devices, such as for organic

photovoltaics, can be performed with roll-to-roll (R2R) techniques.¹⁴⁴ This enables to drastically decrease the fabrication cost.

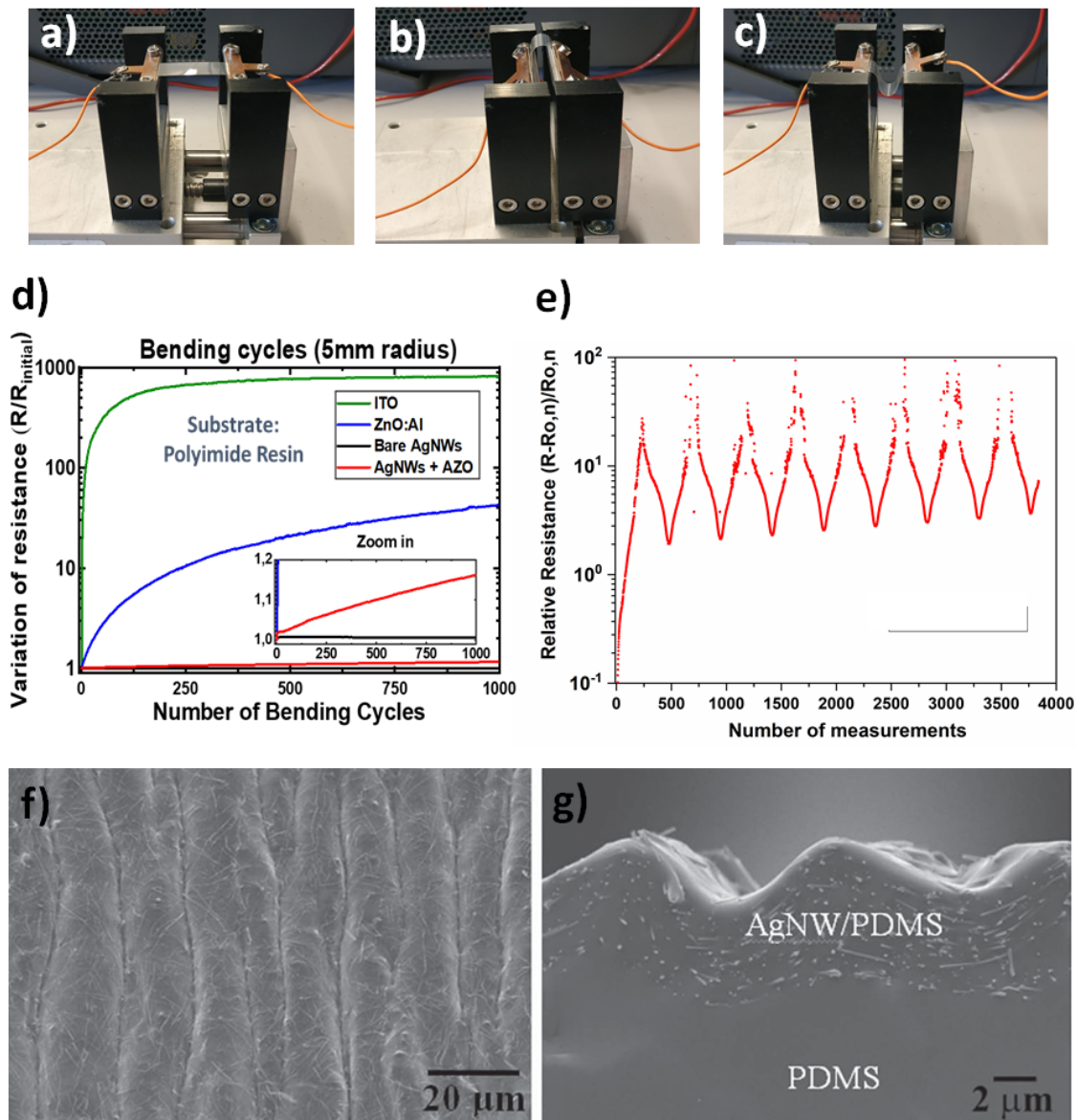


Figure 1-6: a-b-c) Images of a typical bending apparatus for measuring electrical resistance while bending cycles are performed. The two important parameters are the radius of curvature (usually a few millimeters) and the specimen concavity, when the studied layer is on the top (\cap -shape and U-shape are associated to tensile and compressive stress, respectively).²³ d) Experimental data showing the evolution of the relative electrical resistance for three types of TE (ITO, ZnO:Al (AZO) and AgNW network) and the nanocomposite ZnO:Al/AgNW, versus the number of bending cycles. The radius of curvature was 5 mm.³⁷ e) Evolution of the relative electrical resistance of a AgNW-PDMS nanocomposite during 8 cycles of stretching/releasing until 30% elongation. The resistance was measured every second and the initial resistance of the AgNW network was 21 Ohm/sq.²³ f) SEM image of the AgNW/PDMS surface after the stretching and releasing cycles. The image was taken by tilting the sample at an angle of 20° ,¹⁴⁵ g) Cross-sectional SEM image of the previous AgNW/PDMS layer.¹⁴⁵

Flexibility is another property of AgNW networks that can be related to their density (amd) as Park et al. reported with numerical calculations correlated with experimental observations; the

reliability of AgNW networks during bending fatigue was degraded as the density of the network decreased.¹⁴⁶

Concerning the fabrication of stretchable and transparent electrodes, PDMS is the most commonly used polymer, which is also a biocompatible and low-cost material. This time the resistance increases during the stretching and releasing cycles as shown in Figure 1-6e. Denser AgNW networks can be highly stretchable but they exhibit a lower optical transparency.^{44,147} Lee et al. fabricated stretchable LED circuits using AgNW-PDMS electrodes that were operational at over 370% strain without any irreversible degradation, but the electrode was very opaque.¹⁴⁸ However, there are more and more advances on the elaboration of stretchable, transparent electrodes with up-scalable sizes and interesting performances.^{27,149,150} The adhesion or incorporation of AgNWs into elastic substrates is another very important issue. The most widely reported preparation technique involves curing the PDMS at a certain temperature and time followed by peeling off into warm water, so that the NWs are successfully transferred from the initial glass to the polymer.¹⁵¹⁻¹⁵⁴ Furthermore, pre-straining the substrates or curving the MNWs before deposition is an efficient way to reduce the degradation of the nanowires during mechanical stress.^{155,156} Seo et al. used a nondrying glycerogel for the deposition of wavy silver nanowires with a 100% prestrain, without causing kinks and interfacial cracks often found with nanowires layered onto PDMS. The resulting transparent conductor exhibited low electrical resistance even after 5,000 cycles of deformation.¹⁵⁷ Another approach is the selective nanowelding of AgNWs using a high electrostatic potential at the junctions leading to high-performance stretchable electrodes.¹⁵⁸ On the other hand, the elaboration of 3D AgNW conductors in polymeric scaffolds, as reported by Weng et al., leads to novel deformation characteristics suitable for soft electronic skin.¹⁵⁹

From a microscopic point of view, Feng Xu and Yong Zhu have studied *in situ* the AgNW-PDMS surface morphology during stretching-releasing cycles via optical microscopy and examined its buckled wavy shape further with cross-sectional SEM imaging (Figure 1-6f-g).¹⁴⁵ It was observed that the weakening and detachment of the nanowire junctions results in less conductive pathways, and thus an increase of electrical resistance. However, the contribution of the nanowires plastic deformation to the observed electrical change under strain is negligible, because of the very small AgNWs fracture strain (values 1-2%), as measured by Zhu et al.¹⁶⁰ More precisely, these authors performed *in situ* tensile strain tests inside a SEM and showed that the yield strength increases as the nanowire diameter decreases which is attributed to the increase in the NWs Young's modulus.¹⁶⁰

1.2.6. Stability issues and the case of electrical stress

MNW networks can be prone to degradation when subjected to either thermal and/or electrical stress, or to a load of environmental or chemical nature (humidity, radiation, alcohol solvents, acids etc).^{161–166} Stability is currently one of the main limitations for the successful integration of MNW networks in devices and constitutes one of the main axis studied in the present PhD thesis. **Figure 1-7** summarizes the main mechanisms of degradation of MNW networks, such as electrical(a), thermal(b) stress, mechanical(c) and environmental stress(d). There are several approaches developed by researches to study the different instabilities taking place, from single nanowire and the junctions between them (nanoscale) to the macroscopic failure of an entire network.^{167–170} In previous works conducted by the team in LMGP, the effect of thermal annealing on the physical properties was thoroughly studied by macroscopic techniques and also nano-characterization tools, SEM and TEM among other.^{28,30}

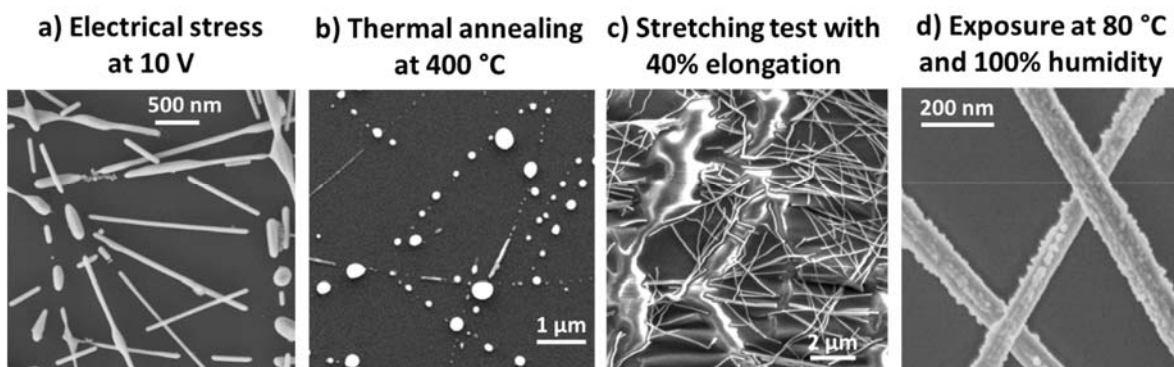


Figure 1-7: SEM images of MNW networks showing the degradation due to different stresses: a) electrical stress by an applied voltage ramp of 0.5 V/min. At 10 V the instabilities lead to partial degradation of the nanowires. b) spheroidised AgNWs after thermal annealing at 400 °C. c) deformed and broken AgNWs deposited on PDMS, at 40% elongation during a stretching test performed in situ inside a SEM. d) environmental stress, when CuNW (copper nanowires) are exposed at 80 °C temperature and 100% humidity for 60 min.¹⁷¹

Sannicolo et al. studied the stability of AgNW networks under electrical stress by applying a voltage ramp (0.5 V/min) and observing the evolution of the electrical resistance, as presented in **Figure 1-8a**. The spatial distribution of temperature was recorded simultaneously by an IR camera (Figure 1-8c), which is a pertinent and well adapted tool for the investigation of local instabilities that arise in transparent electrodes when an electrical bias is applied.³² In more detail, at the beginning of the voltage ramp (Figure 1-8a-i), there is a linear increase in the electrical resistance linked to an increased phonon-induced electron scattering due to the Joule

heating.¹⁶⁹ This relation between the electrical resistance of a metallic component and the temperature is represented by the following equation:

$$R(T_0 + \Delta T) = R_0(T_0)(1 + \beta_R \Delta T) \quad (1-6)$$

where T_0 is the room temperature, ΔT is the increase in temperature, R_0 is the initial resistance and β_R is the temperature coefficient of resistivity, which equals $3.8 \cdot 10^{-3} \text{ K}^{-1}$ for Ag thin films¹⁷², $2.6 \cdot 10^{-3} \text{ K}^{-1}$ for AgNPs films¹⁷³ or $2.2 \cdot 10^{-3} \text{ K}^{-1}$ for AgNW networks.²⁸

At around 15 V, a decrease in the resistance is observed thanks to the electrical sintering phenomenon that occurs at the junctions between nanowires (ii), leading to the optimisation of the network. Subsequently, as the degradation process begins, the resistance starts increasing (iii) and the electrical breakdown of the sample occurs with a sharp increase of the resistance and the loss of conductivity (iv-v). NIR images corresponding to these five periods are shown in Figure 1-8c. At low applied voltage, one can observe a homogeneous distribution of the dissipated heat in the sample, which corresponds to low values of electrical resistance, 10-100 ohms (i). The distribution remains homogeneous until the end of the optimisation process (ii). Then, the sample region with the maximum temperature starts to narrow at a vertical central part of the network parallel to the contact electrodes (iii). The rapid increase in the electrical resistance matches the beginning of a “thermal crack” (iv), which propagates from the bottom of the sample until it splits the sample in two parts (v) in less than two minutes since the beginning of the breakdown. Figure 1-8d shows SEM images of the crack and also the intact network away from it. The region of the crack spans some tens of microns width and includes nanowires completely spheroidised but also some partially damaged. As shown in Figure 1-8e, there are still some filaments connecting the nanowires but with much smaller diameters. Concerning the origin and propagation of the thermal crack, a schematic illustration is shown in Figure 1-8b. Initially, due to local statistical fluctuations in *amd* and random orientation of the nanowires in a sample, some regions with higher current density can occur (“hotspot regions”). The Joule heating is more significant in these spots and the spheroidization occurs faster than in other regions. Consequently, the current can flow only around the hotspot, as shown in Figure 1-8b, creating a new region with increased current density and thus high Joule heating. The nanowires in this region will be subsequently spheroidised too and modify the current distribution around their neighbouring percolating paths in an equivalent fashion. Thus, the defect continues propagating like a domino effect and the final thermal crack leads to the “breakdown” of the sample.

Both thermal and electrical failure mechanisms are in a first approximation induced by Plateau-Rayleigh instability. However, the thermally induced failure occurs over the entire network, while the electrical failure mechanism only leads to a local degradation of the network, which depends on the random fluctuations in *amd*.

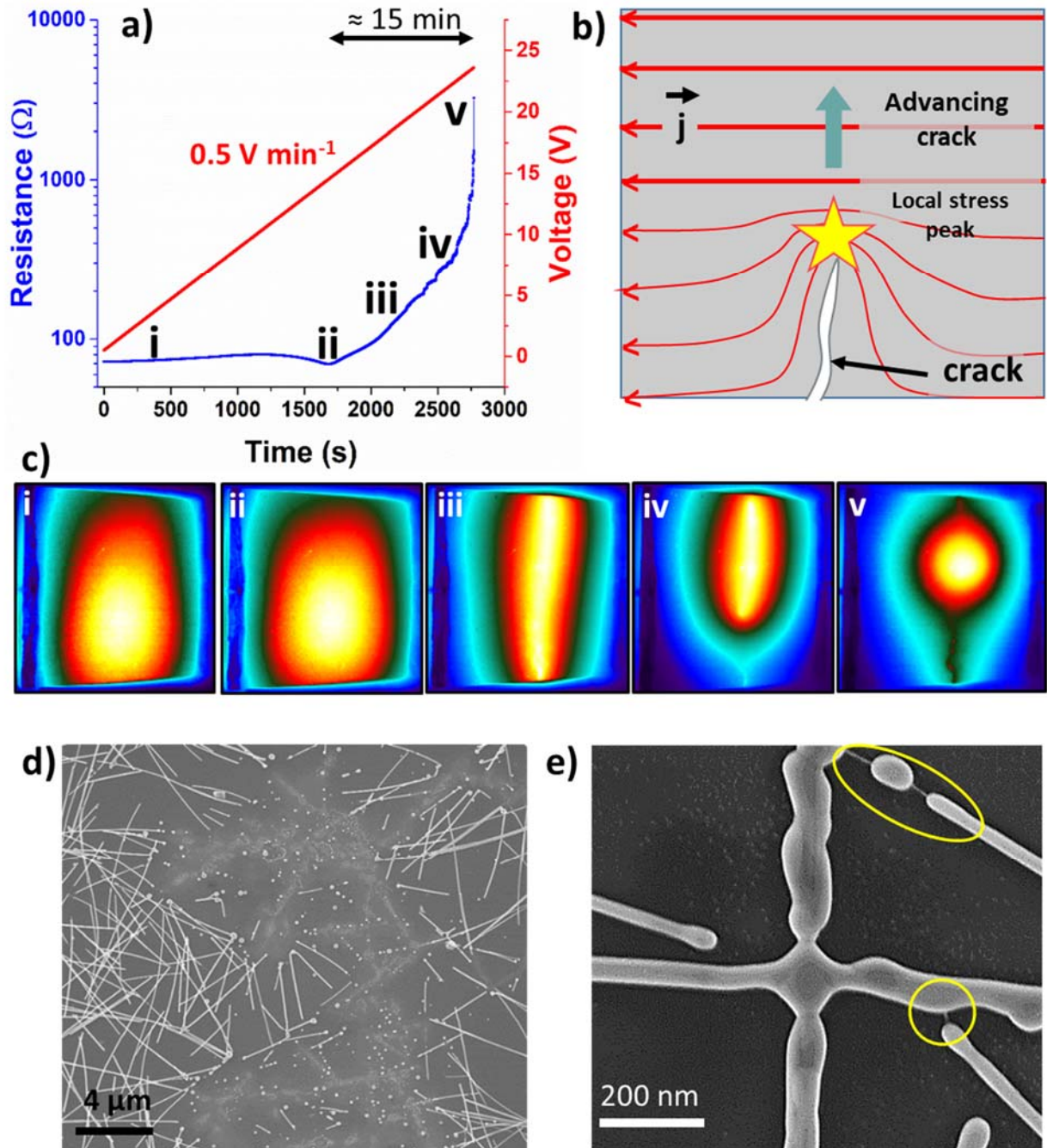


Figure 1-8: a) Electrical resistance of the network when a voltage ramp of 0.5 V/min is applied. b) Schematic of the crack propagation in a AgNW network during the degradation of the network submitted to electrical stress. c) NIR images recorded at different moments (i-v in c). d) SEM images of the sample after electrical breakdown at the crack location. e) Additional SEM images at the same region showing the presence of small Ag filaments (yellow circles) much smaller than AgNWs themselves.³²

1.3. Stability enhancement by oxide coatings

One way to improve thermal and electrical stability of AgNW networks is to deposit a thin conformal and uniform protective layer to prevent atomic surface diffusion and then the morphological instabilities.^{174,175} Several studies have shown stability enhancement of AgNW networks by coating them with thin metal or graphene oxide layers such as titanium oxide (TiO₂),^{169,176} zinc oxide (ZnO),^{35,80,177} aluminium oxide (Al₂O₃),^{178–180} aluminium-doped zinc oxide (AZO),^{37,79,181} or graphene oxide (GO)^{182,183}. However, the deposition techniques mostly used for this purpose, namely, atomic layer deposition (ALD), sputtering, and spin coating, require vacuum for their operation and/or are difficult to scale up. Thus, there is a demand in a simpler and less expensive deposition method. Atmospheric Pressure Spatial Atomic Layer Deposition (AP-SALD), developed in LMGP in the team lead by Dr David Muñoz-Rojas, can fulfil these requirements.^{33,184}

Atomic layer deposition is a chemical vapour phase technique which is used to deposit thin films with low defects and a high degree of thickness control.¹⁸⁵ It consists of injecting successively different precursor vapours into a vacuum chamber which will react with the surface of a substrate. A typical cycle of ALD deposition consists of injecting the first precursor vapour until there are no available reaction sites on the surface and a monolayer of precursor molecules has formed. A purge cycle is then performed to remove any unreacted precursor. The process is continued with the second precursor, generally water when depositing oxides, which will react with the previously deposited layer to form a new layer of oxide. Again, once no active sites are anymore available, a purge is again performed to eliminate excess precursor and reaction by-products, and one cycle of ALD is completed. This deposition technique is powerful because it is self-terminated and surface-limited, thus resulting in a high control over film thickness down to the nanometer and the possibility of depositing highly conformal films on high aspect-ratio or porous substrates. Furthermore, the deposition is performed at relatively low temperatures as compared to chemical vapour deposition (CVD), which enables the use of organic substrates or thermally unstable precursors or samples.¹⁸⁶ The major drawback of this method is that is mostly performed under vacuum, which limits its use for large scale deposition. Additionally, the growth of films is extremely slow due to the intrinsically low growth-per-cycle values and the long cycles cause by the long purging steps. This can be seen as an advantage for the precise control of the deposited thickness (i.e. in microelectronics industry for depositing atomic barrier film) but also as a drawback because it is time consuming.

In order to decrease the deposition time, researchers developed the atmospheric pressure spatial ALD (AP-SALD) technique.³³ The main difference between AP-SALD and ALD is the way in which the separation of the precursors takes place: for the AP-SALD case, they are spatially separated while for the ALD case they are separated in time (Figure 1-9a-b).³³

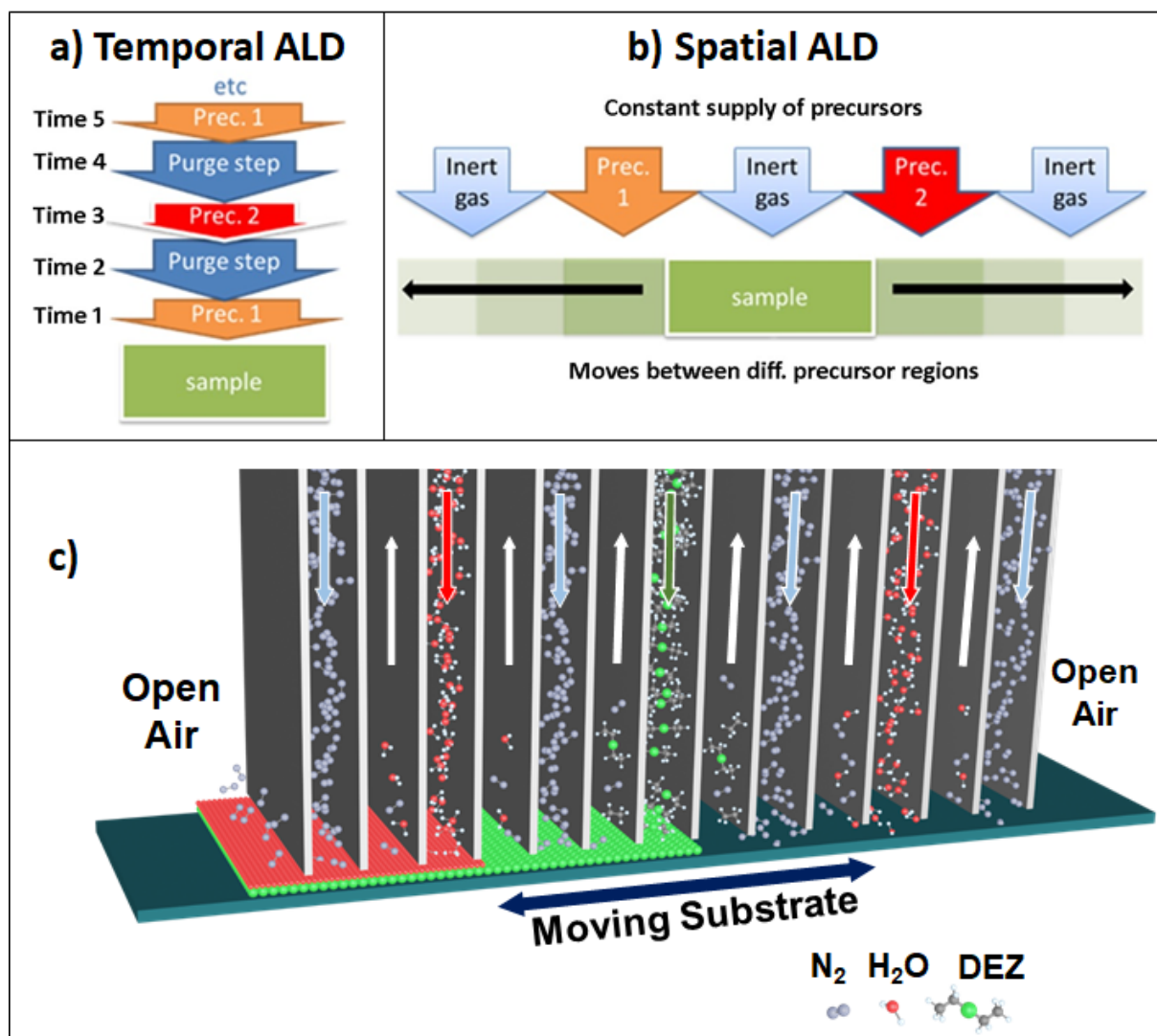


Figure 1-9: a-b) Comparison between a) the temporal and b) spatial ALD: the separation between the two reactive precursors is performed either in time or in space, respectively. In conventional, temporal ALD the substrate is at a fixed position, and the precursors are dosed sequentially, separated by a purge step, while in spatial ALD the precursors are dosed simultaneously and continuously, but at different half-reaction zones. The substrate moves between these regions where the half-reactions take place.³³ c) Schematic of AP-SALD deposition head with the injection of precursor gases that are separated by inert gas N_2 . Precursors are injected through their respective channels and then exhausted through adjacent exhaust channels, thus being exposed to a moving substrate, resulting in the reproduction of the typical ALD cycles. The scheme shows the deposition of ZnO from DEZ (Diethyl zinc) and water.¹⁸⁷

While there are many different ways in which SALD can be performed, in LMGP we use and develop an atmospheric system based on a close/proximity injection head.¹⁸⁸ The head has

parallel inlets used to inject gases, which are exposed to the substrate upon scanning along the perpendicular direction of these inlets. These inlets are linked to the precursors by alternating the different species and the purge gas as shown schematically in Figure 1-9c;¹⁸⁷ one cycle of AP-SALD corresponds to some cycles of ALD depending on the number of channels delivering the metal precursor. The peculiarity of this deposition method is that it requires a close distance between sample and head to avoid mixture of precursors which would then correspond to CVD mode.¹⁸⁹ Typically for the LMGP set-ups the distance between specimen and AP-SALD head is between 100 and 200 microns. This can limit for instance the use of a non-flat substrate. While maintaining the advantages of ALD (low-temperature deposition, thickness control, high-quality materials, and conformity), it can be up to 2 orders of magnitude faster than ALD and it is compatible with R2R and open-air processing. Lately, our team has used AP-SALD³⁵ to fabricate nanocomposite based transparent electrodes in which the AgNW networks are protected by conformal thin oxide layers like ZnO, Al₂O₃ and ZnO:Al.³⁵⁻³⁷

The AP-SALD method was used to deposit thin layers of 15 to 30 nm of ZnO around the AgNWs with the goal of enhancing the network stability.³⁵ **Figure 1-10a** shows TEM and SEM images of bare and ZnO coated AgNWs: they clearly reveal that the ZnO layer deposition is conformal around the AgNWs. The inset exhibits the usual fivefold symmetry twinning of the AgNWs. As demonstrated by Khan et al.³⁵ the ZnO coating improved the adhesion of the AgNW networks to the glass substrate, which is known to be poor for the bare AgNW networks. Electrical and thermal ramps verified that the thicker the deposited ZnO layer the better the stability. The bare AgNW network shows failure at around 9 V, whereas the stability of ZnO-coated AgNW networks increases for thicker ZnO coating, reaching up to 18 V for a 30 nm thick ZnO coating. Similar results have been reported by Celle et al.⁷⁸ in the case of CuNW networks. It was shown that a very thin Al₂O₃ coating deposited by AP-SALD prevents oxidation of the CuNWs. Figure 1-10b reports the dependence of experimental failure voltage measured during a voltage ramp versus thickness of the thin ZnO conformal layer, while the dashed line corresponds to a physical model based on silver atomic diffusion through the oxide coating. The latter is associated to the fact that the ZnO coating hinders the diffusion of the nanowire Ag atoms, avoiding (at least partially) the spheroidization of AgNWs. According to the basic diffusion law in a first approximation, the time delay, $\Delta t^{fail}(L_{ZnO})$, is directly correlated to the oxide layer thickness (L_{ZnO}) as:

$$L_{ZnO} = \sqrt{2 \cdot D \cdot \Delta t^{fail}(L_{ZnO})} \quad (1-7)$$

where D is the diffusion coefficient of Ag atoms through the oxide barrier. Finally, the following equation provides a direct dependency between the voltage failure and ZnO coating thickness L_{ZnO} as:

$$V_{coated\ AgNW}^{fail}(L_{ZnO}) = V_{bare\ AgNW}^{fail} + \frac{\dot{V} \cdot L_{ZnO}^2}{2 \cdot D} \quad (1-8)$$

where \dot{V} is the voltage rate associated with the voltage ramp (equal to 0.1 V min^{-1}). As shown in Figure 1-10b, a good agreement is obtained between experimental data and the proposed model.³⁵

While enhanced stability is observed when increasing the thickness of the ZnO layer, a small and linear decrease in the optical transparency is observed when the coating thickness increases. This is also the case for ZnO:Al/AgNW nanocomposites deposited by AP-SALD and spray coating, respectively. Nguyen et al. reported a 5 % decrease in total transparency but at the same time the charging effect when performing SEM imaging vanishes on the nanocomposite sample since the open spaces between the nanowires are filled by a relatively conductive layer of ZnO:Al.³⁷ This means that the oxide thin film acts as an effective charge collection layer, and when being used for TE applications in solar cells or in OLEDs, for collecting and injecting charges respectively, ZnO:Al/AgNW nanocomposites are expected to be much more efficient than AgNW bare networks. In this study, the thickness of ZnO:Al layer was fixed at 150 nm, an optimized value with a good compromise between the optical transmittance and the prevention of silver diffusion. The density of AgNW networks was the parameter varied from 15 to 105 mg/m². The conductivity of the nanocomposite was studied via physical models too and it was found that the conductivity in ZnO:Al/AgNW nanocomposite originates mainly from i/ the contribution of ZnO:Al thin film for low amd ($< 30 \text{ mg/m}^2$) or ii/ from the AgNW network for high amd ($> 70 \text{ mg/m}^2$). Particularly, it was observed that a contribution of local percolating clusters of AgNWs can be evidenced, even below the macroscopic percolation limit of the network and a simple physical model was then developed based on this idea, showing a high fit quality with the experimental data.³⁷ In terms of stability, Figure 1-10c-d presents the enhanced stability of the nanocomposite under electrical and thermal cycling stress. Finally, the bare AgNW network and the ZnO:Al/AgNW nanocomposites exhibit a good mechanical stability, mainly attributed to the highly flexibility of AgNW networks, although the nanocomposite shows a slight increase of resistance versus number of bending cycles (15% increase after 1000 cycles), as shown in details in the inset of Figure 1-6d.³⁷

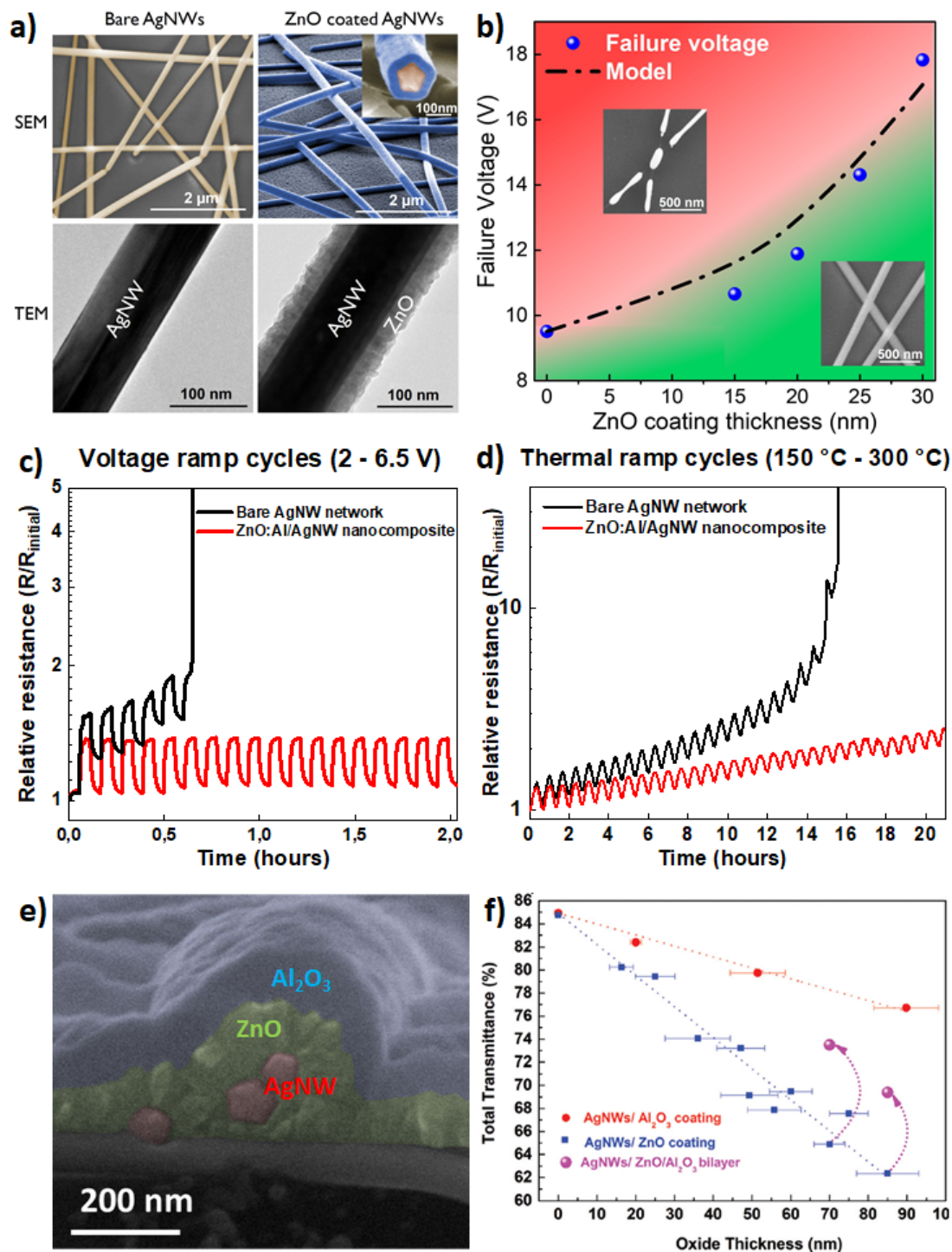


Figure 1-10: AgNW and oxide coatings by AP-SALD. The case of ZnO layers: a) SEM and TEM images of the bare AgNW network and the 25 nm thick ZnO coated, b) failure voltage limit dependence versus ZnO coating thickness. A clear increase of the failure voltage versus ZnO layer thickness is observed (the line corresponds to the physical model based on silver atom diffusion).³⁵ Relative electrical resistance of bare AgNW network and ZnO:Al/AgNW nanocomposite versus time when the samples were subjected to: c) voltage ramp cycles, between 2 V and 6.5 V and d) thermal ramp cycles between 150 °C and 300 °C.³⁷ e) Cross-sectional SEM image of bilayer coatings of 70 nm ZnO/70 nm Al₂O₃ deposited on AgNWs,¹⁸⁰ and f) average total transmittance of Al₂O₃, ZnO and ZnO/Al₂O₃ coated AgNW networks in the visible range versus oxide thickness; this shows that Al₂O₃ coatings induce smaller losses in optical transmittance as compared to ZnO coatings. Two examples at 70 nm and 85 nm confirm the antireflective effect of the Al₂O₃ coating over the ZnO layer.³⁶

Finally, as discussed above, the thin metal oxide coatings enhance drastically the stability of AgNW networks, but at the expense of transparency. However, a recent study of the team in LMGP demonstrated that by depositing a second oxide coating (Al_2O_3), which acts as an antireflective layer, it is possible to obtain highly stable and transparent composite electrodes at the same time. SEM image of such a conformal bilayer coating of ZnO/ Al_2O_3 on top of the AgNWs is presented in Figure 1-10e. Aghazadehchors et al. reported that while a 70 nm thick ZnO coating on AgNW networks shows an average transmittance in the visible range (from 380 to 700 nm) of 64.9%, bilayer coatings consisting of 70 nm ZnO/70 nm Al_2O_3 on AgNWs show an average transmittance of 73.5%, as shown in Figure 1-10f. The electrical, thermal and mechanical enhanced stability of this nanocomposite is also confirmed.¹⁸⁰

1.4. Conclusion

The goal of this first chapter of my thesis manuscript was to offer an overview of transparent electrodes based on MNW networks, in particular AgNW networks. Beginning with the indispensability of such components in a large variety of devices with energy, lighting and heating functionality, we explored briefly the traditional TCM technologies used to date and the emerging ones under investigation. Issues related to Critical raw materials and the superior performances under mechanical stress required by modern applications, led to the search of alternatives to the commonly used ITO, and AgNW networks constitute one of the most promising candidates. In the second part of the chapter, the growth of nanowires and the main MNW networks fabrication techniques were presented. Furthermore, their main properties were demonstrated, as well as the methods to optimise them, with a more detailed mention to the post-deposition thermal annealing treatment. Despite their significant electrical, optical and mechanical properties, MNW lack of stability under different types of stress, is crucial for their successful integration into devices. The scientific interest is highly focused on the stability enhancement and the encapsulation of MNWs with protective, transparent oxide layers by open-air, low cost and up-scalable processes like AP-SALD, as presented in the last part of the chapter. As it was demonstrated, there are still a lot of challenges to tackle and phenomena to study in order to better understand the mechanisms leading to failure and find ways to ensure the stability of AgNW networks when integrated into devices. These were also the main goals of my thesis and the related results, from experiments and simulations, will be described in detail in the chapters to follow.

πολλαὶ γὰρ μεταβολαὶ γίνονται καὶ παντοῖαι τύχαι κατὰ τὸν βίον

Ἀριστοτέλης

« There are many changes and several chances in life »

Aristoteles (384-322 BC)

Chapter 2

2. A review on Transparent Heaters

2.1. Introduction

An overview on TE as presented in the previous chapter. The discussion included general information about the need for emerging TCM and the wide range of applications, the physical properties of metallic nanowire networks and their optimization, their advantages and the instability issues, and finally promising composites based on the encapsulation with TCOs for enhanced performance. It is for over a decade that the nanomaterial-based TE have been more systematically investigated.^{190,191} This field of applied sciences, combining physics, chemistry and other disciplines, has a direct connection with the applications, thus the scientific publications very often include examples of the integration of TCM into devices.

One of the main domains of application concerns transparent heaters (TH). The latter appear to be the first application of TCM in the 1940s, developed in order to increase the visibility of the warplane wind-shields during military actions at elevated heights (defogging and defrosting thanks to a heating element which is optically transparent). Since then, a large variety of more peaceful applications started to grow, with a fast flourishing observed in the last years. Nowadays, TH are indispensable components not only for defrosting windshields but also for healthcare devices, smart buildings, and even everyday-life gadgets with utility beyond imagination. The positive impact of TH on energy, health or transport is significant and, in parallel, we have observed the increasing interest of our scientific community to study further the TH. Consequently, especially the last 5 years, there is a remarkable increase in the publications reporting the heating performance of the featured TCM technology. This is also the case of our team in LMGP and, thus, an important part of my PhD is related to the study and optimization of the fabrication and properties of TH and their implementation in devices. Despite the above, there was only one review-article summarizing the TCM families and the range of devices concerning TH, published by Gupta et al. back in 2016.¹⁹²

For all these reasons, and in collaboration with the scientific team of J.-P. Simonato in CEA-Liten, we decided to write a review article entitled “*Transparent Heaters: a Review*”, by D. T. Papanastasiou, A. Schultheiss, D. Muñoz-Rojas, C. Celle, A. Carella, J.-P. Simonato, and D. Bellet (DOI: <https://doi.org/10.1002/adfm.201910225>).¹, that was submitted and published in *Advanced Functional Materials* in March 2020. Our goal was to provide a thorough literature overview of the current technologies (TCO, CNT and graphene-based, MNW and metallic grids, conducting polymers, hybrids and composites of all the previous) and the target

applications (defrosting-defogging, thermochromic, medical, etc.). In addition, our will was firstly to introduce the thermal physics of TH that has not been previously summarized, starting from the Joule effect (as shown in **Figure 2-1a**) followed by TH main properties such as the power density and the steady-state temperature (Figure 2-1b). In addition, we wanted to provide a critical discussion of the different active materials (Figure 2-1c) and finally, focus on the future challenges in terms of better physical understanding, enhanced performances, and integration of the TH into industrial devices. In the next pages, the published review is reproduced. Afterwards, I present briefly the recent advances from articles published during the very last months, followed by current trends and important prospects.

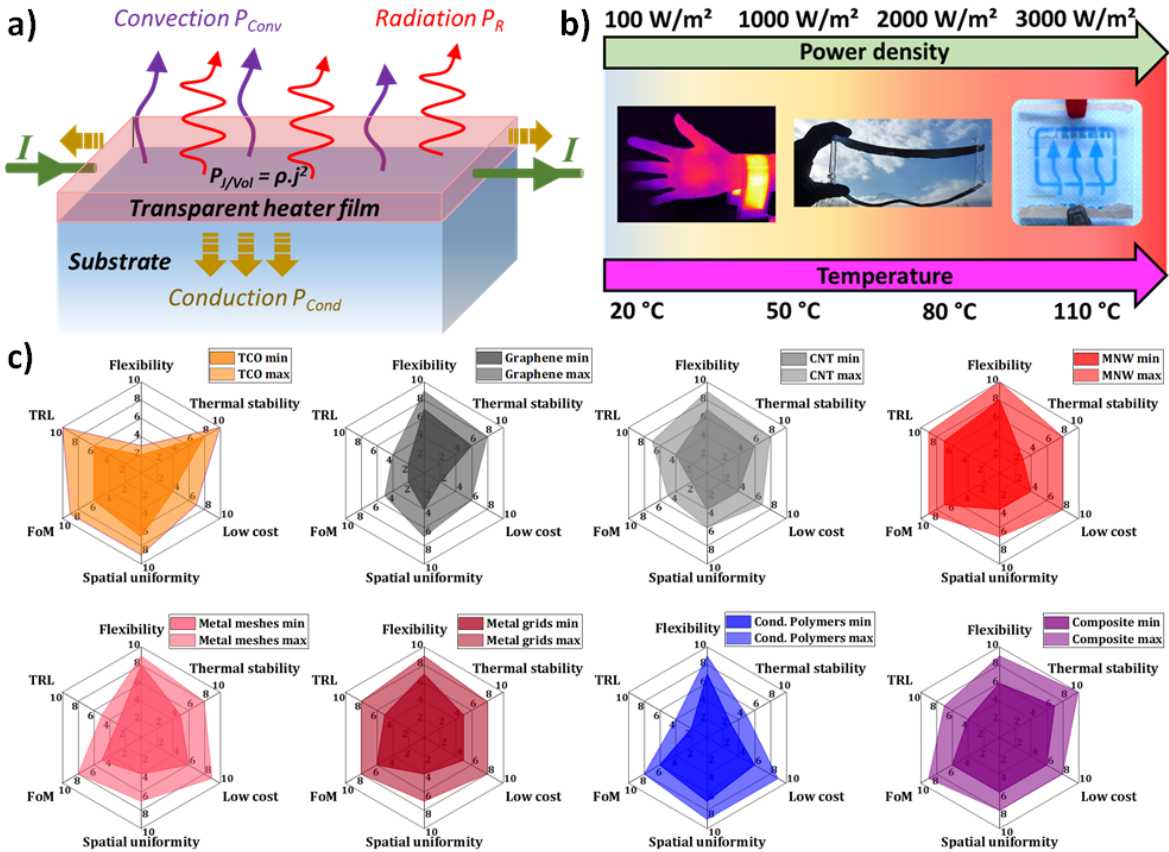


Figure 2-1: a) Schematic of a transparent heater (TH): the thin TH is crossed by an electrical current, generating heat thanks to the Joule effect. A steady state is reached once this generated heat is equal to the sum of the heat losses shown with different colors. b) Main application domains of THs versus areal power density or temperature required. The arrows below represent roughly the typical maximum steady-state temperatures for the main TH technologies. c) Comparison of THs fabricated with the different technologies. This figure shows the general trends with six criteria (clockwise from the top): flexibility, thermal stability, low cost (of both material and process), spatial uniformity, figure of merit (FoM), and technological readiness level (TRL). Depending on the synthesis and usage of experimental THs, a range of figures of merit with minimum and maximum values is proposed. The marks for all criteria for each TH technology are only general indications, since the actual marks are clearly application-dependent.¹

Transparent Heaters: A Review

Dorina T. Papanastasiou, Amélie Schultheiss, David Muñoz-Rojas*, Caroline Celle, Alexandre Carella, Jean-Pierre Simonato*, Daniel Bellet*

* corresponding authors

Keywords: transparent electrode, Joule heating, film heater, composite, stability

D.T. Papanastasiou, Dr. D. Muñoz-Rojas, Pr. D. Bellet

Univ. Grenoble Alpes, CNRS, Grenoble INP, LMGP, F- 38000 Grenoble, France

Email : david.munoz-rojas@grenoble-inp.fr; daniel.bellet@grenoble-inp.fr

A. Schultheiss, Dr. C. Celle, Dr. A. Carella, Dr. J.-P. Simonato

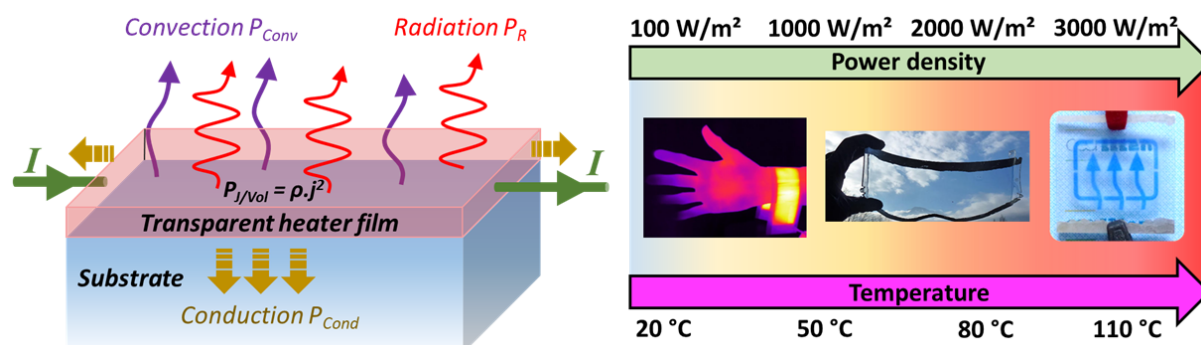
Univ. Grenoble Alpes, CEA, LITEN, DTNM, 17 avenue des Martyrs, F-38054 Grenoble, France

Email: jean-pierre.simonato@cea.fr

Short summary

Transparent heaters (TH) have attracted intense attention from both scientific and industrial actors due to the key role they play in many technologies, including smart windows, deicers, defoggers, displays, actuators and sensors. While transparent conductive oxides have dominated the field for the past five decades, a new generation of THs based on nanomaterials has led to new paradigms in terms of applications and prospects in the past years. Here we will review the most recent developments and strategies to improve the properties, stability and integration of these new THs.

Graphical abstract



1 Introduction

Transparent heaters (THs) are visually transparent devices that contain electrically conductive layers. When an electrical current flows across the transparent heater, it generates heat thanks to the Joule effect. This heat can be efficiently used in many devices. Consequently, numerous applications are concerned by THs, and the associated TH market is growing fast, comprising many types of devices (smart windows, deicers, defoggers, displays, thermotherapy pads, sensors...) for different industrial sectors (transport, buildings, healthcare, sport...). For instance, THs can provide the warmth required to extend the operating temperature of liquid crystal displays (LCDs) in cold environments or can increase the temperature for anti-fogging systems, anti-icing, deicing of optics and optical displays (very useful for transportation). Other applications include the heating of specific industrial processes, of microfluidic chips, of kiosks and handheld devices.^[1] Display technology and smart windows (used in transport or for interior architecture) are among the fastest growing markets related to THs. Importantly, defrosting windows in airplanes enables high-altitude flying.^[2] Smart windows can reduce energy loss in buildings, which currently account for over 40% of the energy consumed. This works thanks to special functional coatings which can regulate solar energy in response to heat (thermochromic material).^[3,4] This heat can be generated by THs within smart windows.^[5] While the required optical transparency depends upon the specific application, in this review we have considered THs having an optical transparency of at least 50%.

The fast control of temperature via the applied current or voltage makes THs a generally better choice when compared to conventional heating elements. This is enabled by the small thermal inertia of thin TH films.

The only technology used for TH before 1995 was based on transparent conductive oxides (TCOs), which were also broadly used as transparent electrodes in many applications including photovoltaics^[6], smart windows^[7], efficient lighting^[8] or displays.^[2,7,9,10] The three main TCO materials are indium tin oxide (ITO)^[11–13], the most well-known and used TCO, fluorine-doped tin oxide (FTO)^[14,15] and aluminum-doped zinc oxide (AZO).^[16–19] TCOs are generally degenerately-doped n-type semiconductors which exhibit a high electrical conductivity of 10^3 - 10^4 S/cm.^[9] They are often fabricated as thin films of approximately 300 nm thickness in order to show high transparency (~90%). While TCOs can exhibit good or even excellent performances in terms of the trade-off between electrical conductivity and optical transparency in the visible range, their two main drawbacks concern their non-flexibility (due to their ceramic nature) and their intrinsic low optical transmittance in the near-infrared (NIR) spectrum due to plasmonic absorption^[13,20]. Therefore, great attention has been devoted to flexible and transparent electrodes^[21] or heaters for three main reasons: i/ the emergence of new-generation devices having flexible or nonplanar substrates, ii/ the potential scarcity of indium for ITO and iii/ the lack of transparency in the NIR. For some applications, even flexibility is not sufficient since stretchability could be a prerequisite, like for the integration of THs within wearable electronics.^[22] For example, flexible but also stretchable THs can be used in thermotherapy^[23,24], a popular treatment in physiotherapy which is particularly useful for the treatment of joint injuries and pain. For such applications, THs should also be soft and thin (and therefore light) so that comfort is not compromised.

It is also worth noting that even for non-flexible devices, we are looking for high throughput fabrication methods which are compatible with an economically viable technology, like the roll-to-roll (R2R) process. Indeed, R2R is a fast processing method associated with little or no loss of material, and which requires that both substrate and active layers be flexible.^[25,26] Therefore TCOs themselves are not compatible with such low-cost methods, except when integrated as very thin films with other materials such as oxides or metals, and thus alternative THs need to be developed.

Several emerging materials have recently been investigated for TH applications, including carbon-based nanomaterials, and mainly carbon nanotubes (CNT)^[27] and graphene^[28]. These new materials are rather cheap and abundant and could therefore follow the fast-growing industrial demand. Moreover, THs made of these building blocks are flexible and can be processed in solution. In parallel, since 2009 metallic nanowire (MNW) networks have started to be more systematically investigated, notably following the seminal articles on: i) the synthesis of MNWs by the groups of Sun^[29] and Wiley^[30–32], among others; ii) the study of the physical properties of MNW networks by Coleman's group^[33,34]; and iii) the integration into efficient devices by Pei's group.^[35,36] Several recent reviews have summarized the main properties, challenges and integration of MNW networks^[20,37–41]. The first article showing that silver nanowire (AgNW) networks could act as efficient THs was published in 2012 by Simonato's group.^[42] As shown below, this ground-breaking paper was followed by many other studies focused on the physics of THs based on MNW networks^[43], on the integration of this type of TH into various devices^[22,44,45] as well as on a better understanding and enhancement of these THs.^[46–48] More recently, great progress has also been reported on conductive polymers which can now be considered as very efficient materials for THs.^[49] For instance, Simonato's group^[50] has also reported the very first efficient TH exclusively based on thin films of conducting polymers.

While many reports show an intense research activity on each of these TH technologies, there is also active research on multi-layered materials or nanocomposites which can combine the advantages of different materials. For instance, Ko et al. showed that high-performance and flexible R2R sputtered ITO/Ag/ITO multilayers can exhibit a high optical transmittance (88.2 %), low sheet resistance (3 Ω /sq) and can be efficiently integrated in a TH device.^[51] Similarly, Park et al. reported that ITO/Cu/ITO multilayer materials can also show promising electrical and optical performances and good TH integration.^[52] The different technologies will be thoroughly discussed in section 3 of this review.

The main scientific and technological features associated with THs can be listed as follows: thermal response time, steady state temperature, homogeneity, mechanical properties (under bending and/or stretching tests), cycling/thermal/electrical/environmental stability including ageing, electrical and optical properties, fabrication process of the TH (the temperature being a potential issue for some applications), the material used, TH size and, finally, the overall fabrication cost, including both materials and processes.

Expected requirements associated to the TH can drastically differ depending on the targeted applications. For instance, smart windows, windscreens or displays require that the THs and their associated substrates exhibit high optical clarity, i.e. high optical transparency and low haziness (defined as the ratio between diffuse and total transmittance of light). Optical engineering related to THs notably concerns matching the optical index to improve reflection

and transmission properties in the desired wavelength band (i.e. visible and/or NIR spectra). The thermal response time is also a crucial parameter. The targeted steady state temperature of THs can be very different depending on the application. For smart windows applications, the thermochromic transition (i.e. metal-insulator transition) associated to hybridized VO₂/Graphene is about 60 °C^[53]. A low temperature is generally required for de-icing or defogging uses (below 30 °C). Some other applications need much higher temperatures, like fast defrosting in automotive or for gas sensors (see section 4 of this review). In these cases the chosen material for the TH should exhibit a very good thermal and electrical stability. TH stability can be a serious issue, especially when numerous cycles are foreseen during the lifetime of the device. It is worth noting that stability is related to several other aspects, including potential cycling/thermal/time/electrical/environmental issues. These crucial aspects will also be addressed in this review. The homogeneity of THs plays a key role for many applications. For example, this is essential for eye comfort when THs are used in windscreens, while hot spots can potentially be at the origin of the TH degradation.^[54]

As for all industrial devices, cost is overwhelmingly important to propel the commercialization and large industrial production (e.g., adding a TH within a ski or motorcycle helmet visor should only cost a few euros), with only a handful of exceptions like spatial applications.

This review is organized as follows. The main physical mechanisms associated with THs are presented in part 2.1, as well as simple physical models developed to better understand TH behavior. The main experimental methods currently used to investigate and explore the critical properties of THs will be described in part 2.2. Stability issues are thoroughly considered in section 2.3, from their physical origin to the solution for stability enhancement. Each TH technology (i.e. associated to specific material) is detailed. A thorough comparison and critical discussion of the different active materials are reported in section 3. Part 4 focuses on the integration of THs in different devices with specific associated requirements and performances. Finally, part 5 gives an overview of the main challenges that lie ahead and the main prospects related to THs in terms of better physical understanding, better performances and stability, as well as their future integration into industrial devices.

2 Principle of transparent heaters (THs):

2.1 Introduction to the thermal physics of THs

As stated above, THs are based on the Joule effect. Joule's law, experimentally demonstrated by J.P. Joule (1818-1889), states that when an electrical current I crosses a homogeneous conductive material with an electrical resistance R , the amount of heat released is equal to I^2R per unit of time. The power dissipated in the material is directly related to the achieved steady-state temperature, through a balance between the Joule effect and heat loss. These thermal losses are schematically presented in **Figure 1a**: they correspond to the total heat transfer from the TH and are associated to three main physical origins: i/ thermal conduction to the substrate or through any conducting connections, ii/ convection to the surrounding air and iii/ radiation emitted from the hot surfaces. Figure 1b exhibits some TH applications (medical, defogging, thermochromic), with characteristic values of temperature and areal power density. Several TH technologies do exist, and their corresponding temperature ranges are roughly presented in

Figure 1b in dashed lines. That being said, these temperatures depend upon the TH fabrication process and the experimental conditions under which the TH is used for a given application. Figure 1c reports the typical performance of the main TH technologies in terms of optical transparency Tr (the substrate transparency being subtracted) versus the electrical sheet resistance R_{sh} . The ongoing efforts by the community are focused on fabricating THs which are, simultaneously, as transparent and as conductive as possible (i.e. with a low sheet resistance). There is a trade-off between these two properties since for a homogeneous transparent conductive layer, the thicker the layer the lower the sheet resistance, but also the lower the optical transparency. This trade-off can be approached thanks to a figure of merit (FoM). For transparent electrodes (TEs), two main figures of merit have been proposed thus far. The first one was derived by Haacke et al. in 1976 who proposed to consider the ratio between the 10th power of the total optical transmittance Tr divided by the sheet resistance R_{sh} : Tr^{10}/R_{sh} .^[55] Haacke's FoM is very often used when dealing with transparent electrodes applications (such as photovoltaic or displays) but also for TH investigations. Another figure of merit was later derived by Coleman's group, who considered the ratio between the electrical conductivity and the optical conductivity (equal to the optical absorption coefficient divided by the free space impedance Z_0 (the latter is equal to: $1/(c \cdot \epsilon_0)$, where c is the speed of light and ϵ_0 the permittivity of free space).^[33] Both these FoMs are used as guides for comparing TEs and THs. Although they make physical sense for homogeneous and continuous thin layers, they have to be considered with more caution for non-homogeneous layers such as CNT networks, metallic grids, or MNW networks. For example, in the case of very long 1D conductive objects, a very high FoM could be obtained even if it does not present high homogeneity or usefulness for device integration. Different values of Haacke's FoM are plotted in Figure 1c, showing that there is a good variety of TH technologies that exhibit very good electrical and optical properties, and that are therefore well suited for TH integration. Other parameters of TH applications have to be taken in consideration as well; for instance, graphene appears to be less conductive and therefore it will not be used alone for fast TH operation, as discussed in section 3.5.4. Chen et al. reported recently copper grid TH with an outstanding Haacke's FoM over $7820 \cdot 10^{-3} \Omega/\text{sq}$ (see Figure 1c), and a fast heating rate at low voltage.^[56] This clearly illustrates the efficiency of such technology as TH.

Figure 1d exhibits the time-dependent temperature of graphene-based THs with two different doping agents, and an ITO-based TH for the sake of comparison.^[57] During the "ON" voltage state, the classical time-dependent behavior shows a linear increase at first, followed by a saturation to a steady-state temperature. The three different materials used have different initial R_{sh} and therefore exhibit different steady-state temperatures for the same applied voltage (here 12 volts).^[57] Sorel et al.^[43] gave a comprehensive and thorough description of the theory of Joule heating in a TH in general, and focused in more detail on THs based on silver nanowire networks. But similar approaches can also be found for other types of TH technologies, such as graphene^[83]. In general, the main key parameters for a TH are the steady-state temperature T_{stab} , and the time needed to approach T_{stab} . Most THs are supposed to reach the desired temperature by using a rather low voltage (< 12 V for standard uses) and after a relatively short response time (i.e. from a few seconds to a few minutes). Considering that the temperature is uniform across the whole TH, the energy balance at a given time t can be written as follows (conduction losses due to external parts of the system are neglected)^[43]:

$$I^2R = (m_1C_1 + m_2C_2) \frac{dT(t)}{dt} + A(h_1 + h_2)(T(t) - T_0) + \sigma A(\varepsilon_1 + \varepsilon_2)(T(t)^4 - T_0^4) \quad (1)$$

For each parameter, the indexes 1 and 2 correspond to the TH and the substrate, respectively; the instantaneous sample temperature is $T(t)$, while the ambient temperature is T_0 . In eq. 1, the term on the left is the dissipated heat per unit of time. The first term on the right is the sum of the heat per unit of time associated to the TH and to the substrate (transported via thermal conduction). This heat is responsible for the temperature elevation of the sample through the specific heat capacities C , with m_1 and m_2 being the mass of the TH itself and of the substrate respectively. The second term represents the heat losses per unit of time by convection, with h_1 and h_2 being the convective heat-transfer coefficients and A the film area, assumed to be equal to the substrate area.

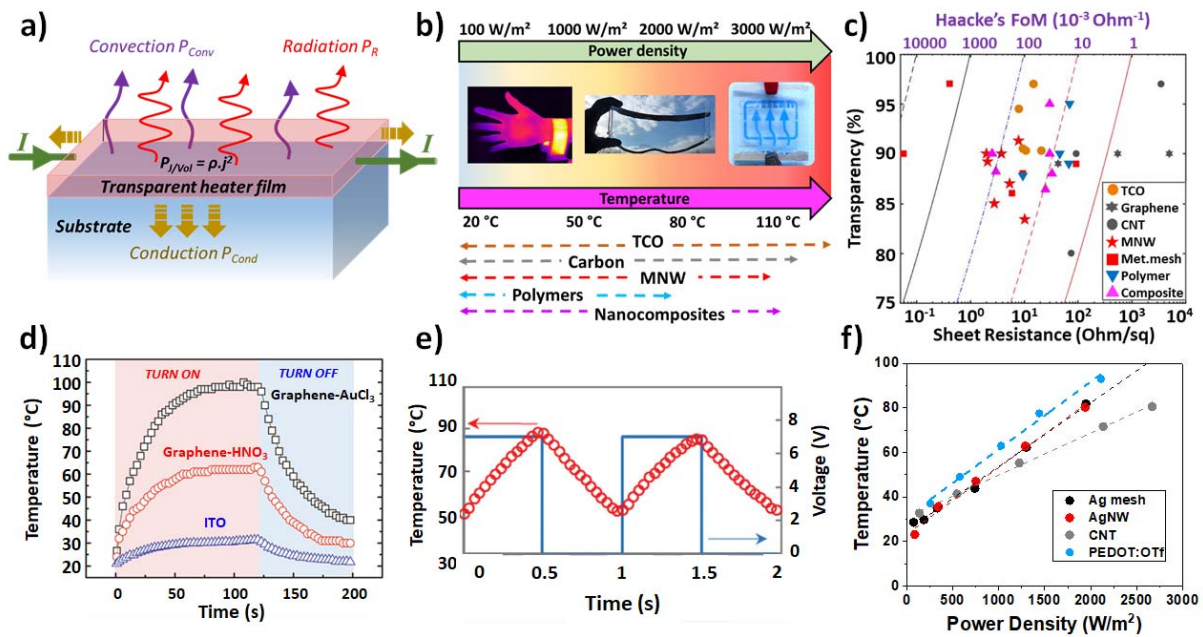


Figure 1. Main features of THs. a) Schematic of a TH: the thin TH is crossed by an electrical current, leading to heat production thanks to the Joule effect. A steady state is reached once this generated heat is equal to the sum of the heat losses shown with different colors. b) Main application domains of THs versus areal power density or temperature required. The arrows below represent roughly the typical maximum steady-state temperatures for the main TH technologies. c) Optical transparency versus sheet resistance diagram for different TH technologies based on: transparent conductive oxides (TCO)^[14,33,58–60], carbon nanotubes (CNT)^[27,33,61], graphene^[57,62,63], metallic nanowire (MNW) networks^[64–70], metallic grids-meshes^[56,71–76], conductive polymers^[49,50,77,78], nanocomposites^[22,48,51,79–81]. The dashed lines correspond to different values of Haacke's *FoM*: 10000, 1000, 100, 10, 1 times $10^{-3} \Omega/\text{sq}^{-1}$. d) Time-dependence of temperature for graphene-based and ITO-based THs, showing the presence of a transitional and steady-state regimes. The optical transmittance of ITO is 95.6% and those of graphene-based THs are 88.5% and 87.5%, respectively for AuCl_3 and HNO_3 doping protocols. Reproduced with permission.^[57] Copyright 2011, American Chemical Society. e) Time-dependence of temperature during voltage cycling showing a very fast thermal response when a TH (here composed of a carbon nanotube network) is deposited on a very thin substrate (12 $\Omega\cdot\text{m}$ thick mica)^[61], in agreement with eq.4. Reproduced with permission.^[61] Copyright 2017, AIP Publishing f) Areal power density dependence of the stabilized temperatures measured for different TH technologies: a linear dependency is generally observed at least for temperatures lower than 100 °C (data for TH based on AgNW^[46], Ag mesh^[82], CNT^[61], PEDOT:OTf^[50]). The slope appears rather similar for the different TH technologies.

Finally, the third term stands for the heat losses by radiation, where σ is the Stefan-Boltzmann constant and ε_1 and ε_2 the emissivity of the TH and of the substrate, respectively. Considering small temperature rises, allowing a linear expansion of eq.1 (the non-linear term associated to radiation losses being neglected) and with the hypothesis that the TH has a much lower heat capacity compared to the substrate ($m_1C_1 \ll m_2C_2$), the energy balance then has the following analytical formula^[43]:

$$\Delta T(t) = T(t) - T_0 \approx \frac{1}{\alpha} \frac{I^2 R}{A} \left[1 - \exp\left(-\frac{\alpha}{m_2 C_2 / A} t\right) \right] \quad (2)$$

where α is the heat transfer constant, which takes into account the parameters of heat losses expressed as follows:

$$\alpha = (h_1 + h_2) + 4(\varepsilon_1 + \varepsilon_2)\sigma T_0^3 \quad (3)$$

Eq. (2) shows that there is a transitional state for a short time, i.e. for a small t compared to the characteristic time τ , while for times much larger than τ , a steady-state temperature is achieved and the saturation temperature is then equal to: $\frac{1}{\alpha} \frac{I^2 R}{A}$. The expression of τ is given by:

$$\tau = \frac{m_2 C_2}{\alpha A} = \frac{\rho_{sub} t_{sub} C_{sub}}{\alpha} \quad (4)$$

where ρ_{sub} , t_{sub} and C_{sub} are, respectively, the density, thickness and specific heat (per unit of volume) of the substrate. After a time $t=\tau$, the temperature reaches 63% of the saturation temperature. Another characteristic time, called the response time, is also often used in the literature: it is defined as the time required to reach 90% of the steady-state temperature, its value being equal to $\text{Ln}(0.1) \tau$, i.e. 2.3τ .

The existence of both transitional and steady-state temperatures is validated by experimental observations, as shown in Figure 1d. τ is generally found to be between 10 and a few hundreds of seconds for the great majority of experimental reports. As a first approximation, this value does not depend much on the material that composes the TH. Accordingly, this range of τ values was observed for THs composed of AgNW networks^[45], CNT networks^[27], TCO^[84], conductive polymers^[50], electrospun nanofibers^[76,85] or graphene^[86]. For efficient THs, the τ value mainly depends on the characteristics of the substrate: the thinner the substrate, the shorter the characteristic time. For example, the steady state temperature was achieved within 10 s when graphene films were deposited on a 50 μm thick polyimide (PI) film, while it took 80 s using 1 mm thick quartz as a substrate^[86]. This is coherent with equation (4). For very small substrate thicknesses τ can be very short too. Kim et al. demonstrated, as depicted in Figure 1e, that the use of single-walled carbon nanotubes (SWNTs) on a very thin polymeric substrate (12 μm thick) leads to a fast response: a temperature of 100 °C could be reached within 1 s with an input voltage of 7 V^[61]. Ke et al. used the same idea and obtained similar results on Al-doped zinc oxide deposited on 25, 65 and 100 micron thick mica substrates^[60].

According to equation (2), the steady-state temperature elevation, ΔT_{stab} , appears to be directly proportional to the applied areal power density and, as a first approximation, does not drastically depend on the TH type. Figure 1f presents the areal power density dependence of the stabilized temperatures measured for different TH technologies and demonstrates this trend. A linear dependency is generally observed (data for TH based on AgNW^[46], Ag mesh^[82], CNT^[61], PEDOT:OTf^[50]) at least for temperatures lower than 100 °C. The slope appears rather similar for the different TH technologies. These slopes depend on the different thermal losses which vary also according to the surface properties of the TH thin film and the substrate^[60]. The

different thermal losses are convection, infra-red radiation and thermal conduction outside the TH itself (through the TH substrate/holder or the electrical connecting wires). Several investigations have tried to estimate the contribution of each thermal loss mechanism, which in turn depends on the substrate, temperature and TH material used. Sorel et al. discussed their dependence versus AgNW network density and showed that there is an increase in convection losses for denser networks which is caused by a higher surface roughness and higher internal area^[43]. The thermal conductivity and thickness of the substrate play a key role for thermal conduction losses. In general, radiative losses are negligible compared to conductive and/or convective losses, at least at low temperatures. Conversely, for high temperatures the radiative losses can contribute significantly, and the linear approximation is not valid anymore. The linear dependence between the steady-state temperature and the areal power density is therefore not valid anymore. For instance, Ji et al. reported the fabrication of highly-stable THs based on ultra-long copper nanofiber networks that can be heated up to 800 °C^[87]. In this case, the steady-state temperature versus heat power does not show a linear dependence in the entire temperature range (as reported in the supplementary information of Ji et al.)^[87] Interestingly, comparing the same TH in air and in vacuum conditions allows us to disentangle convective losses from conduction and radiation losses. Lagrange et al. performed similar experiments on AgNW networks deposited on glass^[46]: in air and in vacuum the temperature elevations increase linearly with the areal power density, but with different slopes. The difference between these two slopes (23.8 and 28.1 W.m⁻².K⁻¹ in vacuum and in air, respectively) allows us to deduce convective thermal losses: $h_{convective}$ could be estimated as 4.3 W.m⁻².K⁻¹.^[46] Another interesting discussion was also reported by Kang et al. regarding the influence of the CNT film density on the different types of heat-transfer losses.^[88] This can be understood through the heat-transfer losses that are directly related to the porous morphology of the CNT network.^[88] One can already classify THs into two different categories: on one side, the homogeneous layers like transparent conductive oxides (TCO), graphene, multilayers (composed of a thin metal surrounded by oxide layers) or conductive polymer films; on the other side, networks composed of carbon nanotubes, metallic nanowires, meshes and fibers. While the first category is supposed to heat homogeneously the whole TH surface, the second category can induce local heating due to its non-homogeneous nature, if heat does not diffuse along both the active material and/or the substrate quickly enough^[54]. These hotspots can induce local degradation within the TH and are therefore an issue to be dealt with. Das et al. investigated scaling in self-heated percolating networks and concluded that hotspot clustering appears to be a mechanism analogous to crystallization physics^[89]. The potential presence of hotspots will be discussed in this review, since their presence can lead to TH instability. In brief, the thermal stability of the TH can be limited to the TH itself (e.g. degradation of the conductive polymer or morphological instability of silver nanowires^[90]) or to the substrate as well. Specifically, for polymeric substrates or low-quality glass substrates, heating can lead to local melting of the polymer or cracking of the glass substrate. For instance, Maize et al. recently used the thermo-reflectance technique to observe “super-Joule” heating hotspots in graphene and AgNW networks^[91], while the latter would have appeared homogeneous using a macroscopic infrared technique. This emphasizes the importance of spatial resolution in temperature observations and this point, among others, is discussed in the following section devoted to the experimental methods used to investigate the main properties of THs. It is worth mentioning that industrial needs require

that a good heater should exhibit uniform thermal distribution over the heating area and achieve the target temperature often with a low voltage (i.e. below 12 V).

2.2 Experimental methods to investigate the main properties of THs

This section aims at introducing the main properties of THs and the experimental methods used to investigate them. Generally speaking, a TH is considered efficient if it shows low electrical resistance, high optical transmittance at least in the visible range, a controllable heating rate, good stability and a low haze factor. We will first focus on electrical resistance and optical transparency. Then, we will present the methods to investigate the basic operating modes of a TH, the heating performances, which are particularly studied by temperature measurements at different length scales. This enables us to measure characteristic features like the heating rate and the relationship between temperature and areal heat power density. Regarding the temperature, there are several ways to measure it through direct contact or contactless means, and with different spatial resolutions, as illustrated below. Since the market appeals prompt research for flexible (or even stretchable) TH, the methods to investigate their mechanical properties are also discussed. Thermal, electrical, humidity and/or mechanical stresses are also reviewed. Finally, other TH features like haze factor, adhesion and roughness are briefly described, as well as their experimental investigation.

Electrical properties. Electrical resistance is a key property of THs, and is evaluated using several experimental methods. The sheet resistance R_{sh} (in Ω/sq) is traditionally used to characterize uniform thin films, since it provides a direct and local measurement of electrical properties, independent of specimen size. The four-point probe method allows a precise measurement of R_{sh} since it eliminates the contributions of electrical wiring and contacts to the global electrical resistance.^[92] This method is generally performed for emerging Transparent Conductive Materials (TCMs) such as thin films or metallic nanowire networks, despite being a direct contact method which can induce local damage. This electrical measurement is very valuable for estimating the electrical homogeneity of a sample by measuring its electrical performance in many different areas. As a first approximation and for a homogeneous layer, R_{sh} is equal to the ratio between electrical resistivity and layer thickness, the latter being often measured by an electronic microscope, a profilometer, Atomic Force Microscopy (AFM) or an ellipsometer. Basic two-point probes can also provide the electrical resistance on samples. In general, two parallel electrodes at opposite sides of the specimen are fabricated using silver inks or metallic layers deposited by evaporation or sputtering. This two-probe method is generally used to follow in-situ the electrical resistance measured during voltage or thermal ramps^[46,90]. For a homogeneous square layer with good electrical conductivity, the 4-probe and 2-probe methods are expected to provide similar results. Another tool to investigate electrical homogeneity is the one-probe electrical mapping, which draws up a cartography of voltage distribution.^[93] In addition, terahertz spectroscopy has been used for non-contact measurement of the conductance of AgNW networks.^[94]

Optical properties. A critical feature of THs is their optical transparency. As shown in **Figure 2a**, TCOs like FTO exhibit a very good transparency in the visible spectrum (390 to 700 nm).

However, their optical transmittances decrease dramatically in the NIR spectrum due to plasmonic absorption (as described in section 3.1). Emerging TCMs such as metallic grids, or metallic nanowire and CNT networks, allow the incident light to be transmitted through the non-covered empty substrate spaces, and thus they remain transparent to a great extent in the whole VIS-NIR spectrum. The transmittance of an AgNW network is shown in Figure 2a: this network is still very transparent in the NIR region. In the case of THs, most applications are in the visible range, which explains why most reports present only visible light measurements. Total transmission can be measured precisely by UV-visible-NIR spectrophotometry with an integrating sphere, as schematically depicted in Figure 2b. There are also small and handy instruments like tint meters, which provide transparency values at a certain visible wavelength, usually 550 nm (light wavelength for maximum efficiency of human eyes). Generally speaking, the optical transparency is either reported in literature at this wavelength of 550 nm or averaged over a typical range of 370-700 nm (i.e. the visible range), but unfortunately it is not always reported whether authors refer to specular (i.e. direct) or total transmittance. The measurement of diffuse transmission is of crucial importance. It is generally expressed through the haze factor, defined as the ratio between the diffuse and total transmittances (Figure 2b). Figure 2c shows a typical example of a low and a highly diffuse/hazy FTO. The non-hazy FTO is the usual FTO layer deposited on a glass substrate, while the diffuse FTO was fabricated by depositing oxide nanoparticles before FTO deposition^[59,95]. The required haze factor values depend drastically upon the desired application. For displays or window defrosting, low haze values are mandatory. For other applications, however, this is less stringent. Although it is an important characteristic, TH haziness is not often reported, preventing the complete benchmarking of TH technologies. In the case of AgNW networks, the haze factor is directly proportional to the areal mass density (usually expressed in mg m^{-2}).^[64] Moreover, it has been reported that decreasing the diameter or extending the length of AgNWs leads to lower haze factors.^[96,97]

Temperature measurement. The accurate measurement of temperature is essential for the fine characterization of THs. Measurements of the temperature produced by THs as a function of the input voltage or other tuned parameters is expected with high temporal and spatial resolutions. One can calculate and/or define other characteristic properties that were discussed in the previous section 2.1, such as steady-state temperature, heating rate, operating voltage, heat power density, thermal resistance or conductivity, heat transfer coefficient, etc. A common choice for measuring the temperature is the use of a thermocouple, directly connected to the studied sample or device. Thermocouples are cheap and cover a wide range of temperatures. There are several suitable types of thermocouples depending on applications and the temperature ranges.^[98] The most reported thermocouple in the case of THs is the type K thermocouple. Another way to measure the temperature by direct contact is the use of resistance temperature detectors (RTD) which are based on the increasing electrical resistance of conductors with increasing temperatures. The platinum RTD in particular displays a superior stability and excellent repeatability, but is more expensive than common thermocouples, and has a narrower range of temperature measurement.^[99] Although these types of thermometers are accurate and easy to use, some studies on THs require a precise mapping of the temperature distribution that cannot be performed properly with the sensors described above.

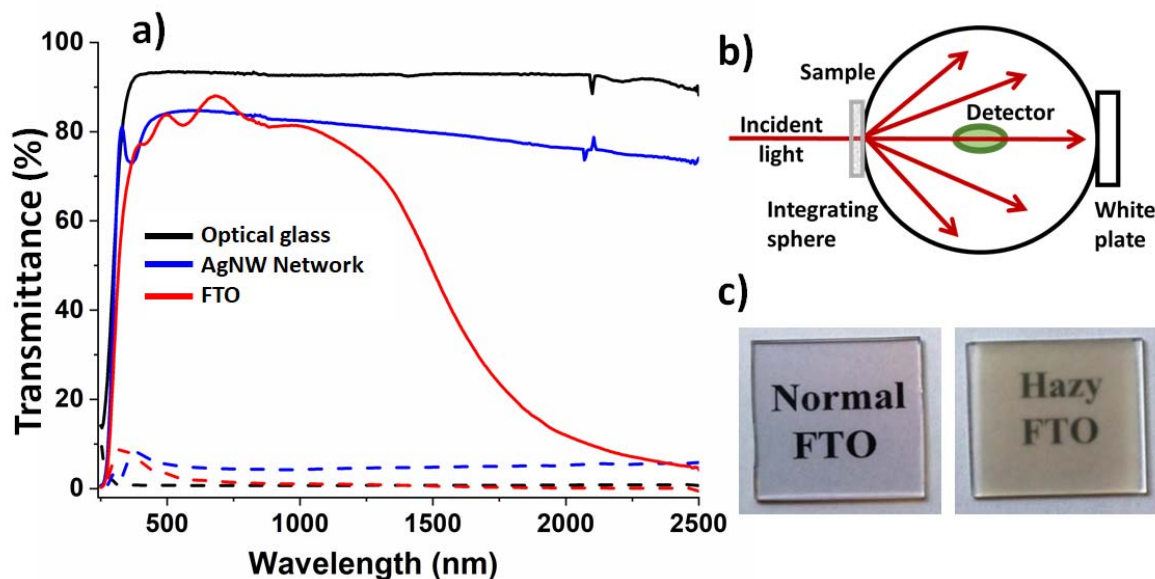


Figure 2. Optical transmittance of transparent heaters (TH). a) Total and diffuse transmittance, shown respectively in continuous and dashed lines, for an AgNW network and an FTO layer deposited on bare optical glass. Both layers have a sheet resistance close to 20 Ω /sq. Metallic nanowire networks are transparent in the NIR region. b) Schematic representation of the spectrophotometer with the integrating sphere. Total (diffuse) transmittance is measured with (without) the white plate to include (exclude) the specular transmittance. c) Pictures of non-hazy (left) and hazy (right) FTO layers on 25x25 mm² glass substrates.

Thermal imaging IR cameras detecting radiations in the mid or long-IR range of the electromagnetic spectrum are appropriate. They have become an indispensable experimental tool for specific temperature measurements. The spatial distribution of temperature is an important advantage of IR imaging since it allows the investigation of heating homogeneity, reveals defects that are optically invisible, and moreover it provides the temperature distribution globally in a device and its environment. Radiative temperature measuring is a non-contact method that can be much more convenient when it is hard or impossible to contact with the studied TH. However, IR imaging gives access only to the surface temperature, which is a clear disadvantage, but this does not appear to be a problem for THs since the active films are very thin. Some key parameters for an IR camera are the temperature range and the thermal sensitivity, the spatial resolution and the frame rate. The pixel pitch of these cameras has decreased to 10 microns, and recent studies suggest that it can be lowered down to 5 microns.^[100] Other critical issues of IR imaging are emissivity and reflection. In modern IR cameras these parameters can generally be set by the operator. Almost all of the reported studies for THs use IR imaging. Emissivity is rarely investigated experimentally^[101,102]; that being said, Kim et al. showed that for AgNW-carbon hybrid THs, the emissivity of the tested film heater decreased linearly with the AgNW content^[102]. This information is useful for the quantitative assessment of thermal losses. Finally, another method with higher sensitivity and a submicron spatial resolution is thermoreflectance (TR). It detects temperature changes near the surface using the relationship between optical reflectance and temperature.^[103] It is used for very specific temperature studies, and not to record the temperature in large areas since it is difficult to define an accurate absolute temperature. In the case of AgNW networks for example, TR

imaging can record hotspots of individual nanowire junctions in the 300x300 nanometer region size.^[91] In another case a picosecond TR technique was used to study the thermal diffusivity of 30 to 70 nm thick ITO thin films.^[104] **Figure 3** presents examples of IR and TR imaging with the corresponding size scales. Figure 3a represents the temperature profile of AgNW-rGO (reduced graphene oxide), measured by an IR camera with a low pixel resolution of 250 μm x 250 μm . This roughly corresponds to an area with more than one hundred nanowires.^[54] A comparable technique used to reveal defects in microelectronic devices is lock-in thermography (LiT).^[105] It can provide an IR emission intensity and a heat timing map^[106] but does not include any thermal calibration or numerical scale. However, as shown in Figure 3b, it appears very useful to visualize the electrical and thermal distribution in the case of MNW networks. It enables us to investigate the activation of efficient percolating pathways and the detection of hot spots under electrical stress.^[107] In the case of the IR camera shown in Figure 3c, the higher resolution of 1.6 μm helps identify the temperature of each channel of the metal crack template.^[108] Finally, Figure 3d shows how advantageous TR can be to perform temperature studies, for example to image hot spots and nanowire junctions.^[91]

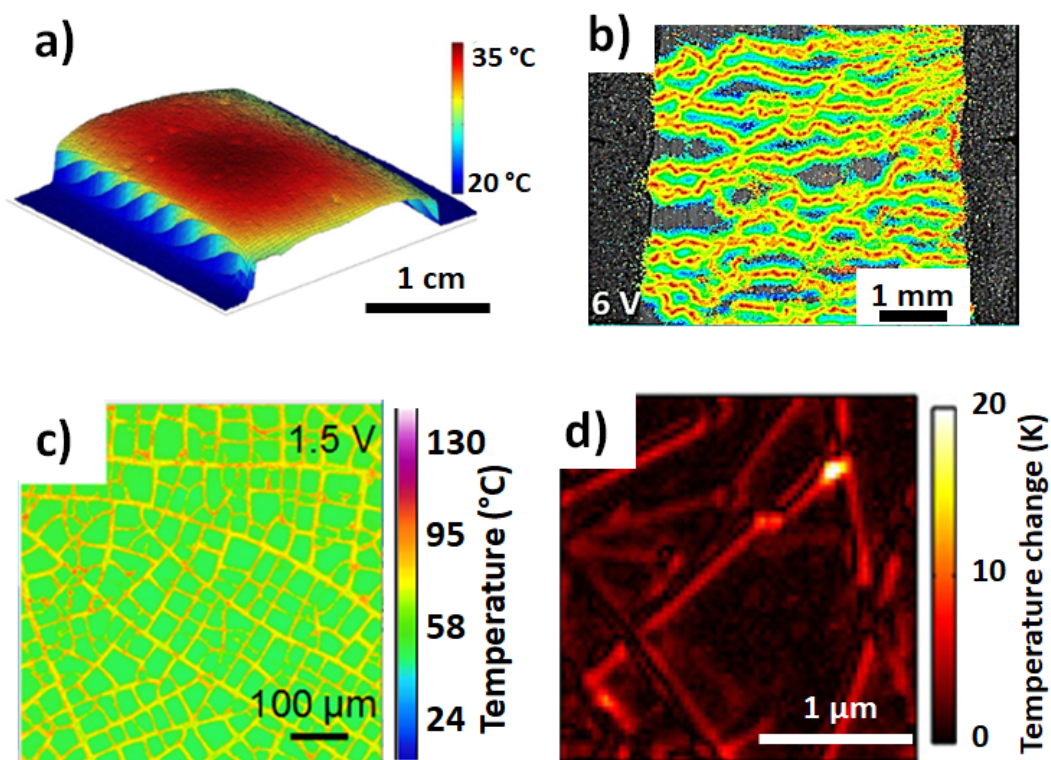


Figure 3. Thermal imaging methods for characterizing THs at different length scales. a) 3D temperature profile measured using an IR camera with 250 μm x 250 μm pixels, for AgNW-rGO after applying an electrical current of 20 mA for 60 s. Reproduced with permission.^[54] Copyright 2017, IOP Publishing. b) LiT image of an AgNW network. The efficient percolating pathways can be detected in brighter colors with a camera of 640 \times 512 pixels resolution with 10 Hz “ON-OFF” voltage cycles of 6V. Reproduced with permission.^[107] Copyright 2016, American Chemical Society. c) Thermal map of a metal mesh network fabricated from a crack template under 1.5 V, with IR imaging with 1.6 μm resolution. Reproduced with permission.^[108] Copyright 2017, American Chemical Society. d) Enlarged region of a nanowire network channel, showing representative hotspots using thermoreflectance (TR) imaging. Reproduced with permission.^[91] Copyright 2015, American Chemical Society.

The different types of temperature measurements are carried out and presented as a function of the electrical properties, since the Joule effect is responsible for the heating. As mentioned previously, the steady-state temperature (T_{steady}) is an important feature for THs and can be studied experimentally by applying a constant voltage or areal power density. The time necessary to reach the steady-state temperature is also measured, and the heating rate is usually calculated and reported with the corresponding value of the applied voltage. Plotting T_{steady} versus the input power density values shows a linear relationship, with the slope coefficient representing the thermal resistance per unit of area. Another typical experiment related to performance measurements of THs is the cyclability or “ON-OFF” test, which consists of switching between the on and off states of the applied bias for a large number of operating cycles.^[102,109]

Mechanical properties. The first application of THs was during World War II, with the use of stiff tin oxide to defrost the cockpit windshields of aircrafts to allow them to fly at higher altitudes.^[2] These past years, the development of nanotechnology and advances in flexible electronics have given rise to a huge variety of applications that require excellent stability under mechanical stresses (flexibility and even stretchability). As explained hereinafter, TCOs cannot be integrated into very flexible devices, despite their excellent electrical and optical properties. The high temperature deposition process makes it rather impossible to use flexible and transparent polymers as substrates, because these do not have high thermal resistance.^[110] When they are deposited on flexible substrates, the electrical performance of TCOs is often limited due to deformations that appear on these thin films. On the other hand, the flexibility of emerging materials such as CNTs, metallic grids, MNWs and conductive polymers is one of the main reasons why their study is constantly increasing. The measurement of electrical resistance over thousands of bending cycles is a standard experiment reported in the literature. In general, the bending radius (usually of several mm) is provided. This value is important since it indicates to what extent the TH can be bent, sometimes crumpled. For THs, electrical conductivity must not be altered by mechanical stresses, and the thermal performance should remain stable. In order to estimate the mechanical behavior of THs, the temperature is usually monitored simultaneously to bending. IR imaging, as a contactless method, is particularly convenient for the direct evaluation of performances. **Figure 4a** presents typical examples of bending tests while Figure 4b exhibits stretching tests with concomitant temperature recording by IR camera. Twisting tests, as shown in Figure 4c, are also sometimes reported, depending on the specific application needs. High flexibility has become a common target for emerging TCMs. Interest has also recently been focused on stretchability, which is intrinsically more complicated. The loss of electrical conductivity can be either total, low or negligible depending on several parameters such as the amount of conductive material or the choice of material itself. Ongoing investigations on stretchable THs with an association of different materials (leading to nanocomposites or hybrid materials, see section 3.5) lead to promising features.^[22,70,111] Finally, the incorporation of TCMs into elastic substrates, and the adhesion to various types of substrates is another issue concerning mechanical properties which could influence the performance of TH applications. Embedded structures can be a promising strategy to tackle adhesion issues.^[81] Measuring performance stability after repeating tape tests^[47,112,113] and microscopic observations of the adhesion between the layers are useful techniques to determine the key drivers that should be studied in depth.

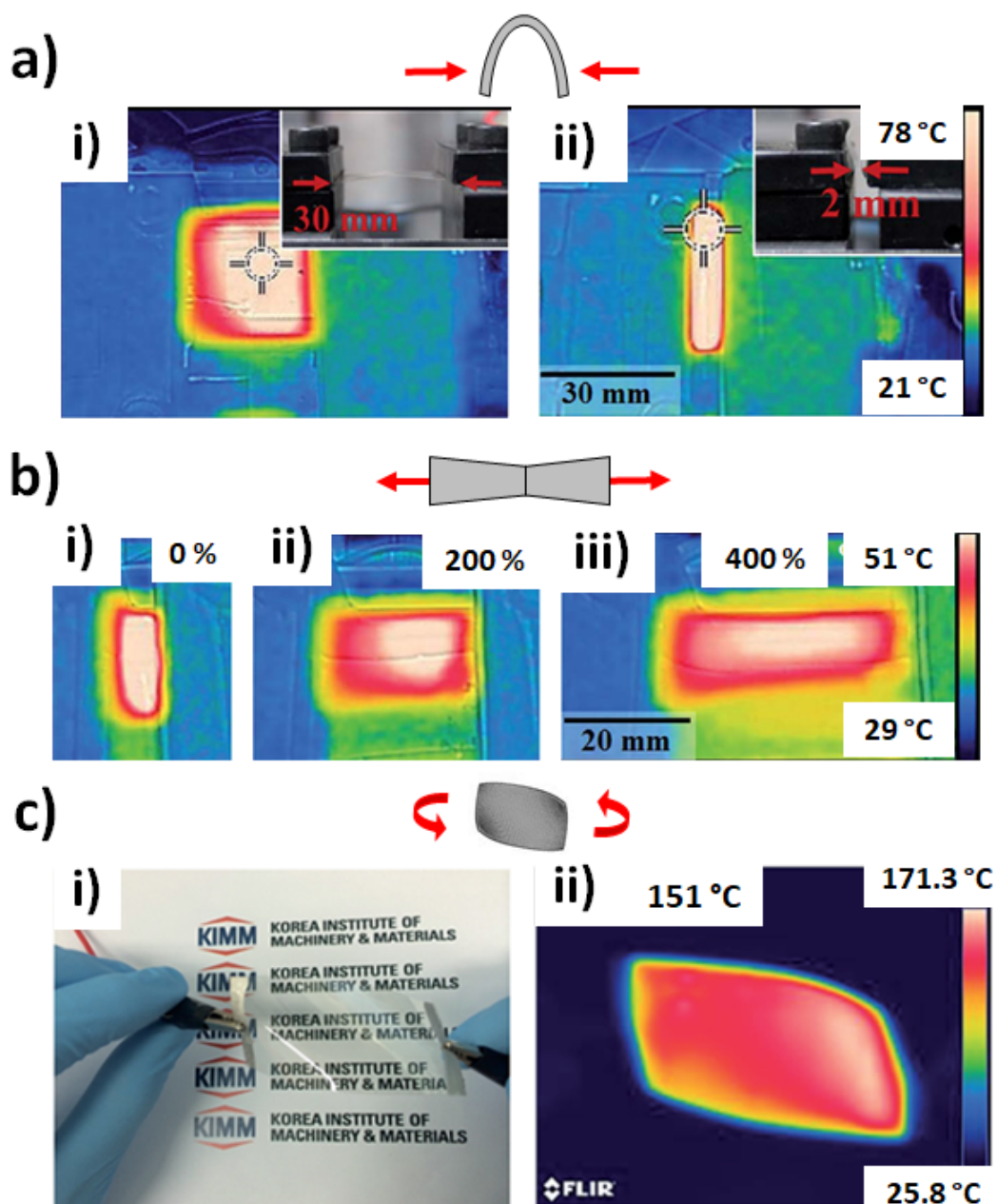


Figure 4. Infrared observations of THs when submitted to different mechanical stress modes. a) Photographs and IR images of an AgNW film during bending tests at i) the initial conformation and ii) the final conformation. The AgNW film ($R_{sh} = 15 \Omega/\text{sq}$, $Tr = 95\%$) was supplied with a voltage of 5 V. b) During the stretching experiment at: i) the initial state ($L = 10 \text{ mm}$), ii) the intermediate stages of stretching with the strain values in percentage shown in the insets, and iii) the final state ($L = 50 \text{ mm}$). The substrate was a stretchable eco-flex. a,b) Reproduced with permission.^[114] Copyright 2017, Royal Society of Chemistry. c) Mechanical flexibility and stability of a CuNi TH on a polymer substrate: i) picture and ii) IR image of the heater at 9 V bias under twisting conditions. Reproduced with permission.^[115] Copyright 2017, Royal Society of Chemistry.

Stability. Electrical, thermal, mechanical and chemical stabilities are key parameters for TH performance. Firstly, it is necessary to verify that electrical conductivity and heat emitted remain stable in the long run when THs undergo electrical stresses. Several tests can be performed, like a voltage ramp and/or plateau cycles with resistance and temperature

recordings. The “ON-OFF” test described above is another typical stability experiment that is performed in most TH studies. The application of a constant voltage/power for hours in order to check if the temperature remains stable^[116] is also usually carried out. In other cases, constantly increasing voltage ramps are applied until the breakdown of the heating performance, followed by the application of lower voltages to investigate potential reversibility.^[46] These experiments have proven that the encapsulation of heating materials with protective coatings is an excellent choice to improve stabilization. Thermal stability is crucial for THs and it is linked to the potential degradation of active materials or surrounding materials due to high operating temperatures and fast heating/cooling rates. A way to study this is to measure electrical resistance under thermal stress (thermal ramps or plateaus) without applying any electrical power (except a very small current for the resistance measurement). It is also important to investigate the intrinsic heat stability of the substrates used to fabricate a TH, especially in the case of flexible polymers, which are known to limit the stability of flexible THs. Regarding chemical oxidation and ageing, typical measurements are carried out in environmental chambers and involve the simultaneous exposure to controlled humidity and temperature, combined with light irradiation^[48,117]. Generally, the relative humidity chosen is over 80 %, and the temperature between 45°C and 90°C, which covers most of the harshest use conditions.^[70,93,118–121] Study durations varies strongly, and usually depends on the anticipated stability of the TH and on the expected lifetime of its components. For example, stability studies for copper nanowire (CuNW)/NPs usually last minutes^[120] or hours^[118,119], while for AgNW the duration of the study can be days^[70] or months^[121]. Of note, there are some large discrepancies in terms of MNW network stability from one research group to another, probably originating from differences in MNW growth conditions and purification processes, leading to different surface chemistries, and consequently to more or less stable MNW networks.

3 The investigated materials technologies for transparent heaters

Several material technologies for TH applications have been thoroughly investigated. The very first type of thin layers were TCOs, which have been investigated for several decades^[2,9,14,17,59]. These thin films of metal oxide have been studied for several applications, including transparent electrodes for solar cells or touch screens, and have already been widely integrated in industrial devices.^[7,10] For THs, like for transparent electrodes, industrial needs have prompted research into other materials^[21]. There are several reasons for this. TCOs, for instance, are ceramic and therefore do not usually withstand any mechanical stress; this makes them incompatible with flexible applications. Moreover, lowering the cost is a strong argument against the vacuum-process and/or the use of indium in the classical indium tin oxide (ITO), due to the scarcity of indium. Likewise, the search for properties that are better adapted to industrial requirements necessitates the exploration of other materials. The goal of this part 3 is to present the main materials categories and their related properties when used for THs. Each type of materials will then be discussed in more detail below, starting with metallic oxide-based materials, then carbon-based nanomaterials (graphene and CNTs), metallic-based materials, conductive polymers and finally nanocomposites or hybrid materials. In this review we consider that *nanocomposites* are materials for which the nanostructures are within a continuous phase such as a matrix, while *hybrid* nanomaterials refer to combination of materials of different natures such as organic-inorganic.

3.1 Metallic oxide-based materials

Among all the different types of TCMs, TCOs were the first to be developed and studied. They have been used industrially for a long time and in many different applications. ITO thin films, in particular, have been employed for the production of THs to defrost aircraft windshields. The basic properties of TCOs have been extensively described in previous works, and we refer the reader to those for additional details^[9,122,123]. Of note, the morphology and structure of TCO thin films play a key role in their conductivity. These thin films usually exhibit polycrystalline structures, as shown in **Figure 5a**, with crystal sizes that depend on the deposition method used and other parameters like film thickness. The latter can easily reach hundreds of nanometers.^[14] Twins are often observed (for FTO for instance), and as in the case of grain boundaries, they are detrimental to charge mobility^[14,59,124]. The fact that grains often become bigger as the film thickness increases has a direct impact on the conductivity of the layers, since the number of grain boundaries and twins decreases (Figure 5b).

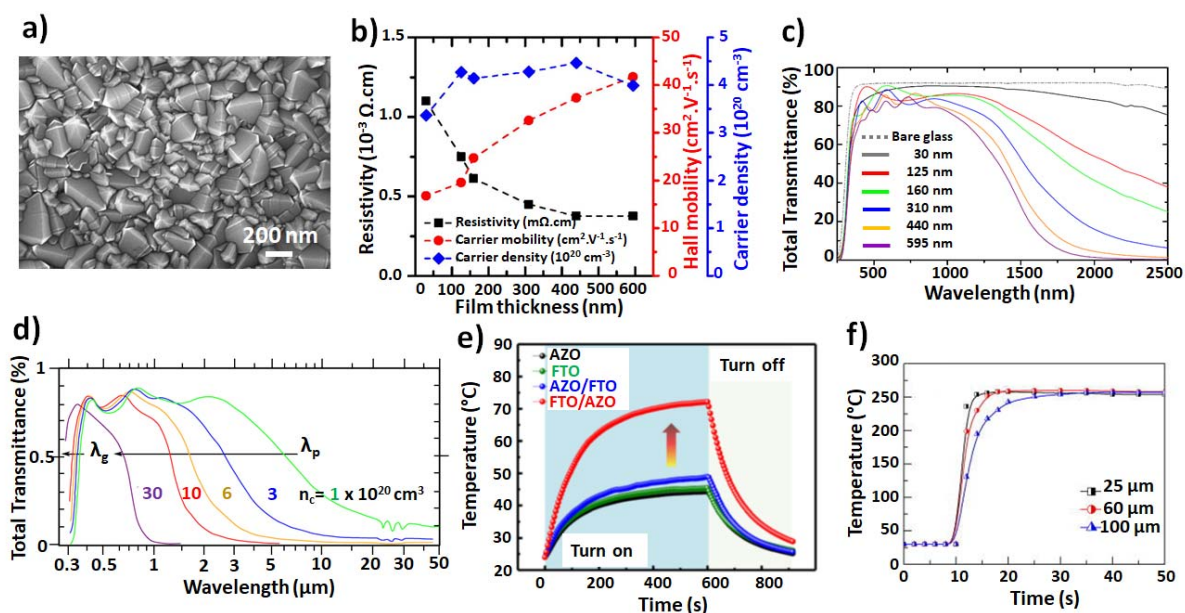


Figure 5. Transparent conductive oxides (TCO) used as THs. a) SEM image of a typical 400 nm thick FTO layer showing the grain-boundary structure of the thin polycrystalline film. b) Main electrical characteristics of FTO layers vs film thickness: electrical resistivity, carrier mobility and carrier density. Reproduced with permission.^[14] Copyright 2013, AIP Publishing. c) Total optical transmittance for different FTO film thicknesses: the thicker the film, the lower the transmittance, specifically in the near infra-red region due to plasmonic absorption. d) Computed spectral normal transmittance of ITO. The values correspond to electron density. Reproduced with permission.^[125] Copyright 1986, AIP Publishing. e) Time dependence of temperature when a 12 V voltage is applied to a TH composed of either an AZO layer (black), a single FTO layer (green), an AZO/FTO (blue) or a FTO/AZO (red) double-layer film on glass which shows different electrical properties. This clearly illustrates the strong influence of the TH electrical properties on the heating performance. Reproduced with permission.^[84] Copyright 2014 John Wiley and Sons. f) Measured temperature vs time for a 100 nm-thick AZO-based TH, deposited on mica substrates of different thicknesses, illustrating the role played by the thermal inertia of the substrate in terms of response time. Reproduced with permission.^[60] Copyright 2018, AIP Publishing.

Another important aspect of TCOs is the fact that transparency in the IR region of the spectrum falls rapidly with film thickness or with carrier concentration due to plasmonic absorption as

shown, respectively, in Figure 5c and 5d.^[20] For TH applications where IR transparency is important, e.g. night vision applications for glasses and binoculars, the TCO technology is therefore not perfectly adapted compared to other TH technologies.

Despite TCOs being the oldest studied TCMs, there are surprisingly few reports in the literature dealing with the application of TCOs as THs. The studies reported so far involve ZnO-based materials, Ga-doped ZnO (GZO)^[126–128] and Al-doped ZnO (AZO)^[60,84,127,129], FTO^[84] and ITO^[130–133]. Indeed, TCOs have been mainly investigated in the framework of industrial research and development, which is generally not associated with scientific publications.

In industry, ITO is routinely deposited by sputtering, a vacuum method that is generally associated with higher costs compared with solution process technologies. Im et al. explored the utilization of ITO nanoparticle (NP) solutions to process ITO thin films^[130] as an alternative to vacuum processing. The films were fabricated by spin-coating the ITO NP solution on a glass substrate, followed by annealing up to 400 °C. The main effect of the annealing step is to sinter the particles. Using these films, a temperature of 163 °C was achieved for a bias voltage of 20 V, and dry-ice was used to demonstrate the defrosting capabilities of the TH.^[130] More recently, Kim et al. used the same approach. However, by increasing the annealing temperature of the deposited ITO NP and by using different atmospheres during the annealing step, they demonstrated that the oxygen vacancies in the film can be controlled^[131]. In this case, temperatures up to 215 °C were reached for a 15V bias, with a thermal efficiency of 162.9 °C/(W/cm²) being obtained for optimized samples. In another study, Yang et al. demonstrated that by adding organic additives such as polymethyl methacrylate and terpineol to the ITO NP solution, the obtained heaters are more efficient and homogeneous. The authors made micro-heaters using this approach, and could reach temperatures of 445 °C for a bias voltage of only 12 V.^[132]

Kim et al. explored the use of bilayers by combining AZO and FTO deposited by sputtering and Chemical Vapor Deposition (CVD), respectively.^[84] They observed that both conductivity and transparency improved for bilayers with respect to single layers of the same thickness, as demonstrated in Figure 5e.^[84] This is attributed to the higher overall particle size in the film, which affects both mobility and transparency. The best results, reported in Figure 5e, were obtained for FTO/AZO bilayers for which temperatures above 70°C were obtained for a bias voltage of 12 V.^[84] Roul et al. studied rigid and flexible AZO-based TCOs by depositing AZO on glass and polyethylene terephthalate (PET) substrates by magnetron sputtering.^[129] The films deposited on glass reached temperatures of approximately 100°C for a 12 V bias for the samples deposited at 200 °C. Flexible heaters made on PET reached 50°C for bias voltages of 8 V. Nevertheless, stability results are only shown for AZO/glass samples, and no study of the effect of bending on the properties of the flexible TH is reported. It is also worth mentioning that ZnO-based TCOs may not be the best candidates for high temperature applications, since ZnO tends to absorb oxygen species in the grain boundaries, which has a detrimental effect on mobility, as explained and modelled recently.^[19] It has been shown that the absorption of oxygen species increases rapidly with temperature^[134], thus most likely limiting the applications of THs based on AZO. Ke et al. showed that despite the ceramic nature of ITO, flexible THs can be obtained by using mica substrates as thin as 15 µm, thanks to their layered structure.^[133] ITO layers of up to 500 nm were deposited by pulsed laser deposition (PLD) at room temperature and annealed at up to 500°C. Flexible THs were fabricated, exhibiting fast ramping.

Temperatures of up to 438 °C were reached in less than 15 s at a bias voltage of 19 V. The same approach was used by the same authors to make flexible THs based on AZO/mica.^[60] Figure 5f shows the measured temperature versus time for a 100 nm-thick AZO-based TH deposited on mica substrates of different thicknesses: this illustrates the role played by the thermal inertia of the substrate,^[60] in agreement with equation (4). Record heating rates of 200 °C/s were obtained in this case. The occurrence of van der Waals epitaxy between the mica substrate and the grown AZO film reasonably explained this superior performance.

Gallium has also traditionally been used to dope ZnO. Jayathilake et al. deposited ZnO co-doped with Al and Ga (AGZO) by aerosol-assisted chemical transport, which showed a lower conductivity than AZO or GZO films^[127]. The films were prepared by dispersing previously prepared AGZO powders (by microwave synthesis) in a methanol solution containing formic acid and cellulose. Then aerosol generated from this suspension was carried by N₂ gas to a glass substrate at 400 °C. Temperatures above 132 °C were achieved in 10 min for bias voltages of 18 V. Older reports on physically deposited GZO films were performed by Kim et al.^[128] and Ahn et al.^[126] In the first case, the films were deposited by rf-magnetron sputtering on glass substrates^[128] and reached 90 °C after 22 s for a bias voltage of 48 V. In the second case, PLD was used to deposit the films on glass substrates, and reached over 88 °C after 48 s for a 12 V bias.^[126]

Thus, while TCOs, and in particular ITO, are the most prominent transparent materials today, with a broad range of industrial applications, fundamental studies involving promising approaches are still being carried out in order to push the limits of these materials in terms of performance and mechanical flexibility. These studies are framed in a wider research that involves the exploration of competing materials, such as carbon-based nanomaterials, which are described in the next section.

3.2 Carbon-based nanomaterials (CNTs & graphene)

Carbon-based thin film heaters were first described in 2007.^[27] Carbon fibers, carbon nanotubes (CNTs) or graphene derivatives have been widely reported in the literature to address several fields of applications including defogging,^[135] anti-icing, de-icing,^[83,136,137] wearable electronics,^[138,139] thermochromic displays^[140,141] or thermomechanical sensors.^[62] Most published studies report the use of carbon-based thin film heaters for the assessment of non-transparent devices. Their high flexibility and stretchability are, without doubt, advantages that make them very interesting for various type of heaters thanks to their remarkable mechanical properties, while conversely they exhibit low transparency.^[57] Since this review focuses on THs, only devices or active materials with good transparency are discussed hereinafter.

Active parts of carbon-based THs can be processed either by dry or solution-based routes, the latter being often more suitable for many supports (PEN, PET, PC, PI or cotton fabrics for example). CNT devices can be produced either through percolative networks implying printing processes^[61], or thanks to CNT forest (aligned CNTs, usually prepared by chemical vapor deposition (CVD) / transfer protocol). For the first method, **Figure 6a** shows an SEM image of a transparent and flexible single wall carbon nanotubes (SWCNT) heater prepared on a plastic substrate, along the associated IR images at various applied voltages.^[61] Regarding graphene and its derivatives, exfoliation of graphite or chemical reduction of GO were reported. Recently, unusual and interesting approaches based on the use of carbon nanosheets from the

carbonization of polymers or from natural carbonaceous by-products of ethylene production were published by Souri et al.^[142] and by Morris et al.^[143], respectively.

Both the deposition processes and the intrinsic properties of the material strongly impact the performances of carbon-based THs. For CNT networks, the trade-off between transparency and conductivity can also be controlled by nanotube types (e.g. single-walled vs multi-walled MWCNT). SWCNTs generally exhibit high transparency and low haze, but rather low conductivity due to the presence of poorly conductive semi-conducting CNTs and resistive CNT-CNT junctions.^[61,144] MWCNT-based electrodes (100% of metallic behavior tubes) are more conductive but less transparent due to their larger size, and exhibit a higher haze value.^[145] Figure 6b exhibits optical and infrared pictures of graphene-based THs illustrating both flexibility and uniformity.^[57] In the case of percolative networks of graphene flakes, each graphene layer decreases the transparency by $\sim 2\text{-}3\%$. However, devices made of a graphene monolayer obtained by dry deposition keep a very high level of transparency, but this technique is somewhat limited to small surfaces. Improvement is still required in terms of uniformity of highly conductive graphene layers and larger surface coverage. Due to the higher electrical contact resistances between the conductive objects of carbon-based networks (CNTs, Carbon flakes) compared to MNW networks, most carbon-based THs require denser systems to reach the same level of conductivity, at the expense of the transparency.

As input voltage and surface temperature are strongly correlated to sheet resistance, in most cases, carbon-based THs are addressed with high input voltages from 10 to 100V for at most a few cm^2 samples. Indeed, transmittances higher than 70% are achievable at several hundreds of Ω/sq .^[146] On polyimide substrates, temperatures higher than 350°C have been reached.^[142] Considering that surface power densities of a few kW/m^2 are required for both thermal comfort and heating, the lifetime and stability of carbon-based materials are a true asset of carbon-based THs. In the case of carbon-based THs, transparency is clearly impaired if one intends to reach low sheet resistance for high heating performance. New developments using carbon nanostructures hybridized with metallic nanowires could provide an interesting alternative since carbon-based materials can significantly enhance the stability of metallic nanowires (See section 3.5.1).

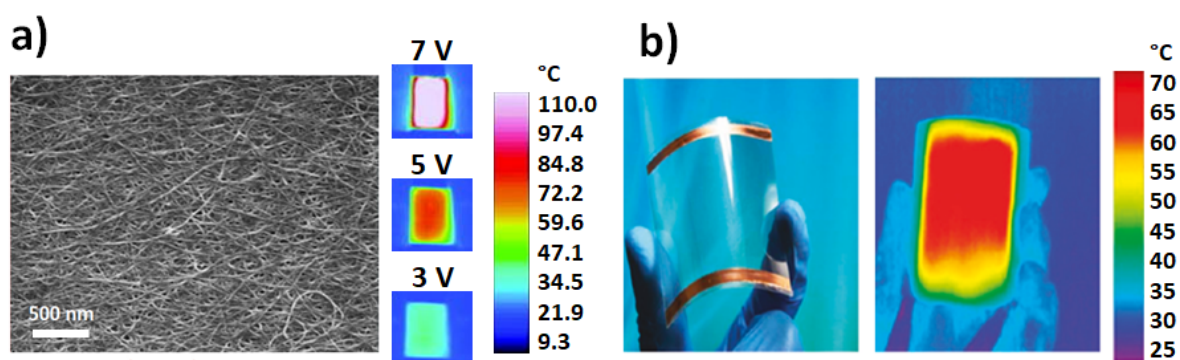


Figure 6. Performances of carbon-based transparent heaters on flexible substrates. a) SEM pictures and infrared pictures of SWCNT-based transparent electrodes when submitted to applied voltages of 3, 5 or 7 volts. Reproduced with permission.^[61] Copyright 2017, AIP Publishing b) Highly flexible graphene-based TH with optical and infrared pictures illustrating both flexibility and uniformity. Reproduced with permission.^[57] Copyright 2011, American Chemical Society.

3.3 Metallic-based materials: metallic grids, metallic meshes, MNW random networks

While TCOs have been largely studied for several decades to be used as transparent electrodes (TEs) or THs, other materials such as metallic-based nanostructures have been considered since the year 2000 approximately^[21,147]. They present additional properties when compared with TCOs, since many of them can be deposited at low temperatures and exhibit good mechanical flexibility. Metals indeed appear attractive as potential TH active materials since they possess very high electrical and thermal conductivities. For instance, silver exhibits the highest conductivities among all materials at room temperature. However, ultrathin metallic films generally do not show an interesting trade-off between optical transparency and sheet resistance, due to both strong light absorption and electron scattering at surfaces or interfaces. As such, the only way to take advantage of metals for TH applications is to engineer metal nanostructures. This can provide interesting opportunities to manipulate photons and electrons in order to achieve electrical, optical and mechanical properties that are not reachable with TCOs. The main metallic patterns that can be efficiently used for TH production are metallic meshes, MNW networks and metallic grids. The difference between metallic grids and meshes in the literature is sometimes confusing. In this review we will consider that *metallic meshes* do not contain privileged directions in terms of conductive lines, while *metallic grids* are constituted by a periodic arrangement of metal lines, generally with a 3- or 4-fold symmetry. In this section, we will briefly examine the different investigated metallic-based materials, by describing their main features, properties and their potential integration into TH devices. Progresses toward low-cost TH fabrication, wire-wire junction resistance, physical properties, adhesion and stability will also briefly be discussed.

Metallic meshes can exhibit some interesting features as THs. As shown by Kiruthika et al. interconnected crackles can be obtained thanks to the spreading of low cost crackle wall paint by using the drop coating technique.^[82] Interconnected Ag meshes can be fabricated by depositing a thin metal layer on top of the obtained crackles and then removing the template. **Figure 7a** shows a typical optical image of an Ag mesh fabricated on glass, while the inset corresponds to the optical profiler image (the thickness is approximately 300 nm).^[82] This type of metallic mesh network exhibits interesting physical properties on large areas. Kiruthika et al. reported a sheet resistance of 1 Ω /sq on an 18x15 cm² area, associated to an optical transmittance of 77%.^[82] Thanks to the low electrical resistance, the use of metallic meshes as THs requires a rather low voltage: an 8.5 V bias was used to reach uniformly heated surfaces of up to 170°C. This efficient defrosting device successfully withstood an ultra-sonication test, as well as many defrosting cycles.^[82] Metallic mesh networks have been the subject of many studies lately, with various metallic species being evaluated, like copper,^[148] silver,^[149,150] nickel,^[151] cupronickel,^[115] gold^[152] and platinum.^[72]

MNW networks have been the subject of a lot of research lately, with a focus on the industrial integration of the networks as transparent electrodes into opto-electronic devices, as recently reviewed by several authors.^[20,38,39,157,158] Among the possible MNW materials, silver has been the most investigated^[33,34,39,159–162], while CuNW networks constitute an interesting alternative.^[48,66,76,163,164] Figure 7b exhibits a high-resolution TEM image of a CuNW showing the 5-fold symmetry.^[66] Figure 7c reports a typical SEM picture of a random AgNW network. The inset shows a TEM image of a well-sintered junction between two AgNWs,^[153] knowing that an efficient local sintering of the junction between the different AgNWs leads to lower

junction's electrical resistance and, therefore, to lower overall network electrical resistance.^[90] While the most used deposition techniques are spin-coating and spray-coating, several original methods have been proposed lately to fabricate AgNW networks with good performances. For instance, Hu et al. proposed a versatile agitation-assisted assembly approach that induces an orientation of AgNWs. This leads to excellent performances with a R_{sh} value of 2.8 Ω/sq , an optical transparency of 85% and a high stretchability of up to 40%.^[68] The electrical resistance of junctions between AgNWs can be reduced by several methods, such as thermal annealing,^[90] UV treatment^[165] or as shown recently by Huang et al. using a self-limited nano-soldering method. This method can decrease R_{sh} from 18.6 to 7.7 Ω/sq while preserving a constant optical transmittance of 90%.^[166] The first demonstration of AgNW networks being efficiently used as THs was published in 2012 by Celle et al.^[42] These authors showed that the intrinsic features of AgNW random networks made it possible to combine bendability, transparency and high heating performances at low voltages (below 12 V), which constitutes a clear asset for integration in many applications.^[42] This demonstration, on both glass and polymeric substrates, was followed by numerous publications. Sorel et al.^[43] published in 2014 a comprehensive physical approach of AgNW network-based THs, including the different regimes associated with low network density (percolative regime) and high network density (bulk-like regime). The authors also provided critical considerations related to electrical conductivity, optical transparency and heat dissipation for efficient THs. Figure 7d shows the relative electrical resistance of different types of TH technologies (ITO, FTO and AgNW) versus the number of bending cycles with a radius of curvature of 5 mm. AgNW networks are much more flexible than TCOs.^[20] However, one of the main issues with MNW networks is their relative low stability under electrical and/or thermal stresses, even at device-operating conditions, as reported in several studies.^[46,54,90,167,168] This is illustrated in Figure 7e, which displays the evolution of the electrical resistance of an AgNW network during a voltage ramp of 0.5 V/min. The electrical resistance exhibits a drastic increase associated to the appearance and propagation of a crack, as revealed by the IR image in the inset (the width of the IR image corresponds to 25 mm).^[93] As reported below (section 3.5.3), the deposition of a thin oxide layer on top of MNW networks drastically enhances their stability or their adhesion.^[47,48,167] These nanocomposites can lead to efficient and stable THs,^[44,46,47,117,169] as discussed further in section 3.5.

Metallic grids have been the subject of a lot of research since they appeared as promising transparent electrodes, with both optical transmittance and sheet resistance being well controlled by adjusting the period and width/thickness of the patterns.^[147,170] The metal lines are thin enough (\sim few μm) to provide a low sheet resistance, while the period of the grid is large enough (\sim 5-200 μm) to provide sufficient transparency but not too large, to ensure heating uniformity over the entire TH. Figure 7f shows a typical optical image of a flexible transparent Au grid electrode with the following geometrical features: grid width of 4.5 μm , grid spacing of 200 μm , Au thickness of \sim 90 nm.^[154] This Au grid electrode exhibits an optical transmittance of 92% at 550 nm and a sheet resistance of 97 Ω/sq .^[154] The fabrication of metal mesh electrodes was originally performed using vapor deposition processes, which require vacuum and generate metal waste. Consequently, many studies have investigated other reliable fabrication methods, and in particular large area printing methods like flexography, slot-casting, screen printing and others. Figure 7g exhibits an AFM profile section of a silver grid, fabricated

by femtosecond laser writing of a silver aqueous solution, which shows the good uniformity of the grid.^[155] This fabrication method possesses advantages in terms of flexibility and adaptability compared to alternative techniques like the combination of metal evaporation and lithography. Figure 7h shows an SEM image of a silver nanoparticle-based (AgNP) metallic grid fabricated by capillary assembly of AgNP.^[156]

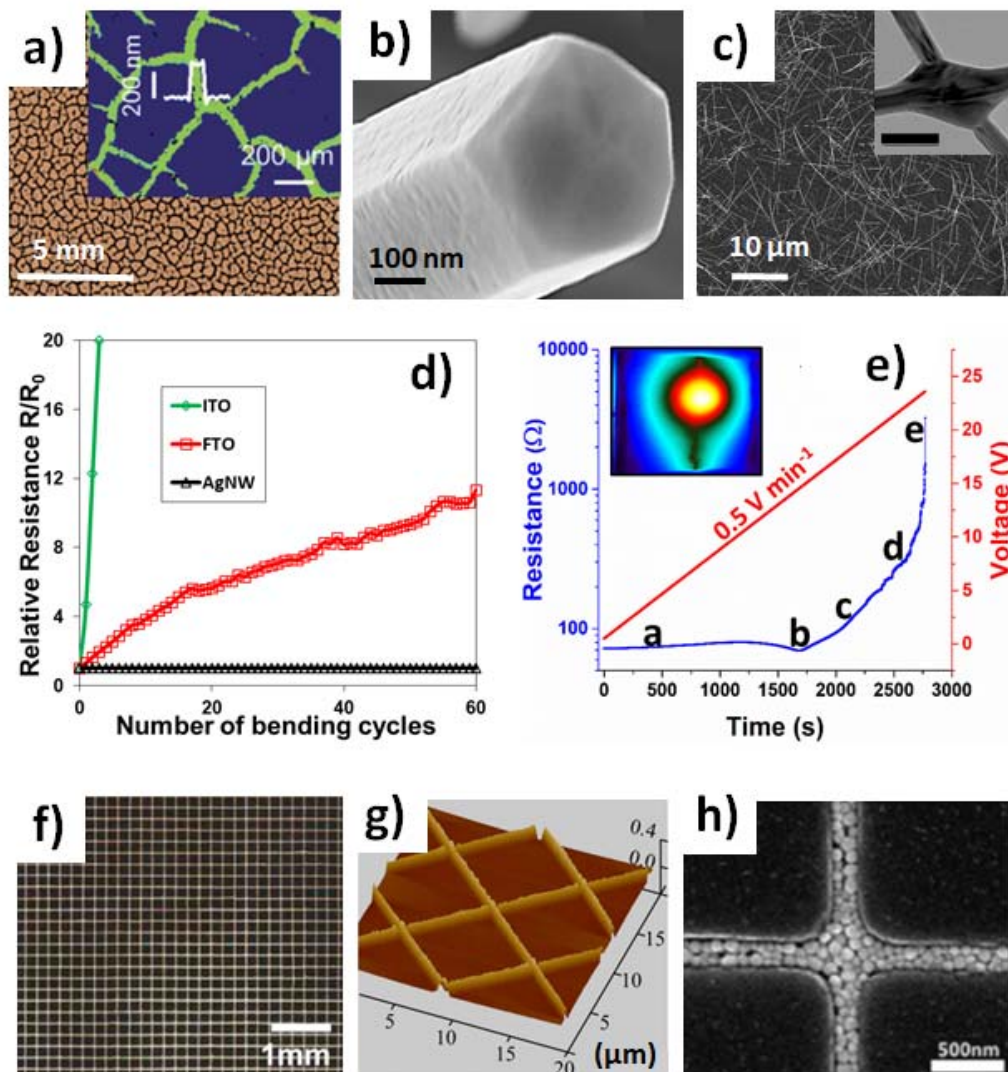


Figure 7. Main features of metallic-based THs. a) Optical image of an Ag mesh fabricated on glass; the inset corresponds to the optical profiler image (thickness of about 300 nm). Reproduced with permission.^[82] Copyright 2014, Royal Society of Chemistry. b) High-resolution SEM image of a copper nanowire (CuNW) with a 5-fold symmetry. Reproduced with permission.^[66] Copyright 2017, John Wiley and Sons. c) Typical SEM picture of an AgNW random network. The inset shows a TEM picture of a sintered junction between two nanowires (bar scale: 100 nm).^[153] d) Relative electrical resistance of different types of TH materials (ITO, FTO and AgNW) versus the number of bending cycles at 5 mm radius of curvature. Reproduced with permission.^[20] Copyright 2016, John Wiley and Sons. e) Evolution of the electrical resistance of an AgNW network during a voltage ramp of 0.5 V/min. The electrical resistance exhibits a drastic increase associated to the appearance and propagation of a crack, as revealed by the IR image in the inset (the width of the IR image corresponds to 25 mm). Reproduced with permission.^[93] Copyright 2018, American Chemical Society. f) Optical microscopy image of a flexible transparent Au grid electrode with the following geometrical features: grid width: 4.5 μm ; grid spacing: 200 μm ; Au thickness: \sim 90 nm. Reproduced with permission.^[154] Copyright 2014, American Chemical Society. g) AFM profile sections of a silver grid fabricated by femtosecond laser writing of a silver aqueous

solution. The profile shows a good uniformity of the grid. Reproduced with permission.^[155] Copyright 2016, AIP Publishing. h) SEM image of the silver nanoparticle (AgNP)-based metallic grid fabricated by capillary assembly of AgNPs. Reproduced with permission.^[156] Copyright 2016, Royal Society of Chemistry.

Of note, metallic grids can exhibit excellent flexibility.^[147] However, one of the potential weaknesses of metal grids is the weak adhesion to the substrate. Lee et al proposed to enhance this adhesion through colloidal deposition and silver enhancement steps. This improves the adhesion of the metal mesh thanks to an intermediate adhesion layer based on 3-aminopropyltriethoxysilane.^[112] This approach results in an optical transmittance of 97.7% and a sheet resistance of 71.6 Ω /sq, and its use as a TH enables to homogeneously reach a temperature of 245°C under an applied voltage of 7 V, showing a clear enhancement of adhesion.^[112] Another very promising strategy to tackle adhesion issues relies on embedded structures since they can: i/ enhance the surface smoothness, ii/ improve drastically the mechanical stability and iii/ induce strong adhesion to the substrate. Khan et al. demonstrated a cost-effective electrodeposition solution process of embedded metal-mesh with excellent mechanical, optical and heating performances.^[74] Of note, metallic fibers (with diameters much larger than nanowires) can exhibit interesting properties. Wang et al. recently demonstrated that percolating networks of Ag nanofibers fabricated by blow-spinning constitute efficient THs.^[73] This TH technology can indeed exhibit good optical and electrical properties, as demonstrated with Ag nanofibers networks that were obtained with an optical transmittance of 95% and a sheet resistance of 16 Ω /sq, enabling to reach temperatures larger than 285°C with a 10 V bias.^[73] Singh et al. reported a TH with low operating voltage based on embedded PVA@Ag nanofiber network. This TCM structure has a smooth surface topology and excellent bending stability after 10 000 bending cycles at 1.0 mm bending radius.^[81] In the case of copper based fibers, Jo et al. demonstrated a highly stretchable and transparent TH with ultra-low sheet resistance that can keep the working temperature constant up to 300 % stretching.^[76]

3.4 Polymer-based materials

Conductive polymers present attractive features for TH fabrication in terms of flexibility/stretchability, cost and processability. However, only few of them exhibit an electrical conductivity suitable for TH applications. Recently, a breakthrough was performed in TH fabrication with the first demonstration of a 100% polymeric TH. Gueye et al. demonstrated the ability of poly(3,4-ethylenedioxythiophene) (PEDOT)-based thin films to be efficient THs, without the need for metal or conductive fillers.^[50] Three conductive polymers were studied (i) PEDOT doped with polystyrene sulfonate (PSS) and with ethylene glycol (EG): PEDOT:PSS-EG, (ii) PEDOT doped with trifluoromethanesulfonate CF_3SO_3^- (OTf): PEDOT:OTf, and (iii) PEDOT:OTf thin films treated with dilute sulfuric acid to further enhance conductivity: PEDOT:Sulf. The chemical structures are displayed in **Figure 8a**.

These conductive polymers show excellent optoelectronic and heating properties^[50], and are flexible, as shown in Figure 8b. The electrical resistance and heating properties of the polymer-based TH remain stable under strong mechanical stress (1000 cycles with a 9 mm bending radius), as shown in Figure 8c. Temperatures higher than 100 °C can be reached in a few minutes with a bias of less than 12 V (Figure 8d). Transparencies higher than 87% are generally

obtained with extremely low light diffusion, the haze value being typically under 1%. This aspect is very important because haziness is a critical parameter for most optoelectronic applications, and such low values are hardly ever achieved with other non-TCO materials.^[38] This polymer-based technology made it possible to reach high power densities, up to 10 000 W/m² (Figure 8d). Heating homogeneity, measured by IR imaging, and extended mechanical stability were demonstrated. Chemical instability could have been anticipated because PEDOT-based materials are known to be sensitive to light and moisture. However, after encapsulation with a barrier film, a loss of only 1°C was measured after 200 h under continuous heating at 55°C, compared to 9°C without encapsulation, which indicates that encapsulation methods should be developed and optimized for the long term durability of these THs.

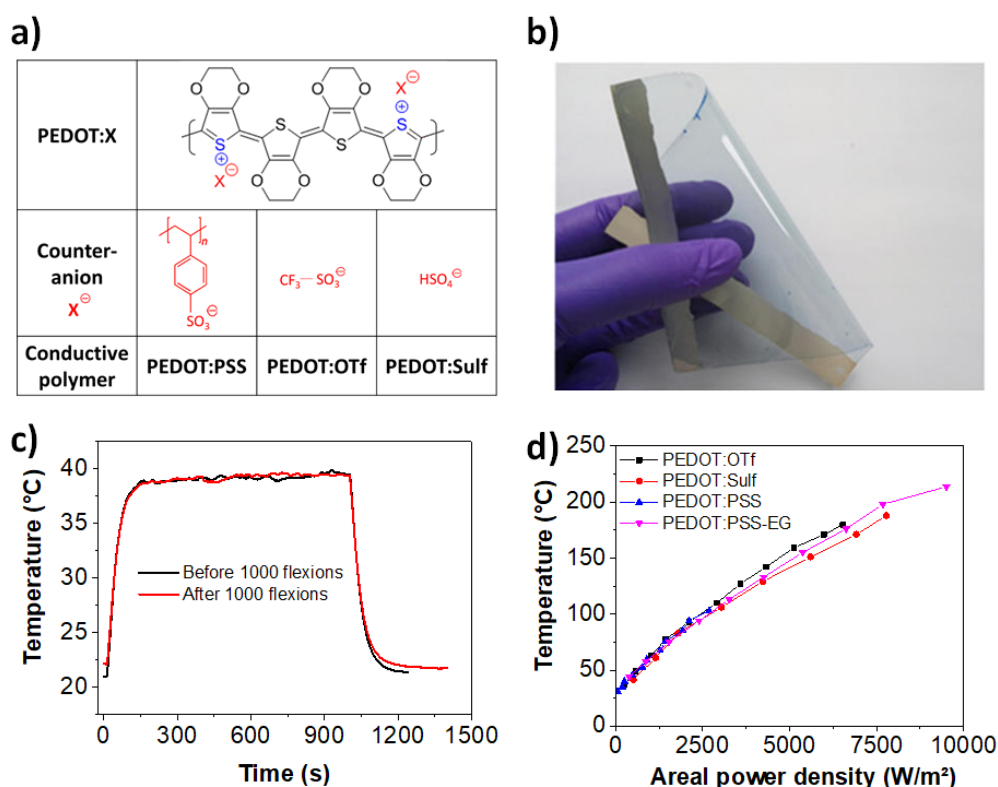


Figure 8. Main features of conductive polymer-based transparent heaters. a) Chemical structures of PEDOT and three main counter-ions forming respectively: PEDOT:PSS-EG, PEDOT:OTf and PEDOT:Sulf. b) Picture of a PEDOT-based TH illustrating its flexibility. c) Temperature increase of PEDOT:PSS-EG-based THs before and after 1000 bending cycles (9 mm radius of curvature) showing its good mechanical stability. d) Temperature increase versus areal power density for conductive polymer-based TH. b-d) Reproduced with permission.^[50] Copyright 2017, American Chemical Society.

Another recently reported approach is based on the use of nanofibers of conductive polymers to form a mesh, which can be used as a TH. An effective and cost-friendly method to produce such nanofibers is electrospinning, which allows the polymer to be deposited onto any curved or flexible surface. Some experiments were carried out on polycaprolactone/carbon black (PCL/CB), polyethylene oxide/polyaniline (PEO/PANI) and PEO/PEDOT:PSS systems.^[85,171] The best results were obtained with the PEO/PEDOT:PSS blend. These polymeric THs show moderate performances in terms of heating properties, requiring a 60V bias to reach 70 °C, at 84 % transparency.^[85] PEDOT:PSS films can also be patterned using a microfluidic post

treatment with solvents. The conductivity is locally boosted by several orders of magnitude, making it possible to obtain localized heating with microscale resolution^[172]. These recent developments based on thin films of intrinsically highly conductive polymers open the way to new high performance and purely organic THs.^[173]

3.5 Nanocomposites and hybrid transparent heaters

THs have gained a constantly increasing attention in research and industry these past years with a recent focus on multilayers, hybrids and nanocomposites. Matching materials with TH requirements is promising since it combines the best properties and advantages of each material, and generally offers much better performances than THs composed of a single material type. In other words, each conductive nanomaterial (TCO, metallic-based materials, carbon-based materials or conductive polymers) has its own advantages and disadvantages, but satisfying all industrial requirements with a single material is nearly impossible. The combination of several of these nanomaterials, however, can offer enhanced properties or better stability. This trend is observed in other modern domains in advanced materials science. This can be illustrated with the case of 1D carbon-based nanocomposites used in electrochemical energy storage devices; these have attracted intensive research interests lately, as an effective way to store energy from renewable energy sources. These aspects have been reviewed recently by Shi et al.^[174] who showed that 1D carbon-based nanocomposites (where CNT are either embedded, coated, encapsulated or supported) can be efficiently integrated into batteries and supercapacitors.

A large family of these hybrids for TH applications includes metallic nanowire networks or grids/meshes coated with protective layers of graphene derivatives or TCOs. These composites exhibit the very high electrical conductivity characteristic of metallic nanomaterials, and the coatings offer higher electrical and thermal stability. Other structures include thin TCO layers and metal nanowires^[47], or MNWs combined with conductive polymers^[175]. The emerging hybrids/nanocomposites based on nanomaterials open the way for flexible devices fabricated using low-cost and up-scalable processes, and leads to a wide variety of modern applications with futuristic shapes and everyday life uses. These nanomaterials can then be successfully integrated into devices since they exhibit an interesting trade-off between electrical and mechanical properties, stability, transparency and haze value. **Figure 9** illustrates the richness and diversity of the materials investigated for TH applications. These materials have been classified according to the main investigated TH technologies: they are composed of either the four primary material types (metallic oxides, metals, conductive polymers and carbon) or of hybrids/nanocomposites composed the combination of these primary materials. The primary material is the main material, while the secondary material is usually present in lesser amounts, and generally added afterwards. The main materials used in each case (primary and hybrids/nanocomposites) are represented in white letters. Each picture illustrates an example of a hybrid category: (from left to right, clockwise) 1) metallic oxides/polymers, 2) polymers/metals, 3) polymers/carbon, 4) carbon/metals, 5) metallic oxides/carbon, 6) metallic oxides/metals. The color code used in Figure 9 applies to the rest of the figures of this review.

To show the recent evolution of TH technologies related either to emerging materials or to nanocomposites, we have investigated the relative number of publications per TH technology. **Figure 10a** shows, through pie-charts, the percentage of scientific articles associated to the different TH technologies, gathered every 4 years since 2004.

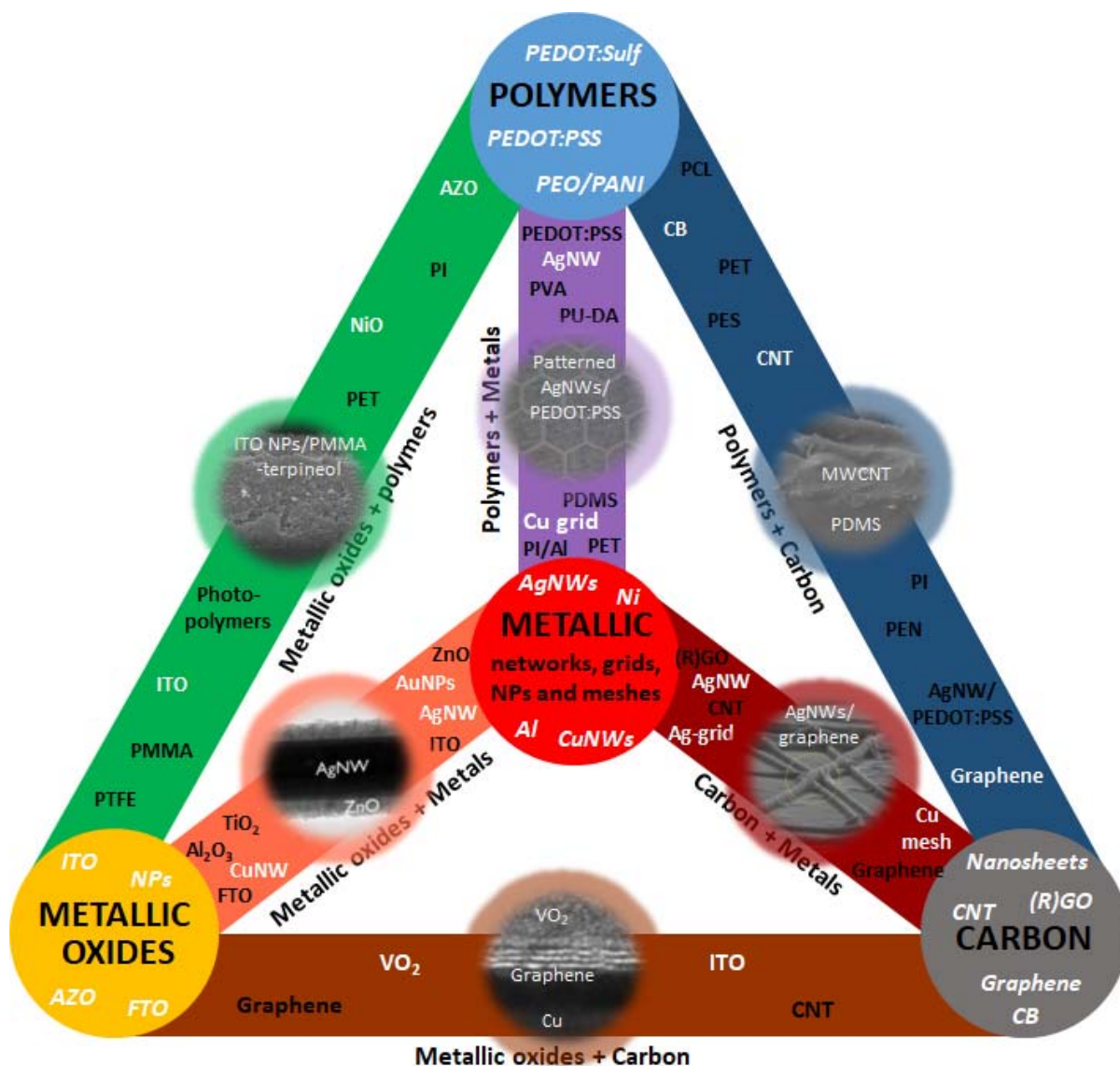


Figure 9. Schematic classification of main TH technologies investigated: they are either composed of the four primary material types (metallic oxides, metals, conductive polymers and carbon) or of hybrids/nanocomposites through combinations. This illustrates the richness and diversity of TH-related advanced materials. The main materials used in each case (primary and hybrid) are represented in white letters. Each picture illustrates an example of a hybrid category: (from left to right, clockwise) 1) metallic oxides/polymers; SEM image of an ITO NP/polymethyl methacrylate (PMMA)-terpineol mixture. Reproduced with permission.^[132] Copyright 2015, Elsevier. 2) polymers/metals; optical micrograph of printed AgNW/PEDOT:PSS composite grids with a hexagonal pattern. Reproduced with permission.^[176] Copyright 2019, MDPI. 3) polymers/carbon; cross-section SEM images of a MWCNT/polydimethylsiloxane (PDMS) bilayer film. Reproduced with permission.^[177] Copyright 2015, Elsevier. 4) carbon/metals; Tilted cross-section SEM image of single-layer graphene/AgNW/glass. Reproduced with permission.^[178] Copyright 2019, John Wiley and Sons. 5) metallic oxides/carbon; HR-TEM of the cross section of graphene-supported VO₂ on a copper substrate which will eventually be etched. Reproduced with permission.^[53] Copyright 2013, American Chemical Society. 6) metallic oxides/metals; TEM image of a 30 nm thick ZnO-coated AgNW. Reproduced with permission.^[47] Copyright 2018, American Chemical Society.

This shows that before 2008 TCOs related to TH were almost the only technology reported in the literature, while carbon materials (graphene and CNTs) were starting to be well studied. From 2009 on, metallic nanowires, meshes and grids have attracted much more attention. These

past years, nanocomposites/hybrids were the focus of many articles, and excellent performances and stability have been reported. Of note, conductive polymer-based THs started to be explored around 2017.^[50] The growing size of the pie-charts with time illustrates the fact that the number of articles per year has been multiplied by 10 between the first period (2004-2008) and the more recent one (2014-2018). It clearly shows the growing interest in THs from the scientific community, driven by the industrial needs. In parallel, there is a strong industrial activity in the TH field, which is not reflected in scientific publications due to intellectual property strategies. Similar trends as those shown in Figure 10a can be surveyed in terms of patent application numbers linked to TH technologies.

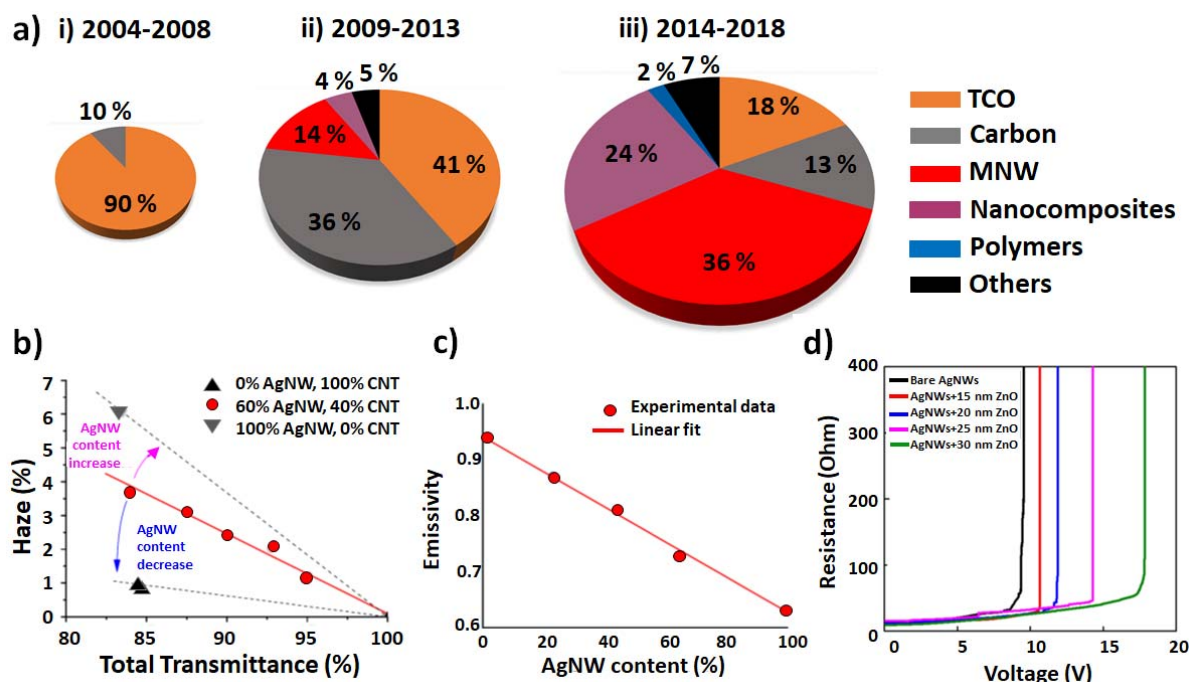


Figure 10. Emergence and examples of the assets of nanocomposite TH technologies. a) Pie-chart representing the percentage of scientific articles associated to the different TH technologies, showing that before 2008 mostly TCOs were mentioned in TH literature, while a small proportion of carbon materials (graphene and CNTs) were starting to be studied. Since 2009 MNW, meshes and grids have attracted much more attention. These past years, nanocomposites have been the focus of many articles, while conductive polymer-based THs have been explored since 2017. The pie-charts are growing with time to illustrate the fact that the number of articles per year has been multiplied by 10 between the first period (2004-2008) and the more recent one (2014-2018), demonstrating a clear growing interest in THs by the scientific community, driven by industrial needs (Sources: Scopus and Web of Science). b) Influence of AgNW content on optical transmittance and haze factor of hybrid conductive films composed of CNTs and AgNWs. c) Emissivity versus AgNW film content of similar film heaters prepared by roll to-roll coating. b,c) Reproduced with permission.^[102] Copyright 2013, Elsevier. d) Variation of electrical resistance versus voltage for bare and ZnO-coated AgNW networks subjected to voltage ramps of 0.1 V/min: the stability of the hybrid composite is clearly enhanced since the failure voltage increases with ZnO thickness. Reproduced with permission.^[47] Copyright 2018, American Chemical Society.

To illustrate the versatility of nanocomposites, Figure 10b and 10c illustrate a typical example where properties can be tuned if the AgNW content is varied in hybrid conductive films composed of CNTs and AgNWs.^[102] Figure 10b shows the influence of AgNW content on optical transmittance and haze value, while Figure 10c shows the emissivity versus AgNW film

content of similar film heaters prepared by roll to-roll coating.^[102] Figure 10d shows the enhancement of the stability of AgNW networks thanks to thin oxide layer (ZnO) coatings. The voltage failure observed during voltage ramps increases from 9 to 18 V for, respectively, bare AgNWs to 30 nm ZnO-coated AgNWs, showing a clear electrical stability enhancement.^[47]

The next sections of 3.5 will focus in more detail on the properties of nanocomposites, discussed per combinations of materials.

3.5.1 Higher thermal efficiency of metallic nanowire and carbon-based materials

Carbon-based materials and MNW hybrid materials have been widely developed for transparent properties enhancements like haze tuning^[102,179,180], but also to improve stability^[181–183] or adhesion.^[184] These hybrids are mainly comprised of 2D MNW networks (copper or silver) combined with CNTs, graphene, GO or rGO. As reported in section 3.2, carbon-based THs suffer from their poor conductivity at high levels of transparency. For heating applications, strong synergies are evidenced when combining the properties of carbon materials and MNWs for efficient, stable and highly flexible THs.

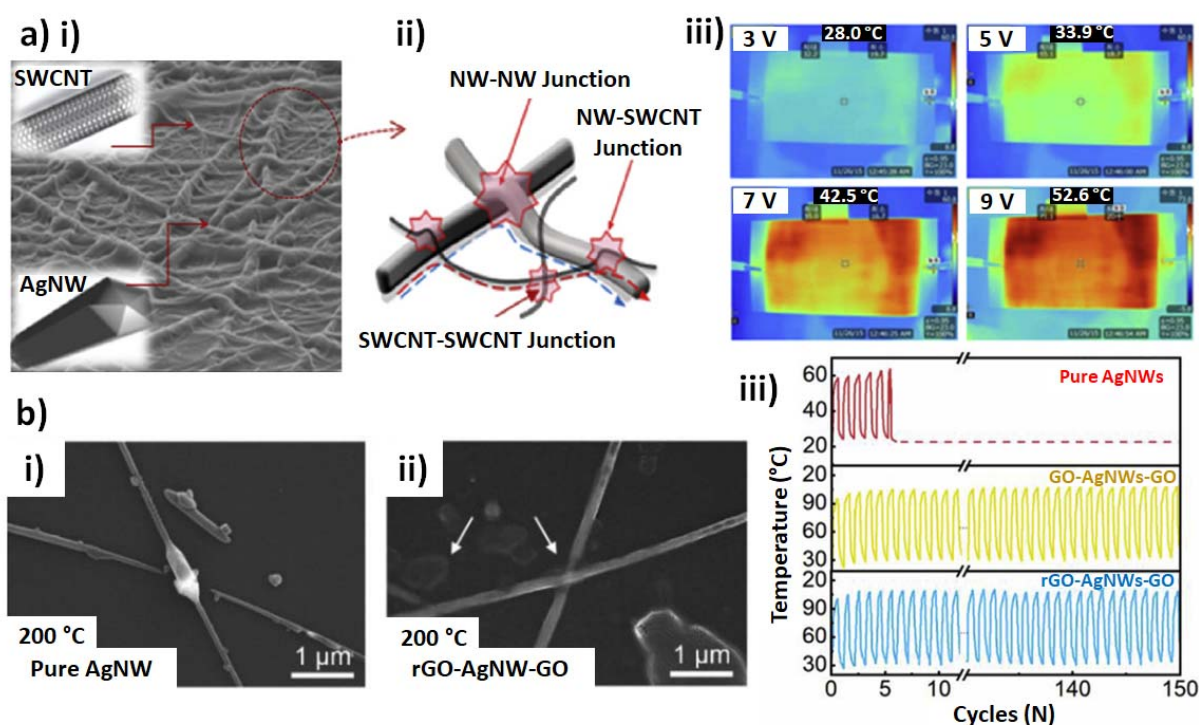


Figure 11. Carbon and MNW-based hybrid THs. a) AgNW-SWCNT hybrid composite layer on TPU: i) FESEM surface image of the hybrid composite layer. ii) schematic representation showing the current pathways. iii) IR thermal images of the SWCNT–AgNW hybrid TH, with a sheet resistance of 30 Ω /sq, under different applied input voltages (3, 5, 7 and 9 V). Reproduced with permission.^[80] Copyright 2018, Elsevier. b) Tri-layer rGO-AgNW-GO composite film i) SEM pictures of pure AgNWs, ii) tri-layer composite film heated at 200°C, iii) heating and cooling tests of pure AgNW, GO-AgNW-GO and rGO-AgNW-GO THs under ON/OFF current cycles of 60 s. Reproduced with permission.^[188] Copyright 2019, Elsevier.

The carbonaceous species (CNTs or Graphene) of the NW-based hybrids significantly improves stability and heat dissipation^[116] of the MNW networks for better thermal efficiency.^[185] Indeed, a more effective spreading of the heat with a small amount of SWCNTs improves the overall thermal stability of the NW network by improving resistance to current shocks.^[185] Moreover, the excellent thermal contact between nanowires and graphene, estimated at 0.5 m.K/W by Gupta et al. prevents Joule heating at the NW/NW junctions.^[186] Sadeque et al. focused their work on thermal transport behaviors in 2D networks of hybrid materials, especially graphene/AgNW composites.^[187] They disentangled contributions from local self-heating (hotspots) and heat spreading from the contacts, using thermorefectance measurements.^[187]

Figure 11a shows SEM pictures of a CNT-AgNW hybrid heater. Highly stretchable and stable hybrid THs were developed, with a very low haze (under 1% at 95% transparency) and elasticity as high as 20%.^[80] As reported very recently by Wang *et al.*, a tri-layer film-based heater of rGO-AgNW-GO, as shown in Figure 11b, exhibits far better chemical, mechanical and thermal performances than pure AgNWs.^[188] They report a significant improvement in long-term stability, with fewer failures on the sandwich-structured film heater.

3.5.2 Adhesion enhancement within metallic nanowire/polymer hybrid transparent heaters

As previously mentioned, polymers are extremely attractive in terms of flexibility/stretchability and processability. Nanocomposite materials relying on MNWs and polymers combine the high conductivity of a MNW network with the desirable mechanical properties of polymers, like flexibility,^[189] stretchability,^[190] and adhesion^[175].

Thanks to the addition of conducting elements in polymer matrices, it is possible to enhance the conductivity while preserving processability. Most of these composite-based THs take advantage of metallic nanofillers, often made of silver or copper. Nanospecies with high form factors are preferred, to favor percolation for the electron pathways. In particular, metallic nanowires can provide efficient networks at low densities, as described by the stick percolation theory.^[191,192] PEDOT:PSS, Polyimide (PI), polydimethylsiloxane (PDMS), PET, polyester (PE), poly(methyl methacrylate) PMMA, and even healable polyurethane (PU-DA) are the most reported matrices for the fabrication of composites for THs.^[79,112,114,175,189,193–204] Biopolymers like chitosan are interesting emerging materials for medical TH applications because of their biocompatibility and biodegradability.^[205] For composites, the choice of the polymer-conducting filler couple depends on the specific properties that are targeted. Polymers generally act as binders to ensure good contacts between nanoparticles and substrate, or they can serve as flexible/stretchable substrates to provide these properties to the system. They do not improve the heating properties, but are interesting nonetheless because of their optical properties (thin film transparency), their potential ability to allow the homogeneous dispersion of conducting nanoparticles, and for their mechanical performances. PEDOT:PSS is also often used as a host for the fabrication of conducting composites, and has mainly been used to improve the adhesion with the substrate. The comparison of film adhesion before and after peeling of 3M Scotch tape is demonstrated in **Figure 12a** and 12b for a pristine AgNW (Figure 12a) and PEDOT:PSS composite film (Figure 12b).^[175] The optical transmittance (measured at 550 nm) was increased from 75% to 81% for the AgNW film, while it remains at 79% for the composite film, demonstrating the enhanced adhesion of the composite.

PEDOT:PSS can also enhance the conductivity by creating conductive pathways between spatially separated nanowires.^[206] In some cases, the conductive polymer can be doped with graphene to improve heating stability.^[116]

Nearly all reported polymer/AgNW hybrid systems show similar performances with a maximal temperature of 100-150 °C, a transparency around 85 % at an operating voltage between 10 and 40 V. Large differences in haze factor are observed, with values ranging from 3%^[189] to 30%.^[194] Screen printing, doctor-blading and drop coating are the main methods reported for the deposition of AgNWs, which are then coated with the polymer.^[175,189,194] AgNWs can be embedded to improve the contact and stability in flexion, with a stable resistance after 1000 bending cycles (with a 500 μm radius of curvature).^[189] Another way to stabilize the system is to add a thin transparent protective layer of poly(vinyl alcohol) (PVA) or insoluble PI.^[194,196] Healable polymers, based on the Diels-Alder reaction, can be cured by simple heat treatment.^[201] Figure 12c shows that after deliberate damage by a knife cut, the AgNW/polyurethane-based TH can heal and recover its original conductivity thanks to a simple heat treatment at 120 °C.^[201]

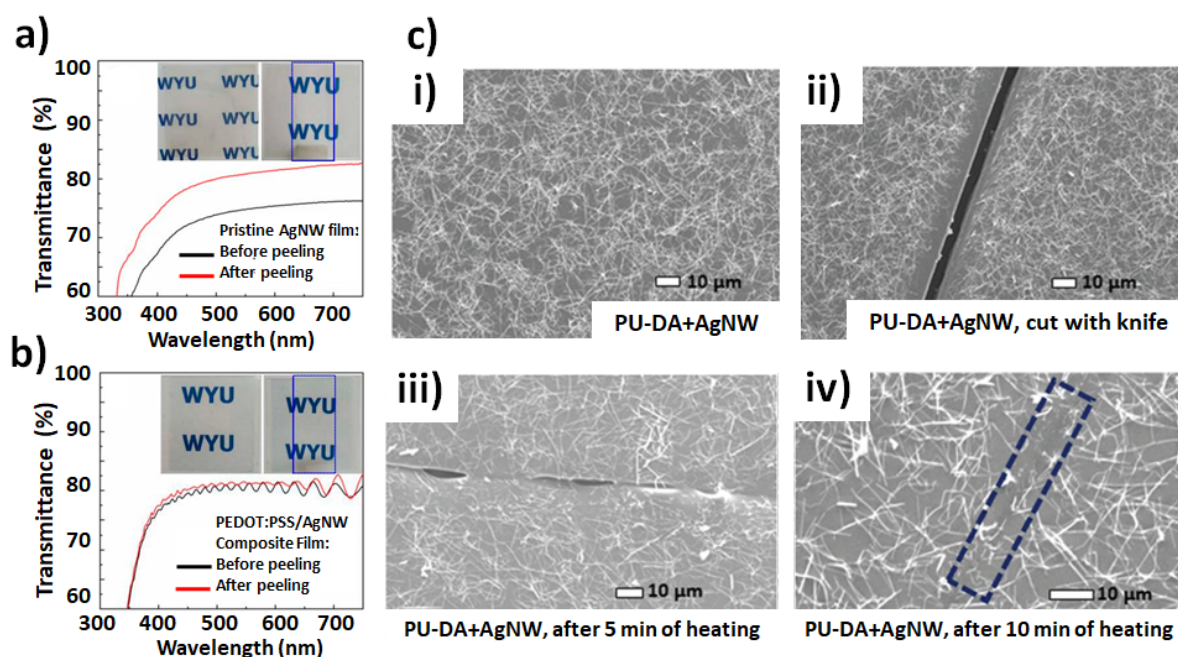


Figure 12. THs based on nanocomposites with AgNW networks and polymers. a) Peeling test of a pristine AgNW film showing a large increase in optical transparency. b) Similar experiment with AgNW and PEDOT:PSS composite showing no increase in optical transparency, associated to a clear improvement in adhesion thanks to the polymer. Reproduced with permission.^[175] Copyright 2017, MDPI. c) FESEM images of the transparent, flexible and healable material with AgNWs and polymers: i) The healable TH as deposited, ii) after a cut with a knife, iii) healing of the electrode at a temperature of 120 °C for 5 min, and (iv) healing of the electrode at a temperature of 120 °C for 10 min. The dotted box indicates the location of the previous cut. Reproduced with permission.^[201] Copyright 2017, Royal Society of Chemistry.

Hybrid materials with a copper/alumina/PI combination are interesting, with a high and stable temperature of 300 °C reached for a 10 V bias, associated with 91% transparency.^[200] Alumina limits the diffusion and oxidation of Cu, while PI is an effective binder to improve the adhesion

strength between the Cu wires and the substrate. Heating stability was demonstrated for 100 cycles with a substantial pulsed current of 1.5 A. Mechanical properties were investigated with bending (1000 cycles, 2 mm radius) and stretching (30 % stretchability on PDMS) experiments, and no significant change in conductance was observed. Similar improvement of adhesion properties of AgNW networks to the substrate due to the use of PI was demonstrated by Lu et al.^[203]

3.5.3 Stability enhancement of metallic nanowires with oxide material

Percolating MNW networks have been shown to act as efficient transparent electrodes^[20,33,34] and can be used in solar cells^[40] and as THs^[42]. The most studied MNWs are AgNWs since their synthesis and properties exhibit strong advantages: silver is the material with the highest thermal and electrical conductivity at room temperature, and the synthesis of AgNWs is well-mastered. However, these metallic nanowire networks suffer from stability issues. MNW thermal instability leads to spheroidization (associated to the loss of the percolating nature of the networks^[90]). Furthermore, electrical instability is observed when the networks undergo electrical stress^[93,168]. CuNW networks are interesting^[30,31] since the price of Cu is much lower than Ag. However, Cu is much more prone to oxidation than Ag and thus the chemical stability of CuNWs is a more critical issue. To enhance the stability of MNWs in general, several solutions have been investigated. The coating of MNWs by a thin oxide layer has shown clear improvements in stability. This strategy has been reported for AgNW/TiO₂^[46], AgNW/ZnO^[47,207], CuNW/Al₂O₃^[48,169], CuNW/ZnO.^[208] **Figure 13** shows SEM (a,b) and TEM (c,d) images of AgNW networks before (a,c) and after (b,d) the deposition of a thin layer of ZnO using atmospheric pressure spatial atomic layer deposition (AP-SALD)^[47]. This technique appears as an ideal approach to protect MNWs since it is a rapid, atmospheric and cheap method for thin film conformal deposition, and therefore does not compromise the low-temperature, atmospheric pressure fabrication of MNW networks.^[208-210] A 25 nm thick coating of ZnO drastically enhances the stability of the TH, as shown in Figure 13e.^[47] Figure 13f shows the relative electrical resistance of the bare AgNW network and the ZnO:Al/AgNW nanocomposite versus time when the samples were subjected to voltage ramp cycles (between 2 V and 6.5 V). The electrical stability is clearly enhanced thanks to the conformal coating when compared to bare AgNWs.^[208] Similarly, Tigan et al. recently reported an extensive study relating CuNW network density and oxide nature (Al₂O₃, ZnO) with electrical and optical properties, as well as stability. These authors were able to reach thermal stability up to 273 °C for CuNW with a thin Al₂O₃ coating, and a remarkably high heating rate of 14 °C/s.^[169]

In addition to improving the network stability, oxide coatings give rise to materials with a much higher adhesion than bare nanowires. Figure 13g shows an optical picture of the peeling off test of a CuNW/Al₂O₃/polyimide(PI) composite film using 3M scotch tape.^[200] Figure 13h reports the variations in optical transmittance (blue) and sheet resistance (black) for Cu wire/Al₂O₃/PI (black circles) and Cu wire/Al₂O₃ (black square) network composite films versus the number of performed tape tests. The composite film (Cu wire/Al₂O₃/PI) clearly exhibits an enhanced adhesion compared to the Cu wire/Al₂O₃, which became insulating after the third tape test.^[200] Of note, an approach has recently been used to enhance the transmittance of AgNW networks coated with protective metal oxide bilayers thanks to an anti-reflective coating.^[211]

While the positive effects of thin oxide coatings on the performance of MNW networks have been reported several times, coating with metallic or oxide nanoparticles (NP) can also be an efficient method. For example, Morgenstern et al. showed that full encapsulation of the AgNW network by a layer of ZnO-NP drastically enhances thermal stability.^[207] Cheong demonstrated that AgNW and AZO can lead to efficient and flexible THs: the AZO coating enables to reach a higher average film temperature of 100 °C (30 °C higher than uncoated AgNWs) as well as a greater heating uniformity.^[212] Cheng et al. also showed that AgNWs can be decorated with gold nanoparticles, leading to a greatly enhanced thermal stability.^[213] Sharma et al. demonstrated that highly stable THs can be obtained with AgNWs decorated with cobalt nanoparticles (CoNPs). It was found that an optimum AgNW-CoNP ratio of 50-50 wt% leads to good performances of the corresponding TH, with a thermal stability up to 350 °C.^[214]

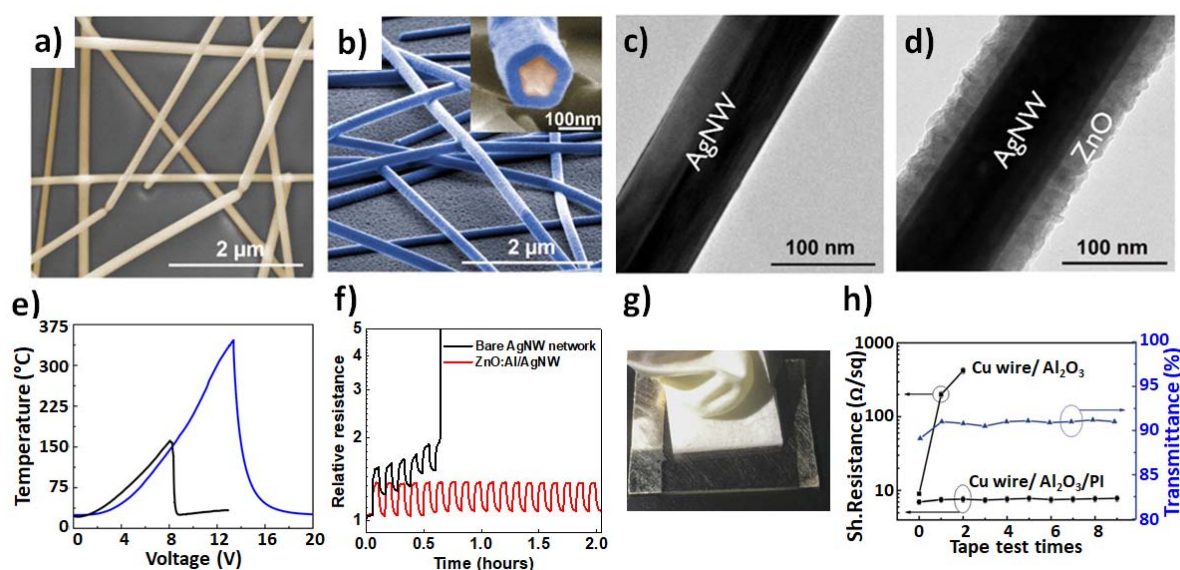


Figure 13. THs based on nanocomposites of MNWs and thin oxide layers. SEM (a,b) and TEM (c,d) observations of AgNW before (a,c) and after (b,d) deposition of a thin layer of ZnO layer using atmospheric pressure spatial atomic layer deposition (AP-SALD). A 25 nm thick ZnO coating drastically enhances the electrical stability of the TH, as shown in e), with the measured temperature during a voltage ramp for a bare and a coated silver nanowire network, in black and blue lines respectively. a-e) Reproduced with permission.^[47] Copyright 2018, American Chemical Society. f) Relative electrical resistance versus time of the bare AgNW network and ZnO:Al/AgNW nanocomposite when the samples were subjected to voltage ramp cycles (between 2 V and 6.5 V): the electrical stability is enhanced thanks to the conformal coating. Reproduced with permission.^[208] Copyright 2019, Royal Society of Chemistry. g) Optical picture showing the peeling off test for the Cu wire/Al₂O₃/polyimide(PI) composite film by 3M scotch tape. h) Variations of sheet resistance (black) versus the number of performed tape tests for Cu wire/Al₂O₃/PI and for Cu wire/Al₂O₃ network composite films; optical transmittance values (blue) Cu wire/Al₂O₃/PI are also plotted. g,h) Reproduced with permission.^[200] Copyright 2016, Royal Society of Chemistry.

3.5.4 Metallic grids and transparent conductive oxides or graphene

Hybrids based on metallic grids combined with graphene exhibit a superior electrical and mechanical stability. Kim et al.^[148] fabricated copper grid meshes by photolithography and deposited a graphene layer on top of the meshes (**Figure 14a**), while Kang et al.^[215] used

electro-hydrodynamic jet printing to write silver grids on a large-area graphene layer. In both cases the hybrids showed improved and more uniform heating performances^[215] compared to each separate material, even after thousands of bending or twisting cycles.^[148] In the case of the Cu grid/graphene, the excellent flexibility is also due to the corona treatment of the PET substrate. Another study on metallic grid-based hybrid THs combined Ag meshes with a thin layer of ITO (Figure 14b). In this study, Kwon et al showed a 12% increase in optical transmittance, followed by a lower power consumption compared to the as-deposited ITO films^[149].

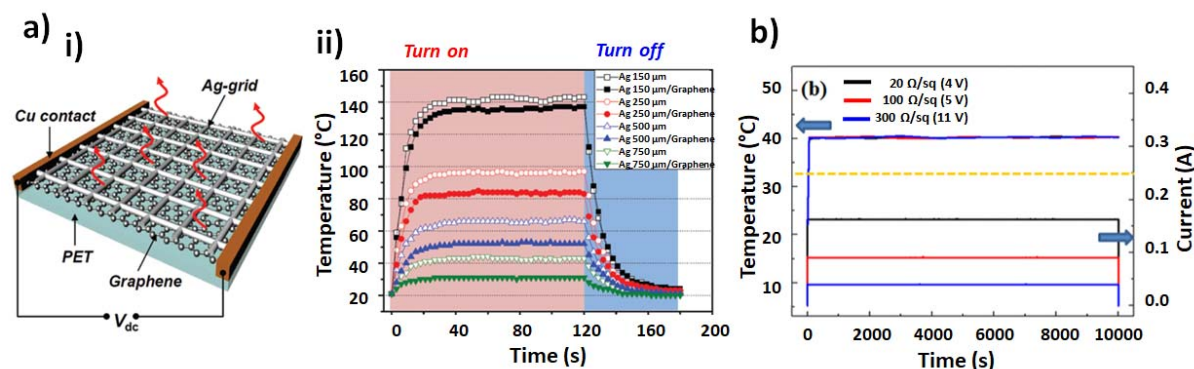


Figure 14. Transparent heaters from metallic grid-based hybrids. a) Ag-grid/graphene heaters: i) schematic illustration of the Ag-grid/graphene film heater connected to Cu electrodes. The size of the heating area was $5 \times 5 \text{ cm}^2$ and ii) time-dependent temperature response of the Ag-grid and Ag-grid coated with graphene heaters. Reproduced with permission.^[215] Copyright 2015, Royal Society of Chemistry. b) Ag mesh-ITO hybrid heaters with sheet resistances of 20, 100, and 300 Ω/sq . The temperature remains very stable for 10,000 s while a voltage of 4, 5 and 11 volts is applied, respectively. Reproduced with permission.^[149] Copyright 2014, IOP Publishing.

3.5.5 Transparent heaters based on metallic or transparent conductive oxide multilayers

Other combinations of materials have been reported in the literature, including multilayers of TCOs or polymers with metallic thin films, or by combining different TCOs and nanoparticles. Several studies deal with the combination of a metallic thin film that is sandwiched between two TCO layers. Kim's group demonstrated that it is possible to make high-performance and flexible THs using continuous roll-to-roll (R2R) sputtering.^[51] In their studies, Ag or Cu was sputtered, from metallic targets, in between 40 nm thick ITO layers. They used a pilot scale system capable of coating 700 mm wide PET substrates at room temperature. In the case of ITO/Ag/ITO films, a transmittance of 88.2% and a sheet resistance of 3 Ω/sq were achieved.^[51] $50 \times 50 \text{ mm}^2$ THs were then fabricated, reaching a steady-state temperature of 100 °C by applying 5 V. In this case, the Ag layer was 12 nm thick and took around 100 s to reach 100 °C. In the case of ITO/Cu/ITO layers, an optical transmittance of 73.9% and a sheet resistance of 11.8 Ω/sq were obtained.^[52] In this study, the best figure of merit was obtained for 12 nm thick Cu layers, and temperatures above 100 °C were obtained under a bias of 8 V. In another study, the ITO layers were replaced by InZnSiO, in combination with Ag, using the same R2R sputtering approach.^[216] The electrodes showed a transmittance of 91.91% and a sheet resistance of 7.83 Ω/sq for a 8 nm thick Ag layer. The electrodes reached 110 °C for a bias of

only 2.4 V. The amorphous nature of the oxide yielded a high thermal stability upon cycling, as well as mechanical stability (no degradation of performance after 10,000 bending tests with a 10 mm bending radius).^[216] The same group presented a similar approach in which ITO was replaced by SnO₂ and the metal layer was composed of a AgPdCu alloy.^[217] In this case, these flexible In-free electrodes were deposited by thermal evaporation, and showed a minimum sheet resistance of 9.42 Ω/sq with transmittance values above 91% for 50 nm thick SnO₂ layers and a 10 nm thick metallic layer.^[217] The metallic layers alone showed a poorer performance than the tri-layer in terms of both conductivity and transmittance, due to the antireflective effects of the multiple coatings. THs made of SnO₂/AgPdCu/SnO₂ multilayers reached different temperatures for different SnO₂ thicknesses. For 10 nm thick oxide layers, temperatures above 110 °C were obtained under a 5.5 V bias, with heating response times between 100 and 200 seconds.^[217] Finally, in a similar approach, Roul *et al.* reported AZO/Ag/AZO electrodes made by sputtering, on PET substrates.^[218] The structural, electrical and optical properties were evaluated as a function of Ag layer thickness. The best results were obtained for a thickness of 5 nm, for which temperatures above 100 °C were obtained for a bias voltage of 10 V.^[218] In another case of a multilayer transparent electrodes, Kang *et al.* proposed the study of polymer/Ag/polymer and polymer/Ag/inorganic (ITO or SiN_x) tri-layer electrodes.^[219] The electrodes were produced by an R2R sputtering system, and the addition of a fluorocarbon polymer led to a higher flexibility, with the electrodes sustaining bending up to a radius of 3 mm, with a sheet resistance of less than 5 Ω/sq and a transmittance of 68%. The use of fluorocarbon polymer also yielded water-repelling electrodes, preventing wetting and removing contamination. THs based on fluorocarbon/Ag/SiN_x reached 180 °C for a bias voltage of 13 V.^[219] Kim *et al.* have presented an asymmetric multilayer TH based on a GZO seed layer, an Ag metallic layer and a GZO optoelectronic control layer.^[220] The electrodes were deposited by sputtering at room temperature, and they showed an optimum sheet resistance of 5.4 Ω/sq for a transmittance of 81.6% (50 nm GZO/12 nm Ag/50 nm GZO). The electrodes were deposited on glass substrates of different thicknesses, in order to evaluate the effect of heat loss through the substrate. The temperature reached on the film and the substrate, as well as the rising time, both depended on the substrate thickness. Heat loss due to conduction needs to be considered for substrates ≥ 3 mm. A model is presented that allows the calculation of heating rates and deicing times.^[220] In a different approach, Im *et al.* proposed THs based of CNT sheets with granular metal (Pd).^[221] The addition of these metal particles boosted the heating efficiency by a factor of 3.6, from 99.9 to 27.3 °C cm²/W. This improvement is attributed to electron-lattice interaction and heat loss suppression. Finally, Hudaya *et al.* reported THs based on FTO with scattered metal nanodots (Cr, NiCr and Ni). The FTO layers were deposited by sputtering, while the metallic nanodots were deposited by electron cyclotron resonance CVD.^[222] The electrodes showed transmittance values over 85% and reached saturation temperatures over 80 °C for a bias voltage of 12 V.

These and other approaches, like TiO₂/Ag/TiO₂ multilayers, have been explored in recent years.^[223] While only the examples described above have been evaluated as THs, it is expected that more electrodes based on the combination of different materials will also be evaluated for TH applications.

3.6 Synthetic comparison between the different TH technologies

As previously described, there are different TH technologies which exhibit diverse characteristics. We have briefly reminded the main features for each technology, and will compare them in more detail in this section. TCOs are the most investigated/used TH technology in industrial devices,^[10] and were discussed in section 3.1. They certainly are the most stable technology, at least in terms of electrical and thermal stability, but they are not compatible with flexible devices nor with solution-based fabrication processes. Moreover, due to indium scarcity, technologies using more abundant or cheaper materials, have been investigated.^[21] Carbon-based materials are mainly represented by carbon nanotubes and graphene, which have already been integrated in TH devices by several research teams (see section 3.2).^[27,61,143] Lately there has been a clear interest in metallic-based THs (as reported in section 3.3). MNW random networks have been well investigated these past years, in particular AgNW^[20,39] and to a lesser extent CuNW.^[48,66,169,224] Interesting properties in terms of TH behavior have been reported with this technology, along with promising flexibility and cost-effective solution process fabrication. MNW-based THs appear compatible with large scale industrial fabrication such as roll-to-roll technology.^[42,44,45] In parallel, metallic mesh networks and grids also exhibit good physical properties and constitute efficient THs.^[72,112,148] However, the thermal and electrical stability of these metallic-based THs can be a severe issue. However, as shown by Chen et al.,^[56] Cu based grids made from a Ag seed layer and a subsequent electroplating of Cu imprinted microgrooves exhibit very good performances. Indeed, sheet resistance down to 0.03 Ω/sq associated with a transmittance of 86% was demonstrated. Furthermore these TH exhibit good stability. The possibility to fabricate them by roll-to-roll manufacturing appears promising for industrial integration. Metal nanofibers present also interesting physical properties in recent studies.^[75,87] Additionally, very recent efforts have led to drastically improve the properties of conductive polymers^[49], reaching the conductivity of state-of-the-art FTO layers (i.e. $3 \cdot 10^{-4} \text{ S/cm}$)^[14]. By investigating different dopants for poly(3,4-ethylenedioxythiophene) (PEDOT)-based materials, Gueye et al. reported thin polymer films with a R_{sh} of 57 Ω/sq , a transparency of 87% and a very low haze factor (i.e. <1%). The use of these conductive polymers enables the fabrication of all-polymer-based THs with excellent performances^[50], with steady-state temperatures exceeding 100 °C when subjected to a 12 V bias.

As described in section 3.5, the association of the different aforementioned materials leads to nanocomposites and/or hybrids, constituting a very rich family of TH technologies that offer a large panel of properties/performances with clearly enhanced electrical and thermal stabilities. The ongoing efforts by the community to fabricate, better understand and optimize THs is notably driven by the growing desire for low-cost, more stable and efficient THs. These efforts can efficiently address several challenges for many applications, the latter being described below in section 4.

The comparison of these different technologies is represented in **Figure 15**, with several criteria being considered. It is worth mentioning that these criteria and the marks associated to each criterion and for each TH technology are subject to discussion, therefore only general trends should be considered. Depending on experimental TH synthesis and usage, a range of figures of merit with minimum and maximum values are proposed. Exceptions ruling out these trends do exist. The flexibility criterion refers to the capacity of a TH technology to withstand

bendability or, for some applications, stretchability tests. TCOs are generally not flexible since oxides belong to the ceramic family, which are brittle materials (see Figure 7d), while other TH technologies are highly flexible. This is the case of all emerging TH technologies. Another critical issue is thermal stability: TCOs are very stable compared to other TH technologies. Thin oxide layers are even used as coatings for other TH technologies, forming efficient and stable nanocomposite THs. Conductive polymers are the least thermally stable among all TH technologies due to their organic nature. Nevertheless high temperatures (above 100°C) can be maintained for a long time, which is sufficient for most applications. The cost of a TH technology depends on several parameters, including the industrial production chain. The learning curves generally show a power law dependency between the cost of a device and the total cumulative production amount. Spatial uniformity is an application-dependent criterion. Homogeneous and continuous thin layers (such as TCOs, conductive polymers or some nanocomposites) are uniform by nature, while networks of carbon nanotubes or metallic nanowires, tiled graphene-based sheets or metallic grids can appear non-homogeneous, as demonstrated by the appearance of hot spots in the worst case.^[187] The use of nanocomposites combining both continuous and discontinuous THs can prevent this non-uniformity. Haacke's figure of merit (FoM) was used (Tr^{10}/R_{sh}): generally speaking, apart from graphene and CNT networks this FoM has rather high values for all TH technologies. Finally, the technological readiness level (TRL) criterion was used. The highest TRL value belongs to the TCO family, which has been investigated and used in industrial devices for several decades. The lowest TRL value is for the conductive polymers, for which the drastic progresses of conductivity making them very promising are only recent.^[49,50]

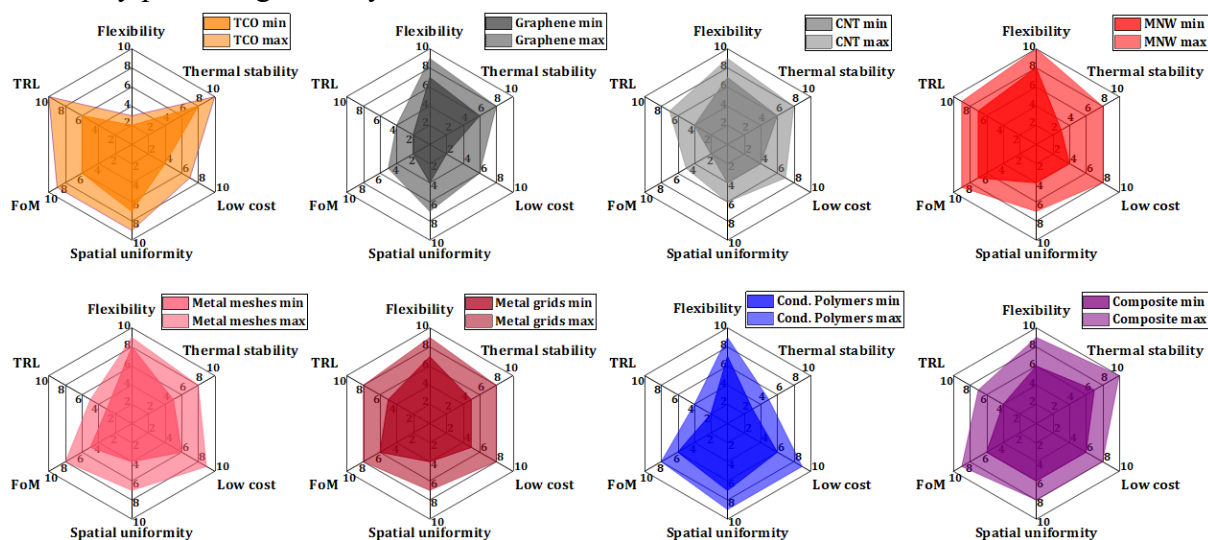


Figure 15. Comparison of THs fabricated with the different technologies. This figure shows the general trends with six criteria (clockwise from the top): flexibility, thermal stability, low cost (of both material and process), spatial uniformity, figure of merit (FoM) and technological readiness level (TRL). Depending on the synthesis and usage of experimental THs, a range of figures of merit with minimum and maximum values is proposed. The marks for all criteria for each TH technology are only general indications, since the actual marks are application-dependent.

Other characteristics could also be of interest. This is the case for the haze factor, which should be low (typically below 2 or 3%) when a TH is placed on windscreens, visors or displays to

ensure eye comfort (preventing blurriness). The haze factor is typically low for TCOs, while it can vary drastically for other TH technologies. For instance, small MNW diameters are preferred to decrease the haze factor^[96] of MNW-based THs. Recently, Ji et al. reported a study of ultra-long copper nanofibers covered with a shell of carbon black, which can provide a high-clarity view (i.e. with low haziness) associated to a transparency of 91% and a sheet resistance of 0.8 Ω/sq .^[87] This once again shows that nanocomposite THs can exhibit excellent properties through efficient combinations of key assets from different TH technologies.

4 Integration of transparent heaters in devices

As described above, THs concern numerous applications. TH fabrication is generally carried out with the goal of implementation in a specific device and for a particular application. As such, active material choice and device design must be considered according to specifications related to the operational use of the device. After pointing out some issues related to TH fabrication (part 4.1), we will describe examples of technical uses. The first one deals with THs for deicing, defrosting or defogging systems (4.2). Then we show how THs can be relevant for thermochromic devices (4.3), medical applications (4.4) and other niche applications (4.5).

4.1 Integration of THs within devices: generalities and potential issues

Even though the intrinsic performances of the materials developed for THs are generally very good, their integration into functional devices can encounter some difficulties. Integration will depend on the nature of the active and support materials, and in general on the environment close to the heating film. In some cases, adhesion can be an issue if the deposited active layer does not stick well to the substrate. This can occur with metallic nanowires, which usually show limited adhesion and can be removed by a simple finger sweep. Layers of graphene- or PEDOT-based materials can be very thin (i.e. less than 20 nm) and thus very fragile and sensitive to mechanical stress. An encapsulating layer needs to be deposited on top of these materials to ensure a good adhesion to the surface, to avoid mechanical damage while preventing the release of the nanomaterials towards end-users. This encapsulation can be carried out through different techniques, like wet processes for transparent polymers, physical deposition of TCOs by atomic layer deposition, lamination with thin glass sheets or transparent adhesive films.

As mentioned earlier, haziness must be finely controlled during the fabrication process since the haze value can vary significantly for some materials. Low haze values are mandatory for TH applications for windscreens or displays, whereas haziness may not be critical for other applications. This means that the fine control of the material itself (e.g. metallic nanowire diameter^[97] or layer thickness of carbon-based material) is crucial to reach the desired specifications and homogeneity on large surfaces. Depending of the TH application, tints induced by the materials should be considered (from a blue- or greenish hue for conductive polymers, blackish for CNTs, metallic greyish or a slight orange color for silver and copper nanowires, respectively, to yellowish with iridescence for TCOs).

Despite their importance, electrical contacts are seldom mentioned in the reported works dealing with TH integration. The fabrication of good and reliable electrical contacts between

the active layer and the voltage generator is usually not straightforward. Silver-based inks or pastes are often used for lab-scale demonstrations, but these materials are not always stable in the long term, and their homogeneous deposition can be tricky. Many other techniques and materials can be envisaged, like vacuum-deposited metals (gold, silver, copper, nickel, etc.), metallic ribbons or wires (usually copper-based materials), liquid metals (e.g. eutectic gallium-indium), or even materials with similar chemical natures to those used in THs, taking into account that these contact electrodes must be much less resistive than the active layers of the TH in order to avoid hotspots and Joule heating at unexpected locations.

Beyond the nature of the electrical contacts, the geometry and patterns of contact electrodes are very important. They will define the heating zones. Depending on their design and voltage input, specific areas can be heated at different areal power densities. In a basic case study with two opposite electrodes on a square TH, the distance between the electrodes must be well designed with respect to the available bias supply. Indeed, the voltage must be increased when the distance between the electrodes is increased to keep good heating properties (generally at least a few hundreds of W/m^2). If this distance increases too much, then high voltages must be used, which can seriously damage the active materials.

TH production should also consider the end-user application requirements. For highly flexible substrates for example, TCOs will not be suitable and polymer materials or metallic nanowires will be preferred. This choice of active material will also define the relevant and available deposition techniques, which are active material-dependent. For large area deposition techniques, special care should be taken to ensure homogeneous deposition, and ideally online analysis techniques should be implemented to check deposition uniformity.

4.2 Deicing, defrosting and defogging

The first application of THs was to avoid condensation in aircraft windshields to increase visibility in warplanes during military actions. At that time, the TCM used was tin oxide, but in modern airplanes it has been replaced by ITO, which is more conductive and thus allows a lower operating voltage (24V).^[2]

The heat produced by THs can also be used for defogging or defrosting applications. Defogging of car headlights is a recent need. Indeed, since the invention of cars, headlights have been based on incandescent bulbs, which inherently produce heat, preventing headlight condensation when they are on. Light-emitting diodes (LEDs) are now gradually replacing conventional incandescent lamps, because of their reduced energy consumption.^[225] Despite this obvious advantage, this new kind of headlight does not produce enough heat to avoid condensation or frosting at the surface of the headlights or inside the headlight housing. This situation creates a new risk, since fog or frost on the headlights can change light refraction and increase light diffusion, which degrades road illumination and thus visibility for the driver.

There is a market for defogging devices based on THs in food distribution, with refrigerated showcases using transparent windows^[2]. Indeed, when products are refrigerated, there is a risk of condensation because of the temperature difference between the two faces of the case. Consumers not being able to see products behind the windows can be detrimental to the store; THs offer an efficient solution to this problem, and patents linked to this topic have existed since the 90s, with ITO technologies.^[226]

LCD panels are used for outdoor applications. A limitation of LCD displays is liquid crystals freezing and electronic performance degradation at low temperatures^[227,228,61]. An ultra-thin film heater at the surface of the screen is an easy and lightweight method to heat the display and avoid degradation linked to low temperatures.

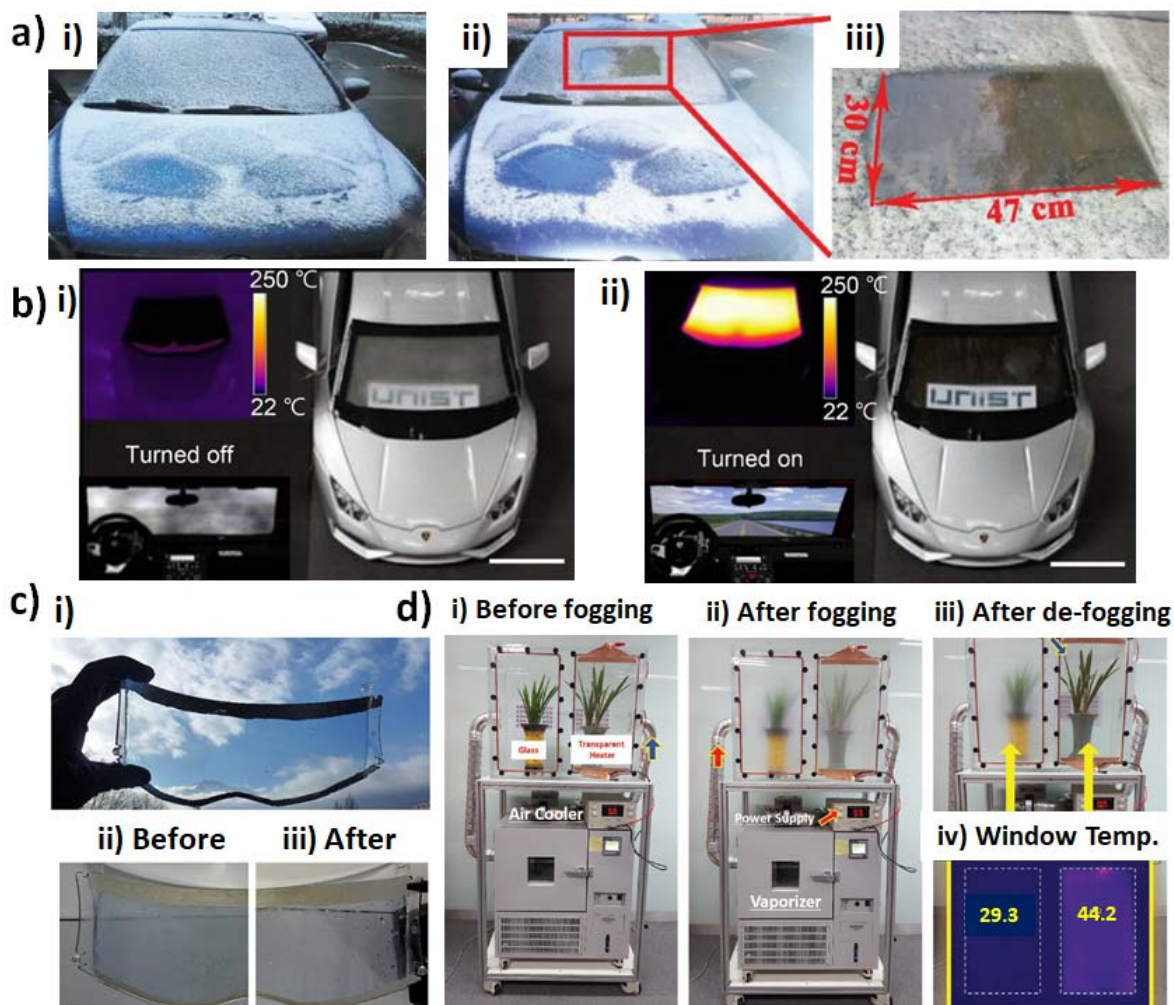


Figure 16. Defrosting and defogging transparent heater applications. a) A car windshield i) before and ii)-iii) after defrosting by applying 20 V for 5 min to a large-size Cu metal-mesh (30 x 47 cm²). Reproduced with permission.^[56] Copyright 2019, John Wiley and Sons. b) Photographs of the Ag/Ag₂O-NF/(index matching layer)IML heater-integrated automobile windshield at i) turn-off and ii) turn-on modes. The applied dc bias was 6 V. The insets show a driver's view through the windshield (lower) and an image captured with an IR camera displaying the temperature distribution of the windshield (upper). Reproduced with permission.^[231] Copyright 2018, American Chemical Society. c) i) a motorcycle visor with a PEDOT:PSS transparent heater, ii) iced in a freezer at -26 °C and iii) after defrosting by the TH. Reproduced with permission.^[50] Copyright 2017, American Chemical Society. d) Pictures describing the quality test of a Zn-Sn-oxide(ZTO)/Ag/ZTO transparent heater (52 x 31 cm²); i) general setting of the test with a normal glass and transparent heater glass placed in front of each orchid before running a test, ii) fog was generated on both windows using a moisturized hot air flow, iii) defogging was carried out on the heater glass for 50 s at 12 V, and (iv) temperature profile of the two glasses during defogging. Reproduced with permission.^[232] Copyright 2019, John Wiley and Sons.

For car windows (windshield and side windows) and external side mirrors, or even for motorcycle helmet visors, the operating voltage should ideally not exceed 12 V, which is the

current standard voltage for cars and motorcycles. This is one of the reasons for the demand for new transparent coatings with lower resistances and similar transparency. The development of the 48 V vehicle will allow, in the near future, to reduce the pressure on the power management of large surface THs and will open up new prospects. Other reasons behind the demand for new transparent coatings concern flexibility and the ability to coat curved surfaces. As previously mentioned, some technologies meet these requirements, especially AgNWs, CNTs, graphene and conducting polymers.

Many demo products have been fabricated, like defoggers/defrosters for car windows or side mirrors (**Figure 16a,b**), made of patterned AgNWs,^[229,230] AgNFs,^[231] Cu grids^[56] or Ni/Ag microgrids.^[195] A demo motorcycle visor (Figure 16c) dip-coated with PEDOT:PSS-EG was fabricated and can be defrosted in a few seconds with a low voltage.^[50] Zn-Sn-oxide(ZTO)/Ag/ZTO was also demonstrated to be of interest for small area defoggers (Figure 16d), as well as for larger areas like the windshield of a commercial car.^[232] Since these systems require low voltages, even sport glasses/ski masks could integrate these new technologies in the coming years.

4.3 Thermochromic applications

The alteration of the color or transmittance of thermochromic materials induced by changes in temperature can be used in a large variety of applications such as smart windows and green buildings, aerospace and military, textile and food packaging.^[233] Thermochromic smart windows are attractive because they are visibly transparent and can intelligently control the amount of solar heat (mainly in the near-infrared region) in response to changes in ambient temperature.^[234] Thermochromic applications are attracting more and more scientific and industrial interests, with efforts being devoted to their successful integration into modern devices. The research discussed in this part shows the Joule effect-based TH influence on thermochromic performance, the associated issues like layer adhesion, and the integration in devices. Vanadium oxide VO₂ materials are often presented, because they exhibit the greatest potential for thermochromic devices and energy-efficient systems^[235] thanks to their electronic structure modification from semi-conducting to metallic behavior when the temperature exceeds 68 °C. Emerging TCMs like CNTs^[236], graphene^[53], AgNWs^[109,199,237,238], conductive polymers^[50] and hybrids^[102,202] have been investigated as the heating elements.

Liu et al.^[236] developed a CNT-based flexible microheater on PET for local heating into a thermochromic display, and tuned the thickness of the materials in order to optimize the thermochromic performance. A first approach was to decrease substrate thickness in order to obtain a good trade-off between mechanical robustness and thermal response. The thermal response of CNT-based films from room temperature to 100 °C was reduced to a few seconds thanks to the use of a 70 μm thick PET layer and with lower CNT coverage.^[236] Indeed, heat dissipation increases inversely with CNT coverage. Finally, a thermochromic display coupled to a driving circuit was made, and Chinese characters were displayed thanks to local heating by the CNT microheater on PET.

In parallel, Kim et al.^[53] reported interesting progress related to the fabrication of flexible VO₂/Graphene-based thermochromic films for energy-saving windows. Graphene acts as a very thin (i.e. atomic film), flexible but robust substrate for the formation of stoichiometric VO₂ crystals. The transfer of the graphene-supported VO₂ onto a plastic substrate enables the

formation of a flexible thermochromic film which shows a decrease of in-house temperature under infrared irradiation in a mock-up house.

In the case of AgNW-based THs, Li et al.^[237] studied the influence of AgNW networks on the VO₂ nanoparticle-based thermochromic performance. The infrared response of this VO₂/AgNW-based device can be controlled thanks to the applied voltage, and the dependence is shown to be highly stable and reversible. **Figure 17a** shows the square-like shape of the dynamic infrared response to the pulse voltage. The response of the VO₂/AgNW-based device exhibits a step variation. The transmittance in the infrared region can therefore quickly be altered when applying either rising or falling input voltage.

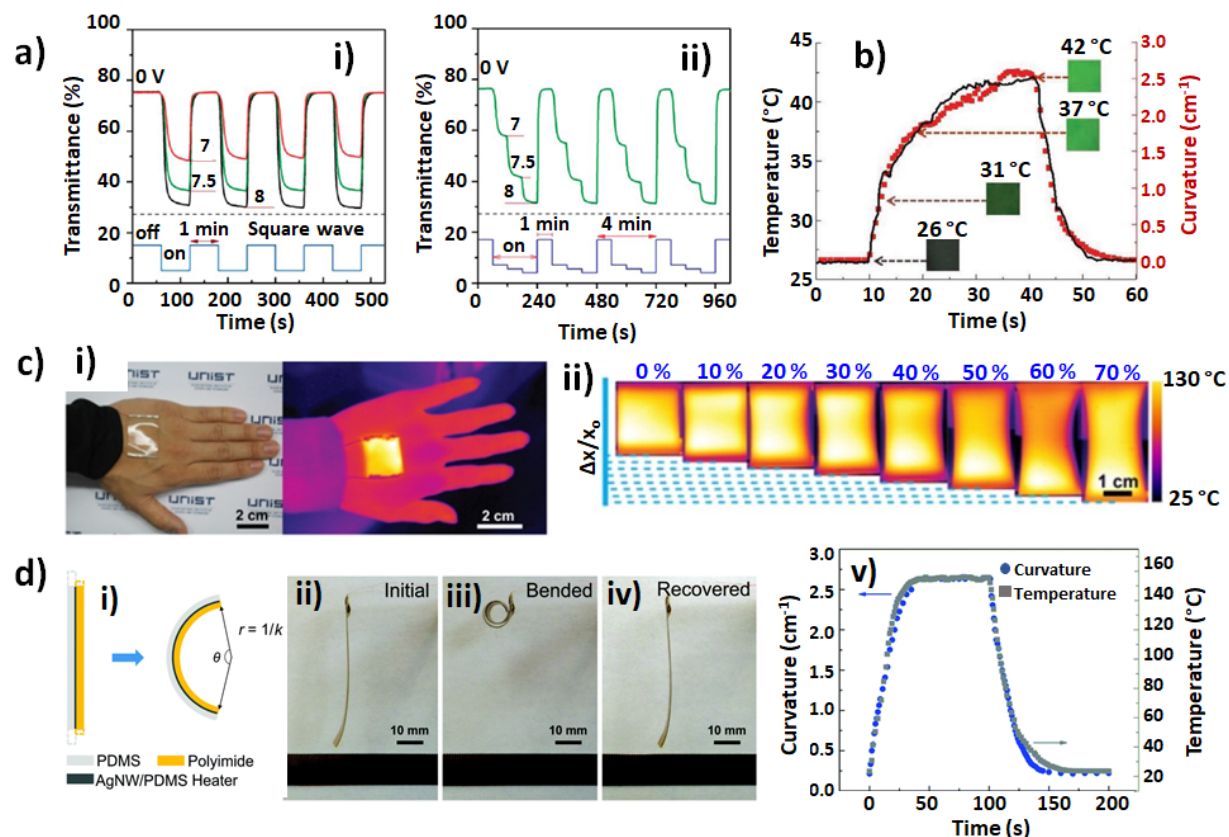


Figure 17. Thermochromic, medical and other transparent heater applications. a) Infrared response at 1.5 μm of a VO₂ NP-electrothermochromic film device based on AgNWs upon input of a pulse voltage with i) a square wave and ii) a square wave with a step variation. The dashed line denotes the lowest transmittance at a constant voltage of 8 V. The pulse wave pattern and its application method are shown below the dashed line, along with the wave parameters. Reproduced with permission.^[237] Copyright 2014, Royal Society of Chemistry. b) The transient behavior of the curvature and temperature of a color-shifting anisotropic soft actuator based on an AgNW network TH. Insets are digital camera images of the actuator's color changes with respect to temperature. Reproduced with permission.^[109] Copyright 2018, John Wiley and Sons. c) Transparent and wearable heaters using nanotrough network of CuZr metallic glasses; i) photograph and IR image of the heater attached to a human hand. The black strap is the custom-made electronic band for a power supply and temperature controller. ii) IR images of the CuZr nanotrough heater under various tensile strains. Reproduced with permission.^[70] Copyright 2016, American Chemical Society. d) Bending and heating performance of the PI/AgNW/PDMS bimorph actuator; i) schematic of the electrothermal bimorph actuation mechanism. k : bending curvature; r : radius of curvature, ii) the initial state, iii) the bent state with the maximum curvature and iv) the recovered state of the U-shaped actuator. One end of the actuator is fixed and the other end can bend freely and reversibly under an applied DC voltage of 4.5 V. v) Curvature and temperature of the actuator as a function of time. Reproduced with permission.^[239] Copyright 2017, Royal Society of Chemistry.

Huang et al.^[238] fabricated a flexible AgNW/PI TH with faster and higher heating temperatures at lower power consumption compared to TCO heaters. The flexible and stable TH was successfully used in a thermochromic device. The obtained AgNW/PI-based TH exhibited a heating temperature of 96°C under a bias of 6V, and a response time of 40 seconds.^[238] Recently, Huang et al.^[199] fabricated a large-area flexible, transparent thermochromic window based on AgNW nylon-meshes. This thermochromic textile could be produced cheap and fast, i.e. 20 minutes for 7.5 m² and a cost of \$15.03.

Another interesting and recent study presented by Kim et al.^[109] used AgNW-based THs as a color-shifting anisotropic soft actuator with a very large bending curvature of 2.5 cm⁻¹ at a low temperature of 40 °C. The transient behavior of the curvature and temperature of the color changing actuators based on AgNW Joule heating is shown in Figure 17b as well as digital camera images of the color of the actuator. The devices have demonstrated a superior long-term stability for more than 10,000 operating cycles. Shi et al.^[202] demonstrated a SiO₂/AgNW/colorless PI composite film heater with an improved transparency of 3.5 % due to the antireflective SiO₂ coating. The haze of both bare and SiO₂-coated AgNW/cPI films are the same, as well as their heating performance. The composite shows good mechanical properties, and was tested in a thermochromic device with a purple to blue color change after 10 s of applied voltage. Kim et al.^[102] fabricated a CNT/AgNW hybrid TH with reduced haze and improved flexibility at 1.5 mm bending radius. The haze of the hybrid film is tuned by AgNW content, and its heating performance is monitored by the color change of a thermochromic dye inside a beaker wrapped with the CNT/AgNW TH film.

4.4 Transparent heaters for Medical applications

This last decade has seen the emergence of new flexible and stretchable electronics to fabricate sensors and actuators with properties similar to skin (namely deformation of up to 15 % and elastic modulus between 10 kPa and a few hundred kPa^[240]). These kinds of devices can be found under several names, namely “electronic skin”, “e-skin”, “epidermal electronics“ and “electronic tattoos”.^[241] They present the advantages of being skin-mountable and thus relevant for continuous health monitoring, drug delivery, thermotherapy, human motion detection, human-machine interfaces and soft robotics.^[241–243]

Since 2013, Webb et al.^[244,245] have worked on the continuous thermal characterization of the skin by using ultrathin arrays of sensors and heaters. Combining sensing and heating allows to monitor physical and chemical parameters (like body temperature, glycemia, blood pressure and oxygen, elastic modulus of the skin^[241]) and potentially immediately diagnosing and delivering a medical treatment by cutaneous contact, keeping in mind that skin permeability or healing can be improved by local heating^[246]. Epidermal drug delivery systems are attractive because of the reduced side effects of topical administration. Bagherifard et al.^[243] used flexible heaters in dermal patches to control the release rates of drugs encapsulated into a thermo-responsive hydrogel (N-Isopropylacrylamide, NIPAM). Currently, sensor heaters are generally made of a bilayer of chromium and gold^[243–245], which are not transparent. Nevertheless, the nanometric thickness of the circuit results in a quasi-transparent device and highlights this line of research.

The most important application of electronic skins is thermotherapy, which is a new but expanding field. Indeed, heating pads are commonly used for a wide range of medical functions, like relieving pain^[247,248], preventing inflammation and improving blood circulation.^[121] Aside from pain relief, beneficial effects of a local heating treatment can be explained by the vasodilation, allowing blood vessels to supply more oxygen and nutrients to the surrounding area. Heating also prevents chronic inflammation by expelling inflammatory exudates.^[249] Moreover, heating pads can be useful in physiotherapy to help tendons, ligaments and muscles gain flexibility.^[250] The two currently available technical solutions for thermotherapy are heat packs and wraps.^[250,251] Heat packs are bulky and heavy and must be pre-heated in water or in a micro-wave, often compromising the fine control of the temperature. Heating wraps allow a better control of the temperature thanks to the Joule heating of resistors, but are usually rigid and heavy, which limits their wearability and their use in hospitals.^[23]

New lightweight and autonomous devices combining a controlled temperature, fast response and high transparency are gaining interest. Using THs for thermotherapy pads would allow to see the heated parts of the body, potentially healing wounds, and to adjust more efficiently the treatment. Different techniques are under development to meet these requirements. The average values of temperature/voltage should be around 40-50 °C/3-5 V, to avoid burning the skin and to operate the devices with common batteries. Two methods are mostly studied: patterned nanocomposites and hybrid films with a network of metallic conductors and an elastomeric substrate.

In 2015, Choi et al.^[23] developed a patterned nanocomposite made of AgNWs and a thermoplastic elastomer (styrene-butadiene-styrene, SBS). In order to obtain a highly conductive nanocomposite, a ligand-exchange reaction was carried out to homogeneously incorporate the AgNWs within the elastomeric matrix. This serpentine mesh-structure allows stable heating (+40 °C, 1 V) while being stretched (17% and 26% for extension or flexion of the wrist and the knee, respectively). The resistance remains stable after 5000 cycles at 30% strain and 48 h under UV exposure. Unfortunately, the device transparency value was not reported.

Other techniques being developed use conductive networks based on MNWs or metallic glasses, coated on elastomeric substrates. CuZr metallic glasses on PDMS display excellent optoelectronic properties, with a resistance of 4 Ω/sq for 90% transparency, combined with a high stretchability (only 30% change in resistance for 70% strain, Figure 17c).^[70] Moreover, a temperature of 60 °C can be reached for a bias of only 3 V. In terms of stability it is demonstrated that the heating performance of the film is stable for 10 days under relatively harsh conditions (85 °C for 85% RH). CuNW-based hybrids also present good performances, with 96 Ω/sq for 91% transparency, using a poly(methyl methacrylate) (PMMA) coating.^[252] To obtain a stretchable device, the elastomer Ecoflex® (blend of cellulose, lignin, poly(lactic acid), poly(hydroxy alcanoate) and starch) was used as a replacement for PMMA, and enabled a stretching of 80% with a constant DC bias of 1.5 V. Under these conditions, however, the maximal reported temperature reached only 30 °C. If the stretching is kept low, a temperature of 50°C can be reached while applying 3 V, which is sufficient for thermotherapy. Percolated AgNW networks deposited on PDMS and encapsulated with PVA were shown to have adequate properties for thermotherapy pads, with high transparency (90%), low sheet resistance (20 Ω/sq and a low operating voltage (3.5 V to reach 45 °C).^[121] Stability under severe thermal (80 °C)

and humidity (80% RH, 45°C) conditions was demonstrated for an extended period of 6 months, in addition to mechanical stability over 10,000 bending cycles (1 mm radius).

Recently, the impact of skin surface heating has been evaluated thanks to tests on porcine skin, to evaluate the efficacy of thermotherapy. A 12 °C temperature raise of the subcutaneous tissue (5 mm beneath the skin surface) was measured.^[190]

Stretchable TCMs demonstrate promising potential for thermotherapy. The stretchability of THs for thermotherapy is an added value. Many research projects on these materials have emerged in recent years, often in strong relationship with the development of flexible and transparent electronics.^[253] Based on the growing interest in wearable devices and the wide range of medical applications, there is no doubt that the research on this topic will gain further momentum.

4.5 Other niche applications

Besides the main applications previously described, THs are clearly interesting for other niche fields like actuators, gas sensors or refractive index tuning. Actuators are devices which are able to convert different types of energy, such as light^[254], electric fields^[255], magnetic fields^[256], pneumatic pressure^[257] or thermal energy, into mechanical energy. Among them, electrothermal actuators are based on either the thermal expansion of a single material or on the difference in thermal expansions between two materials. Their competitive advantages over other actuators are their low actuation voltage, as well as their lightweight and electrolyte-free design. Zhu et al. demonstrated the use of graphene in bimorph actuators.^[258] Graphene contracts upon heating due to a negative thermal expansion coefficient, which is opposite to the common behavior of nearly all materials. This asymmetric thermomechanical response leads to a large bimorph actuation. More recently, transparent electrothermal actuators using CNT-based THs^[259,260] and AgNW-based THs^[109,239] have been reported. Yao et al. demonstrated a remarkable 2.6 cm⁻¹ curvature at a very low actuation voltage of 0.2 V/sq (4.5 V) in electrothermal actuators using AgNW THs (Figure 17d).^[239]

Several studies mention the use of thermal stimuli to address different functions. Zhang et al. developed a transparency-switchable electrothermal actuator using aligned CNT-based THs.^[260] In this paper, the authors used a paraffin wax/polydimethylsiloxane composite. At room temperature, the composite is opaque due to the light scattering induced by the paraffin wax crystallites. Upon heating, actuation occurs simultaneously with wax melting, which results in a dramatic increase in transmittance. Kim et al. demonstrated the use of MNW-based THs for simultaneous actuation and thermochromic color change.^[109]

Transparency becomes an important feature for gas sensors. Since heating gas sensors can improve their performances, the use of Joule heating with THs was reported to improve sensitivity and/or recovery time.^[62,261] Choi et al. developed graphene-based gas sensors, in which graphene was used for both sensing and heating.^[62] They reduced the recovery time of the NO₂ sensor by two orders of magnitude by heating the system up to 250°C. Similarly, Walia et al. improved the response time (from 41 to 13 s) and recovery time (from 112 to 35 s) at 1% H₂, with a moderate Joule heating at 75°C of the transparent conducting palladium network used for sensing.^[261]

In another niche application, Heo et al. demonstrated the use of ITO-based THs for the development of lenticular lenses with a thermally tunable focus, using liquid crystals.^[262] The

temperature can alter the birefringence of a liquid crystal-based lens by changing the refractive index between the active component and the polymer layer. Increasing the temperature from 25 °C to 55 °C altered the focal length from 5.5 mm to 8.5 mm. These lenticular lenses have potential in optical devices like phone cameras.

Finally Won et al.^[263] showed an original concept of stretchable kirigami TE consisting of ultrathin and flexible AgNWs/colorless polyimide cPI composites with laser patterned kirigami structure. A coating thin gold layer enables biocompatibility and enhances electrical stability. The laser patterning technique provides digital and rapid process (without patterning masks) allowing to design kirigami structures.^[263] This leads to achieve tunable stretchability, up to strain of 400%, which extends the scope of applications. Such a soft, thin and highly stretchable features can pave ways for multifunctional transparent and wearable electronic skin applications.

5 Prospects, future challenges and conclusive remarks

Since the first use of THs approximately eighty years ago, tremendous progress has been made in this field. TCOs were the first materials developed and produced at the industrial scale to fabricate efficient THs. These materials have been highly improved over the past decades, and now reach outstanding properties, in particular thanks to an excellent transparency-conductivity trade-off. Although TCOs have been the materials of choice until now, new scientific breakthroughs and new market needs have opened the way for innovative developments, notably based on nano-enabled technologies. The driving forces to search for (improved) substitutes to TCOs not only rely on cost issues, but also on geostrategic considerations, which can be a game-changer, and on the technological evolution of devices. Many devices will require flexibility and stretchability (displays, PV cells, touch screens...), which requires new performances and abilities. The development of these transparent materials could offer an additional value to existing opaque film heaters and permit to see through the active layer. This could be of interest applications in health (*e.g.* patches for thermotherapy) or safety (*e.g.* control of heating elements such as automotive gas pre-heater pipes).

Several relevant approaches appear very promising for TH production with improved functionalities. The recent development of nanomaterials has revealed unforeseen possibilities through the achievement of macroscopic performances relying on ordered or random assemblies of nanospecies, whether carbon-based or metallic. When electrically conductive nanoparticles are assembled on a surface above the percolation threshold, they give access to conductive surfaces at very low coverage values, which allows light to pass through, and to reach both high conductivity and high transparency. Another relevant possibility that needs to be further studied is the recent development based on the use of very thin films of highly conductive polymers. The performances are very promising, and these films have an intrinsically very low haze value.

All these new technologies have managed to meet the expectations at the prototype stage, but certainly need further development to ensure reproducibility, cost-efficiency and stability at the industrial stage. Reproducibility mainly relies on the constant quality and chemical purity of the raw materials (CNTs, graphene, MNWs, polymers), but also on stable large-scale production tools and multiscale characterization techniques. Stability aspects are also

particularly important, and they should be tackled while taking into account the targeted operational conditions. The stability will depend on many parameters like the structure of the device (including chemical compatibility with other layers), the applied voltage, the cyclability, high temperature long-term operating modes, and many others. Concerning the use of nanomaterials, an in-depth nanotoxicity assessment needs to be carried out to ensure the safe use for both the manufacturers' operators and the end-users. Some studies have already been reported^[97,264–268], but further understanding of all the possible toxicity aspects and long-term effects is needed.

To conclude this review, the current production of THs still relies essentially on an “old” technology which has been improved upon over the years, i.e. TCOs. Many existing and future applications will keep using this technology because it is a reliable and well-proven process. However, various ongoing technical developments will provide THs with additional properties (controlled haze factor, flexibility, stretchability, low-cost deposition processes...). We expect that there will not be a single winner among them, but rather several new TH technologies that will find specific industrial applications in the near future.

Acknowledgments:

This project was partially supported by the French National Research Agency in the framework of the “Investissements d’avenir” program (ANR-15-IDEX-02) through the project Eco-SESA. This work was also performed within the framework of the Centre of Excellence of Multifunctional Architected Materials “CEMAM” n° ANR-10-LABEX-44-01 through the project Earth. This work was funded by the Agence Nationale de Recherche (ANR, France) via the program ANR-16-CE05-0021 (DESPATCH), ANR-18-CE09-0041 (Meaning) and ANR-18-CE09-0036 (Panassé). This work was also supported by the Région Auvergne Rhône-Alpes through the project Pack Ambition Recherche 2018 Eternité. The Carnot Energies du Futur is acknowledged through the project FREE. The authors would like to warmly thank Vincent Fitzpatrick for fruitful discussions.

References:

- [1] R. Gupta, K. D. M. Rao, S. Kiruthika, G. U. Kulkarni, *ACS Appl. Mater. Interfaces* **2016**, *8*, 12559.
- [2] R. G. Gordon, *MRS Bulletin* **2000**, *25*, 52.
- [3] S. Long, X. Cao, G. Sun, N. Li, T. Chang, Z. Shao, P. Jin, *Applied Surface Science* **2018**, *441*, 764.
- [4] L. Long, H. Ye, *Scientific Reports* **2015**, *4*, 6427.
- [5] S. T. Heinilä, J. H. Lappalainen, H. M. Jantunen, V. Lantto, *Journal of Electroceramics* **2011**, *27*, 7.
- [6] J. You, L. Meng, T.-B. Song, T.-F. Guo, Y. (Michael) Yang, W.-H. Chang, Z. Hong, H. Chen, H. Zhou, Q. Chen, Y. Liu, N. De Marco, Y. Yang, *Nature Nanotechnology* **2016**, *11*, 75.
- [7] C. G. Granqvist, *Thin Solid Films* **2014**, *564*, 1.
- [8] W. Gaynor, S. Hofmann, M. G. Christoforo, C. Sachse, S. Mehra, A. Salleo, M. D. McGehee, M. C. Gather, B. Lüssem, L. Müller-Meskamp, P. Peumans, K. Leo, *Advanced Materials* **2013**, *25*, 4006.
- [9] K. Ellmer, *Nature Photonics* **2012**, *6*, 809.
- [10] C. G. Granqvist, *Solar Energy Materials and Solar Cells* **2007**, *91*, 1529.
- [11] H. J. Park, J. Kim, J. H. Won, K. S. Choi, Y. T. Lim, J. S. Shin, J.-U. Park, *Thin Solid Films* **2016**, *615*, 8.
- [12] J. Gwamuri, A. Vora, J. Mayandi, D. Ö. Güneş, P. L. Bergstrom, J. M. Pearce, *Solar Energy Materials and Solar Cells* **2016**, *149*, 250.
- [13] M. Morales-Masis, S. De Wolf, R. Woods-Robinson, J. W. Ager, C. Ballif, *Advanced Electronic Materials* **2017**, *3*, 1600529.
- [14] G. Rey, C. Ternon, M. Modreanu, X. Mescot, V. Consonni, D. Bellet, *Journal of Applied Physics* **2013**, *114*, 183713.
- [15] V. Consonni, G. Rey, H. Roussel, B. Doisneau, E. Blanquet, D. Bellet, *Acta Materialia* **2013**, *61*, 22.
- [16] K. Ellmer, A. Klein, B. Rech, Eds., *Transparent Conductive Zinc Oxide*, Springer Berlin Heidelberg, Berlin, Heidelberg, **2008**.
- [17] A. Klein, *J. Am. Ceram. Soc.* **2013**, *96*, 331.
- [18] D. Lincot, *MRS Bulletin* **2010**, *35*, 778.

- [19] V. H. Nguyen, U. Gottlieb, A. Valla, D. Muñoz, D. Bellet, D. Muñoz-Rojas, *Materials Horizons* **2018**, *5*, 715.
- [20] T. Sannicolo, M. Lagrange, A. Cabos, C. Celle, J.-P. Simonato, D. Bellet, *Small* **2016**, *12*, 6052.
- [21] D. S. Hecht, L. Hu, G. Irvin, *Advanced Materials* **2011**, *23*, 1482.
- [22] S. Hong, H. Lee, J. Lee, J. Kwon, S. Han, Y. D. Suh, H. Cho, J. Shin, J. Yeo, S. H. Ko, *Adv. Mater.* **2015**, *27*, 4744.
- [23] S. Choi, J. Park, W. Hyun, J. Kim, J. Kim, Y. B. Lee, C. Song, H. J. Hwang, J. H. Kim, T. Hyeon, D.-H. Kim, *ACS Nano* **2015**, *9*, 6626.
- [24] N.-S. Jang, K.-H. Kim, S.-H. Ha, S.-H. Jung, H. M. Lee, J.-M. Kim, *ACS Applied Materials & Interfaces* **2017**, *9*, 19612.
- [25] S. Bae, H. Kim, Y. Lee, X. Xu, J.-S. Park, Y. Zheng, J. Balakrishnan, T. Lei, H. Ri Kim, Y. I. Song, Y.-J. Kim, K. S. Kim, B. Özyilmaz, J.-H. Ahn, B. H. Hong, S. Iijima, *Nat Nano* **2010**, *5*, 574.
- [26] J. Zhao, Y. Li, G. Yang, K. Jiang, H. Lin, H. Ade, W. Ma, H. Yan, *Nature Energy* **2016**, *1*, 15027.
- [27] Y.-H. Yoon, J.-W. Song, D. Kim, J. Kim, J.-K. Park, S.-K. Oh, C.-S. Han, *Adv. Mater.* **2007**, *19*, 4284.
- [28] J. Du, S. Pei, L. Ma, H.-M. Cheng, *Advanced Materials* **2014**, *26*, 1958.
- [29] Y. Sun, Y. Yin, B. T. Mayers, T. Herricks, Y. Xia, *Chem. Mater.* **2002**, *14*, 4736.
- [30] A. R. Rathmell, S. M. Bergin, Y.-L. Hua, Z.-Y. Li, B. J. Wiley, *Advanced Materials* **2010**, *22*, 3558.
- [31] A. R. Rathmell, B. J. Wiley, *Advanced Materials* **2011**, *23*, 4798.
- [32] A. R. Rathmell, M. Nguyen, M. Chi, B. J. Wiley, *Nano Letters* **2012**, *12*, 3193.
- [33] S. De, T. M. Higgins, P. E. Lyons, E. M. Doherty, P. N. Nirmalraj, W. J. Blau, J. J. Boland, J. N. Coleman, *ACS Nano* **2009**, *3*, 1767.
- [34] S. De, P. J. King, P. E. Lyons, U. Khan, J. N. Coleman, *ACS Nano* **2010**, *4*, 7064.
- [35] J. Liang, L. Li, X. Niu, Z. Yu, Q. Pei, *Nature Photonics* **2013**, *7*, 817.
- [36] L. Li, Z. Yu, W. Hu, C. Chang, Q. Chen, Q. Pei, *Advanced Materials* **2011**, *23*, 5563.
- [37] S. Ye, A. R. Rathmell, Z. Chen, I. E. Stewart, B. J. Wiley, *Adv. Mater.* **2014**, *26*, 6670.
- [38] D. Bellet, M. Lagrange, T. Sannicolo, S. Aghazadehchors, V. H. Nguyen, D. P. Langley, D. Muñoz-Rojas, C. Jiménez, Y. Bréchet, N. D. Nguyen, *Materials* **2017**, *10*, 570.
- [39] D. Chen, J. Liang, Q. Pei, *Sci. China Chem.* **2016**, *1*.
- [40] J. Liu, D. Jia, J. M. Gardner, E. M. J. Johansson, X. Zhang, *Materials Today Energy* **2019**, *13*, 152.
- [41] R. Zhang, M. Engholm, R. Zhang, M. Engholm, *Nanomaterials* **2018**, *8*, 628.
- [42] C. Celle, C. Mayousse, E. Moreau, H. Basti, A. Carella, J.-P. Simonato, *Nano Research* **2012**, *5*, 427.
- [43] S. Sorel, D. Bellet, J. N. Coleman, *ACS Nano* **2014**, *8*, 4805.
- [44] O. Ergun, S. Coskun, Y. Yusufoglu, H. E. Unalan, *Nanotechnology* **2016**, *27*, 445708.
- [45] T. Kim, Y. W. Kim, H. S. Lee, H. Kim, W. S. Yang, K. S. Suh, *Advanced Functional Materials* **2013**, *23*, 1250.
- [46] M. Lagrange, T. Sannicolo, D. Muñoz-Rojas, B. G. Lohan, A. Khan, M. Anikin, C. Jiménez, F. Bruckert, Y. Bréchet, D. Bellet, *Nanotechnology* **2017**, *28*, 055709.
- [47] A. Khan, V. H. Nguyen, D. Muñoz-Rojas, S. Aghazadehchors, C. Jiménez, N. D. Nguyen, D. Bellet, *ACS Applied Materials & Interfaces* **2018**, *10*, 19208.
- [48] C. Celle, A. Cabos, T. Fontecave, B. Laguitton, A. Benayad, L. Guettaz, N. Pélissier, V. H. Nguyen, D. Bellet, D. Muñoz-Rojas, J.-P. Simonato, *Nanotechnology* **2018**, *29*, 085701.
- [49] M. N. Gueye, A. Carella, N. Massonnet, E. Yvenou, S. Brenet, J. Faure-Vincent, S. Pouget, F. Rieutord, H. Okuno, A. Benayad, R. Demadrille, J.-P. Simonato, *Chemistry of Materials* **2016**, *28*, 3462.
- [50] M. N. Gueye, A. Carella, R. Demadrille, J.-P. Simonato, *ACS Appl. Mater. Interfaces* **2017**, *9*, 27250.
- [51] E.-H. Ko, H.-J. Kim, S.-J. Lee, J.-H. Lee, H.-K. Kim, *RSC Advances* **2016**, *6*, 46634.
- [52] S.-H. Park, S.-M. Lee, E.-H. Ko, T.-H. Kim, Y.-C. Nah, S.-J. Lee, J. H. Lee, H.-K. Kim, *Scientific Reports* **2016**, *6*, DOI 10.1038/srep33868.
- [53] H. Kim, Y. Kim, K. S. Kim, H. Y. Jeong, A.-R. Jang, S. H. Han, D. H. Yoon, K. S. Suh, H. S. Shin, T. Kim, W. S. Yang, *ACS Nano* **2013**, *7*, 5769.
- [54] H. H. Khaligh, L. Xu, A. Khosropour, A. Madeira, M. Romano, C. Pradère, M. Tréguer-Delapierre, L. Servant, M. A. Pope, I. A. Goldthorpe, *Nanotechnology* **2017**, *28*, 425703.
- [55] G. Haacke, *Journal of Applied Physics* **1976**, *47*, 4086.
- [56] X. Chen, S. Nie, W. Guo, F. Fei, W. Su, W. Gu, Z. Cui, *Advanced Electronic Materials* **2019**, *5*, 1800991.
- [57] J. Kang, H. Kim, K. S. Kim, S.-K. Lee, S. Bae, J.-H. Ahn, Y.-J. Kim, J.-B. Choi, B. H. Hong, *Nano Lett.* **2011**, *11*, 5154.
- [58] H. Askari, H. Fallah, M. Askari, M. C. Mohmmadiyeh, *arXiv:1409.5293 [cond-mat]* **2014**.
- [59] G. Giusti, V. Consonni, E. Puyoo, D. Bellet, *ACS Appl. Mater. Interfaces* **2014**, *6*, 14096.
- [60] S. Ke, J. Xie, C. Chen, P. Lin, X. Zeng, L. Shu, L. Fei, Y. Wang, M. Ye, D. Wang, *Applied Physics Letters* **2018**, *112*, 031905.
- [61] Y. Kim, H. R. Lee, T. Saito, Y. Nishi, *Applied Physics Letters* **2017**, *110*, 153301.
- [62] H. Choi, J. S. Choi, J.-S. Kim, J.-H. Choe, K. H. Chung, J.-W. Shin, J. T. Kim, D.-H. Youn, K.-C. Kim, J.-I. Lee, S.-Y. Choi, P. Kim, C.-G. Choi, Y.-J. Yu, *Small* **2014**, *10*, 3685.
- [63] P. Blake, P. D. Brimicombe, R. R. Nair, T. J. Booth, D. Jiang, F. Schedin, L. A. Ponomarenko, S. V. Morozov, H. F. Gleeson, E. W. Hill, A. K. Geim, K. S. Novoselov, *Nano Lett.* **2008**, *8*, 1704.
- [64] M. Lagrange, D. P. Langley, G. Giusti, C. Jiménez, Y. Bréchet, D. Bellet, *Nanoscale* **2015**, *7*, 17410.
- [65] H. Yang, S. Bai, X. Guo, H. Wang, *Applied Surface Science* **2019**, *483*, 888.
- [66] M. Bobinger, J. Mock, P. La Torraca, M. Becherer, P. Lugli, L. Larcher, *Advanced Materials Interfaces* **2017**, *4*, 1700568.
- [67] K. D. M. Rao, G. U. Kulkarni, *Nanoscale* **2014**, *6*, 5645.
- [68] H. Hu, S. Wang, S. Wang, G. Liu, T. Cao, Y. Long, *Advanced Functional Materials* **2019**, 1902922.
- [69] H. Wu, D. Kong, Z. Ruan, P.-C. Hsu, S. Wang, Z. Yu, T. J. Carney, L. Hu, S. Fan, Y. Cui, *Nat Nano* **2013**, *8*, 421.

- [70] B. W. An, E.-J. Gwak, K. Kim, Y.-C. Kim, J. Jang, J.-Y. Kim, J.-U. Park, *Nano Letters* **2016**, *16*, 471.
- [71] R. Gupta, K. D. M. Rao, K. Srivastava, A. Kumar, S. Kiruthika, G. U. Kulkarni, *ACS Applied Materials & Interfaces* **2014**, *6*, 13688.
- [72] D. Lordan, M. Burke, M. Manning, A. Martin, A. Amann, D. O'Connell, R. Murphy, C. Lyons, A. J. Quinn, *ACS Applied Materials & Interfaces* **2017**, *9*, 4932.
- [73] H. Wang, S. Lin, D. Zu, J. Song, Z. Liu, L. Li, C. Jia, X. Bai, J. Liu, Z. Li, D. Wang, Y. Huang, M. Fang, M. Lei, B. Li, H. Wu, *Advanced Materials Technologies* **2019**, 1900045.
- [74] A. Khan, S. Lee, T. Jang, Z. Xiong, C. Zhang, J. Tang, L. J. Guo, W.-D. Li, *Small* **2016**, *12*, 3021.
- [75] S. An, H. S. Jo, D.-Y. Kim, H. J. Lee, B.-K. Ju, S. S. Al-Deyab, J.-H. Ahn, Y. Qin, M. T. Swihart, A. L. Yarin, S. S. Yoon, *Advanced Materials* **2016**, *28*, 7149.
- [76] H. S. Jo, S. An, J.-G. Lee, H. G. Park, S. S. Al-Deyab, A. L. Yarin, S. S. Yoon, *NPG Asia Materials* **2017**, *9*, e347.
- [77] N. Kim, H. Kang, J.-H. Lee, S. Kee, S. H. Lee, K. Lee, *Advanced Materials* **2015**, *27*, 2317.
- [78] Y. Wang, C. Zhu, R. Pfattner, H. Yan, L. Jin, S. Chen, F. Molina-Lopez, F. Lissel, J. Liu, N. I. Rabiah, Z. Chen, J. W. Chung, C. Linder, M. F. Toney, B. Murmann, Z. Bao, *Science Advances* **2017**, *3*, e1602076.
- [79] J. Li, J. Liang, X. Jian, W. Hu, J. Li, Q. Pei, *Macromol. Mater. Eng.* **2014**, *299*, 1403.
- [80] B.-Y. Hwang, S.-H. Choi, K.-W. Lee, J.-Y. Kim, *Composites Part B: Engineering* **2018**, *151*, 1.
- [81] S. B. Singh, Y. Hu, T. Kshetri, N. H. Kim, J. H. Lee, *Journal of Materials Chemistry C* **2017**, *5*, 4198.
- [82] S. Kiruthika, R. Gupta, G. U. Kulkarni, *RSC Adv.* **2014**, *4*, 49745.
- [83] J. J. Bae, S. C. Lim, G. H. Han, Y. W. Jo, D. L. Doung, E. S. Kim, S. J. Chae, T. Q. Huy, N. Van Luan, Y. H. Lee, *Adv. Funct. Mater.* **2012**, *22*, 4819.
- [84] A.-Y. Kim, K. Lee, J. H. Park, D. Byun, J. K. Lee, *physica status solidi (a)* **2014**, *211*, 1923.
- [85] S. Duzyer, S. Sinha-Ray, S. Sinha-Ray, A. L. Yarin, *Macromolecular Materials and Engineering* **2017**, *302*, 1700188.
- [86] D. Sui, Y. Huang, L. Huang, J. Liang, Y. Ma, Y. Chen, *Small* **2011**, *7*, 3186.
- [87] S. Ji, J. Park, Y. Jo, Y.-B. Kim, J. Jang, S.-K. Kim, S. Jeong, J.-U. Park, *Applied Surface Science* **2019**, *483*, 1101.
- [88] T. J. Kang, T. Kim, S. M. Seo, Y. J. Park, Y. H. Kim, *Carbon* **2011**, *49*, 1087.
- [89] S. R. Das, A. M. S. Mohammed, K. Maize, S. Sadeque, A. Shakouri, D. B. Janes, M. A. Alam, *Nano Lett.* **2016**, *16*, 3130.
- [90] D. P. Langley, M. Lagrange, G. Giusti, C. Jiménez, Y. Bréchet, N. D. Nguyen, D. Bellet, *Nanoscale* **2014**, *6*, 13535.
- [91] K. Maize, S. R. Das, S. Sadeque, A. M. S. Mohammed, A. Shakouri, D. B. Janes, M. A. Alam, *Applied Physics Letters* **2015**, *106*, 143104.
- [92] F. M. Smits, *Bell System Technical Journal* **1958**, *37*, 711.
- [93] T. Sannicolo, N. Charvin, L. Flandin, S. Kraus, D. T. Papanastasiou, C. Celle, J.-P. Simonato, D. Muñoz-Rojas, C. Jiménez, D. Bellet, *ACS Nano* **2018**, *12*, 4648.
- [94] N. Hoof, M. Parente, A. Baldi, J. G. Rivas, *Advanced Optical Materials* **2019**, 1900790.
- [95] S.-T. Zhang, M. Foldyna, H. Roussel, V. Consonni, E. Pernot, L. Schmidt-Mende, L. Rapenne, C. Jiménez, J.-L. Deschanvres, D. Muñoz-Rojas, D. Bellet, *J. Mater. Chem. C* **2016**, *5*, 91.
- [96] T. Araki, J. Jiu, M. Nogi, H. Koga, S. Nagao, T. Sugahara, K. Sugauma, *Nano Res.* **2014**, *7*, 236.
- [97] D. Toybou, C. Celle, C. Aude-Garcia, T. Rabilloud, J.-P. Simonato, *Environmental Science: Nano* **2019**, *6*, 684.
- [98] P. R. N. Childs, in *Practical Temperature Measurement*, Elsevier, **2001**, pp. 98–144.
- [99] B. Liptak, Ed., *Instrument Engineers' Handbook, Fourth Edition, Volume One: Process Measurement and Analysis*, CRC Press, **2003**.
- [100] A. Rogalski, P. Martyniuk, M. Kopytko, *Reports on Progress in Physics* **2016**, *79*, 046501.
- [101] Y.-A. Li, Y.-J. Chen, N.-H. Tai, *Materials Research Express* **2014**, *1*, 025605.
- [102] D. Kim, L. Zhu, D.-J. Jeong, K. Chun, Y.-Y. Bang, S.-R. Kim, J.-H. Kim, S.-K. Oh, *Carbon* **2013**, *63*, 530.
- [103] D. Pierścińska, *Journal of Physics D: Applied Physics* **2018**, *51*, 013001.
- [104] T. Yagi, K. Tamano, Y. Sato, N. Taketoshi, T. Baba, Y. Shigesato, *Journal of Vacuum Science & Technology A: Vacuum, Surfaces, and Films* **2005**, *23*, 1180.
- [105] O. Breitenstein, W. Warta, M. Langenkamp, *Lock-in Thermography: Basics and Use for Evaluating Electronic Devices and Materials*, Springer Science & Business Media, **2010**.
- [106] Ch. Schmidt, F. Altmann, O. Breitenstein, *Materials Science and Engineering: B* **2012**, *177*, 1261.
- [107] T. Sannicolo, D. Muñoz-Rojas, N. D. Nguyen, S. Moreau, C. Celle, J.-P. Simonato, Y. Bréchet, D. Bellet, *Nano Letters* **2016**, *16*, 7046.
- [108] R. Gupta, A. Kumar, S. Sadasivam, S. Walia, G. U. Kulkarni, T. S. Fisher, A. Marconnet, *ACS Applied Materials & Interfaces* **2017**, *9*, 13703.
- [109] H. Kim, H. Lee, I. Ha, J. Jung, P. Won, H. Cho, J. Yeo, S. Hong, S. Han, J. Kwon, K.-J. Cho, S. H. Ko, *Advanced Functional Materials* **2018**, *28*, 1801847.
- [110] V. Zardetto, T. M. Brown, A. Reale, A. Di Carlo, *Journal of Polymer Science Part B: Polymer Physics* **2011**, *49*, 638.
- [111] J. Jang, B. G. Hyun, S. Ji, E. Cho, B. W. An, W. H. Cheong, J.-U. Park, *NPG Asia Materials* **2017**, *9*, e432.
- [112] S. M. Lee, S. Oh, S. T. Chang, *ACS Applied Materials & Interfaces* **2019**, *11*, 4541.
- [113] F. Oytun, O. Alpturk, F. Basarir, *Materials Research Bulletin* **2019**, *112*, 53.
- [114] J.-G. Lee, J.-H. Lee, S. An, D.-Y. Kim, T.-G. Kim, S. S. Al-Deyab, A. L. Yarin, S. S. Yoon, *Journal of Materials Chemistry A* **2017**, *5*, 6677.
- [115] H.-J. Kim, Y. Kim, J.-H. Jeong, J.-H. Choi, J. Lee, D.-G. Choi, *Journal of Materials Chemistry A* **2015**, *3*, 16621.
- [116] M. Cao, M. Wang, L. Li, H. Qiu, Z. Yang, *ACS Applied Materials & Interfaces* **2018**, *10*, 1077.
- [117] D. Doganay, S. Coskun, S. P. Genlik, H. E. Unalan, *Nanotechnology* **2016**, *27*, 435201.
- [118] S. Xie, T. Li, Z. Xu, Y. Wang, X. Liu, W. Guo, *Nanoscale* **2018**, *10*, 6531.

- [119] Y. Tang, H. Ruan, Z. Huang, D. Shi, H. Liu, S. Chen, J. Zhang, *Nanotechnology* **2018**, *29*, 455706.
- [120] J. Kwon, H. Cho, Y. D. Suh, J. Lee, H. Lee, J. Jung, D. Kim, D. Lee, S. Hong, S. H. Ko, *Advanced Materials Technologies* **2017**, *2*, 1600222.
- [121] W. Lan, Y. Chen, Z. Yang, W. Han, J. Zhou, Y. Zhang, J. Wang, G. Tang, Y. Wei, W. Dou, Q. Su, E. Xie, *ACS Applied Materials & Interfaces* **2017**, *9*, 6644.
- [122] D. Levy, E. Castellón, *Transparent Conductive Materials: From Materials via Synthesis and Characterization to Applications*, **2018**.
- [123] D. Ginley, H. Hosono, D. C. Paine, *Handbook of Transparent Conductors*, Springer Science & Business Media, **2010**.
- [124] V. Consonni, G. Rey, H. Roussel, D. Bellet, *Journal of Applied Physics* **2012**, *111*, 033523.
- [125] I. Hamberg, C. G. Granqvist, *Journal of Applied Physics* **1986**, *60*, R123.
- [126] B. D. Ahn, S. H. Oh, D. U. Hong, D. H. Shin, A. Moujoud, H. J. Kim, *Journal of Crystal Growth* **2008**, *310*, 3303.
- [127] D. S. Y. Jayathilake, J. S. Sagu, K. G. U. Wijayantha, *Materials Letters* **2018**, *237*, 249.
- [128] J. H. Kim, B. D. Ahn, C. H. Kim, K. A. Jeon, H. S. Kang, S. Y. Lee, *Thin Solid Films* **2008**, *516*, 1330.
- [129] M. K. Roul, B. Obasogie, G. Kogo, J. R. Skuza, R. M. Mundle, A. K. Pradhan, *Journal of Applied Physics* **2017**, *122*, 135110.
- [130] K. Im, K. Cho, J. Kim, S. Kim, *Thin Solid Films* **2010**, *518*, 3960.
- [131] C. Kim, J.-W. Park, J. Kim, S.-J. Hong, M. J. Lee, *Journal of Alloys and Compounds* **2017**, *726*, 712.
- [132] K. Yang, K. Cho, K. Im, S. Kim, *Materials Research Bulletin* **2015**, *63*, 194.
- [133] S. Ke, C. Chen, N. Fu, H. Zhou, M. Ye, P. Lin, W. Yuan, X. Zeng, L. Chen, H. Huang, *ACS Applied Materials & Interfaces* **2016**, *8*, 28406.
- [134] V. H. Nguyen, D. Bellet, B. Masenelli, D. Muñoz-Rojas, *ACS Applied Nano Materials* **2018**, *1*, 6922.
- [135] L. Li, S. K. Hong, Y. Jo, M. Tian, C. Y. Woo, S. H. Kim, J.-M. Kim, H. W. Lee, *ACS Applied Materials & Interfaces* **2019**, *11*, 16223.
- [136] X. Yao, S. C. Hawkins, B. G. Falzon, *Carbon* **2018**, *136*, 130.
- [137] N. Karim, M. Zhang, S. Afroj, V. Koncherry, P. Potluri, K. S. Novoselov, *RSC Advances* **2018**, *8*, 16815.
- [138] H. Souri, D. Bhattacharyya, *ACS Applied Materials & Interfaces* **2018**, *10*, 20845.
- [139] M. Yang, J. Pan, A. Xu, L. Luo, D. Cheng, G. Cai, J. Wang, B. Tang, X. Wang, *Polymers* **2018**, *10*, 568.
- [140] P. Liu, D. Zhou, Y. Wei, K. Jiang, J. Wang, L. Zhang, Q. Li, S. Fan, *ACS Nano* **2015**, *9*, 3753.
- [141] B. Zhou, X. Han, L. Li, Y. Feng, T. Fang, G. Zheng, B. Wang, K. Dai, C. Liu, C. Shen, *Composites Science and Technology* **2019**, *183*, 107796.
- [142] H. Souri, S. J. Yu, H. Yeo, M. Goh, J.-Y. Hwang, S. M. Kim, B.-C. Ku, Y. G. Jeong, N.-H. You, *RSC Advances* **2016**, *6*, 52509.
- [143] O. P. Morris, X. Zang, A. Gregg, B. Keller, B. Getachew, S. Ingersoll, H. A. Elsen, M. M. Disko, N. Ferralis, J. C. Grossman, *Advanced Materials* **2019**, *31*, 1900331.
- [144] E. J. Spadafora, K. Saint-Aubin, C. Celle, R. Demadrille, B. Grévin, J.-P. Simonato, *Carbon* **2012**, *50*, 3459.
- [145] H.-S. Jang, S. K. Jeon, S. H. Nahm, *Carbon* **2011**, *49*, 111.
- [146] T. L. Chen, D. S. Ghosh, M. Marchena, J. Osmond, V. Pruneri, *ACS Applied Materials & Interfaces* **2015**, *7*, 5938.
- [147] L. Hu, H. Wu, Y. Cui, *MRS Bulletin* **2011**, *36*, 760.
- [148] B.-J. Kim, J.-S. Park, R. Yoo, J.-S. Park, *RSC Advances* **2017**, *7*, 53025.
- [149] N. Kwon, K. Kim, J. Heo, I. Yi, I. Chung, *Nanotechnology* **2014**, *25*, 265702.
- [150] P. Li, J. G. Ma, H. Y. Xu, D. Lin, X. D. Xue, X. Z. Yan, P. Xia, Y. C. Liu, *Journal of Alloys and Compounds* **2016**, *664*, 764.
- [151] A. Khan, C. Liang, Y.-T. Huang, C. Zhang, J. Cai, S.-P. Feng, W.-D. Li, *Advanced Engineering Materials* **2019**, *1900723*.
- [152] E. Thouti, C. Mistry, A. Chandran, D. K. Panwar, P. Kumar, H. Suman, J. Akhtar, *Journal of Physics D: Applied Physics* **2019**, *52*, 5301.
- [153] T. Sannicolo, Transparent Electrodes Based on Silver Nanowire Networks: Electrical Percolation, Physical Properties, and Applications, PhD thesis, University of Grenoble Alpes (France), **2017**.
- [154] J. H. Park, D. Y. Lee, Y.-H. Kim, J. K. Kim, J. H. Lee, J. H. Park, T.-W. Lee, J. H. Cho, *ACS Appl. Mater. Interfaces* **2014**, *6*, 12380.
- [155] Y.-Y. Zhao, M.-L. Zheng, X.-Z. Dong, F. Jin, J. Liu, X.-L. Ren, X.-M. Duan, Z.-S. Zhao, *Applied Physics Letters* **2016**, *108*, 221104.
- [156] J. Kang, C.-G. Park, S.-H. Lee, C. Cho, D.-G. Choi, J.-Y. Lee, *Nanoscale* **2016**, *8*, 11217.
- [157] J. Xue, J. Song, Y. Dong, L. Xu, J. Li, H. Zeng, *Science Bulletin* **2017**, *62*, 143.
- [158] H. Sohn, C. Park, J.-M. Oh, S. W. Kang, M.-J. Kim, *Materials* **2019**, *12*, 2526.
- [159] C. G. da Rocha, H. G. Manning, C. O'Callaghan, C. Ritter, A. T. Bellew, J. J. Boland, M. S. Ferreira, *Nanoscale* **2015**, *7*, 13011.
- [160] A. T. Bellew, H. G. Manning, C. Gomes da Rocha, M. S. Ferreira, J. J. Boland, *ACS Nano* **2015**, *9*, 11422.
- [161] S. Coskun, E. Selen Ates, H. Emrah Unalan, *Nanotechnology* **2013**, *24*, 125202.
- [162] Y. Goliya, A. Rivadeneyra, J. F. Salmeron, A. Albrecht, J. Mock, M. Haider, J. Russer, B. Cruz, P. Eschlewech, E. Biebl, M. Becherer, M. R. Bobinger, *Advanced Optical Materials* **2019**, 1900995.
- [163] M. Bobinger, J. Mock, M. Becherer, P. L. Torraca, D. Angeli, L. Larcher, P. Lugli, *IEEE*, **2017**, pp. 151–154.
- [164] I. E. Stewart, S. Ye, Z. Chen, P. F. Flowers, B. J. Wiley, *Chemistry of Materials* **2015**, *27*, 7788.
- [165] E. C. Garnett, W. Cai, J. J. Cha, F. Mahmood, S. T. Connor, M. Greyson Christoforo, Y. Cui, M. D. McGehee, M. L. Brongersma, *Nature Materials* **2012**, *11*, 241.
- [166] Y. Huang, Y. Tian, C. Hang, Y. Liu, S. Wang, M. Qi, H. Zhang, J. Zhao, *ACS Applied Materials & Interfaces* **2019**, *11*, 21850.

- [167] D. Chen, F. Zhao, K. Tong, G. Saldanha, C. Liu, Q. Pei, *Advanced Electronic Materials* **2016**, *2*, 1600167.
- [168] H. H. Khaligh, I. A. Goldthorpe, *Nanoscale research letters* **2013**, *8*, 1.
- [169] D. Tigan, S. P. Genlik, B. Imer, H. E. Unalan, *Nanotechnology* **2019**, *30*, 325202.
- [170] M.-G. Kang, L. J. Guo, *Adv. Mater.* **2007**, *19*, 1391.
- [171] B. Bessaire, M. Mathieu, V. Salles, T. Yeghoyan, C. Celle, J.-P. Simonato, A. Brioude, *ACS Applied Materials & Interfaces* **2017**, *9*, 950.
- [172] L. J. Romasanta, P. Schäfer, J. Leng, *Scientific Reports* **2018**, *8*, 16227.
- [173] M. N. Gueye, A. Carella, J. Faure-Vincent, R. Demadrille, J.-P. Simonato, *Progress in Materials Science* **2019**, *100*, 100616.
- [174] C. Shi, K. A. Owusu, X. Xu, T. Zhu, G. Zhang, W. Yang, L. Mai, *Small* **2019**, 1902348.
- [175] X. He, R. He, Q. Lan, W. Wu, F. Duan, J. Xiao, M. Zhang, Q. Zeng, J. Wu, J. Liu, *Materials* **2017**, *10*, 220.
- [176] X. He, G. Shen, R. Xu, W. Yang, C. Zhang, Z. Liu, B. Chen, J. Liu, M. Song, *Polymers* **2019**, *11*, 468.
- [177] J. Yan, Y. G. Jeong, *Materials & Design* **2015**, *86*, 72.
- [178] S.-B. Yang, H. Choi, D. S. Lee, C.-G. Choi, S.-Y. Choi, I.-D. Kim, *Small* **2015**, *11*, 1293.
- [179] L. Dou, F. Cui, Y. Yu, G. Khanarian, S. W. Eaton, Q. Yang, J. Resasco, C. Schildknecht, K. Schierle-Arndt, P. Yang, *ACS Nano* **2016**, *10*, 2600.
- [180] H. J. Han, Y. C. Choi, J. H. Han, *Synthetic Metals* **2015**, *199*, 219.
- [181] Y. Ahn, Y. Jeong, D. Lee, Y. Lee, *ACS Nano* **2015**, *9*, 3125.
- [182] C. Wu, J. Jiu, T. Araki, H. Koga, T. Sekitani, H. Wang, K. Suganuma, *RSC Adv.* **2016**, *6*, 15838.
- [183] Y. Tang, H. Ruan, Y. Chen, J. Xiang, H. Liu, R. Jin, D. Shi, S. Chen, J. Zhang, *Nanotechnology* **2020**, *31*, 045704.
- [184] S. M. Lee, J. H. Lee, S. Bak, K. Lee, Y. Li, H. Lee, *Nano Research* **2015**, *8*, 1882.
- [185] Y. Cai, X. Piao, X. Yao, W. Gao, E. Nie, Z. Zhang, Z. Sun, *Nanotechnology* **2019**, *30*, 225201.
- [186] M. P. Gupta, N. Kumar, S. Kumar, *IEEE Transactions on Nanotechnology* **2018**, *17*, 829.
- [187] S. Sadeque, Y. Gong, K. Maize, A. K. Ziabari, A. M. Mohammed, A. Shakouri, D. B. Janes, *IEEE Transactions on Nanotechnology* **2018**, *17*, 276.
- [188] S. Wang, Y. Tian, C. Wang, C. Hang, Y. Huang, C. Liao, *Composites Science and Technology* **2019**, *174*, 76.
- [189] K. Pyo, J.-W. Kim, *Current Applied Physics* **2016**, *16*, 1453.
- [190] D. Han, Y. Li, X. Jiang, W. Zhao, F. Wang, W. Lan, E. Xie, W. Han, *Composites Science and Technology* **2018**, *168*, 460.
- [191] K. Barros, P. L. Krapivsky, S. Redner, *Physical Review E* **2009**, *80*, 040101.
- [192] M. Žeželj, I. Stanković, A. Belić, *Phys. Rev. E* **2012**, *85*, 021101.
- [193] J.-S. Bae, Y.-S. Lee, J. Li, J. Liang, D. Chen, Q. Pei, S.-B. Lee, *Advanced Materials Technologies* **2018**, 1700364.
- [194] S. Ji, W. He, K. Wang, Y. Ran, C. Ye, *Small* **2014**, *10*, 4951.
- [195] K. Lee, J. Park, H. Kim, H.-S. Park, H.-K. Song, K.-H. Kim, K. Seo, *Journal of Materials Chemistry A* **2018**.
- [196] C.-Y. Chou, H.-S. Liu, G.-S. Liou, *RSC Advances* **2016**, *6*, 61386.
- [197] M. Patel, K. R. Chauhan, J. Kim, J.-W. Kim, D. Lim, *Sensors and Actuators A: Physical* **2017**, *267*, 8.
- [198] Y. Cai, X. Piao, X. Yao, E. Nie, Z. Zhang, Z. Sun, *Materials Letters* **2019**, *249*, 66.
- [199] W.-R. Huang, Z. He, J.-L. Wang, J.-W. Liu, S.-H. Yu, *iScience* **2019**, *12*, 333.
- [200] P. Li, J. Ma, H. Xu, X. Xue, Y. Liu, *J. Mater. Chem. C* **2016**, *4*, 3581.
- [201] N. Tiwari, A. Ankit, M. Rajput, M. R. Kulkarni, R. A. John, N. Mathews, *Nanoscale* **2017**, *9*, 14990.
- [202] X. Shi, W. Xu, J. Zhang, R. Wang, X. Li, W. Shen, G. Chen, X. Fang, W. Song, *Materials Research Express* **2019**, *6*, 095069.
- [203] H.-Y. Lu, C.-Y. Chou, J.-H. Wu, J.-J. Lin, G.-S. Liou, *Journal of Materials Chemistry C* **2015**, *3*, 3629.
- [204] X. Shi, W. Xu, W. Shen, G. Wang, R. Wang, X. Li, W. Song, *Journal of Materials Science: Materials in Electronics* **2019**, *30*, 2089.
- [205] Z. R. Ramadhan, J. W. Han, D. J. Lee, S. A. N. Entifar, J. Hong, C. Yun, Y. H. Kim, *Materials Research Letters* **2019**, *7*, 124.
- [206] J. Li, S. Qi, J. Liang, L. Li, Y. Xiong, W. Hu, Q. Pei, *ACS Applied Materials & Interfaces* **2015**, *7*, 14140.
- [207] F. S. F. Morgenstern, D. Kabra, S. Massip, T. J. K. Brenner, P. E. Lyons, J. N. Coleman, R. H. Friend, *Applied Physics Letters* **2011**, *4*, 183307.
- [208] V. H. Nguyen, J. Resende, D. T. Papanastasiou, N. Fontanals, C. Jiménez, D. Muñoz-Rojas, D. Bellet, *Nanoscale* **2019**, *11*, 12097.
- [209] D. Muñoz-Rojas, V. H. Nguyen, C. Masse de la Huerta, S. Aghazadehchors, C. Jiménez, D. Bellet, *Comptes Rendus Physique* **2017**, *18*, 391.
- [210] V. H. Nguyen, J. Resende, C. Jiménez, J.-L. Deschanvres, P. Carroy, D. Muñoz, D. Bellet, D. Muñoz-Rojas, *Journal of Renewable and Sustainable Energy* **2017**, *9*, 021203.
- [211] S. Aghazadehchors, V. H. Nguyen, D. Muñoz-Rojas, C. Jiménez, L. Rapenne, N. D. Nguyen, D. Bellet, *Nanoscale* **2019**, *11*, 19969.
- [212] H.-G. Cheong, J.-H. Kim, J.-H. Song, U. Jeong, J.-W. Park, *Thin Solid Films* **2015**, *589*, 633.
- [213] H. Chen, L. Wang, J. Li, Y. Yu, X. Bi, *Materials Letters* **2018**, *217*, 52.
- [214] B. Sharma, J.-S. Kim, A. Sharma, *Microelectronic Engineering* **2019**, *205*, 37.
- [215] J. Kang, Y. Jang, Y. Kim, S.-H. Cho, J. Suhr, B. H. Hong, J.-B. Choi, D. Byun, *Nanoscale* **2015**, *7*, 6567.
- [216] H. Khachatryan, M. Kim, H.-J. Seok, H.-K. Kim, *Materials Science in Semiconductor Processing* **2019**, *99*, 1.
- [217] D.-H. Kim, K.-S. Cho, H.-K. Kim, *Scientific Reports* **2017**, *7*, 2550.
- [218] M. K. Roul, S. K. Pradhan, K. D. Song, M. J. Bahoura, *Journal of Materials Science* **2019**, *54*, 7062.
- [219] T.-W. Kang, S. H. Kim, C. H. Kim, S.-M. Lee, H.-K. Kim, J. S. Park, J. H. Lee, Y. S. Yang, S.-J. Lee, *ACS Applied Materials & Interfaces* **2017**, *9*, 33129.
- [220] G. Kim, J. W. Lim, C. Yeon, T. Kim, H. C. Lee, S. J. Yun, *Journal of Alloys and Compounds* **2019**, *774*, 1092.

- [221] H. Im, E. Y. Jang, A. Choi, W. J. Kim, T. J. Kang, Y. W. Park, Y. H. Kim, *ACS Applied Materials & Interfaces* **2012**, *4*, 2338.
- [222] C. Hudaya, B. J. Jeon, J. K. Lee, *ACS Appl. Mater. Interfaces* **2015**, *7*, 57.
- [223] K.-D. Kim, T. Pfadler, E. Zimmermann, Y. Feng, J. A. Dorman, J. Weickert, L. Schmidt-Mende, *APL Materials* **2015**, *3*, 106105.
- [224] Y. Cheng, H. Zhang, R. Wang, X. Wang, H. Zhai, T. Wang, Q. Jin, J. Sun, *ACS Applied Materials & Interfaces* **2016**, *8*, 32925.
- [225] R. Singh, R. Kuzhikkali, N. Shet, N. Sekarapandian, G. Kizhedath, M. Arumugum, SABIC Tech Center, **2016**, p. 9.
- [226] B. Vandecastelle, *Heated window for refrigerated showcase and method of manufacturing same*, **1992**, EP0502775.
- [227] “Heater Circuits and LCD monitors,” can be found under <https://www.allflexinc.com/blog/heater-circuits-and-lcd-monitors/>, **2015**.
- [228] “Transparent Heaters and LCD Heaters,” can be found under <http://touchinternational.com/products/touch-display-enhancements/transparent-heaters/>, **n.d.**
- [229] S.-S. Yoon, D.-Y. Khang, *ACS Applied Materials & Interfaces* **2016**, *8*, 23236.
- [230] L. Veeramuthu, B.-Y. Chen, C.-Y. Tsai, F.-C. Liang, M. Venkatesan, D.-H. Jiang, C.-W. Chen, X. Cai, C.-C. Kuo, *RSC Advances* **2019**, *9*, 35786.
- [231] S.-W. Kim, B. W. An, E. Cho, B. G. Hyun, Y.-J. Moon, S.-K. Kim, J.-U. Park, *Nano Letters* **2018**, *18*, 3865.
- [232] W. Cheong, Y. Kim, J. Lee, C. Hong, H. Choi, Y. Kwak, Y. J. Kim, Y. S. Kim, *Advanced Materials Technologies* **2019**, *4*, 1800550.
- [233] Y. Cheng, X. Zhang, C. Fang, J. Chen, Z. Wang, *Journal of Materials Science & Technology* **2018**, *34*, 2225.
- [234] Y. Gao, H. Luo, Z. Zhang, L. Kang, Z. Chen, J. Du, M. Kanehira, C. Cao, *Nano Energy* **2012**, *1*, 221.
- [235] Z. Shao, X. Cao, H. Luo, P. Jin, *NPG Asia Materials* **2018**, *10*, 581.
- [236] P. Liu, L. Liu, K. Jiang, S. Fan, *Small* **2011**, *7*, 732.
- [237] M. Li, S. Ji, J. Pan, H. Wu, L. Zhong, Q. Wang, F. Li, G. Li, *J. Mater. Chem. A* **2014**, *2*, 20470.
- [238] Q. Huang, W. Shen, X. Fang, G. Chen, J. Guo, W. Xu, R. Tan, W. Song, *RSC Advances* **2015**, *5*, 45836.
- [239] S. Yao, J. Cui, Z. Cui, Y. Zhu, *Nanoscale* **2017**, *9*, 3797.
- [240] Xing Liang, S. A. Boppart, *IEEE Transactions on Biomedical Engineering* **2010**, *57*, 953.
- [241] Y. Liu, M. Pharr, G. A. Salvatore, *ACS Nano* **2017**, *11*, 9614.
- [242] M. Amjadi, K.-U. Kyung, I. Park, M. Sitti, *Advanced Functional Materials* **2016**, *26*, 1678.
- [243] S. Bagherifard, A. Tamayol, P. Mostafalu, M. Akbari, M. Comotto, N. Annabi, M. Ghaderi, S. Sonkusale, M. R. Dokmeci, A. Khademhosseini, *Advanced Healthcare Materials* **2016**, *5*, 175.
- [244] R. C. Webb, A. P. Bonifas, A. Behnaz, Y. Zhang, K. J. Yu, H. Cheng, M. Shi, Z. Bian, Z. Liu, Y.-S. Kim, W.-H. Yeo, J. S. Park, J. Song, Y. Li, Y. Huang, A. M. Gorbach, J. A. Rogers, *Nature Materials* **2013**, *12*, 938.
- [245] R. C. Webb, R. M. Pielak, P. Bastien, J. Ayers, J. Niittynen, J. Kurniawan, M. Manco, A. Lin, N. H. Cho, V. Malychuk, G. Balooch, J. A. Rogers, *PLOS ONE* **2015**, *10*, e0118131.
- [246] J.-H. Park, J.-W. Lee, Y.-C. Kim, M. R. Prausnitz, *International Journal of Pharmaceutics* **2008**, *359*, 94.
- [247] S. F. Nadler, K. Weingand, R. J. Kruse, *Pain physician* **2004**, *7*, 395.
- [248] H. Cramer, C. Baumgarten, K.-E. Choi, R. Lauche, F. J. Saha, F. Musial, G. Dobos, *European Journal of Integrative Medicine* **2012**, *4*, e371.
- [249] S. K. Barua, M. Z. A. Chowdhury, *Chattagram Maa-O-Shishu Hospital Medical College Journal* **2014**, *13*, 60.
- [250] H. Lee, *Medical Science Monitor* **2013**, *19*, 661.
- [251] S. Michlovitz, L. Hun, G. N. Erasala, D. A. Hengehold, K. W. Weingand, *Archives of Physical Medicine and Rehabilitation* **2004**, *85*, 1409.
- [252] H. Zhai, R. Wang, X. Wang, Y. Cheng, L. Shi, J. Sun, *Nano Research* **2016**, *9*, 3924.
- [253] T. Q. Trung, N.-E. Lee, *Journal of Materials Chemistry C* **2017**, *5*, 2202.
- [254] W. Jiang, D. Niu, H. Liu, C. Wang, T. Zhao, L. Yin, Y. Shi, B. Chen, Y. Ding, B. Lu, *Advanced Functional Materials* **2014**, *24*, 7598.
- [255] R. H. Baughman, C. Cui, A. A. Zakhidov, Z. Iqbal, J. N. Barisci, G. M. Spinks, G. G. Wallace, A. Mazzoldi, D. D. Rossi, A. G. Rinzler, O. Jaschinski, S. Roth, M. Kertesz, *Science* **1999**, *284*, 1340.
- [256] T. Kimura, Y. Umehara, F. Kimura, *Soft Matter* **2012**, *8*, 6206.
- [257] R. V. Martinez, A. C. Glavan, C. Keplinger, A. I. Oyetibo, G. M. Whitesides, *Advanced Functional Materials* **2014**, *24*, 3003.
- [258] S.-E. Zhu, R. Shabani, J. Rho, Y. Kim, B. H. Hong, J.-H. Ahn, H. J. Cho, *Nano Lett.* **2011**, *11*, 977.
- [259] L. Chen, M. Weng, W. Zhang, Z. Zhou, Y. Zhou, D. Xia, J. Li, Z. Huang, C. Liu, S. Fan, *Nanoscale* **2016**, *8*, 6877.
- [260] W. Zhang, M. Weng, P. Zhou, L. Chen, Z. Huang, L. Zhang, C. Liu, S. Fan, *Carbon* **2017**, *116*, 625.
- [261] S. Walia, R. Gupta, K. D. M. Rao, G. U. Kulkarni, *ACS Applied Materials & Interfaces* **2016**, *8*, 23419.
- [262] K. C. Heo, S. H. Yu, J. H. Kwon, J. S. Gwag, *Appl. Opt., AO* **2013**, *52*, 8460.
- [263] P. Won, J. J. Park, T. Lee, I. Ha, S. Han, M. Choi, J. Lee, S. Hong, K.-J. Cho, S. H. Ko, *Nano Letters* **2019**, *19*, 6087.
- [264] L. Ou, B. Song, H. Liang, J. Liu, X. Feng, B. Deng, T. Sun, L. Shao, *Particle and Fibre Toxicology* **2016**, *13*, 57.
- [265] M. Charehsaz, S. Coskun, H. E. Unalan, R. Reis, S. Helvacioglu, A. K. Giri, A. Aydin, *Toxicological & Environmental Chemistry* **2017**, *99*, 837.
- [266] S. G. Lehmann, D. Toybou, A.-E. Pradas del Real, D. Arndt, A. Tagmount, M. Viau, M. Safi, A. Pacureanu, P. Cloetens, S. Bohic, M. Salomé, H. Castillo-Michel, B. Omaña-Sanz, A. Hofmann, C. Vulpe, J.-P. Simonato, C. Celle, L. Charlet, B. Gilbert, *Proceedings of the National Academy of Sciences* **2019**, *116*, 14893.
- [267] D. Mohanta, S. Patnaik, S. Sood, N. Das, *Journal of Pharmaceutical Analysis* **2019**, *9*, 293.
- [268] Y. Tabei, A. Sonoda, Y. Nakajima, V. Biju, Y. Makita, Y. Yoshida, M. Horie, *Metallomics* **2015**, *7*, 816.

2.2 Recent advances and prospects.

TH have gained a significant interest among the TCM applications, serving a large spectrum of devices with rather different needs on temperature ranges, sizes, substrates and operation. However, as discussed thoroughly in our review article, the TH stable and efficient heating performance are key parameters to ensure successful integration within industrial devices. Research is focused on improving such parameters for the case of emerging TCM technologies that show better properties compared to traditional ones. Therefore, they will be able to replace successfully the ITO for some applications, and the industry will take advantage of their superior flexibility and versatility for the future devices.

Examples of pertinent studies published just after the review article, concern highly flexible and more stable composites. For instance, Jang et al. reported a rapid, flexible defrosting Zn-doped SnO_x/Ag/Zn-doped SnO_x (ZTO/Ag/ZTO) multilayer thin film with high durability against humidity, achieved by the incorporation of nitrogen.¹⁹³ Another oxide/Ag/oxide based composite, showed high mechanical and chemical stability, designed for defogging-defrosting applications too.¹⁹⁴ Concerning AgNW based TH, Lee et al. deposited an AlO_x protection layer on the AgNWs and showed that the composite had a fast response and uniform temperature distribution.¹⁹⁵ Related to another TCM family, wrapping of a AgNW network with reduced graphene oxide (rGO) can improve the maximum electrical heating temperature of the resulting TH, due to the effective suppression of the oxidation and the diffusion of surface silver atoms.¹⁹⁶ In addition, the transmittance of the composite remained unchanged compared to the bare network. Further research on graphene-based TH combining experiments and simulations, reported an enhanced performance compared to metal-based thin-film heaters.¹⁹⁷ In addition, a graphene film demonstrated a superior performance thanks to intentionally increased defects and uniformly distributed wrinkles. When integrated on anti-icing coatings freezing was delayed by 1.25 h at -15 °C or 2.8 h at -10 °C.¹⁹⁸

Furthermore, Park et al. conducted an interesting study about the control of the evaporation rate of water droplets on TH, previously not reported.¹⁹⁹ Similarly, Kim et al. investigated the droplet evaporation characteristics and the wettability control on a Cu mesh based transparent heater, and reported the vanishing of coffee-rings during the water evaporation by the deposition of a hydrophobic amorphous fluoropolymer on top of the nanowires.²⁰⁰ Increasing interest is given on TH deposited on flexible polyimide films that withstand higher temperatures than other common plastic substrates, and are compatible with TH heating performances that reach even 400 °C.^{201–203} Emerging applications include the combination of flexible TH, like

AgNW networks, with phase-changing polymer films for the application on smart, thermochromic windows.²⁰⁴ Another approach that have gained increasing interest is the combination of emerging TH like CNT or MNW networks with self-healable substrates in order to improve the stability under extreme mechanical stress. A recent example is a 3D printed, biodegradable and stretchable carbon-based TH, mixed in wheat flour and water which is an intrinsically self-healing dough and recovers after cutting.²⁰⁵ In addition, Zhao et al. fabricated a biocompatible, wearable epidermal sensor based on ultra-long AgNWs embedded in a hydrogel with high self-healing effectiveness and strong adhesiveness.²⁰⁶ Furthermore, the low-cost CuNW networks when encapsulated by protective oxides or polymers can show significant resistance to oxidation, which is a crucial stability issue for this type of nanowires. For instance, as reported by Kim et al., patterned CuNW embedded on polyurethane acrylate are promising candidates for flexible TH in futuristic devices, like the replication of the feeling of heat in virtual reality applications.²⁰⁷ Concerning other emerging applications, wearable TH can be significantly useful in devices of personal thermal management, like personal heating or thermotherapy.²⁰⁸ Finally, it would be interesting to use TH as auxiliary heating elements of positive temperature coefficient ceramic thermistors in degaussing circuits.

The variety of applications can be very vast, as well as our imagination about gadgets or large area TH devices, or the combination of TCM technologies for enhanced performances, and the elaboration of hybrids that serve several operations on the same time. There a still a lot of challenges to be tackled, properties to be further investigated, physical and chemical phenomena to be better understood. From our side, the studies conducted during my PhD to better understand the origin of failure on AgNW networks (Chapter 4) and the impact of non-homogeneity and local heating (Chapter 5), can contribute to the advancement of the aforementioned issues. Finally, we manage to fabricate AgNW-oxide based TH with enhanced stability and integrated them to lab-on-chip bio applications (Chapter 6.1). Taking advantage of the beauty of a simple and so commonly used effect as the Joule heating, our results are encouraging for elaborating low-cost, environmentally-friendly, energy-efficient devices, adapted to present and future needs.

οὐδὲν ἀτέκμαρτον οὐδὲ τυφλὸν

Πλούταρχος

« Nothing is irrational, nothing is concealed »

Plutarch (47-120 AD)

Chapter 3

3. Experimental techniques and simulation methods: generalities and few preliminary results.

In this chapter the experimental techniques that were used during the present PhD thesis, are reported, including: the fabrication steps of AgNW networks by spray coating, the characterization of their electrical, optical and mechanical properties, the morphological characterization by electronic microscopy, and the temperature measurements. In addition, the comparison between spray, rod and spin coating for the deposition of ultra-long AgNWs will be presented, based on the research article entitled “*Rapid synthesis of ultra-long silver nanowires for high performance transparent electrodes*”, published recently on *Nanoscale Advances* by A. Madeira, D.T. Papanastasiou, T. Toupance, L. Servant, M. Tréguer-Delapierre, D. Bellet, I.A. Goldthorpe, July 2020, DOI: [10.1039/D0NA00392A](https://doi.org/10.1039/D0NA00392A).³⁸ In the last part, the simulation methods used and developed during my PhD thesis are introduced and preliminary results such as the effect of nanowire lengths and diameters on the electrical performances are presented. The results of such simulations are compared with the experimental ones from the deposition of AgNW networks of different nanowire dimensions. These AgNWs were kindly provided by the team of J.-P. Simonato at CEA-Liten (Grenoble, France), as well as for the majority the AgNWs that I have used for the fabrication and study of transparent electrodes during my thesis. Finally, I briefly introduce a COMSOL Multiphysics® model of Ag thin films that we use for the electrical and thermal properties of both homogeneous and non-homogeneous AgNW networks.

3.1. Fabrication of MNW networks by spray coating and comparison with other methods.

Spray coating in LMGP. In order to achieve optimised performances of AgNW networks, we need to assess their random and homogeneous spatial distribution,³² and for this reason, we use a home-made spray coating set-up in LMGP, designed by the Engineer Dominique De Barros. This allows depositing networks without preferential orientation of the nanowires as opposed to what occurs when spin coating is used. In addition, much larger surfaces can be coated, and the suspension loss during the deposition is minimized, which are both clear assets discussed also in Chapter 1.2.2. However, the ultrasonic nozzle of the spray can lead to AgNW fragmentation especially in the case of (ultra)long nanowires. As Ko et al. have demonstrated, ultrasonic spraying exhibits a significant decrease in the length of AgNWs as compared to air spraying and, therefore, an increase of the networks sheet resistance.¹⁰⁵ Thus, our team in

LMGP replaced the traditional spray coating head with a commercial aerograph by Harder&Steenbeck (airbrush “Infinity”). Then, thanks to the assistance of Silas Kraus (internship 2017-18), we optimized the deposition characteristics as mentioned below, when we were both doing our internships in the lab and in the beginning of my PhD. A schematic representation of the spray coating is shown in **Figure 3-1a**.

Spraying parameters. The airbrush is fixed in a mechanical set-up connected with a programmable automation controller (PAC) and the deposition is easy, quick, and controllable. Given that the maximum airbrush movement is 25x30 cm², and the samples fabricated within the frame of this thesis were 2.5x2.5 cm², 5x5 cm² and even 10x10 cm², several samples can be prepared at one time. In this way, we can apply different characterization techniques in series of samples with the same electrical and optical properties. The key deposition parameters that should be carefully tuned and selected are: the spraying distance, the substrate’s temperature, the spraying pressure and the flow rate, which in our case is controlled by the needle’s position inside the air brush. For an optimised procedure, the evaporation of the solvents of the nanowires suspensions is quick and uniform and the droplets have such size that the so-called “coffee rings” can be avoided.²⁰⁹⁻²¹¹ These parameters need to be optimised for each MNW suspensions with different concentrations and solvents. The deposition is performed in the following way: the diluted suspension is inserted in a spray cup with a syringe, and is then sprayed in the form of microscopic droplets, using dry nitrogen (N₂). The spray cup can contain 5 ml of suspension and it is often refilled between the spraying cycles. The airbrush moves in X and Y directions above an aluminum plate, enabling the deposition on a glass or plastic substrates. One cycle is completed after a “zig-zag” movement that covers the whole substrate twice and then the airbrush comes back to its initial position; this movement is represented schematically by the light blue arrows in Figure 3-1b. The plate holding the samples is heated up to 110 °C, which is high enough given the evaporation temperature of the solvents commonly used (methanol-64.7 °C, ethanol-78.2 °C, isopropanol-82.5 °C),¹¹¹ but also lower than the melting point of a big variety of plastic substrates.²¹² An air pump, when it is released, pushes a button that moves the airbrush lever allowing the N₂ to enter and activate the spraying. The N₂ pressure and the position of the needle can adjust the flow of the suspension. We have optimised the gas pressure at 1.4 bar and the flow of the suspension is tuned each time according to the MNW suspension and depending on the suspension concentration. The way we use to do so, is to measure the number of droplets per second (dr/s) dropping from the airbrush without spraying. We optimized the flow rate between 0.3 and 0.5 dr/s for concentrations around 0.1

g/kg, which means 6 to 10 droplets per 20 s (time in which we usually measure). The spraying distance between the airbrush head and the plate is another important parameter to control and we have optimised it at 7 cm. The procedure is repeated several cycles, until the desired AgNW network density and electrical resistance is obtained. The spray set-up is enclosed within a chamber with a ventilation system connected to the laboratory's nanomaterials fume hoods, in order to pump off the gases from the solvents evaporation. A double Plexiglas door protection separates the user during deposition along with the appropriate nanomaterials mask, safety goggles, gloves and lab coat indispensably worn throughout the whole procedure of preparation, deposition and post-cleaning. The entire protocol and photos can be found in **Annexe I**.

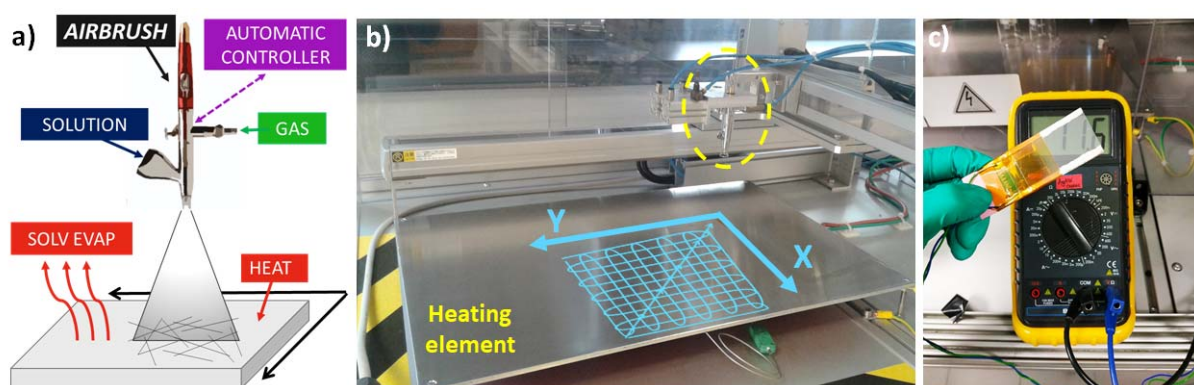


Figure 3-1: a) Schematic representation of the spray coating set-up used in LMGP. b) Photo showing the spray coating area with the heating element where the substrates are placed and the airbrush (inside dotted yellow circle) connected to the set-up branches whose movement is automatically controlled. The arrows in light blue represent the zig-zag movement of the airbrush during one spraying cycle (the typical represented area is in an order of magnitude of $100 \times 100 \text{ mm}^2$). c) Photo of the monitor, used to measure *in situ* the electrical resistance inside the chamber during deposition, connected with long cables to an external multimeter. Here a typical example after deposition, back to room temperature showing an electrical resistance of 11.6 Ohm.

***In situ* resistance monitoring.** The electrical resistance of the deposited networks can be measured by removing a sample between the spray cycles and measuring with a multimeter directly between the edges of a sample (*ex situ* measurement). However, there is a high risk of damaging the nanowires and misestimating the value of the resistance. In order to measure the resistance in a fast and reliable way, avoiding the errors associated with by-hand measurements, an *in situ* monitor set up was elaborated by Silas Kraus, João Resende (post-doc 2018-19) and Nil Fontanals (internship 2018). The monitor consists of a glass substrate with two sides, parallel electrodes connected to a multimeter outside the deposition chamber (Figure 3-1c). The electrodes are made with copper tape and silver paste that is painted between the copper tape and the glass to ensure good contact with the nanowires, since the thickness of the copper tape is much larger in comparison to the size of the nanowires. The copper tape is then in electrical

contact with a pair of long cables connected to a multimeter. Kapton® tape, or other high heat-resistant tape, is used to hold the above assembly and, since it is an electrical insulator, it serves also as a mask to draw the area of deposition on top of the monitor. This area has to be of a size proportional to the target samples so that the resistance measured *in situ* is equivalent to that of the samples. Consequently, we can study and optimise directly the deposition of a new AgNW suspension, follow the evolution of the electrical resistance constantly during the whole spray deposition and identify potential problems during the cycles (i.e. flow rate variation, nanowires blocked in the nozzle, thus non-deposited etc.) and finally stop when the desired electrical resistance is reached.

Nanowire suspension. Concerning the MNW used during my thesis, I mostly worked with the suspensions provided by the team of J.-P. Simonato at CEA-Liten, that improved the purification step of the polyol process using decantation.²¹³ The networks deposited with these laboratory nanowires do not require thermal annealing post-treatment³⁰ as in the case of commercial nanowires we also use, like the ACS Materials®. The last years there is an increasing industrial production of MNW in suspensions and recently, we have started testing other commercial AgNWs from companies such as R&Bnano (France) and NanoAmor, Inc. (USA). In the framework of the collaboration with Alexandra Madeira during her PhD in ICMCB (with Prof. Tréguer-Delapierre) and University of Waterloo (Prof. Goldthrope), and afterwards in the framework of the ANR project MEANING (more details in Chapter 6.3.3), we have the opportunity to test ultra-long AgNWs provided by the team of M. Tréguer-Delapierre (ICMCB, France) and compare them with other deposition techniques in a laboratory (rod coating) and even industrial scale (R2R deposition by the industrial partner Armor in Nantes, France).

Substrates nature. As already mentioned, the rather low temperatures needed for the evaporation of the solvents during the spray deposition, allow us to use a large variety of substrates, flexible or not, better always of high transparency. Apart from the simple glass slides that are low cost and commonly used in laboratories, Corning® 1737F glass is often preferred, thanks to its advanced properties, for the deposition and tests of thin films at high temperatures experiments or the optical characterization. Despite its elevated cost, this alkali-free borosilicate glass possesses high thermal shock resistance, low micro-roughness and an excellent optical quality.²¹⁴ Thus, it is suitable for the high thermal and electrical stress tests and as a reference for the optical measurements (around 92 % total transmittance). Concerning the investigation of the mechanical properties of AgNW networks, we choose transparent,

flexible and low-cost thermoplastic polymer substrates such as polyethylene naphthalate (PEN) and polyethylene terephthalate (PET). The AgNWs have also shown a good adhesion to these substrates when they undergo tape tests.^{212,215,216} However, for the elaboration of composites of AgNW networks with oxides by ALD-based deposition techniques that require deposition temperatures above 180 °C, the previous transparent polymers are not suitable, as they begin to deform or melt. Polyimide (PI) substrates with high glass transition temperatures but lower optical transparency can be an option for the mechanical studies of AgNW/oxide composites. Fortunately, the last years there has been a considerable progress on the development and commercialization of colourless and transparent PI films.²¹⁷ In LMGP we have been using Neopulim® made by Mitsubishi, to compare e.g. the properties of bare AgNW and AgNW/Al:ZnO composites.²¹⁸ Last but not least is the use of the elastomer (rubber) polydimethylsiloxane (PDMS) as a substrate for the elaboration of stretchable and transparent electrodes based on AgNW/PDMS composites. PDMS is a biocompatible, low cost, easy to manipulate, optically transparent material that has been used in a large variety of applications.²¹⁹ In our field it has gained a lot of interest too, concerning the fabrication of AgNW networks embedded in PDMS, i.e. composites that retain low resistances under strain tests.²²⁰ Its fabrication techniques are rather facile to reproduce and all the details and mechanical properties of the composites are presented in Chapter 6.2. In the same part, we will discuss the elaboration of AgNW/PDMS composites for piezoelectric sensors and actuators in the framework of the Carnot project FREE in collaboration with the laboratories G2Elab and TIMA (both in Grenoble). Our goal here is to use the AgNW networks as stretchable electrodes in energy harvesting devices where elastomers like PDMS form the dielectric medium.^{221,222}

Substrate preparation. Concerning the cleaning of the substrates before the AgNWs deposition, the protocol followed is inspired by the glass cleaning for thin films deposition found in literature.²²³ A well-adapted cleaning is an essential step to avoid the residues that can create defects within AgNW networks. It consists of i/ rubbing the substrates with acetone to remove glass residues from the cutting of the glasses to the desired sizes, ii/ ultrasound bath in alcohol (IPA or EtOH) for 15 min, iii/ rinsing with deionized water and iv/ blow drying with N₂ gun. This protocol is adapted when dealing with plastic substrates limitations (i.e. avoid acetone step). In the case of PDMS films, which are prepared from “scratch” in the lab to obtain the needed thickness and shape, the whole procedure is quite different (see Chapter 6.2).

3D printed masks. One of the advantages of the spray coating, as already mentioned above, is the large deposition area which allows us to deposit simultaneously several samples with no

restriction in the size and the type of the substrate. In addition, thanks to the low-cost and fast 3D printing techniques available at LMGP, we had the opportunity to design and fabricate masks in order to deposit AgNW networks with different configurations. Indeed, as it will be presented in Chapter 5, it has been proven very interesting to explore the cases of non-homogeneous/patterned transparent electrodes. For this experiments, we have been using the *Formlabs* “Form 2” 3D printer with the *Clear* resin provided by *Formlabs*.

Electrical contacts. A final and crucial step in the fabrication of AgNW networks is the deposition of electrical conductive contacts to the two edges of the samples, in order to make electrical characterization, such as two-point probe electrical resistance measurements. A common approach used for AgNW networks that are deposited on glass or flexible polymer substrates is to deposit silver paste that dries in air. Another typical physical vapour deposition method is the Joule effect induced evaporation. An Edwards Auto306 evaporator is available at LMGP and it is appropriate for the deposition of silver or gold contacts on AgNW networks even on top of PDMS substrates or for the cases that we need ultra-thin contacts of sub-micron thickness. The Eutectic Gallium-Indium (EGaIn) liquid metal alloy is a better choice for the stretching tests, during which we have faced some technical problems to measure the real electrical resistance of the AgNW network because of the movement of the set-up and sample. Finally, in the case of integration of the AgNW networks in devices like transparent heaters for the lab-on-chip bio applications, more particular configurations have been explored (as detailed in Chapter 6.1).

Comparison of deposition methods and FoM of ultra-long AgNW networks. In the framework of the collaboration between LMGP and laboratories at University of Bordeaux (France) and University of Waterloo (Canada), where Alexandra Madeira was doing her PhD, we investigated the properties of ultra-long AgNWs deposited by different techniques.³⁸ Ultra-long nanowires are promising for applications requiring high transparency like touch screens and the results presented in this part are originated from our common article.³⁸ A. Madeira used 1,2-propanediol instead of ethylene glycol as the solvent in the polyol process and selected the optimal silver concentration in the reaction. Therefore, ultra-long AgNWs were obtained ($L = 130 \pm 36 \mu\text{m}$ and $D = 124 \pm 25 \text{ nm}$) with reduced reaction time and temperatures, 1 h and 140 °C, respectively, with no addition of foreign ions. Furthermore, we studied the Mayer rod and spray coating techniques that showed both better results compared to spin coated electrodes, in terms of networks homogeneity, since the radial orientation of the ultra-long AgNWs is very prominent. This is clearly revealed in the SEM images presented in **Figure 3-2a** as well as the

orientation particularities of the other two methods. This directly influences the electrical performance as already explained in Chapter 1.2.2.³² Spray coating offers a much more homogeneous network but the nanowires are curved due to their length. Finally, the rod-coated nanowires are more straight than the spray-coated, and they seem aligned along the four orthogonally directed coats.²²⁴ Such alignment has been shown in the past to lead to a higher figure of merit,^{225,226} confirmed in our case too. Rod coating has proven to be the best technique for the case of ultra-long AgNWs and the resulting transparent electrodes present one of the highest *FoM* among all the reported nanowire electrodes deposited using a scalable process (comparison in Figure 3-2b). Their sheet resistance is $5 \Omega/\text{sq}$, at a transparency of 94% and they do not require any post-processing such as thermal annealing that is often used for industrial nanowires. This is presented in Figure 3-2c, where we can also notice that our electrodes remain stable until higher thermal stress.

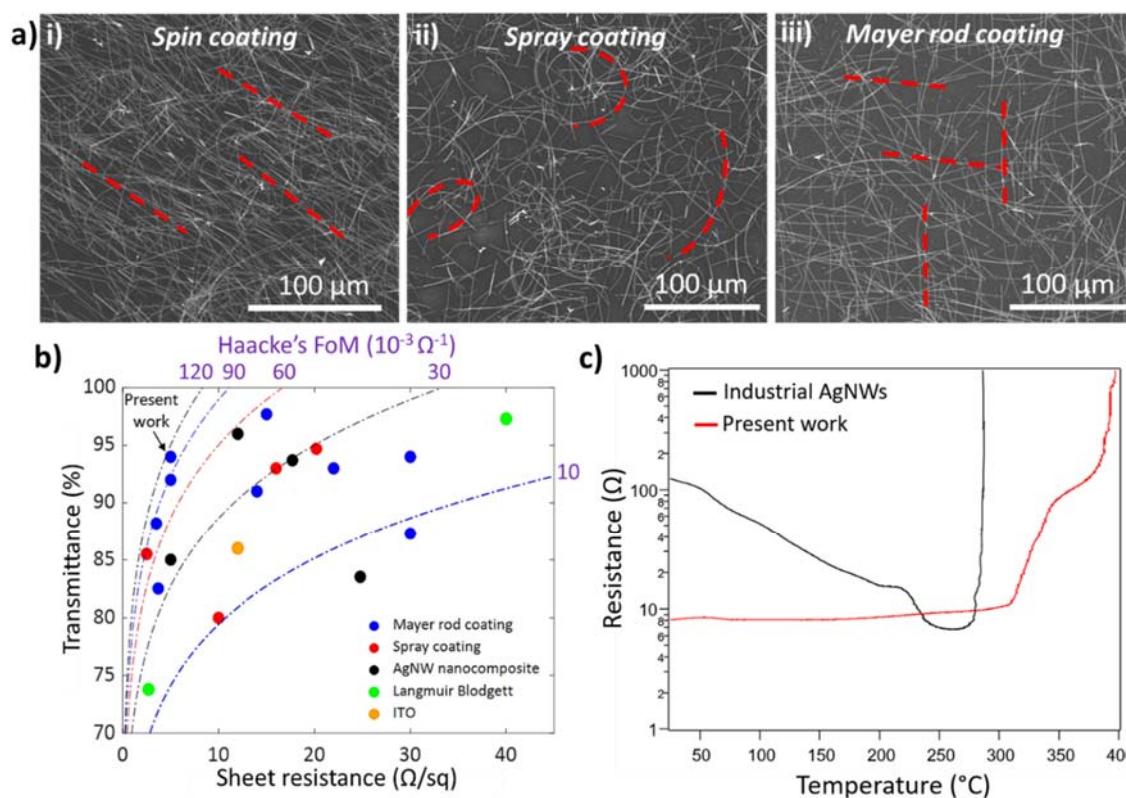


Figure 3-2: a) SEM images of ultra-long AgNW networks deposited by i) spin-, ii) spray- and iii) Mayer rod- coating. The red dashed lines highlight the nanowires deposition states onto the substrates: radial orientation, curved nanowires and orthogonally oriented coatings, respectively.³⁸ b) Transmittance versus sheet resistance of transparent electrodes based on AgNWs deposited using scalable processes: Mayer rod, spray coating, and Langmuir Blodgett, as well as AgNW nanocomposites and ITO.³⁸ c) Temperature evolution of the electrical resistance of electrodes made with industrial AgNWs ($d = 117 \text{ nm}$ and $L = 44 \mu\text{m}$, Seashell Technology, black curve) and with the $130 \mu\text{m}$ long nanowires (red curve) during a thermal ramp of $5 \text{ }^\circ\text{C}/\text{min}$ in air.³⁸

3.2. Experimental characterization techniques

Electrical properties. One of the basic properties of conductive materials is the electrical resistance is. A measurement with a multimeter using two probes positioned on opposite the side contacts is a common and easy method. However, for further studies of the electrical conductivity under electrical and/or thermal stress, we use specific configurations that consist of a hot plate connected to a thermocouple or a sample holder and two probes connected to a sourcemeter (like Keithley). The heat and the electrical power source can be controlled by a software (often LabVIEW), following the user's recipes for the electrical and thermal studies (plateaux and /or ramps), and record the needed parameters (time, voltage, current, resistance, temperature). However, in order to continue our studies in an accurate way and with highly precision, our team in LMGP decided to elaborate a new home-made characterization bench, designed by the engineer Dominique De Barros (short protocol and photos in **Annexe II**). During my thesis, I contributed to the construction of this new set-up with the assistance of Martin Bordas (internship 2018). The featured advantages of the new set-up include the possibility to perform electrical measurements under several conditions, such as high temperature (up to 800 °C), variable pressure down to vacuum (10^{-4} mbar), possibility to use different atmospheres or UV illumination. Thus, I had the chance to manipulate several materials (i.e. cut metal panels) to build the bench, build an electrical table and find possible malfunctions, and get an official training for the electrical security measures.

Another common way to characterize and compare thin layers in general, and transparent conductive materials, is to measure the sheet resistance, derived from a four point probe set-up.²²⁷ A schematic representation is given in the inset of **Figure 3-3a**. The four-point probe is used to compensate the effect of the electrical wiring and contact contributions to the global electrical resistance. A software collects the measurements, performs the finite size corrections and finally provides the mean sheet resistance with its standard deviation out of 5 different points of the sample. Theoretically for thin films, the relation between the sheet resistance, given in a first approximation by: $R_{sh} = \rho/t$, and the resistance R , measured between the side contacts, is as follows:

$$R = \rho \frac{L}{S} = \rho \frac{L}{W*t} = R_{sh} * \left(\frac{L}{W}\right) \Rightarrow \frac{R_{sh}/R}{W/L} = 1 \quad (3-1)$$

where ρ the resistivity (Ohm.m), t the thickness of the thin film, S the cross-sectional area, W and L the lateral dimensions of the sample. On the contrary to the thin oxide films, it is more

complicated to estimate the resistance of AgNW networks due to their morphology.²²⁸ The “thin film” hypothesis would be acceptable if the areal mass density is very high so that the percolating networks can be considered as almost continuous and behaving as a thin silver film. If not, the measurement error becomes very elevated for sparser networks, close to $amd_c=43.4$ mg/m^2 , as it is shown in Figure 3-3a. For statistical reasons, the smaller the number of NWs, the less uniform the deposition is, leading to a high deviation of the sheet resistance at low density. In addition, the bare AgNW networks have poor adhesion to most substrates and it is rather easy to remove them during such direct probe measurements, thus affecting the measurement. Other techniques for the electrical characterization, along with any important details for specific techniques used in each study during my thesis, are presented along with the experimental results in the chapters to follow.

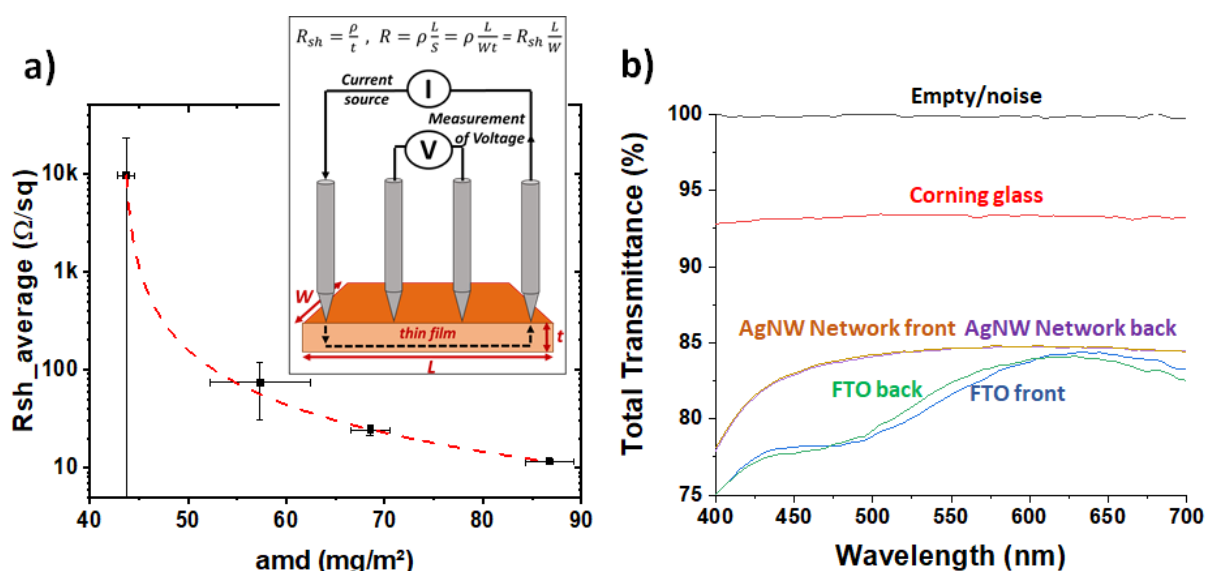


Figure 3-3: a) Sheet resistance measured by four point probes for AgNW networks of four different densities, while the amd_c is equal to $43.4 \text{ mg}/\text{m}^2$. The inset is a schematic representation of a thin film resistivity and sheet resistance estimation by four probes measurement. b) Total transmittance measurements with a spectrophotometer for Corning glass (reference substrate), AgNW network and diffuse FTO. Two different measurements are performed for each sample regarding the substrate and the incident light position: the “front” (“back”) is when the incident light transverses the AgNW or the FTO before (after) the glass and then enters the integrating sphere of the spectrophotometer.

Optical properties. During my thesis, I used a Lambda 950 UV/Vis/NIR spectrophotometer (Perkin Elmer) with an integrated sphere, available at LMGP, and I optimised the protocol that we use for AgNW networks, especially in the case of diffuse transmittance (see **Annexe III**). The optical measurements are delicate and sensitive to changes of the lamp intensity, the integrating sphere sensitivity (InGaAs detector), lens alignment, frequent maintenance and protection from dust and residues from other samples. In the beginning of the measurements,

after checking the last calibration date, performing the lens alignment and baseline measurement, it is essential to measure without any sample and verify that the total and diffuse transmittance is close to 100 % and 0 % respectively, with small error (± 0.2 %). In addition, these values are necessary for the correct calculation of the haze factor. At a specific wavelength, this is given by the equation:

$$\text{Haze Factor}(\%) = 100 * \left(\frac{T_4}{T_2} - \frac{T_3}{T_1} \right) \quad (3-2)$$

where T_4 and T_2 are the diffuse and total transmittance of the sample, respectively, and T_3 and T_1 are the reference diffuse and total transmittance values, respectively, when no sample is present. It is always important to measure the bare substrate transmittance so that its contribution can be removed or solely taken into account as reference in the results showing the optical transmittance of the resulting AgNW-based samples. Finally, I performed some tests to establish the parameters that can influence the optical measurements, for example whether the position of the AgNW network with respect to the incident light and the substrate may influence the measured values, the importance of the samples size and homogeneity, etc. For the first one, it was proven that there is no difference whether the incident light transverses first the substrate and then the AgNWs before entering the integrated sphere, or the other way around. On the contrary, this differs for diffuse thin films like FTO (grown also on Corning glass in LMGP) as it is shown in Figure 3-3b. However, as intuitively expected, when it comes to samples that are much bigger than the spectrophotometers aperture (especially if their homogeneity during deposition is not assured) it is suggested to perform measurements on several regions of the same sample and derive a mean value.

Mechanical properties. To perform bending and stretching tests, we use a home-made set up with two metallic jaws between which the sample is positioned. A motor can displace one jaw while the other is fixed. The metallic jaws are also connected with a Keithley for *in situ* measurement of the electrical resistance during the mechanical test. The motor and the Keithley are connected to a LabVIEW software that controls the movement of the jaw (stretch-release with the desired speed and number of repeating cycles), the applied voltage/current and the recording of the electrical resistance values. Photos of the set-up can be found in **Annexe IV**. For the evaluation of the flexibility of AgNW networks and their composites, it is necessary to estimate and report the bending radius. In the case of the stretchability investigation, we should measure with precision the length elongation and calculate the normalised resistance difference

from the initial one, in order to directly compare with other technologies. For a fair comparison, we take into account the initial width and length of the measured sample as follows:

$$R_{normalised} = \frac{R_{measured} \cdot Width}{Length} \quad (3-3)$$

Nanocharacterization. Scanning Electron Microscopy (SEM) is an accurate method to observe the local morphology of AgNW networks. In LMGP we have been using a field emission gun-scanning electron microscopy (FEG-SEM Environmental FEI QUANTA 250) and recently we have the chance to use another high resolution SEM (ZEISS-Gemini 300) with immersion lens (InLens) detector that provides an enhanced, sub-nanometer spatial resolution at low kV. The FEI QUANTA 250 allows the de-acceleration of the electron beam over non-conductive samples and thus permits to achieve 1.2 nm resolution at 30 kV with high vacuum, while the ZEISS Gemini300 offers a resolution of 1.2 nm at only 1 kV and 0.7 nm at 15 kV. SEM images are analysed by ImageJ software to provide an estimation of the *amd*. More specifically, the software recognises the nanowires from Back Scattered Electron images where they appear white, thanks to their electrical conductivity, on top of the non-conductive, black substrate (glass or plastic), using the “Ridge detection” plug-in.²²⁹ The crucial part is the selection of pixel analysis/size in order to count precisely the true nanowire coverage in the images. Once the nanowires are detected and the software counts their total length in pixels, we divide this value by the SEM image surface in pixels to obtain the so-called geometrical density $d_g = \frac{L_{tot}}{S_{tot}}$. Knowing the D_{NW} diameter of the AgNWs used for to fabricate the sample and considering the nanowires approximately as cylinders, we can calculate the *amd* of a network by the following equation (3-4). The *amd* is defined as the number of nanowires N per unit area S (or the geometrical density divided by the average length of the nanowires L_{NW}) multiplied by the mass of a nanowire m_{NW} . Thus:

$$amd = \frac{N}{S} \cdot m_{NW} = \frac{d_g}{L_{NW}} m_{NW} = d_g \cdot \rho_m \cdot \frac{\pi \cdot D_{NW}^2}{4} \quad (3-4)$$

where ρ_m is the mass density of bulk silver, equal to 10.49 g/cm³.

Transmission electron microscopy (TEM, JEOL JEM-2010 microscope, operated by the engineer Laetitia Rapenne in LMGP) is a very sensitive technique for the evaluation of the AgNW diameter distribution, as well as the morphology of single AgNWs and their junctions, before and after post-deposition treatments. In addition, it provides important analysis for the interfaces between the nanowires and the oxide encapsulating them.

Temperature measurements. This parameter has had an essential role in the experimental work during my thesis, for two entangled objectives; the study of the stability under electrical stress and the evaluation of the performance of transparent heater devices. The experimental techniques have been already reported thoroughly in Chapter 2, included in our review article on transparent heaters.¹ I will provide here just a quick reminder on the tools we mostly use in LMGP. Firstly, resistance temperature detectors (RTD) like Pt100 (platinum sensor with a resistance of 100 ohms in 0 °C) can measure in a very accurate way the temperature, based on the linear increase of the resistivity of platinum with the increase of temperature. Flexible RTD sensors are easily placed on the samples and connected to the same software we use for the electrical characterization, and they offer a quick and precise measurement of the average temperature of our samples. However, IR imaging is a much more powerful and versatile tool because it offers a spatial distribution of the temperature with a sub-micron resolution. There are parameters that should be carefully taken into account, such as the choice of the emissivity coefficient and the conditions during measurement (light, shadow, reflections) that can disturb the radiation signal. In addition, the mounting of the set-up can be delicate, but in any case, the information retrieved about the temperature is significant for our studies, as it is demonstrated in the chapters to follow.

3.3. Simulation models.

A significant work has been done in modelling the physical properties of AgNW networks by the LMGP team in order to further understand some experimentally observed phenomena and investigate ways to predict their performance. Firstly, Daniel Langley created during his PhD thesis (2011-14) a Monte Carlo code in MATLAB® to generate random AgNW networks and explore the impact of the nanowire shape, size and orientation on the percolation critical density.²³⁰ Then, Thomas Sannicolo, during his PhD thesis (2014-17), and Shujun Xian (internship 2016), optimized several aspects of the MATLAB® code and created a link with COMSOL Multiphysics® in order to simulate the network electrical and thermal properties. During my internship (2017) in LMGP, I optimized some parts of the COMSOL model, and I used it to study the impact of network density and nanowire dimensions on the electrical properties. In the beginning of my PhD, I used this numerical approach to compare networks with different nanowire dimensions to those that I fabricated experimentally by using AgNW suspensions provided by the team of J.-P. Simonato at CEA-Liten. These results will be presented in the following pages, after a brief introduction to the basic simulation principles.

Finally, I will also introduce a different simulation approach that I developed during my PhD with the contribution of Vladimir Tsukanov (internship 2019). In this case, we used an approximation of a silver thin film to simulate the electrical and thermal properties of samples with the same size as the experimental ones, which is not doable with the previous approach for time computation reasons, as it will be explained below.

Monte Carlo simulations using MATLAB®. In the last decades, stick percolation has attracted significant interest due to its potential application in carbon nanotube and metallic nanowire-based networks.²³¹ According to Langley et al.²³⁰ the percolation threshold N_C , defined as the critical number of nanowires required to have a percolation probability of $\frac{1}{2}$, depends on the relative length between the stick length L_{NW} and the length of a square system L_s . In order to simulate a realistic network, a square frame with left and right electrodes is generated that corresponds to the real substrate with the two metallic contact electrodes. The 1D AgNWs (diameter is not considered) are distributed randomly within this space with a random angle, to mimic the spray coating deposition. Various networks with different system size (length and width of the substrate), nanowire length and network densities (simply referred as x times the percolation threshold n_c) can be generated.²³² Once the generation has been completed, MATLAB® provides an image of the network (**Figure 3-4a**) by classing the NWs into three different colours (**Figure 3-4c**): 1) “blue” wires are the ones that intercept the percolating cluster, 2) “magenta” wires intercept the percolating cluster but are not likely to participate to the electrical conduction, and 3) “black” wires that do not intercept any other wire. It is indeed critical to make the distinction between the different types of percolating wires if we aim to apply the simulations for certain applications. For example, in devices such as displays or antennas, the nanowires other than “blue” ones can be not taken into consideration, since they are not likely to participate to the electrical current transfer between the two electrodes. On the other hand, in solar cells, the magenta wires have to be taken into account in the simulation, since they can participate to the collection of the photo-generated electrons, and transfer them to the electrically active percolating wires (blue ones) connected to them.²³³

AgNW network simulations using COMSOL Multiphysics®. Once a network is generated, MATLAB provides all the architecture information, such as the nanowires number, their position (x and y coordinates and rotation angle), and the cluster they belong to. By using a Livelink software, all this information can be transferred from MATLAB to COMSOL Multiphysics®, which is a software used to simulate different processes and devices from

various fields of engineering, manufacturing, and scientific research using the Finite Element Method (FEM).^{234,235} In COMSOL the nanowires are rectangles whose length is L_{NW} , and width equal to the diameter D_{NW} . Simulation of the network electrical properties is performed in 2D and “Electric Currents” physics model is chosen. Since, the electrical current is supposed to be homogeneously distributed in the z axis, the simulation results of a 3D network lead to the same results as in 2D. An electric potential difference is applied between the left and right contacts. COMSOL solves the Maxwell’s equations and calculates the voltage level and surface current density in each point of the nanowire network. The voltage equipotential lines are highlighted with rainbow colours from blue (0 V) to red (1 V), as shown in Figure 3-4b.

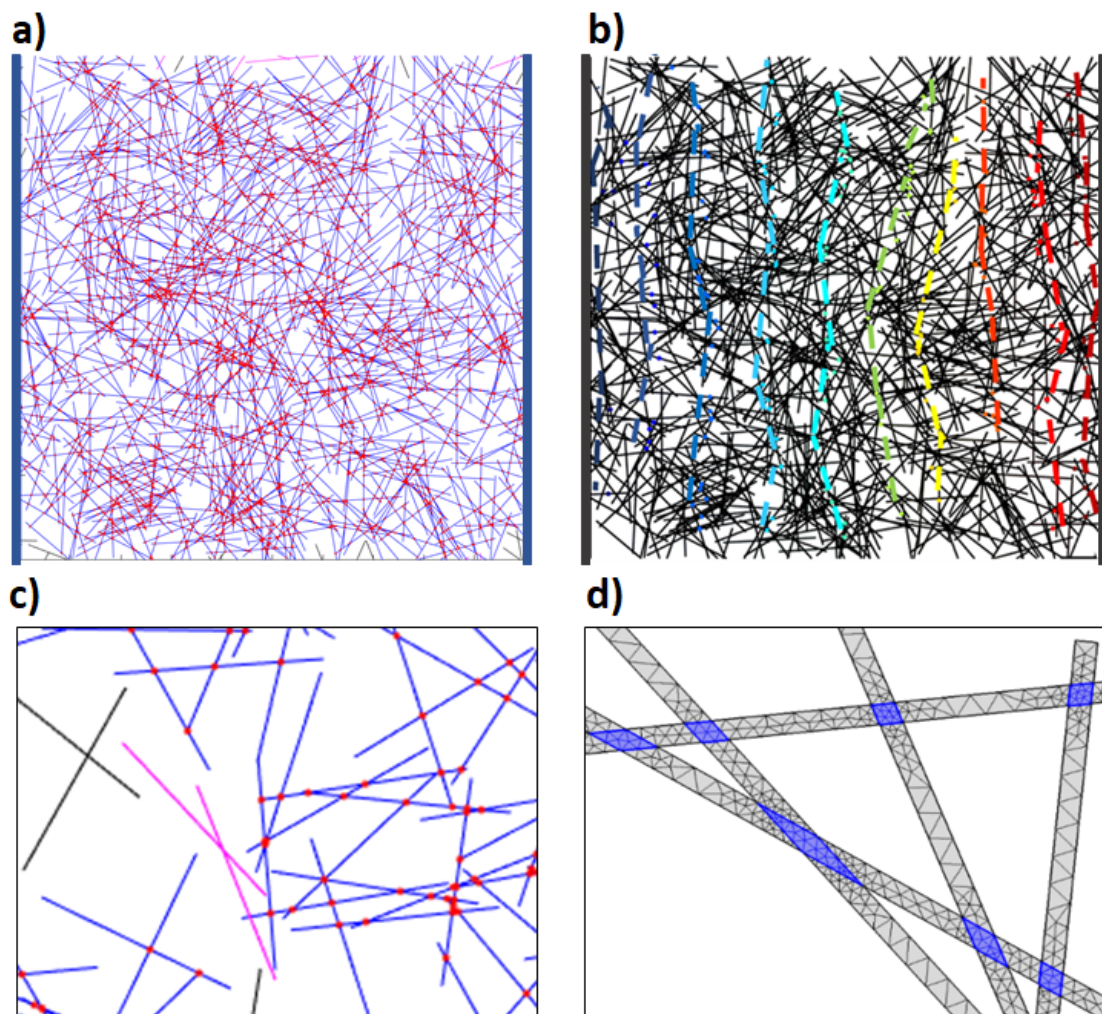


Figure 3-4: From MATLAB to COMSOL. a) A 2D stick nanowire network randomly generated by MATLAB, with density 5 times the percolation threshold ($5n_c$), $50 \times 50 \mu\text{m}^2$ substrate size, $L_{NW} = 10 \mu\text{m}$. b) The same network simulated in COMSOL with 1 volt applied between the left and right contacts. The dashed colored lines represent the voltage equipotential lines. c) Zoom in the 2D stick network: the blue sticks are connected to the percolation pathways, the magenta ones are the end wires on percolation pathways and the black ones are not connected to any pathway. The red dots highlight the junctions between active/blue nanowires. d) Zoom in the mesh geometry between interconnected AgNWs in COMSOL model. A finer meshing (smaller element size) is chosen at the junction areas for a more precise computation.²³⁶

For the COMSOL calculations, several parameters have to be taken into account. For example, the AgNWs electrical resistivity that depends on the D_{NW} , as it is described in section 1.2.3., has to be considered. Another critical parameter that drastically impacts the simulation results is junction sintering, i.e. nanowire-to-nanowire resistance. This can be tuned by changing the contact impedance value of the nanowire-to-nanowire boundaries. The values that are implemented for the contact impedance rely on experimental measurements of the electrical resistance of several single nanowire-to-nanowire junctions with different level of optimization.²³⁷ Another way to compute with higher precision the electrical contribution of the junctions is to choose smaller element size than for the rest of the nanowires (Figure 3-4d).²³⁶ It is important to note that the systems we generate have a maximum size of $100 \times 100 \mu\text{m}^2$. This is a mandatory condition for saving time and then extracting more results. COMSOL solving is indeed very time-consuming. For example, it can take almost a day to extract the simulation results of samples having a relatively high density ($5n_c$). Even though such dimensions are far lower than the real networks ($2.5 \times 2.5 \text{ cm}^2$), the values of electrical resistance that are extracted from the simulations are in the same range as the experimental ones. To further verify this, it is necessary to compare with experimental data. Therefore, I fabricated series of transparent electrodes with different nanowire dimensions and varying amd , using AgNW suspensions provided by CEA-Liten. Two examples are presented in **Figure 3-5**, with $L_{NW} = 5 \mu\text{m}$ - $D_{NW} = 58 \text{ nm}$, and for longer ones with $L_{NW} = 27 \mu\text{m}$ - $D_{NW} = 70 \text{ nm}$. The amd was calculated by SEM images and *ImageJ* software for the experimental samples and with the related equations and nanowires number and dimensions for the simulated ones. The dimensions of the experimental substrates are $25 \times 25 \text{ mm}^2$ and the system size of the simulated AgNW networks is $25 \times 25 \mu\text{m}^2$ for the shorter, and $100 \times 100 \mu\text{m}^2$ for the longer nanowires. As it is shown in Figure 3-5, the simulations are in agreement with the experimentally fabricated AgNW networks; the plots present the electrical resistance versus the ratio of areal mass density (amd) and critical areal mass density (amd_c). The resistance for both simulations and experiments was calculated and measured using 2 point probes. The amd/amd_c ratio is necessary for the true comparison, since the size of the simulated networks is an order of magnitude smaller than the experimental ones and can lead to statistical errors. In the simulations, the nanowire length is comparable to the system size leading to a lower percolation threshold: for $L_{NW} = 5 \mu\text{m}$ - $D_{NW} = 58 \text{ nm}$ the simulated amd_c is 32 mg/m^2 (for $25 \times 25 \mu\text{m}^2$), while the experimental one is 43.9 mg/m^2 (for $25 \times 25 \text{ mm}^2$). For $L_{NW} = 27 \mu\text{m}$ - $D_{NW} = 70 \text{ nm}$ the simulated amd_c is 14.6 mg/m^2 (for $100 \times 100 \mu\text{m}^2$), while the experimental one is 25

mg/m²(for 25 x 25 mm²). Despite the dimension differences, the model seems be useful to predict the electrical performances of MNW networks.

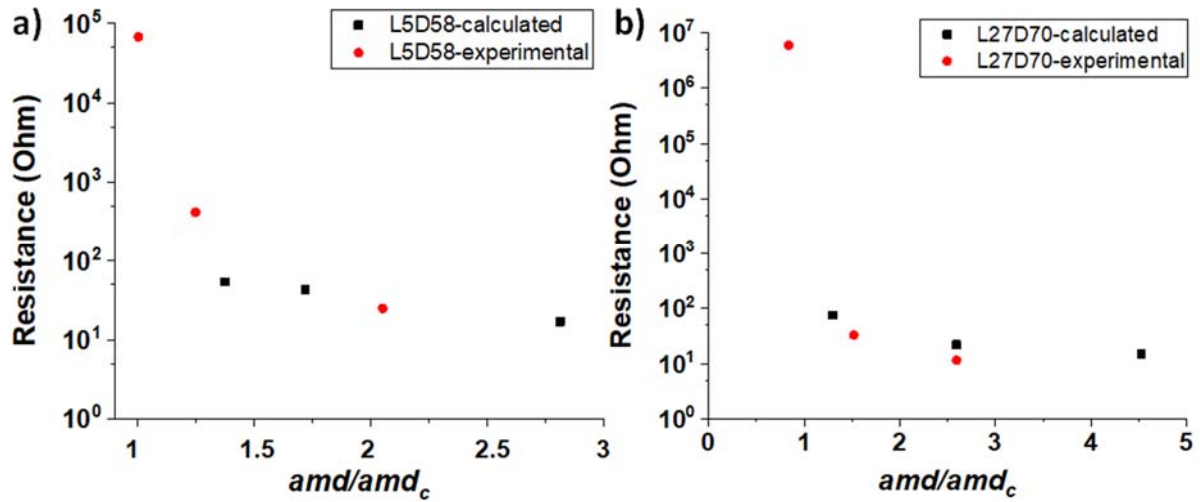


Figure 3-5: Comparison between experimental and calculated electrical resistance (2 point probes) versus the ratio of areal mass density over the critical areal mass density, for AgNW networks deposited by spray coating on 25 x 25 mm² glass substrates and for networks simulated by COMSOL with a size of 25 x 25 and 100 x 100 μm², respectively. Two different couples of nanowires dimensions are used: a) $L_{NW} = 5$ and $D_{NW} = 58$ nm, and b) $L_{NW} = 27$ μm and $D_{NW} = 70$ nm.

Ag thin film approximation in COMSOL Multiphysics®. In order to avoid the size restrictions imposed by the computation time and the software mesh limitations, and in order to focus more macroscopically on the electrical and thermal properties of applications, we chose an additional approach: a thin Ag layer with properties proportional to those of a AgNW network. A thin Ag film with some nm thickness on top of a Corning glass substrate of 25 x 25 x 0.11 cm³ size, can be simulated by a 3D model using the modules “Electric Currents, Shell” and “Heat transfer in solids” of COMSOL version 5.2. In this case, the architecture of the model is much simpler than the 2D stick-MATLAB based previously presented. What is more delicate is the choice and/or calculation of parameters such as the film thickness, the heat transfer coefficients and other losses, in order to produce a correct analogy of the Ag thin film with the AgNW network. The results demonstrate the voltage and surface current distribution on the Ag film and the temperature distribution in the film plus the substrate, heat that is induced by the Joule effect. This way we are able to compare with AgNW networks experimentally fabricated with non-homogeneous distribution, of several kinds of patterns, but also investigate the impact of small defects in the electrical and thermal distribution, and their relation with the occurring instabilities. The impact of non-homogeneity and the origin of degradation during electrical stress is one of the main objectives of my PhD thesis and it will be thoroughly discussed in Chapter 4 and 5, along with the details of this COMSOL modelling.

ἄνθρωποι τύχης εἶδωλον ἐπλάσαντο πρόφασιν ἰδίης ἀβουλίας.

Δημόκριτος

« People created an idol for chance, a pretext for their own reluctance »

Democritus (460-370 BC)

Chapter 4

4. Exploring the degradation of AgNW networks under electrical and thermal stress.

Thermal annealing is a commonly used technique for the optimization of AgNW networks and it has been extensively studied by our team in LMGP.^{28,30} As discussed in Chapter 1.2.4, the thermally activated atomic diffusion of silver atoms between adjacent nanowires, improves the sintering of the nanowire junctions, leading then to the overall optimization of the electrical resistance. However, the excess of heating can destabilize the morphology of the nanowires; due to the Plateau-Rayleigh instability, the nanowires become spheroidised and, as a result, the electrical pathways break and the electrical conductivity is lost.³⁰ Thus, the electrical stability is a crucial parameter for the integration of AgNW-based TE into devices. In addition to temperature, the failure of the networks can be also triggered by Joule heating when an electrical bias is applied to the network.^{161,163} In this case, the dynamics of failure is different to the one observed for networks subjected to thermal stress, and the infrared (IR) imaging has revealed valuable information about the spatial distribution of temperature during electrical stress, as previously studied by our team.³² The local formation of hotspots, and their propagation, have been observed in AgNW networks under an applied voltage ramp, leading to the conductivity loss of the electrode, as introduced in Chapter 1.2.6. The presence of spatial statistical fluctuations of AgNW dimensions or network density, and thus of local current density inhomogeneities, can lead to an elevated Joule heating in highly localized areas of the network, triggering further damaging effects. Consequently, a deeper study of the origin of degradation and the propagation of hotspots in AgNW networks was conducted in the framework of the project EARTH, between LMGP and LEPMI-Bourget-du-Lac, funded by the labex CEMAM. The main results of this study, focusing on the electrical and thermal simulations of a local defect performed using COMSOL Multiphysics®, and their correlation with other electrical simulations and experimental data, will be discussed in the present chapter. The first part of this chapter is highly inspired by the article entitled “*Dynamic degradation of metallic nanowire networks under electrical stress: a comparison between experiments and simulations*” published recently on *Nanoscale Advances* by N. Charvin, J. Resende, D. T. Papanastasiou, D. Muñoz-Rojas, C. Jiménez, A. Nourdine, D. Bellet, and L. Flandin, January 2021, DOI: <https://doi.org/10.1039/D0NA00895H>.

An important observation concerning the degradation under electrical stress, in contrast to the thermally induced failure that occurs over the entire network, is that the electrical failure

mechanism only leads to a local damage of the network in a tiny region of a few microns large. However, for both mechanisms, the temperature induced instabilities seem to be the main force of breakdown of the overall AgNW network. It is important to indicate that, when the electrical bias is applied, it is hard to disentangle the thermal and electrical effects on the network breakdown. To date, the majority of the related studies deal with the thermal and electrical stress separately, but both of them simultaneously affect the performance of AgNW based transparent electrodes. Therefore, our objective is to better explain these mechanisms of failure, by studying the *in situ* evolution of electrical resistance, when the stress is associated to a given applied temperature and to a given applied electrical current. In addition, for a successful integration of AgNW networks into devices, it would be useful to build a model that predicts the time of failure for given conditions of temperature and/or applied electrical current and, if possible, AgNW network densities to which we can associate a given electrical resistance. For the above reasons, we conducted a combined temperature-current experiment ($T-I$) to explore the time of failure of MNW networks. This work was performed during the post-doc of Dr. João Resende, with the contribution of Nil Fontanals and Dominik Moritz (internships 2018), and also during my Thesis. The main results and the associated discussion are reported in the second part of the present chapter, which is highly inspired by the article entitled “*Endurance tests on silver nanowire networks under constant thermal and electrical stress*” to be submitted, by J. Resende, D. T. Papanastasiou, D. Moritz, N. Fontanals, C. Jiménez, and D. Bellet.

4.1. Degradation of AgNW networks under electrical stress investigated by experiments and simulations

In order to investigate the origins of failure under electrical stress, we measured *in situ* the electrical resistance of AgNW networks under increasing electrical bias and in parallel we observed by IR imaging the spatial distribution of the temperature dissipated at the surface of the networks due to Joule heating. Moreover, we compared the experimental results on AgNW networks with:

- static simulations of the power-induced heating phenomena in a Ag thin film with initial defects, mimicking the initial hotspots experimentally observed in AgNW network.
- dynamic simulations of randomly deposited 2D sticks, including structural changes within the resistive network to mimic its progressive degradation under electrical stress.

Experimental results of electrical stress. Beginning with the fabrication of the transparent electrodes, we used the spray deposition with our homemade airbrush set-up. AgNW solutions were provided by the research team of Dr. Jean-Pierre Simonato from CEA-LITEN, synthesized according to the process developed by Mayousse et al.²¹³ The AgNWs present an average diameter of 70 ± 10 nm and an average length of 8 ± 3 μm being dispersed in methanol with initial concentration of 3.1 g/kg and diluted (30 times) to obtain a concentration of 0.1 g/L. The Corning glass substrates were cut in size of 25 x 25 mm². The results presented in this section concern a AgNW network with a corresponding *amd* of 93 mg/m², and an initial macroscopic resistance of 8.9 Ω , similar to previous studies,^{238,239} in which we base our calculations for values such as the contact resistance between the nanowires in the simulations. The spray coating protocol and details of the characterization techniques by SEM and the areal mass density calculation can be found in chapter sections 3.1-3.2. We applied a voltage ramp of 1 V/min using a Keithley 2400 sourcemeter, from 3 V up to the beginning of the breakdown. Meanwhile, *in situ* IR imaging was performed, to record the temperature distribution on the surface of the sample and extract the maximum temperature, T_{max} , using a FLIR A320G IR camera placed above the setup. During all the electrical tests, the samples were held hanging in mid-air, to avoid the thermal conduction losses by heat-transfer to any holder.

The AgNW network was subjected to the continuous voltage ramp, as shown in **Figure 4-1a**. As the voltage increases, so does the temperature, due to Joule effect; the metallic nature of the conducting element leads to a slight increase of the resistance as temperature increases. The induced heating is confirmed by the temperature measured by the IR camera; the evolution of maximum temperature, T_{max} , is also reported in Figure 4-1a. When the voltage bias reaches about 10 V, around 420 seconds after the beginning of the experiment, a significant and sharp increase in the resistance values is observed. Indeed, in less than 10 seconds, a sharp increase of five orders of magnitude is observed (from 10 Ω to M Ω). This is simultaneously accompanied by a sharp increase of T_{max} , as shown by Figure 4-1a. The series of IR images in Figure 4-1b reveals that the location of the hotspot also moved quickly throughout the entire sample. The green areas correspond to isothermal zones, i.e. where the temperature exceeds a specified threshold, here 195°C according to the camera range chosen for the experiment. According to the series of images, the hotspots gradually shift from the center of the specimen to the top and bottom edges in 2.5 seconds. The resulting path follows a somewhat linear course parallel to the opposite silver paste contacts (vertical in the IR images). This extensive propagation is consistent with the electrical resistance increase, until the moment where the

network is largely damaged and the electrical percolation is not spanning anymore from one electrode to the other. However, as previously described,^{32,167} one might observe that R_s returns to the 1 k Ω range after some time at rest under almost zero applied bias. The critical current density $j_{failure}$ was calculated from the following equation, provided by Lagrange et al., for the current density associated to the failure under electrical bias:²⁴⁰

$$j_{failure} = \frac{2 \cdot V_{failure}}{\pi \cdot \rho \cdot W} \quad (4-1)$$

where $V_{failure}$ in our case is equal to 10 V, ρ is $1.98 \cdot 10^{-8} \Omega \cdot m$, i.e. the AgNW electrical resistivity calculated according to the equation (1-1) by Bid et al.,²⁴¹ and W is the distance between the two parallel electrodes, equal to 19.8 mm. The resulting value is $1.63 \times 10^{10} \text{ A} \cdot m^{-2}$, which is in good agreement with previously reported ones.²⁴⁰ SEM images reveal a region with degraded nanowires, where the network had been deteriorated, as shown in Figure 4-1c. These bands with a width of several microns result from the local degradation of AgNW and provoke the sharp increase of the measured resistance.

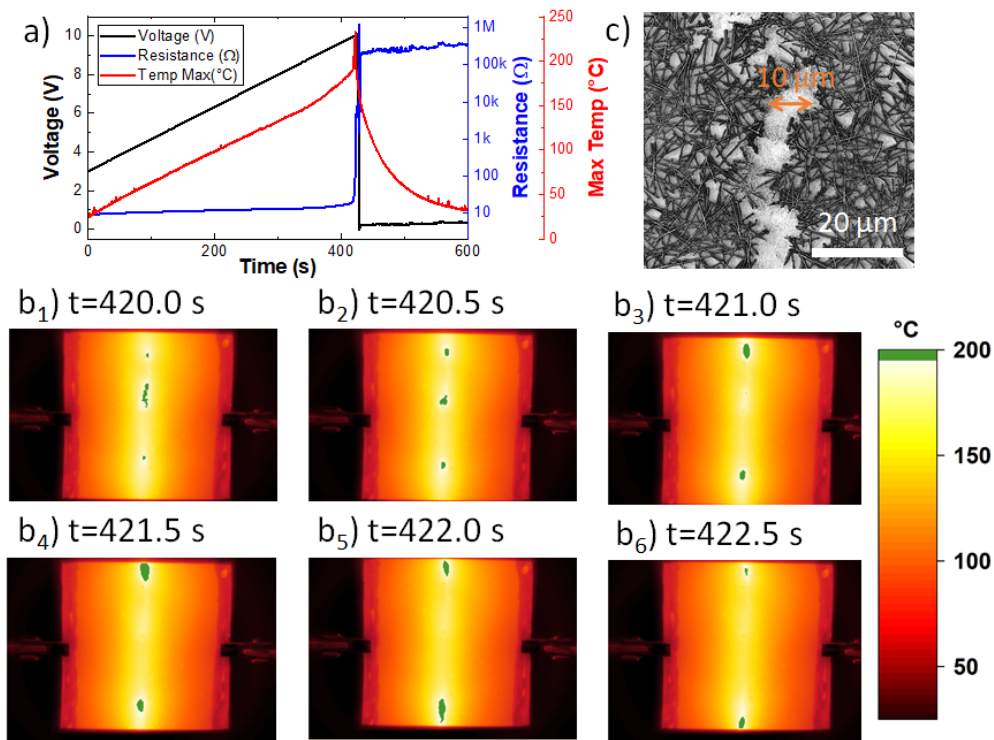


Figure 4-1: Experimental observation of the electrical degradation of a spray deposited AgNW network. a) Time evolution of resistance and maximum temperature of a AgNW network sample with an initial resistance of 8.9Ω when applying a voltage ramp of 1 V/min, starting from 3V, until voltage breakdown observed around 10V. b) b_1 to b_6 : Infrared images corresponding to the crack formation during the voltage ramp at different times between 420 and 422.5 s. Green areas represent the hottest regions, above $195 \text{ }^\circ\text{C}$. A visible propagation of the hot-spot from the center of the specimen to the edges, following a parallel line to the vertically aligned electrodes, is observed. c) SEM image of the AgNW network degradation or "crack" visible due to the differences in charging effect on the secondary electron detector. The width of the crack is about $10 \mu\text{m}$.

The origin of a hotspot; simulation approaches. In order to better understand the mechanisms controlling the crack propagation, simulated networks were prepared with a well-defined notch in a known position, as shown by **Figure 4-2a**. Our objective is to compare the effect of the macroscopic temperature from both a numerical and an experimental standpoint. COMSOL Multiphysics® was used to simulate macroscopically the electrical performance of AgNW networks as well as the locally induced increase of temperature. As discussed in Chapter 3.3, the fine element method (FEM) limits impose a simplified model, therefore a thin Ag layer was used instead of the discrete AgNW network, allowing a comparison between modelled and experimental samples of the same size. The thickness of the homogenized Ag layer (for instance 10 nm) was chosen to use a similar amount metal than the discrete network (for instance *amd* of 105 mg/m²). With this method, the size of the simulated specimens is the same than that of the experimentally fabricated ones (25 x 25 mm²), with the same used substrate (25 x 25 x 1.1 mm³). The modules “Electric Currents, Shell” and “Heat transfer in solids” of AC/DC COMSOL model were used for the computations. The electrical and heat transfer coefficients of thin Ag and Corning glass were applied. Therefore, the surface current density and temperature of a homogenous Ag film with the initial notch were calculated using COMSOL. To do so, the silver material was removed on a stripe of 10 µm wide. A 1V voltage bias was then applied between the two opposite contacts. As expected, the surface current density indicates a rather homogeneous distribution, apart from the area that contains the notch, as clearly shown by **Figure 4-2b**. In this case, the COMSOL simulation results locally in a 10 times increase of the current density at the tip of the simulated defect, compared to the homogeneous specimen case. During the present study, I performed several simulations with varying sizes and a large tip-effect is obtained, even for rather short notch of only 20 µm long. This intense current density values result in a corresponding localized higher temperature. A steady-state temperature analysis is shown in **Figure 4-2c**, with the sample at 1V bias. The rather small defect in the Ag thin film impacts directly the distribution of surface temperature even at very low voltage. The difference between the maximum and minimum temperature is 0.5 °C at room temperature. At higher voltages it increases drastically, i.e. 33 °C at 8 V and 50 °C at 10 V. The min-max values are 66 °C-99 °C and 90 °C-140 °C, respectively.

As seen in **Figure 4-2b**, locally the 2D current density can be equal to 20 A/m for a bias of 1V, which corresponds to a current density $j=2.10^9$ A/m² for the 10 nm Ag film used here. If one wants to apply this observation to the failure one has to consider the bias at which the AgNW network losses its percolation nature: 10 V. Therefore COMSOL simulations indicate that the

current density that would be associated to the network degradation would be about $2 \cdot 10^{10}$ A/m², this is a value very close to the one obtained previously thanks to eq.(4-1): 1.63×10^{10} A.m⁻². This local severe increase of the current density is at the origin of the hotspot creation in an experimental AgNW network, as the temperature is higher in this region, and can cause a locally spheroidization of the nanowires with the corresponding loss of the network electric conduction.

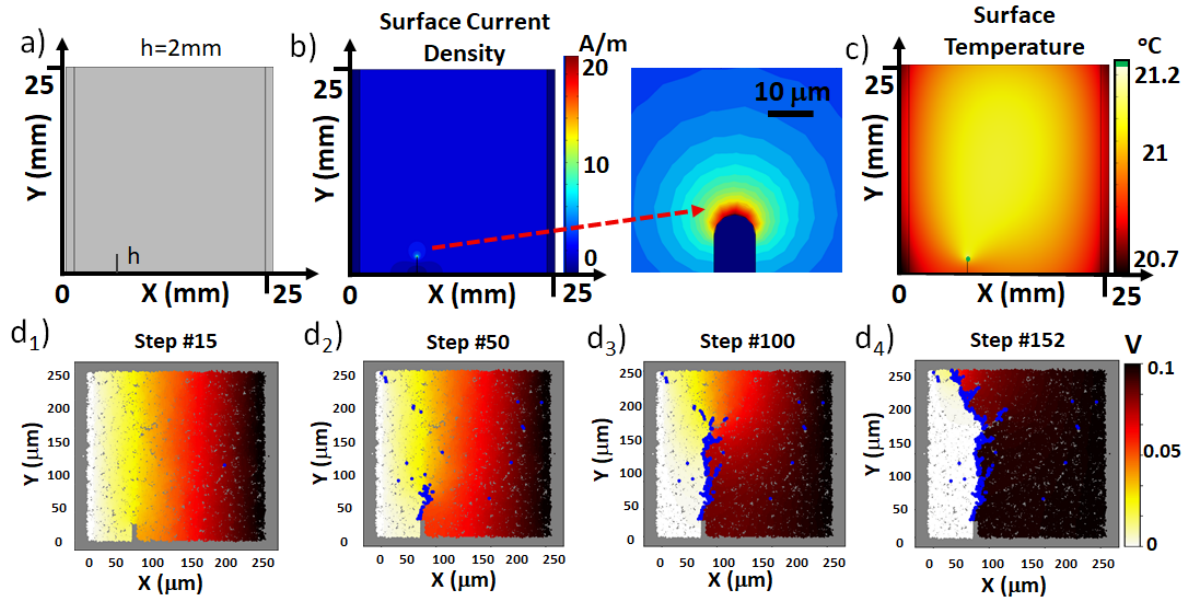


Figure 4-2: Modelling the degradation in a AgNW network with an initial notch. a) Scheme of a silver film with a 2 mm vertical notch at the bottom left of a 25 x 25 mm² sample. b) COMSOL simulation of the surface current density under a 1 V bias applied between the vertical opposite electrodes. Entire sample (left), and zoom (right) on the notch area. c) COMSOL steady-state simulation of the surface temperature distribution under a 1 V bias. d) Voltage maps at different steps (15, 50, 100 and 152) representing the formation of the crack in a network with a vertical notch on a 200 x 253 µm² 2D stick network obtained by the electrical simulations with Python code.

Dynamic simulation of a crack propagation. In addition to the COMSOL simulations, the notched specimens were modelled with simulation based on random 2D sticks to determine the voltage and current maps. This numerical method was developed by the Engineer Nicolas Charvin (LEPMI, Bourget-du-Lac) with a homemade Python code. The goal is to build a time dependent simulation, including structural changes within the resistive network to mimic its progressive degradation under electrical stress. The proposed dynamic approach is based on the evaluation of the currents distribution on a simulated network. As mentioned in Chapter 3.3, a metallic discontinuous nanowire network may be simulated with a random arrangement of 2D segments on a rectangular area ($L_{sx} \times L_{sy}$).^{242,243} Each segment is represented as an electrical resistor with a R_{wire} proportional to the length of the corresponding sub-segment. Each

intersection is represented as a contact resistor (R_c) with values adjusted to correspond to the macroscopic resistance of the real sample R_s (in the previous experiment, it was reported to be 8.9Ω). R_c value could either be determined for individual junctions by a direct-measurement,²³⁸ or assumed as an average R_c value by adjusting the simulated sheet resistance of the sample, R_s , in order to mimic the real characteristics of similar experimental networks, using R_c as a fitting parameter.²³⁹ From a linear relation between R_c and R_s , we could derive that the corresponding contact resistance is equal to $14 \pm 2 \Omega$. Given the small size of the simulated networks ($200 \times 253 \mu\text{m}^2$), the electrical bias values were also adjusted to offer a fair comparison to the real networks. The electrical potential value can then be calculated on every node of the 2D segments graph structure, using Kirchoff's Current Law. This then results in a unique electrical potential map over the whole sample, and a corresponding sheet resistance of the sample, R_s .

We consider the degradation of a single AgNW at a microscopic level to be directly linked to the temperature of that particular wire due to Joule effect. This temperature is directly dependent on the energy dissipated in the wire. An iterative damage phenomenon was thus simulated at a very individual and local scale by progressively and irreversibly modifying the nanowire network model, depending on the thermal destruction of single wires. Under a given voltage bias, the electrical current density j is determined in every resistor (either R_{wire} or R_c type). At each iteration step, the resistor with the highest j , among all resistors whose j is larger than a defined threshold value $j_{failure}$ is selected and removed from the graph, considered as broken. This process is repeated, until the network loses its percolating nature between the two opposite electrodes. The experimental critical current density $j_{failure}$ can be derived from the observed voltage bias $V_{failure}$ at which failure occurs on a real sample.²⁴⁰ If we adjust the simulated voltage bias according to ratio of the system size ($200 \times 253 \mu\text{m}^2$) and the sample real size ($25 \times 25 \text{mm}^2$), $L_{sx,simul} / L_{sx,exp}$, the $j_{failure}$ can then be used as a realistic threshold.

The dynamic model was applied to alter the simulated structure under 0.1 V voltage bias. In the series of voltage map runs shown in Figure 4-2d, we observe the origin of the crack formation at the tip of the vertical defect, already from Step #50. This origin point for the crack propagation is the region where the electrical power is the highest, associated with higher local temperature, and therefore causing a local degradation on the nanowires in this area. This dynamic model mimics the hotspot creation and the associated defect propagation to the nearby region, the Joule heating induced region turns it to a hotspot, which degrades drastically the next nearby nanowires. As it is shown in Step #100 and #152, this catastrophic phenomenon propagates as a domino effect until the final loss of percolation between the opposite electrodes.

Defects on real AgNW networks are related to local variations of the network density, leading consequently to local variations of the electrical resistance and the dynamic simulations confirm that indeed such defects can be the origin of failure. Finally, dynamic simulations show that the propagation process happens along a rather vertical crack (parallel to the contacts), by analogy with a mechanical crack, not only in the case of networks with initial defects, but also for a homogeneous thin film. Further experiments and simulations will be demonstrated in chapter 5, which is dedicated to the investigation of the non-homogeneous AgNW networks, their effect on the electrical and thermal properties and their relation with the origin of failure. Before this, we would like to link the mechanisms of failure under electrical stress with the degradation during thermal stress and investigate their simultaneous effect on the AgNW network failure, this issue is the subject of the following section 4.2.

4.2. Time to Failure of AgNW networks under thermal and/or electrical stress: The so-called “*T-I* experiments”

After we have explored the impact of electrical stress separately from the thermal stress, which was the issue in previous work of the team,³⁰ we can now focus on when both are applied simultaneously on a AgNW network and investigate the evolution of its electrical properties. Our goal is to apply several values of temperature (T) and current (I) and investigate the degradation mechanism which is prevailing for each coupled $T-I$ conditions in networks with varying density. By measuring the time of failure in each experiment, we aim to develop a physical model that can predict the performance limits under arbitrary temperature and electrical bias. Such estimation could be useful for the successful integration of AgNW networks into industrial devices, according to the characteristics of each device and the related working conditions.

Experimental protocol for endurance tests and time-of-failure estimation. In order to investigate the endurance of AgNW networks under electrical and thermal stresses, we measured the time of failure (ToF) or time at which a sample degrades or “fails”, meaning that the electrical resistance diverges, while subjected to a constant temperature (T) and applied electrical current (I). The lifetime of the networks also depends on the sample initial resistance, being related to its network density. A large number of samples is required to obtain statistically sufficient data of time to failure, for each temperature and current conditions. Thus, for the fabrication of AgNW networks, this time Corning glass substrate were cut in smaller squares

of 12.5 x 12.5 mm². This size of substrates allowed us to obtain a set of 30 samples from each deposition. **Figure 4-3a** shows the dispersion of all initial resistances used for the experiment. Our goal was to deposit AgNW networks with resistance between 10 and 20 Ω. The total number of tested samples is over 200 and the mean resistance value and standard deviation are 13.7 Ω and 5.0 Ω, respectively. Figure 4-3b shows the calculated *amd* of 4 samples with an initial resistance from 8.1 to 19.5 Ω. For 8.1 Ω, we obtain an *amd* of 118 mg/m², whereas for 19.5 Ω an *amd* of 73 mg/m² is calculated. Even if the network resistance could be influenced by network defects or non-homogeneities from the deposition, it is assumed that all samples show an *amd* between 70 and 120 mg/m². As already discussed in section 1.2.3 and shown also in Figure 3-3a of section 3.2, the dependence of the resistance with *amd* follows the power law:

$$(amd - amd_c)^{-\gamma} \quad (4-2)$$

with γ equal to 4/3 and the amd_c is estimated to be 43.4 mg/m², for the AgNWs that we have been using (diameter=70 nm, length=8 μm). The same fitting is plotted for the samples in Figure 4-3b.

The thermal and electrical endurance tests are performed in a characterization set-up including a hot plate, connected to a thermocouple with a National Instruments™ input module, and two-point probes mounted on the hot plate and connected with a Keithley 2400 sourcemeter. Two pairs of two-point probes can be used; thus we are able to measure simultaneously two different samples under the same experimental conditions. The thermocouple module and the sourcemeters are connected with a LabVIEW software that controls and records every second the data related to: time, voltage, current, resistance and temperature.

With the *T-I* experiment, one can expect to collect all the possible failure conditions for AgNW networks having different nanowire densities, therefore different initial electrical resistance (*R*) values at a sufficient range of low resistance samples. These data will then be useful to create an approximate model that predicts the time of failure. To do so, three main experimental tests have been conducted:

- Performing measurements over samples with different *R* (initial resistance) when the same conditions of *T* and *I* are applied, to obtain a tendency of *ToF* with *R* variation.
- Performing measurements over sets of samples with similar values of *R* for the same applied *T* but varying *I*, to deduce the tendency of *ToF* with *I*. The current values applied are 0 A, 0.1 A, 0.25 A, 0.5 A and 0.75 A.

- Performing measurements over sets of samples with similar values of R for the same applied I but varying T , to deduce the tendency of ToF with T . The temperature conditions that are tested during the T-I experiment vary from 50 to 400 °C, with 25 °C increasing step value.

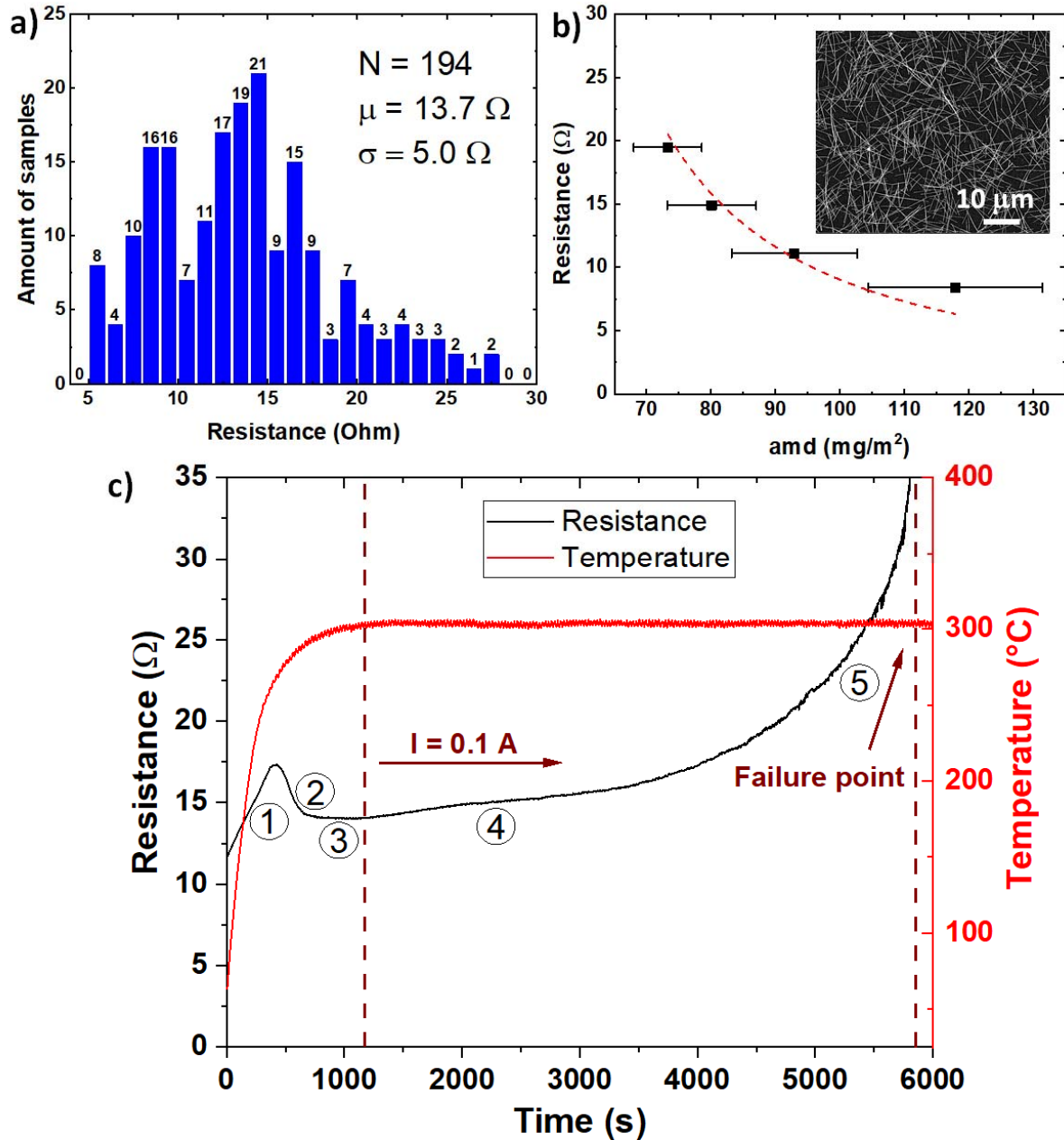


Figure 4-3: a) Resistance distribution of all the studied AgNW networks in the electrical and thermal endurance ($T-I$) experiment. b) Resistance versus areal mass density (amd) of AgNW networks for the $T-I$ experiment. The dashed line represents the power law between R versus amd . Inset represents a SEM picture of a network with a density of $73 \pm 5 mg/m^2$. c) Exemplary time evolution of a AgNW network resistance during T-I experiment. In the beginning the sample is being heated with a rate of 15 $^{\circ}C/min$ until a certain set temperature, here 300 $^{\circ}C$. Then, it is subjected to electrical stress as well, in this case 0.1 A, until the resistance starts diverging. The breaking point is considered at the moment when the resistance reaches 5 k Ω . The regions observed during the $T-I$ experiments are related to: 1/ linear increase of resistance at constant heating rate, 2/ sintering processes which leads to a resistance decrease, 3/ steady state region, 4/ slow degradation of AgNW network due to both electrical and thermal stress, and 5/ fast degradation of network associated to the failure.

To perform the measurements, for each T - I couple, it is required that the temperature reaches first a steady-state T , and only afterwards the constant current I can be applied. Figure 4-3c shows the steps of the T - I experiment. At first, the specimens are heated up to the set temperature T with a heating rate of 15 °C/min. At the same time, a low current is applied with a value of 5 mA, enough to measure the electrical resistance but with a negligible electrical impact. Once the temperature stabilizes, the target current I can be then applied. That is the moment “zero” of the experiment and both temperature and current are from now on imposed to the sample. Starting from this moment, we measure the time until the resistance reaches 5 k Ω and this duration is denoted as the ToF . This value is chosen because the AgNW networks have been observed to follow kilo-Ohm range values after their breakdown under electrical stress tests, as discussed in section 4.1.

In Figure 4-3c we can also observe the time evolution of the resistance during the T - I experiment on a sample heated up to 300 °C and afterwards exposed to a constant current of 0.1 A. This can be divided into 5 different regions. Region 1 shows the linear increase of resistance with increasing temperature at constant heating rate, in accordance with the metallic behavior of AgNW networks. From this linear relation, one can calculate the temperature coefficient of electrical resistance, β , using eq. (1-6) as discussed in chapter 1.2.6. The thermal coefficient for AgNW networks in the present experiment β_{Ag} is calculated as $2.1 \times 10^{-3} \text{ K}^{-1}$ and is in the same range as already reported by Lagrange et al, $2.1 \pm 0.1 \times 10^{-3} \text{ K}^{-1}$.²⁸ At a temperature of around 200 °C, the resistance begins to decrease again (region 2). The surrounding PVP layer of the nanowire exhibits a glass transition temperature of 174 °C and a melting point at 220 °C.¹²¹ The PVP layer degradation could enlarge the contact area between the nanowires at the junction. Due to the heat treatment the junctions start sintering by temperature activated process which leads finally to an improvement of the AgNW network and thus to a decrease of the overall resistance. Then, when the applied temperature stabilizes, in this example at 300 °C, the resistance shows almost no further decrease, as observed in region 3. At this temperature, we start applying the current corresponding to the examined T - I couple, here $I = 0.1 \text{ A}$. Thus, apart from the temperature T imposed to the sample through the hot plate, the power, during current flow, is dissipated by Joule heating in the AgNW network and be expressed by: $P_{in} = I^2 R$. According to Sorel et al. the increase of temperature of the AgNW network due to Joule heating can be approximated as:¹¹⁴

$$T(t) \approx T_0 + \frac{1}{\alpha} \frac{I^2 R}{A} [1 - e^{-\frac{t}{\tau}}] \quad (4-3) \text{ with } T_{stab} = T_0 + \left(\frac{1}{\alpha} \frac{I^2 R}{A} \right) \quad (4-4)$$

where α and τ are referred as heat and time constant, respectively, and $\frac{I^2 R}{A}$ stands for the areal power density, while A is the specimen area. On closer examination at region 4, the bounded increase in resistance can be observed. However, this time there is no steady state visible; instead there is a smooth continuity between region 4 and 5, without any abrupt change. Region 5 describes the accelerating degradation of the network, with a sharp increase of the electrical resistance, at the failure point.

Initial resistance influence. As introduced previously, a part of the measurements is performed under the same temperature and current values for a large number of samples with different initial electrical resistance R , with the objective of obtaining the dependence of ToF versus R . The samples chosen for this experiment have initial resistance values from 8 to 18 Ω , and are exposed to a constant temperature of 150 $^{\circ}\text{C}$ and a constant applied current of 0.5 A. The ToF for each sample is then measured and three cases are plotted in Figure 4-4a, where the evolution in time of the electrical resistance during the $T-I$ experiment is presented, with the time in log-scale. The initial resistances are 10.5, 12.4 and 17.4 Ω , selected to cover the range of resistances of the tested samples. The resistance follows the evolution described previously in Figure 4-3, but the ToF is clearly varying with the initial resistance. The three presented samples demonstrate the general trend of the $T-I$ experiment: the lower the electrical resistance, the longer the time of failure.

Influence of temperature. During this group of measurements, we tested samples with similar R values, applying a constant current, I , and varying the values of temperature, T . The case of $I = 0.25$ A and $R = 16.0 \pm 0.9$ Ω is presented in Figure 4-4b. With such data sets, the objective was to predict failure conditions for a certain AgNW network and therefore associated to its own network density (amd value) and initial electrical resistance, for a given temperature T at a certain applied electrical current I . The temperatures applied to the group of the Figure 4-4b are: 175, 200, 225, 250, 275, and 300 $^{\circ}\text{C}$. The ToF data over the variation of temperature show what was expected according to the impact of thermal annealing and the Plateau-Rayleigh instability as discussed previously in the present chapter. If the applied temperature, thus the thermal stress, increases then the failure of the networks will be promoted and the associated time to failure will be shorter. For instance, for temperatures lower than 200 $^{\circ}\text{C}$, the samples are stable for more than 24 hours, while for temperatures above 300 $^{\circ}\text{C}$ the electrical breakdown is very fast, occurring in less than 10 minutes.

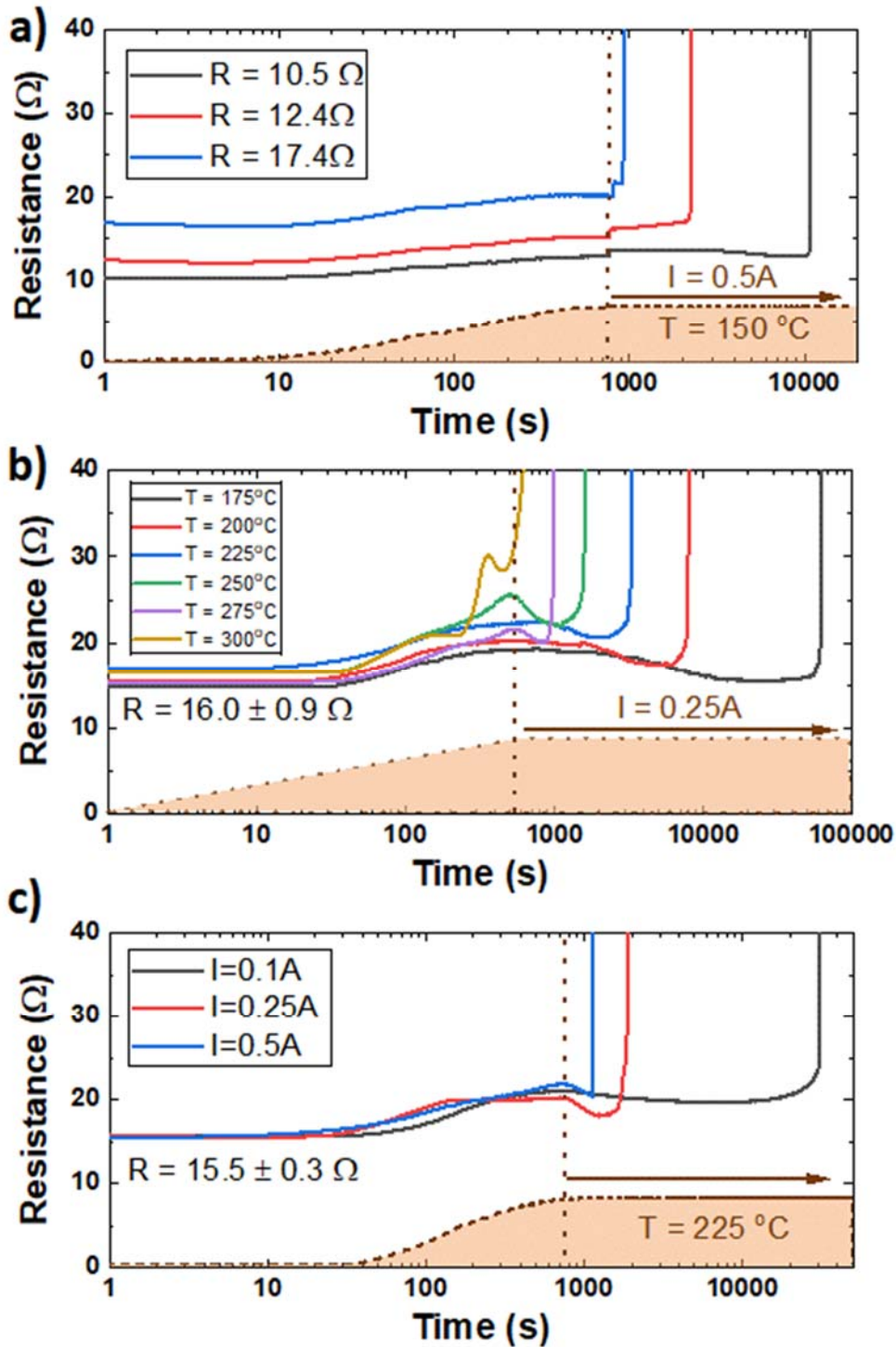


Figure 4-4: Influence of a) initial resistance, b) applied temperature and c) applied current on the time of failure, depicted by the evolution of resistance during the T-I experiment. In each case, the investigated parameter (resistance, current or temperature) is varied while the other two are maintained constant. The orange regions represent schematically the temperature evolution and the dashed vertical line shows the moment when the set temperature is reached and the current starts to be applied. a) Three samples with initial resistance from 10.5 to 17.4 Ω are tested under the same temperature and current (150 $^\circ\text{C}$, 0.5 A). b) Various temperatures from 175 to 300 $^\circ\text{C}$ are applied in a set of samples with similar $R = 16.0 \pm 0.9 \Omega$ under constant current of 0.25 A. c) Three different values of current (0.1, 0.25, 0.5 A) are applied in a group of samples with similar $R = 15.5 \pm 0.3 \Omega$, at a constant temperature of 225 $^\circ\text{C}$.

Influence of electrical bias. Similar trends are observed in the case of different electrical bias values. As expected, the higher the current applied on AgNW networks, the shorter the time of failure. As shown in Figure 4-4c, for a group of samples with similar initial resistance of $R = 15.5 \pm 0.3 \Omega$, at the same applied temperature equal to $225 \text{ }^\circ\text{C}$, the AgNW networks remain stable for more than 8 hours under a low applied current of 0.1 A. On the other hand, at higher electrical current of 0.5 A, the time of failure is much shorter, less than 15 minutes. At even higher values of current, we observe an almost instant divergence of the electrical resistance.

Figure 4-5 illustrates through SEM images the 3 general regimes of degradation after thermal and electrical stress, these 3 regimes are: a) the thermal stress is dominant (low or almost zero current bias and high applied temperatures over $300 \text{ }^\circ\text{C}$), b) the thermal and the electrical stress both play a key role, and c) the electrical stress is solely considered and the impact of temperature is negligible. In the case that the electrical stress is dominant, the AgNW networks appear intact on the whole network except from the regions where the hotspots have propagated, in accordance to the results of electrical stress demonstrated in the first part 4.1 of the present chapter. Such highly localized regions contain damaged nanowires, partially or fully spheroidised, like the ones in Figure 4-5i. The degradation of the nanowires is present mostly in the very thin region of the crack, where the hotspots have propagated, as observed by the IR camera. In the intermediate cases, where both the temperature and the current applied are significant, with high values, the SEM images reveal similar damages (Figure 4-5ii) but this time they are observable in the whole AgNW network. Finally in the case where the thermal stress dominates, SEM images, like the one on Figure 4-5iii, confirm the complete spheroidization of AgNW over the whole network, as previously observed during the thermal annealing studies.³⁰

Towards the time-of-failure model; temperature contribution. As mentioned above, almost 200 samples were tested under different temperature and current conditions to allow building a semi-empirical model predicting the time to failure for the AgNW networks. Our goal is to fit the experimental observations with the physical laws that describe, in the most pertinent way, the mechanisms of failure linked to thermal and/or electrical stress. Firstly, we consider the impact of the temperature; as Lagrange et al.²⁸ have shown, the nanowires diameter plays a key role in the morphological instabilities, which are driven by the surface energy reduction. Experimental data appeared compatible with the Gibbs-Thomson equation, meaning that the decrease of spheroidization temperature is inversely proportional to the nanowires diameter.²⁸

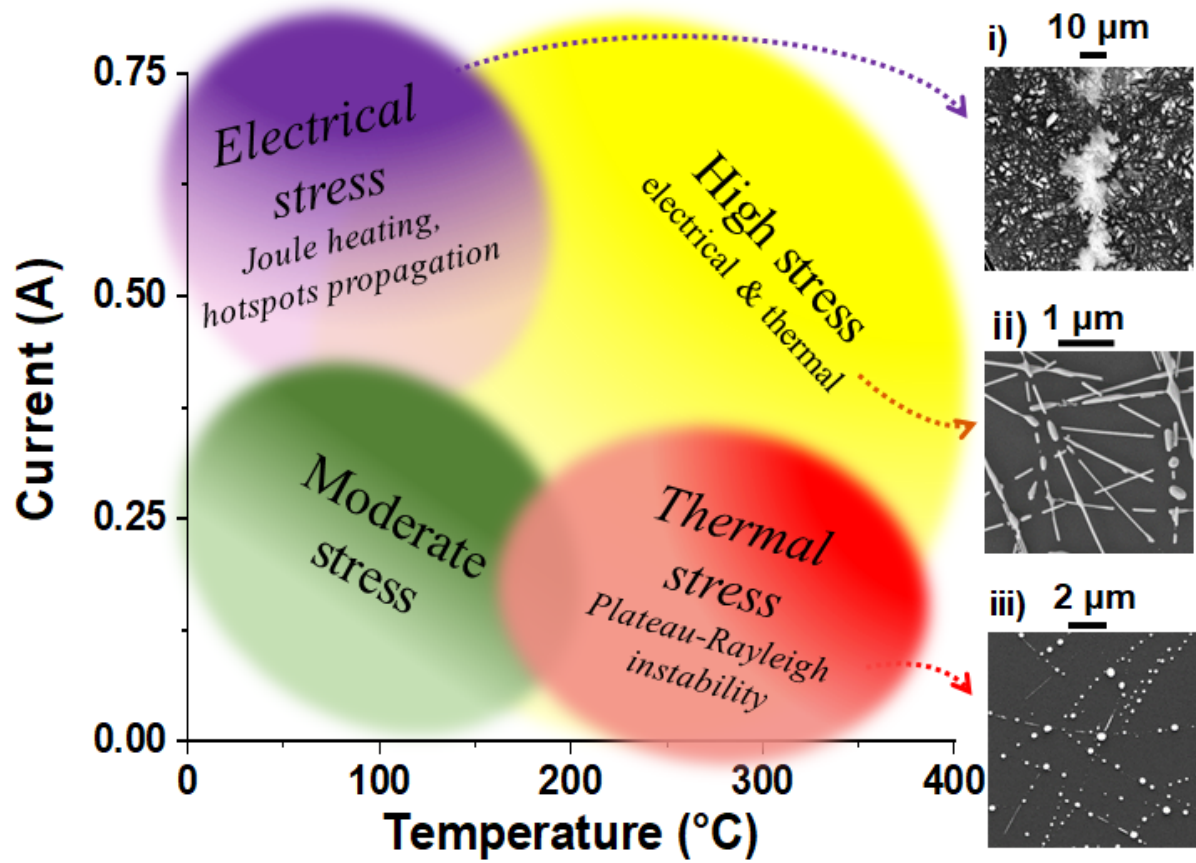


Figure 4-5: Schematic representation of the T - I experiment, showing the ranges of the applied temperature and current. The extreme cases where temperature and/or current are high lead to fast degradation of the AgNW and they are associated with different mechanisms of failure. SEM images correspond to the 3 general regimes of the degradation, when: i) solely a high current is applied, i.e. 0.75 A, and the impact of the temperature is negligible (below 100 °C), Hotspots are induced locally due to Joule heating and propagation of a crack along a very narrow area (as shown by the SEM picture in i)). ii) high stress by both electrical and thermal stress, with values above 0.3 A and 200 °C respectively, iii) the thermal stress is dominant, with applied temperatures over 300 °C, and the current bias is roughly lower than 0.2 A, and the Plateau-Rayleigh instability causes the spheroidization of the nanowires.

Similarly, we could assume an initial crude model where atomic diffusion operates over a characteristic distance, L_{therm} , to allow the AgNW morphological instability occurrence. This can be described by the following equation:

$$L_{therm} = \sqrt{2 \cdot D \cdot t_{therm}} \quad (4-5)$$

where D is the diffusion coefficient, $D = D_0 \cdot \exp\left(-\frac{\epsilon_{therm}}{k_B T}\right)$ and t_{therm} is the characteristic thermal time, and D_0 and ϵ_{therm} are the pre-exponential factor and a thermal activation energy, respectively. This concerns only the thermal stress. To generalize this concept also for electrical stress, one can use eq. (4-5), which considers that the applying electrical bias can be seen as a way to increase the temperature through Joule heating, by using the steady state temperature

described in eq. (4-3). Therefore, one can combine both eq. (4-3) and eq. (4-5) to estimate the ToF :

$$t_{therm} = \frac{L_{therm}^2}{2D_0} \exp\left(\frac{\varepsilon_{therm}}{k_B T}\right) = A_{therm}^{-1} \cdot \exp\left(\frac{\varepsilon_{therm}}{k_B T}\right) \quad (4-6)$$

with parameter A_{therm} depending on the nanowires properties. **Figure 4-6** shows the average values of ToF for each set of samples tested as a function of temperature, for different electrical currents.

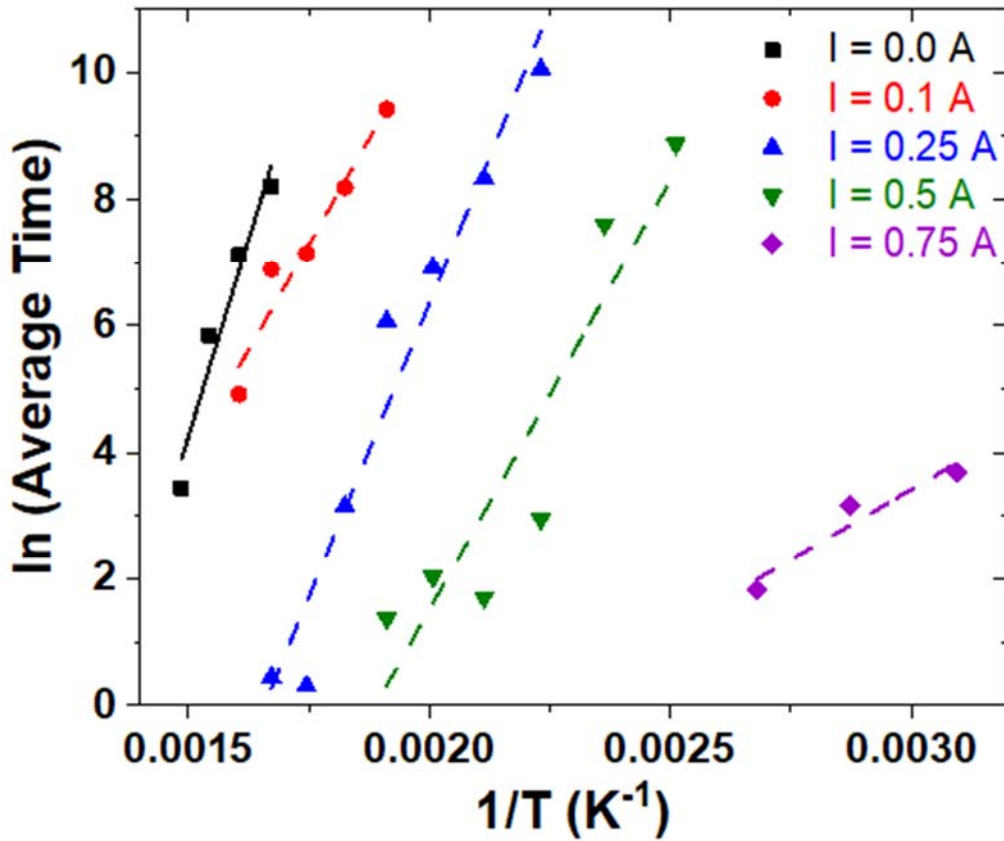


Figure 4-6: T - I experiment: natural logarithm of average ToF of samples with similar resistance versus the inverse of temperature. The data are separated in colour groups corresponding to the same applied current. For the zero current group (in black) the activation energy E can be extracted from the linear relation by Arrhenius plots and the calculation gives 2.15 ± 0.35 eV. In the rest of the cases the dashed lines are guide to the eye to show the tendency of degradation with the increase of applied current.

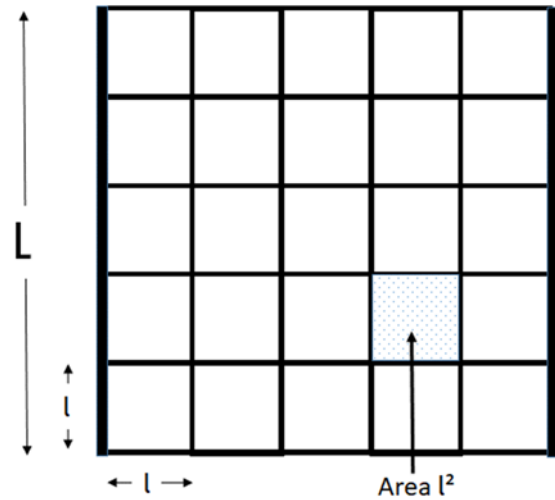
Based on the logarithmic scale one can observe linear tendencies changing with the inverse of temperature, which is an evidence for thermally activated processes, in agreement with eq. (4-6). In the case of zero electrical stress, one can extract by Arrhenius plot, the activation energy related to the thermal component of the degradation mechanism. The estimated value is 2.15 ± 0.35 eV, which is rather high compared to the ones observed during previous thermal annealing experiments, i.e. from 0.3 to 1 eV.²⁴⁴ The rest of the slopes, concerning the application of non-

zero current, decrease with the increase of applied current; higher current means higher Joule heating and thus, lower thermal energy is needed to reach the same degradation state related with the atomic diffusion occurring at the nanoscale.

The next step of this investigation deals without considering anymore the applied current intensity I , but focusing more on the current density j .

From applied current I to the estimation of current density j . All experimental data so far in part 4.2 have been presented by considering the electrical current I at the network scale. It can appear more pertinent to consider a more local analysis, replacing then I by the current density j . Such an approach has three main advantages: i/ the analysis does not depend anymore on the network dimension, therefore comparison with data from literature is more straightforward, ii/ in the same vein the comparison between failure at the network scale (as in this work) and at the AgNW scale (as one can find some in literature) can be done; iii/ one can then consider what has been seen in part 4.1 for the electrical degradation with the local increase of the current density once the crack has been created.

In what follows we first focus on the way to convert the electrical intensity, I , into current density, j . To do so, one has first to calculate the cross section of the AgNW network. For the sake of simplicity, one can imagine that we rearrange all AgNWs so they constitute a regular quadratic periodic mesh of parallel AgNWs, the mesh having the same silver mass (as well the same areal mass density) than AgNW network. This is schematically



shown on the right, with two opposite vertical electrodes at each side. The whole specimen area is L^2 , while in the hatched area we can count 4 associated wires of length l , counting each for half for one square area l^2 . Therefore the areal density of sticks of length l is then $n = 2/l^2$. The areal mass density, amd , can be equal (by definition) to the mass of silver within any zone, simply divided by the zone's area. If one considers for instance a small square of edge l (hatched area) then amd can be written as :

$$amd = \frac{mass}{area} = \frac{2 \cdot (mass\ of\ a\ wire\ of\ length\ l)}{l^2} = \frac{\rho_{Ag}^m \pi D_{NW}^2}{2 l} \quad (4-7)$$

with D_{NW} the diameter of the nanowires and ρ_{Ag}^m silver mass density, equal to $10.5 \times 10^4 \text{ kg/m}^3$. Now we have to estimate the cross section, i.e. the surface which is crossed by the electrical current along the horizontal directions (perpendicular to the vertical electrodes each side). The cross section, CS , is equal to the number of wires crossed (L/l) times the cross section of each of them ($\pi D^2/4$), therefore the cross section can be written as:

$$CS = \frac{L}{l} \cdot \frac{\pi D^2}{4} = \frac{L \cdot amd}{2 \cdot \rho_{Ag}^m} \quad (4-8)$$

For instance, if one considers typical values associated to this work: an electrical intensity I of 0.5 A, an amd of 100 mg/m^2 , $L=12.5 \text{ mm}$, then the current density is equal to 10^{10} A/m^2 or 10^6 A/cm^2 , sometimes as well expressed as 1 MA/cm^2 . This value is coherent with the result discussed in section 4.1, equal to $1.63 \times 10^{10} \text{ A/m}^2$ or 1.63 MA/cm^2 , and to values found in literature; Lagrange et al. have reported a current density of failure equal to 3.1 MA/cm^2 at 7.5 V.²⁴⁰ In addition, Khaligh et al. have estimated by simulations that AgNW networks can be stable when carrying an average current density of 0.12 MA/cm^2 .¹⁶²

***T-j* experimental results.** By replacing the applied current with the corresponding current density, $CS = \frac{I}{j}$, we can consider all the samples, no average values are needed and we can take in consideration the resistance variations, since they can be associated to amd variation. The relation of $\log(ToF)$ with the reciprocal temperature for all the samples of the $T-I$ experiment, is depicted in Figure 4-7a, as a function of the calculated j . Focusing now to the electrical origin of AgNW network failure, one can observe the ToF of all the samples as a function of the current density in Figure 4-7b. The ToF is also plotted here in log scale and the color map represents the applied temperature in each sample. It is shown more clearly that in the extreme case of high current density, i.e. 1.5 MA/cm^2 , the AgNW networks degrade fast, with a corresponding ToF lower than 100 seconds, even when exposed to low temperatures below $150 \text{ }^\circ\text{C}$. In the other extreme case, close to zero electrical bias, the failure occurs mainly for the samples that undergo high applied temperatures over $300 \text{ }^\circ\text{C}$. The intermediate cases of 0.5 to 1 MA/cm^2 show a larger variation in the time of failure and temperature ranges. The results are more mixed, indicating the entanglement of the electrical and thermal load. However, observing the evolution of $\log(ToF)$ for the same current density, we can notice a general trend of a linear increase of $\log(ToF)$ as the temperature decreases.

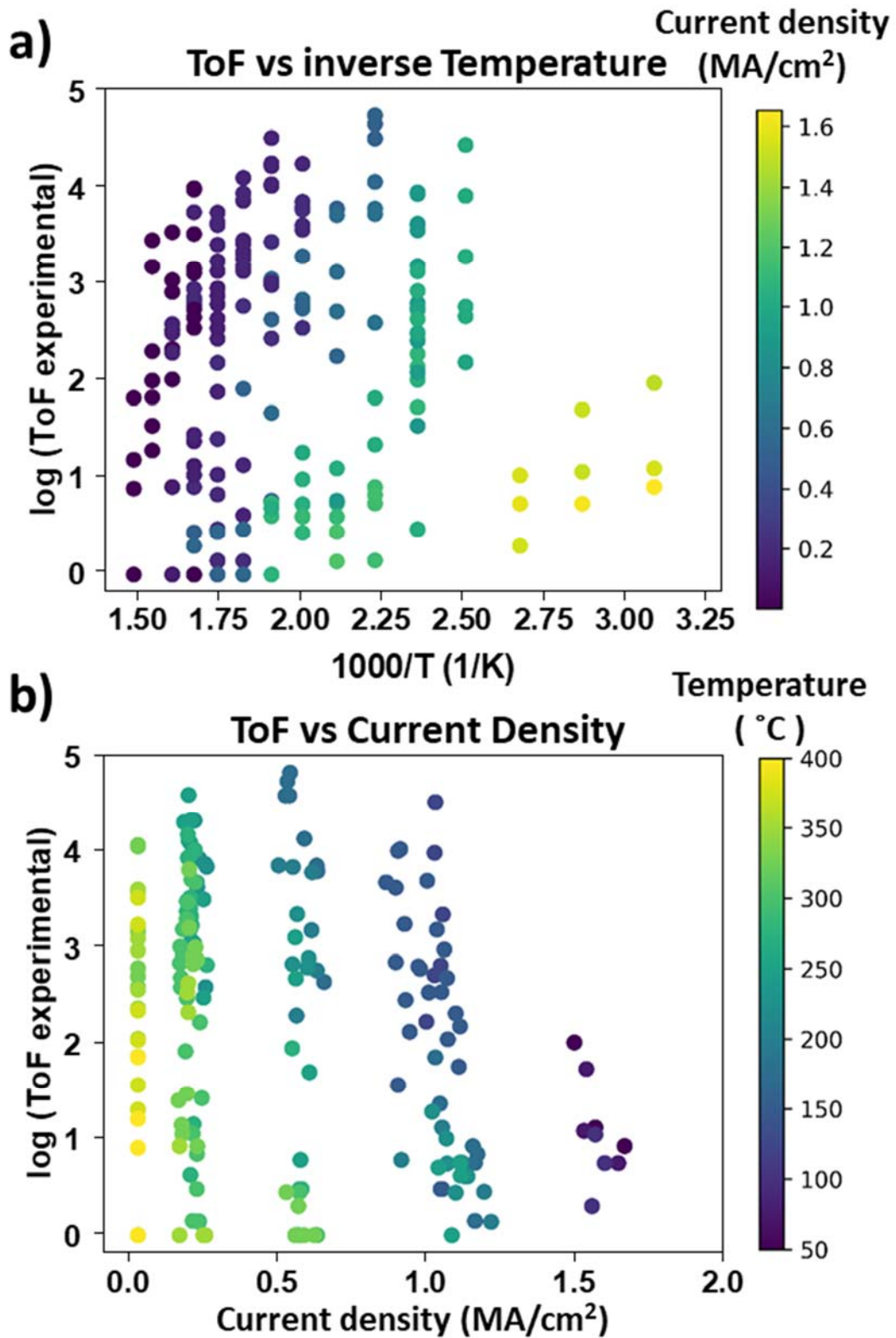


Figure 4-7: Time-of-failure, ToF (in seconds), for all samples of the $T-I$ experiment plotted in log scale, with the current density calculated by the applied electrical bias and the initial resistance of each sample. The graphs demonstrate the relation of ToF with a) the reciprocal temperature and b) the current density. The color of each data corresponds to the current density and the applied temperature, respectively.

T-j model. In order to build a model that can estimate the *ToF* during both electrical and thermal stresses, one can consider the increase of temperature in eq. (4-2), replacing then T_0 by $T_0 + \Delta T$, where the temperature increase ΔT is being induced by Joule heating. Then, using eq. (4-6), which associates the time to failure associated to the thermal stress, we can make a first approximation introducing also the electrical stress. The *ToF* can be now written such as:

$$ToF = B. \exp\left(\frac{E}{k_B.(T+\Delta T_{local})}\right) \quad (4-9)$$

where T is the applied temperature and ΔT_{local} is induced by Joule heating.

The previous approach is valid at the macroscopic level. As already mentioned, the goal is to obtain an expression of time of failure associated to the local level. Instead of considering macroscopic parameters, such as the electrical resistance R and the electrical current I , one can consider the local parameters: the areal mass density amd and the electrical current density j . This allows to consider the local physical mechanisms. The relation between electrical resistance R and amd is eq. (4-2), while the dependence between I and j is simply given by:

$$I=j.CS \quad (4-10)$$

where the cross section CS is given by eq. (4-8). Therefore locally the increase of temperature, ΔT_{local} , can be written in a way equivalent to eq. (4-6), which follows a macroscopic perspective. For a local perspective one gets now:

$$\Delta T_{local} = \frac{areal\ power}{\alpha^{local}} = \frac{(\rho^{el}.j^2).(Vol^{all\ AgNWs})}{\alpha^{local}.A} \quad (4-11)$$

where ρ^{el} is the electrical resistivity of AgNWs, α^{local} is the local heat transfer constant, $Vol^{all\ AgNWs}$ is the total volume of AgNWs in the whole network and A the network's geometric area (equal to L^2). $Vol^{all\ AgNWs}$ can be estimated from the total mass of silver within AgNW network, $M^{all\ AgNWs}$, given by:

$$M^{all\ AgNWs} = \rho_{Ag}^m.Vol^{all\ AgNWs} = amd.A \quad (4-12)$$

where ρ_{Ag}^m is the silver bulk density. Inserting the expression of the total volume of AgNWs from eq. (4-12) into eq. (4-11), this last equation becomes now:

$$\Delta T_{local} = \frac{\rho^{el}.j^2.amd}{\alpha^{local}.\rho_{Ag}^m} = C.j^2.amd \quad (4-13) \text{ with } C \text{ a constant equal to } C = \frac{\rho^{el}}{\alpha^{local}.\rho_{Ag}^m} \quad (4-14)$$

Equation (4-13) can be easily understood if one considers that the local temperature increase, ΔT_{local} , should linearly increase with: ρ^{el} , j^2 and amd . Consequently, this model allows us now

to write the time of failure of a AgNW network along with its dependence with T, j and amd , as follows:

$$ToF = B. \exp\left(\frac{E}{k_B \cdot \left(T + \frac{\rho^{el} \cdot j^2 \cdot amd}{\alpha^{local} \cdot \rho_{Ag}^m}\right)}\right) \Rightarrow$$

$$ToF = B. \exp\left(\frac{E}{k_B \cdot (T + C \cdot j^2 \cdot amd)}\right) \quad (4-15)$$

This last equation possesses only three unknown parameters: B, E and α^{local} .

Before comparing experimental data with eq. (4-15), one should keep in mind the limitations of the model associated to several hypotheses that have been considered:

- We first assumed that the ToF can be expressed with an equation form equivalent to eq. (4-6). This is based on the fact that the surface atomic diffusion can be activated either by temperature and/or Joule effect in order to trigger the nanowires morphology change (from wire shape to spheres, i.e. from percolating to non-percolating AgNW networks), while the associated driving force is the reduction of the total surface energy.
- We considered that AgNW networks are homogeneous (identical amd everywhere in the network), leading to a I - j relation which resembles the approaches considered in the framework of mean field theory. According to this, in a stochastic model, the effect of all other entities on any given entity is approximated by a single averaged effect. Thus, a many-body problem reduces to a one-body problem.
- We assumed that all AgNWs in the network have identical diameter, and therefore identical electrical resistivity ρ^{el} since the latter depends upon AgNW diameter (chapter 1.2.3),²⁴¹ in our case $\rho^{el} = 1.985 \times 10^{-6}$ Ohm.cm for D_{NW} equal to 70 nm. However, we do know that any AgNW solution (and then network) does have a diameter distribution.^{38,213} Larger diameter distributions can affect the ToF , since thinner nanowires fail sooner.¹⁶³

Therefore, the model proposed here aims to give only the main tendencies in terms of dependence of the time of failure of AgNW networks with temperature, current density and areal mass density. It aims as well to predict, in a first approximation, which is the main mechanism responsible to AgNW network degradation. This can be helpful to disentangle the electrical from the thermal mechanism of failure. However as exposed just above there are several hypotheses which make this model a semi-empirical model.

The results of the modelling are presented in Figure 4-8, in an current density-applied temperature diagram where the rainbow color map corresponds to the range of the ToF (in log scale). The values of ToF were calculated for an average R equal to 13.7 ohms, associated to amd equal to 81.6 mg.m⁻². Concerning the fitting parameters, the activation energy E , which can be extracted when no current is applied by using an Arrhenius plot, i.e. $\log (ToF)$ vs $(1/T)$ as previously demonstrated for the experimental results of $T-I$ experiment. Its value in the model is equal to (1.1 ± 0.1) eV, which is in a close range to the ones observed during previous thermal annealing experiments, i.e. from 0.3 to 1 eV.²⁴⁴ In addition, the model provides the parameter C equal to $(1.97 \pm 0.1) \times 10^{-14}$ K.A⁻².m⁶.kg⁻¹, thus, the heat constant α can be calculated as (96 ± 4.8) W.m⁻².K⁻¹ from eq. (4-14). This value is in the same range with other metallic nanostructures, graphene or carbon nanotubes, i.e. from 15 to 123 W.m⁻².K⁻¹, as summarized by Sorel et al.¹¹⁴

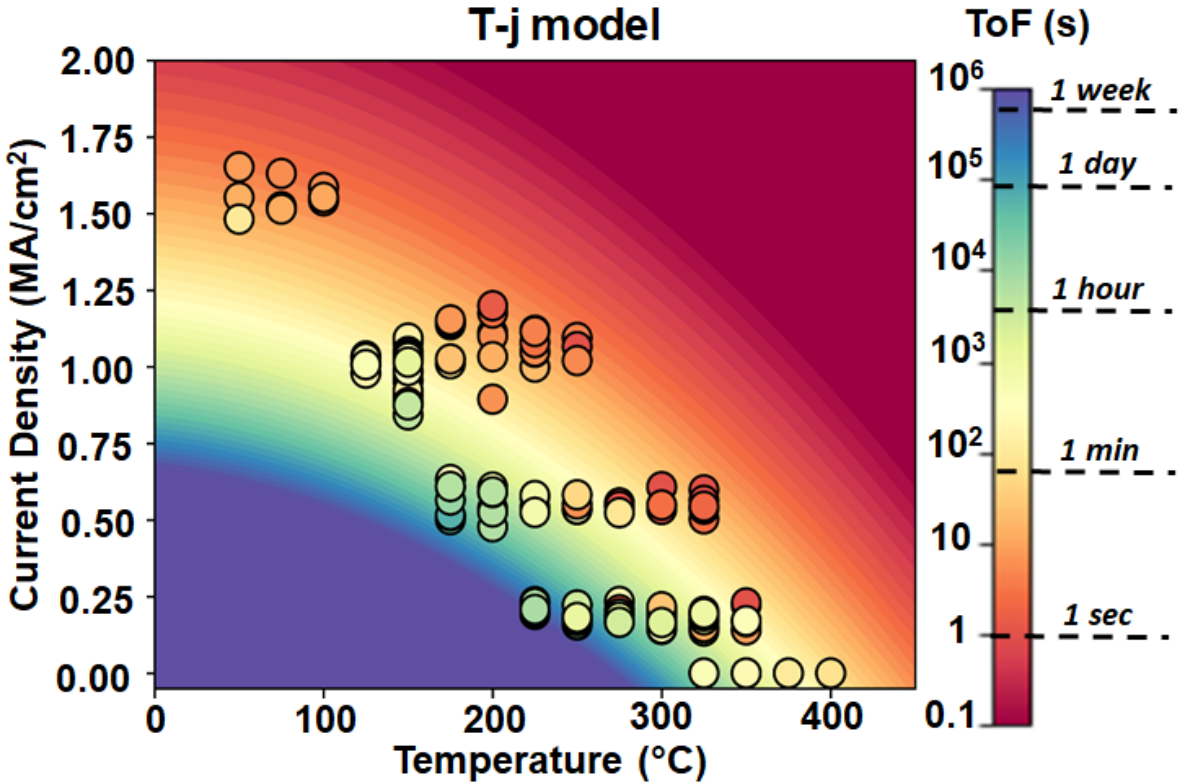


Figure 4-8: T-j model: Current Density-Temperature diagram showing both calculated and experimental values of the time of failure (ToF) for AgNW networks. The color map represents the calculated Time of Failure and duration examples are noted in the rainbow scale, i.e. 1 second, 1 minute, 1 hour etc. The small circles correspond to experimental T-I couples and their inside color corresponds to the experimentally measured ToF .

Among the three parameters already discussed, the parameter B can also be estimated as $(5.47 \pm 0.1) \times 10^{-8}$ s. Concerning this obtained value, starting from eq.(4-5) and (4-6), B is equal to the square of the characteristic distance, L_{therm} , divided by 2 times D_0 , where D_0 is the pre-factor of the diffusion coefficient. L_{therm} was considered as the characteristic distance over which the atomic diffusion operates to induce the degradation of the AgNW network, which means the diffusion required for the morphological instability of AgNWs. For the sake of simplicity one can consider for L_{therm} the wavelength of the perturbations of a cylinder that generates Plateau-Rayleigh instability of a cylinder of radius R : $2\pi R$.²⁴⁵ Therefore, B can be estimated as:

$$B = \frac{\pi^2 D_{NW}^2}{2D_0} \quad (4-16)$$

Since we know B and D_{NW} (70 nm) one can estimate the value for the pre-factor D_0 . Its value is: 4.4×10^{-7} m²/s. Such value has to be discussed. The simplest way to consider the pre-factor diffusion D_0 is to compare it with its simplest expression, which is $v \cdot d^2/4$, where v is the attempt frequency for atoms diffusion, considered as 10^{13} s⁻¹ for silver,²⁴⁶ and d is the minimum distance between atoms on the (100) surface, $d = \frac{a}{\sqrt{2}}$, where a is the silver lattice parameter, equal to 0.409 nm. Such a simple calculation leads to the value of 2.1×10^{-7} m²/s which is of the same order of magnitude than the one obtained above. A more precise way for the comparison is to consider the pre-factor diffusion associated to the atomic surface diffusion on silver (100) crystallographic planes which was estimated, for large surfaces, by Jamnig et al. as 3.7×10^{-7} m²/s.²⁴⁶ Although the geometry is very different between silver bulk planar (100) surfaces and the surfaces of AgNWs, these two values are rather close. This way, the calculated value of B can be explained.

For the sake of comparison, the T - j experimental data are presented also with the small circles, and we can observe that the model offers a good first approximation to the experimental measurements. At first glance, 3 different regimes are revealed by the model. The first two concern extreme cases with either instant or very long time of failure, represented by the red and blue regions respectively. In the first case, the thermal and electrical stress have both high values, i.e. in a range of 250-400 °C and 0.75-2 MA/cm², respectively, corresponding to the “high stress” region that is schematically presented in Figure 4-5. On the other hand, when the stress is moderate (blue region), i.e. current density below 0.75 MA/cm² and temperature below 250 °C, it can take several days for the degradation of the AgNW networks to degrade. Between the two extremes, there is a rainbow region, with a continuous increase of the ToF , with an entangled contribution of both electrical and thermal stress. However, this is less prominent for

temperatures below 100 °C, where the increase of $\log(ToF)$ seems independent of the thermal stress but almost linear to the electrical one. Above this temperature threshold, it becomes harder to distinguish which mechanism of failure is dominant. In any way, the degradation of the AgNW network is thermally activated from both the high applied temperatures and the Joule heating. Other studies concerning the current flow, usually attribute the failure not only to Joule heating but also to electromigration, inspired by microelectronics and the Black's median time to failure for semiconductor circuits.^{247,248} However, the scale of the macroscopic physical approach related to AgNW networks is different from the scale of individual nanowires, and therefore a direct comparison is not trivial.²⁴⁹ Indeed, it is very tricky to prove that the dominant mechanism for the morphological instabilities is the electromigration, in large scale, dense, randomly oriented AgNW networks. Even when the data fit with the Black's equation it is usually the case for low bias and temperatures.²⁴⁷ In our case, we observed by experiments and simulation that the degradation is mainly driven by thermally induced morphological instabilities, either directly related to high imposed temperatures (Plateau-Rayleigh) or indirectly by the power-induced heating (local high current density). Using this approach, we combined the electrical and thermal contribution to the thermally activated atomic diffusion in order to calculate the ToF . Thanks to its rather good agreement with experimental values (as shown by Figure 4-8), the proposed model can be used to estimate the lifetime of a device where AgNW networks are used if significant electrical or thermal stress are being used.

4.3. Conclusions and prospects

The stability under electrical and thermal stress is a crucial parameter for the performance and integration of AgNW networks. Thus, in the present chapter we explored the failure of the networks by experimental and simulation approaches. The electrical measurements during a voltage ramp, combined with the recording of the spatial distribution of the temperature by IR imaging, offered significant results about the mechanisms of failure under electrical stress. The principal observation is that the network degradation originates from a randomly localized elevated Joule-heating, which consequently leads to the local degradation of the sample. This localized damage propagates as a domino effect within the network, leaving behind a very thin, vertical region like a crack where the percolation paths of the network are not active anymore. To further study and understand the origin of failure, we used electrical and thermal simulations. The model verified that regions with small defects can be the source of such hotspots, therefore inducing the electrical degradation of the whole specimen. This occurs since a microscopic

defect induces a large local increase of the current density values along very short distance (about one micron). Consequently, these simulations show also that the Joule heating in the edge of defects is much more significant than for the rest of the specimen, and thus it represents a plausible origin of a hotspot, as those experimentally observed. Such deeper explanation of the AgNW network degradation is a necessary step to overcome instability issues in order to successfully integrate such transparent electrodes into industrial devices. The stability enhancement can be achieved by oxide thin films, used to block atomic diffusion and prevent the degradation caused by overheating. The investigation of such protective layers, as well as a further study of the non-homogeneities on AgNW networks, is another significant part of my PhD thesis, presented in the chapter 5 that follows.

Furthermore, to better understand as well as predict AgNW network instability, we considered useful to build a model that predicts the time of failure, for given conditions of temperature and/or electrical bias, and if possible for different nanowires dimensions and network densities, to which we can associate a given electrical resistance. This objective led us to the T - I (temperature-current) experiment during which we measured the time of failure (ToF), meaning the time from the beginning of a thermal and electrical load until the electrical failure of the network (i.e. associated to the divergence of the electrical resistance). We have explored what occurs experimentally when these two stresses are applied, thus the aim was to understand better how the sample fails when controlling both temperature and current. The experiment was conducted over 200 samples, with various initial electrical resistances and applied temperature and current values. Consequently, we achieved a statistically sufficient amount of data and we could extract the prevailing tendencies for both thermal and electrical stresses. Therefore, we proposed a semi-empirical model in order to compare the experimental and calculated data in phase diagram j - T in order to predict the ToF . Three main regions are depicted in this phase diagram; two extreme cases of high and moderate stress, and a region where both thermal and electrical stress are considerable. In the extreme cases, the failure can be either ultra-fast or take several days, while in the intermediate cases it is rather hard to distinguish which stress is the prevailing failure mechanism. In addition, for low temperatures below 100 °C, the ToF seems mostly dependent from the electrical than thermal stress and the decrease of $\log(ToF)$ with the inverse of the squared current density, is now more prominent, according to eq. (4-15). The electrical pathways of the network are damaged by the morphological instabilities of the nanowires as soon as the atomic diffusion is activated. This can be driven by mechanisms purely thermally induced (Plateau-Rayleigh) or purely electrically induced (local high current density).

Thus, our approach to the model was to consider that the temperature used in the diffusion activated term can be equal to the applied temperature plus the increase of temperature included by the power-induced Joule heating. This simple semi-empirical model offers a rather good first approximation to the experimental results and it provides useful information about the limitations of the AgNW networks for the industrial implementation as TE. However, further data are needed in order to make a more reliable fitting of the physical parameters, and understand better the physics of the term that is related to the purely electrical impact on network failure. Extra measurements of moderate temperature-current couples could help in this direction, and the IR imaging during such measurements could be helpful to investigate the dominant mechanism of failure. This could also be combined with a study of the proportion of the spheroidised nanowires as a function of the $T-I$ couples, with the help of SEM images and a software like *ImageJ*. Finally, the whole $T-I$ experiment could be repeated for composites of AgNW networks coated with oxide thin film, in order to study the impact of the oxides on the AgNW performance and build an equivalent model to predict the ToF of the composites.

πάντα χωρεῖ καὶ οὐδὲν μένει

Ἡράκλειτος

« Everything flows and nothing stays still »

Heraclitus (535 – 475 BC)

Chapter 5

**5. Non-homogeneity on silver nanowire networks:
investigation of their effects thanks to experiments and simulations.
Stability enhancement by oxide coatings.**

As demonstrated in the previous chapters, despite their highly promising properties, AgNW networks present instabilities under electrical and thermal stress that lead to the degradation of their electrical conductivity. This is still the main challenge to tackle for their successful integration into devices, with the electrical stability being crucial. In Chapter 4, we explored the degradation mechanism in AgNW networks, focusing on the formation of hot spots at a very local scale and its destructive propagation through the network. Simulations confirmed the correlation of initial defects with the origin of failure, as it was also observed experimentally. The occurrence of zones with different current density, followed by a locally elevated power-induced Joule heating, is the key parameter for these instabilities. Therefore, we decided to go a step further and investigate the effect of non-homogeneity in a more macroscopic way, always combining experimental and simulation approaches. In this chapter, we investigate different patterns of AgNW networks by one-probe electrical mapping and IR imaging, and we compare the results with simulations of electrical and thermal distribution by physical modelling. In addition, we study the influence of zinc oxide (ZnO) coatings on the electrical distribution and the performance enhancement of non-homogeneous specimens. The present chapter is highly inspired by the article entitled “*Effects of non-homogeneity and oxide coating on silver nanowire networks under electrical stress: comparison between experimental and modeling approaches*” by the following authors: D.T. Papanastasiou, N. Charvin, J. Résende, V. H. Nguyen, A. Sekkat, D. Muñoz-Rojas, C. Jiménez, L. Flandin and D. Bellet, and which is submitted. This work has been performed in the framework of the collaboration between LMGP and LEPMI-Bourget du Lac through the project EARTH funded by CEMAM. Vladimir Tsukanov, who I co-supervised (M2 internship 2019), contributed also to the simulations developed by COMSOL Multiphysics®. The ZnO coatings were deposited by AP-SALD by Dr. Viet H. Nguyen (PhD thesis 2015-18, Post-Doc 2019) and Abderrahime Sekkat (on-going PhD thesis since 2018), and the masks used to generate the different patterns were 3D-printed by Dr. César A. Masse de la Huerta (PhD thesis 2016-19).

5.1. Materials fabrication and experimental characterization.

AgNW solution was provided by the research team of Dr. Jean-Pierre Simonato from CEALITEN, synthesized according to the process developed by Mayousse et al.²¹³ The AgNWs present an average diameter of 70 ± 10 nm and an average length of 8 ± 3 μm being dispersed in methanol with initial concentration of 3.1 g/kg and diluted afterwards 30 times to obtain a concentration of 0.1 g/L. For the deposition of the nanowires we used spray deposition with our homemade airbrush set-up. For the sake of reproducibility, during each AgNW spray deposition, the resistance was measured *in situ* with the resistance monitor. Corning glass 1737 1.1 mm in thickness, and cut in squares of 25×25 mm², was used as substrate. Three different specimen geometries are used throughout the present work, as shown in **Figure 5-1a**; i) a reference group related to homogenous networks (Hom), and two non-homogeneous networks with ii) either AgNW-free triangles, called empty triangles (ET) or iii) triangles with denser AgNW density than the rest of the specimen, called denser triangles (DT).

Non-homogeneous specimens were fabricated thanks to the use of masks with triangle shapes; two types of masks were printed using the *Formlabs* “Form 2” 3D printer with the *Clear* resin, and their designs are presented in **Figure 5-1b**. For each type of network geometry, both bare AgNW and 30 ± 5 nm thick ZnO coated AgNW were studied. ZnO thin films were deposited with the AP-SALD home-made system of LMGP.^{33,250} **Figure 5-1c** presents a SEM image of a bare, spray-deposited AgNW network. The TEM image of **Figure 5-1d** shows the conformal ZnO film coating on the AgNW. Finally, all six types of specimen (three geometries, each one with either bare or coated AgNW) exhibit resistance from 10.2 to 27.6 Ω and average *amd* for the AgNW network of 114 ± 4 mg/m². The triangular areas are either free of AgNWs or presenting a higher *amd* value (134 mg/m²), compared to the rest of the network. The trend observed in each one of the deposited series, is that the non-homogeneous samples show higher resistance than the homogeneous case, with the one having ET showing the highest value, meaning $R_{Hom} < R_{DT} < R_{ET}$. In addition, the presence of the ZnO coating is beneficial for the electrical conduction and for example there is a reduction in the electrical resistance from 20.7 to 15.9 Ω in the case of bare and ZnO coated homogeneous AgNW network, respectively. **Figure 5-2a** represents the total and diffuse transmission for a bare and a ZnO coated AgNW network. There is a minor influence of the oxide coating on the optical transmittance mainly in the UV range due to the band gap of ZnO and the absorption from the ZnO coated free spaces between AgNWs, but the AgNW/ZnO maintain very high transmittance; the average of total transmittance decreases from 83.3 % to 82.1 %, for bare and coated network. Similarly, the

coated network becomes slightly more diffuse, with the average diffuse transmittance increasing from 10.7% to 11.2 %.

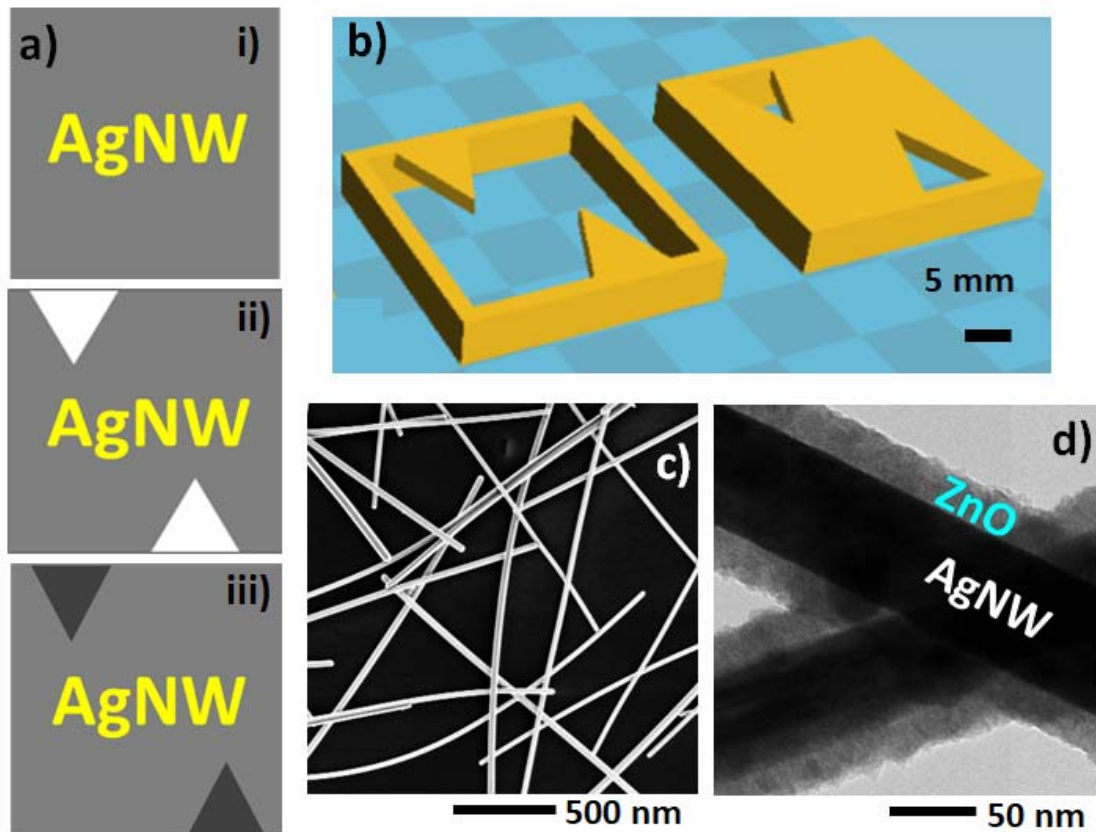


Figure 5-1: a) Schematic representation of the 25*25 mm² fabricated AgNW networks, for which the grey color is associated to the same AgNW density: i) homogenous density of AgNW on the whole glass substrate, ii) empty triangles (ET) case: specimen without AgNW in the top-left and bottom-right triangles (white color), iii) denser triangles (DT) case: specimen with larger AgNW density in the triangles (dark gray color). b) Design of the 3D printed masks for the fabrication of non-homogeneous spray-deposited AgNW networks. The left mask is used for transparent electrodes with absence of AgNW on the triangle regions (empty triangles, named ET). The right one is used to mask the sample except the triangle regions so that these triangles become more conductive (denser triangles, named DT). c) SEM image of a bare AgNW network. d) TEM image of AgNW coated with a conformal layer of ZnO deposited by SALD.

Two main experimental techniques were used in this study: one-probe (1P) mapping of the electrical distribution, and the measurement of the evolution of electrical resistance during a voltage ramp of 0.5 V/min with a parallel recording of the surface temperature by IR imaging. The combination of such electrical and thermal analyses contributes to a deeper understanding of the dynamics of failure. These techniques were used to investigate the effects on the main properties of the two following features: the non-homogeneity of AgNW networks and the oxide coating. Figure 5-2b shows a schematic representation of the experimental 1P-mapping

set-up, which measures point by point the electrical potential. The left contact of the measured specimen was connected to the ground, while an electric potential of 1 V was applied to the right one. The probe is positioned on periodically distributed locations on the AgNW network, monitored by a LabVIEW software, and each time its tip touches the network, the local electric potential is measured. A distance between the measured points (step size) of 1 mm was chosen. Thus, when plotting the values of each local measurement, an electrical map is obtained, such as the ones discussed in section 5.2, enabling to detect any spatial variations of the electrical distribution. IR imagery has already been proved in our previous work to suit well for the detection of defects, such as the presence of resistive hotspots and their associated propagation observed during the electrical breakdown of AgNW networks.³² A classical 2-probe set-up in the edge of the specimen, using metallic forceps, was used to apply the voltage by means of a Keithley 2602 source-measure-unit during the voltage ramps. In parallel, the surface temperature spatial distribution of the specimens during the voltage ramp was measured by a FLIR A320G IR camera. More detailed information about the spray deposition of AgNW networks and the characterization techniques are provided in Chapter 3.

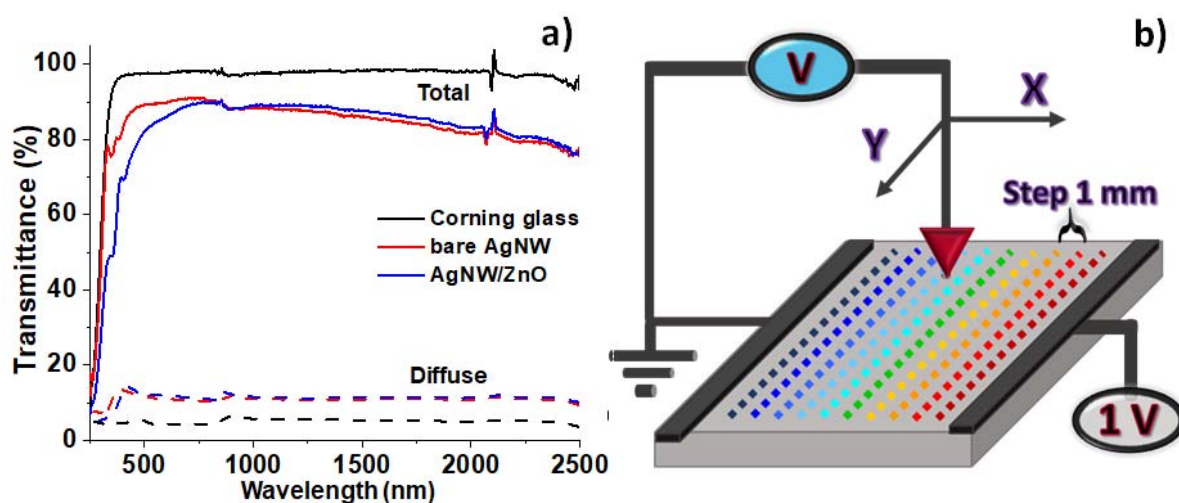


Figure 5-2: a) Total and diffuse optical transmittance, plotted respectively with straight and dashed lines, for bare and ZnO coated AgNW network, of the same AgNW deposition series. The transmittance of the Corning glass substrate is plotted in black. b) Schematic representation of the one-probe (1P) mapping: the left silver-paste contact of the specimen is connected to the ground, while a 1 V bias between opposite electrodes is applied. A tip automatically moves above the studied specimen and touches it point by point to measure the local electric potential. A distance between the measured points (step size) of 1 mm was chosen.

5.2. Bare AgNW network and non-homogeneity.

Firstly, we focus on bare AgNW networks through experiments and simulations, starting with the 1P-mapping results that are presented in **Figure 5-3a-c** for bare networks. In the homogenous case the equipotential lines are almost parallel to the left and right electrodes, as theoretically expected. On the contrary, the tortuosity of the equipotential lines increases for the non-homogeneous cases.

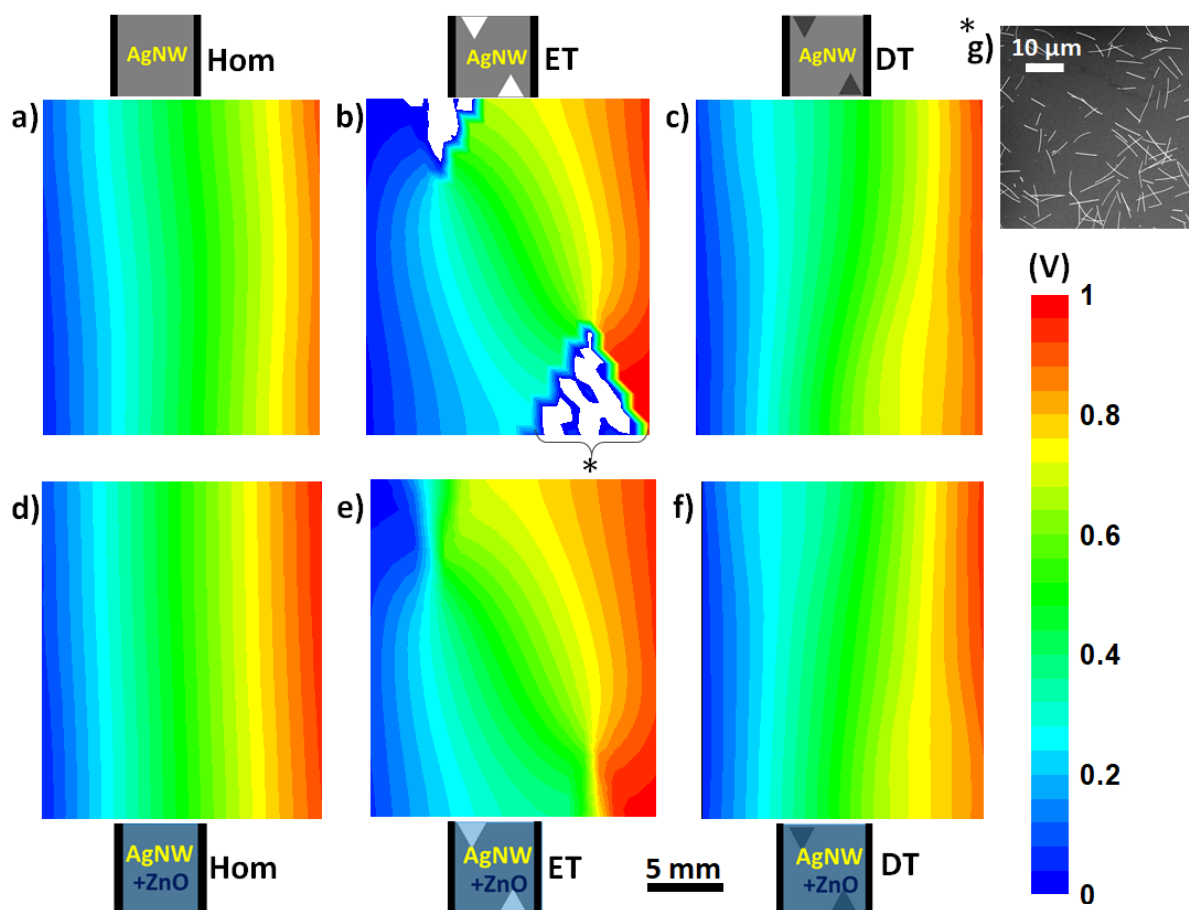


Figure 5-3: Experimental one-probe electrical maps associated to six types of AgNW networks with 1 V bias applied between parallel silver-paste vertical electrodes. Bare AgNW networks are shown on the top row (a-c) and AgNW networks coated with 30 nm thick ZnO layer on the bottom row (d-f). Left column is associated to homogeneous AgNW networks (Hom) (a,d), middle column is associated to empty triangles (ET), (b,e) and right column to denser triangles (DT) (c,f). The non-homogenous deposition of AgNW networks has a direct impact on the tortuosity of equipotential lines. However, the ZnO coating has a beneficial effect in every network configuration, by smoothing the electrical potential distribution. g) SEM image of a specimen of AgNW/ZnO network showing an unexpected presence of nanowires in the (supposedly empty) triangular region that was masked during the AgNW deposition.

The largest deviation from the vertical equipotential lines, reaching a 30° inclination, can be observed close to the empty triangles. While, contrary to our expectations, there are still conductive areas in the triangular regions for this specimen as one can see from the blue points inside the triangles. SEM imaging in Figure 5-3g confirmed a sporadic presence of nanowires in these regions, due to an imperfect protection from the mask. Concerning the third configuration of AgNW network fabrication in this study, the presence of denser triangles leads to 5 to 10° deviation from the vertical alignment, which is smaller compared to the ET case.

Figure 5-4a-c reports the evolution of electrical resistance of these types of specimen under an electrical stress ramp. For bare AgNW networks, the degradation for the non-homogeneous cases appears at different voltage values: from 12.8 V for the homogeneous, to 11.2 and 11 V for the ET and DT, respectively. In the beginning of the voltage ramp, V increases slowly and then follows a steep increase in some seconds reaching $M\Omega$ or even $G\Omega$ during the degradation. After 3-4 minutes V decreases to some $k\Omega$ and stays stable around these value until 15 V, moment in which the voltage ramp is stopped. In Figure 5-4 the evolution of maximum temperature is also plotted, as depicted from the IR sequences. The highest values achieved are 207-211 °C, followed by a decrease that is similar to the cooling down of a metallic component when no voltage bias is applied. Although the voltage ramp is always applied, there is no Joule heating for 3-4 minutes since the conductivity is lost and almost no current flows through the sample. This drop of temperature is interrupted around 40-50 °C, when the resistance falls back to $k\Omega$ range. Then finally the temperature exhibits a small increase and remains around 60 °C until the end of the voltage ramp.

In parallel, the IR sequences offer interesting information related to the spatial distribution of the temperature in the homogeneous and non-homogeneous cases, and the phenomena that occur during the electrical stress/voltage ramp can be discussed as follows:

i/ Before degradation, the homogeneous sample heats more in the center while for the non-homogeneous cases the high temperatures are observed: a) for the ET, close to the triangle edges and between them, diagonally at the center of the specimen, b) for DT, outside, left and right, close to the triangles. If one compares these last two thermal mappings with the 1P-electrical mapping in Figure 5-3b-c, there is a clear direct relation between them. The local denser equipotential lines correspond to local higher heating exactly for similar regions. It is also worth noting that the difference in temperature between hotter and colder regions (on the same

sample) varies, being more important for both non-homogeneous cases (60 °C of difference) compared for the homogeneous one (45 °C).

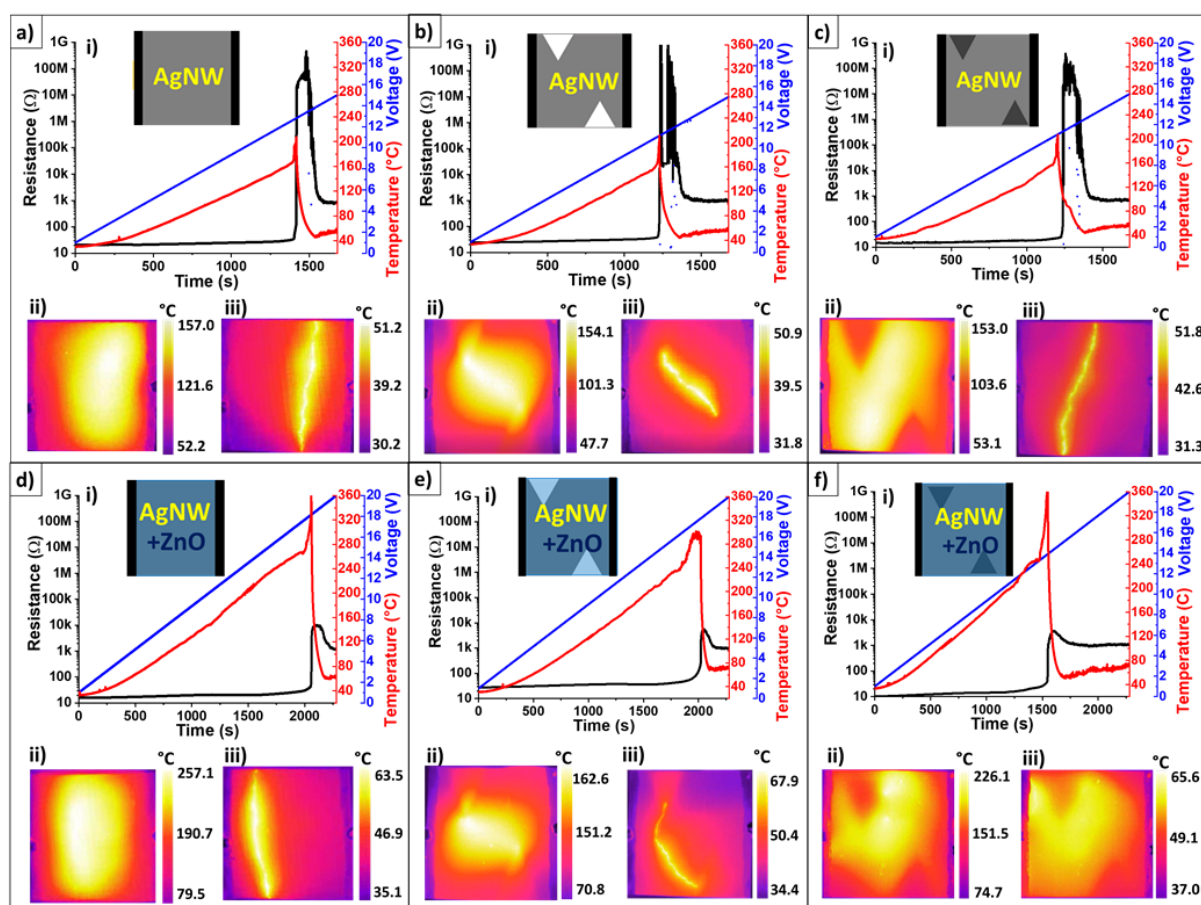


Figure 5-4: Electrical resistance (black), voltage (blue) and maximum surface temperature (the latter being measured from IR imaging and represented in red) during the voltage ramp of 0.5 V/min applied to: a-c) bare AgNW networks and d-f) 30 nm ZnO coated AgNW networks. For each network configuration the associated schemas are shown (homogeneous, empty triangles and denser triangles, respectively from left to right). In each case the IR pictures on the left (ii) were taken just before the propagation of network failure, while the ones on the right (iii) were taken after the degradation when the resistance had dropped at some kΩ. The size of all specimens is 25*25 mm².

ii/ During the degradation, some hotspots appear locally along very narrow regions tens of microns wide; these same regions will contain hotspots after degradation too, giving the impression of a thermal crack in the IR sequences. This narrow line is visible also in SEM, as shown in **Figure 5-5a**, with the charging contrast effects helping to distinguish the damaged nanowires (bright/white nanowires) from the rest of the intact network (dark/black nanowires). This voltage contrast has been recently reported to distinguish the non-conducting AgNW networks by Suemori et al.²⁵¹ The homogeneous case presents this crack more or less in the middle of the sample parallel to the silver paste contacts: this can be understood since the

network's borders experience larger thermal losses than the center, and therefore, are the colder regions of the specimen. The hotspots for the ET case propagate between the edges of the triangles while for the DT case the hotspots are close to the sides of the triangles, along the diagonal, at regions where the local electric field is larger, as shown by 1-P mapping in Figure 5-3b-c.

iii/ Concerning the spatial distribution of temperature after degradation, the crack continues to have a higher temperature compared with the rest of the sample. This is due to the presence of new conductive paths where the local degradation of nanowires occurred, as verified from SEM images (Figure 5-5b-c), which increases the resistivity locally.

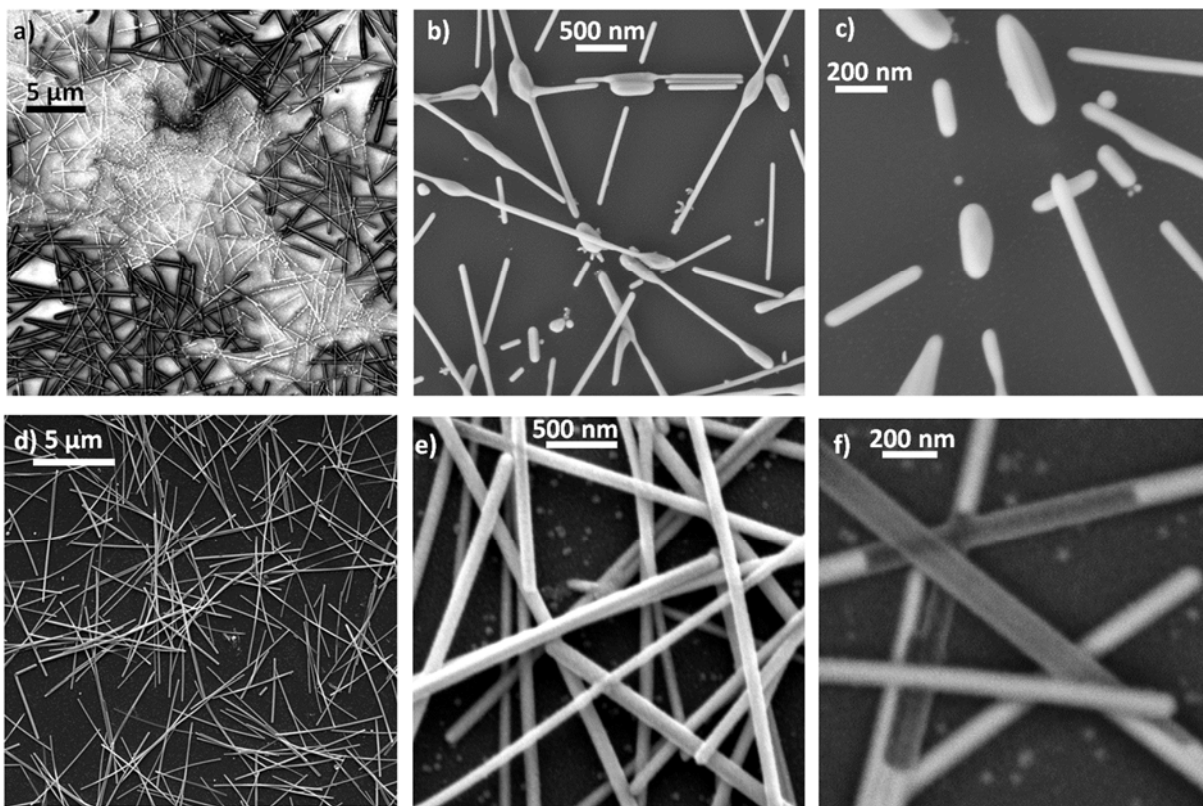


Figure 5-5: SEM images after the electrical stress with a voltage ramp of 0.5 V/min for a-c) bare AgNW and d-f) ZnO coated networks. a, d, e) The great majority of the silver nanowires remain intact after the electrical degradation. However, in the region at the vicinity of the hotspots (thermal crack) there is a very thin and elongated zone with severely damaged nanowires. b, c) the bare AgNW are partially destroyed and f) in the case of coated networks, while atomic diffusion of Ag has also occurred in this case, the shell of ZnO around the AgNWs appears intact.

Another parameter that is important to investigate to better understand the mechanisms of failure is the maximum power, P_{\max} that can flow to the network. For a given voltage, the power for the three network configurations follows the inverse trend compared to the electrical resistance; which means that from higher to lower initial resistance, the P_{\max} is inversely,

ET<Hom<DT, 3.3-5-5.5 W. However, between the ET and DT, the different P_{\max} (3.3 and 5.5 W) corresponds to the same temperature, 154 and 153 °C, while the voltage values are similar (10.5 and 10.8 V), and the ET shows higher resistance at that moment, 35.5 Ω , compared with 20.1 Ω for the DT. Therefore, the ET configuration can be interesting to obtain high local heating at a lower power applied.

Furthermore, concerning the degradation, **Figure 5-6** shows in details the evolution of resistance, temperature and power, instead of voltage, for the different samples, starting from the maximum power observed until the increase of resistance and/or its drop to k Ω range. Throughout the applied voltage ramp, the surface temperature of the AgNW network increases in a linear way (except a short delay during the 1-2 initial minutes), until the moment degradation starts. The resistance follows a slight increase, less than 50% higher than the initial values just before degradation for all cases. Then, during degradation, the temperature increases much faster, followed by a stiff increase of the electrical resistance to non-conductive values. The power time dependence shows that the quick increase of temperature occurs after the maximum of power is reached. This observation combined with the IR sequences suggest that at a certain electrical stress, the Joule heating in specific points becomes too significant and leads to a local degradation of the network. At the nanoscale, this is associated with the fact that above a given Joule heating power, AgNW undergo a morphological instability. At the macroscopic view, this damage represented by the hotspots, propagates to the rest of the sample, resulting in a generalized increase of the electrical resistance since conductive pathways between both sides of the thermal crack are not efficient anymore. Comparing the position of the hotspots with the electrical distribution, there is a clear dependence on the non-homogeneity of the AgNWs distribution shown by these electrical 1P mappings (Figure 5-3a-c) and the appearance of regions with excess heating revealed by IR imaging (Figure 5-4a-c, ii-IR photos before degradation).

Concerning the dynamics of the crack propagation, it is different for the three different configurations of the bare AgNW electrodes. Figure 5-6a-c indicate that the electrical resistance and power exhibit maximum values in a different timing for each one (see the dashed arrows eye guides). For instance, P_{\max} does not occur at the same voltage, thus time, for the three cases: at 12.1 V for Hom, 10.8 V for ET and 10.5 V for the DT case. Moreover, once the maximum power has been reached, the duration, before the temperature itself exhibits a maximum value, depends upon the configuration: 80 s, 47 s and 63 s, for Hom, ET and DT, respectively. The fastest appears for ET; this stems from the position of the two hotspots in the triangle pointy

edges and the close distance between them, locally leading to larger electrical stress. Concerning the increase of temperature and resistance, for the homogeneous case these two parameters rise simultaneously, after P_{\max} . In the non-homogeneous cases, the increase of temperature and resistance are clearly separated: 7 s for ET and 34 s for DT. In order to explain these time differences, a closer look needs to be taken. In particular, for the ET case, the rise of temperature takes place just a few seconds after a resistance steep rise takes place, with hotspots forming from the edges of the triangles, and the whole middle of the sample showing an excess heating. But in parallel, no current can flow through the top and bottom fractions of the network, including the empty triangles. The DT case is particular because the temperature rises and falls while the power remains in its maximum plateau and the resistance has not reached its maximum yet. This means that the local degradation does not affect the whole sample at the exact same time. Indeed, from the beginning of the voltage ramp, the denser triangle areas heat less than the regions beside them (top right and bottom left). The hotspots propagate diagonally between these two regions while the top and bottom fractions of the sample are 80 °C colder and the current can still flow through these bands until the thermal crack splits completely the network.

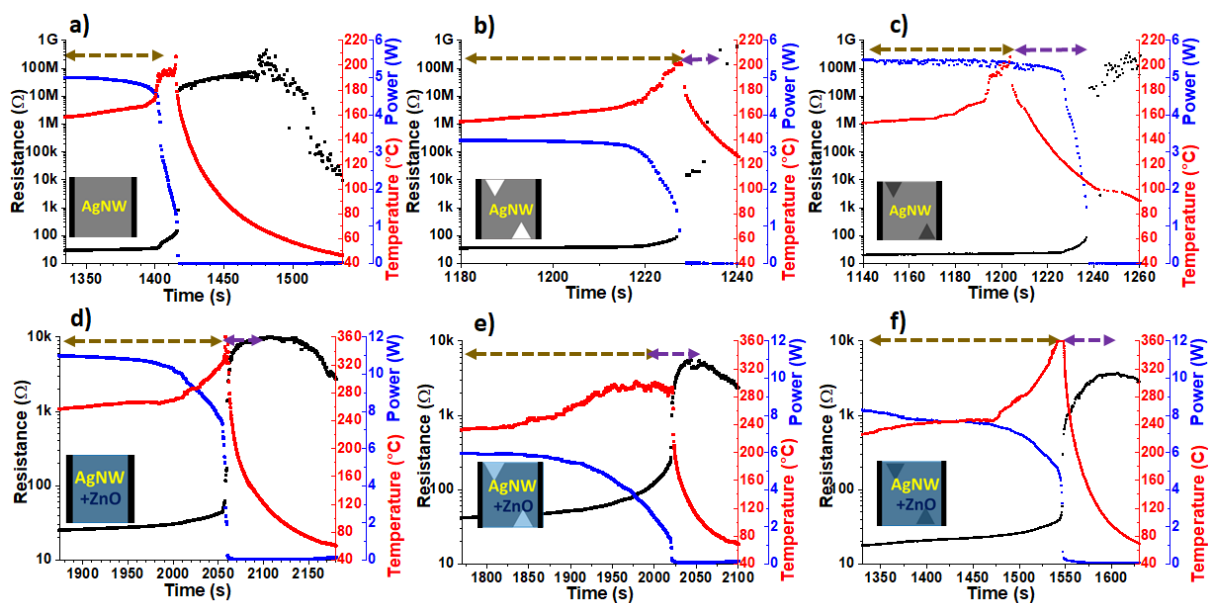


Figure 5-6: Electrical resistance, power and maximum surface temperature (extracted from IR imaging) during the voltage ramp of 0.5 V/min applied to: a-c) bare AgNW networks and d-f) 30 nm ZnO coated AgNW networks, for the three configurations shown in the inset schemas (Hom, ET and DT). The size of all specimens is 25*25 mm². For each case, the plots start when the power is maximum, while the dashed arrows indicate the duration between a) maximum power and maximum temperature (ochre/brown line) and b) maximum temperature and maximum resistance (purple line).

5.3. Simulations of electrical and thermal distribution.

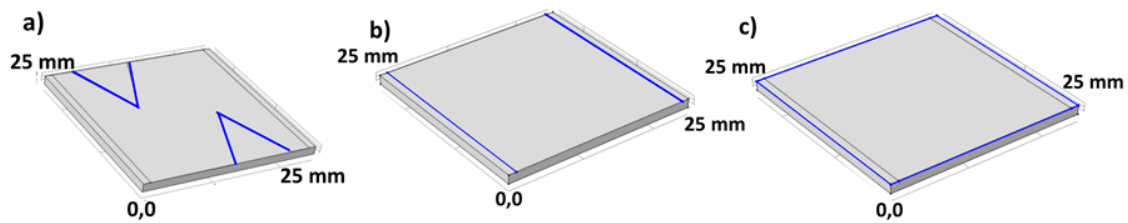
The simulations of the electric model and Joule heating offer a fair comparison between: i/ the electric potential distribution obtained by the model and the experimental ones measured by 1P-mapping, and ii/ the surface temperature distributions obtained by the model and the IR camera. We use the Ag film approximation in COMSOL, as discussed in Chapter 3, coupling both electrical and thermal models and thus calculating the spatial distributions of the electric potential, current density and surface temperature. Ag films of 0.79 nm thickness on top of Corning glass are simulated to represent the AgNW networks. The size of the simulated specimens is the same as the experimentally fabricated ones (25*25 mm²) as well as the glass substrate size (25*25*1.1 mm³). In the case of ET, Ag is removed from the inside of the triangles, while for the DT the Ag conductivity is varied between the inside of the triangles and the rest of the specimen. The geometry is presented in **Figure 5-7a**. A work plane is added, where rectangular 1 mm wide contacts are added on the left and right sides with the appropriate electric boundary conditions, as presented in Figure 5-7b-c. The version of COMSOL used allows the simulation of a single shell, thus the same thickness is applied in all cases in order to get a sheet resistance of 20 Ω/sq.

Concerning the conductivity of the Ag layer, the standard bulk Ag value $\sigma=63*10^6$ S/m is used in the case of Hom and the ET. The same conductivity is applied in the third case for the DT, while $50*10^6$ S/m is approximately applied in the rest/middle of the sample (less conductive experimentally). In order to perform thermal simulations, three main mechanisms of heat losses must be taken into account: convection, conduction, and radiation. Considering the temperature is uniform across the sample and neglecting the conduction losses to external parts of the system (for instance through the connecting wires), one can write the energy balance:¹¹⁴

$$I^2R = (m_1C_1 + m_2C_2) \frac{dT(t)}{dt} + A(h_1 + h_2)(T(t) - T_0) + \sigma A(\varepsilon_1 + \varepsilon_2)(T(t)^4 - T_0^4) \quad (1)$$

where the subscripts 1 and 2 denote respectively the Ag thin film and the substrate, I is the electric current, R is the resistance of the film, A is the substrate area, σ is the Stefan – Boltzmann constant, m is the mass, C is the specific heat capacity, h is the convective heat transfer coefficient, and ε is the emissivity of the sides of the samples. $T(t)$ denotes instant temperature of the sample, and the ambient temperature T_0 used in the model is 20 °C. From equation (1) one can see that the heat generated by the Joule effect (the left term) is dissipated through the temperature elevation in the conductive film and the substrate (first term on the right), the heat losses by convection (second term) and radiation (third term). In the model, the

two layers are not physically separated so the conduction between them is considered ideal and any external conduction losses are neglected. To consider the radiation losses, the emissivity of both Corning glass and Ag are considered (given in Figure 5.7d). To consider the convection losses, the following range values of convective heat transfer coefficient has been reported in the literature for nanostructured or metallic films: $h= 8-92 \text{ W}/(\text{m}^2\cdot\text{K})$.¹¹⁴ In the present work values of $h= 10 \text{ W}/(\text{m}^2\cdot\text{K})$ and $h= 50 \text{ W}/(\text{m}^2\cdot\text{K})$ are applied for the glass substrate and for the silver layer, respectively. For the DT case, an $h=40 \text{ W}/(\text{m}^2\cdot\text{K})$ is used for the less dense/conductive part in the middle of the DT. All the details of each material properties such as electrical and thermal conductivity, emissivity and heat transfer coefficients are listed in the table of Figure 5-7d .



d)	Material	Corning glass	Thin Ag film
	Thermal conductivity $k, \frac{W}{m\cdot K}$	0.91	429
	Electrical conductivity $\sigma, S/m$	10^{-14}	$63 \cdot 10^6$
	Heat capacity at constant pressure $C_p, J/(kg \cdot K)$	707.6	235
	Density $\rho, kg/m^3$	2540	10490
	Coefficient of thermal expansion $\alpha, 1/K$	$4.2 \cdot 10^{-7}$	$18.9 \cdot 10^{-6}$
	Emissivity ε	0.92	0.02
	Heat transfer coefficient $h, W/(m^2K)$	10	50

Figure 5-7: a) Geometry of the physical simulations in COMSOL for a thin Ag layer on top of Corning glass substrate with the presence of the two diagonally aligned triangles, which are either empty or denser/ more conductive than the rest of the film. b) Boundary conditions of the electric model (blue lines): the left contact is connected to the ground and the right to the applied bias (1 V etc) c) Boundary conditions (blue lines) of the electrical insulation on the sides of the Ag thin film. d) Physical parameters for Corning glass and silver thin film. The Corning glass substrate is 1.1 mm thick, while the Ag thin layer has a sheet resistance of $20 \Omega/\text{sq}$. For DT, the triangles have the same σ and h value as the Ag thin film (in Hom and ET samples), while the rest of the thin film, which is less conductive, is simulated with lower values of $50 \text{ S}/\text{m}$ and $40 \text{ W}/(\text{m}^2\cdot\text{K})$.

Figure 5-8 reports the spatial distribution of the electrical stress, for a 5 V bias, through the simulations, as well as the comparison with experimental surface temperature data. In the homogeneous case, the electrical potential lines are perfectly parallel (Figure 5-8a), which is almost the case for the experimental too, as revealed by 1P-electrical mapping (Figure 5-3a). Thus the simulated current density (Figure 5-8d) has the same value all over the surface. Figure 5-8g and j report the surface temperature, respectively obtained by simulation and experiment, showing similar hotspots that result in the thermal cracks taking place the middle of the specimen (the hottest location), which are parallel to the voltage lines. Simulations of the surface temperature (Figure 5-8g) show that the difference between the middle and the edges of the sample appears small at low bias, 0.2 °C at 1 V, but it becomes more significant when higher voltages are considered, 5 °C at 5 V. Although this increase of temperature in the middle of the specimen seems low, one has to keep in mind that AgNW networks do exhibit local spatial distributions of network density (associated for instance to AgNW diameter and junction area distribution), which all lead to a non-homogeneous temperature distribution. Therefore, increasing macroscopically the temperature will increase the probability that one location gets much hotter than the average value, therefore becoming a hotspot from which the thermal crack will be initiated.

Concerning the non-homogeneous cases, both simulations of the voltage show that the tortuosity increase, especially in the ET case, as reported in Figure 5-8e and f. As a consequence, the calculated current density has no longer a constant value all over the surface. For ET, the electrical lines have the highest density around the edges of the triangles (Figure 5-8b) whereas the simulated current density shows its maximum value too (Figure 5-8e). This maximum value is highly localized and is followed accordingly by the highest temperatures appearing outside and around of the triangle edges, and extended also to the space between them (Figure 5-8h). For DT, (Figure 5-8f), the electric potential lines are more tortuous than for Hom samples, but less marked than when ET are present (Figure 5-8e). The presence of more AgNWs in the triangle regions increases the current density values; there are some paths with higher current density that, linked to the experimental voltage ramp, are still available for the current to flow during the degradation, exactly before the thermal crack divides the sample in two. If one compares the two non-homogeneous cases, they show an inverted electrical and thermal behavior; the corresponding mappings of ET and DT seem like complementary stamps of each other.

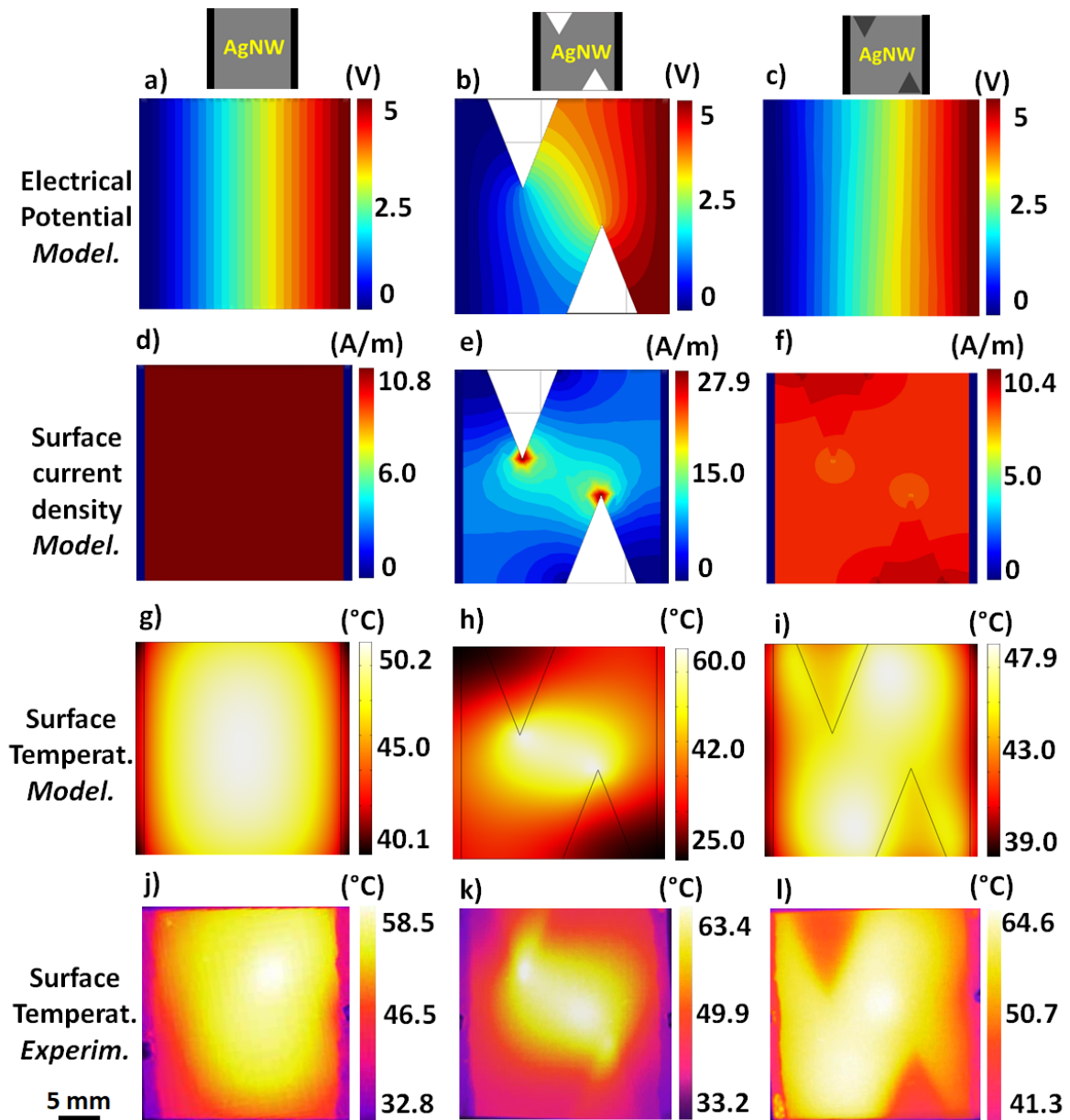


Figure 5-8: Comparison between the simulated and experimental data of the distribution of the electrical stress and of surface temperature, for the three specimen geometries. a-i) Modelling results for the distribution of electrical potential (a-c), surface current density (d-f) and surface temperature distribution (g-i), when 5 V bias is applied between the parallel contacts (left and right vertical sides). j-l) Experimental results for the spatial distribution of temperature obtained by IR imaging at 5 V, during a voltage ramp of 0.5 V/min. Three configurations are used (vertical columns): homogeneous layer (a, d, g, j), networks with empty triangles, (b, e, h, k) and with more conductive triangles (c, f, i, l).

However, the dispersion of the current density values is proven to be the significant factor for the local electrical stress and the source of instabilities. It is important not only to search for the case with the highest values of surface current density or Joule heating, but for the one having the highest difference between its maximum and minimum values. For example, at 5 V, for ET

4 times higher ΔI_{surf} is observed as compared to DT; for the first, the current density varies from almost 0 A/m close to the contacts to 27.9 A/m in the triangle edges, while for DT, the surface current density is 6.5 A/m in the triangle edges and the maximum is over 10 A/m at the bottom of the triangles. This is reflected in the surface temperatures, with the simulations showing a similar trend for the temperature maximum and minimum values. The temperature difference ΔT is around 8 °C for Hom and DT samples, while for ET it is more than 4 times higher, 35 °C, and very localized, as described above.

Comparing simulations (Figure 5-8g-i) and experiments (Figure 5-8j-l), focusing now on the surface temperature: the thermal maps are almost identical in terms of spatial distribution. The temperature ranges are also similar and the differences between the three types of electrodes (Hom-ET-DT) follow qualitatively the same trend: the ET case has more significant and localized power induced heating. However, the temperature dispersion is more significant in the experiments than the simulations. This can be due to the fact that the modeling is made for a macroscopic thin film with ideal of current flow and thermal losses equilibrium. However, it is rather encouraging to observe that such a simple modelling approach can predict the electrical and thermal behavior of an entire AgNW network with a fair comparison with experimental observations.

5.4. ZnO coated AgNW networks and its effect on the electrical distribution and the degradation of the networks.

This part of the chapter deals with the effects of ZnO coating on AgNW degradation. As clearly shown by Figure 5-4 and Figure 5-6, a first, main difference between bare and ZnO coated electrodes is that for the latter the resistance increase is much more progressive, with no sharp increase, and values always lower to 10 k Ω . More importantly, the conformal ZnO coating induces a clear enhanced stability for AgNW by preventing the silver atomic diffusion.³⁵ First of all, while the conductivity of the electrodes stems basically from the nanowires, since the *amd* value is over 110 mg/m²,²¹⁸ the thin ZnO layer decreases the electrical resistance, for example from 20 to 15 Ω for the homogeneous case. Since the ZnO layer covers the whole specimen area, in spite of its low electrical conductivity, it enhances the electrical homogeneity, since the equipotential lines are more parallel for all three configurations for the coated AgNW (Figure 5-3d-f) compared with bare AgNW (Figure 5-3a-c). The most striking case being the ET configuration for which the “empty” triangles have much less effects after ZnO coating. The

increase of overall electrical homogeneity of the AgNW network strongly limits the macroscopic degradation of the whole specimen in terms of electrical resistance and AgNW morphology impacts. Indeed, SEM images after an electrical stress experiment show that the entire bare AgNW network is intact except within the thermal crack region (Figure 5-5a), where the AgNWs are partially or totally damaged, as shown in Figure 5-5b-c. However, after ZnO coating, the degradation is much smoother since the hotspots are partially short-circuited by the ZnO thin layer and AgNW undergo much less damage (since the ZnO coating prevents the Ag atom surface diffusion), as shown in SEM images in Figure 5-5d-f.

Concerning the non-homogeneous cases, similarly to bare AgNW networks observations, ZnO coated networks degrade at lower voltage compared with homogeneous specimen: Figure 5-4 shows that the degradation occurs at 18.5 V for Hom, 17.5 V for ET and 13.8 V for DT. The comparison between homogeneous ZnO bare and coated AgNW network shows an increase in voltage of 6.7 V associated to the degradation (12.8 V and 18.1 V, respectively) in agreement with our previous works.^{35,218} For the non-homogeneous networks, ET configuration exhibits the highest benefit from ZnO coating with a 56 % increase of the voltage failure (11.2 V to 17.5 V for bare and coated AgNW, respectively) while for DT case the increase is of 25 % (11 V to 13.8 V). In conclusion, the AgNW/ZnO composite presents a significantly enhanced electrical performance. Concerning the thermal performance, the composites showed also remarkably higher maximum temperatures before degradation; for the homogeneous and the non-homogeneous DT, the higher temperature is 360 °C, and for the ET 301.5 °C, at the moment when the degradation begins (Figure 5-6d-f).

Being functional at higher voltages also means that the maximum power running in the ZnO coated samples is increased from 0.88 to 1.33 W/cm² for the DT, 0.53 to 0.96 W/cm² for the ET, and from 0.8 to 1.76 W/cm² for the homogeneous case. The ZnO coating decelerates the degradation also in terms of time of failure propagation. Already the bare non-homogeneous specimens offered a better view of the dynamics of failure, but the oxide presence disentangles even more the events. The time between the maximum power and maximum temperature is now from 2 to 4 times longer than for bare AgNW networks. Even more important is the distinction between the rise of temperature and the rise of resistance, when for the homogeneous bare AgNW reference case they occur simultaneously. In the nanocomposite case the dynamics of failure appears different. First of all, the ZnO coating protects the nanowires from atomic diffusion, so they can be stable at high power induced heating. Still, the local electrical stress and thus the Joule heating is so high locally that the degradation is inevitable. Therefore, this is

the reason why the non-homogeneous AgNW/ZnO coated electrodes again degrade faster than the homogeneous AgNW/ZnO, since they present higher local stress and heating in the same regions as the bare corresponding cases (see in Figure 5-4 with IR photos before degradation). Secondly, the ZnO, as discussed above, works as a minor electron pathway. This means that during the increase of temperature, it takes more time for the resistive hotspots to propagate in the network. The resistance of the coated electrodes increases smoother than the bare networks and it takes longer to reach its highest value. When in the bare homogeneous AgNW network the temperature rises simultaneously with the resistance (Figure 5-6a), in the coated homogeneous one it takes another 46 s for the resistance to increase (Figure 5-6d). Accordingly, for the non-homogeneous cases it takes half to one-minute extra time. The dashed arrows in the Resistance-Power-Temperature plots guide us to see this difference.

The third parameter linked to the ZnO effect during the electrical stress is the distribution of heat within AgNW networks. In **Figure 5-9**, the temperature profiles are depicted from the IR observations, in lines parallel to x-axis that run the middle of the specimens. The oxide coating contributes to a smoother temperature distribution, which means that it can lower down the local thermal stress, where the instability of the AgNW networks originates. The temperature profiles for the bare cases show that the difference between the middle and the edge points becomes more and more significant as the voltage and maximum temperature increases (Figure 5-9a-c). This is more prominent for the ET case that receives the high local electrical stress, proven by experiments and simulations in the first part of the results section. In the beginning of the degradation at 11 V, the temperature in the edges is 87 °C while in the middle is 156 °C, almost the double. Comparing each homogeneous or non-homogeneous case with its corresponding ZnO coated network (Figure 5-9d-f), there are three differences: i) the temperature differences between the middle and edges are lower, ii) the distribution is spatially smoother, without any notable peaks in the middle of the specimen, iii) the local stress is higher when the power reaches its maximum value (orange lines) and not at the maximum of the temperature (red lines). This can be explained by the dynamics of failure in the AgNW/ZnO case, the longer propagation of the failure and more homogeneous heat dissipation. Additionally, the DT AgNW/ZnO has a quite different temperature profile. As the IR videos show the crack, on this case, propagated close to the upper denser triangle and there is also a thin line parallel to left silver paste contact that showed hotspots during the degradation. This is probably due to the high conformal coating over the nanowires; the high heat finds a way to dissipate only close to the edges and at the interface with the contacts. One can observe the

same thermal behavior along the diagonal for the bare AgNW networks. These plots are presented in Figure 5-9g and h.

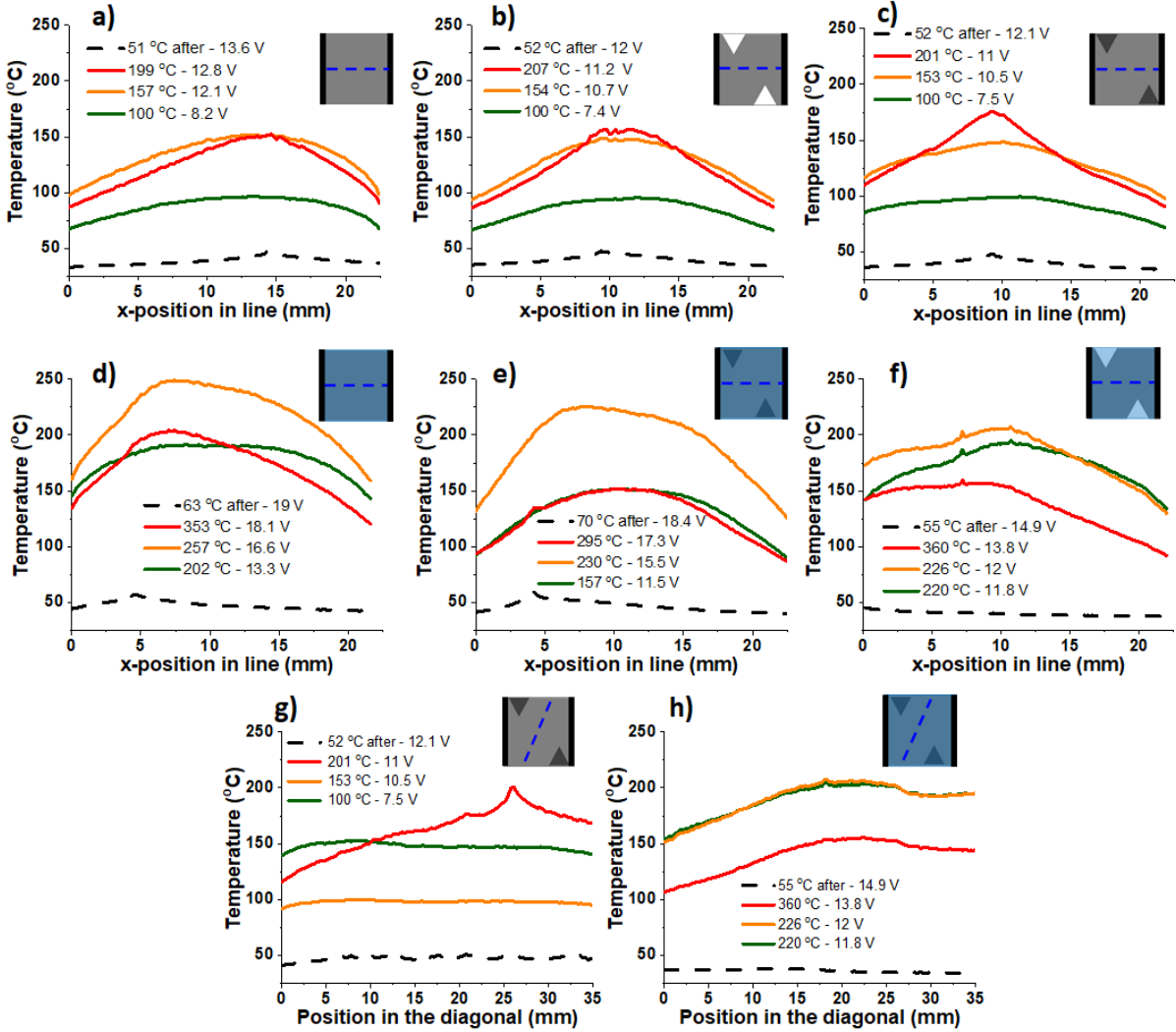


Figure 5-9: a-f) Experimental temperature profiles corresponding to a line parallel to the x axis, in the middle of the samples (see dash lines in the insets). As indicated schematically by the grey or blue insets, the first line corresponds to the bare AgNW networks and the second to the ZnO coated ones, for the three configurations Hom-ET-DT. The temperatures are extracted from the IR sequences during the voltage ramp of 0.5 V/min. Four different moments of the voltage ramp are chosen each time: far before degradation (green lines), at maximum power (orange lines), at maximum temperature (red lines) and after degradation, when the resistance is restored to kΩ range (black dash lines). The maximum surface temperatures of the specimens at each of the four moments is reported in the inset legends. The size of all specimens is 25*25 mm². g-h) Experimental temperature profiles corresponding to a diagonal line (see dash lines in the insets) for DT networks.

5.5. Additional examples, conclusions and prospects

The local variation of network homogeneity in electrodes composed of silver nanowires has a significant impact on the electrical and consequently thermal distribution of the specimens, as shown above. In particular, the presence of triangular zones with absence of nanowires (ET) or denser nanowire network regions (DT) showed the appearance of higher electrical potential variations. In the regions where the density of the network changed drastically in space, the electrical potential presented higher tortuosity accordingly, as revealed by the 1P-mappings. This fact led to the creation of spots with a high surface current density, when compared to the rest of the network. Therefore, an increased heating at these points was observed, when a significant voltage was applied. Such specimen configurations were helpful to further understand the AgNW network breakdown under electrical stress, as the edge effects and variations in the local distribution of the network density lead to local hotspots from where the thermal instabilities and defects started propagating. In addition, the experimental results were confirmed by simulations of both voltage and surface temperature maps. Thus, the comparison of the non-homogenous transparent electrodes with the homogenous ones, both experimentally and by modelling, showed two different thermal effects: i) the temperature variation between a hotter and cooler region on a non-homogenous electrode is larger than in a homogenous sample; ii) non-homogenous electrodes can be designed in order to obtain regions with a higher maximum local temperature than in the homogeneous case, at lower applied voltages. These regions can be simulated by simple, macroscopic, physical models and patterned easily during the AgNW network deposition. In addition, to further test the reliability of the modelling, another geometry of AgNW network patterning was studied, by keeping the areal mass density the same, as it is presented in **Figure 5-10**. In this alternative geometry, the had a ring shape and the contacts were placed in the outer circular periphery and in the central hole. The region with higher current density, as it is calculated by simulations (a), is close to the small, inner contact and corresponds to the same region that heats more during a voltage ramp, as demonstrated by the IR image (b).

The second effect on the AgNW networks stability that was investigated is the presence of a ZnO coating on top the AgNW networks and its impact on the electrical and thermal distribution, especially in the case of non-homogeneous transparent electrodes. The 1P-mappings showed a reduction of the tortuosity of the electrical equipotential lines, when compared with the bare AgNW networks. This enhancement of electrical homogeneity is achieved thanks to the electrical conduction through the oxide. Even if the resistivity of ZnO is

much higher than that of AgNWs, the conduction through this oxide plays a relevant role in the less dense network regions, contributing as a mean for electrical conduction. Additionally, the ZnO increased significantly the stability with a 50 % higher voltage failure, while maintaining the high optical transparency of the electrodes. Furthermore, the presence of a thin oxide layer allowed the electrodes to reach higher temperatures above 300 °C generated by Joule heating.

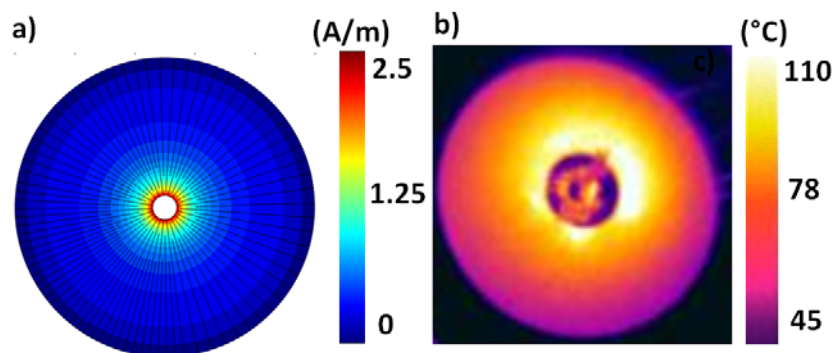


Figure 5-10: a) Surface current density obtained by COMSOL simulations for a round Ag thin film. One contact is in the outer periphery and the other is placed in the central hole. b) IR images of round AgNW network deposited on a round glass (same contact configuration a for the modelling in a)) during a voltage ramp. The diameter of the rounded sample is 25 mm.

While this study is related to AgNW networks, the proposed methods as well as the main results can be applied to copper nanowire networks. The latter would be a low-cost solution, when compared to silver nanowires but are more prone to oxidation; however as for AgNW, an oxide coating drastically enhances the stability⁷⁸. Therefore, one of the perspectives of this research work would be to explore other metallic nanowires networks and not only those based on AgNW. Finally, these results can contribute to the future of transparent electrodes based on metallic nanowire networks as the present study proposes a way to engineer new generation of transparent heaters with specific hotter regions, only by controlling the local network density. An example is given in **Figure 5-11**. 3D printed masks (Figure 5-11i) are used during the spraying of the nanowires leading to vertical bands with different network density (Figure 5-11ii). As it is shown in the IR images of Figure 5-11iii, the vertical bands demonstrate different power-induced heating, due to the varying density thus electrical distribution. This is confirmed and can be designed by physical modelling too (Figure 5-11d). Such configurations can be attractive for the transparent heaters serving experiments on biomedical lab-on-a-chip and other microfluidic applications, as it will be discussed in the following chapter. The presence of the ZnO layer can ensure the stability of these electrodes, and increase their heating performance for potential application in defrosting/defogging devices such as optical masks or vehicle windows that need high steady-state temperatures and fast heating rates.

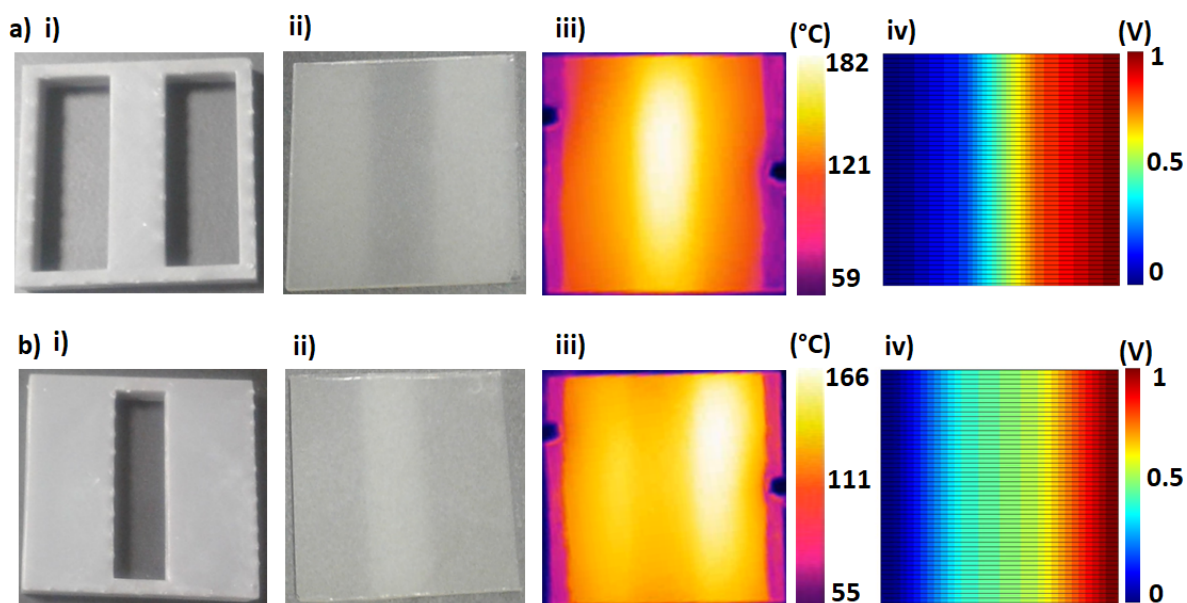


Figure 5-11: Two examples of non-homogeneous AgNW networks with varying areal mass density (amd) in different vertical bands; a) lower amd in the middle band, and thus higher resistance, b) higher amd in the middle band and thus lower resistance. For each case: i) the 3D printed mask used for the deposition of the AgNWs, ii) a photo of the fabricated sample; the bands that appear whiter have more nanowires, iii) IR image during a voltage ramp; the whiter regions are hotter, iv) the voltage mapping by physical modelling of the corresponding Ag thin film associated to similar sheet resistance than AgNW networks. The size of all square samples is $25 \times 25 \text{ mm}^2$.

*Ου γαρ το ειπεῖν καλῶς καλόν,
ἀλλὰ τῷ ειπόντι δράσας τα εἰρημένα.*

Ζήνων ο Κιτιεύς

*« The good is not the one who say things well,
but the one who puts them into action »*

Zeno of Citium (334 – 262 BC)

Chapter 6

6. Integration of Ag-based nano-objects into devices.

Following our contribution towards the elaboration of a more robust technology, as presented in the previous chapters, this last one is dedicated to the applications. One of the main goals of my thesis was to explore deeper the performance and the failure of AgNW networks and investigate ways to improve their stability. This paved the way to proceed on the integration of AgNW networks and other Ag-based nanomaterials into devices, through several projects and collaborations that I had the great chance to work on and also expand my knowledge on diverse topics.

✎ In the first part of the present chapter, AgNW-based transparent heaters (TH) for bio applications are presented. The ultimate goal of the study we performed with a biologist at LMGP, Prof. Franz Bruckert, is to develop *in situ* quantitative polymerase chain reaction (qPCR) for DNA amplification in a microchannel chip with direct monitoring of the fluorescence observed through a microscope. For this, we embedded the AgNW networks on the chip and apply certain voltage steps in order to induce the heating and cooling cycles and obtain the temperatures needed for the PCR assay. Thanks to the optical transparency of the AgNW-based TH, the fluorescent signal is not affected and thus we could study its variation *in situ*, during successive, power-induced thermal cycles. The AgNW/ZnO nanocomposites, fabricated by AP-SALD thanks to Abderrahime Sekkat (on-going PhD thesis since 2018) and Dr. Viet H. Nguyen (PhD thesis 2015-18, Post-Doc 2019), enhance the electrical stability and the thermal performance of the TH. In addition, we demonstrate a simple, up-scalable approach to prepare AgNW-based TH for specific lab-on-a-chip devices. The bio measurements were conducted with the contribution of Phelma Biomedical Engineering students, in the framework of Instrumentation Projects during 2017-18 (Carolina Naomi Nakamura and Sara Öhman) and 2018-19 (Melvin Buton, Benjamin Delecourt, Davy Uthayasooriyar and Loïc Hermant).

✎ In the second part, the integration of AgNW networks on flexible energy harvesters will be presented. In the framework of the Carnot Energies du Futur project *FREE* (Flexible, transparent electrodes for Robust Electrostatic generators for Energy harvesting) in collaboration with Prof. Alain Sylvestre from G2Elab (Grenoble Génie Electrique laboratory) and Prof. Skandar Basrour from laboratory TIMA (Techniques de l'Informatique et de la Microélectronique pour l'Architecture des systèmes intégrés) in Grenoble, we aim to elaborate electrostatic generators with superior mechanical properties to fit in applications including

smart clothes, hybrid vehicles, haptic screens, autonomous biocompatible harvesters. For this, it is necessary to replace the traditional electrical contacts, like gold thin films, with a technology that is (semi)transparent and retains its electrical conductivity under mechanical stress. Transparent electrodes based on AgNW networks are a promising candidate thanks to their excellent stability under bending and their propitious performance under stretching tests, as it has been introduced in chapter 1.2.5. In LMGP, starting from my master internship (2017) and the PhD thesis of Dr. Thomas Sannicolo (2014-17), we have been able to elaborate AgNW networks embedded in biocompatible elastomers like PDMS, and investigate their electrical performance under stretching tests. Then during my PhD thesis, we further characterized the electrical resistance of AgNW/PDMS composites under mechanical stresses. In the framework of Carnot project *FREE*, we have been searching as well for efficient ways to integrate AgNW networks in PDMS composites and “sandwiches” with components that constitute the dielectric medium of energy harvesting devices. In section 6.2, I will present the main results of this study, performed also with the contribution of Tomy Chatin (M2 internship 2019), whom I co-supervised.

✎ Continuing with the integration of AgNWs into devices, in section 6.3, we will discuss the research topic and selected results from the two on-going French ANR (*Agence nationale de la recherche*) projects of our team with laboratory and industrial collaborators. The first one, named *PANASSE* (Planar Assembly of NAnowires for Sidewalls Emission, ANR 2019-2022), concerns the fabrication of MNW-based cold cathodes for compact X-ray sources in future medical applications. In collaboration with TRT (Thales Research and Technology) in Palaiseau that have years of experience in the development of CNT cathodes, and the IEMN (Institut d’Electronique, de Microélectronique et de Nanotechnologie) in Lille that are experts in nano-characterization, we investigate the vacuum electron emission from planar MNWs, aiming at robust and low-cost miniaturized electron sources. The second project *MEANING* (MEtAllic Nanowire networks: from fundamental aspects towards INdustrial integration, ANR 2019-2022) is related to the integration of MNW networks in emerging organic photovoltaics (OPV). In the framework of this project, we are collaborating with the team of Prof. Mona Tréguer-Delapierre in ICMCB (Institut de Chimie de la Matière Condensée de Bordeaux) that has reported great advances in the growth of novel nanostructures, and the Solar Power Films team of the industrial enterprise ARMOR in Nantes that nowadays are focusing in the large scale printing of OPV. This means that a consortium with very complementary expertise is gathered including for instance growth of metallic nanostructures, fabrication and physics of

MNW networks, modeling of their physical properties and engineering for an efficient integration in industrial organic solar cells. Some results of the electrical characterization performed in LMGP to AgNW networks deposited in large plastic substrates by ARMOR, will be presented in section 6.3.

☞ The last part of chapter 6 is related to the study of a different material than MNW networks. It concerns the characterization of nanocomposites consisting of silver nanoparticles (AgNPs) on polymer coatings, which were elaborated by Dr. Lavinia Balan and Marine Dabert (PhD thesis 2017-20) in IS2M (Institute of Materials Science of Mulhouse) and CEMHTI (Conditions Extrêmes et Matériaux: Haute Température et Irradiation, laboratory in Orléans). The Ag@polymer coatings demonstrate promising electrical and optical properties, such as high reflectivity in NIR, which is interesting for their integration to a wide variety of energy-saving applications. During our collaboration, in LMGP we performed the characterization of the electrical properties of the metallized coatings, focusing on the effects of thermal annealing. The main results are presented in the section 6.4 of this chapter, which is highly inspired by the article entitled “*Exploring the Effects of Thermal Annealing on the Optical and Electrical Properties of a Photo-generated Ag@polymer Metallized Coating*” by M. Dabert, D. T. Papanastasiou, L. Vidal, S. Hajjar-Garreau, D. Bellet, L. Balan. This article is in the phase of submission.

6.1. Transparent Heaters (TH) for lab-on-a-chip applications

In this first part of the present chapter related to devices, the AgNW-based Transparent Heater for biological applications are presented. To start with, a brief introduction to the PCR principle and some PCR technologies will be presented, focusing on the ones which use TH as heating elements. The goal of the study we performed with Prof. Franz Bruckert, is to develop *in situ* qPCR for DNA amplification in a microfluidic chip with direct monitoring of the fluorescence by a microscope. The properties of AgNW based TH and the advantages of ZnO coating on the AgNWs will be presented. Our approach to develop the TH lab-on-a-chip will be presented along with the prevailing technical issues and limitations we should tackle. Then, the heating using AgNW/ZnO TH will be discussed, showing *in situ* fluorescence measurements that allows us to calculate the actual temperature in the microchannel. Furthermore, preliminary experiments demonstrating that DNA amplification indeed takes place in the device will be discussed, as well as prospects for future optimization.

“Abundance and distinction”;²⁵² **a brief introduction to qPCR.** It was back to 1983 when K. B. Mullis invented the nowadays-very-popular polymerase chain reaction (PCR) method. Thanks to the PCR, small amounts of target DNA template (amplicon) are exponentially amplified in a series of thermal cycles.²⁵³ Ten years later, Mullis was awarded the 1993 Nobel Prize in Chemistry (shared with Michael Smith) and, at the same year, Higuchi et al. demonstrated the discovery of real-time or quantitative PCR (qPCR), by adding a fluorescent label that binds to the accumulating PCR product and monitoring the thermal cycling with a spectrofluorometer.²⁵⁴ As the concentration of the PCR product increases, the intensity of the fluorescent signal also increases, thus with the qPCR minimal amounts of DNA could be replicated rapidly and detected easily. Since then, the PCR technique has been adapted for numerous molecular biology applications and qPCR is the key-method for the gene expression analysis with promising developments towards a more sensitive, faster and affordable technology.^{255,256} Nowadays, real-time Reverse Transcriptase qPCR (RT-qPCR) has routinely been used for the detection of infectious diseases, including those by bacteria or viruses. Reverse Transcriptase is an enzyme used to copy RNA in the form of DNA, which is called cDNA (complementary DNA). Only today though, we could claim that the PCR is a term that everyone around the world have heard of, related to the unprecedented pandemic of coronavirus disease that we are facing since March 2020.³⁹⁻⁴¹ The RT-qPCR assay for SARS-CoV-2 using upper and lower respiratory tract specimens is the gold standard for diagnosing COVID-19.⁴²

Thermal cyclers or thermocyclers are the instruments used to amplify DNA or cDNA samples by the PCR, by raising and lowering the temperature of the samples in a holding block in discrete, preprogrammed steps.²⁵⁷ Another step in PCR has been the development of digital droplet PCR (ddPCR). In this technique, the sample is fractionated into small droplets that contain a single biological object to analyze, and the qPCR reagents. The qPCR results are analyzed in single droplets with real-time PCR. This allows detecting low-abundance targets in a mixture, for instance mutants cells in a cell population.²⁵⁸ This technique is nowadays used for the monitoring of patients with Chronic Myeloid Leukemia.²⁵⁹

Among the several detection methods for the indirect measurement of template in qPCR, two reporter systems are commonly used;²⁶⁰ the intercalating SYBR Green assay by Wittwer et al.²⁶¹ and the TaqMan probe system by Holland et al.²⁶² Double-stranded DNA (dsDNA) binding dyes are popular because they offer a low-cost detection and do not require additional design considerations. The most commonly used dye, SYBR[®] Green I, which we also use in our experiments in LMGP, functions as intercalating and/or minor groove binding agent and emits detectable fluorescence when bound to dsDNA, but has a very low background when free in solution. Therefore, fluorescent signal intensity, which can be detected by the thermal cycler, increases proportionally to the quantity of the amplicon.²⁶³ Thus, the fluorescent signal of the sample is collected at the end of the elongation step of each PCR cycle to determine the relative change in amplified products. Each cycle of the DNA amplification includes three main steps, which are schematically presented in **Figure 6-1a**²⁶⁴: i) *denaturation*, in which dsDNA templates are heated at around 95 °C for 20–30 seconds to break the hydrogen bonds and separate the DNA strands (DNA melting), ii) *annealing*, in which the reaction temperature is lowered to 55–65 °C for 20-40 seconds, allowing short DNA molecules called primers to bind to flanking regions of the target DNA, iii) *extension*, in which DNA polymerase extends the 3'-hydroxy group at the end of each primer along the template strands, at a temperature of 72 °C.^{265–268} Finally, at the end of the cycle, we get two completely identical strands. We can therefore multiply the amplicon by 2 each cycle. For about n cycles, we have in theory 2^n DNA, i.e. for 20 cycles we get an increase in the concentration per 10^6 . Practically, SYBR Green fluorescence is measured at the end of the annealing step.

A commonly employed method to quantify gene expression by RT-qPCR relies on plotting fluorescence against the number of cycles on a logarithmic scale. When the DNA is in the log-linear phase of amplification,²⁶⁹ the amount of fluorescence increases above the background. The point at which the fluorescence becomes measurable is called the Quantification Cycle (C_q)

or crossing point. By using multiple dilutions of a known amount of standard DNA, a standard curve can be generated of log concentration against C_q . The amount of DNA or complementary DNA (cDNA) in an unknown sample can then be calculated from its C_q value.²⁷⁰ The different phases of the reaction:

i) *exponential*, the first phase of PCR amplification, in which the target yield has reached the detection threshold, the reaction components are in excess and there is an exact doubling of product each cycle. Real-Time qPCR measures the C_q value at this phase of PCR;

ii) *linear*, in which the reaction components are being consumed, amplification slows, and the reaction rate decreases;

iii) *plateau*, the final phase of the amplification, in which there is insufficient free enzyme to continue amplification, the reaction is complete and at its maximum yield, this is called the plateau phase.²⁷¹

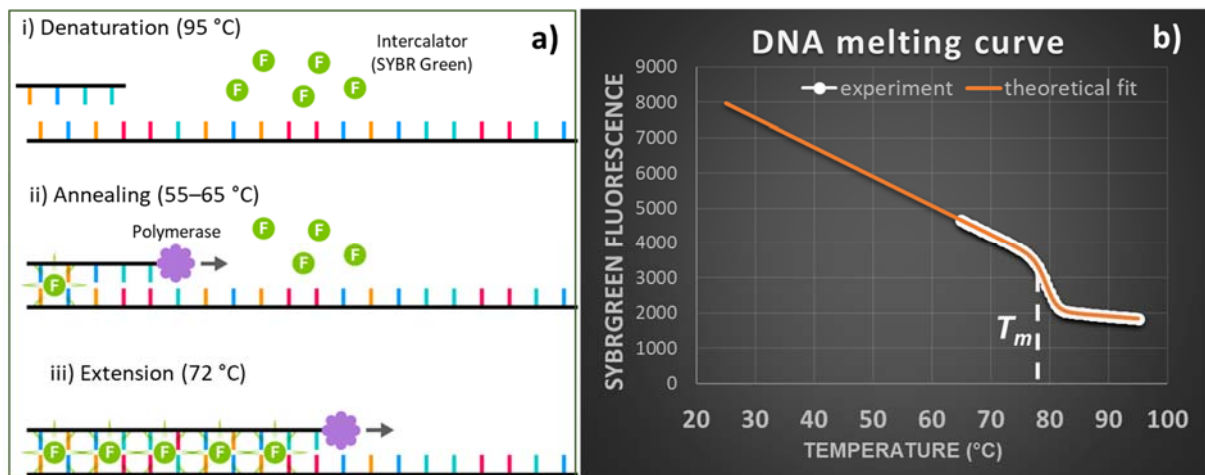


Figure 6-1: a) Principle of a DNA melting experiment.²⁶⁴ b) DNA melting curve during a cycle of the PCR assay for SYBR Green dye we used for our experiments. The experimental data (white dots) correspond to the fluorescence, which is extracted by the qPCR Bio-Rad instrument, as a function of the temperature. The melting temperature $T_m = 79.52$ °C is derived from the fit of the data by the Savitzky–Golay filter (orange line) and corresponds to the temperature in which a sharp transition of the fluorescence values is observed.

DNA melting curve. As already mentioned, in quantitative PCR, DNA amplification is monitored at each cycle of PCR. The signal of fluorescence obtained with SYBR Green is maximum when the DNA is in the form of double strand while it is at its minimum when denatured. This property is exploited to check that the amplified product is the correct one by measuring the melting temperature T_m , which is characteristic of the DNA fragment length and

percentage of G and C nucleobases in the sequence. Therefore, when the melting temperature is reached, the fluorescence should decrease.

Figure 6-1b demonstrates the melting curve of the DNA plasmid that we used in our latest experiments in LMGP. It is the plasmid pQE30-Syn8 and two primers com-5' and com-3' and we have used the qPCR Bio-Rad of CIME-Nanotech platform of Grenoble-INP. To calculate the melting temperature, we smooth the fluorescence versus temperature curves using a Savitzky–Golay filter, which increases the precision of the data without distorting the fluorescence signal trend,²⁷² according to the following equation:

$$F(T) = F_0 - \frac{aT+b+ce^{\frac{T_m-T}{w}}}{1+e^{\frac{T_m-T}{w}}} \quad (6-1)$$

where F the measured fluorescence, F_0 its initial value equals to 1003 both F and F_0 have arbitrary units), the parameters $a= 13.73 \text{ K}^{-1}$, $b= 6886$ and $c= 82.74 \text{ K}^{-1}$, w is the temperature width, which will limit the temperature accuracy for estimating T_m , equal to $0.9672 \text{ }^\circ\text{C}$. We obtain finally $T_m= 79.52 \text{ }^\circ\text{C}$.

TH based PCR technologies. The implementation of microfluidic systems has led to the development of an entirely new family of PCR devices, like chip-based and droplet-based qPCR and digital PCR (dPCR).²⁷³ In parallel, there is a global, great need of IoT related to healthcare, including portable, user-friendly and light diagnostic devices.²⁷⁴ A miniaturized PCR, that is safe to use, even if part of the diagnostics is performed out of the classic laboratory conditions, would be really useful at times when vast infectious disease outbreaks occur. This could be realized if the heating element is a flexible TH, especially if this film is an independent, removable piece from the PCR device that could be removed and reused on top of other biochips. To date, the current continuous-flow PCR uses two or more heating sheets to achieve temperature cycling,²⁷⁵ and/or with devices that are bulky and inconvenient to carry.²⁷⁶ Reports so far include water bath containers, which in some cases are heated by candles, heating and show use of cooling by Peltier elements, IR laser for heating, cooling by fans, thermal reservoirs from metallic blocks etc.^{268,277–279} Concerning the use of transparent materials in PCR-based devices, to date there are few, and not very recent reports. The following studies report a high optical transparency (80-90%) but they use two or three TH layers to obtain the amplification temperatures from each layer. Even if the heating rates can be efficient, the fabrication techniques can be complicated or expensive to reproduce in large scale. Sun et al. proposed a microchannel chip for continuous-flow PCR with two ITO films operating at two different temperatures (one zone for the denaturation and one for the extension step), but they did not

apply it for monitoring PCR amplification.²⁸⁰ The dsDNA dyes liquid could potentially circulate in the channels of the chip and get heated continuously by the two different ITO heaters amplification. They calibrated the power supply to the ITO films in order to achieve the two-stage (94 and 67.8 °C) thermal cycling inside the microchannels but they do not provide any information about the consumed power.²⁸⁰ Similarly, Chung et al. reported a reverse transcription RT-qPCR with two graphene-based TH to achieve a thermal cycling between two temperatures as the previous study. One side (hot side) of the chip was heated by graphene heater up to 95-105 °C for denaturation, and the opposite side (cold side) was cooled by pressurized air blowing down to 50-65 °C for annealing and extension steps. The power consumption for the heater was less than 500 mW and gel-electrophoresis PCR results demonstrated that the quantities of amplified DNA copies from the chip were nearly equivalent to those from the thermocycler. The results are presented in **Figure 6-2a**. However, different chip geometry would be necessary in order to optimize and control the heating conditions in a highly reproducible way, especially the part of cooling down which is done by air blowing.²⁸¹

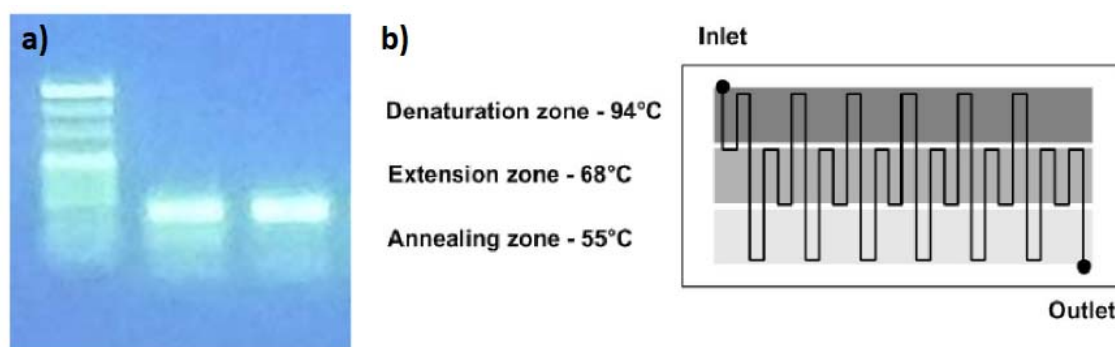


Figure 6-2: a) Gel electrophoresis of PCR product. (From the left) Lane 1: size marker ladder, lane 2: result using a PCR chip based on graphene TH, lane 3: control result using a PCR thermocycler.²⁸¹ b) Schematic presentation of continuous-flow PCR chip based on ITO heaters on PDMS microchannel, showing the three regions of the chip with different temperatures corresponding to the amplification temperatures.²⁸²

Going a step further, Joung et al. fabricated an ITO-coated glass/PDMS chip with three different zones of temperature and performed the continuous-flow PCR.²⁸² The liquid circulates in the channels of the chip, as shown in Figure 6-2b, and transverses continuously the three different temperatures corresponding to the three steps of the DNA amplification. The authors reported an applied power of about 1100 mW to get 94 °C for denaturation at the first region. Gel electrophoresis analysis was used also by these authors to PCR product collected at the end of the microchannel. The impact of the liquid flow rate for the DNA amplification was investigated and the amplification of two plasmids was achieved. However, the fabrication techniques used for the ITO heaters and the PDMS microchannel requires photolithography,

spin coating and etching techniques that are complicated to reproduce in large scale. Moreover, in all above study cases, the continuous flow approach is not suitable for *in situ* observation by a fluorescent microscope, at a specific steady point of the liquid.²⁸²

AgNW-based TH. Regarding the above, it is necessary to elaborate a transparent, flexible, versatile heating element with a straightforward way to control the thermal cycles between the same temperatures and heating-cooling rates comparable to the qPCR laboratory kits. By using AgNW-based TH, we aim to provide a versatile, low-cost and easy-to-use thermocycler for lab-on-a-chip PCR research. Emerging TH like those based on AgNW have also the great advantage that they need very low power supply to function. A future step could be the further commercial use of miniaturized PCR devices, based on a reliable and low-cost technology. In our studies we use a simple approach of a single heating film based on AgNW network, placed on top of the microchannel chip to heat it by thermal conduction. Concerning the AgNW network density, we can fabricate: i) a homogenous network to heat at the same temperature all four channels of the bio chip simultaneously, ii) a non-homogenous network, like the ones discussed in chapter 5.5, to obtain under the same electrical bias, a given temperature in each channel, depending on the network local *amd* (or equivalently its R_{sh}). The advantage of our approach is that in all cases, we just need one power sourcemeter connected to the AgNW-based TH. The Keithley sourcemeter is connected to a LabVIEW software where we can program the voltage ramps and plateaus and repeat them as many times as the PCR thermal cycles. Thus, we manage to heat the AgNW network by Joule effect and then, through thermal conduction, the amplicons inside the microchannels of the lab-chip. As already mentioned above, the temperatures at each PCR step are very specific: if they do not precisely correspond to the expected value at the expected time, the amplification of DNA will not be achieved. The power supply is programmed as a function of the AgNW network resistance, the heat conduction to the bio chip and the rest of thermal losses of the system during the Joule heating. The physics related to the Joule heating and the TH technologies was presented in details in chapter 2. In the present section we will discuss the aspects that concern in particular the integration of AgNW-based TH to the lab-on-a-chip applications.

AgNW/ZnO for enhanced performance. The electrical stability and the heating performance are crucial for the *in situ* qPCR that we aim to perform. The TH stability can be enhanced and ensured by the encapsulation of the nanowires with protective, transparent oxides, i.e. the AgNW/ZnO nanocomposites.^{35,36,218} This thin, conformal oxide layers are deposited by AP-

SALD in LMGP, in the similar, optimized way already demonstrated in chapter 5.4. In **Figure 6-3a** one can observe the minor effect of ZnO layers of different thicknesses (50 and 90 nm) on the optical transparency of the AgNW network. In the visible range, i.e. at 550 nm, the ZnO induces a slight decrease in the total transmittance of bare AgNW from 82.5% to 81.6% and 79.3%, for 50 or 90 nm ZnO, respectively. Conversely, the thicker ZnO layer is even beneficial in the NIR range, showing a possible antireflective behavior.²⁸³ Moreover, the ZnO offers a significant improvement of the electrical stability when subjected to thermal stress of 20 heating-cooling cycles from 50 to 120 °C, with a rate of 5 °C/min, in agreement with previous studies performed at LMGP.³⁵ Such an example comparing the bare and 50 nm ZnO-coated AgNW networks is demonstrated in Figure 6-3b. In order to compare the stability under electrical stress and the Joule heating performance, we perform 20 consecutive voltage cycles between 4 and 9 V, with a rate of 0.5 V/min. As demonstrated in Figure 6-3c, we can observe reversible and non-reversible changes in the resistance. The reversible increase and decrease of resistance during each voltage cycle is related to the linear dependence of the resistance to the temperature, due to electron-phonon interactions,²⁸⁴ which increases and decreases respectively, by Joule heating. Both cases are quite stable; the initial and final resistance for the bare AgNW is 16.7 and 18.5 Ohm respectively, while the ZnO coated networks is more stable showing a smaller increase, i.e. from 13.4 to 14.3 Ohm. This observation, as well as the overall behavior of the resistance during the 20 voltage cycles, are linked to non-reversible changes due to either sintering and/or damaging phenomena occurring to the nanowires.²⁴⁰ The bare AgNW network presents an increase in the electrical resistance, followed by a decrease which is probably due to a slight optimization of the nanowires junctions, thanks to the power-induced heating. This can also be observed in Figure 6-3d, where the relative resistance is plotted versus the Joule-effect generated temperature.

The ZnO coated case presents less non-reversible resistance changes as compared with bare AgNWs, meaning that there is nearly no sintering nor degradation for coated AgNWs. This means that the thin oxide layer at the surface of AgNWs can successfully prevent the atomic surface diffusion from the power-induced heating, as previously demonstrated too.³⁵ It should be also noted that the difference in max and min temperatures derives from the different initial resistance, i.e. 16.7 and 13.4 Ohm for the bare and coated network, respectively. However, the heating ranges are similar: 70 to 140 °C for the bare and 60 to 120 °C for the nanocomposite. Finally, during successive voltage ramps and plateaus, the resistance of the nanocomposite is increasing in a more stable way, if one compares the bare (Figure 6-3e) and coated case (Figure 6-3f). For the above reasons, for such experiments, the AgNW/ZnO or other MNW/oxide

nanocomposites is an efficient and stable TH technology, offering the advantage of low-cost fabrication when AP-SALD is used. Moreover, this technology exhibits a very low specific heat with a small thermal inertia, therefore the thermal response can follow the electrical inputs quickly.

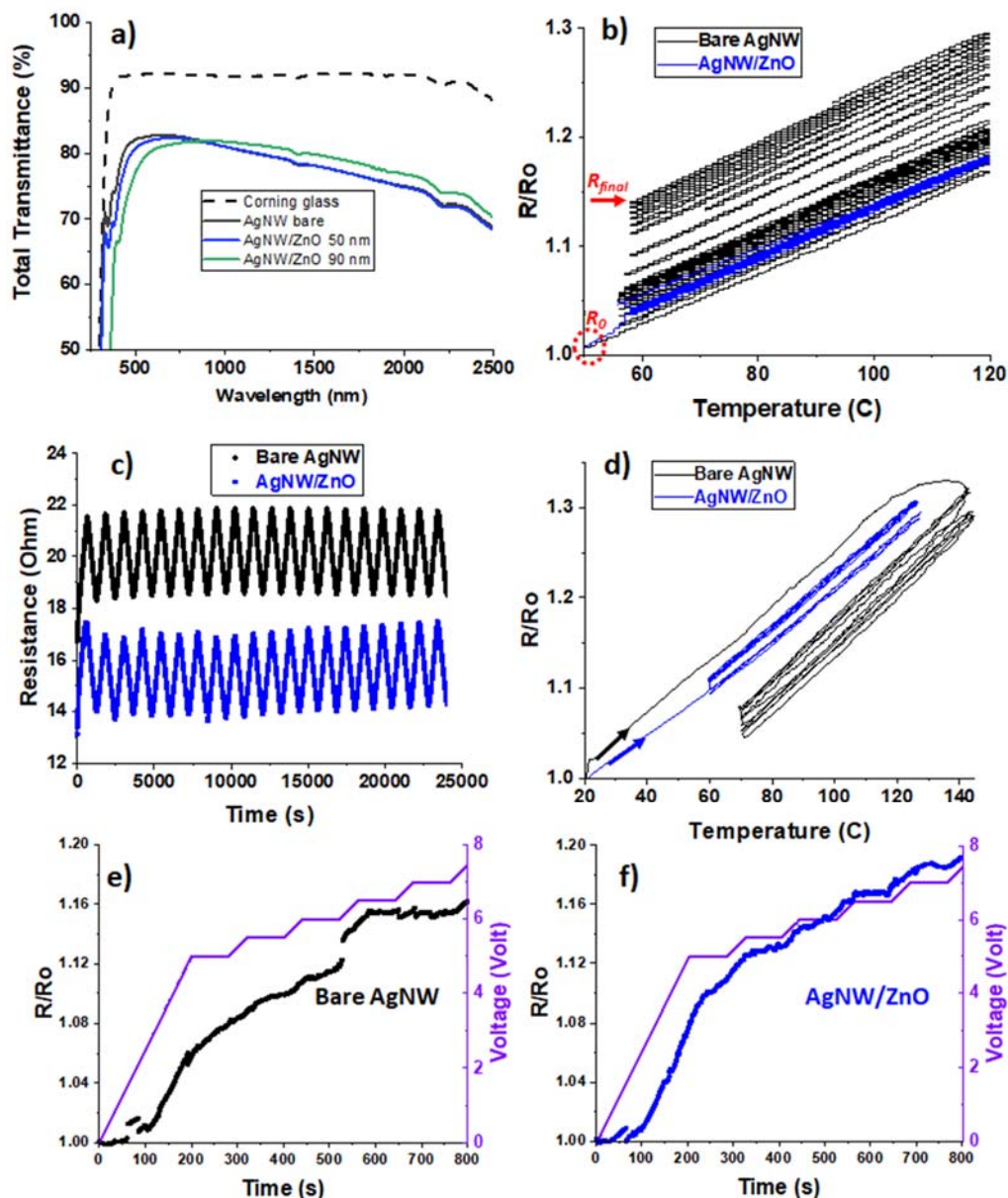


Figure 6-3: Comparison between networks composed of bare AgNWs (i.e. as deposited by spray deposition) and AgNW coated with a thin layer of ZnO deposited by AP-SALD. a) Total transmittance in UV-VIS-NIR spectrum for bare AgNW and 50 and 90 nm ZnO coated AgNW networks. b) Relative electrical resistance as a function of temperature during 20 cycles of successive heating-cooling between 50 and 120 °C, with a heating or cooling rate of 5 °C/min, for bare and 50 nm ZnO coated AgNW network. The ZnO coated case in blue line is very stable and reaches back almost the same initial value. c) Electrical resistance evolution during 20 consecutive voltage ramps of 0.5 V/min between 4 and 9 V, for bare and 50 nm ZnO coated AgNW networks. d) The same electrical test, with the resistance plotted versus the Joule-effect generated temperature. The temperature is measured by Pt100 thermocouple and the plot is zoomed in the 1st, 2nd, 10th, 11th, 17th and 18th voltage cycles for a better view of the values. e-f) The evolution of electrical resistance during increasing voltage stress (ramps and plateaus in red) for bare and 50 nm ZnO coated AgNW network, respectively.

Towards a versatile TH for a lab-on-a-chip device. During our study to integrate the AgNW-based TH on the lab-on-a-chip devices and perform the *in situ* qPCR, we have been handling several practical issues, i.e.:

- the electrical contacts configuration and the connection of the TH,
- the assembly of the *in situ* qPCR components, avoiding the contact of the TH nanomaterials with the biological substances,
- the measurement of the temperature (IR camera, Pt100) and the estimation of the temperature inside the microchannels,
- the fluorescent microscope (choice/calibration corresponding to the wavelengths of excitation and emission of the dye, minimize photo-bleaching of the dye),
- overheating of the plastic microchannel chip above 100 °C that leads to local melting and the apparition of air bubbles in the DNA solution, disturbing the fluorescent signal.

Furthermore, there are two important limitations of our TH system to handle. The first concerns the thermal inertia effect, due to thickness of the intermediate glass or plastic layers between the AgNW-based TH and the DNA, and the heat losses to the surrounding air. It is rather complex to be anticipated and, for the moment, a calibration experiment with DNA-SybrGreen is the only way to adjust the heating and cooling steps in PCR amplification, as it is presented later on. In addition, the AgNW based TH is slower compared to commercial apparatus, which is an issue to overcome for a potential use in diagnostic devices. Commercial apparatus cyclers dispose a rate of ± 3 °C /sec, even ± 10 °C per sec for the fastest ones. The problem is that, for the sake of simplicity of our system, spontaneous air convection is the only source of cooling it down. The AgNW networks does not cool down as fast as Peltier elements used in most commercial systems. Forced air convection using a fan could be very useful. In the present thesis, we will discuss the most significant features of the above aspects and the chosen parameters of the lab-on-a-chip application that we optimized for the *in situ* qPCR.

In the beginning, we have investigated several configurations to embed the AgNW-TH into the microchannel chip, thanks to the versatility of the spray coating set-up in LMGP. For example, we have deposited the AgNWs directly on top of the plastic chips, in order to avoid using an intermediate glass or plastic substrate. With such a compact configuration we can apply less power to achieve the same heating by conduction inside the microchannel, regarding the temperature gradient from the heating AgNW network to the underneath layers. However, the problem that appeared frequently during the electrical or thermal tests is the delamination of side contacts from the chip, probably due to weak adhesion between the silver paste and the

plastic material. Therefore, after similar essays we decided to use the “classic” deposition of the AgNWs on a substrate and fix the sample on top of the microchannel chip as shown in the photos of **Figure 6-4a** and b.

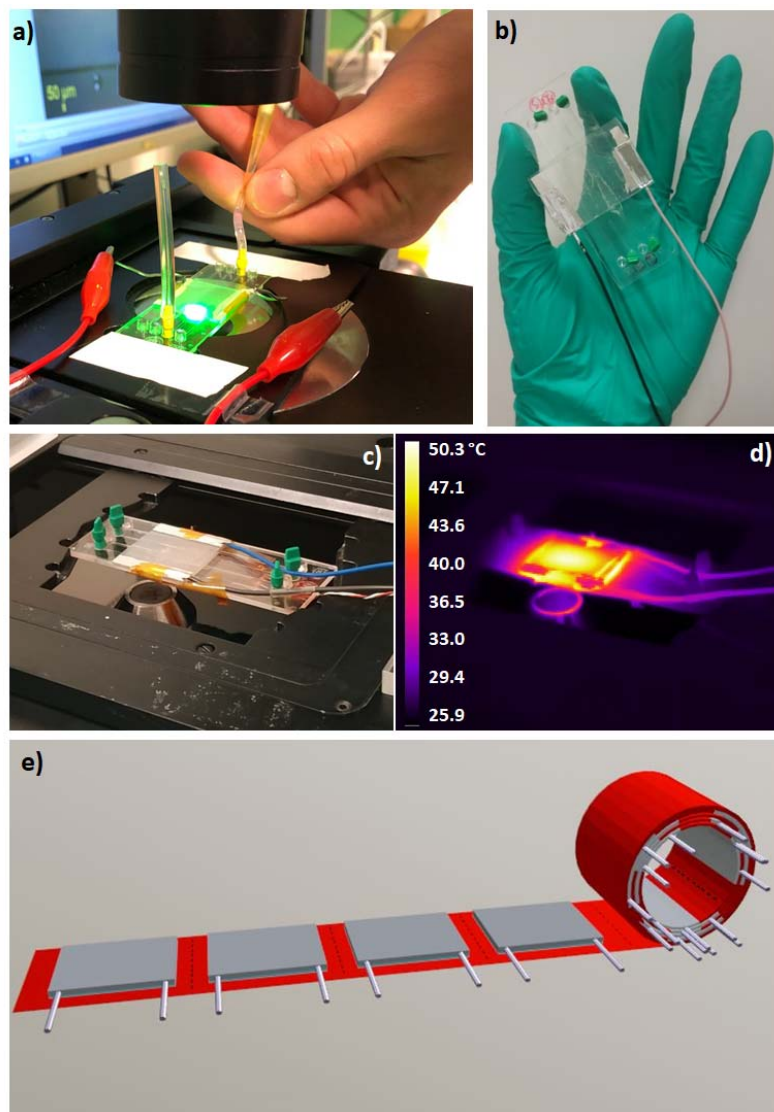


Figure 6-4: Lab-on-a-chip device for *in situ* qPCR studies, based on AgNW-based TH. a) Photo of the TH-bio chip placed on top of the microscope for the fluorescence measurements of the DNA-binding dye. The AgNW network is deposited on 25x25 mm² Corning glass and the plastic chip has 25x75 mm² size. b) Photo of the AgNW/ZnO TH nanocomposite embedded on the microchannel chip by double sided tape. The electrical contacts are also encapsulated on the left and right sides of the TH and are connected to longer wires for power supply. c) Another photo of the lab-on-a-chip system; a Pt100 thermocouple is placed below the chip to measure and compare the temperature with the IR camera measurements on the top side of the TH-AgNW network. d) IR image of the previous assembly, during the power-induced thermal cycling of the DNA. e) Illustration (using Blender software) showing the previous configuration but designed on a large scale, with a double sided tape roll fabricated to provide several ready-to-use TH films. Each AgNW/ZnO TH film is encapsulated between a flexible substrate (top film) and the double sided tape (bottom film) and it can be separated when cut along the dashed lines. Then, the surrounding protective wrap (red color) can be removed and the TH can be stuck on top of the microchannel chip, as shown on the photo (c). The TH is ready-to-use when a voltage bias is applied between its wires, which are already embedded in the TH film of the tape roll. The size of the microchannels is 25x75 mm² and the TH 40x30 mm².

The temperature measurements can be performed through conduction or radiation. For the first, we can place a Pt100 thermocouple below the chip, as it is shown in Figure 6-4c. Also, we use an IR camera close to the fluorescent microscope and measure the surface temperature of the AgNW-based TH, like the IR sequence presented in Figure 6-4d. Moreover, we have used a Pt100 between the chip and the corning glass, always being careful not to cover the region of the microchannel that is being observed by the fluorescent microscope. In this way, we obtain important information about the temperature gradient between the AgNW network surface and the channels of the microchips, in order to calibrate the power supply accordingly. More details about the spray coating and the temperature measurements were presented in chapter 2 and 3. While investigating a simple and reproducible way to prepare the TH for the bio-chips and thinking of the protection of the DNA and the user from the nanomaterials, we came up with the idea of the double sided tape. This can be useful to encapsulate the AgNW-based TH and also facilitate its integration on the microchannel chip, thinking towards a large-scale bio-TH tape. As shown in the photo of Figure 6-4b, we can fabricate a compact and always transparent lab-on-a-chip device suitable for the qPCR. In particular, the AgNWs are spray deposited on a flexible thin substrate like PI-Neopulim® (see chapter 3.1) and the ZnO layer can be then deposited by AP-SALD to enhance AgNW stability. Then, we fix the silver paste contacts and the long wires on the sides of the AgNW/ZnO nanocomposite. Next step is to place one of the adhesive sides of the tape on top of the ZnO-contacts. As a result, we ensure the encapsulation of the AgNW-based TH and the electrical contacts between the plastic substrate and the tape. This is ready to be stuck on top of the bio-chip when needed, just by peeling off the protective wrap from the second side of the tape. Moreover, with this configuration, we replace the Corning glass with the tape, as the medium between the TH and the microchannel chip. This means that by choosing the right tape we can increase the heat conduction and lower the thermal inertia, therefore improving the device efficiency. For this, we searched for double sided tapes based on polymers that combine excellent adhesion with plastics, high thermal conductivity and optical transparency. In addition, the tape should be resistive to temperatures at least until 100 °C for the in situ qPCR. There are several commercial tapes made from polyester that fulfil these criteria.²⁸⁵ Finally, in the same way to its integration, the AgNW-based TH on the tape can be easily removed from the chip and re-used to another one without losing its electrical properties. For this reason, it is important to note that the TH should exhibit a great flexibility for the assembly of the in situ qPCR. An ITO or other TCO film would lose their electrical conductivity from the first application on a chip, since they show an increase in the electrical resistance already from the beginning of bending tests.¹ Ultimately, this AgNW-based flexible

TH can be deposited by R2R processes and thus, double sided tapes containing a large amount of ready-to-use TH could be fabricated in an industrial scale, therefore compatible with low cost fabrication. This is presented schematically in Figure 6-4e by an illustration made with Blender software, thanks to Phelma engineering students, and especially to Elise Langagne, in the framework of a PHELMA 1st year project on TH, during 2019-20. Once the TH is cut from the tape roll and the protective wrap (here in red color) is removed, we can easily stick the TH to the bio-chip and apply the power supply for the *in situ* qPCR. As presented in the following paragraphs, the bias needed for the thermal cycles at this size of lab-on-a-chip device, is quite low, usually below 5 V for a sample resistance below 15 ohms. Thus, the required electrical power can be supplied from a handy set-up too. For the moment, for our tests in LMGP we use a Keithley sourcemeter controlled by a LabVIEW program, like the usual experiments demonstrated in the present thesis, however simpler and cheaper tools can be envisaged for this purpose.

Measuring in situ temperature in the microchannel upon heating with AgNW based TH.

Since we are able to fabricate a stable and efficient TH and we manage to integrate it successfully in thermal contact with the microchannels chip, we will focus now on the in situ experiments. The goal is to choose the suitable electrical bias applied on the TH to obtain the temperatures corresponding to the PCR thermal cycles, as described in the beginning of this section. We have performed several series of tests to determine the heating and cooling conditions of the specific lab-on-a-chip device. The first steps are related to the steady state temperatures reached at constant 4 V bias. As demonstrated in **Figure 6-6a**, the temperature of the AgNW/ZnO surface measured by an IR camera appears to be 13 °C hotter than the surface below the chip (see photos in Figure 6-4 for the experiment configuration). This was intrinsically expected due to the temperature gradient, when the heat is conducted through the Corning glass and the plastic chip. The temperature below the chip and between the chip and the Corning glass has a similar difference, during consecutive voltage ramps and plateaus, demonstrated in Figure 6-6b. Therefore, considering these results, we need to adapt the voltage values that we applied during the in situ PCR, to avoid the over or under estimation of the temperature of the DNA inside the channel.

Concerning the main steps for measurement of the fluorescence during the *in situ* experiments, first of all, we use the software of the microscope, which allows us to program the number and the frequency of the images. We choose these parameters depending on the experiment that we perform, the steps and the number of the PCR assays we try to reproduce. In order to avoid the

photo-bleaching of the dye, especially when the experiments last long, i.e. more than an hour for 20 cycles of qPCR, we activate the light of the microscope only for the time of exposure, usually 10 seconds, during which the sensor measures the fluorescence and captures the fluorescent image. In the end of the experiment we can extract the histogram of fluorescence in each image and then its mean value. From the quantification of the fluorescence, we can know whether the DNA was amplified or not; if the fluorescence increases in the end of each consecutive PCR cycle, it means that the DNA has been amplified. Moreover, we can use the fluorescent signal obtained from the Bio-Rad qPCR as a temperature reference and deduce, for the *in situ* fluorescent experimental data, the temperature inside the lab-on-a-chip microchannel.

We used pre-amplified DNA with SYBR Green to measure the temperature in a microchannel during a voltage ramp of 0.5 V/min until 4.5 V. As shown on Figure 6-5c the fluorescence decreases in two phases as the voltage increases. A slow decline related to the decrease of SYBR Green DNA complex fluorescence due to the increase frequency of molecular collisions as temperature increases, and a sharp decline due to the dissociation of DNA strands. This transition temperature depends on the presence of molecules that affect H-bond formation (related to the varying urea concentration, data not shown here) proving that it is related to DNA denaturation. In the absence of DNA (SYBR Green alone), the SYBR Green fluorescence is lower and uniformly varies with time. When the heating is stopped, the fluorescence level is rapidly restored as the temperature lowers (after 1400 sec).

Equation (6.1) was then inverted to calculate the temperature in the microchannel from room temperature up to the denaturation temperature, 80 °C. Plotting the temperature in the microchannel as a function of the temperature measured by a Pt100 thermocouple under a chip shows a linear relationship in the range (20-80 °C). The difference is explained by heat loss in the microchannel. This experiment was reproduced 10 times with 2 different types of TH (AgNW and AgNW/ZnO) and 3 different DNA-SYBR Green preparations. The internal temperature of the microchannels can be deduced using the fluorescence reference values obtained from the Bio-Rad instrument. The evolution of fluorescence and estimated DNA temperature, during the heating by AgNW TH shown in Figure 6-5c, is demonstrated in Figure 6-5d. There is an expected difference of temperature underneath the chip (left) and inside the microchannel (right), which should be taken into account for the calibration of the TH voltage cycles.

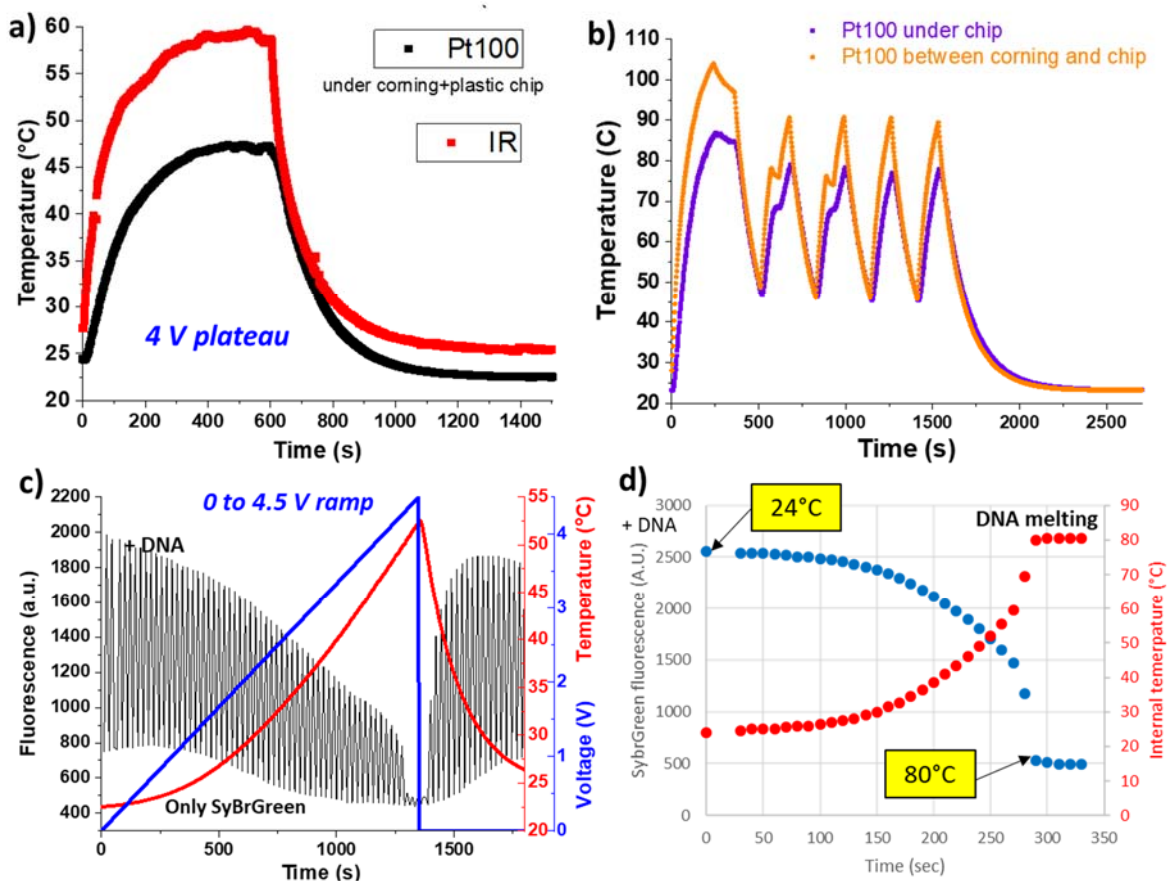


Figure 6-5: a) Comparison of the temperatures measured by an IR camera, on the surface of the AgNW network (red line) and a Pt100 thermocouple placed below the plastic chip (black line), during an ON-OFF voltage plateau at constant voltage of 4 V. b) Comparison of the temperatures measured by one Pt100 thermocouple placed below the plastic chip (purple line) and one in between the AgNW corning glass substrate and the plastic chip (orange line), during variable voltage plateaus. c) Evolution of fluorescence (black line) of pre-amplified DNA with SYBR Green, measured by fluorescent microscope during heating induced by AgNW TH under a voltage ramp of 0.5 V/min (blue line). The temperature of the set-up is measured by a Pt100 placed under the chip (red line). d) Evolution of the fluorescence and the estimated internal temperature of the microchannel-DNA, for the same experiment.

***In situ* amplification of DNA in the microchannel using the AgNW/ZnO TH.** The information obtained in the thermal ramp assay was then used to define a heating profile allowing *in situ* DNA amplification. Since the system presents a certain thermal inertia (the time to modify the thermal exchanges between the microchannel and the ambient air), the duration and the voltage applied during the three PCR stages should be adjusted, to reach the desired temperature. A pre-amplified DNA-SYBR Green solution was used to check the temperature profile, as the one shown in Figure 6-5d. Then, a DNA-SYBR Green mixture was prepared and 8 cycles were performed with a PCR machine in order to reach an intermediate fluorescence level, close to 1400, as demonstrated by the initial value of the *in situ* experiment in **Figure 6-6a**. To minimize photo-bleaching, the sample was illuminated for a few seconds at

each time step. In the beginning of the *in situ* experiment, two amplification cycles were performed while the fluorescence was measured every 10 sec. A small increase of fluorescence can be noticed between the first and second cycles, i.e. around 800 sec. Furthermore, when the device was cooled down, a clear fluorescence increase was measured at room temperature: the fluorescence level was 1842. Subtracting the basal value (300) this indicates that a 36% amplification occurred: $(1800-300)/(1400-300) = 0.36$. This is a minimum value, since photo-bleaching of DNA-SYBR Green complexes may reduce the fluorescence level. This experiment was reproduced twice. It remains to be demonstrated that DNA was indeed amplified, by using electrophoresis, but these first results look already promising.

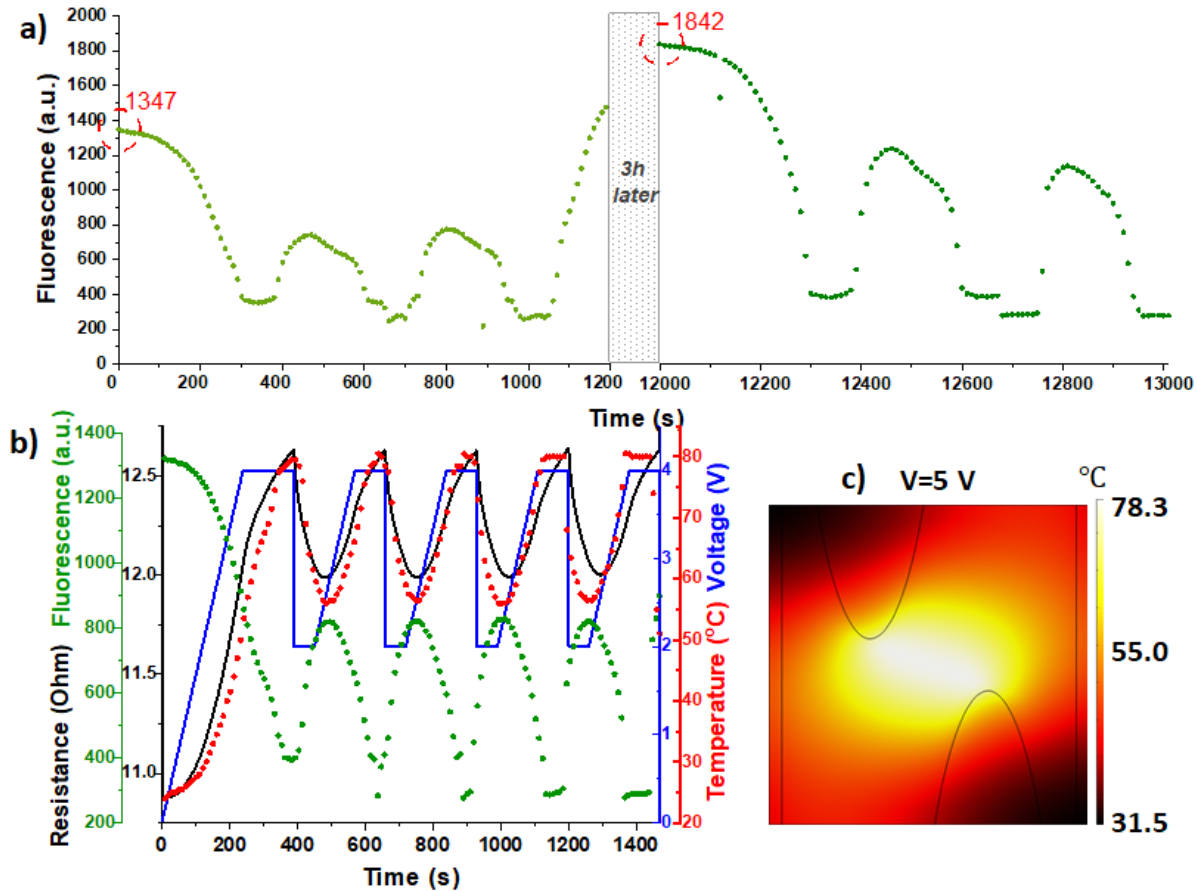


Figure 6-6: a) *In situ* fluorescent measurements of the SYBR Green binding dye during four amplification cycles performed using power-induced heating by AgNW/ZnO TH. A small increase of fluorescence can be noticed between the first and second (left). The third and fourth cycle are performed after 3 hours (right). Cooling down the set-up at room temperature revealed a 36% amplification from the increase of the fluorescence at 1842. b) Temperature (red line) of the DNA inside a microchannel, derived from the fluorescence signal of the SYBR Green binding dye, measured *in situ* during 5 consecutive thermal cycles. The heating and cooling is achieved by the voltage ramps and plateaus (blue line) applied to a AgNW/ZnO TH, whose electrical resistance follows a stable performance as shown in the plot (black line). The fluorescent measurements are performed every 10 sec c) Simulation of the surface temperature for a thin Ag (absence of Ag within the rounded edge triangles) showing the localized power-induced hot region, when 5 V bias is applied between the vertical opposite electrodes.

Another example of *in situ* fluorescence measurements during thermal cycles induced by the AgNW/ZnO nanocomposite TH is demonstrated in Figure 6-6b. The DNA-SYBR Green solution was not pre-amplified this time. In this test we applied five cycles of heating-cooling, between plateaus of 4 V and 2 V respectively, by using a voltage ramp of 1 V/min. The electrical resistance demonstrated a very stable performance, which was also confirmed by the reproducible increase and decrease of the temperature inside the microchannel. This last was extracted by the fluorescent values that we measured *in situ* with the microscope. However, the maximum temperature obtained in this experiment was 80 °C, which is lower than the PCR denaturation temperature, explaining why the fluorescence did not increase after each cycle.

To date, we have performed series of experiments carefully varying the voltage ramps and plateaus, the time to remain in each temperature and the combination of all these parameters. Indeed, we have now a better control of the temperatures related to the denaturation, annealing and extension of the PCR array. Still, technical issues that occur during the experiments, as discussed previously in this section 6.1, can complicate the procedure and need to be controlled in higher precision. Furthermore, we aim to combine this with the patterned AgNW networks, like the ones presented in chapter 5.5 and obtain a highly localized heating. Another example is given here in Figure 6-6c, with the simulation of a non-homogeneous thin Ag film with empty rounded, triangles diagonally placed on top and bottom edges of the AgNW network surface. The steady-state temperature reached at constant 5 V, shows a highly localized maximum value of 78 °C in the center of the film between the triangle edges. We can tune with ease the patterning of the TH (by using masks during spray deposition) and obtain regions of different temperatures under the same power supply. This could be very useful if adapted to the four microchannels geometry in the bio chip and proves why AgNW-based TH appear promising for lab-on-a-chip devices, not only in laboratory research but also for future developing of miniaturized, fast and low power consumption diagnostic kits.

6.2. Stretchable transparent electrodes for energy harvesters

Nowadays, embedded sensors have gained in precision, reliability, robustness, miniaturization and are widely used in the IoT.^{26,43} Therefore, it is a great challenge to make these sensors autonomous by developing energy generators that convert ambient mechanical energy into electricity.²⁸⁶ This way we could make more compact device configurations and also reduce significantly their energy consumption. In addition, transparent electrodes with excellent mechanical properties are essential components in achieving stretchable electronics and AgNW networks are one of the most promising candidates for such applications.⁴⁴⁻⁴⁶ In this context and in the framework of Carnot project *FREE*, our team in LMGP collaborates with two other laboratories in Grenoble, G2Elab and TIMA, which have developed great expertise on electroactive polymers and MEMS over the last years.^{222,287} Our goal is to develop flexible energy generators designed from electro-active elastomers, based on the deformation of materials incorporated between two deformable electrodes and operating in an electrostatic mode. From our side we aim to optimize the mechanical properties of AgNW-based stretchable electrodes and improve their integration on elastomers, in order to replace other commonly used electrodes with conductive pastes that are fragile or non-stable when submitted to mechanical stress.

Introduction to piezoelectric materials and the role of electrical contacts. Some porous polymers can exhibit a ferroelectric-like behaviour after undergoing an important voltage, we call this kind of materials ferroelectrets or piezoelectret.²⁸⁸⁻²⁹⁰ This performance occurs due to the huge applied voltage which leads to a corona poling process of the gas contained into the polymer cavities, as shown in **Figure 6-7a** by Zhang et al.²⁹¹ The gas breakdown results in charge separation and charges are distributed in opposite sides of the pores. This charge separation acts similarly to an atomic dipole into a ferroelectric material as schematized in **Figure 6-7b**.²⁹¹ The cavities can be created in a controlled way with homogeneous size and shape,²⁸⁷ or they can be made in a random way.^{292,293} Accordingly, the surface charges are free to flow in an electric circuit, shown in **Figure 6-7c**, which is the basic macroscopic mechanism for ferroelectrets used for sensing and energy harvesting applications. Subsequently, as the material is soft and flexible, a pressure ($\pi\acute{\epsilon}\zeta\omega$ -*piezo* in greek for the word *press*) can be applied on the foam which will reduce the size of the pores and thus the distance between the dipolar charges. If the distance between the charges becomes smaller, the amount of charges in the contacts needed to neutralize them will be lower. If we connect the two contacts to each other,

these supplementary charges will create a current that we can collect through the top and bottom electrodes. Various cellular micro-structured polymers, have been developed by researchers in the last years for use as piezoelectret materials. The scientific teams of S. Basrouer and A. Sylvestre have proposed a low-cost technique to create a mold by UV-lithography for the fabrication of a cellular micro-structured PDMS material, as shown by SEM imaging in Figure 6-7d.²⁹⁴ The PDMS presents a very low elastic modulus compared to other polymers already used as piezoelectrets, which is advantageous for mechanical micro-sensors and actuators.²⁸⁷ Metallic thin films, like gold, have been used for the top and bottom electrodes, but this material cannot withstand large tensile stress, which is not adapted to flexible devices. That is the reason why we choose to use AgNW networks, which can be bent or stretched, to replace the gold films. In addition, PDMS is a commonly used substrate for the fabrication of AgNW network based transparent, stretchable electrodes, as we develop the last years in LMGP too. Thus, our initial idea for the elaboration of flexible, piezoelectric energy harvesters is to work on a three-layer system, which means to pattern a layer of PDMS using a photo-active resin to create an array of holes, as described by Kachroudi et al.,²⁹⁴ and then to sandwich it between two AgNW/PDMS composites to perform the electrical breakdown and collect the electric current. This sandwich is schematically demonstrated in Figure 6-7e. In the following part, we will focus on the AgNW/PDMS layer fabrication and its electrical performance under mechanical stress. Then, the different techniques for the AgNW/PDMS-PDMS-PDMS/AgNW sandwich fabrication will be demonstrated. The intermediate PDMS layer is the piezoelectric material elaborated in by our collaborators, with the contribution of students performing their internship in TIMA and G2Elab. The mold method for the cavities patterning²⁹⁴ has been reproduced and optimized by Jean-Michel Pichonat (2nd year Phelma internship 2018) and a new method has been studied by Yuji Kachiwazaki (M1 internship 2019). This last method of PDMS foam preparation involves the mixing of liquid PDMS with sugar that, when is dissolved, leaves random voids in the polymer.^{295,296}

Fabrication of AgNW/PDMS composites. In order to obtain transparent, conductive and stretchable electrodes, we need to combine the AgNW networks with a polymer matrix. As mentioned earlier, PDMS is chosen as a host material for its mechanical properties, its biocompatibility and its simple fabrication. To fabricate AgNW network embedded in PDMS, we use a protocol inspired by those frequently reported in literature, and schematically presented in **Figure 6-8a**.

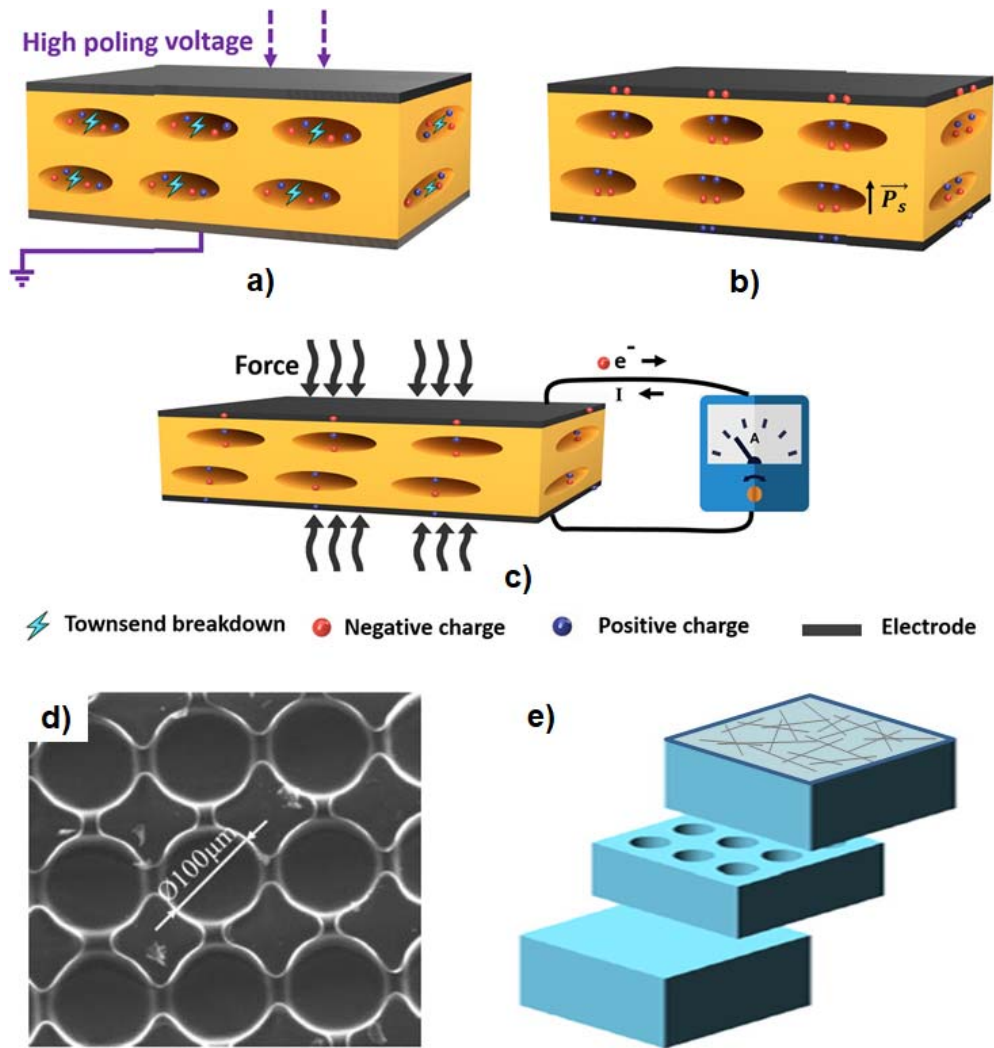


Figure 6-7: a-c) Schematic of the working mechanism of ferroelectret: a) Townsend breakdown under a high poling voltage, e.g. direct contact poling or corona poling.²⁹¹ b) Charged sample having positive/negative electrical charges on the opposite faces of the polymer surfaces with the polarization of \vec{P}_s .²⁹¹ c) Piezoelectrically induced charge flow when an external force is applied along the polarization direction.²⁹¹ d) SEM top view of the micro-structured PDMS layer with bottom bulk layer. The cavities, made from a mold created by UV-lithography, have a diameter of 100 μm .²⁹⁴ e) Schematic of a three layered PDMS for energy harvester applications, with the layer in the middle used as the micro-structured piezoelectret.²⁸⁷ In the present design, proposed in the framework of our collaboration with G2ELAB and TIMA, the top and bottom Au contacts are replaced by AgNW networks embedded in PDMS for the charge collection.

Firstly, we deposit a AgNW network on Corning glass of 50x50 mm² size by spray coating (Figure 6-8a-i) as previously introduced in chapter 3.1. For the PDMS, we use a Sylgard 184 Silicone Elastomer kit composed of the prepolymer (dimethyl-vinyl terminated silicone base polymer) and the curing agent. We mix them with a ratio of 10:1 in a beaker and then deposit the liquid PDMS by spin coating on top of the AgNW network. The spin-coater allows us to control the rotation speed, acceleration and the time of rotation, and thus the thickness of the

deposited layer. After several tests where different values of these parameters were tested, the optimized rotation speed was set at 500 rpm with an acceleration of 500 rpm/s during 30 seconds (Figure 6-8a-ii). Like this, we can obtain a final PDMS layer of 200-300 μm thickness, as the one measured by SEM image of the PDMS cross section in Figure 6-8b. On the same figure, the total transmittance of a 250 μm thick PDMS layer compared to a bare, corning glass is demonstrated (Figure 6-8c). The AgNW network covered by liquid PDMS is baked in 160°C during 30 minutes, in order to cure and solidify the polymer. The final step consists of peeling-off the PDMS layer from the glass substrate (Figure 6-8a-iii). This step is crucial for the successful transfer of the AgNW network from the glass to the polymer, which defines if the AgNW/PDMS composite is well conductive or not. In order to optimize the ratio of nanowires transferred to PDMS, we use a water-assisted process that consists of peeling-off the layer into a distilled water bath heated at 50°C. Kim et al. studied this process and justified the transfer improvement thanks to the affinity of the water with the different materials.⁹⁹ Indeed, the work of separation of the PDMS with AgNW network and glass has a negative value in the water medium. The work of separation is given by the following equation, using the surface tension between material x and y denoted γ_{x-y} :⁹⁹

$$W = (\gamma_{PDMS-water} + \gamma_{AgNWs-water} + \gamma_{water-glass}) - (\gamma_{PDMS-glass} + \gamma_{AgNWs-glass}) \quad (6-2)$$

When the PDMS is spread on the glass, it is not falling when we flip the substrate, thus the work function is positive. With a negative separation work, we are expecting a spontaneous peel off of the PDMS from the glass when it's immersed into a water bath. Thanks to this energetic argument, we can affirm that the transfer of AgNW into PDMS is more effective into a water bath. Another practical tip, which is very important before peeling-off, is to cut a small square frame of less than 5 mm, around the edges of the cured AgNW/PDMS, in order to remove the thick PDMS borders which were created during the spin coating, and separate the film from the PDMS that have licked and covered the glass sides. This way, we facilitate the peeling off and improve the transfer of the nanowires to the polymer.

Electrical stability under stretching tests. In order to evaluate the electrical stability of the AgNW/PDMS composites, we study the electrical resistance evolution of our samples under different stretching conditions. For this, we use a home-made set-up where the AgNW/PDMS cut bands are placed between two metallic jaws, as shown in the photo in Figure 6-8d. One of the jaws is fixed and the other one can move thanks to a motor controlled by a LabVIEW software. In addition, the metallic jaws are connected to a Keithley 2400 sourcemeter that

allows us to measure *in situ* the electrical resistance of the composite during the mechanical test.

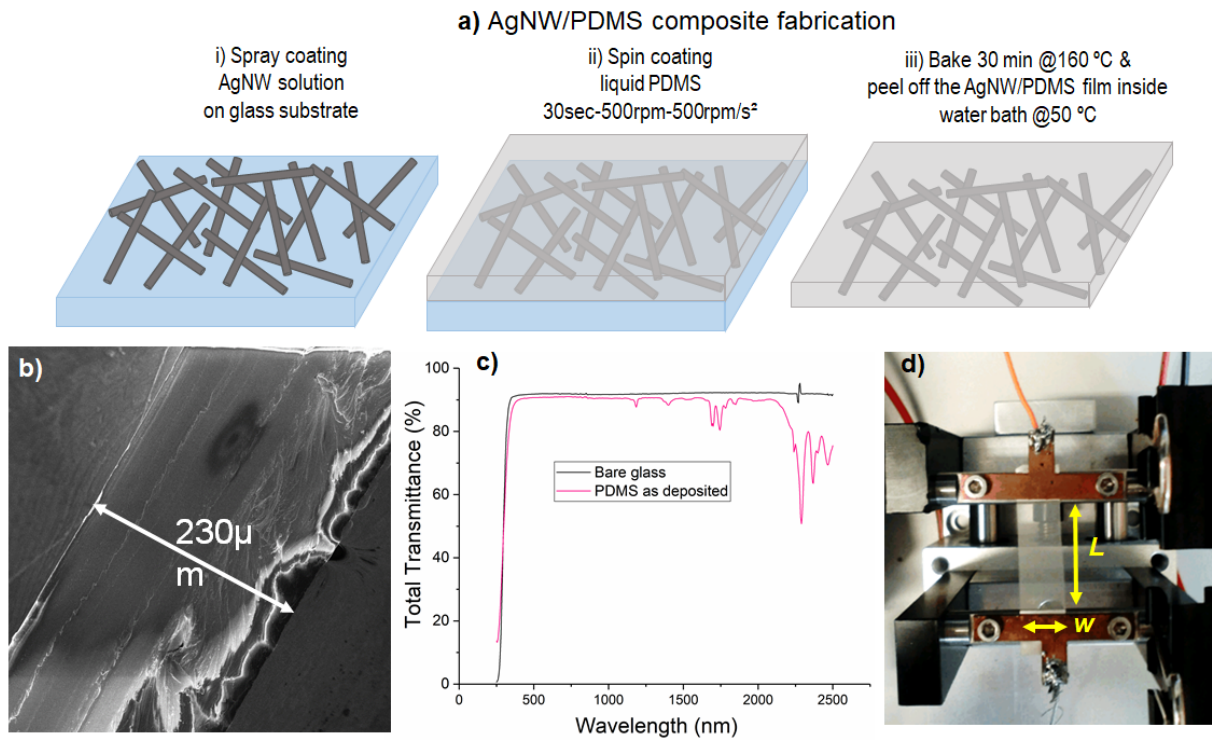


Figure 6-8: a) Schematic representation of AgNW/PDMS composite main fabrication steps: i) AgNWs spray deposition on glass substrate, ii) spin coating of the liquid elastomer, followed by iii) its curing in an oven and the final water-assisted peeling-off of the AgNW/PDMS film from the glass substrate. b) SEM image of the cross-section of the PDMS layer deposited by the previous method. c) Total transmittance of the bare PDMS layer of the same thickness and preparation, compared to the bare Corning glass substrate. d) View from the top photo of the set-up used for the mechanical stress of the AgNW/PDMS composites (elongation along its length L axis), with an *in situ* measurement of the electrical resistance by the side metallic jaws.

Thanks to the different LabVIEW softwares developed by the engineer Mikhail Anikin, we can define the type of stretching cycle that we will apply: the “fast” or the “slow” stretching. For a fair comparison between the AgNW/PDMS composites, we should remove the geometrical variation of the resistance, induced by different cutting and sample size. This is why we calculate the “normalized” resistance defined by the following equation:

$$R_n = \frac{R_{meas} \cdot w}{L} \quad (6-3)$$

where R_n the “normalized” resistance, R_{meas} the measured one by the sourcemeter, w the width of the PDMS band and L its length (see photo in Figure 6-8d). Finally, the appropriate selection of contacts between the edges of the sample and the metallic jaws, is important for the characterization. Previously, we used evaporated gold or silver contacts on the edges of the

sample, as mentioned in chapter 3.1. However, we observed an increase on the electrical resistance that originated from the damage of the interface during stretching and not from a real increase of the AgNW network resistance. Thus, we decided to change the type of contacts and test the Eutectic Gallium-Indium (EGaIn) liquid metal alloy, to form a bridge between the jaws and the sample top surface. Indeed, we obtained a drastic improvement in the junction between jaws and the nanowire network, as it is demonstrated in **Figure 6-9**. For samples of similar initial resistance (each time for two different network densities, one sparse around 50 mg/m² and one denser over 100 mg/m²), fabricated by the same method and being tested under the same elongation and stretching cycles, the change in resistance is in a totally different order of magnitude, as illustrated by the different y-axis scale in Figure 6-9. The silver-evaporated contacts artefact leads to large degradation (resistance values hundred times more the initial one), which is avoided when EGaIn contacts are used (some tens of increase).

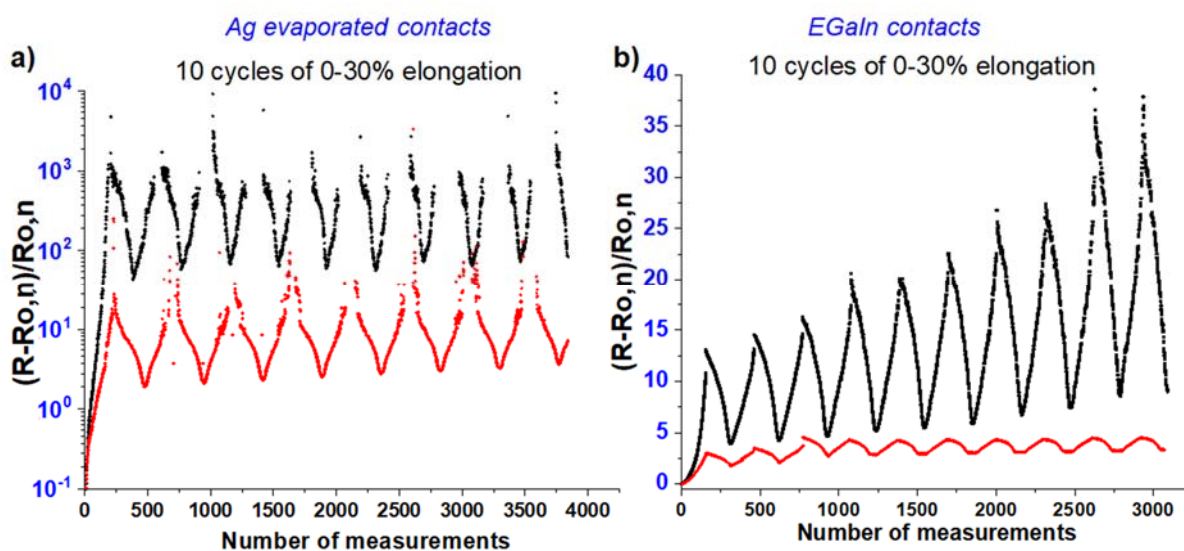


Figure 6-9: Resistance relative change during 10 cycles of stretching until 30 % of elongation for two different types of contact configuration: a) silver evaporated contacts between the AgNW/PDMS film and the metallic jaws, b) EGaIn liquid metallic alloy placed as a bridge on top of the jaws and the nanowires (please note the semi-logarithmic and linear y-axis, respectively, for silver evaporated and EGaIn contacts). In each case, two different AgNW network densities are tested, a sparse (black) and a denser one (red points).

➤ Fast stretching

During this experiment, the AgNW/PDMS composite is quickly stretched and released at a speed of 15 mm/sec. This experiment consists of performing 100 cycles at each 5% elongation (5%, 10%, 15%, ...) until 30%. Each stretching value will be separated by 20 cycles at 0%, which simply corresponds to measure twenty times the resistance of the sample at rest. A cycle

consists of stretching the polymer until a certain elongation, come back to the initial position and perform an electrical resistance measurement. The graph on the Figure 6-10a shows the relative, normalized resistance variation during the fast stretching experiment of a sample with an initial, normalized resistance of 8.6 Ω . There is a strong increase of the resistance, observed from the 20% elongation and on. Furthermore, for each elongation step, we can observe a linear increase of the relative resistance variation with an increasing gradient α . It can be transcript into a mathematical form by the following equation:

$$R_n = R_{n,0} \cdot (1 + \alpha(\sigma) \cdot N) \quad (6-4)$$

with R_n the normalized resistance, $R_{n,0}$ the initial normalized resistance, α the ramp of resistance gain, σ the stretching value and N the number of cycles. The plot of the ramp of resistance gain as a function of the elongation in Figure 6-10b, presents almost the same linear increase until 15 %. For higher elongation step, the degradation of AgNW network is no longer linearly advancing but instead increases rapidly. This behavior can be explained by the fact that at low stretching, there is a certain degradation of the AgNW network and the nanowires that are displaced during the stretching and do not return to their exact initial position after releasing. Still, the nanowires get back in contact, even if they are no longer well sintered as when firstly embedded to the PDMS layer. At higher stretching, as we have previously observed by *in situ* SEM during stretching,²³⁶ some cracks appear on the polymer substrate, perpendicular to the direction of the stretching in order to relax some elastic energy. At the location of the mechanical crack, the nanowires are broken and thus the corresponding percolation paths are disconnected, which leads to an important degradation of the network, measurable by the sharper electrical resistance increase. These cracks are partially reversible/healable, because we observe a small decrease of resistance after the 100th cycle at 25% and 30%. This means that if we waited longer, the polymer would start healing and the nanowires into the cracks could get back in contact and reform a percolative path. It is interesting to check if we could reach back to the initial resistance value. To verify this, we performed the same test on the same sample eight days later and we plot the normalized resistance in Figure 6-10c. Firstly, we see on this graph that the initial resistance of the PDMS band of 8.6 Ω is not recovered one week afterwards, but the resistance is now 84.9 Ω . However, an important improvement of 68% is visible compared to the last resistance measured after the 30% elongation. Then, we repeated the previous measurement and this time the increase in the electrical resistance occurs faster. This could be explained due to the existing damages on the AgNW network and the polymer

substrate. In particular, the nanowires junctions are still non-optimized and even a small mechanical stress of the polymer matrix can further destroy these already weak junctions.

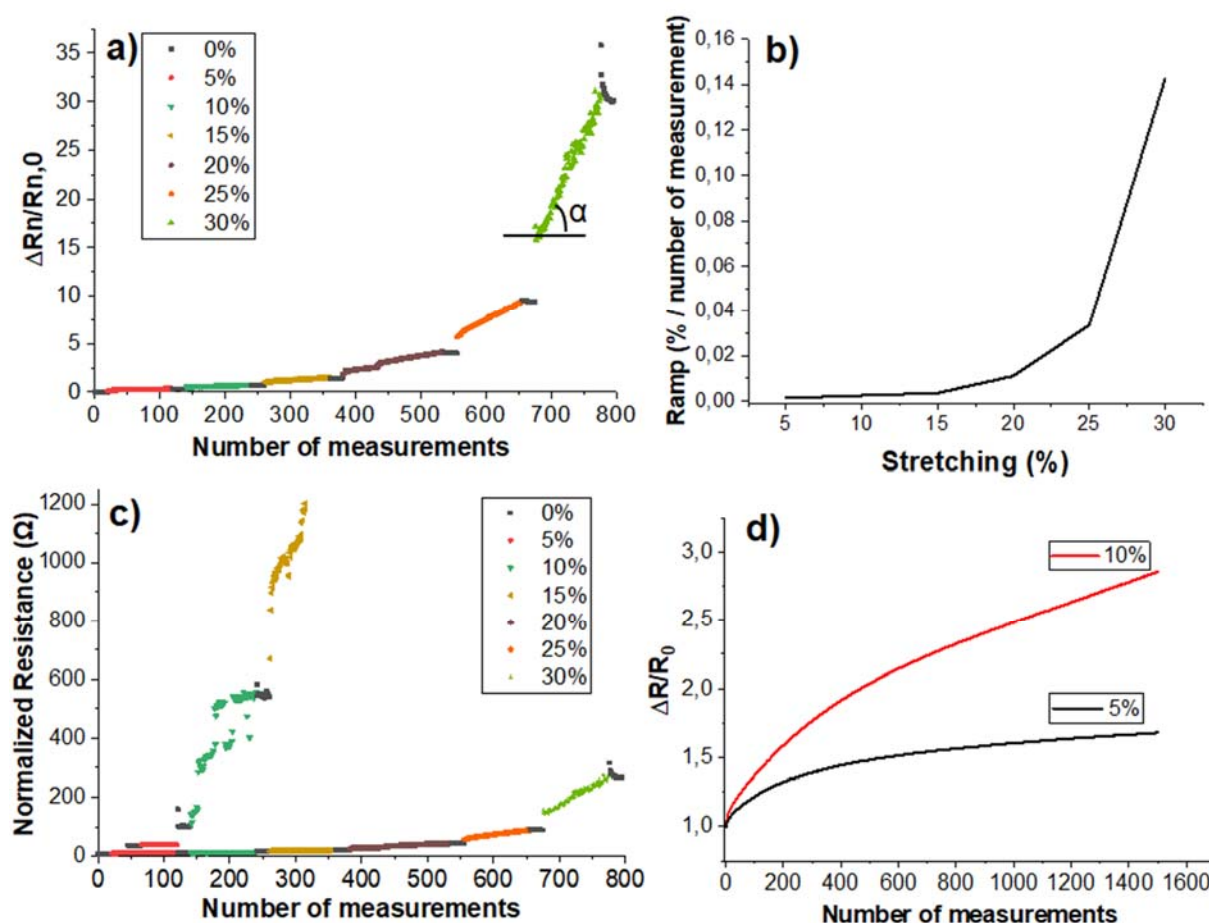


Figure 6-10: a) Fast stretching test of a AgNW/PDMS composite were 100 stretching cycles we performed at each 5% of elongation until 30%, separated by 20 stretching cycles at 0%. An example of ramp calculation is shown for 30% of elongation. b) Degradation ramp as a function of the stretching value. c) Comparison between first and second fast stretching measurement on the same sample. d) Endurance of the AgNW/PDMS composite during 1500 fast stretching cycles at 5 and 10% of elongation.

The previous experiment is useful to better understand the properties of the composite. It is necessary also to study the endurance of the electrical properties. Thus, we perform mechanical tests of 1500 fast stretching cycles at a constant elongation of 5% and 10% to AgNW/PDMS bands cut from the same sample. The initial resistance of the bands presented here, is 17.8 Ω and 21.8 Ω , respectively. A more important degradation is expected for the sample that undergoes a higher elongation, similarly to the previous experiment. The results in Figure 6-10d demonstrate that after 1500 cycles at 5% of elongation, the increase of the resistance is only 2.5 times compared to its initial value, which corresponds to a final resistance of 29.9 Ω . Moreover, the increase of resistance between each cycle reduces and seems to stabilize after

approximately 500 cycles. It seems that there is a certain deformation of the AgNW network in the beginning of stretching, most probably due to the cracks appearing on the polymer substrate. This has a direct impact to the increase of the electrical resistance of the network. Since the stretching elongation is the same, after the deformation, the network shows a more stable performance; during the rest of the cycles, there is a slight increase in the electrical resistance. A similar behavior is observed for the stretching at 10% of elongation but with a larger increase of the electrical resistance. Actually, the resistance measured after 1500 cycles is 4 times higher than the initial one. Also, the resistance has not reached the saturation regime as it was observed for the 5 % elongation, meaning that the deformation of the polymer substrate and subsequently of the network is continuing.

➤ Slow stretching

In this part, we investigate the stretching speed impact on the electrical resistance of the AgNW network embedded in the PDMS. For this purpose, we choose a slower elongation mode of stretching and releasing, during which we measure the electrical resistance at each second. We usually repeat 10 consequent stretching-releasing cycles. The electrical response of two bands cut from the same AgNW/PDMS sample is compared in **Figure 6-11**, for a maximum elongation of 30 %.

Their initial normalized resistance is 16.8 Ω and 10.7 Ω , and the stretching speeds 0.04 mm/s and 0.08 mm/s. The experiments reveal a clear impact of the speed elongation on the increase of the electrical resistance. Indeed, we observe that the final resistance of the stretched sample with the lower speed is higher than the resistance of the sample that is stretched faster. We could assume that this variation is due to the total time the samples are exposed to mechanical stress, as it takes the double time for the AgNW/PDMS composite with the lower elongation speed, to reach the maximum 30 % elongation.

Three-layered AgNW/PDMS/AgNW fabrication. As mentioned in the beginning of this sub-chapter 6.2, our aim is to integrate in an efficient and reproducible way the AgNW/PDMS composites in piezoelectrets for energy harvesting applications. For this, we need a sandwich-like configuration with the AgNW network being the top and bottom stretchable electrodes, while the active material, like a PDMS with charged cavities, is in the middle (see Figure 6-7e). By contacting the top and bottom AgNW networks we are able to collect the current from the piezoelectret and measure its dielectric properties, like its capacitance. Roughly, our approach to fabricate the above configuration is to stick the AgNW/PDMS layers to the PDMS

piezoelectret, which means create a robust PDMS/PDMS bonding. In the paragraphs to follow the different techniques, which we tested to bond the PDMS/PDMS layers, are presented. The PDMS is one of the most used polymer in microfluidics, thus its adhesive properties have been well explored and some bonding techniques have been already studied.²⁹⁷ However, in our case we have the AgNW network embedded on the PDMS, and special attention should be given in order not to damage the nanowires by techniques, like plasma or UV treatment. All the tested techniques are listed in **Figure 6-12**. We list the techniques into two groups to separate the method where the bonding is performed, before or after the peeling-off of the AgNW/PDMS layer from the glass substrate.

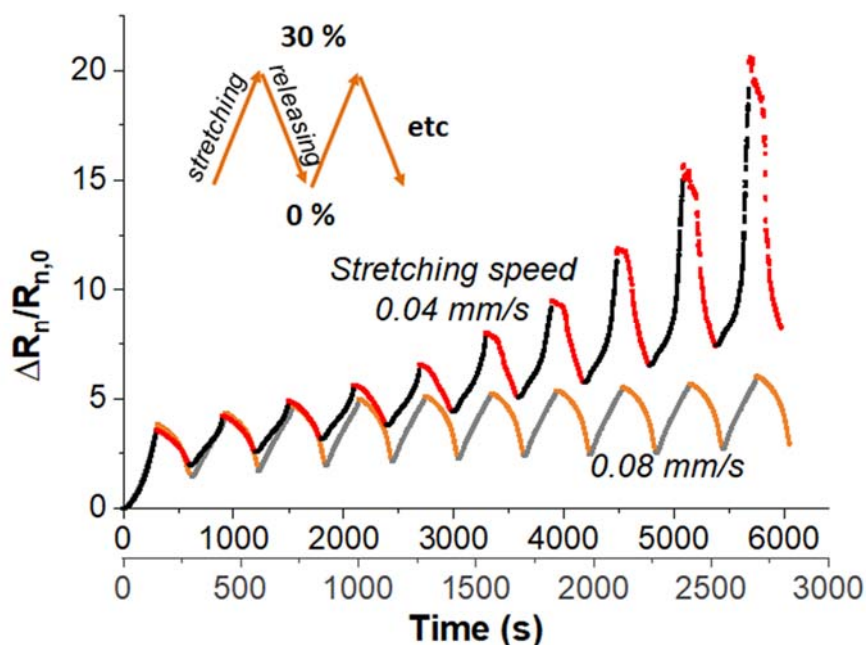


Figure 6-11: Comparison of the stretching speed impact on the relative variation of the normalized resistance during the slow stretching measurement. For an easier comparison, two different time axes are plotted because of the different elongation speeds; the upper x-axis corresponds to the slower stretching (0.04 mm/s) and the lower x-axis to the higher speed (0.08 mm/s). The measurement of the resistance is performed continuously at every second, during the 10 cycles of stretching up to 30 % and the releasing to 0 %.

➤ Plasma O₂ bonding before peeling-off

Plasma O₂ bonding is one of the most used techniques for the surface modification of polymers to improve their adhesion.²⁹⁷ When the PDMS is undergoing a plasma etching, there are hydroxyl groups which are formed and create adhesive forces with a substrate or another PDMS

layer.²⁹⁸ The process we followed is to deposit the PDMS and bake two AgNW/PDMS layers on Corning glass, as described in the previous paragraph, without the peeling-off step. Then, we put the samples into an oxygen plasma machine for 2 min with an RF power at 12 W and a pressure of 0.4 Torr. After the treatment, we directly bonded them by hand pressure for around 1 minute and we obtained a AgNW/PDMS/AgNW sandwich, encapsulated by two Corning glass substrates. Finally, we peeled-off the sandwich into a water bath to remove the glass substrates. The result was not very successful because the bonding was not strong enough to separate the sandwich from the glass substrates. Indeed, when we tried to bind the two layers, we noticed that mostly the corners of the PDMS layers are in good contact. The corners of the PDMS layer are thicker due to the border effects created during the spin coating of the liquid PDMS to the 50x50 mm² square substrates. In addition, due to weak contact between the PDMS layers, some water can pass through the interface and destroy the hydroxyl group. Then, we decided to change the plasma parameters to optimized values reported by Bhattacharya et al.²⁹⁹ We repeated the same process, this time with a plasma treatment of 30 seconds, the RF power at 20 W and pressure at 0.7 Torr. We tested the peeling-off both in and out of the water bath and also we tried the removal of a larger band on the edges, in order to reduce the border effects, but still without success. In all the cases, the problem originates mostly from the roughness of the cured PDMS layer. The surface parts which are in well contact are not enough to ensure a strong adhesion between the two PDMS layers during the peeling-off.

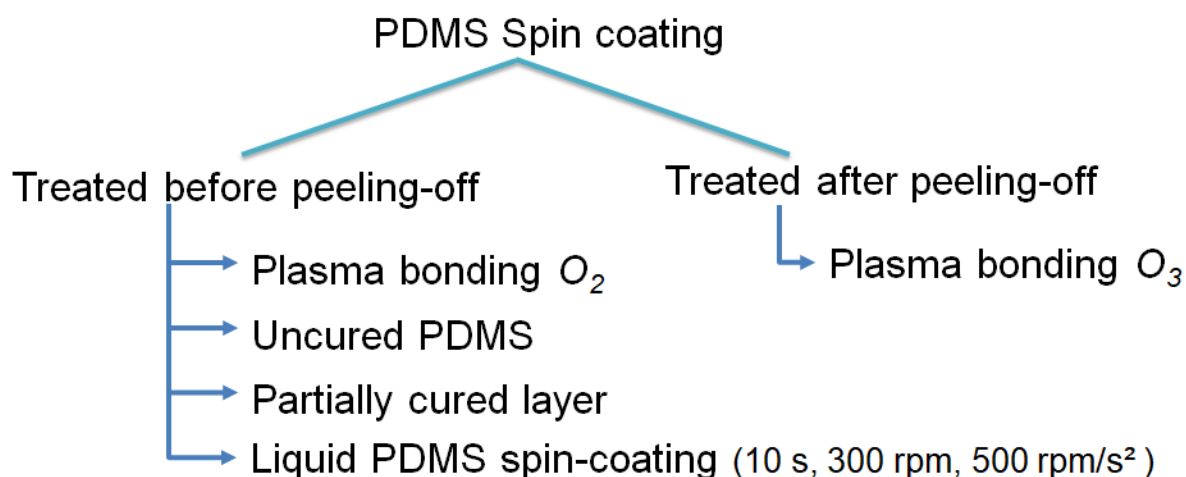


Figure 6-12: The different techniques tested for the PDMS/PDMS bonding, related to the fabrication of AgNW/PDMS/AgNW sandwiches for piezoelectric applications.

➤ Plasma O₃ bonding after peeling-off

We decided to peel-off the PDMS layers before the plasma treatment and bonding, in order to reduce the adhesive forces between the glass substrate and the PDMS. We also switched to ozone plasma. After the peeling-off step, we placed again the layer on the Corning glass with the same configuration as before (from bottom to top: Corning glass/AgNW/PDMS). The result was successful and we obtained our first composite sandwich. This time even when removing the glass substrate directly in air and not by the water-assisted procedure, the separation from the glass substrate was smooth. However, with this technique, we still need to peel-off the composite layer before the bonding. In addition, the adhesive force is rather low due to the non-homogeneity of the cured PDMS layer thickness, as discussed for the previous technique. We should be able to find an easier and more efficient process in terms of adhesion.

➤ Uncured layer

After some researches, we decided to use directly the PDMS properties to proceed to the bonding, which way should offer a better adhesive force.²⁹⁷ One of the techniques is called “stamp-and-stick” bonding technique and it consists of using a liquid layer of PDMS as a glue.³⁰⁰ According to this, we deposited a layer of liquid PDMS on a glass substrate by the following spin coating parameters: 8-9 min, 8000 rpm, 500 rpm/s. This way the layer fabricated should be very thin, around 1-1.5 μm thick. After 15 minutes, we transferred the liquid PDMS layer to the surface of one of the AgNW/PDMS composites already deposited and cured on glass substrates. Finally, we bonded the two AgNW/PDMS and cured the sandwich at 90°C for 15 minutes to solidify the intermediate adhesive liquid PDMS layer. However, once more the problem was coming from the border effects, the intermediate adhesive layer is badly transferred to the already cured AgNW/PDMS composite and the desired sandwich was not successfully fabricated by this protocol. Therefore, we decided to modify it by removing the transfer step. Indeed, we directly deposited the PDMS by spin coating on the cured composite. We changed also the parameter of the spin-coater (1 min, 1000 rpm, 500 rpm/s) in order to obtain a thicker glue layer, which could be able to fill efficiently the air gaps between the composite layers during bonding. The final result with this modified protocol is successful apart from some big bubbles appearing in the PDMS. The formation of the bubbles can be avoided if we increase even more the thickness of the PDMS glue layer, or by a more progressive bonding, starting the stamp from one edge and not directly stick the opposite PDMS surfaces. Finally, it is important to note that this technique allowed us to reduce the post-process step. In this case, we just need to deposit a PDMS layer after the AgNW/PDMS composites fabrication.

However, we can look for a further reduction of the number of fabrication steps thanks to the next technique.

➤ Partially cured layer

Unlike the previously presented bonding processes, this one is performed during the AgNW/PDMS composite fabrication. Indeed, instead of performing the full curing of the PDMS, we perform a partial curing. The latter consists of reducing the annealing temperature to 55°C and the curing time to 24 minutes. These parameters have been reported as optimal by Go et Shoji.³⁰¹ After this baking, we obtained a PDMS layer not totally cured and still rather sticky. Then, we proceeded to the bonding of the AgNW/PDMS partially cured composites, by hand pressing and finished the curing of the sandwich. We decided to put a weight (0.5 kg over an area of 25 mm²) on it to maintain the compressive force and then we placed it inside an oven at 160°C for 30 minutes. Finally, we performed the same water-assisted peeling-off procedure as before and obtained successfully the sandwich. This technique requires two ovens at different temperature, but the bonding is performed directly during the composite fabrication. The main drawback is that we do not control the thickness of the PDMS layer because some crushing can occur during hand-pressing bonding. In a next test, we should try to place a spacer of known thickness between the Corning glasses. This spacer can be easily fabricated thanks to the 3D-printers at our disposal in the lab.

➤ Liquid PDMS

This last technique is not a new bonding technique but includes a different configuration; instead of depositing PDMS on top of the AgNW networks in two separate Corning glass substrates and then try to bond them, we deposited the PDMS by spin coating only to one of the two glass substrates and then embedded the second substrate with the AgNW network directly on top of the liquid PDMS. We obtained a layer of liquid PDMS with AgNW network on each face, enclosed between two Corning glasses that we cured it as described previously. After peeling-off in water bath, we obtained the desired sandwich. This technique is successful for the fabrication of the AgNW/PDMS/AgNW composite but we cannot easily control the thickness of this layer. Here again, some PDMS can flow out of the glass substrates during the hand pressing bonding. In order to solve this problem, we decided to build a 3D-printed mask. This mask is a spacer with square shape of 47.5 mm side and of 0.5 mm height. This allowed us to control the distance between the two glass substrates and remove the borders. We repeated the last process by changing the spin coating parameters in order to obtain a thick layer (10s, 300rpm, 500rpm/s). We added the mask on the liquid layer before bonding with the other glass

substrate and proceeded to the curing. The final sandwich could be successfully separated by the glass substrates and it possesses a known thickness of 200-300 μm . In addition, this technique needs only one oven and no supplementary step to produce the final product.

Comparison and conclusions. We have tested several techniques of sandwich preparation, in order to apply them to the piezoelectret fabrication. Apart from the process simplicity and reproducibility, in order to choose the most appropriate technique, we searched for the one that provides AgNW networks with the best electrical performance. Thus, we will compare the electrical resistance of each AgNW network side of the sandwiches. The results are summarized in the table of **Figure 6-13a**, results which correspond to the as-deposited AgNW network resistance and the one after the AgNW/PDMS/AgNW fabrication. The results show that there is always one AgNW side of the sandwich which is more resistive than the other. This difference occurs during the peeling off process. In fact, when we remove the first glass substrate, the peeling off separates directly the whole glass from the PDMS layer, which is practically not favorable for the transfer of the nanowires to the polymer, as it schematized in Figure 6-13b. Instead, it can leave parts of the AgNW network on the glass, visibly seen like the ones showed in photo in Figure 6-13c. On the contrary, for the second glass substrate, the peeling off is done more progressively, because here we touch and tear off the polymer film that is flexible. Besides, we notice that the uncured layer technique is the less affected by such phenomenon, showing similar resistances between its two sides. However, it shows a significant increase in the electrical resistance compared to the initial value of the corresponding as-deposited AgNW network. Thus, in terms of the difference between the initial and final resistance and not between the two AgNW/PDMS sides, the most efficient technique is the partially cured layer. Ultimately, all these techniques have to be adapted to the final piezoelectric system. Actually, as the interleaved layer is beforehand functionalized with the cavities array, we cannot use easily the glue polymer solution for the bonding. Concerning the uncured layer technique, the PDMS film deposited on the composite film has to be as thin as possible in order to avoid an important volume variation of the cavities. Finally, the most adapted technique seems to be the partially cured one because the PDMS has already started to crosslink. Thus, with a gentle pressing, we can expect to fabricate our piezoelectret without interfering with the size of the cavities. Further experimental investigations are still needed to improve the process of sandwich separation from holders in order to obtain approximately the same resistance for both faces. The use of a flexible substrate, like Teflon, could be beneficial for the peeling-off step. In addition, we could also try to mix PDMS with Zonyl FS-300, a fluorosurfactant which is an

effective compound to lower the surface tension of aqueous solutions,³⁰² in order to improve the adhesion between the nanowires and the polymer, as already reported by Wang et al.³⁰³

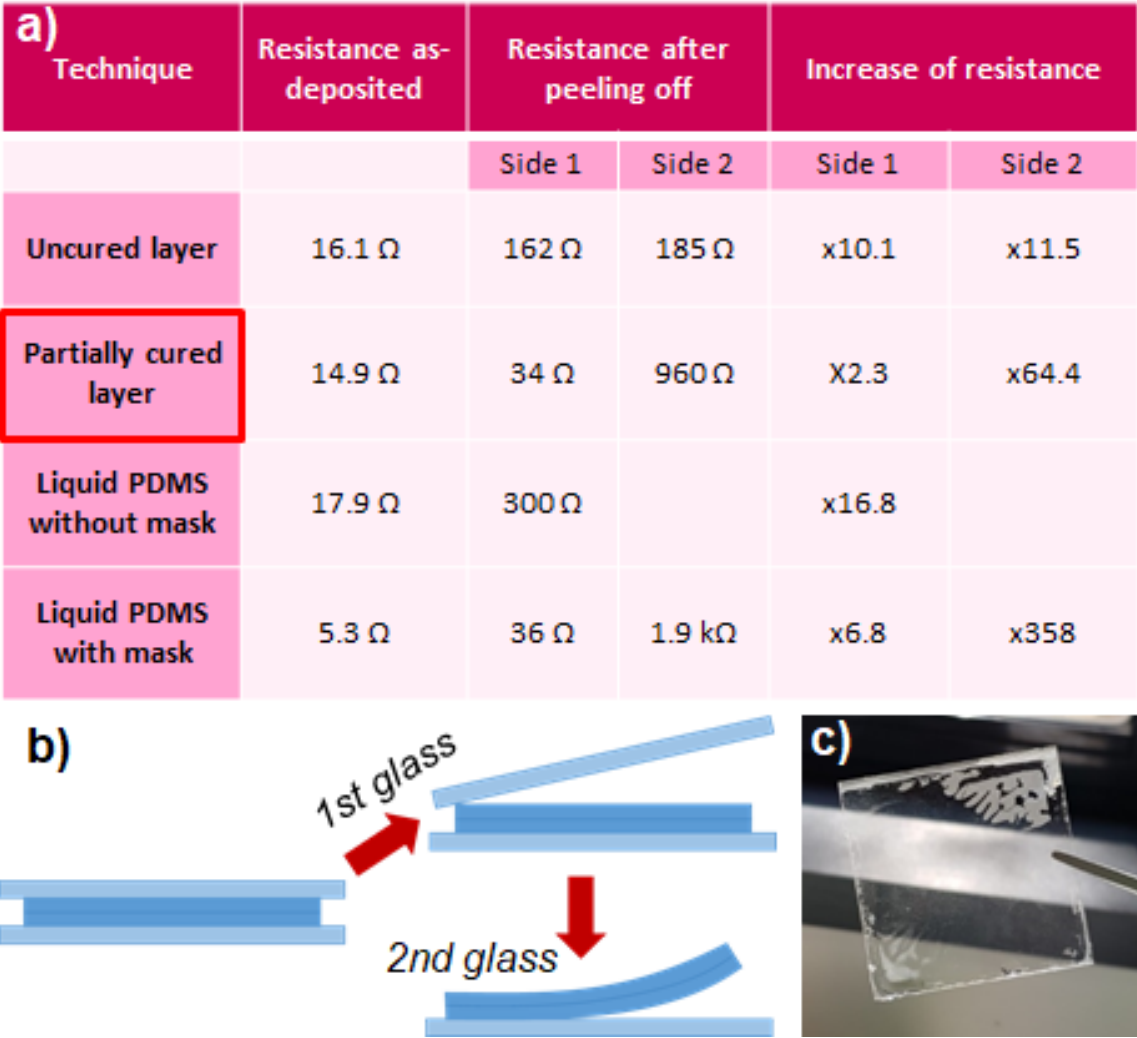


Figure 6-13: a) Table summarizing the electrical resistance before and after the sandwich fabrication for different PDMS bonding or curing techniques. b) Schematic of the AgNW/PDMS composite separation from the Corning glass substrates. c) Photo of the Corning glass substrate after peel-off, showing the remaining nanowire network.

6.3. Industrial collaborations on medical and energy applications

In this section, we continue presenting the applications related to AgNWs, with a brief presentation of the two ANR projects, in which our team is participating, in collaboration with laboratory and industrial partners.

PANASSE: MNW based cold cathodes for miniaturized X-ray sources. The first project, named *PANASSE*, concerns the developing of MNW-based cold cathodes for X-ray emission in future, compact micro-devices. In general, electron sources are used in many applications, and can be based on the thermionic emission mechanism, where electrons are emitted from heated filaments. Besides, when they are subjected to high external electric field, electrons near Fermi level can tunnel through the energy barrier and escape to the vacuum level. This field emission is a preferred mechanism for certain applications because no heating is required and the emission current is almost solely controlled by the external field.³⁰⁴ Such an extremely high field can be obtained on a sharp tip of a very thin needle, because electric fields concentrate at the sharp points. CNTs possess properties favorable for field emitters such as high aspect ratio and a sharp tip.³⁰⁵ That is why since the beginning of 90s and the discovery of CNTs, these carbon nanomaterials have been recognized as one of the most promising electron field emitters in various vacuum microelectronic devices like cold cathode flat panel displays, with the ability to provide single or multiple electron sources.³⁰⁶ Inspired by the nowadays state-of-the-art CNT cold cathode developed by Thalès Research and Technology (TRT) at Palaiseau,³⁰⁷ the consortium in *PANASSE* ANR project (2019-2022) is working on an alternative geometry for the field emission: a planar MNWs configuration, that can offer significant advantages compared to the classical tip emission. There is already proof-of-concept about planar emission structures reported in literature for CNTs,^{308,309} and also from our preliminary studies in the framework of *PANASSE* for AgNWs. Dr. Jean-Paul Mazellier is the project coordinator and with his scientific team in TRT, they prepare Si wafers with the sub-cells of different contact geometries for the electron emission measurements, also performed in TRT after the final steps of the cathodes preparation. Apart from the experimental processing, they have developed numerical simulations to determine the ideal configuration of the cold cathode. The experimental and modeling results obtained during the internship of Enzo Rongione in TRT (M2 internship 2019) are very promising for the future development of the miniaturized devices. Moreover, the laboratory partners from IEMN in Lille, Dr. Maxime Berthe, Dr. Dominique Deresmes and Dr. Thierry Melin, have a significant expertise in the nano-characterization. The charge monitoring by AFM measurements and the 4-point probe electrical

measurements by Scanning Tunneling Microscope (STM-Nanoprobe) integrated in SEM, can reveal essential information about the nanowires and the dielectric spacers properties and configuration.^{310,311}

From our side in LMGP, we are performing the MNWs deposition by spray coating and the oxide thin films deposition by AP-SALD, aiming to functionalize and optimize it for the purposes of the specific device. The main fabrication steps are presented schematically in **Figure 6-14a**, starting from the spray coating. SEM image in Figure 6-14b shows AgNWs deposited on Si/SiO₂ wafers with Ti-Au contacts patterned by UV-lithography in TRT. The nanowires have a surface planar configuration, which means to be arranged on the surface with one of their (100) crystallographic plans parallel to the substrate, as they are laid down in a horizontal position, with one side of their pentagonal cross section on top of the insulator SiO₂ layer. Therefore, their opposite tip can serve as top emitting edges as we will discuss in details later on the present section. This time, the concept of the device differs from the nanowire network configuration, because in *PANASSE* we focus on a single nanowire device fabrication, in order to achieve the desired size reduction and the efficient control of its performance, avoiding the screening of the field emission by neighboring nanowires. Our will is to keep the advantage of the simplicity of the nanowires spray deposition and on the same time achieve the highest possible amount of devices where only one single nanowire is placed between the contacts. We optimized the areal mass density to a very low value around 2 mg/m², which was also verified by numerical simulations. As already mentioned, Konishi et al. have shown that the emission current from the sidewalls is larger than the emission from the tip of MWNTs, and even dominates the tip-based emission current by one order of magnitude, reaching the microampere.³⁰⁸ Thus, planar nanowires based cold cathode could offer higher emission current thus higher brightness. Also they would provide enhanced thermal management, flexible design and larger surface production, fabrication cost reduction etc.^{308,312} However, the side walls of the MWNTs have weaker electric field concentrations on their surface, which results in a higher turn-on voltage than that of the tip of MWNT, thus one should apply a higher voltage to obtain same emission order of magnitude as in tip-based emission case.³⁰⁸ Therefore, one of the main goals of the *PANASSE* project is to explore ways to increase this factor for the sidewall emission, linked with parameters as the system geometry. On the same time, we need a high permittivity material to partially passivate the nanowires. This feature is achieved by the deposition of so-called spacer, a dielectric layer like Al₂O₃, as schematically presented in Figure 6-14a-iii. As we have already demonstrated in our studies presented in the previous chapters,

the AP-SALD build up in LMGP, is a versatile, fast and low-cost method for the deposition of such oxide thin films. A last step in the fabrication of the cold cathodes is the semi-encapsulation or the partial top-uncapping, in order to remove a part of the dielectric spacer, as it illustrated by the schema of Figure 6-14a-iii and tangibly shown by the SEM images in Figure 6-14c and d, before and after this process, respectively. This plays a twofold role on the resulting electron emission. First of all, the partial top-uncapping is essential as it allows the electron field emission from silver to flow and enhance the top side tip emission. Then, the presence of the spacer in the bottom can minimize the electrical impact of the nanowire to the insulator layer below, because a possible charging of the insulator layer can lead to the breakdown of the local electric field. The partial top-uncapping is performed thanks to the Ion Beam Etching (IBE) method in TRT and the resulting height of the etching is crucial and needs to be further investigated and optimized, since the emission is favored in the pentagonal edges of the nanowire and there are potentially three tips of the pentagonal exposed directly to the etching.

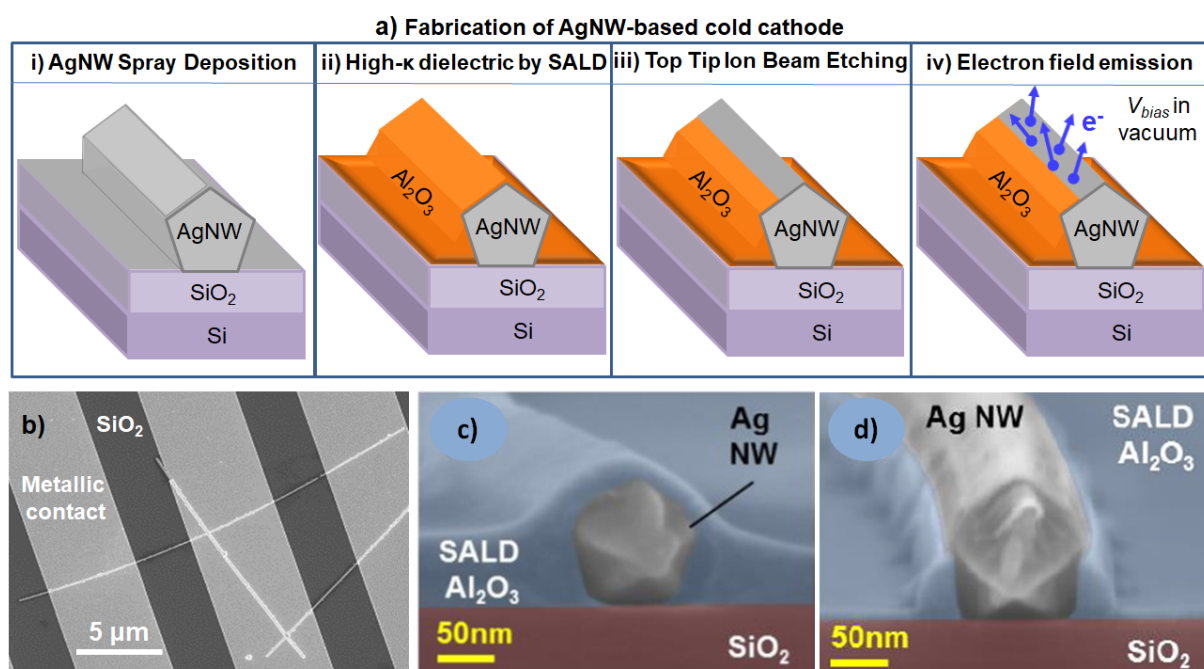


Figure 6-14: a) Schematic representation of the main fabrication steps of AgNW-based cold cathodes including i) the AgNWs spray deposition, ii) the encapsulation of the AgNWs by a high- κ dielectric oxide, like Al_2O_3 by AP-SALD, iii) the partial top-uncapping of the AgNW top tip sides by ion beam etching (IBE), iv) the electrons planar emission when submitted to an electrical bias in vacuum. b) SEM top-view of the sprayed nanowires on top of the Si/ SiO_2 wafers patterned with Ti-Au metallic contacts by UV-lithography. c) SEM image of the fully encapsulated AgNW by Al_2O_3 (step ii). d) SEM image of the partially top-uncapping of AgNW (step iii). The SEM (b-c-d) is performed by TRT.

In addition, we have investigated several other parameters such as different patterns and materials for the cold-cathodes contacts and variable SiO_2 insulator layer thicknesses. The results so far appear promising since we have measured experimentally a field emission starting

at a threshold voltage of $V_{th} = 60$ V and the electron emission reaching a maximum current of $I_{max} = 300$ pA. Moreover, when switching twice the bias from 60 V to 80 V, there is no observed hysteresis, which means that the spacer can reduce effectively the charge injection into the insulator substrate. At present and future work, we are testing: i/ various nanowires dimensions to fit better the patterned contacts, ii/ different AgNWs provenance (associated with different synthesis conditions for instance) from other laboratory and commercial sources, iii/ CuNWs, which could lower down even more the cost production, iv/ other dielectric spacers, since today the team of AP-SALD at LMGP can elaborate several thin oxide films. Future steps of *PANASSE* project include the elaboration of a collective emission cathode and the emission enhancement, leading to a progressive upscaling, in order to maximize chances to reach high current delivering cathodes. Our work aims to the production of innovative field emission structure for future compact X-ray imaging systems, and in particular computed tomography equipment for 3D reconstruction. Still, there is a large variety of electronic technologies that could use miniaturized field emission devices and in general, the study of the planar metallic nanowires electron emission properties, coupled with thin dielectric films, can be useful for other topics too.

MEANING: up-scalable fabrication of MNW network based transparent electrodes (TE) for organic photovoltaic (OPV). In collaboration between chemists and physicists on MNW networks and an industrial partner, developing organic solar cells, we aim, through the *MEANING* project, to contribute to the large scale production of flexible OPV. The team of Prof. Mona Tréguer-Delapierre in ICMCB, with whom we have collaborated in other projects too (see Chapter 3),³⁸ have a great expertise in the synthesis of novel nano-objects and the functionalization of hybrid nanostructures.^{313,314} Thus, the rapid and upscaling growth of AgNW and CuNW will be studied towards mass, low cost production processes. Then, our role in LMGP related to the *MEANING* project, includes the optimization of electrical, optical and mechanical properties by varying the deposition methods and applying post-treatment techniques, such as the thermal annealing previously searched by our team (see Chapter 1.2.4). Once more, the investigation and enhancement of stability is crucial for the further industrial applications of MNW networks. Apart from the stability, some other issues that we aim to improve concerning the performance of MNW networks on OPV, is the reduced charge collection efficiency due to the empty space between the nanowires,²¹⁸ the homogeneity of the network that can influence the electrical properties (see Chapter 5), the surface roughness of

the nanowires that can create electrical shorting problems with the OPV layers,³¹⁵ and the poor adhesion with the substrate.³¹⁶ To address this, MNW based nanocomposites with polymers, carbon nanomaterials or oxide thin films, are being investigated, like in our previous studies, where AgNW/oxide nanocomposites can lead to a clear stability enhancement (more details were presented for example in Chapter 1.3 and 5.4). The ultimate goal of *MEANING* project is the efficient integration of this robust technology into organic solar cells, developed by the project's industrial partner, ARMOR. Being founded almost a century ago, ARMOR was the first company to produce carbon films in France and continued being innovative in several applications during the 20th century. Since they have developed a great expertise in the formulation of high-quality inks and in the high-speed coating of fine layers on ultra-thin films, they have focused the last decade, on the production of non-toxic, environmentally friendly, organic photovoltaic films, ASCA®.³¹⁷ **Figure 6-15** presents preliminary tests that we have performed in LMGP, on 2.5x2.5 cm² samples cut from AgNW networks deposited by ARMOR on 30x30 cm² flexible substrates (PET) with R2R. The samples are very stable under bending with a curvature radius of 5 mm. As shown in Figure 6-15a, the electrical resistance increases only 3 % after 10,000 bending cycles. The inset photo shows an example of OPV film developed by ARMOR. The AgNW networks demonstrate also excellent electrical performance under electrical and thermal stress, during several plateau and repetitive ramp cycles, respectively (Figure 6-15b-c). Finally, the electrical resistance is very stable when the samples are constantly heated for 6 hours on 120 °C, as presented in Figure 6-15d. The results are promising for the future integration of the MNW networks in the OPV films of the project.

As we are currently continuing our studies, a conclusive remark here would be that *MEANING* is a great example describing the entire procedure behind the development of a new application; starting from the first fabrication attempts and fundamental studies of the physical and chemical properties, followed by the optimization, reproducibility and stability enhancement, leading finally to the industrial integration, testing and feed-back, before the ultimate mass production. Every step of this academic and industrial R&D is crucial and there is a significant importance on the efficient coordination and interaction between the different steps and partners, rather than on a straightforward, linear process.

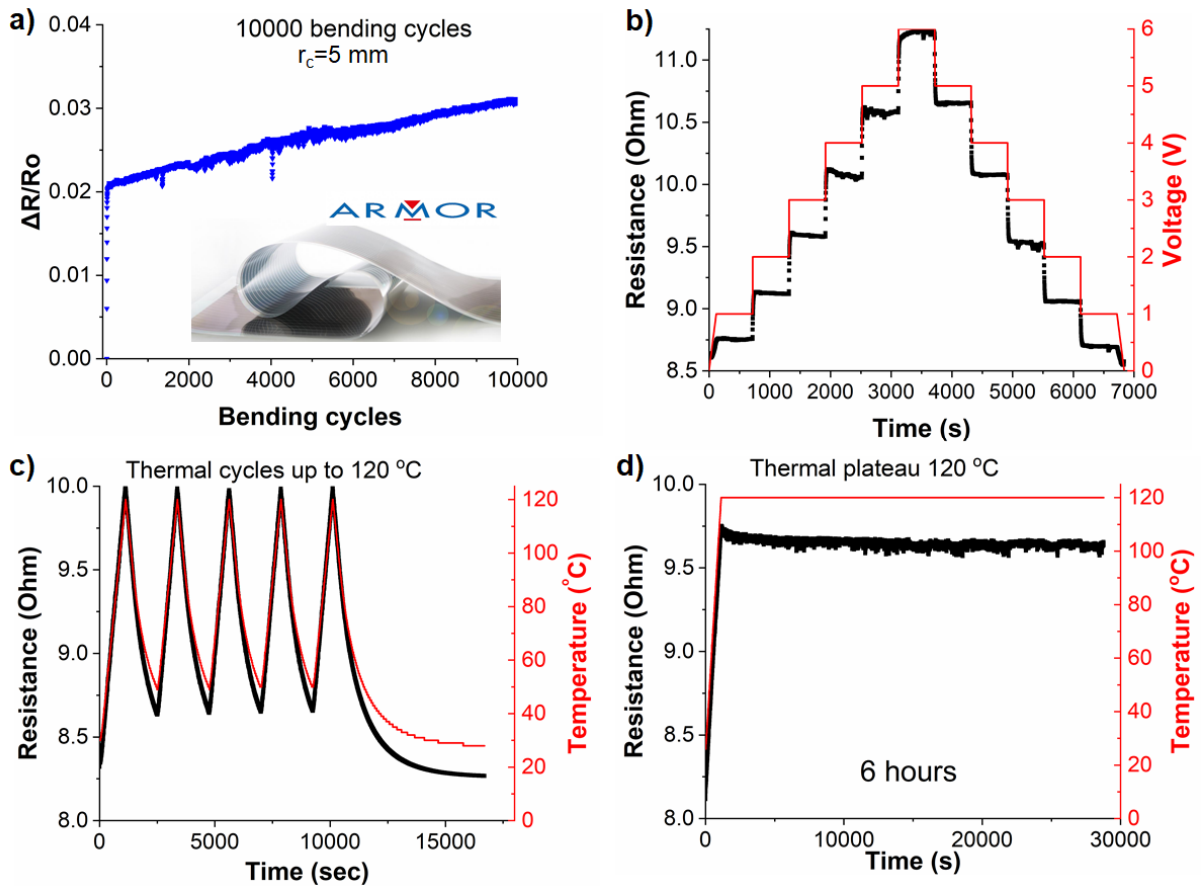


Figure 6-15: Electrical resistance characterization, performed in LMGP, for AgNW networks deposited on PET substrate by R2R techniques developed by ARMOR: a) 10,000 bending cycles with 5 mm radius curvature. The inset is a photo of the OPV films developed by ARMOR.³¹⁸ b) Increasing and decreasing voltage plateaus, staying 10 min at each voltage bias. c) Five thermal cycles between 50 and 120 °C with a thermal ramp of ± 5 °C/min. d) Thermal plateau of 120 °C for 6 hours. The samples size is 2.5×2.5 cm², cut from the 30×30 cm² films, and the bias applied for the electrical measurements during the mechanical and thermal tests is 1 V.

6.4. Thermal annealing effects on Ag@polymer reflective conductive coatings

This last part of chapter 6 concerns a different technology than the transparent conductive materials, those of Ag@polymer coatings that are elaborated by the scientific team of Dr. Lavinia Balan (IS2M-Mulhouse, CEMHTI-Orleans), and investigated also during the PhD thesis of Marine Dabert, conducted on the same period of time with my thesis. In the framework of our collaboration, we performed the electrical characterization of these hybrid materials in LMGP, focusing on the effect of thermal annealing. Such nanocomposites filled with AgNPs can provide attractive optical, electrical or antimicrobial properties, by tuning the nature of the metal and their synthesis.

Photo-induced synthesis. Many strategies to obtain metal nanoparticles have been developed,³¹⁹ and can be distinguished by two types of preparation : top-down and bottom-up approaches. The first one focuses on the formation of nanoparticles from bulk metal. Simakin et al. have used laser ablation of silver, gold, or titanium to generate nanoparticles in liquid media in order to obtain colloidal solutions³²⁰. On the other hand, the bottom up approach refers to a synthesis of nanoparticles by mostly chemical or photochemical routes from metal precursor salts, particularly in the case of silver. Several steps are required, as studied by Gupta et al.; the first step is the reduction of citrate which leads to silver nanoparticles and the second is the polymerization in the presence of particles.³²¹ In order to optimize this synthesis, Southward et al. developed a one-step process to obtain Ag@polymer nanomaterials. Curing and reduction of silver are managed at the same time, however the process requires long time at high temperature, typically 4 hours at 300 °C.³²²⁻³²⁴ In order to minimize the temperature and the process time, the photochemical approach appears to be a seductive alternative since it combines photo-reduction and photo-polymerization processes at ambient temperature that require only a few minutes to generate the target material.^{325,326} Following this approach, the scientific team of Dr. L. Balan has previously introduced a new method to create metalized surfaces (Ag or Au) by nano-assembling metal and polymer using an one-pot, one-step photo-induced process.^{326,327} This nano-assembling has a very specific in-depth gradient concentration profile of AgNPs in the polymer matrix. As a result, the as-synthesized coating has a mirror aspect on its surface, like a metalized silvered coating, as reported previously.^{326,327}

Thermal annealing. Silver-filled materials exhibit good electrical conductivity and high temperature treatments have been used to improve more the conductivity, as it is described in chapter 1.2.4 for the case of AgNW networks. Similarly, Li et al. treated commercial silver

fillers at 600 – 800 °C for few seconds in order to remove surface lubricant initially responsible for the particle stabilization.³²⁸ Concerning Ag@polymer nanomaterials, Fantino et al. printed 3D polymer structures and then generated silver nanoparticles by heating at 200°C. This treatment was carried out under vacuum and resulted in a decrease of electrical resistivity by an order of magnitude.³²⁹ In all these thermal annealing processes, sintering is the main driving force to reduce electrical resistance at junctions between Ag nanoparticles or Ag nanowires; its origin being the reduction of surface energy.³⁰ This phenomenon increases the compactness of the layer formed by the nanoparticles and induces a multiplication of the conductive contacts between them and therefore a lower junction resistance.¹⁶

In our work, we studied the effects of heat treatment on the structural gradient that develops in the metallized coating and its influence on its main physical properties: electrical and optical. One of the priorities was to induce sintering between the nanoparticles in order to enhance electrical conductivity. In LMGP, we performed the post-treatment on top of a heating plate in ambient air. At first, several maximum temperatures were tested; at temperatures above 360 °C the polymer degrades and below 270 °C, no decrease in the electrical resistance is observed. Thus, the optimum maximum temperature is chosen at 350 °C. Before annealing, the samples were cut in 1.2x1.2 cm² pieces from the initial as-synthesized films and silver-paste contacts were placed in two parallel edges. The thermal ramp used from room temperature to 350°C, was set at a 5°C/min rate by a Eurotherm PLC driven by LabVIEW. This heating stage was followed by a cooling stage with a decreasing temperature ramp also of 5°C/min. The electrical resistance was measured *in situ* with a Keithley 2400 sourcemeter, using two probes and a very low voltage (0.2 V) to avoid any risk of electrical degradation. Additionally, the effects of heat treatment on AgNPs were studied by SEM and TEM imaging, X-ray diffraction analysis and photoelectron spectroscopy (XRD, XPS), optical reflectivity and contact angle measurements, conducted in IS2M-Mulhouse, with the contribution of our team in LMGP to the morphological analysis of TEM images by *ImageJ* and the crystallographic analysis. Several series of samples were tested with varying coating thicknesses, three different Ag concentrations and two different types of polymer matrices. In the paragraphs to follow, the main results of our study will be presented, concerning four different thicknesses of Ag@polymer coatings (10, 25, 50, 100 μm) with the same concentration of metal precursor Ag⁺ (5 wt. %) mixed with the photosensitizer to the polyethylene glycol (600) diacrylate monomer (PEG600DA).

Morphological characterization. The as-synthesized Ag@polymer coatings were characterized by SEM to observe the surface morphology of the metal top layer after UV photo-

generation (**Figure 6-16a**, left column) and after thermal post-treatment at 350°C (**Figure 6-16a**, right column). The average nanoparticles sizes after UV synthesis and after thermal treatment are reported on the table of **Figure 6-16b** and plotted in **Figure 6-16c** as a function of the thickness of the photo-generated metallized coating. First of all, after UV synthesis, we observe spherical nanoparticles near the surface, with an average diameter ranging from 25 to 200 nm, while the thickness of the coating increases from 10 to 100 μm (**Figure 6-16b**). The thermal post-treatment increases the particles size and induces the formation of a AgNP network near the surface. More specifically, the particle size increases by factors varying from 2.5 to 7, becoming more significant as the thickness of the films decreases, providing in all cases an increase of the surface roughness. The diameter of the smaller NPs, which corresponds to the thinner 10 μm coating, increases from 25 to 185 nm, while the larger ones from 200 to 500 nm, in the case of the thicker films. These observations stem from two main phenomena that reduce the total surface energy of the system: sintering and coalescence. This is related also to a slight oxidative degradation of the polymer, catalyzed by silver during thermal annealing at the air/coating interface. Southward et al. observed such a behavior when they heated silver/polyimide films between 300°C (non conductive surface) and 340 °C (conductive surface).³²³ Subsequently, the spherical AgNPs begin to aggregate into more elongated shapes, as also reported by Bhattacharyya et al.,³³⁰ which ultimately creates a silver network near the upper surface.

After observation of the upper surfaces, cross sections of the photo-generated coating obtained by microtome cutting were analyzed by TEM (insets of **Figure 6-17**). As reported in previous work by Balan et al.,³²⁶ a typical gradient distribution of silver nanoparticles was observed after UV synthesis, with a concentration increasing from the depth to the samples surface. It is interesting to note that the density and thickness of the silver top layer, which accumulates near the sample surface, both increase as the overall thickness of the coating increases. In addition, the thicker the nanocomposite layer the greater the amount of silver in the Ag@polymer coating. The top layer consists of elementary silver nanoparticles and aggregates separated by finely divided polymer zones. It can also be observed that the aggregates form a more interconnected (i.e. more compact and denser) network of AgNPs near the upper surface with a marked increase in the atomic density of Ag as one approaches the interface.³²² At the same time, the deeper layer of the samples was almost completely empty of nanoparticles, which had been accumulated close to the metallic upper surface with a clear delineation between these two domains.

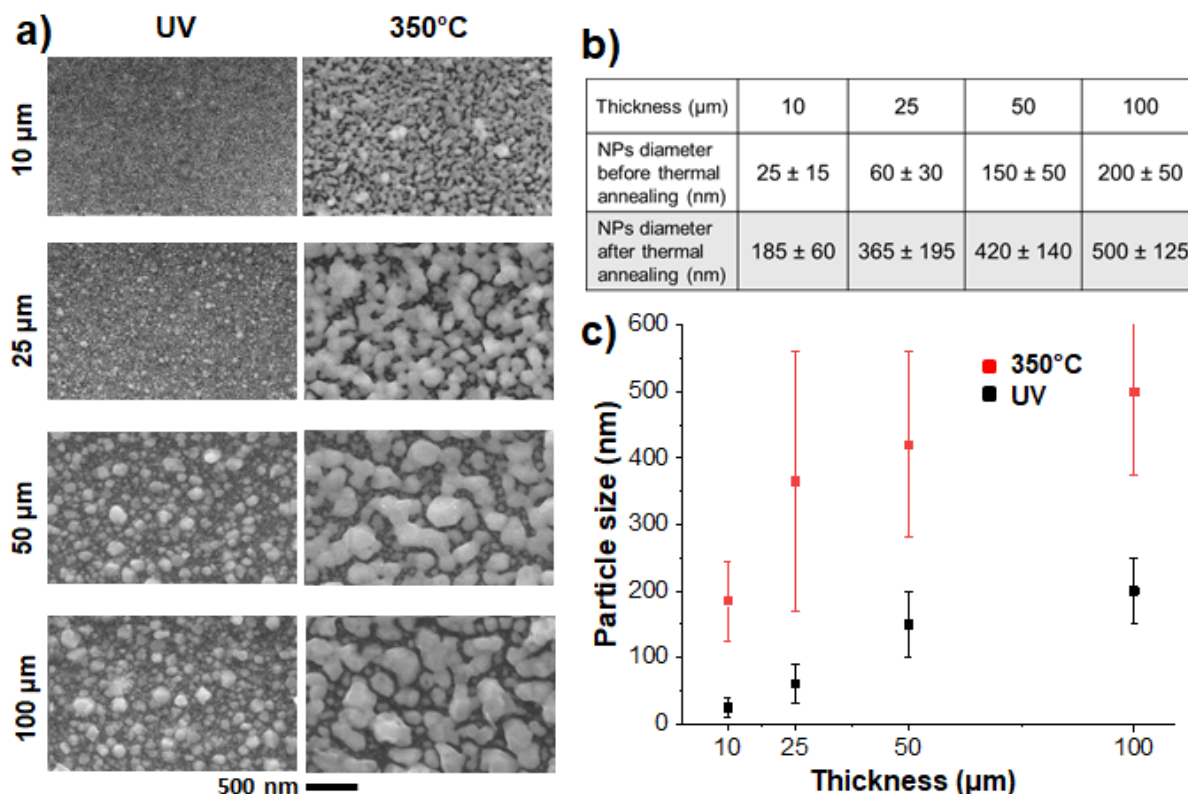


Figure 6-16: Scanning electron microscopy (SEM) observations: a) Top images of the surfaces of Ag@polymer samples after UV synthesis (UV, left), and after thermal annealing (350°C, right), for increasing coating thickness (10, 25, 50 and 100 μm). The bar scale is the same for all SEM images. b) Average size of the silver particles deduced from the SEM images after UV synthesis (second line) and thermal annealing (third line). c) Average particles size at the surface versus the coating thickness.

One way to semi-quantitatively analyze these TEM images is to plot their grey level value as a function of the depth using *ImageJ*. These curves, presented in Figure 6-17, give quantitative indications on the depthwise distribution of Ag atoms and its evolution after the heat treatment for a set of four thicknesses ranging from 10 to 100 μm. For example, in the case of a 10 μm-sample (Figure 6-17a) the curves show, after thermal treatment, a narrower and stronger peak, near the coating surface, bounded to a more compact top metal layer. On the other hand, for a 100 μm-sample, the result shown in Figure 6-17d indicates an increase of the metal top layer thickness. We assume that thermal annealing induces an increase in the mobility of the polymer chains and AgNPs reorganize spontaneously. Moreover, this migration phenomenon is related to the particles size; the smaller the particles, the more easily they migrate through the polymer chains. This observation could be indicative of a coalescence phenomenon, also associated with local sintering. Interestingly, from the TEM images, inset in Figure 6-17, it can be seen that in the case of the 100 μm thick sample, after UV synthesis, the metal particles present in the deep

layers have sizes from 25 to 75 nm. After annealing, the densification of the upper layer is less pronounced, which confirms a less easy migration of the NPs. In the intermediate cases of 50 and 25 μm thick samples (Figure 6-17b-c), the particles are smaller (20-40 nm and 10-30 nm, respectively); their spatial redistribution under the effect of thermal annealing is more pronounced and a clear delineation appears between deep layers empty of particles and the compact upper layer. In the case of the 10 μm coating, the particles are even smaller (5 to 20 nm), so much so that they have migrated during UV synthesis before being trapped by the vitrification of the polymer binder as a result of photo-crosslinking.

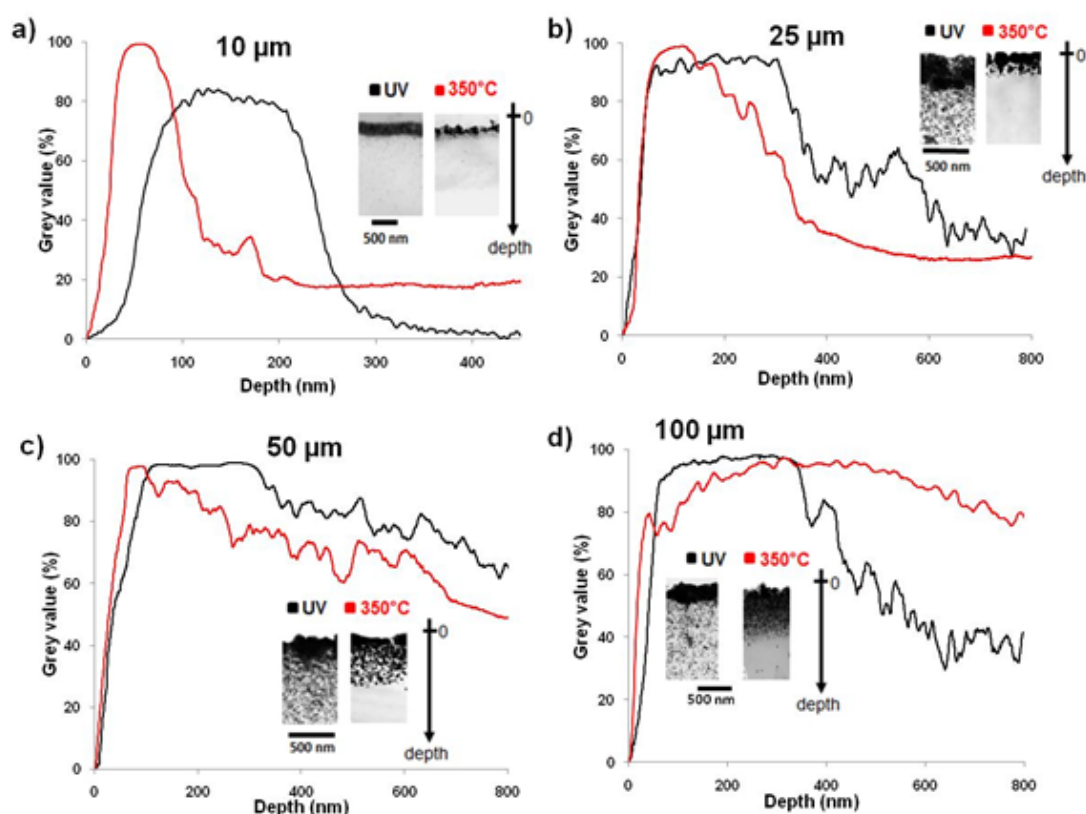


Figure 6-17: Transmission electron microscopy (TEM) analysis of cross sections of four samples with increasing thicknesses (10, 25, 50 and 100 μm) after UV synthesis (black curves) and after thermal annealing (red curves): the grey levels are plotted versus depth, normally to the surface.

Electrical properties. In their initial state (UV, as-synthesized), the electrical characteristics of the Ag@polymer coatings show a strong dependence on the coating thickness. As shown in Figure 6-18a, the thicker the initial film, the lower the electrical resistance. Indeed, the 10 and 25 μm thick coatings are definitely non-conductive (resistance close to 10^8 - 10^9 ohms) while 50 and 100 μm thick coatings are conductive with a resistance of 80 and 8 ohms, respectively. These differences are clearly related to the characteristics of the AgNPs constituting the upper layer of the coating: their size, the morphology and the compactness of their spatial

arrangement. As shown in Figure 6-16b-c, the size of AgNPs clearly increases from 25 to 200 nm, along with the increase of layer thickness. From an electrical point of view, the size of AgNPs should be compared to the electron mean free path λ in bulk Ag, which is close to 50 nm in bulk silver at room temperature.¹¹⁰ It is well known that for particle sizes smaller than λ , the electrical resistivity increases due to the enhanced electron surface scatterings, as it has been already discussed for AgNWs in chapter 1.2.3. Therefore, the small particle size of the 10 and 25 μm coatings, combined with the probably low percolative nature of the AgNP network, explains the very high electrical resistance of the thinner coatings (10 and 25 microns).

Nevertheless, as shown in Figure 6-18a, the thermal annealing is very efficient, especially for thinner films where the electrical resistance drops by 8 orders of magnitude. This can be explained by the combination of two phenomena: i/ local sintering between AgNPs which creates extra conduction paths between AgNPs (see SEM images in Figure 6-16a), ii/ migration and coalescence of AgNPs (see TEM images in Figure 6-17). The combination of these two phenomena results in a general improvement of the percolating character of the network formed by the silver nanostructures even more marked near the top surface of the samples. As a general observation, thermal post-treatment induces a drastic decrease in the electrical resistance of the coatings. This effect seems to be most pronounced in the temperature range from 270 to 300°C. After this thermal treatment all samples present a final, very low resistance at room temperature, in the range of 2.2 - 2.6 ohms, as shown clearly in Figure 6-18b.

During the cooling down step, the measured electrical resistance decreases linearly with the decreasing temperature as one can see even more clearly in a zoomed image of the same plot during cooling down in Figure 6-18b. This is also well observed in Figure 6-18c for the 100 μm thick coating during three successive thermal annealing cycles. This linear dependence appears reversible, despite the slight effects of sintering (at temperature larger than 300°C), and can be understood thanks to the metallic (electrons-phonons interaction) behavior of the AgNP network. Moreover, these measurements demonstrate that the Ag@polymer coatings are very stable under repeated thermal stress. From the linear dependence of the electrical resistance with temperature after the thermal annealing, one can calculate the temperature coefficient of electrical resistance, β , which can be derived from equation (1-6) discussed also in chapter 1.2.6. The calculated values for each coating thickness after the thermal annealing (also reported in Figure 6-18e as a function of the AgNPs diameter that corresponds to each coating) vary from $0.8 \cdot 10^{-3}$ to $1.5 \cdot 10^{-3} \text{ K}^{-1}$. These values appear smaller than $3.8 \cdot 10^{-3} \text{ K}^{-1}$ which is the value for Ag thin film¹⁷² or $2.6 \cdot 10^{-3} \text{ K}^{-1}$ for AgNPs film¹⁷³ or $2.2 \cdot 10^{-3} \text{ K}^{-1}$ for AgNW network.²⁸ A

possible explanation of such difference can be the sparser AgNP network in our present work, possibly associated with defects or small polymer residues between AgNPs.

Finally, another type of thermal annealing was performed to study the behavior of electrical resistance this time at constant temperature, 200 °C. Figure 6-18f reports the time dependence of the electrical resistance for a 25 μm thick coating. In a similar way to the thermal ramp, the resistance follows a drastic and fast decrease during the thermal plateau: while the initial resistance was 10⁷ ohms, it went to 20 ohms after only 8 minutes and appears stable with 10.4 ohm resistance after 50 minutes of constant heating. It is worth noticing that the main part of the drastic optimization occurs within the first minutes of the thermal treatment at 200 °C.

Optical properties. The raw samples (UV, as-synthesized) had reflective surfaces with a nice mirror effect as shown by photographs in **Figure 6-19**. Reflectance was measured over a range from 200 to 800 nm. All the experimental curves, which refer to four samples with increasing thicknesses of the upper silver layer, are shown in Figure 6-19a for the as-synthesized samples and Figure 6-19b after the thermal treatment. For comparison of optical reflection characteristics, these plots also include two simulated curves (20 nm and 1 μm thick bulk silver layer on top of an acrylate polymer substrate). These were calculated using an online software for thin films optical properties estimation.³³¹ In Figure 6-19c, one can see the top metal layer thickness of each Ag@polymer coating, measured from TEM cross section images, for the as-synthesized (UV) and the thermally post-treated samples (350 °C). An important shoulder was observed below 400 nm for the 50 and 100 μm thick nanomaterials, due to the particles size influence (150 ± 50 nm and 200 ± 50 nm respectively). However, in the case of 10 and 25 μm, the particles are smaller and with lower size dispersion (25 ± 15 nm and 60 ± 30 nm respectively), and no shoulder in the reflectance spectra was observed.

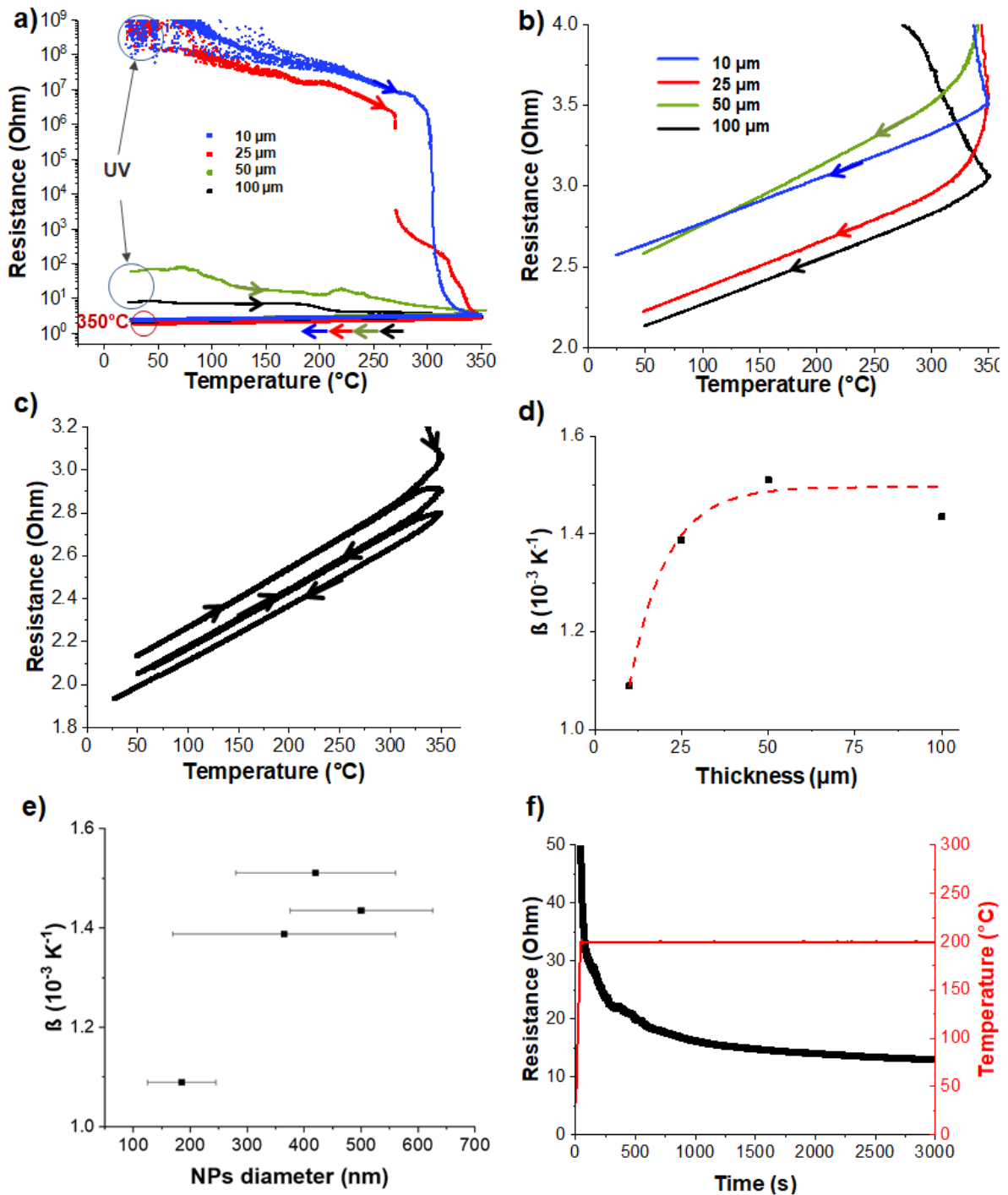


Figure 6-18: Thermal annealing and electrical properties of the Ag@polymer coating. a) The electrical resistance behaviour during thermal ramp up to 350 °C for samples of four different thicknesses: 10, 25, 50 and 100 μm . The thermal ramp was 5 °C/min for both heating and cooling. b) Linear zoom-in of the previous plots, during the cooling down, presenting the final electrical resistance after thermal annealing. c) The electrical resistance versus temperature during 3 repeated similar thermal ramp cycles for a sample of 100 μm thickness. d) The temperature coefficient of resistance β calculated for the four different coating thicknesses. e) The same coefficient as a function of the average AgNPs diameter that corresponds to each coating thickness of 10 to 100 μm f) Evolution of the electrical resistance versus time during a thermal annealing at 200 °C during 50 min, for a 25 μm thick sample.

In addition, some interference phenomena were observed experimentally in the visible range especially for the thinner samples (10 and 25 μm). They most probably stem from the reflection between coupled air/metal and metal/polymer interfaces. Following the thermal annealing, the interference phenomena disappeared and the reflectance seems to be affected, as presented in Figure 6-19b; the 25, 50 and 100 μm samples show similar behavior with a decrease of their reflectance values about 20 % at 450 nm. A less noticeable effect is observed for the 10 μm coating which exhibits a 75 % reflectance at 450 nm. This decrease of the reflectance spectra is probably due to the coalescence of the NPs, the formation of bigger particles and the increase of surface roughness during thermal treatment as shown by SEM analysis (Figure 6-16). Moreover, the shoulder initially observed only for the 100 and 50 μm cases at 380 and 365 nm respectively, was found for all the samples after thermal annealing: 355 nm for 10 μm (soft change), 365 nm for 25 μm and 380 nm for 50 and 100 μm . This observation is linked to the particles size on the top layer. Comparing to the calculated curves, the 100 μm thick Ag@polymer nanomaterial thickness, which corresponds to the 0.8-1 μm top metal layer (see table Figure 6-19c), is quite different from the calculated 1 μm silver bulk layer. This difference can be due to the presence of a clear non-homogeneity of the nanoparticles size and network creation. This favors the roughness of the surface, which is well-known that favors the diffuse reflection at the expense of specular reflection. In addition, it is related to a slightly whitening aspect induced after thermal treatment on the surface of the samples, for 100 μm and 50 μm thicknesses, as seen in the photos in Figure 6-19b. On the other hand, the 10 μm thick Ag@polymer coating, which corresponds to the 0.2-0.3 μm thick top metal layer, shows quite similar trend with the calculated 1 μm silver bulk in terms of curved shape. This trend could stem from the more homogeneous size distribution of the coating on the surface (see SEM images recorded after thermal annealing reported in Figure 6-16a).

Wettability. Contact angle of water droplets on the sample surfaces was determined with a DSA100 - Krüss goniometer in IS2M, before and after the thermal annealing, in order to evaluate the influence of the restructuring induced by this post-treatment. As shown in Figure 6-19d, as the thickness of the as-synthesized samples increases, the contact angle increases slightly and then stabilizes when thickness is larger than 50 μm . After thermal annealing, a dramatic increase of the contact angle is observed, especially for the thinner coatings. The smaller the sample thickness the greater the difference; for 10 μm thickness this increase is from 25° to 92° while for 100 μm from 40° to 79°. This change in surface wettability, i.e. towards more pronounced hydrophobicity after thermal annealing, can be explained by the

sintering/coalescence phenomenon induced by thermal annealing. This treatment reduced the surface energy and allowed the creation of a more compact AgNP network. In addition, it induced an increase in the surface roughness as already observed by SEM images presented in Figure 6-16. It is well known that in the case of materials with low surface energy, high surface roughness leads to a reduction in wettability (higher contact angle).³¹ This situation corresponds well to what is experimentally observed before and after heat treatment.

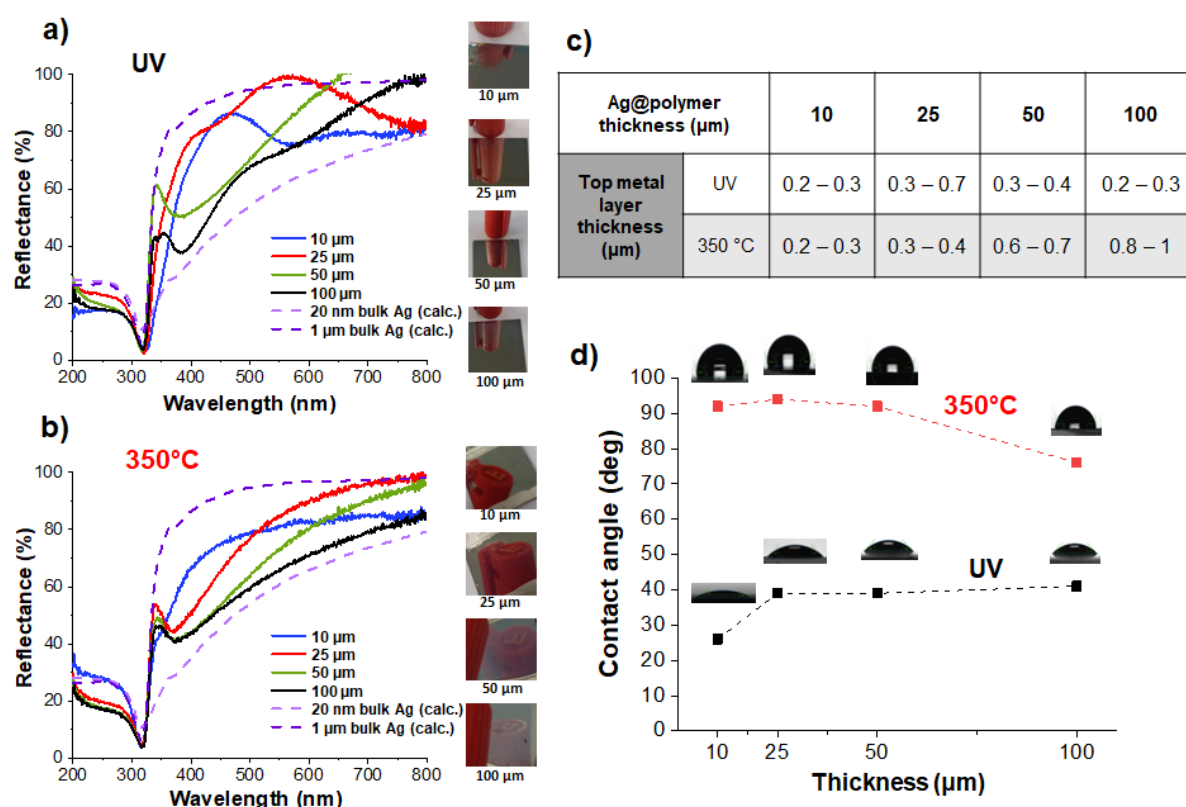


Figure 6-19: Reflectance spectra of Ag@polymer metallized coating of different thicknesses: a) after UV synthesis and b) after thermal annealing. Dotted lines show the reflection spectra calculated for 20 nm and 1 μm thick solid silver layers on polyacrylate substrate. Inset: photographs of the reflections provided by the different mirrors. c) Top metal layer thickness (extracted from TEM images) before (UV, as-synthesized) and after thermal annealing treatment (350 °C) for each case of Ag@polymer thickness values. d) Contact angles of a water droplet with the surface of the Ag@polymer coating for different thicknesses after UV synthesis (black dots) and after thermal treatment (red dots) (inset: photographic images of the deposited droplet).

Conclusion. In the present work, we studied the effect of thermal annealing on a metallized Ag@polymer coating, in collaboration with the Dr. L. Balan and the PhD candidate M. Dabert that elaborate and investigate such hybrid nanomaterials. As we have previously observed in LMGP for the case of AgNW networks,³⁰ thermal annealing enhances the electrical, optical and other properties of metal-based nanomaterials. Such post-treatment increases the mobility of

the polymer chains that reorganize spontaneously and, at the same time, AgNPs migrate from the depths towards the surface. Therefore, the metal network become denser and more interconnected near the surface due to coalescence and local sintering. The creation of a dense and compact AgNP network near the surface improves significantly the electrical conductivity, thus underlining the close correlation between spatial organization and intimate structure of the material, enhancing for instance the (111) crystallographic texturation. During and after the annealing process, it is also observed that the surface of the Ag@polymer coating becomes significantly more hydrophobic and reflective. This properties variation is even more pronounced for the thinner samples. More specifically, the thinnest coating (10 μm) offers the best compromise between all the above studied properties: high reflectance (75%), low electrical resistance (2 ohm) and a very marked hydrophobic character (water contact angle of 92°). Thus, these results represent an important step forward in multifunctional, metalized coatings technology and pave the way for a promising integration into a wide variety of devices, i.e. in the field of printed circuit boards. Thanks to their excellent reflectivity in the NIR, they could also be integrated in interesting devices such as efficient and low-cost reflectors or thermal barriers.

Ἐν οἶδα ὅτι οὐδέν οἶδα.

Σωκράτης

« the one thing I know is that I know nothing »

Socrates (470 – 399 BC)

Chapter 7

7. Conclusions and prospects

The field of transparent conductive materials (TCM) has been increasingly developing the last years thanks to the advances in nanosciences and emerging technologies like AgNW networks. It has been more than a decade that research in this field started, exploring the properties of such transparent electrodes (TE). Nowadays we have reached a more mature state that deals with their integration in energy, lighting and heating devices. The main goal of the present PhD thesis was to deal with degradation issues of AgNW networks, towards a successful proof of concept of devices either at the laboratory or industrial scale.

The electrical, optical and mechanical properties of AgNW networks were thoroughly discussed in chapter 1, as well as studies performed so far concerning the mechanisms of failure.^{32,240,333} In addition, the strategies to enhance the stability under thermal and/or electrical stress were introduced in chapter 1, focusing on the deposition of transparent protective oxides by AP-SALD, developed in LMGP.^{33,35,36,218} Chapter 2 was dedicated to transparent heaters (TH) and the review-article we have published recently in collaboration with Dr. J-P Simonato's team in CEA-Liten,¹ including the discussion of all TH technologies, from traditional TCO to novel nanocomposites and hybrids. TH can be significantly beneficial for energy, health or transport and especially in the last 5 years, there has been an increasing interest of our scientific community to further study this application. Another important part of my PhD is related to the study and optimization of the fabrication and properties of TH and their implementation in devices. For this reason, in our review-article we highlighted the physical principles associated with TH and the physical models that have been developed to understand better their performance. In chapter 3 that followed, the experimental techniques used during the present PhD thesis were introduced, including the fabrication of AgNW networks and the characterization of their properties. The optimization of these processes and preliminary results were presented as well, like the comparative study of the deposition of ultra-long AgNWs using three different techniques, namely, spray, rod and spin coating, that we conducted in collaboration with Dr. A. Madeira and the scientific teams of Prof. I.A. Goldthorpe and Prof. M. Tréguer-Delapierre.³⁸ The utilization of capping agents during the growth of AgNWs, the rapid growth and the precise control of the nanowires dimensions and the networks fabrication with techniques that are compatible to large scale processes, are very important aspects for the industrial use of AgNW-based TE. Our team in LMGP has the opportunity to collaborate with several laboratories with years of expertise in nanochemistry and other industrial partners which specialize in the fabrication of MNWs. Thus, there is a great potential to explore and advance

together towards green and sustainable axis for the TE elaboration, by reducing the overall fabrication cost and the waste of raw materials as well.

Concerning the simulations, indeed this is a versatile approach that serves to better understand and explain fundamental aspects of AgNW network properties and also to model their performance under applied electrical power. In the last part of chapter 3 the main simulation techniques, developed in the present PhD thesis were briefly introduced. In preliminary results generated with COMSOL Multiphysics®, the calculated resistance of networks with different nanowires length and diameter, adjusted to the size of real samples, was in good accordance with spray deposited samples. However, due to computation limits, a simpler and much faster approach of a thin Ag film approximation was adopted for the rest of the studies, allowing the comparison between experimental and numerical samples of identical size. There are several ideas to be explored by future works related to physical modelling, for instance the impact of different substrates to the thermal performance of AgNW networks under power supply. For this, we could replace the Corning glass by plastic substrates that we have already used for the experiments and also explore silicon, quartz, sapphire etc.

The remaining three chapters of the present manuscript were related to the experiments and simulations of the main axis of my PhD thesis: the failure mechanisms of AgNW networks and their integration into devices in the framework of collaborations and projects.

The electrical stability is one of the most crucial parameters for a robust performance of AgNW networks as TE. To achieve this, we should first of all better explain the underlying physical mechanisms that are at the origin of failure. Continuing the work of the previous PhD T. Sannicolo, and in collaboration with Prof. L. Flandin and Engineer N. Charvin in LEPMI,³² we further explored the origin of degradation, including this time simulation approaches. As presented in the first part of chapter 4, we followed both the electrical performance of AgNW networks and the spatial distribution of temperature during electrical stress by IR imaging. The main observation is that the network degradation originates from a localized elevated Joule-heating that can occur randomly or due to an initial morphological defect in the sample. Furthermore, we used electrical and thermal simulations to better explain the experimental observations. The first approach concerned the representation of the TE as a random net of 2D stick resistors and the evaluation of electrical current, using a homemade code in Python (developed by Engineer N. Charvin in LEPMI). At each run, the sticks that showed a power density value above a certain threshold were removed by the network. These morphological changes mimicked finally the crack propagation and the model verified that when regions with

small defects were built-in, they represented also the origin of instabilities. Similar results were obtained by simulating a thin Ag film with an initial tiny structural defect, in COMSOL Multiphysics®. This macroscopic approach allowed the evaluation of the electrical and thermal properties of a model with the same size and initial resistance as a spray-coated AgNW network and the notable impact of micro-defects. The simulated current density had the same value over almost the entire Ag film, apart from the region in front of the edge of the microscopic defect; the current density can be 5 times higher along 50 microns from it. Consequently, these simulations also demonstrated that the Joule heating difference between the edge of defects and the rest of the sample is significant, and thus it represents a plausible origin of a hotspot, as those experimentally observed.

A further step to the experimental study of network degradation was the evaluation of the evolution of electrical performance under a simultaneous electrical and thermal stress. This could be useful for the devices not only from a fundamental point of view but also to predict the AgNW based devices lifetime. The effect of thermal annealing had been thoroughly investigated previously in LMGP, during the PhD thesis of D. Langley and M. Lagrange,^{28,30} revealing the spheroidization of nanowires in the entire network induced by the Plateau-Rayleigh instability, and allowed by atomic diffusion which is activated at high temperatures.^{30,240} Concerning the influence of electrical stress applied to the AgNW networks, as we have demonstrated recently, inhomogeneities occurring locally impact the electrical conduction of the whole network as well. The electrical and thermal phenomena are entangled due to the Joule heating, as other teams have studied too by experimental and simulation approaches like the team of Prof. I. Goldthorpe.¹⁶² However, we believe it is necessary to combine the electrical and thermal stress to AgNW networks, to which we can associate a given electrical resistance. As presented in the second part of chapter 4, during the post-doc of João Resende, we conducted the so-called T - I (temperature-current) experiments during which we measured the time of failure (ToF), meaning the time from the beginning of a thermal and electrical load until the electrical breakdown of the network, i.e. associated to the divergence of the electrical resistance. The experiment was conducted on nearly 200 samples, with various initial electrical resistances, applied temperature and current values. Consequently, we achieved a statistically sufficient amount of data in order to compare it with a semi-empirical model. The latter has been proposed by considering a supplementary term within the expression of the thermal ToF , linked to the power-induced Joule heating. For a straightforward comparison with all experimental data, we included the areal mass density (amd) in the electrical term and finally

fitted the data of ToF using the current density instead of the applied current. The model showed a rather good first approximation to the experimental results. For each amd , the modelled phase diagram offers a prediction of the ToF as a function of the current density and temperature, with three main regions depicted from the plot; two extreme cases of high and moderate stress, and a region where both thermal and electrical stress are considerable. In the extreme cases, the failure can be either ultra-fast or take several days, while in the intermediate cases it is rather hard to distinguish which stress is the prevailing failure mechanism. From both experiments and simulations presented in the two parts of chapter 4, we concluded that the degradation is mainly driven by thermally induced morphological instabilities, either directly related to high imposed temperatures (Plateau-Rayleigh) or indirectly by the power-induced heating (local high current density). However, further data are needed in order to make a more reliable fitting of the physical parameters. To this direction, extra measurements focused on moderate temperature-current couples are necessary. The fabrication of the new home-made characterization bench is certainly helpful from an experimental point of view, because it increases the number of samples we can study under the same conditions and enhances the reliability of the measurements. In addition, we could repeat the $T-I$ experiment under controlled atmospheric pressure or inserted gases, and vary the humidity as well. Another idea is to use the NIR imaging during the $T-I$ measurements, in order to investigate further the dominant mechanism of failure. This could be combined as well with a study of the proportion of the spheroidized nanowires as a function of the $T-I$ couples, with the help of SEM images and a software like *ImageJ*. Finally, we could repeat the $T-I$ experiment and build an equivalent model to predict the ToF of the AgNW/oxide composites. This would help to evaluate in a more complete way the influence of thin oxide films and potentially enlighten the mechanisms of failure.

The large variations of the current density around defects on AgNW networks, as estimated by the simulations, and consequently the Joule heating variations and hotspots formation, observed experimentally by IR imaging as well, led us to fabricate and investigate non-homogeneous networks. The morphological non-homogeneities on AgNW networks have a direct impact on the electrical distribution and the performance of the networks when implemented into devices.³² Designing and fabricating non-homogeneous networks can offer several advantages. From a fundamental point of view, they revealed interesting information about the mechanisms of failure. In particular, we engineered the presence of triangular zones with either absence of nanowires or denser nanowire network regions and we measured the electrical distribution by

one-probe electrical mappings. In the points where the density of the network changed drastically, the electrical potential presented higher tortuosity too. The simulated cases presented the same distribution of electrical potential with the experiments. Furthermore, the modelled Ag thin films presented spots where the calculated surface current density is higher compared to the rest of the specimen. At the same spots the simulated temperature due to Joule heating was elevated too. The same image of an increased heating was observed experimentally by NIR imaging, when a significant voltage was applied to the AgNW networks with the empty or denser triangular regions. Experiments and simulations of different AgNW network patterns justified that the edge effects and variations in the local distribution of the network density lead to local hotspots from where the instabilities and defects start propagating. The physical model is reliable and useful to predict the regions of high electrical stress and generated temperature.

Therefore, another advantage is that non-homogeneous networks can address devices specific needs, for example TH with regions of different heating performance under the same power supply. Compared to the synthesis of TCO or the fabrication of metallic grids, the solution-processed deposition of MNWs is much more versatile and controllable.^{316,334} As we demonstrated, this becomes even more interesting when combined with: i/ nowadays fast and low-cost 3D printing of patterns used during the deposition of AgNWs and ii/ simple modelling approaches to engineer the electrical and thermal performance of the networks. In addition, lately there is a growing interest to investigate patterning methods such as ink-jet printing and screen printing, whose lower cost can make large-area manufacturing possible.^{335,336} This is a fabrication aspect that we should definitely consider in our future work, especially for the development of large size wearable TH or body motion electrostatic generators (Carnot project *FREE*).

Apart from the spatial mapping of the temperature and the detection of inhomogeneities and defects from IR imaging, the information related to emissivity and radiation losses is very important for applications such as clothes for personal thermal management, energy-efficient buildings or smart automobile windows.^{208,337–339} The energy-saving domains are of high interest and this aspect of AgNW networks has been little investigated to date. As discussed by Hu et al. in a recent review article,²⁰⁸ we can achieve a heating textile by coating with AgNW network. Since the human body radiation has a dominant thermal wavelength at around 9 μm , if the nanowire spacing is much smaller than this length scale, most IR radiation will be reflected and thus a thermal radiation reflection layer is achieved. Meanwhile, AgNWs are preferred for the breathability and stretchability that they offer compared to metallic or other ceramic thin

films.³³⁹ Concerning smart buildings, Lin et al. reported recently a cost-effective, large scale spray-coating technique to fabricate IR blocking window coatings with AgNWs.³³⁷ In addition, Li et al., in their study for low-emissivity coatings, demonstrated that the reflectivity of AgNW/polymer coatings increases in the IR with decreasing diameter of nanowires, while the hybrid remains highly transparent in the visible range.³³⁸ Still, a good compromise should be found between breathability and stretchability, reflectivity and electrical conductivity. For this reason, it is necessary to investigate the impact of network density (*amd*) and other AgNW network features (sizes, post-deposition treatment, coating...) on their properties. Moreover, tuning the network density in non-homogeneous networks, like the ones presented in chapter 5, could be very promising for a large variety of heating-cooling devices. The use of high-resolution tools will certainly help on this direction, like the promising preliminary tests, performed with the help of the Engineer François Bonnel, with a new IR camera obtained by CMTC (Consortium des Moyens Technologiques Communs) of Grenoble INP.

Apart from better understanding the physical properties and performance limitations under electrical and thermal stress, we continued the studies related to the stability enhancement of AgNW networks with protective oxide layers by the Atmospheric Pressure SALD (AP-SALD), method developed in LMGP by the team of Dr David Muñoz-Rojas.^{33,35} ZnO coating on the AgNW networks demonstrated a beneficial impact on the electrical and thermal distribution, especially in the case of non-homogeneous transparent electrodes, as presented in chapter 5. The 1P-mappings showed a reduction of the tortuosity of the electrical equipotential lines, when compared with the bare AgNW networks, thanks to the electrical conduction through the oxide. In addition, the thin, conformal oxide ZnO increased significantly the stability with a 50 % higher voltage failure, while maintaining the high optical transparency of the electrodes, and allowed the electrodes to reach temperatures above 300 °C generated by Joule heating. This is surely very advantageous for all types of applications. Deeper investigation of the anti-reflective properties of AgNW/ZnO composites due to ZnO band gap properties would be interesting to applications too. Meanwhile, we have achieved the reduction of charging effects with the deposition of ZnO:Al coating on top of the nanowires which can be beneficial for either collecting or injecting electrical charges when being used for TE applications in solar cells or in OLEDs, respectively.²¹⁸

Nowadays, an increasing number of materials have started to be tested by the SALD team, as well as the influence of such thin, oxide layers, like SnO₂ and HfO₂, in AgNW networks. The large variety of materials that can be deposited by AP-SALD is also crucial in order to find the

most appropriate dielectric spacer for the AgNW-based cold cathodes that we aim to fabricate in the framework of *PANASSE* project with Thalès and IEMN, as discussed in chapter 6.3. In addition, the area-selective deposition that has been elaborated by SALD could offer a great advantage to the networks, because it could retain the optical transparency of AgNW networks, by preserving the oxide deposition on top of the spaces between the nanowires. Meanwhile, we have started collaborating recently with the scientific team of Prof. Christophe Vallée at LTM in order to investigate the properties of AgNW composites with nitrides and oxides deposited by thermal or plasma enhanced ALD (PEALD). Preliminary results presented in **Figure 7-1** demonstrate the robust performance compared to bare networks for a) AgNW/TiN under electrical stress, and b) AgNW/HfO₂ under thermal stress. The list of hybrid materials and AgNW-based composites that can be elaborated is getting larger and larger, with emergent technologies like MXenes being lately reported.³⁴⁰⁻³⁴² As demonstrated by Miao et al. the mechanical robustness and electromagnetic interference (EMI) shielding effectiveness of such composites is highly interesting for aerospace and smart electronic devices.³⁴³ Such materials could also be explored in LMGP, in collaboration with the team of Prof. Thierry Ouisse, whose research focuses on MAX phases, MXenes and other nano-lamellar phases. Last but not least, the future study of AgNW/oxide composites is related to physical modelling of their electrical and optical properties, as well as their heating performances.

The stable and reproducible performance of AgNW networks leads to our ultimate goal, the successful integration into devices and their efficient performance. In chapter 6, the main collaborations and projects during my PhD thesis were presented and they concern different types of applications; TH for lab-on-a-chip devices, stretchable energy harvesters, cold cathodes for miniaturized X-ray sources, flexible R2R fabricated OPV. Some ideas and prospects related to AgNW networks optimization have been already stated in the present conclusive chapter. Additionally, concerning the TH for bio microfluidic applications, an important issue to be tackled is the precise control of the power-induced temperature. Biological substances are very sensitive to temperature and, in order to fabricate accurate lab-on-a-chip devices, it would be useful to study the temperature gradient from the AgNW network to the microfluidic channels by physical modeling. The heating and cooling rates are also very important for the *in situ* PCR array we aim to reproduce and this means that the heating losses (conduction, convection, radiation) should be optimized and tuned too. Furthermore, another type of *in situ* measurement based on AgNW network TH that we plan to explore in LMGP, concerns the variation of optical transmittance of vanadium oxide (VO₂) under heating. Dr.

Jean-Luc Deschanvres is an expert in the growth of VO₂ by CVD techniques, a promising material for RF switches³⁴⁴ and energy efficiency buildings,³⁴⁵ while AgNW-based TH have successfully been integrated in thermochromic devices.¹ This time, we would like to investigate the transition temperature of VO₂ by measuring its transmittance *in situ* while heating the sample inside the spectrophotometer chamber by using AgNW TH.

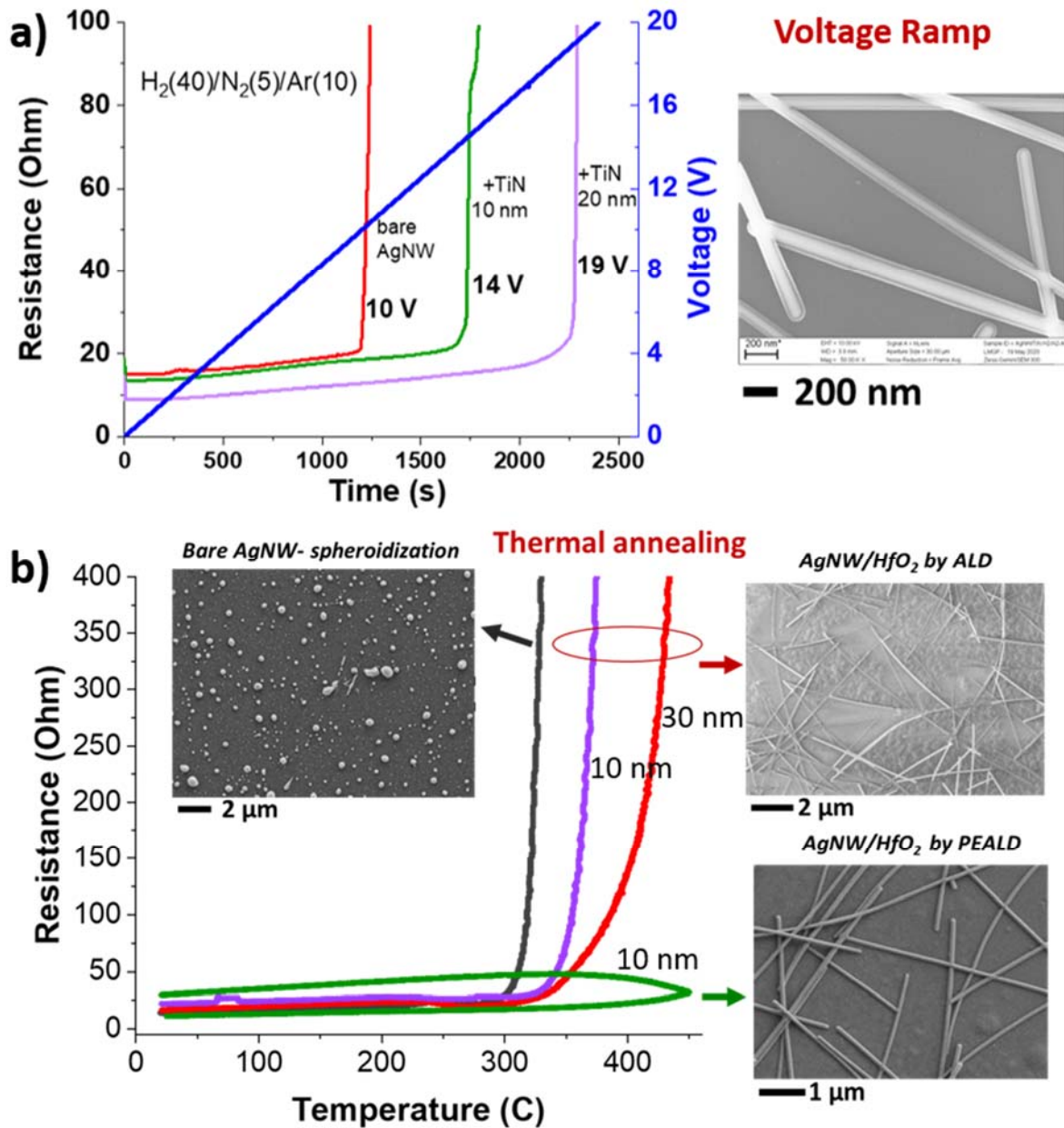


Figure 7-1: a) Evolution of resistance during a voltage ramp 0.5 V/min for bare AgNW and coated with 10 and 20 nm TiN by PEALD. SEM image showing the conformal layer of TiN. b) Resistance versus temperature during thermal annealing with a ramp of 5 °C/min for bare AgNW and coated with HfO₂ by ALD (10 and 30 nm oxide thickness) and PEALD (10 nm). SEM observations after the thermal stress revealing the complete degradation of bare nanowires, the partial degradation of the ones coated with ALD and the stable AgNW network encapsulated by HfO₂ by PEALD that retains a low electrical resistance.

Furthermore, despite the fact that AgNW networks have been widely studied for energy, electronic and heating devices, there are other types of applications that have not been well investigated yet such as wound healing, surface coating and drug delivery.^{346,347} Another emerging application concerns water disinfection.^{348,349} As recently demonstrated by Bahcelioglu et al, AgNW glass filters are highly promising for the removal of E. coli from water.³⁵⁰ In addition, there is a highly increasing interest for the antibacterial performance of AgNW networks and nanocomposites with cellulose nanofibrils.^{351–355} In general, AgNWs have attracted significant attention for future green, flexible organic electronics, compared with other alternatives thanks to their advantageous physical properties, solution-processability and low-cost fabrication.³⁵⁶

The variety of emerging applications related to AgNW networks is vast and proves the importance of such technology to nowadays energy and electronic transitions. Our studies should be directed towards non-toxic materials and environmental-friendly procedures, and insist on recycling materials and recover critical metals from old devices, following Japan's example.³⁵⁷ In order to develop robust and sustainable devices, fundamental research on materials is indispensable to know the limits, better understand, look for alternatives, measure the advantages and pitfalls, and choose a compromise between properties. It is not easy to find the golden mean; this is something that I learnt during my PhD thesis. But it is worth trying. We have no other option than to search deeper and let it flow. The beauty of Materials Science lies on the unlimited combination of materials and its multidisciplinary character. And as Richard Feynman had so accurately stated decades before the flourishing of nanotechnology, “there's plenty of room at the bottom”.

References

- (1) Papanastasiou, D. T.; Schultheiss, A.; Muñoz-Rojas, D.; Celle, C.; Carella, A.; Simonato, J.-P.; Bellet, D. Transparent Heaters: A Review. *Advanced Functional Materials* **2020**, *30* (21), 1910225. <https://doi.org/10.1002/adfm.201910225>.
- (2) Sannicolo, T.; Lagrange, M.; Cabos, A.; Celle, C.; Simonato, J.-P.; Bellet, D. Metallic Nanowire-Based Transparent Electrodes for Next Generation Flexible Devices: A Review. *Small* **2016**, *12* (44), 6052–6075. <https://doi.org/10.1002/sml.201602581>.
- (3) Ellmer, K. Past Achievements and Future Challenges in the Development of Optically Transparent Electrodes. *Nature Photonics* **2012**, *6* (12), 809–817. <https://doi.org/10.1038/nphoton.2012.282>.
- (4) Kumar, A.; Zhou, C. The Race To Replace Tin-Doped Indium Oxide: Which Material Will Win? *ACS Nano* **2010**, *4* (1), 11–14. <https://doi.org/10.1021/nn901903b>.
- (5) Afre, R. A.; Sharma, N.; Sharon, M.; Sharon, M. Transparent Conducting Oxide Films for Various Applications: A Review. *REVIEWS ON ADVANCED MATERIALS SCIENCE* **2018**, *53* (1), 79–89. <https://doi.org/10.1515/rams-2018-0006>.
- (6) Kulkarni, G. U.; Kiruthika, S.; Gupta, R.; Rao, K. Towards Low Cost Materials and Methods for Transparent Electrodes. *Current Opinion in Chemical Engineering* **2015**, *8*, 60–68. <https://doi.org/10.1016/j.coche.2015.03.001>.
- (7) Li, D.; Lai, W.-Y.; Zhang, Y.-Z.; Huang, W. Printable Transparent Conductive Films for Flexible Electronics. *Advanced Materials* **2018**, *30* (10), 1704738. <https://doi.org/10.1002/adma.201704738>.
- (8) Zhou, Y.; Azumi, R. Carbon Nanotube Based Transparent Conductive Films: Progress, Challenges, and Perspectives. *Sci Technol Adv Mater* **2016**, *17* (1), 493–516. <https://doi.org/10.1080/14686996.2016.1214526>.
- (9) Rosli, N. N.; Ibrahim, M. A.; Ahmad Ludin, N.; Mat Teridi, M. A.; Sopian, K. A Review of Graphene Based Transparent Conducting Films for Use in Solar Photovoltaic Applications. *Renewable and Sustainable Energy Reviews* **2019**, *99*, 83–99. <https://doi.org/10.1016/j.rser.2018.09.011>.
- (10) Xu, Y.; Liu, J. Graphene as Transparent Electrodes: Fabrication and New Emerging Applications. *Small* **2016**, *12* (11), 1400–1419. <https://doi.org/10.1002/sml.201502988>.
- (11) Gueye, M. N.; Carella, A.; Demadrille, R.; Simonato, J.-P. All-Polymeric Flexible Transparent Heaters. *ACS Appl. Mater. Interfaces* **2017**, *9* (32), 27250–27256. <https://doi.org/10.1021/acsami.7b08578>.
- (12) Gueye, M. N.; Carella, A.; Faure-Vincent, J.; Demadrille, R.; Simonato, J.-P. Progress in Understanding Structure and Transport Properties of PEDOT-Based Materials: A Critical Review. *Progress in Materials Science* **2020**, *108*, 100616. <https://doi.org/10.1016/j.pmatsci.2019.100616>.
- (13) Xu, G.; Li, Y. Metal-microstructure Based Flexible Transparent Electrodes and Their Applications in Electronic Devices. *Nano Select* **2020**, *1* (2), 169–182. <https://doi.org/10.1002/nano.202000006>.
- (14) Lee, H. B.; Jin, W.-Y.; Ovhal, M. M.; Kumar, N.; Kang, J.-W. Flexible Transparent Conducting Electrodes Based on Metal Meshes for Organic Optoelectronic Device Applications: A Review. *J. Mater. Chem. C* **2019**, *7* (5), 1087–1110. <https://doi.org/10.1039/C8TC04423F>.
- (15) Langley, D.; Giusti, G.; Mayousse, C.; Celle, C.; Bellet, D.; Simonato, J.-P. Flexible Transparent Conductive Materials Based on Silver Nanowire Networks: A Review.

- Nanotechnology* **2013**, *24* (45), 452001. <https://doi.org/10.1088/0957-4484/24/45/452001>.
- (16) Bellet, D.; Lagrange, M.; Sannicolo, T.; Aghazadehchors, S.; Nguyen, V. H.; Langley, D. P.; Muñoz-Rojas, D.; Jiménez, C.; Bréchet, Y.; Nguyen, N. D. Transparent Electrodes Based on Silver Nanowire Networks: From Physical Considerations towards Device Integration. *Materials* **2017**, *10* (6), 570. <https://doi.org/10.3390/ma10060570>.
 - (17) Morales-Masis, M.; De Wolf, S.; Woods-Robinson, R.; Ager, J. W.; Ballif, C. Transparent Electrodes for Efficient Optoelectronics. *Adv. Electron. Mater.* **2017**, *3* (5), n/a-n/a. <https://doi.org/10.1002/aelm.201600529>.
 - (18) Singh, M.; Rana, S. Silver and Copper Nanowire Films as Cost-Effective and Robust Transparent Electrode in Energy Harvesting through Photovoltaic: A Review. *Materials Today Communications* **2020**, *24*, 101317. <https://doi.org/10.1016/j.mtcomm.2020.101317>.
 - (19) Sohn, H.; Park, C.; Oh, J.-M.; Kang, S. W.; Kim, M.-J. Silver Nanowire Networks: Mechano-Electric Properties and Applications. *Materials* **2019**, *12* (16), 2526. <https://doi.org/10.3390/ma12162526>.
 - (20) Langley, D. P.; Giusti, G.; Lagrange, M.; Collins, R.; Jiménez, C.; Bréchet, Y.; Bellet, D. Silver Nanowire Networks: Physical Properties and Potential Integration in Solar Cells. *Solar Energy Materials and Solar Cells* **2014**, *125*, 318–324. <https://doi.org/10.1016/j.solmat.2013.09.015>.
 - (21) Guo, F.; Li, N.; Radmilović, V. V.; Radmilović, V. R.; Turbiez, M.; Spiecker, E.; Forberich, K.; Brabec, C. J. Fully Printed Organic Tandem Solar Cells Using Solution-Processed Silver Nanowires and Opaque Silver as Charge Collecting Electrodes. *Energy Environ. Sci.* **2015**, *8* (6), 1690–1697. <https://doi.org/10.1039/C5EE00184F>.
 - (22) Aurang, P.; Doganay, D.; Bek, A.; Turan, R.; Unalan, H. E. Silver Nanowire Networks as Transparent Top Electrodes for Silicon Solar Cells. *Solar Energy* **2017**, *141*, 110–117. <https://doi.org/10.1016/j.solener.2016.11.021>.
 - (23) Papanastasiou, D. T.; Sannicolo, T.; Resende, J.; Nguyen, V. H.; Jimenez, C.; Munoz-Rojas, D.; Nguyen, N. D.; Bellet, D. Recent Progress in the Study of Silver Nanowire Networks and Their Applications. In *Advances toward the development of nanotechnology*; 2019; p 472.
 - (24) Celle, C.; Mayousse, C.; Moreau, E.; Basti, H.; Carella, A.; Simonato, J.-P. Highly Flexible Transparent Film Heaters Based on Random Networks of Silver Nanowires. *Nano Research* **2012**, *5* (6), 427–433. <https://doi.org/10.1007/s12274-012-0225-2>.
 - (25) Zhang, S.; Li, S.; Xia, Z.; Cai, K. A Review of Electronic Skin: Soft Electronics and Sensors for Human Health. *J. Mater. Chem. B* **2020**, *8* (5), 852–862. <https://doi.org/10.1039/C9TB02531F>.
 - (26) Yao, S.; Ren, P.; Song, R.; Liu, Y.; Huang, Q.; Dong, J.; O'Connor, B. T.; Zhu, Y. Nanomaterial-Enabled Flexible and Stretchable Sensing Systems: Processing, Integration, and Applications. *Adv. Mater.* **2020**, *32* (15), 1902343. <https://doi.org/10.1002/adma.201902343>.
 - (27) Jeong, H.; Noh, Y.; Ko, S. H.; Lee, D. Flexible Resistive Pressure Sensor with Silver Nanowire Networks Embedded in Polymer Using Natural Formation of Air Gap. *Composites Science and Technology* **2019**, *174*, 50–57. <https://doi.org/10.1016/j.compscitech.2019.01.028>.
 - (28) Lagrange, M.; Langley, D. P.; Giusti, G.; Jiménez, C.; Bréchet, Y.; Bellet, D. Optimization of Silver Nanowire-Based Transparent Electrodes: Effects of Density,

- Size and Thermal Annealing. *Nanoscale* **2015**, *7* (41), 17410–17423.
<https://doi.org/10.1039/C5NR04084A>.
- (29) Langley, D. P.; Lagrange, M.; Nguyen, N. D.; Bellet, D. Percolation in Networks of 1-Dimensional Objects: Comparison between Monte Carlo Simulations and Experimental Observations. *Nanoscale Horizons* **2018**, *3* (5), 545–550.
<https://doi.org/10.1039/C8NH00066B>.
- (30) Langley, D. P.; Lagrange, M.; Giusti, G.; Jiménez, C.; Bréchet, Y.; Nguyen, N. D.; Bellet, D. Metallic Nanowire Networks: Effects of Thermal Annealing on Electrical Resistance. *Nanoscale* **2014**, *6*, 13535–13543. <https://doi.org/10.1039/C4NR04151H>.
- (31) Sannicolo, T.; Muñoz-Rojas, D.; Nguyen, N. D.; Moreau, S.; Celle, C.; Simonato, J.-P.; Bréchet, Y.; Bellet, D. Direct Imaging of the Onset of Electrical Conduction in Silver Nanowire Networks by Infrared Thermography: Evidence of Geometrical Quantized Percolation. *Nano Letters* **2016**, *16* (11), 7046–7053.
<https://doi.org/10.1021/acs.nanolett.6b03270>.
- (32) Sannicolo, T.; Charvin, N.; Flandin, L.; Kraus, S.; Papanastasiou, D. T.; Celle, C.; Simonato, J.-P.; Muñoz-Rojas, D.; Jiménez, C.; Bellet, D. Electrical Mapping of Silver Nanowire Networks: A Versatile Tool for Imaging Network Homogeneity and Degradation Dynamics during Failure. *ACS Nano* **2018**, *12* (5), 4648–4659.
<https://doi.org/10.1021/acsnano.8b01242>.
- (33) Muñoz-Rojas, D.; Nguyen, V. H.; Masse de la Huerta, C.; Aghazadehchors, S.; Jiménez, C.; Bellet, D. Spatial Atomic Layer Deposition (SALD), an Emerging Tool for Energy Materials. Application to New-Generation Photovoltaic Devices and Transparent Conductive Materials. *Comptes Rendus Physique* **2017**, *18* (7), 391–400.
<https://doi.org/10.1016/j.crhy.2017.09.004>.
- (34) Muñoz-Rojas, D.; MacManus-Driscoll, J. Spatial Atmospheric Atomic Layer Deposition: A New Laboratory and Industrial Tool for Low-Cost Photovoltaics. *Materials Horizons* **2014**, Doi:10.1039/c3mh00136a.
<https://doi.org/10.1039/c3mh00136a>.
- (35) Khan, A.; Nguyen, V. H.; Muñoz-Rojas, D.; Aghazadehchors, S.; Jiménez, C.; Nguyen, N. D.; Bellet, D. Stability Enhancement of Silver Nanowire Networks with Conformal ZnO Coatings Deposited by Atmospheric Pressure Spatial Atomic Layer Deposition. *ACS Applied Materials & Interfaces* **2018**, *10* (22), 19208–19217.
<https://doi.org/10.1021/acsmi.8b03079>.
- (36) Aghazadehchors, S.; Nguyen, V. H.; Muñoz-Rojas, D.; Jiménez, C.; Rapenne, L.; Nguyen, N. D.; Bellet, D. Versatility of Bilayer Metal Oxide Coatings on Silver Nanowire Networks for Enhanced Stability with Minimal Transparency Loss. *Nanoscale* **2019**, *11* (42), 19969–19979. <https://doi.org/10.1039/C9NR05658K>.
- (37) Nguyen, V. H.; Resende, J.; Papanastasiou, D. T.; Fontanals, N.; Jiménez, C.; Muñoz-Rojas, D.; Bellet, D. Low-Cost Fabrication of Flexible Transparent Electrodes Based on Al Doped ZnO and Silver Nanowire Nanocomposites: Impact of the Network Density. *Nanoscale* **2019**, *11* (25), 12097–12107.
<https://doi.org/10.1039/C9NR02664A>.
- (38) Madeira, A.; Papanastasiou, D. T.; Toupance, T.; Servant, L.; Tréguer-Delapierre, M.; Bellet, D.; Goldthorpe, I. A. Rapid Synthesis of Ultra-Long Silver Nanowires for High Performance Transparent Electrodes. *Nanoscale Adv.* **2020**, *2* (9), 3804–3808.
<https://doi.org/10.1039/D0NA00392A>.
- (39) WHO. Coronavirus disease (COVID-19) pandemic
<https://www.who.int/emergencies/diseases/novel-coronavirus-2019>.

- (40) WHO. Diagnostic detection of 2019-nCoV by real-time RT-PCR https://www.who.int/docs/default-source/coronaviruse/protocol-v2-1.pdf?sfvrsn=a9ef618c_2 (accessed Mar 17, 2020).
- (41) Wang, Y.; Kang, H.; Liu, X.; Tong, Z. Combination of RT-qPCR Testing and Clinical Features for Diagnosis of COVID-19 Facilitates Management of SARS-CoV-2 Outbreak. *J Med Virol* **2020**, *92* (6), 538–539. <https://doi.org/10.1002/jmv.25721>.
- (42) Sethuraman, N.; Jeremiah, S. S.; Ryo, A. Interpreting Diagnostic Tests for SARS-CoV-2. *JAMA* **2020**, *323* (22), 2249. <https://doi.org/10.1001/jama.2020.8259>.
- (43) Wang, J.; Lou, H.; Meng, J.; Peng, Z.; Wang, B.; Wan, J. Stretchable Energy Storage E-Skin Supercapacitors and Body Movement Sensors. *Sensors and Actuators B: Chemical* **2020**, *305*, 127529. <https://doi.org/10.1016/j.snb.2019.127529>.
- (44) Zhang, Y.; He, P.; Luo, M.; Xu, X.; Dai, G.; Yang, J. Highly Stretchable Polymer/Silver Nanowires Composite Sensor for Human Health Monitoring. *Nano Res.* **2020**, *13* (4), 919–926. <https://doi.org/10.1007/s12274-020-2730-z>.
- (45) Zhou, W.; Yao, S.; Wang, H.; Du, Q.; Ma, Y.; Zhu, Y. Gas-Permeable, Ultrathin, Stretchable Epidermal Electronics with Porous Electrodes. *ACS Nano* **2020**, *14* (5), 5798–5805. <https://doi.org/10.1021/acsnano.0c00906>.
- (46) Zhu, H.-W.; Gao, H.-L.; Zhao, H.-Y.; Ge, J.; Hu, B.-C.; Huang, J.; Yu, S.-H. Printable Elastic Silver Nanowire-Based Conductor for Washable Electronic Textiles. *Nano Res.* **2020**, *13* (10), 2879–2884. <https://doi.org/10.1007/s12274-020-2947-x>.
- (47) Papanastasiou, D. T.; Schultheiss, A.; Muñoz-Rojas, D.; Celle, C.; Carella, A.; Simonato, J.-P.; Bellet, D. Transparent Heaters: A Review. *Advanced Functional Materials* **2020**, 1910225. <https://doi.org/10.1002/adfm.201910225>.
- (48) Husain, A. A. F.; Hasan, W. Z. W.; Shafie, S.; Hamidon, M. N.; Pandey, S. S. A Review of Transparent Solar Photovoltaic Technologies. *Renewable and Sustainable Energy Reviews* **2018**, *94*, 779–791. <https://doi.org/10.1016/j.rser.2018.06.031>.
- (49) O'Regan, B.; Grätzel, M. A Low-Cost, High-Efficiency Solar Cell Based on Dye-Sensitized Colloidal TiO₂ Films. *Nature* **1991**, *353* (6346), 737–740. <https://doi.org/10.1038/353737a0>.
- (50) LG Transparent OLED <https://www.lg-informationdisplay.com/ISE2019>.
- (51) Samsung secures flexible display patent for foldable smartphones <https://www.cbronline.com/uncategorised/samsung-secures-flexible-display-patent-for-foldable-smartphones/>.
- (52) Transparent Antennas <https://metamaterial.com/solutions/transparent-antennas-2/>.
- (53) SwissTech Convention Center to the EPFL campus <https://www.itsliquid.com/swisstech-convention-center.html>.
- (54) SageGlass LightZone <https://www.sageglass.com/en/products/sageglass-lightzone>.
- (55) New developments in transparent heating polymer films http://www.cea-tech.fr/cea-tech/english/Pages/ec_2017/transparent-heating-polymer-films-nanomaterials-processes.aspx.
- (56) Al-Kuhaili, M. F. Electrical Conductivity Enhancement of Indium Tin Oxide (ITO) Thin Films Reactively Sputtered in a Hydrogen Plasma. *J Mater Sci: Mater Electron* **2020**, *31* (4), 2729–2740. <https://doi.org/10.1007/s10854-019-02813-9>.
- (57) Alzoubi, K.; Hamasha, M. M.; Lu, S.; Sammakia, B. Bending Fatigue Study of Sputtered ITO on Flexible Substrate. *Journal of Display Technology* **2011**, *7* (11), 593–600. <https://doi.org/10.1109/JDT.2011.2151830>.
- (58) Martin Lokan; Roderick Eggert; Michael Redlinger. *The Availability of Indium: The Present, Medium Term, and Long Term*; NREL-Colorado School of Mines, 2015; p 79.

- (59) Wegscheider, S.; Steinlechner, S.; Leuchtenmüller, M. Innovative Concept for the Recovery of Silver and Indium by a Combined Treatment of Jarosite and Electric Arc Furnace Dust. *JOM* **2017**, *69* (2), 388–394. <https://doi.org/10.1007/s11837-016-2192-7>.
- (60) Graedel, T. E.; Allwood, J.; Birat, J.-P.; Buchert, M.; Hagelüken, C.; Reck, B. K.; Sibley, S. F.; Sonnemann, G.; United Nations Environment Programme; Working Group on the Global Metal Flows. *Recycling Rates of Metals: A Status Report*; 2011.
- (61) Ylä-Mella, J.; Pongrácz, E. Drivers and Constraints of Critical Materials Recycling: The Case of Indium. *Resources* **2016**, *5* (4), 34. <https://doi.org/10.3390/resources5040034>.
- (62) Wang, H. G.; Wu, Y. F.; Gu, Y. F.; Mu, X. Z. An Evaluation of Potential Yield of Indium Recycled from Waste Mobile Phone in China. *MSF* **2016**, *847*, 335–343. <https://doi.org/10.4028/www.scientific.net/MSF.847.335>.
- (63) Zhang, K.; Wu, Y.; Wang, W.; Li, B.; Zhang, Y.; Zuo, T. Recycling Indium from Waste LCDs: A Review. *Resources, Conservation and Recycling* **2015**, *104*, 276–290. <https://doi.org/10.1016/j.resconrec.2015.07.015>.
- (64) Ciacci, L.; Werner, T. T.; Vassura, I.; Passarini, F. Backlighting the European Indium Recycling Potentials. *Journal of Industrial Ecology* **2019**, *23* (2), 426–437. <https://doi.org/10.1111/jiec.12744>.
- (65) Hecht, D. S.; Hu, L.; Irvin, G. Emerging Transparent Electrodes Based on Thin Films of Carbon Nanotubes, Graphene, and Metallic Nanostructures. *Advanced Materials* **2011**, *23* (13), 1482–1513. <https://doi.org/10.1002/adma.201003188>.
- (66) Jeon, I.; Yoon, J.; Kim, U.; Lee, C.; Xiang, R.; Shawky, A.; Xi, J.; Byeon, J.; Lee, H. M.; Choi, M.; Maruyama, S.; Matsuo, Y. High-Performance Solution-Processed Double-Walled Carbon Nanotube Transparent Electrode for Perovskite Solar Cells. *Adv. Energy Mater.* **2019**, *9* (27), 1901204. <https://doi.org/10.1002/aenm.201901204>.
- (67) Edgar J.Lopez-Naranjo; Luis J. González-Ortiz, E. J.; Luis M. Apátiga; Eric M. Rivera-Muñoz, L. J.; Alejandro Manzano-Ramírez. Transparent Electrodes: A Review of the Use of Carbon-Based Nanomaterials. *Journal of Nanomaterials* **2016**, *2016*, 4928365. <https://doi.org/10.1155/2016/4928365>.
- (68) Li, L.; Hong, S. K.; Jo, Y.; Tian, M.; Woo, C. Y.; Kim, S. H.; Kim, J.-M.; Lee, H. W. Transparent, Flexible Heater Based on Hybrid 2D Platform of Graphene and Dry-Spun Carbon Nanotubes. *ACS Applied Materials & Interfaces* **2019**, *11* (17), 16223–16232. <https://doi.org/10.1021/acsami.9b02225>.
- (69) Choi, H.; Choi, J. S.; Kim, J.-S.; Choe, J.-H.; Chung, K. H.; Shin, J.-W.; Kim, J. T.; Youn, D.-H.; Kim, K.-C.; Lee, J.-I.; Choi, S.-Y.; Kim, P.; Choi, C.-G.; Yu, Y.-J. Flexible and Transparent Gas Molecule Sensor Integrated with Sensing and Heating Graphene Layers. *Small* **2014**, *10* (18), 3685–3691. <https://doi.org/10.1002/sml.201400434>.
- (70) Yang, J.; Liu, Y.; Liu, S.; Li, L.; Zhang, C.; Liu, T. Conducting Polymer Composites: Material Synthesis and Applications in Electrochemical Capacitive Energy Storage. *Mater. Chem. Front.* **2017**, *1* (2), 251–268. <https://doi.org/10.1039/C6QM00150E>.
- (71) Gueye, M. N.; Carella, A.; Massonnet, N.; Yvenou, E.; Brenet, S.; Faure-Vincent, J.; Pouget, S.; Rieutord, F.; Okuno, H.; Benayad, A.; Demadrille, R.; Simonato, J.-P. Structure and Dopant Engineering in PEDOT Thin Films: Practical Tools for a Dramatic Conductivity Enhancement. *Chem. Mater.* **2016**, *28* (10), 3462–3468. <https://doi.org/10.1021/acs.chemmater.6b01035>.
- (72) Chen, X.; Nie, S.; Guo, W.; Fei, F.; Su, W.; Gu, W.; Cui, Z. Printable High-Aspect Ratio and High-Resolution Cu Grid Flexible Transparent Conductive Film with

- Figure of Merit over 80 000. *Advanced Electronic Materials* **2019**, 5 (5), 1800991. <https://doi.org/10.1002/aelm.201800991>.
- (73) Kim, W.-K.; Lee, S.; Hee Lee, D.; Hee Park, I.; Seong Bae, J.; Woo Lee, T.; Kim, J.-Y.; Hun Park, J.; Chan Cho, Y.; Ryong Cho, C.; Jeong, S.-Y. Cu Mesh for Flexible Transparent Conductive Electrodes. *Scientific Reports* **2015**, 5 (1). <https://doi.org/10.1038/srep10715>.
- (74) Xu, J.-L.; Liu, Y.-H.; Gao, X.; Sun, Y.; Shen, S.; Cai, X.; Chen, L.; Wang, S.-D. Embedded Ag Grid Electrodes as Current Collector for Ultraflexible Transparent Solid-State Supercapacitor. *ACS Appl. Mater. Interfaces* **2017**, 9 (33), 27649–27656. <https://doi.org/10.1021/acsami.7b06184>.
- (75) Sorel, S.; Bellet, D.; Coleman, J. N. Relationship between Material Properties and Transparent Heater Performance for Both Bulk-like and Percolative Nanostructured Networks. *ACS Nano* **2014**, 8 (5), 4805–4814. <https://doi.org/10.1021/nn500692d>.
- (76) Ahn, Y.; Jeong, Y.; Lee, D.; Lee, Y. Copper Nanowire–Graphene Core–Shell Nanostructure for Highly Stable Transparent Conducting Electrodes. *ACS Nano* **2015**, 9 (3), 3125–3133. <https://doi.org/10.1021/acs.nano.5b00053>.
- (77) Chen, J.; Chen, J.; Li, Y.; Zhou, W.; Feng, X.; Huang, Q.; Zheng, J.-G.; Liu, R.; Ma, Y.; Huang, W. Enhanced Oxidation-Resistant Cu–Ni Core–Shell Nanowires: Controllable One-Pot Synthesis and Solution Processing to Transparent Flexible Heaters. *Nanoscale* **2015**, 7 (40), 16874–16879. <https://doi.org/10.1039/C5NR04930J>.
- (78) Celle, C.; Cabos, A.; Fontecave, T.; Laguitton, B.; Benayad, A.; Guettaz, L.; Pélissier, N.; Nguyen, V. H.; Bellet, D.; Muñoz-Rojas, D.; Simonato, J.-P. Oxidation of Copper Nanowire Based Transparent Electrodes in Ambient Conditions and Their Stabilization by Encapsulation: Application to Transparent Film Heaters. *Nanotechnology* **2018**, 29 (8), 085701. <https://doi.org/10.1088/1361-6528/aaa48e>.
- (79) Cheong, H.-G.; Kim, J.-H.; Song, J.-H.; Jeong, U.; Park, J.-W. Highly Flexible Transparent Thin Film Heaters Based on Silver Nanowires and Aluminum Zinc Oxides. *Thin Solid Films* **2015**, 589, 633–641. <https://doi.org/10.1016/j.tsf.2015.06.047>.
- (80) Pham, A.-T.; Nguyen, X.-Q.; Tran, D.-H.; Ngoc Phan, V.; Duong, T.-T.; Nguyen, D.-C. Enhancement of the Electrical Properties of Silver Nanowire Transparent Conductive Electrodes by Atomic Layer Deposition Coating with Zinc Oxide. *Nanotechnology* **2016**, 27 (33), 335202. <https://doi.org/10.1088/0957-4484/27/33/335202>.
- (81) Hoeng, F.; Denneulin, A.; Krosnicki, G.; Bras, J. Positive Impact of Cellulose Nanofibrils on Silver Nanowire Coatings for Transparent Conductive Films. *J. Mater. Chem. C* **2016**, 4 (46), 10945–10954. <https://doi.org/10.1039/C6TC03629E>.
- (82) He, X.; Shen, G.; Xu, R.; Yang, W.; Zhang, C.; Liu, Z.; Chen, B.; Liu, J.; Song, M. Hexagonal and Square Patterned Silver Nanowires/PEDOT:PSS Composite Grids by Screen Printing for Uniformly Transparent Heaters. *Polymers* **2019**, 11 (3), 468. <https://doi.org/10.3390/polym11030468>.
- (83) Lin, P.-C.; Hsieh, C.-T.; Liu, X.; Chang, F.-C.; Chen, W.-C.; Yu, J.; Chueh, C.-C. Fabricating Efficient Flexible Organic Photovoltaics Using an Eco-Friendly Cellulose Nanofibers/Silver Nanowires Conductive Substrate. *Chemical Engineering Journal* **2021**, 405, 126996. <https://doi.org/10.1016/j.cej.2020.126996>.
- (84) Mallikarjuna, K.; Kim, H. Highly Transparent Conductive Reduced Graphene Oxide/Silver Nanowires/Silver Grid Electrodes for Low-Voltage Electrochromic Smart Windows. *ACS Appl. Mater. Interfaces* **2019**, 11 (2), 1969–1978. <https://doi.org/10.1021/acsami.8b14086>.

- (85) Tang, Y.; Ruan, H.; Chen, Y.; Xiang, J.; Liu, H.; Jin, R.; Shi, D.; Chen, S.; Zhang, J. A Flexible, Room-Temperature and Solution-Processible Copper Nanowire Based Transparent Electrode Protected by Reduced Graphene Oxide Exhibiting High Performance and Improved Stability. *Nanotechnology* **2020**, *31* (4), 045704. <https://doi.org/10.1088/1361-6528/ab4c03>.
- (86) Wang, J.; Zhang, Z.; Wang, S.; Zhang, R.; Guo, Y.; Cheng, G.; Gu, Y.; Liu, K.; Chen, K. Superstable Copper Nanowire Network Electrodes by Single-Crystal Graphene Covering and Their Applications in Flexible Nanogenerator and Light-Emitting Diode. *Nano Energy* **2020**, *71*, 104638. <https://doi.org/10.1016/j.nanoen.2020.104638>.
- (87) Ricciardulli, A. G.; Yang, S.; Wetzelaer, G.-J. A. H.; Feng, X.; Blom, P. W. M. Hybrid Silver Nanowire and Graphene-Based Solution-Processed Transparent Electrode for Organic Optoelectronics. *Advanced Functional Materials* **2018**, *28* (14), 1706010. <https://doi.org/10.1002/adfm.201706010>.
- (88) Hwang, Y.; Choi, J.; Kim, J.-W.; Lee, J.-W.; Kim, J. G.; Hwang, H.; Choi, K. W.; Lee, W.; Ju, B.-K. Ag-Fiber/Graphene Hybrid Electrodes for Highly Flexible and Transparent Optoelectronic Devices. *Sci Rep* **2020**, *10* (1), 5117. <https://doi.org/10.1038/s41598-020-62056-1>.
- (89) Deschamps, A.; Lagier, J.-P.; Fievet, F.; Aeiyaach, S.; Lacaze, P.-C. New Chemical One-Step Process for Preparing Fine Metallic Particles Embedded in a Polymer Matrix. *J. Mater. Chem.* **1992**, *2* (11), 1213–1214. <https://doi.org/10.1039/JM9920201213>.
- (90) Wiley, B.; Sun, Y.; Mayers, B.; Xia, Y. Shape-Controlled Synthesis of Metal Nanostructures: The Case of Silver. *Chemistry – A European Journal* **2005**, *11* (2), 454–463. <https://doi.org/10.1002/chem.200400927>.
- (91) Sun, Y.; Mayers, B.; Herricks, T.; Xia, Y. Polyol Synthesis of Uniform Silver Nanowires: A Plausible Growth Mechanism and the Supporting Evidence. *Nano Lett.* **2003**, *3* (7), 955–960. <https://doi.org/10.1021/nl034312m>.
- (92) Nengduo, Z.; Xuesong, Y.; Hao, G. Highly Conductive and Flexible Transparent Films Based on Silver Nanowire/Chitosan Composite. *RSC Advances* **2016**, *6* (53), 47552–47561. <https://doi.org/10.1039/C6RA05448J>.
- (93) Coskun, S.; Aksoy, B.; Unalan, H. E. Polyol Synthesis of Silver Nanowires: An Extensive Parametric Study. *Crystal Growth & Design* **2011**, *11* (11), 4963–4969. <https://doi.org/10.1021/cg200874g>.
- (94) Hwang, J.; Shim, Y.; Yoon, S.-M.; Lee, S. H.; Park, S.-H. Influence of Polyvinylpyrrolidone (PVP) Capping Layer on Silver Nanowire Networks: Theoretical and Experimental Studies. *RSC Adv.* **2016**, *6* (37), 30972–30977. <https://doi.org/10.1039/C5RA28003F>.
- (95) Wang, J.; Jiu, J.; Araki, T.; Nogi, M.; Sugahara, T.; Nagao, S.; Koga, H.; He, P.; Saganuma, K. Silver Nanowire Electrodes: Conductivity Improvement Without Post-Treatment and Application in Capacitive Pressure Sensors. *Nano-Micro Lett.* **2015**, *7* (1), 51–58. <https://doi.org/10.1007/s40820-014-0018-0>.
- (96) Madeira, A.; Plissonneau, M.; Servant, L.; Goldthorpe, I. A.; Tréguer-Delapierre, M. Increasing Silver Nanowire Network Stability through Small Molecule Passivation. *Nanomaterials* **2019**, *9* (6), 899. <https://doi.org/10.3390/nano9060899>.
- (97) Li, Y.; Guo, S.; Yang, H.; Chao, Y.; Jiang, S.; Wang, C. One-Step Synthesis of Ultra-Long Silver Nanowires of over 100 Mm and Their Application in Flexible Transparent Conductive Films. *RSC Adv.* **2018**, *8* (15), 8057–8063. <https://doi.org/10.1039/C7RA13683H>.

- (98) Azani, M.; Hassanpour, A. Synthesis of Silver Nanowires with Controllable Diameter and Simple Tool to Evaluate Their Diameter, Concentration and Yield. *ChemistrySelect* **2019**, *4* (9), 2716–2720. <https://doi.org/10.1002/slct.201900298>.
- (99) Kim, J.; Park, J.; Jeong, U.; Park, J.-W. Silver Nanowire Network Embedded in Polydimethylsiloxane as Stretchable, Transparent, and Conductive Substrates. *Journal of Applied Polymer Science* **2016**, *133* (33). <https://doi.org/10.1002/app.43830>.
- (100) Wang, H.; Wang, Y.; Chen, X. Synthesis of Uniform Silver Nanowires from AgCl Seeds for Transparent Conductive Films via Spin-Coating at Variable Spin-Speed. *Colloids and Surfaces A: Physicochemical and Engineering Aspects* **2019**, *565*, 154–161. <https://doi.org/10.1016/j.colsurfa.2018.11.050>.
- (101) Yang, C.; Gu, H.; Lin, W.; Yuen, M. M.; Wong, C. P.; Xiong, M.; Gao, B. Silver Nanowires: From Scalable Synthesis to Recyclable Foldable Electronics. *Advanced Materials* **2011**, *23* (27), 3052–3056. <https://doi.org/10.1002/adma.201100530>.
- (102) Lee, J.-Y.; Connor, S. T.; Cui, Y.; Peumans, P. Solution-Processed Metal Nanowire Mesh Transparent Electrodes. *Nano Letters* **2008**, *8* (2), 689–692. <https://doi.org/10.1021/nl073296g>.
- (103) Chen, D.; Liang, J.; Liu, C.; Saldanha, G.; Zhao, F.; Tong, K.; Liu, J.; Pei, Q. Thermally Stable Silver Nanowire–Polyimide Transparent Electrode Based on Atomic Layer Deposition of Zinc Oxide on Silver Nanowires. *Adv. Funct. Mater.* **2015**, *25* (48), 7512–7520. <https://doi.org/10.1002/adfm.201503236>.
- (104) Liu, C.-H.; Yu, X. Silver Nanowire-Based Transparent, Flexible, and Conductive Thin Film. *Nanoscale Research Letters* **2011**, *6* (1), 75–82. <https://doi.org/10.1186/1556-276X-6-75>.
- (105) Ko, Y.-H.; Lee, J.-W.; Choi, W.-K.; Kim, S.-R. Ultrasonic-Sprayed Graphene Oxide and Air-Sprayed Silver Nanowire for the Preparation of Flexible Transparent Conductive Films. *Chem. Lett.* **2014**, *43* (8), 1242–1244. <https://doi.org/10.1246/cl.140220>.
- (106) Wang, J.-L.; Wang, Z.-H.; Liu, J.-W.; Yu, S.-H. Recycling Valuable Silver from Waste Generated in Diverse Nanotemplate Reactions. *Sci. China Mater.* **2016**, *59* (7), 538–546. <https://doi.org/10.1007/s40843-016-5078-x>.
- (107) Yoo, B.; Kim, Y.; Han, C. J.; Oh, M. S.; Kim, J.-W. Recyclable Patterning of Silver Nanowire Percolated Network for Fabrication of Flexible Transparent Electrode. *Applied Surface Science* **2018**, *429*, 151–157. <https://doi.org/10.1016/j.apsusc.2017.07.285>.
- (108) Omaña-Sanz, B.; Toybou, D.; Lesven, L.; Gaucher, V.; Fadel, A.; Addad, A.; Recourt, P.; Yeghicheyan, D.; Arndt, D.; Celle, C.; Simonato, J.-P.; Vulpe, C.; Charlet, L.; Sobanska, S.; Gilbert, B.; Hofmann, A. An Electrochemical Method to Rapidly Assess the Environmental Risk of Silver Release from Nanowire Transparent Conductive Films. *NanoImpact* **2020**, *18*, 100217. <https://doi.org/10.1016/j.impact.2020.100217>.
- (109) Bid, A.; Bora, A.; Raychaudhuri, A. K. Temperature Dependence of the Resistance of Metallic Nanowires of Diameter $\geq 15\text{nm}$: Applicability of Bloch-Grüneisen Theorem. *Phys. Rev. B* **2006**, *74* (3), 035426–035426–035428. <https://doi.org/10.1103/PhysRevB.74.035426>.
- (110) Gall, D. Electron Mean Free Path in Elemental Metals. *Journal of Applied Physics* **2016**, *119* (8), 085101. <https://doi.org/10.1063/1.4942216>.
- (111) Rumble, J. R.; Lide, D. R.; Bruno, T. J. *CRC Handbook of Chemistry and Physics [2019-2020]: A Ready-Reference Book of Chemical and Physical Data*; 2019.
- (112) Stauffer, D.; Aharony, A. *Introduction to Percolation Theory, 2nd Revised Ed.*; Taylor and Francis: London, 1994.

- (113) Li, J.; Zhang, S.-L. Finite-Size Scaling in Stick Percolation. *Phys. Rev. E* **2009**, *80* (4), 040104-040104–4. <https://doi.org/10.1103/PhysRevE.80.040104>.
- (114) Sorel, S.; Bellet, D.; Coleman, J. N. Relationship between Material Properties and Transparent Heater Performance for Both Bulk-like and Percolative Nanostructured Networks. *ACS Nano* **2014**, *8* (5), 4805–4814. <https://doi.org/10.1021/nn500692d>.
- (115) Bergin, S. M.; Chen, Y.-H.; Rathmell, A. R.; Charbonneau, P.; Li, Z.-Y.; Wiley, B. J. The Effect of Nanowire Length and Diameter on the Properties of Transparent, Conducting Nanowire Films. *Nanoscale* **2012**, *4* (6), 1996. <https://doi.org/10.1039/c2nr30126a>.
- (116) Giusti, G.; Consonni, V.; Puyoo, E.; Bellet, D. High Performance ZnO-SnO₂:F Nanocomposite Transparent Electrodes for Energy Applications. *ACS Appl. Mater. Interfaces* **2014**, *6* (16), 14096–14107. <https://doi.org/10.1021/am5034473>.
- (117) Araki, T.; Jiu, J.; Nogi, M.; Koga, H.; Nagao, S.; Sugahara, T.; Suganuma, K. Low Haze Transparent Electrodes and Highly Conducting Air Dried Films with Ultra-Long Silver Nanowires Synthesized by One-Step Polyol Method. *Nano Res.* **2014**, *7* (2), 236–245. <https://doi.org/10.1007/s12274-013-0391-x>.
- (118) Marus, M.; Hubarevich, A.; Fan, W. J.; Wang, H.; Smirnov, A.; Wang, K.; Huang, H.; Sun, X. W. Optical Haze of Randomly Arranged Silver Nanowire Transparent Conductive Films with Wide Range of Nanowire Diameters. *AIP Adv.* **2018**, *8* (3), 035201. <https://doi.org/10.1063/1.5020033>.
- (119) Haacke, G. New Figure of Merit for Transparent Conductors. *Journal of Applied Physics* **1976**, *47* (9), 4086–4089. <https://doi.org/10.1063/1.323240>.
- (120) De, S.; Higgins, T. M.; Lyons, P. E.; Doherty, E. M.; Nirmalraj, P. N.; Blau, W. J.; Boland, J. J.; Coleman, J. N. Silver Nanowire Networks as Flexible, Transparent, Conducting Films: Extremely High DC to Optical Conductivity Ratios. *ACS Nano* **2009**, *3* (7), 1767–1774. <https://doi.org/10.1021/nn900348c>.
- (121) Tokuno, T.; Nogi, M.; Karakawa, M.; Jiu, J.; Nge, T. T.; Aso, Y.; Suganuma, K. Fabrication of Silver Nanowire Transparent Electrodes at Room Temperature. *Nano Research* **2011**, *4* (12), 1215–1222. <https://doi.org/10.1007/s12274-011-0172-3>.
- (122) Lee, J.; Lee, P.; Lee, H.; Lee, D.; Lee, S. S.; Ko, S. H. Very Long Ag Nanowire Synthesis and Its Application in a Highly Transparent, Conductive and Flexible Metal Electrode Touch Panel. *Nanoscale* **2012**, *4* (20), 6408–6414. <https://doi.org/10.1039/C2NR31254A>.
- (123) Stewart, I. E.; Rathmell, A. R.; Yan, L.; Ye, S.; Flowers, P. F.; You, W.; Wiley, B. J. Solution-Processed Copper–Nickel Nanowire Anodes for Organic Solar Cells. *Nanoscale* **2014**, *6* (11), 5980–5988. <https://doi.org/10.1039/C4NR01024H>.
- (124) Han, S.; Hong, S.; Ham, J.; Yeo, J.; Lee, J.; Kang, B.; Lee, P.; Kwon, J.; Lee, S. S.; Yang, M.-Y.; Ko, S. H. Fast Plasmonic Laser Nanowelding for a Cu-Nanowire Percolation Network for Flexible Transparent Conductors and Stretchable Electronics. *Adv. Mater.* **2014**, *26* (33), 5808–5814. <https://doi.org/10.1002/adma.201400474>.
- (125) Liu, Y.; Zhang, J.; Gao, H.; Wang, Y.; Liu, Q.; Huang, S.; Guo, C. F.; Ren, Z. Capillary-Force-Induced Cold Welding in Silver-Nanowire-Based Flexible Transparent Electrodes. *Nano Letters* **2017**, *17* (2), 1090–1096. <https://doi.org/10.1021/acs.nanolett.6b04613>.
- (126) Xu, F.; Xu, W.; Mao, B.; Shen, W.; Yu, Y.; Tan, R.; Song, W. Preparation and Cold Welding of Silver Nanowire Based Transparent Electrodes with Optical Transmittances >90% and Sheet Resistances <10 Ohm/Sq. *Journal of Colloid and Interface Science* **2018**, *512*, 208–218. <https://doi.org/10.1016/j.jcis.2017.10.051>.
- (127) Wang, Y.; Zhang, L.; Wang, D. Ultrastretchable Hybrid Electrodes of Silver Nanowires and Multiwalled Carbon Nanotubes Realized by Capillary-Force-Induced

- Welding. *Adv. Mater. Technol.* **2019**, *4* (11), 1900721. <https://doi.org/10.1002/admt.201900721>.
- (128) Zhang, K.; Li, J.; Fang, Y.; Luo, B.; Zhang, Y.; Li, Y.; Zhou, J.; Hu, B. Unraveling the Solvent Induced Welding of Silver Nanowires for High Performance Flexible Transparent Electrodes. *Nanoscale* **2018**, *10* (27), 12981–12990. <https://doi.org/10.1039/C8NR01648H>.
- (129) Coskun, S.; Selen Ates, E.; Emrah Unalan, H. Optimization of Silver Nanowire Networks for Polymer Light Emitting Diode Electrodes. *Nanotechnology* **2013**, *24* (12), 125202. <https://doi.org/10.1088/0957-4484/24/12/125202>.
- (130) D. Vollath. *Nanomaterials: An Introduction to Synthesis, Properties and Applications*; Wiley-VCH Verlag GmbH & Co. KGaA: Weinheim, 2008.
- (131) Zhang, S.; Li, S.; Xia, Z.; Cai, K. A Review of Electronic Skin: Soft Electronics and Sensors for Human Health. *J. Mater. Chem. B* **2020**, *8* (5), 852–862. <https://doi.org/10.1039/C9TB02531F>.
- (132) Wang, J.; Lou, H.; Meng, J.; Peng, Z.; Wang, B.; Wan, J. Stretchable Energy Storage E-Skin Supercapacitors and Body Movement Sensors. *Sensors and Actuators B: Chemical* **2020**, *305*, 127529. <https://doi.org/10.1016/j.snb.2019.127529>.
- (133) Han, Q.; Chen, Y.; Song, W.; Zhang, M.; Wang, S.; Ren, P.; Hao, L.; Wang, A.; Bai, S.; Yin, J. Fabrication of Agarose Hydrogel with Patterned Silver Nanowires for Motion Sensor. *Bio-des. Manuf.* **2019**, *2* (4), 269–277. <https://doi.org/10.1007/s42242-019-00051-w>.
- (134) Araki, T.; Uemura, T.; Yoshimoto, S.; Takemoto, A.; Noda, Y.; Izumi, S.; Sekitani, T. Wireless Monitoring Using a Stretchable and Transparent Sensor Sheet Containing Metal Nanowires. *Adv. Mater.* **2020**, *32* (15), 1902684. <https://doi.org/10.1002/adma.201902684>.
- (135) Zhao, M.; Li, D.; Huang, J.; Wang, D.; Mensah, A.; Wei, Q. A Multifunctional and Highly Stretchable Electronic Device Based on Silver Nanowire/Wrap Yarn Composite for a Wearable Strain Sensor and Heater. *J. Mater. Chem. C* **2019**, *7* (43), 13468–13476. <https://doi.org/10.1039/C9TC04252K>.
- (136) Veeramuthu, L.; Chen, B.-Y.; Tsai, C.-Y.; Liang, F.-C.; Venkatesan, M.; Jiang, D.-H.; Chen, C.-W.; Cai, X.; Kuo, C.-C. Novel Stretchable Thermochromic Transparent Heaters Designed for Smart Window Defroster Applications by Spray Coating Silver Nanowire. *RSC Advances* **2019**, *9* (61), 35786–35796. <https://doi.org/10.1039/C9RA06508C>.
- (137) Jo, M.; Bae, S.; Oh, I.; Jeong, J.; Kang, B.; Hwang, S. J.; Lee, S. S.; Son, H. J.; Moon, B.-M.; Ko, M. J.; Lee, P. 3D Printer-Based Encapsulated Origami Electronics for Extreme System Stretchability and High Areal Coverage. *ACS Nano* **2019**, *13* (11), 12500–12510. <https://doi.org/10.1021/acsnano.9b02362>.
- (138) Jo, H. S.; An, S.; Park, C.-W.; Woo, D.-Y.; Yarin, A. L.; Yoon, S. S. Wearable, Stretchable, Transparent All-in-One Soft Sensor Formed from Supersonically Sprayed Silver Nanowires. *ACS Appl. Mater. Interfaces* **2019**, *11* (43), 40232–40242. <https://doi.org/10.1021/acsmi.9b12847>.
- (139) Yao, S.; Yang, J.; Poblete, F. R.; Hu, X.; Zhu, Y. Multifunctional Electronic Textiles Using Silver Nanowire Composites. *ACS Appl. Mater. Interfaces* **2019**, *11* (34), 31028–31037. <https://doi.org/10.1021/acsmi.9b07520>.
- (140) Jayathilaka, W. A. D. M.; Qi, K.; Qin, Y.; Chinnappan, A.; Serrano-García, W.; Baskar, C.; Wang, H.; He, J.; Cui, S.; Thomas, S. W.; Ramakrishna, S. Significance of Nanomaterials in Wearables: A Review on Wearable Actuators and Sensors. *Adv. Mater.* **2019**, *31* (7), 1805921. <https://doi.org/10.1002/adma.201805921>.

- (141) Kwon, J.; Suh, Y. D.; Lee, J.; Lee, P.; Han, S.; Hong, S.; Yeo, J.; Lee, H.; Ko, S. H. Recent Progress in Silver Nanowire Based Flexible/Wearable Optoelectronics. *Journal of Materials Chemistry C* **2018**, *6* (28), 7445–7461. <https://doi.org/10.1039/C8TC01024B>.
- (142) Jung, J.; Cho, H.; Yuksel, R.; Kim, D.; Lee, H.; Kwon, J.; Lee, P.; Yeo, J.; Hong, S.; Unalan, H. E.; Han, S.; Ko, S. H. Stretchable/Flexible Silver Nanowire Electrodes for Energy Device Applications. *Nanoscale* **2019**, *11* (43), 20356–20378. <https://doi.org/10.1039/C9NR04193A>.
- (143) Kim, D.-J.; Shin, H.-I.; Ko, E.-H.; Kim, K.-H.; Kim, T.-W.; Kim, H.-K. Roll-to-Roll Slot-Die Coating of 400 Mm Wide, Flexible, Transparent Ag Nanowire Films for Flexible Touch Screen Panels. *Scientific Reports* **2016**, *6* (1). <https://doi.org/10.1038/srep34322>.
- (144) Hauger, T. C.; Al-Rafia, S. M. I.; Buriak, J. M. Rolling Silver Nanowire Electrodes: Simultaneously Addressing Adhesion, Roughness, and Conductivity. *ACS Appl. Mater. Interfaces* **2013**, *5* (23), 12663–12671. <https://doi.org/10.1021/am403986f>.
- (145) Xu, F.; Zhu, Y. Highly Conductive and Stretchable Silver Nanowire Conductors. *Advanced Materials* **2012**, *24* (37), 5117–5122. <https://doi.org/10.1002/adma.201201886>.
- (146) Park, M.; Kim, W.; Hwang, B.; Han, S. M. Effect of Varying the Density of Ag Nanowire Networks on Their Reliability during Bending Fatigue. *Scripta Materialia* **2019**, *161*, 70–73. <https://doi.org/10.1016/j.scriptamat.2018.10.017>.
- (147) Chen, S.-P.; Liao, Y.-C. Highly Stretchable and Conductive Silver Nanowire Thin Films Formed by Soldering Nanomesh Junctions. *Phys. Chem. Chem. Phys.* **2014**, *16* (37), 19856–19860. <https://doi.org/10.1039/C4CP02808B>.
- (148) Lee, P.; Lee, J.; Lee, H.; Yeo, J.; Hong, S.; Nam, K. H.; Lee, D.; Lee, S. S.; Ko, S. H. Highly Stretchable and Highly Conductive Metal Electrode by Very Long Metal Nanowire Percolation Network. *Adv. Mater.* **2012**, *24* (25), 3326–3332. <https://doi.org/10.1002/adma.201200359>.
- (149) Hong, S.; Lee, H.; Lee, J.; Kwon, J.; Han, S.; Suh, Y. D.; Cho, H.; Shin, J.; Yeo, J.; Ko, S. H. Highly Stretchable and Transparent Metal Nanowire Heater for Wearable Electronics Applications. *Adv. Mater.* **2015**, *27* (32), 4744–4751. <https://doi.org/10.1002/adma.201500917>.
- (150) Liu, H.-S.; Pan, B.-C.; Liou, G.-S. Highly Transparent AgNW/PDMS Stretchable Electrodes for Elastomeric Electrochromic Devices. *Nanoscale* **2017**, *9* (7), 2633–2639. <https://doi.org/10.1039/C6NR09220A>.
- (151) Kim, J.; Park, J.; Jeong, U.; Park, J.-W. Silver Nanowire Network Embedded in Polydimethylsiloxane as Stretchable, Transparent, and Conductive Substrates. *J. Appl. Polym. Sci.* **2016**, *133* (33), n/a-n/a. <https://doi.org/10.1002/app.43830>.
- (152) Huang, G.-W.; Xiao, H.-M.; Fu, S.-Y. Wearable Electronics of Silver-Nanowire/Poly(Dimethylsiloxane) Nanocomposite for Smart Clothing. *Scientific Reports* **2015**, *5*, 13971. <https://doi.org/10.1038/srep13971>.
- (153) Amjadi, M.; Pichitpajongkit, A.; Ryu, S.; Park, I. Piezoresistivity of AG NWS-PDMS Nanocomposite. In *2014 IEEE 27th International Conference on Micro Electro Mechanical Systems (MEMS)*; 2014; pp 785–788. <https://doi.org/10.1109/MEMSYS.2014.6765758>.
- (154) Ho, X.; Nie Tey, J.; Liu, W.; Kweng Cheng, C.; Wei, J. Biaxially Stretchable Silver Nanowire Transparent Conductors. *Journal of Applied Physics* **2013**, *113* (4), 044311-044311–044315. <https://doi.org/doi:10.1063/1.4789795>.

- (155) Lim, G.-H.; Ahn, K.; Bok, S.; Nam, J.; Lim, B. Curving Silver Nanowires Using Liquid Droplets for Highly Stretchable and Durable Percolation Networks. *Nanoscale* **2017**, *9* (26), 8938–8944. <https://doi.org/10.1039/C7NR02615C>.
- (156) Ho, X.; Cheng, C. K.; Tey, J. N.; Wei, J. Tunable Strain Gauges Based on Two-Dimensional Silver Nanowire Networks. *Nanotechnology* **2015**, *26* (19), 195504. <https://doi.org/10.1088/0957-4484/26/19/195504>.
- (157) Seo, Y.; Kim, B. S.; Ballance, W. C.; Aw, N.; Sutton, B.; Kong, H. Transparent and Flexible Electronics Assembled with Metallic Nanowire-Layered Nondrying Glycerogel. *ACS Appl. Mater. Interfaces* **2020**, *12* (11), 13040–13050. <https://doi.org/10.1021/acscami.9b21697>.
- (158) Lee, H.-J.; Oh, S.; Cho, K.-Y.; Jeong, W.-L.; Lee, D.-S.; Park, S.-J. Spontaneous and Selective Nanowelding of Silver Nanowires by Electrochemical Ostwald Ripening and High Electrostatic Potential at the Junctions for High-Performance Stretchable Transparent Electrodes. *ACS Appl. Mater. Interfaces* **2018**, *10* (16), 14124–14131. <https://doi.org/10.1021/acscami.8b00837>.
- (159) Weng, C.; Dai, Z.; Wang, G.; Liu, L.; Zhang, Z. Elastomer-Free, Stretchable, and Conformable Silver Nanowire Conductors Enabled by Three-Dimensional Buckled Microstructures. *ACS Appl. Mater. Interfaces* **2019**, *11* (6), 6541–6549. <https://doi.org/10.1021/acscami.8b19890>.
- (160) Zhu, Y.; Qin, Q.; Xu, F.; Fan, F.; Ding, Y.; Zhang, T.; Wiley, B. J.; Wang, Z. L. Size Effects on Elasticity, Yielding, and Fracture of Silver Nanowires: *In Situ* Experiments. *Physical Review B* **2012**, *85* (4). <https://doi.org/10.1103/PhysRevB.85.045443>.
- (161) Fantanas, D.; Brunton, A.; Henley, S. J.; Dorey, R. A. Investigation of the Mechanism for Current Induced Network Failure for Spray Deposited Silver Nanowires. *Nanotechnology* **2018**, *29* (46), 465705. <https://doi.org/10.1088/1361-6528/aaded>.
- (162) Khaligh, H. H.; Xu, L.; Khosropour, A.; Madeira, A.; Romano, M.; Pradère, C.; Tréguer-Delapierre, M.; Servant, L.; Pope, M. A.; Goldthorpe, I. A. The Joule Heating Problem in Silver Nanowire Transparent Electrodes. *Nanotechnology* **2017**, *28* (42), 425703. <https://doi.org/10.1088/1361-6528/aa7f34>.
- (163) Khaligh, H. H.; Goldthorpe, I. A. Failure of Silver Nanowire Transparent Electrodes under Current Flow. *Nanoscale research letters* **2013**, *8* (1), 1–6.
- (164) Chen, D.; Zhao, F.; Tong, K.; Saldanha, G.; Liu, C.; Pei, Q. Mitigation of Electrical Failure of Silver Nanowires under Current Flow and the Application for Long Lifetime Organic Light-Emitting Diodes. *Advanced Electronic Materials* **2016**, *2* (8), 1600167. <https://doi.org/10.1002/aelm.201600167>.
- (165) Mayousse, C.; Celle, C.; Fraczkiewicz, A.; Simonato, J.-P. Stability of Silver Nanowire Based Electrodes under Environmental and Electrical Stresses. *Nanoscale* **2015**, *7* (5), 2107–2115. <https://doi.org/10.1039/C4NR06783E>.
- (166) Arefpour, M.; Almasi Kashi, M.; Bagheli, M. High Chemical and Thermal Stability of Ag Nanowire-Based Transparent Conductive Electrodes Induced by Electroless Ag Nanoparticle Decoration. *Phys. Status Solidi A* **2020**, 1900957. <https://doi.org/10.1002/pssa.201900957>.
- (167) Kholid, F. N.; Huang, H.; Zhang, Y.; Fan, H. J. Multiple Electrical Breakdowns and Electrical Annealing Using High Current Approximating Breakdown Current of Silver Nanowire Network. *Nanotechnology* **2016**, *27* (2), 025703. <https://doi.org/10.1088/0957-4484/27/2/025703>.
- (168) Batra, N. M.; Syed, A.; Costa, P. M. F. J. Current-Induced Restructuring in Bent Silver Nanowires. *Nanoscale* **2019**, *11* (8), 3606–3618. <https://doi.org/10.1039/C8NR08551J>.

- (169) Lagrange, M.; Sanniccolo, T.; Muñoz-Rojas, D.; Lohan, B. G.; Khan, A.; Anikin, M.; Jiménez, C.; Bruckert, F.; Bréchet, Y.; D Bellet. Understanding the Mechanisms Leading to Failure in Metallic Nanowire-Based Transparent Heaters, and Solution for Stability Enhancement. *Nanotechnology* **2017**, *28* (5), 055709. <https://doi.org/10.1088/1361-6528/28/5/055709>.
- (170) Maize, K.; Das, S. R.; Sadeque, S.; Mohammed, A. M. S.; Shakouri, A.; Janes, D. B.; Alam, M. A. Super-Joule Heating in Graphene and Silver Nanowire Network. *Applied Physics Letters* **2015**, *106* (14), 143104. <https://doi.org/10.1063/1.4916943>.
- (171) Zhai, H.; Wang, R.; Wang, X.; Cheng, Y.; Shi, L.; Sun, J. Transparent Heaters Based on Highly Stable Cu Nanowire Films. *Nano Res.* **2016**, *9* (12), 3924–3936. <https://doi.org/10.1007/s12274-016-1261-0>.
- (172) Leonard, W. F.; Ramey, R. L. Temperature Coefficient of Resistance in Thin Metal Films. *Journal of Applied Physics* **1966**, *37* (9), 3634–3635. <https://doi.org/10.1063/1.1708921>.
- (173) Sandouk, E. J.; Gimzewski, J. K.; Stieg, A. Z. Multistate Resistive Switching in Silver Nanoparticle Films. *Science and Technology of Advanced Materials* **2015**, *16* (4), 045004. <https://doi.org/10.1088/1468-6996/16/4/045004>.
- (174) Morgenstern, F. S. F.; Kabra, D.; Massip, S.; Brenner, T. J. K.; Lyons, P. E.; Coleman, J. N.; Friend, R. H. Ag-Nanowire Films Coated with ZnO Nanoparticles as a Transparent Electrode for Solar Cells. *Applied Physics Letters* **2011**, *4* (11), 183307-183307–3. <https://doi.org/10.1063/1.3656973>.
- (175) Muñoz-Rojas, D.; MacManus-Driscoll, J. Spatial Atmospheric Atomic Layer Deposition: A New Laboratory and Industrial Tool for Low-Cost Photovoltaics. *Mater. Horiz.* **2014**, *1* (3), 314–320. <https://doi.org/10.1039/C3MH00136A>.
- (176) Song, T.-B.; Rim, Y. S.; Liu, F.; Bob, B.; Ye, S.; Hsieh, Y.-T.; Yang, Y. Highly Robust Silver Nanowire Network for Transparent Electrode. *ACS Appl. Mater. Interfaces* **2015**, *7* (44), 24601–24607. <https://doi.org/10.1021/acsami.5b06540>.
- (177) Go, M.; Hwang, B.; Lim, S. Highly Reliable Mulberry Paper (Hanji)-Based Electrode with Printed Silver Nanowire/Zinc Oxide Hybrid for Soft Electronics. *Materials and Manufacturing Processes* **2019**, *34* (14), 1605–1611. <https://doi.org/10.1080/10426914.2019.1594266>.
- (178) Hwang, B.; An, Y.; Lee, H.; Lee, E.; Becker, S.; Kim, Y.-H.; Kim, H. Highly Flexible and Transparent Ag Nanowire Electrode Encapsulated with Ultra-Thin Al₂O₃: Thermal, Ambient, and Mechanical Stabilities. *Scientific Reports* **2017**, *7* (1). <https://doi.org/10.1038/srep41336>.
- (179) Lee, J.-M.; Kim, Y.-H.; Kim, H.-K.; Kim, H.-J.; Hong, C.-H. Effect of AlO_x Protection Layer on AgNWs for Flexible Transparent Heater. *Scientific Reports* **2020**, *10* (1). <https://doi.org/10.1038/s41598-020-61449-6>.
- (180) Aghazadehchors, S.; Nguyen, V. H.; Muñoz-Rojas, D.; Jiménez, C.; Rapenne, L.; Nguyen, N. D.; Bellet, D. Versatility of Bilayer Metal Oxide Coatings on Silver Nanowire Networks for Enhanced Stability with Minimal Transparency Loss. *Nanoscale* **2019**, *11* (42), 19969–19979. <https://doi.org/10.1039/C9NR05658K>.
- (181) Göbelt, M.; Keding, R.; Schmitt, S. W.; Hoffmann, B.; Jäckle, S.; Latzel, M.; Radmilović, V. V.; Radmilović, V. R.; Spiecker, E.; Christiansen, S. Encapsulation of Silver Nanowire Networks by Atomic Layer Deposition for Indium-Free Transparent Electrodes. *Nano Energy* **2015**, *16*, 196–206. <https://doi.org/10.1016/j.nanoen.2015.06.027>.
- (182) Chae, W. H.; Sanniccolo, T.; Grossman, J. C. Double-Sided Graphene Oxide Encapsulated Silver Nanowire Transparent Electrode with Improved Chemical and

- Electrical Stability. *ACS Appl. Mater. Interfaces* **2020**, acsami.0c03587. <https://doi.org/10.1021/acsami.0c03587>.
- (183) Wang, S.; Tian, Y.; Wang, C.; Hang, C.; Huang, Y.; Liao, C. Chemical and Thermal Robust Tri-Layer RGO/Ag NWs/GO Composite Film for Wearable Heaters. *Composites Science and Technology* **2019**, *174*, 76–83. <https://doi.org/10.1016/j.compscitech.2019.02.022>.
- (184) Nguyen, V. H. et al. Deposition of ZnO Based Thin Films by Atmospheric Pressure Spatial Atomic Layer Deposition for Application in Solar Cells. *Journal of Renewable and Sustainable Energy* **2017**, *9* (2), 021203. <https://doi.org/10.1063/1.4979822>.
- (185) Levy, D. H.; Nelson, S. F. Thin-Film Electronics by Atomic Layer Deposition. *Journal of Vacuum Science & Technology A: Vacuum, Surfaces, and Films* **2012**, *30* (1), 018501. <https://doi.org/10.1116/1.3670748>.
- (186) Johnson, R. W.; Hultqvist, A.; Bent, S. F. A Brief Review of Atomic Layer Deposition: From Fundamentals to Applications. *Materials Today* **2014**, *17* (5), 236–246. <https://doi.org/10.1016/j.mattod.2014.04.026>.
- (187) de la Huerta, C. A. M.; Nguyen, V. H.; Sekkat, A.; Crivello, C.; Toldra-Reig, F.; Veiga, P.; Jimenez, C.; Quessada, S.; Muñoz-Rojas, D. Facile Patterning of Functional Materials via Gas-Phase 3D Printing. *arXiv:2006.05235 [cond-mat, physics:physics]* **2020**. <https://doi.org/10.1002/admt.202000657>.
- (188) Muñoz-Rojas, D.; Huong Nguyen, V.; Masse de la Huerta, C.; Jiménez, C.; Bellet, D. Spatial Atomic Layer Deposition. In *Chemical Vapor Deposition for Nanotechnology*; Mandracci, P., Ed.; IntechOpen, 2019. <https://doi.org/10.5772/intechopen.82439>.
- (189) Masse de la Huerta, C.; Nguyen, V. H.; Dedulle, J.-M.; Bellet, D.; Jiménez, C.; Muñoz-Rojas, D. Influence of the Geometric Parameters on the Deposition Mode in Spatial Atomic Layer Deposition: A Novel Approach to Area-Selective Deposition. *Coatings* **2019**, *9* (1), 5. <https://doi.org/10.3390/coatings9010005>.
- (190) Hecht, D. S.; Hu, L.; Irvin, G. Emerging Transparent Electrodes Based on Thin Films of Carbon Nanotubes, Graphene, and Metallic Nanostructures. *Adv. Mater.* **2011**, *23* (13), 1482–1513. <https://doi.org/10.1002/adma.201003188>.
- (191) De, S.; Higgins, T. M.; Lyons, P. E.; Doherty, E. M.; Nirmalraj, P. N.; Blau, W. J.; Boland, J. J.; Coleman, J. N. Silver Nanowire Networks as Flexible, Transparent, Conducting Films: Extremely High DC to Optical Conductivity Ratios. *ACS Nano* **2009**, *3* (7), 1767–1774. <https://doi.org/10.1021/nn900348c>.
- (192) Gupta, R.; Rao, K. D. M.; Kiruthika, S.; Kulkarni, G. U. Visibly Transparent Heaters. *ACS Appl. Mater. Interfaces* **2016**, *8* (20), 12559–12575. <https://doi.org/10.1021/acsami.5b11026>.
- (193) Jang, J.; Parmar, N. S.; Choi, W. K.; Choi, J.-W. Rapid Defrost Transparent Thin Film Heater with Flexibility and Chemical Stability. *ACS Appl. Mater. Interfaces* **2020**, acsami.0c10852. <https://doi.org/10.1021/acsami.0c10852>.
- (194) Lee, S. Y.; Hwang, J. Y. Transparent Heater with Meshed Amorphous Oxide/Metal/Amorphous Oxide for Electric Vehicle Applications. *Sci Rep* **2020**, *10* (1), 9697. <https://doi.org/10.1038/s41598-020-66514-8>.
- (195) Lee, J.-M.; Kim, Y.-H.; Kim, H.-K.; Kim, H.-J.; Hong, C.-H. Effect of AlO_x Protection Layer on AgNWs for Flexible Transparent Heater. *Sci Rep* **2020**, *10* (1), 4592. <https://doi.org/10.1038/s41598-020-61449-6>.
- (196) Yang, Y.; Chen, S.; Li, W.; Li, P.; Ma, J.; Li, B.; Zhao, X.; Ju, Z.; Chang, H.; Xiao, L.; Xu, H.; Liu, Y. Reduced Graphene Oxide Conformally Wrapped Silver Nanowire Networks for Flexible Transparent Heating and Electromagnetic Interference Shielding. *ACS Nano* **2020**, *14* (7), 8754–8765. <https://doi.org/10.1021/acs.nano.0c03337>.

- (197) Zhang, Y.; Liu, H.; Tan, L.; Zhang, Y.; Jeppson, K.; Wei, B.; Liu, J. Properties of Undoped Few-Layer Graphene-Based Transparent Heaters. *Materials* **2019**, *13* (1), 104. <https://doi.org/10.3390/ma13010104>.
- (198) Li, Z.; Zhen, Z.; Chai, M.; Zhao, X.; Zhong, Y.; Zhu, H. Transparent Electrothermal Film Defoggers and Antiicing Coatings Based on Wrinkled Graphene. *Small* **2020**, *16* (4), 1905945. <https://doi.org/10.1002/sml.201905945>.
- (199) Park, J.; Lee, S.; Kim, D.-I.; Kim, Y.-Y.; Kim, S.; Kim, H.-J.; Kim, Y. Evaporation-Rate Control of Water Droplets on Flexible Transparent Heater for Sensor Application. *Sensors* **2019**, *19* (22), 4918. <https://doi.org/10.3390/s19224918>.
- (200) Kim, H.-J.; Kim, J.; Kim, Y. Fluoropolymer-Coated Nanometer-Thick Cu Mesh Film for Robust and Hydrophobic Transparent Heater. *ACS Appl. Nano Mater.* **2020**, *acsanm.0c01404*. <https://doi.org/10.1021/acsanm.0c01404>.
- (201) Wang, Z.; Li, J.; Xu, J.; Huang, J.; Yang, Y.; Tan, R.; Chen, G.; Fang, X.; Zhao, Y.; Song, W. Robust Ultrathin and Transparent AZO/Ag-SnO₂/AZO on Polyimide Substrate for Flexible Thin Film Heater with Temperature over 400 °C. *Journal of Materials Science & Technology* **2020**, *48*, 156–162. <https://doi.org/10.1016/j.jmst.2020.01.058>.
- (202) Lim, S.-H.; Kim, H.-K. Deposition Rate Effect on Optical and Electrical Properties of Thermally Evaporated WO_{3-x}/Ag/WO_{3-x} Multilayer Electrode for Transparent and Flexible Thin Film Heaters. *Sci Rep* **2020**, *10* (1), 8357. <https://doi.org/10.1038/s41598-020-65260-1>.
- (203) Goak, J. C.; Kim, T. Y.; Kim, D. U.; Chang, K. S.; Lee, C. S.; Lee, N. Stable Heating Performance of Carbon Nanotube/Silver Nanowire Transparent Heaters. *Applied Surface Science* **2020**, *510*, 145445. <https://doi.org/10.1016/j.apsusc.2020.145445>.
- (204) Xie, Y.; Guan, F.; Li, Z.; Meng, Y.; Cheng, J.; Li, L.; Pei, Q. A Phase-Changing Polymer Film for Broadband Smart Window Applications. *Macromol. Rapid Commun.* **2020**, 2000290. <https://doi.org/10.1002/marc.202000290>.
- (205) Guo, B.; Zhang, J.; Ananth, K. P.; Zhao, S.; Ji, X.; Bai, J. Stretchable, Self-Healing and Biodegradable Water-Based Heater Produced by 3D Printing. *Composites Part A: Applied Science and Manufacturing* **2020**, *133*, 105863. <https://doi.org/10.1016/j.compositesa.2020.105863>.
- (206) Zhao, W.; Qu, X.; Xu, Q.; Lu, Y.; Yuan, W.; Wang, W.; Wang, Q.; Huang, W.; Dong, X. Ultrastretchable, Self-Healable, and Wearable Epidermal Sensors Based on Ultralong Ag Nanowires Compositing Binary-Networked Hydrogels. *Adv. Electron. Mater.* **2020**, *6* (7), 2000267. <https://doi.org/10.1002/aelm.202000267>.
- (207) Kim, D.; Bang, J.; Lee, W.; Ha, I.; Lee, J.; Eom, H.; Kim, M.; Park, J.; Choi, J.; Kwon, J.; Han, S.; Park, H.; Lee, D.; Ko, S. H. Highly Stretchable and Oxidation-Resistive Cu Nanowire Heater for Replication of the Feeling of Heat in a Virtual World. *J. Mater. Chem. A* **2020**, *8* (17), 8281–8291. <https://doi.org/10.1039/D0TA00380H>.
- (208) Hu, R.; Liu, Y.; Shin, S.; Huang, S.; Ren, X.; Shu, W.; Cheng, J.; Tao, G.; Xu, W.; Chen, R.; Luo, X. Emerging Materials and Strategies for Personal Thermal Management. *Adv. Energy Mater.* **2020**, *10* (17), 1903921. <https://doi.org/10.1002/aenm.201903921>.
- (209) Wang, X.; Kang, G.; Seong, B.; Chae, I.; Yudistira, H. T.; Lee, H.; Kim, H.; Byun, D. Transparent Arrays of Silver Nanowire Rings Driven by Evaporation of Sessile Droplets. *J. Phys. D: Appl. Phys.* **2017**, *50* (45), 455302. <https://doi.org/10.1088/1361-6463/aa8c23>.

- (210) Choi, D. Y.; Kang, H. W.; Sung, H. J.; Kim, S. S. Annealing-Free, Flexible Silver Nanowire–Polymer Composite Electrodes via a Continuous Two-Step Spray-Coating Method. *Nanoscale* **2013**, *5* (3), 977–983. <https://doi.org/10.1039/C2NR32221H>.
- (211) Cai, Z.; Deng, S.; Liao, H.; Zeng, C.; Montavon, G. The Effect of Spray Distance and Scanning Step on the Coating Thickness Uniformity in Cold Spray Process. *J Therm Spray Tech* **2014**, *23* (3), 354–362. <https://doi.org/10.1007/s11666-013-0002-0>.
- (212) Zardetto, V.; Brown, T. M.; Reale, A.; Di Carlo, A. Substrates for Flexible Electronics: A Practical Investigation on the Electrical, Film Flexibility, Optical, Temperature, and Solvent Resistance Properties. *Journal of Polymer Science Part B: Polymer Physics* **2011**, *49* (9), 638–648. <https://doi.org/10.1002/polb.22227>.
- (213) Mayousse, C.; Celle, C.; Moreau, E.; Mainguet, J.-F.; Carella, A.; Simonato, J.-P. Improvements in Purification of Silver Nanowires by Decantation and Fabrication of Flexible Transparent Electrodes. Application to Capacitive Touch Sensors. *Nanotechnology* **2013**, *24* (21), 215501.
- (214) 1737F Alkali-free boro-aluminosilicate glass <https://www.pgo-online.com/intl/1737.html>.
- (215) Fonrodona, M.; Escarre, J.; Villar, F.; Soler, D.; Asensi, J.; Bertomeu, J.; Andreu, J. PEN as Substrate for New Solar Cell Technologies. *Solar Energy Materials and Solar Cells* **2005**, *89* (1), 37–47. <https://doi.org/10.1016/j.solmat.2004.12.006>.
- (216) Kiran Kumar, A. B. V.; wan Bae, C.; Piao, L.; Kim, S.-H. Silver Nanowire Based Flexible Electrodes with Improved Properties: High Conductivity, Transparency, Adhesion and Low Haze. *Materials Research Bulletin* **2013**, *48* (8), 2944–2949. <https://doi.org/10.1016/j.materresbull.2013.04.035>.
- (217) Ni, H.; Liu, J.; Wang, Z.; Yang, S. A Review on Colorless and Optically Transparent Polyimide Films: Chemistry, Process and Engineering Applications. *Journal of Industrial and Engineering Chemistry* **2015**, *28*, 16–27. <https://doi.org/10.1016/j.jiec.2015.03.013>.
- (218) Nguyen, V. H.; Resende, J.; Papanastasiou, D. T.; Fontanals, N.; Jiménez, C.; Muñoz-Rojas, D.; Bellet, D. Low-Cost Fabrication of Flexible Transparent Electrodes Based on Al Doped ZnO and Silver Nanowire Nanocomposites: Impact of the Network Density. *Nanoscale* **2019**, *11* (25), 12097–12107. <https://doi.org/10.1039/C9NR02664A>.
- (219) Victor, A.; Ribeiro, J.; F. Araújo, F. Study of PDMS Characterization and Its Applications in Biomedicine: A Review. *JMEB* **2019**, *4* (1), 1–9. <https://doi.org/10.24243/JMEB/4.1.163>.
- (220) Jung, J.; Cho, H.; Yuksel, R.; Kim, D.; Lee, H.; Kwon, J.; Lee, P.; Yeo, J.; Hong, S.; Unalan, H. E.; Han, S.; Ko, S. H. Stretchable/Flexible Silver Nanowire Electrodes for Energy Device Applications. *Nanoscale* **2019**, *11* (43), 20356–20378. <https://doi.org/10.1039/C9NR04193A>.
- (221) Kachroudi, A.; Basrou, S.; Rufer, L.; Sylvestre, A.; Jomni, F. Dielectric Properties Modelling of Cellular Structures with PDMS for Micro-Sensor Applications. *Smart Materials and Structures* **2015**, *24* (12), 125013. <https://doi.org/10.1088/0964-1726/24/12/125013>.
- (222) Lagomarsini, C.; Jean-Mistral, C.; Lombardi, G.; Sylvestre, A. Hybrid Piezoelectric–Electrostatic Generators for Wearable Energy Harvesting Applications. *Smart Mater. Struct.* **2019**, *28* (3), 035003. <https://doi.org/10.1088/1361-665X/aaf34e>.
- (223) Birch, W. R. Cleaning Glass Surfaces. In *Sol-Gel Technologies for Glass Producers and Users*; Aegerter, M. A., Mennig, M., Eds.; Springer US: Boston, MA, 2004; pp 19–34. https://doi.org/10.1007/978-0-387-88953-5_2.

- (224) Dong, J.; Goldthorpe, I. A. Exploiting Both Optical and Electrical Anisotropy in Nanowire Electrodes for Higher Transparency. *Nanotechnology* **2018**, *29* (4), 045705. <https://doi.org/10.1088/1361-6528/aa9ab2>.
- (225) Kang, S.; Kim, T.; Cho, S.; Lee, Y.; Choe, A.; Walker, B.; Ko, S.-J.; Kim, J. Y.; Ko, H. Capillary Printing of Highly Aligned Silver Nanowire Transparent Electrodes for High-Performance Optoelectronic Devices. *Nano Lett.* **2015**, *15* (12), 7933–7942. <https://doi.org/10.1021/acs.nanolett.5b03019>.
- (226) Chiang, K.-M.; Huang, Z.-Y.; Tsai, W.-L.; Lin, H.-W. Orthogonally Weaved Silver Nanowire Networks for Very Efficient Organic Optoelectronic Devices. *Organic Electronics* **2017**, *43*, 15–20. <https://doi.org/10.1016/j.orgel.2016.12.054>.
- (227) Smits, F. M. Measurement of Sheet Resistivities with the Four-Point Probe. *Bell System Technical Journal* **1958**, *37* (3), 711–718. <https://doi.org/10.1002/j.1538-7305.1958.tb03883.x>.
- (228) Margulis, G. Y.; Christoforo, M. G.; Lam, D.; Beiley, Z. M.; Bowring, A. R.; Bailie, C. D.; Salleo, A.; McGehee, M. D. Spray Deposition of Silver Nanowire Electrodes for Semitransparent Solid-State Dye-Sensitized Solar Cells. *Adv. Energy Mater.* **2013**, *3* (12), 1657–1663. <https://doi.org/10.1002/aenm.201300660>.
- (229) Steger, C. An Unbiased Detector of Curvilinear Structures. *IEEE Transactions on Pattern Analysis and Machine Intelligence* **1998**, *20* (2), 113–125. <https://doi.org/10.1109/34.659930>.
- (230) Langley, D. P.; Lagrange, M.; Nguyen, N. D.; Bellet, D. Percolation in Networks of 1-Dimensional Objects: Comparison between Monte Carlo Simulations and Experimental Observations. *Nanoscale Horizons* **2018**, *3* (5), 545–550. <https://doi.org/10.1039/C8NH00066B>.
- (231) De, S.; Coleman, J. N. The Effects of Percolation in Nanostructured Transparent Conductors. *MRS Bulletin* **2011**, *36* (10), 774–781. <https://doi.org/10.1557/mrs.2011.236>.
- (232) Daniel P. Langley. Silver Nanowire Networks: Effects of Percolation and Thermal Annealing on Physical Properties. October 2014.
- (233) Kumar, A.; Kulkarni, G. U. Evaluating Conducting Network Based Transparent Electrodes from Geometrical Considerations. *Journal of Applied Physics* **2016**. <https://doi.org/10.1063/1.4939280>.
- (234) COMSOL Multiphysics. The Finite Element Method (FEM) <https://www.comsol.com/multiphysics/finite-element-method>.
- (235) Thangaraju, S. K.; Munisamy, K. M. Electrical and Joule Heating Relationship Investigation Using Finite Element Method. *IOP Conf. Ser.: Mater. Sci. Eng.* **2015**, *88*, 012036. <https://doi.org/10.1088/1757-899X/88/1/012036>.
- (236) Sannicolo, T. Transparent Electrodes Based on Silver Nanowire Networks: Electrical Percolation, Physical Properties, and Applications. PhD thesis, University of Grenoble Alpes (France), 2017.
- (237) Bellew, A. T.; Manning, H. G.; Gomes da Rocha, C.; Ferreira, M. S.; Boland, J. J. Resistance of Single Ag Nanowire Junctions and Their Role in the Conductivity of Nanowire Networks. *ACS Nano* **2015**. <https://doi.org/10.1021/acs.nano.5b05469>.
- (238) Selzer, F.; Floresca, C.; Kneppe, D.; Bormann, L.; Sachse, C.; Weiß, N.; Eychmüller, A.; Amassian, A.; Müller-Meskamp, L.; Leo, K. Electrical Limit of Silver Nanowire Electrodes: Direct Measurement of the Nanowire Junction Resistance. *Applied Physics Letters* **2016**, *108* (16), 163302. <https://doi.org/10.1063/1.4947285>.
- (239) Bellew, A. T.; Manning, H. G.; Gomes da Rocha, C.; Ferreira, M. S.; Boland, J. J. Resistance of Single Ag Nanowire Junctions and Their Role in the Conductivity of

- Nanowire Networks. *ACS Nano* **2015**, *9* (11), 11422–11429. <https://doi.org/10.1021/acsnano.5b05469>.
- (240) Lagrange, M.; Sannicolo, T.; Muñoz-Rojas, D.; Lohan, B. G.; Khan, A.; Anikin, M.; Jiménez, C.; Bruckert, F.; Bréchet, Y.; D Bellet. Understanding the Mechanisms Leading to Failure in Metallic Nanowire-Based Transparent Heaters, and Solution for Stability Enhancement. *Nanotechnology* **2017**, *28* (5), 055709. <https://doi.org/10.1088/1361-6528/28/5/055709>.
- (241) Bid, A.; Bora, A.; Raychaudhuri, A. K. Temperature Dependence of the Resistance of Metallic Nanowires of Diameter ≥ 15 Nm: Applicability of Bloch-Grüneisen Theorem. *Phys. Rev. B* **2006**, *74* (3), 035426. <https://doi.org/10.1103/PhysRevB.74.035426>.
- (242) Forró, C.; Demkó, L.; Weydert, S.; Vörös, J.; Tybrandt, K. Predictive Model for the Electrical Transport within Nanowire Networks. *ACS nano* **2018**, *12* (11), 11080–11087.
- (243) da Rocha, C. G.; Manning, H. G.; O’Callaghan, C.; Ritter, C.; Bellew, A. T.; Boland, J. J.; Ferreira, M. S. Ultimate Conductivity Performance in Metallic Nanowire Networks. *Nanoscale* **2015**, *7* (30), 13011–13016.
- (244) Lagrange, M. Physical Analysis of Percolating Silver Nanowire Networks Used as Transparent Electrodes for Flexible Applications. PhD thesis, University of Grenoble Alpes (France), 2015.
- (245) de Gennes, P.-G.; Brochard-Wyart, F.; Quéré, D. *Capillarity and Wetting Phenomena - Drops, Bubbles, Pearls, Waves*; Springer New York, 2004.
- (246) Jamnig, A.; Sangiovanni, D. G.; Abadias, G.; Sarakinos, K. Atomic-Scale Diffusion Rates during Growth of Thin Metal Films on Weakly-Interacting Substrates. *Sci Rep* **2019**, *9* (1), 6640. <https://doi.org/10.1038/s41598-019-43107-8>.
- (247) Wang, K.; Jin, Y.; Wang, X.; Qian, B.; Wang, J.; Xiao, F. Investigation into the Failure Mechanism of Silver Nanowire Network Film under Electrical Stress. In *2020 IEEE 70th Electronic Components and Technology Conference (ECTC)*; IEEE: Orlando, FL, USA, 2020; pp 1218–1224. <https://doi.org/10.1109/ECTC32862.2020.00195>.
- (248) Black, J. R. Electromigration—A Brief Survey and Some Recent Results. *IEEE Transactions on Electron Devices* **1969**, *16* (4), 338–347. <https://doi.org/10.1109/T-ED.1969.16754>.
- (249) Stahlmecke, B.; Meyer zu Heringdorf, F.-J.; Chelaru, L. I.; Horn-von Hoegen, M.; Dumpich, G.; Roos, K. R. Electromigration in Self-Organized Single-Crystalline Silver Nanowires. *Applied Physics Letters* **2006**, *88* (5), 053122. <https://doi.org/10.1063/1.2172012>.
- (250) Nguyen, V. H.; Resende, J.; Jiménez, C.; Deschanvres, J.-L.; Carroy, P.; Muñoz, D.; Bellet, D.; Muñoz-Rojas, D. Deposition of ZnO Based Thin Films by Atmospheric Pressure Spatial Atomic Layer Deposition for Application in Solar Cells. *Journal of Renewable and Sustainable Energy* **2017**, *9* (2), 021203. <https://doi.org/10.1063/1.4979822>.
- (251) Suemori, K.; Watanabe, Y.; Fukuda, N.; Uemura, S. Voltage Contrast in Scanning Electron Microscopy to Distinguish Conducting Ag Nanowire Networks from Nonconducting Ag Nanowire Networks. *ACS Omega* **2020**, *acsomega.9b04222*. <https://doi.org/10.1021/acsomega.9b04222>.
- (252) The Polymerase Chain Reaction, Kary B. Mullis, 1993 Chemistry Nobel Lecture <https://www.nobelprize.org/prizes/chemistry/1993/mullis/lecture/>.
- (253) Saiki, R.; Scharf, S.; Faloona, F.; Mullis, K.; Horn, G.; Erlich, H.; Arnheim, N. Enzymatic Amplification of Beta-Globin Genomic Sequences and Restriction Site

- Analysis for Diagnosis of Sickle Cell Anemia. *Science* **1985**, *230* (4732), 1350–1354. <https://doi.org/10.1126/science.2999980>.
- (254) Higuchi, R.; Fockler, C.; Dollinger, G.; Watson, R. Kinetic PCR Analysis: Real-Time Monitoring of DNA Amplification Reactions. *Nat Biotechnol* **1993**, *11* (9), 1026–1030. <https://doi.org/10.1038/nbt0993-1026>.
- (255) VanGuilder, H. D.; Vrana, K. E.; Freeman, W. M. Twenty-Five Years of Quantitative PCR for Gene Expression Analysis. *BioTechniques* **2008**, *44* (5), 619–626. <https://doi.org/10.2144/000112776>.
- (256) Gadkar, V. yJ; Filion, M. New Developments in Quantitative Real-Time Polymerase Chain Reaction Technology. *Curr Issues Mol Biol* **2014**, *16*, 1–6.
- (257) Biocompare. PCR Thermocyclers <https://www.biocompare.com/PCR-Real-Time-PCR/PCR-Thermal-Cyclers-PCR-Thermocycler/>.
- (258) Milbury, C. A.; Zhong, Q.; Lin, J.; Williams, M.; Olson, J.; Link, D. R.; Hutchison, B. Determining Lower Limits of Detection of Digital PCR Assays for Cancer-Related Gene Mutations. *Biomolecular Detection and Quantification* **2014**, *1* (1), 8–22. <https://doi.org/10.1016/j.bdq.2014.08.001>.
- (259) Petiti, J.; Lo Iacono, M.; Dragani, M.; Pironi, L.; Fantino, C.; Rapanotti, M. C.; Quarantelli, F.; Izzo, B.; Divona, M.; Rege-Cambrin, G.; Saglio, G.; Gottardi, E. M.; Cilloni, D.; Fava, C. Novel Multiplex Droplet Digital PCR Assays to Monitor Minimal Residual Disease in Chronic Myeloid Leukemia Patients Showing Atypical BCR-ABL1 Transcripts. *JCM* **2020**, *9* (5), 1457. <https://doi.org/10.3390/jcm9051457>.
- (260) Smith, C. J.; Osborn, A. M. Advantages and Limitations of Quantitative PCR (Q-PCR)-Based Approaches in Microbial Ecology: Application of Q-PCR in Microbial Ecology. *FEMS Microbiology Ecology* **2009**, *67* (1), 6–20. <https://doi.org/10.1111/j.1574-6941.2008.00629.x>.
- (261) Wittwer, C. T.; Herrmann, M. G.; Moss, A. A.; Rasmussen, R. P. Continuous Fluorescence Monitoring of Rapid Cycle DNA Amplification. *BioTechniques* **1997**, *22* (1), 130–138. <https://doi.org/10.2144/97221bi01>.
- (262) Holland, P. M.; Abramson, R. D.; Watson, R.; Gelfand, D. H. Detection of Specific Polymerase Chain Reaction Product by Utilizing the 5'----3' Exonuclease Activity of *Thermus Aquaticus* DNA Polymerase. *Proceedings of the National Academy of Sciences* **1991**, *88* (16), 7276–7280. <https://doi.org/10.1073/pnas.88.16.7276>.
- (263) Sigma Aldrich. Quantitative PCR and Digital PCR Detection Methods <https://www.sigmaaldrich.com/technical-documents/articles/biology/quantitative-pcr-and-digital-pcr-detection-methods.html>.
- (264) Takara. One-step RT-qPCR kits <https://www.takarabio.com/learning-centers/real-time-pcr/overview/one-step-rt-qpcr-kits>.
- (265) ThermoFisher Scientific. PCR Basics <https://www.thermofisher.com/fr/fr/home/life-science/cloning/cloning-learning-center/invitrogen-school-of-molecular-biology/pcr-education/pcr-reagents-enzymes/pcr-basics.html>.
- (266) Wikipedia. Polymerase Chain Reaction https://en.wikipedia.org/wiki/Polymerase_chain_reaction.
- (267) Ponchel, F.; Toomes, C.; Bransfield, K.; Leong, F. T.; Douglas, S. H.; Field, S. L.; Bell, S. M.; Combaret, V.; Puisieux, A.; Mighell, A. J.; Robinson, P. A.; Inglehearn, C. F.; Isaacs, J. D.; Markham, A. F. Real-Time PCR Based on SYBR-Green I Fluorescence: An Alternative to the TaqMan Assay for a Relative Quantification of Gene Rearrangements, Gene Amplifications and Micro Gene Deletions. *BMC Biotechnol* **2003**, *3* (1), 18. <https://doi.org/10.1186/1472-6750-3-18>.

- (268) Hsieh, Y.-F.; Yonezawa, E.; Kuo, L.-S.; Yeh, S.-H.; Chen, P.-J.; Chen, P.-H. Polymerase Chain Reaction with Phase Change as Intrinsic Thermal Control. *Appl. Phys. Lett.* **2013**, *102* (17), 173701. <https://doi.org/10.1063/1.4803442>.
- (269) Ramakers, C.; Ruijter, J. M.; Deprez, R. H. L.; Moorman, A. F. M. Assumption-Free Analysis of Quantitative Real-Time Polymerase Chain Reaction (PCR) Data. *Neuroscience Letters* **2003**, *339* (1), 62–66. [https://doi.org/10.1016/S0304-3940\(02\)01423-4](https://doi.org/10.1016/S0304-3940(02)01423-4).
- (270) Sigma Aldrich. Universal SYBR Green qPCR Protocol <https://www.sigmaaldrich.com/technical-documents/protocols/biology/sybr-green-qpcr.html>.
- (271) BJS Biotechnologies. What are the phases of PCR amplification? <https://www.xpresspcr.com/faq-items/phases-pcr-amplification/>.
- (272) Gaudreault, C.; Salvas, J.; Sirois, J. Savitzky–Golay Smoothing and Differentiation for Polymerase Chain Reaction Quantification. *Biochem. Cell Biol.* **2018**, *96* (3), 380–389. <https://doi.org/10.1139/bcb-2016-0194>.
- (273) Zhu, H.; Zhang, H.; Xu, Y.; Laššáková, S.; Korabečná, M.; Neuzil, P. PCR Past, Present and Future. *BioTechniques* **2020**, btn-2020-0057. <https://doi.org/10.2144/btn-2020-0057>.
- (274) Zhu, H.; Podesva, P.; Liu, X.; Zhang, H.; Teply, T.; Xu, Y.; Chang, H.; Qian, A.; Lei, Y.; Li, Y.; Niculescu, A.; Iliescu, C.; Neuzil, P. IoT PCR for Pandemic Disease Detection and Its Spread Monitoring. *Sensors and Actuators B: Chemical* **2020**, *303*, 127098. <https://doi.org/10.1016/j.snb.2019.127098>.
- (275) Kopp, M. U. Chemical Amplification: Continuous-Flow PCR on a Chip. *Science* **1998**, *280* (5366), 1046–1048. <https://doi.org/10.1126/science.280.5366.1046>.
- (276) Li, B.; Li, Y.; Manz, A.; Wu, W. Miniaturized Continuous-Flow Digital PCR for Clinical-Level Serum Sample Based on the 3D Microfluidics and CMOS Imaging Device. *Sensors* **2020**, *20* (9), 2492. <https://doi.org/10.3390/s20092492>.
- (277) Chen, J.; Luo, Z.; Li, L.; He, J.; Li, L.; Zhu, J.; Wu, P.; He, L. Capillary-Based Integrated Digital PCR in Picoliter Droplets. *Lab Chip* **2018**, *18* (3), 412–421. <https://doi.org/10.1039/C7LC01160A>.
- (278) Ahrberg, C. D.; Manz, A.; Chung, B. G. Polymerase Chain Reaction in Microfluidic Devices. *Lab Chip* **2016**, *16* (20), 3866–3884. <https://doi.org/10.1039/C6LC00984K>.
- (279) Zhang, W.; Li, N.; Koga, D.; Zhang, Y.; Zeng, H.; Nakajima, H.; Lin, J.-M.; Uchiyama, K. Inkjet Printing Based Droplet Generation for Integrated Online Digital Polymerase Chain Reaction. *Anal. Chem.* **2018**, *90* (8), 5329–5334. <https://doi.org/10.1021/acs.analchem.8b00463>.
- (280) Sun, K.; Yamaguchi, A.; Ishida, Y.; Matsuo, S.; Misawa, H. A Heater-Integrated Transparent Microchannel Chip for Continuous-Flow PCR. *Sensors and Actuators B: Chemical* **2002**, *84* (2–3), 283–289. [https://doi.org/10.1016/S0925-4005\(02\)00016-3](https://doi.org/10.1016/S0925-4005(02)00016-3).
- (281) Chung, K. H.; Choi, Y. H.; Choi, H. K.; Kim, J. T.; Yu, Y.-J.; Choi, J. S.; Youn, D.-H.; Choi, C.-G. Convection-Based Realtime Polymerase Chain Reaction (PCR) Utilizing Transparent Graphene Heaters. In *IEEE SENSORS 2014 Proceedings*; IEEE: Valencia, Spain, 2014; pp 1006–1009. <https://doi.org/10.1109/ICSENS.2014.6985173>.
- (282) Joung, S.-R.; Kim, J.; Choi, Y. J.; Kang, C. J.; Kim, Y.-S. ITO-Coated Glass/Polydimethylsiloxane Continuous-Flow PCR Chip. In *2007 2nd IEEE International Conference on Nano/Micro Engineered and Molecular Systems*; IEEE: Bangkok, 2007; pp 691–694. <https://doi.org/10.1109/NEMS.2007.352113>.
- (283) Simya, O. K.; Balachander, K.; Dhanalakshmi, D.; Ashok, AnuradhaM. Performance of Different Anti-Reflection Coating and TCO Layers for Kesterite Based Thin Film

- Photovoltaic Devices Using Essential Macleod Simulation Program. *Superlattices and Microstructures* **2020**, *145*, 106579. <https://doi.org/10.1016/j.spmi.2020.106579>.
- (284) Stojanovic, N.; Maithripala, D. H. S.; Berg, J. M.; Holtz, M. Thermal Conductivity in Metallic Nanostructures at High Temperature: Electrons, Phonons, and the Wiedemann-Franz Law. *Phys. Rev. B* **2010**, *82* (7), 075418. <https://doi.org/10.1103/PhysRevB.82.075418>.
- (285) Adezif. Double-sided polyester adhesive tape <https://www.adezif.fr/ruban-adhesif-double-face-polyester>.
- (286) Wu, H.; Huang, Y.; Xu, F.; Duan, Y.; Yin, Z. Energy Harvesters for Wearable and Stretchable Electronics: From Flexibility to Stretchability. *Adv. Mater.* **2016**, *28* (45), 9881–9919. <https://doi.org/10.1002/adma.201602251>.
- (287) Kachroudi, A.; Basrou, S.; Rufer, L.; Sylvestre, A.; Jomni, F. Micro-Structured PDMS Piezoelectric Enhancement through Charging Conditions. *Smart Materials and Structures* **2016**, *25* (10), 105027. <https://doi.org/10.1088/0964-1726/25/10/105027>.
- (288) Wang, Y.; Wu, L.; Zhang, X. Energy Harvesting from Vibration Using Flexible Fluoroethylenepropylene Piezoelectret Films with Cross-Tunnel Structure. *IEEE Transactions on Dielectrics and Electrical Insulation* **2015**, *22* (3), 1349–1354. <https://doi.org/10.1109/TDEI.2015.7116321>.
- (289) Zhang, X.; Pondrom, P.; Sessler, G. M.; Ma, X. Ferroelectret Nanogenerator with Large Transverse Piezoelectric Activity. *Nano Energy* **2018**, *50*, 52–61. <https://doi.org/10.1016/j.nanoen.2018.05.016>.
- (290) Shi, J.; Yong, S.; Beeby, S. An Easy to Assemble Ferroelectret for Human Body Energy Harvesting. *Smart Materials and Structures* **2018**, *27* (8), 084005. <https://doi.org/10.1088/1361-665X/aabdbc>.
- (291) Zhang, Y.; Bowen, C. R.; Ghosh, S. K.; Mandal, D.; Khanbareh, H.; Arafa, M.; Wan, C. Ferroelectret Materials and Devices for Energy Harvesting Applications. *Nano Energy* **2019**, *57*, 118–140. <https://doi.org/10.1016/j.nanoen.2018.12.040>.
- (292) Wu, N.; Cheng, X.; Zhong, Q.; Zhong, J.; Li, W.; Wang, B.; Hu, B.; Zhou, J. Cellular Polypropylene Piezoelectret for Human Body Energy Harvesting and Health Monitoring. *Advanced Functional Materials* **2015**, *25* (30), 4788–4794. <https://doi.org/10.1002/adfm.201501695>.
- (293) Wang, B.; Zhong, J.; Zhong, Q.; Wu, N.; Cheng, X.; Li, W.; Liu, K.; Huang, L.; Hu, B.; Zhou, J. Sandwiched Composite Fluorocarbon Film for Flexible Electret Generator. *Advanced Electronic Materials* **2016**, *2* (4), 1500408. <https://doi.org/10.1002/aelm.201500408>.
- (294) Kachroudi, A.; Basrou, S.; Rufer, L.; Jomni, F. Piezoelectric Cellular Micro-Structured PDMS Material for Micro-Sensors and Energy Harvesting. *J. Phys.: Conf. Ser.* **2015**, *660*, 012040. <https://doi.org/10.1088/1742-6596/660/1/012040>.
- (295) Bilent, S.; Dinh, T. H. N.; Martincic, E.; Joubert, P.-Y. Porous Polymer Based Flexible Pressure Sensors for Medical Applications. *Proceedings* **2018**, *2* (13), 849. <https://doi.org/10.3390/proceedings2130849>.
- (296) Rinaldi, A.; Tamburrano, A.; Fortunato, M.; Sarto, M. A Flexible and Highly Sensitive Pressure Sensor Based on a PDMS Foam Coated with Graphene Nanoplatelets. *Sensors* **2016**, *16* (12), 2148. <https://doi.org/10.3390/s16122148>.
- (297) Eddings, M. A.; Johnson, M. A.; Gale, B. K. Determining the Optimal PDMS–PDMS Bonding Technique for Microfluidic Devices. *Journal of Micromechanics and Microengineering* **2008**, *18* (6), 067001. <https://doi.org/10.1088/0960-1317/18/6/067001>.

- (298) Tang, L.; Lee, N. Y. A Facile Route for Irreversible Bonding of Plastic-PDMS Hybrid Microdevices at Room Temperature. *Lab on a Chip* **2010**, *10* (10), 1274. <https://doi.org/10.1039/b924753j>.
- (299) Bhattacharya, S.; Datta, A.; Berg, J. M.; Gangopadhyay, S. Studies on Surface Wettability of Poly(Dimethyl) Siloxane (PDMS) and Glass under Oxygen-Plasma Treatment and Correlation with Bond Strength. *Journal of Microelectromechanical Systems* **2005**, *14* (3), 590–597. <https://doi.org/10.1109/JMEMS.2005.844746>.
- (300) Satyanarayana, S.; Karnik, R. N.; Majumdar, A. Stamp-and-Stick Room-Temperature Bonding Technique for Microdevices. *Journal of Microelectromechanical Systems* **2005**, *14* (2), 392–399. <https://doi.org/10.1109/JMEMS.2004.839334>.
- (301) Go, J. S.; Shoji, S. A Disposable, Dead Volume-Free and Leak-Free in-Plane PDMS Microvalve. *Sensors and Actuators A: Physical* **2004**, *114* (2–3), 438–444. <https://doi.org/10.1016/j.sna.2003.12.028>.
- (302) Kovalchuk, N. M.; Trybala, A.; Starov, V.; Matar, O.; Ivanova, N. Fluoro- vs Hydrocarbon Surfactants: Why Do They Differ in Wetting Performance? *Advances in Colloid and Interface Science* **2014**, *210*, 65–71. <https://doi.org/10.1016/j.cis.2014.04.003>.
- (303) Wang, J.; Yan, C.; Kang, W.; Lee, P. S. High-Efficiency Transfer of Percolating Nanowire Films for Stretchable and Transparent Photodetectors. *Nanoscale* **2014**, *6* (18), 10734–10739. <https://doi.org/10.1039/C4NR02462A>.
- (304) Cheng, Y.; Zhou, O. Electron Field Emission from Carbon Nanotubes. *Comptes Rendus Physique* **2003**, *4* (9), 1021–1033. [https://doi.org/10.1016/S1631-0705\(03\)00103-8](https://doi.org/10.1016/S1631-0705(03)00103-8).
- (305) Saito, Y.; Uemura, S. Field Emission from Carbon Nanotubes and Its Application to Electron Sources. *Carbon* **2000**, *38* (2), 169–182. [https://doi.org/10.1016/S0008-6223\(99\)00139-6](https://doi.org/10.1016/S0008-6223(99)00139-6).
- (306) Bonard, J.-M.; Kind, H.; Stöckli, T.; Nilsson, L.-O. Field Emission from Carbon Nanotubes: The First Five Years. *Solid-State Electronics* **2001**, *45* (6), 893–914. [https://doi.org/10.1016/S0038-1101\(00\)00213-6](https://doi.org/10.1016/S0038-1101(00)00213-6).
- (307) Mazellier, J.-P.; Sabaut, L. Vacuum Electron Tube with Planar Cathode Based on Nanotubes or Nanowires. US20180012723A1.
- (308) Konishi, Y.; Hokushin, S.; Tanaka, H.; Pan, L.; Akita, S.; Nakayama, Y. Comparison of Field Emissions from Side Wall and Tip of an Individual Carbon Nanotube. *Jpn. J. Appl. Phys.* **2005**, *44* (4A), 1648–1651. <https://doi.org/10.1143/JJAP.44.1648>.
- (309) Chai, G.; Chow, L. Electron Emission from the Side Wall of an Individual Multiwall Carbon Nanotube. *Carbon* **2007**, *45* (2), 281–284. <https://doi.org/10.1016/j.carbon.2006.09.030>.
- (310) Thomas, L.; Guérin, D.; Quinard, B.; Jacquet, E.; Mattana, R.; Seneor, P.; Vuillaume, D.; Mélin, T.; Lenfant, S. Conductance Switching at the Nanoscale of Diarylethene Derivative Self-Assembled Monolayers on La_{0.7}Sr_{0.3}MnO₃. *Nanoscale* **2020**, *12* (15), 8268–8276. <https://doi.org/10.1039/C9NR09928J>.
- (311) Eschimese, D.; Hsia, P.; Vaurette, F.; Deresmes, D.; De Bettignies, P.; Schreiber, J.; Chaigneau, M.; Arscott, S.; Lévêque, G.; Mélin, T. Comparative Investigation of Plasmonic Properties between Tunable Nanoobjects and Metallized Nanoprobes for Optical Spectroscopy. *J. Phys. Chem. C* **2019**, *123* (46), 28392–28400. <https://doi.org/10.1021/acs.jpcc.9b09977>.
- (312) Zhao, Q.; Huang, C.-K.; Zhu, R.; Xu, J.; Chen, L.; Yu, D. 2D Planar Field Emission Devices Based on Individual ZnO Nanowires. *Solid State Communications* **2011**, *151* (22), 1650–1653. <https://doi.org/10.1016/j.ssc.2011.08.010>.

- (313) Madeira, A.; Plissonneau, M.; Servant, L.; Goldthorpe, I. A.; Tréguer-Delapierre, M. Increasing Silver Nanowire Network Stability through Small Molecule Passivation. *Nanomaterials (Basel)* **2019**, *9* (6), 899. <https://doi.org/10.3390/nano9060899>.
- (314) Le Beulze, A.; Gomez-Graña, S.; Gehan, H.; Mornet, S.; Ravaine, S.; Correa-Duarte, M.; Guerrini, L.; Alvarez-Puebla, R. A.; Duguet, E.; Pertreux, E.; Crut, A.; Maioli, P.; Vallée, F.; Del Fatti, N.; Ersen, O.; Treguer-Delapierre, M. Robust Raspberry-like Metallo-Dielectric Nanoclusters of Critical Sizes as SERS Substrates. *Nanoscale* **2017**, *9* (17), 5725–5736. <https://doi.org/10.1039/C7NR00969K>.
- (315) Kumar, D.; Stoichkov, V.; Brousseau, E.; Smith, G. C.; Kettle, J. High Performing AgNW Transparent Conducting Electrodes with a Sheet Resistance of $2.5 \Omega \text{ Sq}^{-1}$ Based upon a Roll-to-Roll Compatible Post-Processing Technique. *Nanoscale* **2019**, *11* (12), 5760–5769. <https://doi.org/10.1039/C8NR07974A>.
- (316) Singh, M.; Rana, S. Silver and Copper Nanowire Films as Cost-Effective and Robust Transparent Electrode in Energy Harvesting through Photovoltaic: A Review. *Materials Today Communications* **2020**, *24*, 101317. <https://doi.org/10.1016/j.mtcomm.2020.101317>.
- (317) ARMOR Solar Power Films <https://www.armor-group.com/fr/aspf>.
- (318) Photovoltaic: ARMOR and Opvius join forces <https://www.armor-group.com/en/content/photovoltaic-armor-and-opvius-join-forces>.
- (319) Jamkhande, P. G.; Ghule, N. W.; Bamer, A. H.; Kalaskar, M. G. Metal Nanoparticles Synthesis: An Overview on Methods of Preparation, Advantages and Disadvantages, and Applications. *Journal of Drug Delivery Science and Technology* **2019**, *53*, 101174. <https://doi.org/10.1016/j.jddst.2019.101174>.
- (320) Simakin, A. V.; Voronov, V. V.; Kirichenko, N. A.; Shafeev, G. A. Nanoparticles Produced by Laser Ablation of Solids in Liquid Environment. *Applied Physics A* **2004**, *79* (4–6), 1127–1132. <https://doi.org/10.1007/s00339-004-2660-8>.
- (321) Gupta, K.; Jana, P. C.; Meikap, A. K. Optical and Electrical Transport Properties of Polyaniline–Silver Nanocomposite. *Synthetic Metals* **2010**, *160* (13–14), 1566–1573. <https://doi.org/10.1016/j.synthmet.2010.05.026>.
- (322) Southward, R. E.; Thompson, D. W. Metal–Polyimide Nanocomposite Films: Single-Stage Synthesis of Silvered Polyimide Films Prepared from Silver(I) Complexes and BPDA/4,4'-ODA. *Chemistry of Materials* **2004**, *16* (7), 1277–1284. <https://doi.org/10.1021/cm030425v>.
- (323) Southward, R. E.; Thompson, D. W.; St. Clair, A. K. Control of Reflectivity and Surface Conductivity in Metallized Polyimide Films Prepared via in Situ Silver(I) Reduction. *Chemistry of Materials* **1997**, *9* (2), 501–510. <https://doi.org/10.1021/cm960349e>.
- (324) Southward, R. E.; Thompson, D. S.; Thompson, D. W.; St. Clair, A. K. Inverse Chemical Vapor Deposition: A Novel Single Stage Synthesis of Highly Reflective and Conductive Silvered Polymeric Films. *Chemistry of Materials* **1999**, *11* (2), 501–507. <https://doi.org/10.1021/cm981014v>.
- (325) Jradi, S.; Balan, L.; Zeng, X. H.; Plain, J.; Lougnot, D. J.; Royer, P.; Bachelot, R.; Akil, S.; Soppera, O.; Vidal, L. Spatially Controlled Synthesis of Silver Nanoparticles and Nanowires by Photosensitized Reduction. *Nanotechnology* **2010**, *21* (9), 095605. <https://doi.org/10.1088/0957-4484/21/9/095605>.
- (326) Zaier, M.; Vidal, L.; Hajjar-Garreau, S.; Balan, L. Generating Highly Reflective and Conductive Metal Layers through a Light-Assisted Synthesis and Assembling of Silver Nanoparticles in a Polymer Matrix. *Scientific Reports* **2017**, *7* (1). <https://doi.org/10.1038/s41598-017-12617-8>.

- (327) Schejn, A.; Ott, M.; Dabert, M.; Vidal, L.; Balan, L. Photo-Induced Design of Reflective Metallized Gold@polymer Coatings with Tuned Architecture. *Materials & Design* **2018**, *160*, 74–83. <https://doi.org/10.1016/j.matdes.2018.08.051>.
- (328) Li, C.; Li, Q.; Cheng, L.; Li, T.; Lu, H.; Tang, L.; Zhang, K.; E, S.; Zhang, J.; Li, Z.; Yao, Y. Conductivity Enhancement of Polymer Composites Using High-Temperature Short-Time Treated Silver Fillers. *Composites Part A: Applied Science and Manufacturing* **2017**, *100*, 64–70. <https://doi.org/10.1016/j.compositesa.2017.05.007>.
- (329) Fantino, E.; Chiappone, A.; Calignano, F.; Fontana, M.; Pirri, F.; Roppolo, I. In Situ Thermal Generation of Silver Nanoparticles in 3D Printed Polymeric Structures. *Materials* **2016**, *9* (7), 589. <https://doi.org/10.3390/ma9070589>.
- (330) Bhattacharyya, S. R.; Datta, D.; Chini, T. K.; Ghose, D.; Shyjumon, I.; Hippler, R. Morphological Evolution of Films Composed of Energetic and Size-Selected Silver Nanocluster Ions. *Nuclear Instruments and Methods in Physics Research Section B: Beam Interactions with Materials and Atoms* **2009**, *267* (8–9), 1432–1435. <https://doi.org/10.1016/j.nimb.2009.01.124>.
- (331) Optical constants of Ag (Silver)
<https://refractiveindex.info/?shelf=main&book=Ag&page=Johnson>.
- (332) Gu, C. D.; Xu, X. J.; Tu, J. P. Fabrication and Wettability of Nanoporous Silver Film on Copper from Choline Chloride-Based Deep Eutectic Solvents. *The Journal of Physical Chemistry C* **2010**, *114* (32), 13614–13619. <https://doi.org/10.1021/jp105182y>.
- (333) Sannicolo, T.; Lagrange, M.; Cabos, A.; Celle, C.; Simonato, J.-P.; Bellet, D. Metallic Nanowire-Based Transparent Electrodes for Next Generation Flexible Devices: A Review. *Small* **2016**, *12* (44), 6052–6075. <https://doi.org/10.1002/sml.201602581>.
- (334) Tan, D.; Jiang, C.; Li, Q.; Bi, S.; Song, J. Silver Nanowire Networks with Preparations and Applications: A Review. *J Mater Sci: Mater Electron* **2020**, *31* (18), 15669–15696. <https://doi.org/10.1007/s10854-020-04131-x>.
- (335) Li, W.; Yarali, E.; Bakytbekov, A.; Anthopoulos, T. D.; Shamim, A. Highly Transparent and Conductive Electrodes Enabled by Scalable Printing-and-Sintering of Silver Nanowires. *Nanotechnology* **2020**, *31* (39), 395201. <https://doi.org/10.1088/1361-6528/ab9c53>.
- (336) Park, J.; Kim, G.; Lee, B.; Lee, S.; Won, P.; Yoon, H.; Cho, H.; Ko, S. H.; Hong, Y. Highly Customizable Transparent Silver Nanowire Patterning via Inkjet-Printed Conductive Polymer Templates Formed on Various Surfaces. *Adv. Mater. Technol.* **2020**, *5* (6), 2000042. <https://doi.org/10.1002/admt.202000042>.
- (337) Lin, S.; Wang, H.; Zhang, X.; Wang, D.; Zu, D.; Song, J.; Liu, Z.; Huang, Y.; Huang, K.; Tao, N.; Li, Z.; Bai, X.; Li, B.; Lei, M.; Yu, Z.; Wu, H. Direct Spray-Coating of Highly Robust and Transparent Ag Nanowires for Energy Saving Windows. *Nano Energy* **2019**, *62*, 111–116. <https://doi.org/10.1016/j.nanoen.2019.04.071>.
- (338) Li, T.; Gao, Y.; Zheng, K.; Ma, Y.; Ding, D.; Zhang, H. Achieving Better Greenhouse Effect than Glass: Visibly Transparent and Low Emissivity Metal-Polymer Hybrid Metamaterials. *ES Energy Environ.* **2019**. <https://doi.org/10.30919/esee8c325>.
- (339) Hsu, P.-C.; Liu, X.; Liu, C.; Xie, X.; Lee, H. R.; Welch, A. J.; Zhao, T.; Cui, Y. Personal Thermal Management by Metallic Nanowire-Coated Textile. *Nano Letters* **2015**, *15* (1), 365–371. <https://doi.org/10.1021/nl5036572>.
- (340) Chen, W.; Liu, L.-X.; Zhang, H.-B.; Yu, Z.-Z. Flexible, Transparent and Conductive Ti3C2Tx MXene-Silver Nanowire Films with Smart Acoustic Sensitivity for High-Performance Electromagnetic Interference Shielding. *ACS Nano* **2020**, [acsnano.0c01635](https://doi.org/10.1021/acsnano.0c01635). <https://doi.org/10.1021/acsnano.0c01635>.

- (341) Liu, L.; Chen, W.; Zhang, H.; Wang, Q.; Guan, F.; Yu, Z. Flexible and Multifunctional Silk Textiles with Biomimetic Leaf-Like MXene/Silver Nanowire Nanostructures for Electromagnetic Interference Shielding, Humidity Monitoring, and Self-Derived Hydrophobicity. *Advanced Functional Materials* **2019**, *29* (44), 1905197. <https://doi.org/10.1002/adfm.201905197>.
- (342) Tang, H.; Feng, H.; Wang, H.; Wan, X.; Liang, J.; Chen, Y. Highly Conducting MXene–Silver Nanowire Transparent Electrodes for Flexible Organic Solar Cells. *ACS Appl. Mater. Interfaces* **2019**, *11* (28), 25330–25337. <https://doi.org/10.1021/acsami.9b04113>.
- (343) Miao, M.; Liu, R.; Thaiboonrod, S.; Shi, L.; Cao, S.; Zhang, J.; Fang, J.; Feng, X. Silver Nanowires Intercalating Ti_3C_2Tx MXene Composite Films with Excellent Flexibility for Electromagnetic Interference Shielding. *J. Mater. Chem. C* **2020**, *8* (9), 3120–3126. <https://doi.org/10.1039/C9TC06361G>.
- (344) Lee, J.; Lee, D.; Cho, S. J.; Seo, J.-H.; Liu, D.; Eom, C.-B.; Ma, Z. Epitaxial VO_2 Thin Film-Based Radio-Frequency Switches with Thermal Activation. *Appl. Phys. Lett.* **2017**, *111* (6), 063110. <https://doi.org/10.1063/1.4998452>.
- (345) Gonçalves, A.; Resende, J.; Marques, A. C.; Pinto, J. V.; Nunes, D.; Marie, A.; Gonçalves, R.; Pereira, L.; Martins, R.; Fortunato, E. Smart Optically Active VO_2 Nanostructured Layers Applied in Roof-Type Ceramic Tiles for Energy Efficiency. *Solar Energy Materials and Solar Cells* **2016**, *150*, 1–9. <https://doi.org/10.1016/j.solmat.2016.02.001>.
- (346) Jones, R.; Draheim, R.; Roldo, M. Silver Nanowires: Synthesis, Antibacterial Activity and Biomedical Applications. *Applied Sciences* **2018**, *8* (5), 673. <https://doi.org/10.3390/app8050673>.
- (347) Fang, Y.; Li, Y.; Li, Y.; Ding, M.; Xie, J.; Hu, B. Solution-Processed Submicron Free-Standing, Conformal, Transparent, Breathable Epidermal Electrodes. *ACS Appl. Mater. Interfaces* **2020**, *12* (21), 23689–23696. <https://doi.org/10.1021/acsami.0c04134>.
- (348) Chen, W.; Jiang, J.; Zhang, W.; Wang, T.; Zhou, J.; Huang, C.-H.; Xie, X. Silver Nanowire-Modified Filter with Controllable Silver Ion Release for Point-of-Use Disinfection. *Environ. Sci. Technol.* **2019**, *53* (13), 7504–7512. <https://doi.org/10.1021/acs.est.9b01678>.
- (349) Bahcelioglu, E.; Unalan, H. E.; Erguder, T. H. Silver-Based Nanomaterials: A Critical Review on Factors Affecting Water Disinfection Performance and Silver Release. *Critical Reviews in Environmental Science and Technology* **2020**, 1–35. <https://doi.org/10.1080/10643389.2020.1784666>.
- (350) Bahcelioglu, E.; Doganay, D.; Coskun, S.; Unalan, H. E.; Erguder, T. H. A Point-of-Use (POU) Water Disinfection: Silver Nanowire Decorated Glass Fiber Filters. *Journal of Water Process Engineering* **2020**, *38*, 101616. <https://doi.org/10.1016/j.jwpe.2020.101616>.
- (351) Spieser, H.; Denneulin, A.; Deganello, D.; Gethin, D.; Koppolu, R.; Bras, J. Cellulose Nanofibrils and Silver Nanowires Active Coatings for the Development of Antibacterial Packaging Surfaces. *Carbohydrate Polymers* **2020**, *240*, 116305. <https://doi.org/10.1016/j.carbpol.2020.116305>.
- (352) Wang, Z.; Zhao, S.; Hong, L.; Huang, J. Preparation and Properties of Silver-Based Cellulose/Polyvinyl Alcohol Antibacterial Materials. *J Inorg Organomet Polym* **2020**, *30* (11), 4382–4393. <https://doi.org/10.1007/s10904-020-01669-5>.
- (353) Peng, X.; Dong, K.; Ye, C.; Jiang, Y.; Zhai, S.; Cheng, R.; Liu, D.; Gao, X.; Wang, J.; Wang, Z. L. A Breathable, Biodegradable, Antibacterial, and Self-Powered Electronic

- Skin Based on All-Nanofiber Triboelectric Nanogenerators. *Sci. Adv.* **2020**, *6* (26), eaba9624. <https://doi.org/10.1126/sciadv.aba9624>.
- (354) Xu, Y.; Yuan, Y.; Fan, X.; Cui, M.; Xiao, J.; Du, J.; Pan, Z.; Feng, G.; Lv, B.; Song, C.; Wang, T. Silver Nanowire-Carbon Nanotube/Coal-Based Carbon Composite Membrane with Fascinating Antimicrobial Ability and Antibiofouling under Electrochemical Assistance. *Journal of Water Process Engineering* **2020**, *38*, 101617. <https://doi.org/10.1016/j.jwpe.2020.101617>.
- (355) Kim, J.-H.; Ma, J.; Jo, S.; Lee, S.; Kim, C. S. Enhancement of Antibacterial Performance of Silver Nanowire Transparent Film by Post-Heat Treatment. *Nanomaterials* **2020**, *10* (5), 938. <https://doi.org/10.3390/nano10050938>.
- (356) Li, W.; Zhang, H.; Shi, S.; Xu, J.; Qin, X.; He, Q.; Yang, K.; Dai, W.; Liu, G.; Zhou, Q.; Yu, H.; Silva, S. R. P.; Fahlman, M. Recent Progress in Silver Nanowire Networks for Flexible Organic Electronics. *J. Mater. Chem. C* **2020**, *8* (14), 4636–4674. <https://doi.org/10.1039/C9TC06865A>.
- (357) Charles, R. G.; Douglas, P.; Dowling, M.; Liversage, G.; Davies, M. L. Towards Increased Recovery of Critical Raw Materials from WEEE– Evaluation of CRMs at a Component Level and Pre-Processing Methods for Interface Optimisation with Recovery Processes. *Resources, Conservation and Recycling* **2020**, *161*, 104923. <https://doi.org/10.1016/j.resconrec.2020.104923>.

ANNEXE I: Spray coating-Airbrush protocol

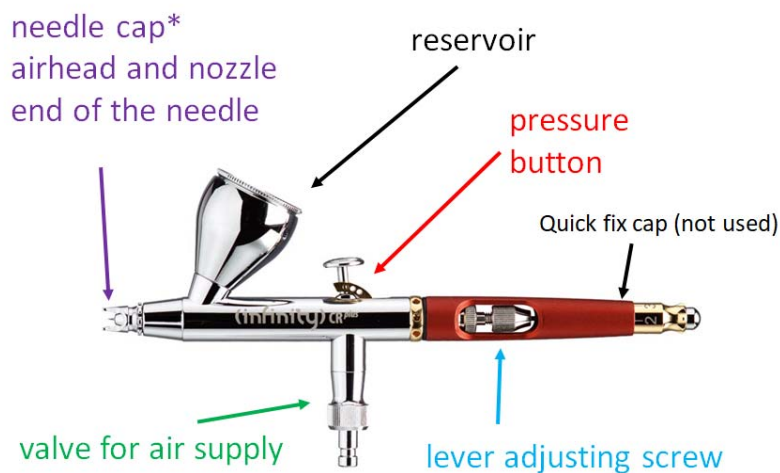
General safety instructions:

- Always wear the **appropriate clothing**: closed-toe shoes, clothes that fully cover the legs and lab coat
- Protect your **eyes** with safety goggles
- Confine **long hair**
- Use **gloves** according to the solvents used
- Never forget the special **mask** for nanomaterials
- No **food** or **drink** allowed
- Don't use **headphones/ear buds**
- Don't forget, besides the safety clothing, mask and gloves, to use the proper **bin for nano-waste!**
- Be vigilant with the use of **inserted gases**: N₂-Azote and O₂-Air comprimé

The Airbrush (**Figure A-1**) is placed inside the spray coating set-up (**Figure A-2**~~Erreur ! Source du renvoi introuvable.~~) and is linked with an automatic runner connected to the program “Programmable Automation Controller (PAC) Display Runtime Professional” which enables the movement in X and Y direction with different spray parameters (**Figure A-3**).

The samples are placed in a heating template in order to have the appropriate temperature during the deposition of the solution.

BASIC AIRBRUSH PARTS



*We usually don't put the red cap but one should try if it's needed for its deposition or not.

Figure A-1: Photo of the Airbrush with its main parts (left), placed inside the spray coating set-up (right).

***One must be careful not to be burnt from the heating element, although one of the many automations of the setup is that the temperature stops arising when the inside protection door is open. Still, the temperature does not turn from 100 to 20 °C in just one second. Maximum temperature: 110 °C.

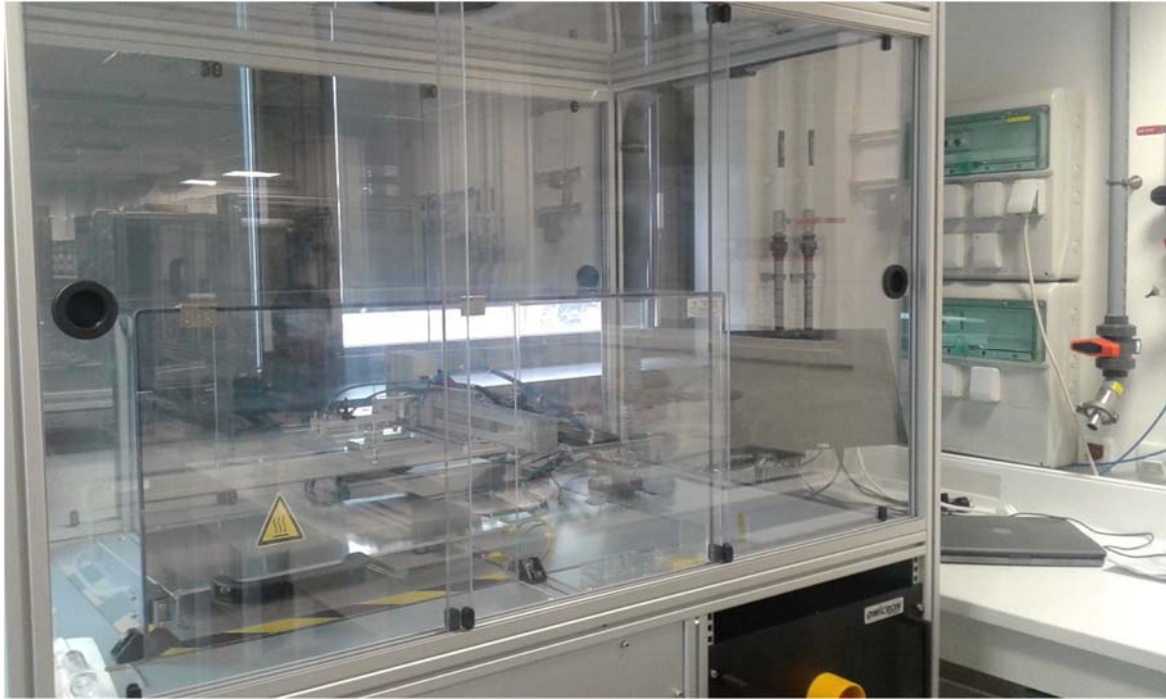
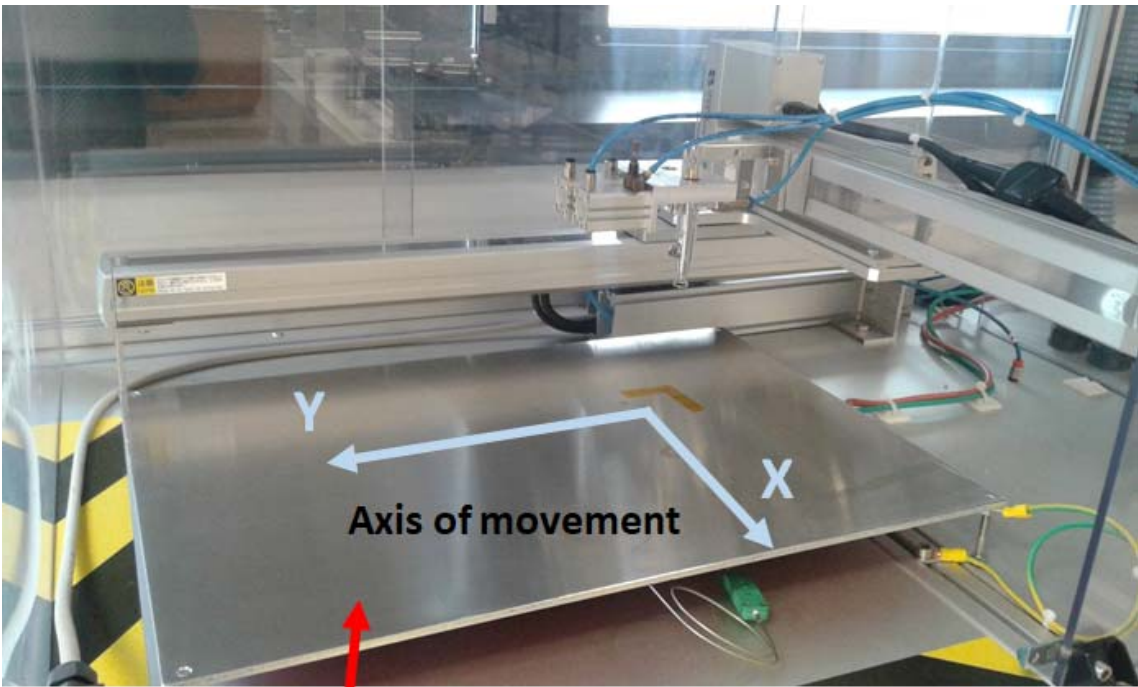


Figure A-2: General photo of the spray coating set-up in LMGP.



Heating element

Figure A-3: Photo of the inside of the spray coating set-up showing the Airbrush and the heating element on top of which the samples are placed during deposition. The Airbrush moves on the X and Y direction thanks to a PAC.

A. First steps to open and prepare the system:

- We put the 2 plugs in (machine+laptop)
- We put on the first red of the 3 buttons in the machine (Power Switch) and the second button in the machine (green ON) (**Figure A-4**)

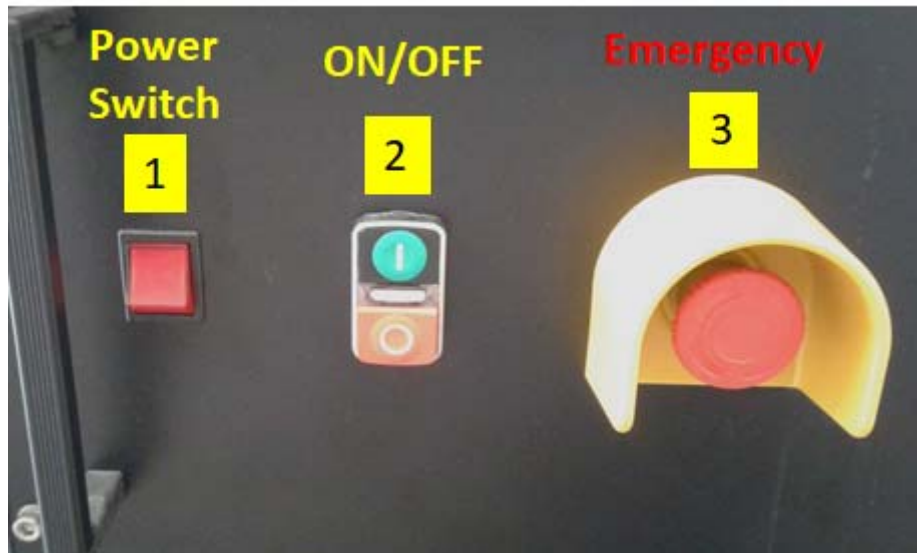


Figure A-4: Main power and safety buttons of the spray coating set-up.

Steps in the PC before starting the deposition (**Figure A-5**)

- Open the PAC Display Runtime Professional
- Open the “Administrator (login)” (normally it doesn’t require password)
- Go to Motion Debug Mode
- Click “Enable Power Switch” (it must go green)
- Click the option that appears “Enable Watchdog” (it must go green). You should hear a sound from the machine that means it will start working normally.
- Don’t click very quickly one button after the other. Sometimes software bugs occur...
- Go to Monitoring

We open the air and the azote pipe. (**Figure A-6**)

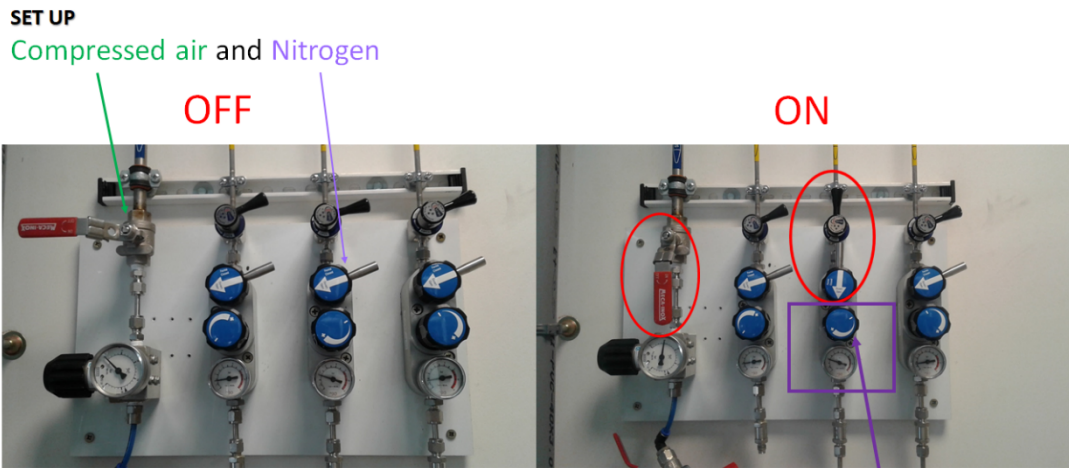
Before monitoring the deposition’s parameters:

- Choose or be sure that you use the pair of needle+nozzle that fits better your deposition. There are different sizes: 0,15-0,20-0,40 mm.
- Fix manually the distance of the air brush from the sample. There are already two indicated distances: point 1 (7.5cm), point 2 (6.5cm) and the lower level (4.2cm). In these, consider to add the 2mm of the distance between the nozzle and the edge of the needle cap that protects it.
- Put some solvent to the reservoir in order to clean the spray again before use
- Put the samples the template. Concerning their correct position according to the spray deposition, do some motion tests without enabling the solution to flow, in order to set each time, the appropriate X and Y position. We can also change the height of the aluminium plate.

*** Always close all the doors before starting a deposition***



Figure A-5: PAC interface of the Administrator(login) page.



Turn to modify the pressure of the spray
The 1.4 bars were found optimal for some depositions.

Figure A-6: Photos of the air and azote supply when turned off (left) and turned on (right).

B. Monitoring and parameters of our deposition (Figure A-7)

- “Start Spray” Play and Stop buttons: they open and close respectively the lever that allows the solution exit from the beck.
- “Vent SetPoint”: 100%
- “Temp1 Set Point”: The temperature of the aluminium plate. Its maximum is 110C

- The rest temperature set points are for future use, do not click on them.

Always press “ENTER” from the keyboard in order to save the changes in the values described below

- “Speed”, “Deceleration”, “Distance X”, “Distance Y”, “Cycle” : tuneable parameters. Be careful in their min and max values as described beside.
- We keep usually the deceleration in 1000
- The X and Y distances must be determined each time according to the samples as described above. X and Y values must be dividable by 5.
- Prefer a small number of cycles. Sometimes software bugs occur but in any case we have to control step by step the deposition to prevent undesirable deposition effects. In case of small reservoir that contains max 7 ml, we have to fill it often especially.
- Once the deposition has started, the Airbrush will move and spray as many times as the number of cycles and then it will return automatically to its initial position without pressing any other key.
The ‘STOP MOTION’ button can be used if we absolutely need to interrupt the deposition in the middle of a cycle. In that case the spraying stops and by keeping the button pressed the Airbrush goes back to its initial position.

There is the emergency button of course for the case that something gets really wrong and we have to force down the setup (Figure A-4)

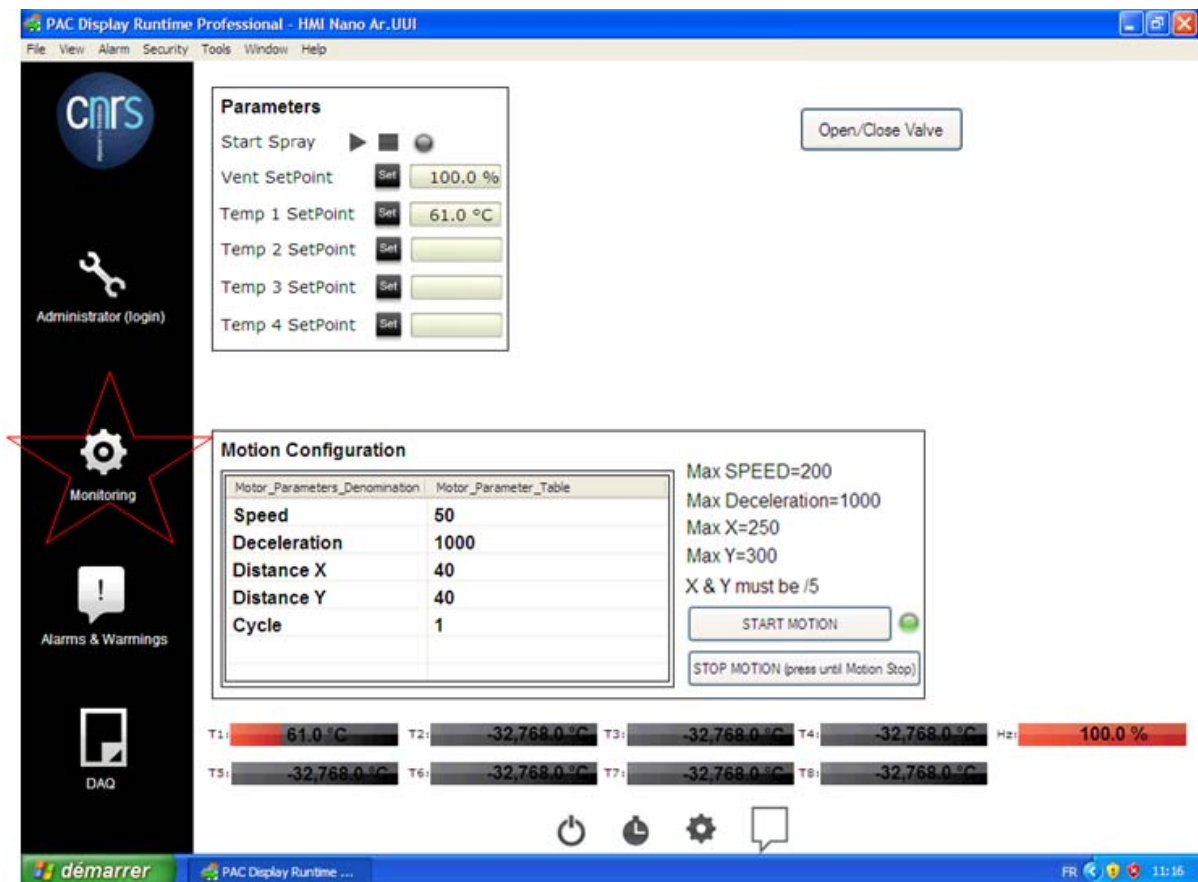


Figure A-7: PAC interface of the “Monitoring” page.

C. Fill the reservoir:

- Fill the reservoir with the solution. There is small hole in the Airbrush's reservoir that we fill with a glass syringe with metallic needle. The small reservoir contains maximum 7 ml.
- Unscrew and turn the lever in order to fix the flow rate of the solution. We use to count the number of droplets per 20 sec. A low rate like ~5-10 droplets/20 sec is a good choice but this depends on a lot of parameters especially the concentration of the solution, the type of solvent etc. Each time that a parameter changes we have to re-optimize the whole procedure.
- Droplets can fall even if the Airbrush isn't spraying so put a short beaker under it in its initial position.

*** Always close all the doors before starting a deposition***

Ready for deposition:

- When the parameters are set, click the "start motion" and the air brush starts moving.
- When the air brush stands back in the initial position: click the "STOP" button of "Start Spray" to stop the spraying.

*** In case of bug you can try the Initialize in Administrator (login) or restart the whole procedure. First close correctly (see end page) the machine and the software, close the gas supplies and then restart everything***

DAQ

It provides us the graphs where we can choose a parameter and see its values on the screen.

D. Turn off and clean

- Be sure that the spray is stopped.
- Put the temperature in 0 C.

Remember to wait for the plate's cooling down, even if everything is closed, until we remove our sample

- Clean carefully the air brush in order to have it proper for the next use. Put an amount of ethanol or isopropanol in the air brush reservoir and make several depositions. Make sure firstly that the sprayed samples are removed from the template.
- Take off the needle, the nozzle, the airhead, the reservoir and the syringe and clean it in ultrasound bath for 10 minutes.
- Clean the aluminium plate. Make sure it is already cooled down.

Shut down the PC and the rest of the setup:

- Administrator: turn off the "Enable Watchdog" and then the "Enable Power"
- Turn off the program.
- Close the compressed air and azote piping.
- Turn OFF the ON/OFF (green and red button) by pressing the red one.
- Turn off the Power Switch red button (first) on the machine.
- Turn off the PC.
- Take off the 2 plugs (machine+laptop).

ANNEXE II: Electrical characterization bench short protocol

The home-made electrical characterization bench (**Figure A-8a**) is used for *in situ* measurements of the electrical resistance of samples, under electrical and thermal applied stress, under several conditions, such as high temperature (up to 800 °C), variable pressure down to vacuum (10^{-4} mbar).

- Put the sample in the middle of the sample carrier (top surface of the heating element, Figure A-8b) and fix well the two tips connected to the Keithley for the electrical measurements. A Pt100 sensor is fixed on the top of the sample carrier for the measurement of the temperature on the sample and shown in the user interface. Connect the cables of Keithley for the 2 points mode (red and black on the right, up and down). Close the sample holder with the top metallic lid protection. (Figure A-8c)
- Plug the electric cables of Keithley, laptop and electric box.
- Turn on the Keithley. If you don't turn the Keithley before the main machine, a bug will occur in the software in "Run Strategy" (details later below).
- Turn on the electric box, buttons in front panel: i. Power Switch on (button on the right to turn right) and the "sous tension" indicator button should turn on, ii. ON-OFF button (MARCHE/ARRET on the left) to open: push the green button. After each button you should hear a sound from the inside the electric box which is coming from the connection of the contactor. *If the urgency button is pressed, the ON button does not work.
- Turn on the electric supply "Sorensen" on the other side of the electric bench, outside the electric box.
- Turn on the laptop, code: 12Ertyu.
- Open the "PAC Control Basic". Go to "File" -> "Strategy" -> "1- Strategy PAC BdC".
- Click the "Debug" to download the Strategy.
- Click "Run Strategy" and the Keithley connects directly with the laptop-PAC.
- If Keithley does not connect with the program, the problem may come from the order of connecting-opening the devices. First we should connect and turn on the Keithley before the electric box and laptop.
- Click "Online" to be able to pass on the Strategy's user interface program.
- Without closing the "PAC Control Basic" open the "PAC Run Time". Automatically the resistance of the sample will be measured by the Keithley with an output of 100 μ A and in the main page the measuring mode is "Resistance".
- In the "Main" page of the interface, click "Power Supply" to turn it on (the button colour should go green and listen to the sound of contactor connecting). If it does not open, check the electric supply ("Sorensen") on the back of the electric box, it may be closed.
- Turn on the "Heater Switch" (the button colour should go green and listen to the sound of contactor connecting).
- It is important to settle the "Current limit" of the power supply. This is connected to the current applied in order to heat and control the temperature of the heating element. The values can vary from 1 to 5 A. The heating element is made of SiC, it is a semiconductor that can reach very high temperatures and then it heats by radiation the plate of sample carrier. In the interface we can see the temperature of the heating element, the temperature of the sample carrier ("Pt100") and the temperature that we have imposed to the system during a recipe. The difference between the first two is normal that is why the regulation of the power, in order to reach the desired temperature imposed by the step of the user recipes, is done indirectly using the temperature of the Pt100 sensor close to the sample.
- Go to "Recipes" in order to start the measurements. You can choose the Time-Temperature-Power-Voltage-Current values on the same time by writing in the recipe

lines/table. This means that you can perform experiments with variable temperature and electric supply. The time lines are showing the time value in continuous and not by steps; this means that you need to add the previous line value and not just the value of time period. You can write a recipe and then “Upload” it (button in the Recipes page, below the recipe lines) so that you can use it another time directly by “Download” it (button).

- When you perform measurements with variable voltage or current, change the mode to voltage or current respectively. The resistance is always calculated and its value is shown in the interface.
- When you are ready, click on the “Start Recipe” to perform the measurement. In the end of your experiment click on the “End recipe”.
- The data are saved in Libraries -> Documents -> PAC BdC -> HMI
- To close the system firstly close the PAC Run Time: File -> Exit
- Then in the PAC Control Debug, “Stop Strategy” and close the file.
- Turn OFF button and Power Switch OFF button in the electric box/machine and the supply of “Sorensen”
- Close the Keithley and remove its electric cables.
- Unplug the electric box, the Keithley and the laptop.

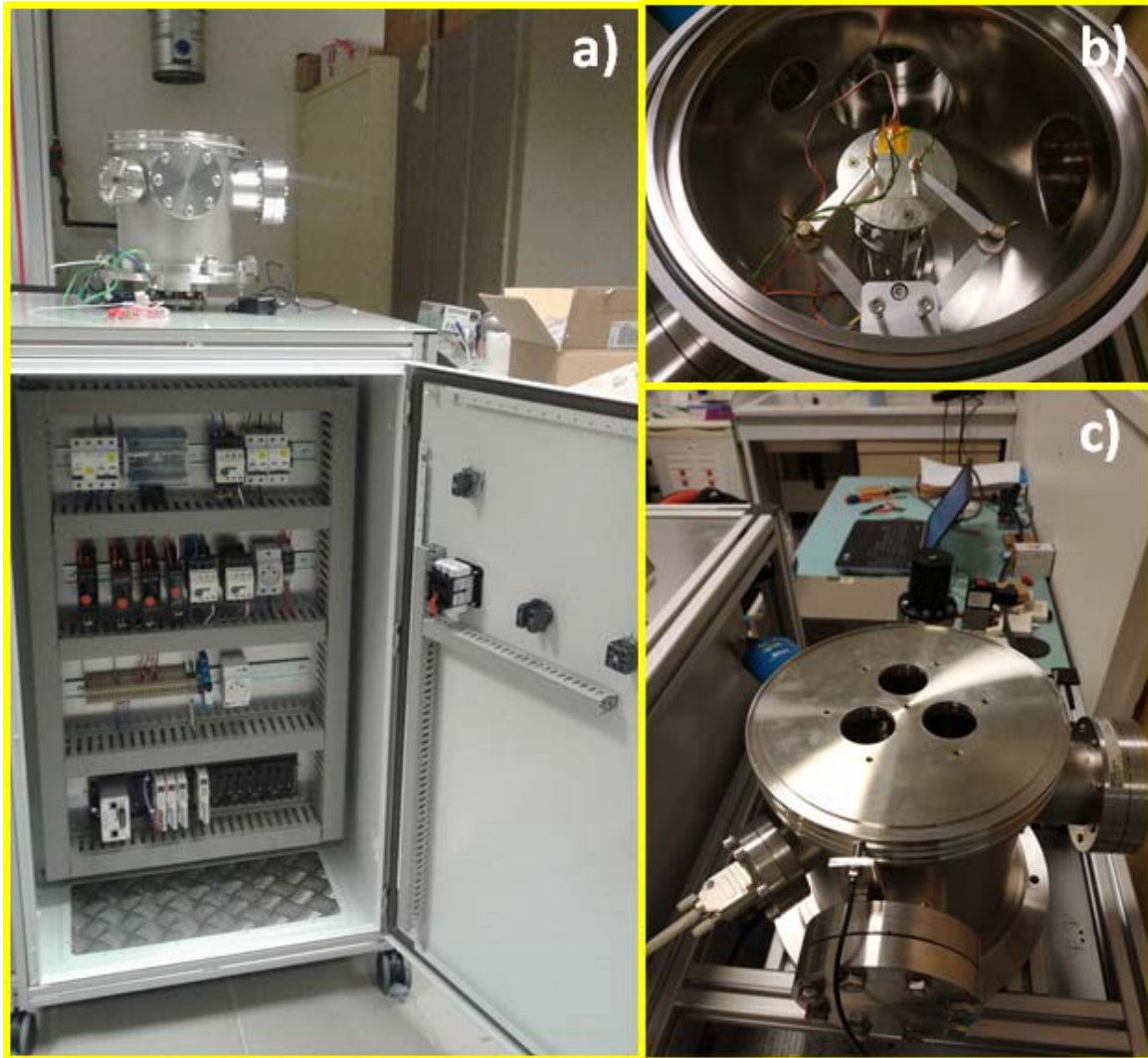


Figure A-8: Photos of the home-made electrical characterization bench. a) The electrical table and the sample holder box on top of it. b) The sample holder with two electrical probes connected on the side contacts of a sample. c) The sample holder box with the metallic lid protection.

ANNEXE III: Spectrophotometer protocol

This following protocol focuses on the total and diffuse transmittance measurements with the Spectrophotometer Lambda 950 by PerkinElmer (**Figure A-9a**) and the way to estimate the haze factor of a transparent sample. Lambda950 is a double beam spectrophotometer which utilizes two beams of light, i.e. a reference beam and a sampling beam that passes through the sample, and two detectors, inside an integrating sphere, that allow the two beams to be measured at one time. In Figure A-9b one can see a photo of the part of the optical lens that the sampling beam passes through and reaches the sample transmittance port/aperture, with a sample placed on this port/aperture. The integrating sphere is inside the right part of the port.

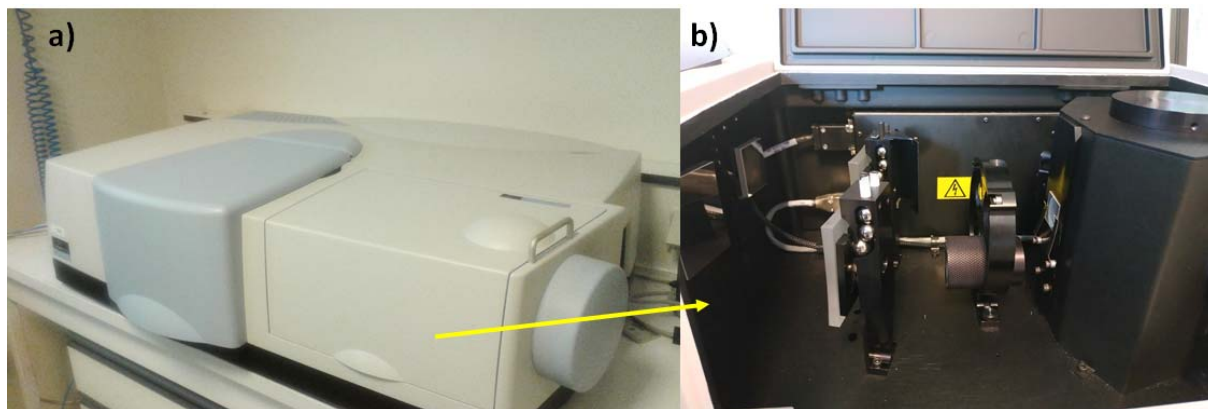


Figure A-9: a) Photo of the Spectrophotometer Lambda 950 by PerkinElmer. b) Photo of the optical lens and sample transmittance port where the sampling beam passes through. On the right part of the port it is the integrating sphere.

General steps:

1. Turn on the spectrophotometer (button on the top, on the back right corner). Wait 30 minutes so the lamps can stabilize before the first measurement. Open the software PerkinElmer UV Winlab (on the desktop) and log in as an analyst.
2. If you are planning to make spectrum, click on the shortcut called “Users” on the left column “base methods”. This will launch a general sequence with good parameters.
3. Check and note in your data sheet for C29-Spectrophotometer and lab-book the date of the last calibration. This calibration sheet should be visible in front of the equipment. In case it has been long time (more than 1-2 months) contact the responsible.
4. Data Collection section
 - i. λ interval : (default) widest settings with the integrating sphere: from 2500 to 250 nm.
 - ii. Data interval: space between two adjacent points (5nm or 2nm if a good accuracy is needed).
 - iii. %T, %R or A depending on the kind of measurement, i.e. transmittance, reflectance, absorbance
 - iv. Integrating time: 0.52s.
 - v. Amplification InGaAs: around 14.
 - vi. Slit width PMT : 4nm.

Numerous other parameters can also be changed (height of the beam, attenuators, slit width, etc).

5. Correction section

- Before any measurement, baselines have to be done (100% and/or 0%). The time needed for one baseline is exactly the same as the time needed for a normal scan. The 0% baseline is more and more important as the sample absorbs more light.
- If you are making reflection measurements, the spectralon has to be corrected (it does not have a reflection coefficient of 100% over the whole spectral range) by using the menu in the correction section. To do so, %R has to be selected in Data Collection.

6. Sample Info section

- You can enter as many samples as needed and change their name and description. The column “user” has to be filled with your name. Don’t forget to include:
 - i. a measurement without sample (“empty” sample). It is also needed for the haze factor calculations. Do not confound it with the baseline corrections.
 - ii. the substrate-reference of your samples.
- The sub-section “Graphs” displays the spectrum of the samples. View->Overlay samples displays all the spectrum acquired on the same graph.

7. Note in your data sheet for C29 and lab-book the samples you are measuring and the specific setup you use for the measurements (sample position, spot size...)

8. Lens alignment (Figure A-10)

When all the parameters are filled and before starting the acquisition, check if the beam is aligned and it does not exceed the slit. Press the button “Align” and when the beam is ready, you can open the outside coverage and use a square paper both at the entrance and the reflectance port to check the beam as shown as in the photo below. Click again the button “Align” before proceeding to the measurements. In case of problem, report it to the responsible.

Do not try to align it by yourself! Ask the responsible of the spectrophotometer.

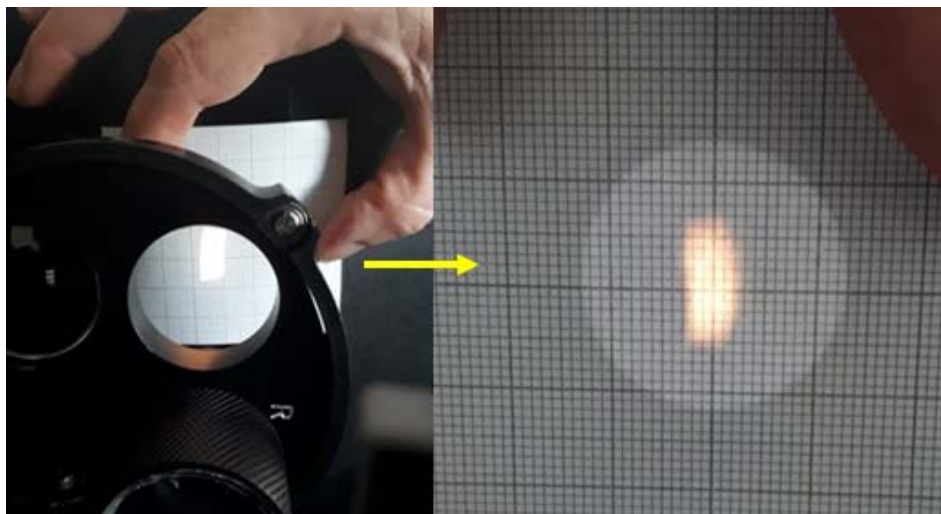


Figure A-10: Checking the lens alignment of the sampling beam.

9. Start the acquisition

- Click on the “Start” button. The spectrophotometer will first do the baseline(s) required and will continue with the samples entered in the “Sample Info” section.
- **Always perform firstly a measurement of the Total (and Diffuse) Transmittance without any sample** at all, just empty port. These measurements are essential for the calculation of the Haze Factor (see step 12. for the calculation).

To measure Total Transmittance place the Spectralon (white standing plate, Figure A-11a) in the Reflectance Port.

To measure Diffuse Transmittance remove the Spectralon in the Reflectance Port and replace it with Reflectance Port Light Trap (Figure A-11b). Always cover the black circular area with the plastic cover that is black on the inside and pale blue on the other side.

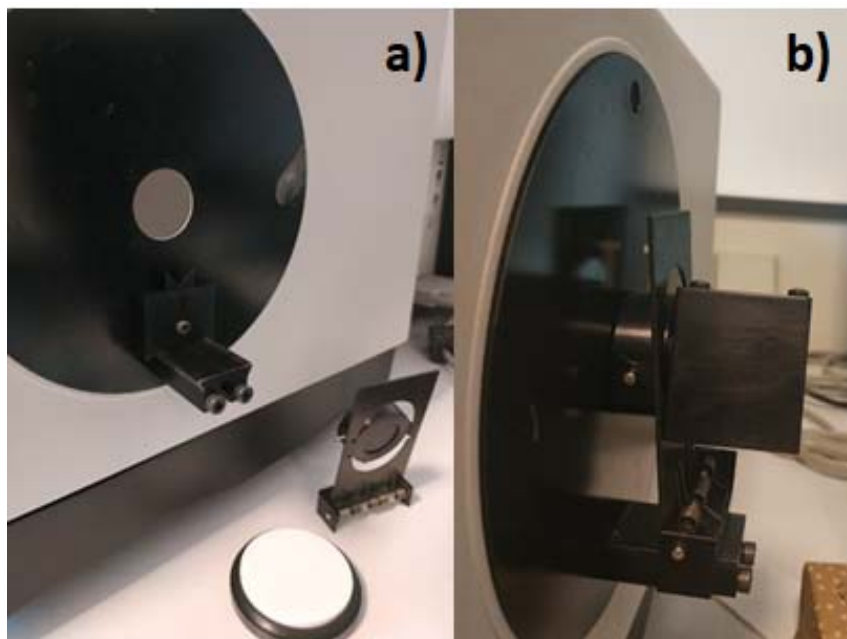


Figure A-11: a) White plate/Spectralon in the Reflectance Port, certificated for Total Transmittance measurements. b) Light trap in the Reflectance Port, for Diffuse Transmittance measurements.

- Do not forget also to measure total and diffuse transmittance with a clean substrate, same that you use to fabricate for your samples.
- Then continue with your samples. Be careful to fit well the size of the sample in the slit. If the sample is even slightly smaller, we must use a mask to decrease the slit.
- Diffuse transmittance measurement: remove the white standard plate of the Reflectance Port and thus the direct transmittance is excluded. Close well the outside light blue rounded port. The most precise and easier way to perform this measurement is to
 - i. put a sample,
 - ii. measure its total transmittance,
 - iii. remove the plate and measure the diffuse transmittance,
 - iv. replace the plate, change sample and repeat the same procedure.

Suggestions

- In case of very diffuse samples it is possible to perform the measurements on both sides of the samples to check if there is a difference between the case that the light passes firstly from the glass substrate and then the sample deposited and the opposite case. Don't forget to write in the data sheet for C29 the configuration
- In the case of homogenous samples (**Figure A-12a**) a measurement in one position of the sample (i.e. in the middle) gives a quite representative value for the optical properties. But in case of not homogenous samples (**Figure A-12b**) it is suggested to perform several measurements by changing the position of the beam on the sample each time. This allow to have a statistic information of the inhomogeneity.

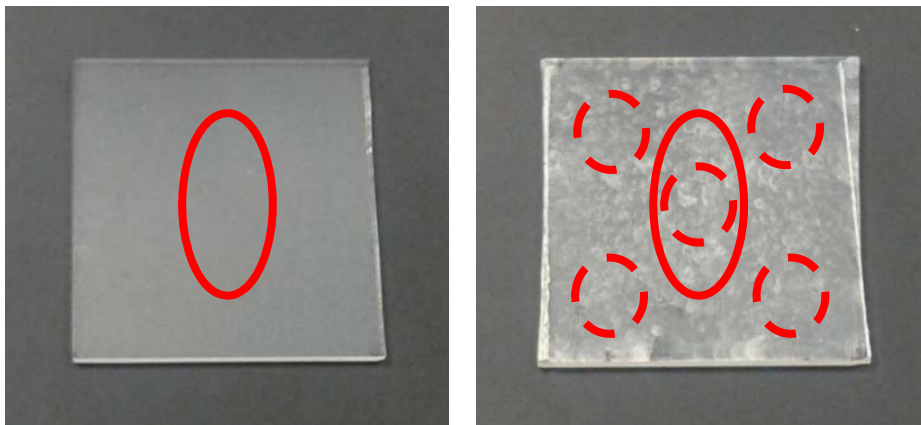


Figure A-12: Photos of a) homogenous AgNW network, b) non-homogenous case of AgNW network.

10. Processing section

- You can treat your data in this section with different mathematical operation. The calculated spectrum will be exported like normal spectrum (*.csv).
- For example, the smooth option allows you to smooth your spectrum on a desired spectral range.

11. Output section

- The export folder has to be changed (Output>Data Export: Setup) and has to correspond to your personal folder. If you do not have a personal folder yet, you can create it in C:\Users\LMGP (the name of this folder has to be the same like the name of your personal folder in "Transfert Manip").

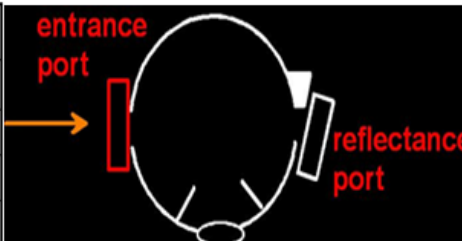
12. When all the samples have been run, you have to save the sequence. This will automatically export the data in the folder entered in Output>Data Export: Setup. To save your sequence: File>Save Results>As a new task. You should give an explicit name to your sequence: Surname_Name_Date and you can also add a description. Your sequence can be opened and continued later. After saving it, it will appear in the "Tasks" menu of the software. It is important that you move this sequence to your personal folder within the software. In case of problem of saving by this way, you can use the File>Export.

13. Fill the "Document of Measurements" that is always next to the machine, with the information required.

14. Haze Factor calculation (usually reported for $\lambda = 550$ nm)

$$\text{Haze Factor}(\%) = 100 * \left(\frac{T_4}{T_2} - \frac{T_3}{T_1} \right)$$

Measurement	Entrance Port	Reflectance Port
T ₁	no sample	(TT) with white plate
T ₂	sample	(TT) with white plate
T ₃	no sample	(DT) without white plate
T ₄	sample	(DT) without white plate



where TT= Total Transmittance and DT= Diffuse Transmittance.

ANNEXE IV: Photos of the mechanical test (bending/stretching) set up

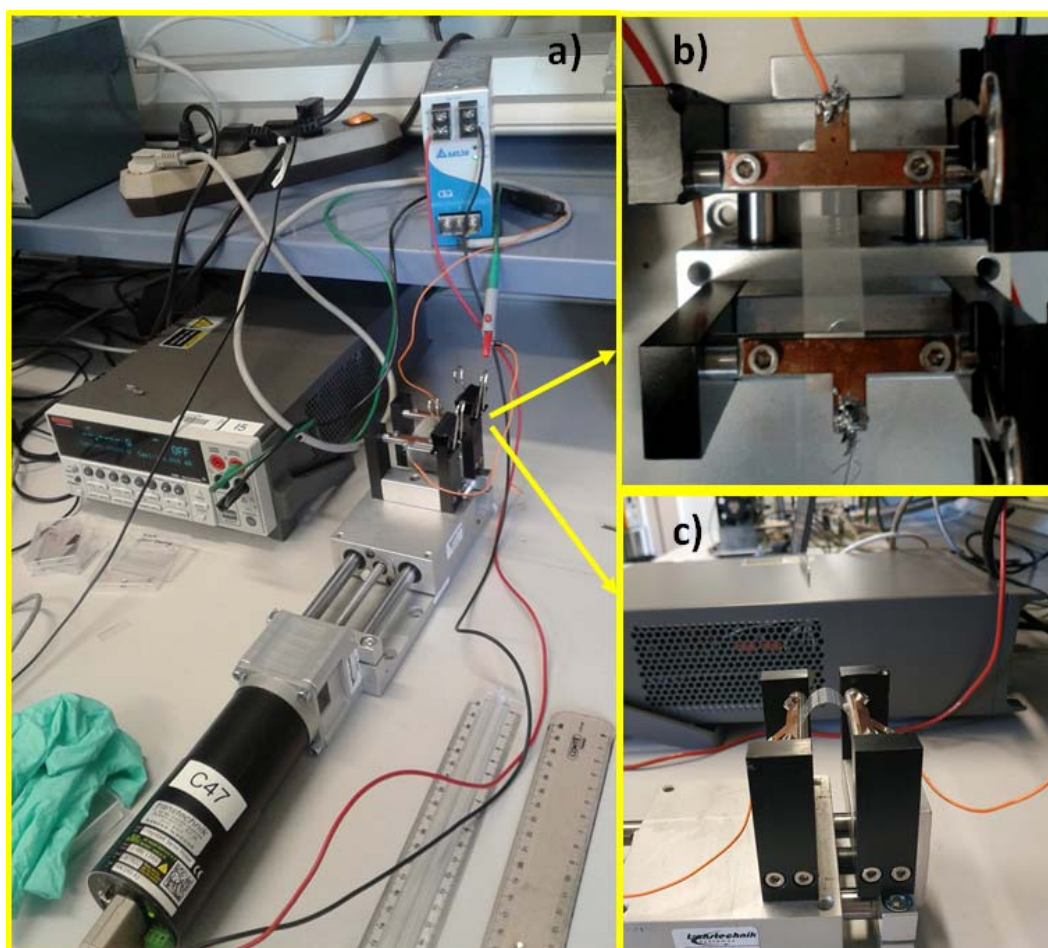


Figure A-13: a) Mechanical test set up: the sample holder with metallic jaws, connected to the Keithley (on the left) for *in situ* electrical measurements. One of the jaws can move thanks to the motor (black cylinder) connected to a movement controller, up and behind the sample holder. Both the Keithley and the movement controller are connected and controlled by LabVIEW. b) a band of AgNW network on PDMS during stretching test. c) photo of AgNW on Neopulim during bending test.

List of publications

Articles published in peer-reviewed journals:

1. N. Charvin, J. Resende, D.T. Papanastasiou, D. Muñoz-Rojas, C. Jiménez, Ali Nourdine, D. Bellet, L. Flandin, «*Dynamic degradation of metallic nanowire networks under electrical stress: a comparison between experiments and simulations*» *Nanoscale Adv.* 2021, 3, 675-681, <https://doi.org/10.1039/D0NA00895H>
2. A. Madeira, D. T. Papanastasiou, T. Toupance, L. Servant, M. Tréguer-Delapierre, D. Bellet, I. Goldthorpe «*Rapid synthesis of ultra-long silver nanowires for high performance transparent electrodes*», *Nanoscale Adv.* 2020, 2, 3804-3808, <https://doi.org/10.1039/D0NA00392A>
3. D. T. Papanastasiou, A. Schultheiss, D. Muñoz-Rojas, C. Celle, A. Carella, J.-P. Simonato, D. Bellet «*Transparent Heaters-A Review*», *Adv. Funct. Mater.* 2020, 1910225, <https://doi.org/10.1002/adfm.201910225>
4. V. H. Nguyen, J. Resende, D.T. Papanastasiou, N. Fontanals, C. Jimenez, D. Muñoz-Rojas, D. Bellet «*Low-cost fabrication of flexible transparent electrodes based on Al doped ZnO and silver nanowire nanocomposites: impact of the network density*», *Nanoscale* 2019, 11 (25), 12097-12107, <https://doi.org/10.1039/C9NR02664A>
5. E. Norton, L. Farrell, A. Zhussupbekova, D. Mullarkey, D. Caffrey, D.T. Papanastasiou, D. Oser, D. Bellet, I.V. Shvets, K. Fleischer «*Bending stability of Cu_{0.4}CrO₂ – A transparent p-type conducting oxide for large area flexible electronics*», *AIP Advances* 2018, 8, 085013, <https://aip.scitation.org/doi/10.1063/1.5027038>
6. T. Sannicolo, N. Charvin, L. Flandin, S. Kraus, D.T. Papanastasiou, C. Celle, J.-P. Simonato, D. Muñoz-Rojas, C. Jiménez, D. Bellet et al., «*Electrical Mapping of Silver Nanowire Networks: A Versatile Tool for Imaging Network Homogeneity and Degradation Dynamics during Failure*», *ACS Nano* 2018, 12, 4648-4659, <https://doi.org/10.1021/acsnano.8b01242>

Book chapters:

1. D. Bellet, D.T. Papanastasiou, J. Resende, V.H. Nguyen, C. Jiménez, N.D. Nguyen, D. Muñoz-Rojas, «*Metallic nanowire percolating networks: from main properties to applications*», ouvrage : «*Nanosystems*», *Intech Open* 2019, <https://doi.org/10.5772/intechopen.89281>
2. D.T. Papanastasiou, T. Sannicolo, J. Resende, V.H. Nguyen, C. Jiménez, D. Muñoz-Rojas, N.D. Nguyen, D. Bellet «*Physics and applications of silver nanowire networks*», ouvrage : «*Advances toward the development of nanotechnology*», Verlag 2019, <https://www.worldcat.org/isbn/9786202220996>

Submitted articles:

1. D.T. Papanastasiou, N. Charvin, J. Resende, V.H. Nguyen, A. Sekkat, D. Muñoz-Rojas, C. Jiménez, L. Flandin, D. Bellet «*Effects of non-homogeneity and oxide coating on silver nanowire networks under electrical stress: comparison between experiment and modeling*»
2. M. Dabert, D. T. Papanastasiou, L. Vidal, S. Hajjar-Garreau, D. Bellet, L. Balan «*Exploring the Effects of Thermal Annealing on the Optical and Electrical Properties of a Photo-generated Ag@polymer Metallized Coating*»

Dorina (Theodora) PAPANASTASIOU, thèse doctorat 2017-20, LMGP- UMR 5628
« *Étude des réseaux de nanofils d'argent : propriétés physiques, stabilité et intégration dans les dispositifs* »
Directeur et co-directeur de thèse : Prof. Daniel BELLET, Dr. David MUÑOZ-ROJAS

Résumé en français : Les matériaux conducteurs transparents (TCM) sont essentiels pour une grande variété d'applications émergentes telles que les dispositifs photovoltaïques, l'éclairage efficace, les capteurs, détecteurs mais aussi les films chauffants transparents (**Figure 1**).^[1,2] La transition numérique et énergétique du 21^e siècle, ainsi que les enjeux géostratégiques liés aux matériaux critiques, ont poussé à la recherche de nouveaux matériaux afin de remplacer les oxydes conducteurs transparents (TCO) traditionnels utilisés actuellement.^[3] En particulier, l'oxyde d'indium et d'étain (ITO) a dominé le domaine des électrodes transparentes (TE) dans les dispositifs durant près de quatre décennies, grâce à ses très bonnes propriétés physiques, telles qu'une bonne transparence optique et conductivité électrique, et sa grande stabilité. Mais malgré ces atouts, ITO souffre de sérieuses limitations liées au coût de fabrication, à la fragilité associée aux contraintes mécaniques et à la rareté de l'indium.^[4,5] Pour répondre à la nécessité d'économiser des matières premières et de la demande croissante de dispositifs flexibles, légers et intelligents, des TE alternatives sont donc nécessaires.^[6,7] C'est pourquoi une variété d'autres TCM a été étudiée de manière intensive pendant plus d'une décennie. Le vaste développement des nanosciences dans le monde entier a effectivement aidé à l'avancement dans ce domaine, où de nombreux nanomatériaux différents ont été proposés en tant que TCM alternatif. En particulier, des progrès significatifs ont été reportés grâce notamment à des matériaux comme les réseaux de nanotubes de carbone (CNT),^[8] les couches minces de graphène,^[9,10] les polymères conducteurs,^[11,12] les grilles métalliques,^[13,14] et les réseaux de nanofils métalliques.^[15,16] Les propriétés électriques, optiques et mécaniques, la fabrication durable et à faible coût, les matières premières disponibles et leur recyclabilité, la stabilité (thermique, chimique, électrique) et la compatibilité avec d'autres matériaux sont des caractéristiques clés pour sélectionner la technologie appropriée pour chaque application.^[17]

Les réseaux à base de nanofils d'argent (AgNW) apparaissent comme l'un des candidats les plus prometteurs dans la course au remplacement de l'ITO car : i/ ils présentent des propriétés optiques et électriques très prometteuses, ii/ contrairement à l'ITO et à de nombreux autres TCM, ils se sont avérés très flexibles, et iii/ ils peuvent être fabriqués par des techniques à faible coût basées sur des solutions adaptées à la production industrielle à grande échelle.^[16,18,19] Un autre avantage est que grâce au facteur d'aspect très élevé des nanofils, la quantité d'argent peut être considérablement réduite par rapport à la quantité d'indium dans une électrode à base

d'ITO.^[2] Grâce à leurs propriétés, les réseaux de AgNW ont déjà été intégrés dans de nombreux appareils qui couvrent un large spectre allant des films chauffants transparents, des cellules solaires, des antennes radiofréquences, des écrans tactiles, de l'éclairage à la récupération d'énergie.^[23] Les réseaux AgNW permettent d'allier flexibilité, transparence et hautes performances de chauffage à basse tension, ce qui constitue un atout évident pour l'intégration dans des chauffages transparents (TH).^[1,24] De plus, les TE à base de AgNW peuvent être des composants essentiels de dispositifs électroniques de faible consommation et portables pour la détection des mouvements et la surveillance de la santé.^[25-27]

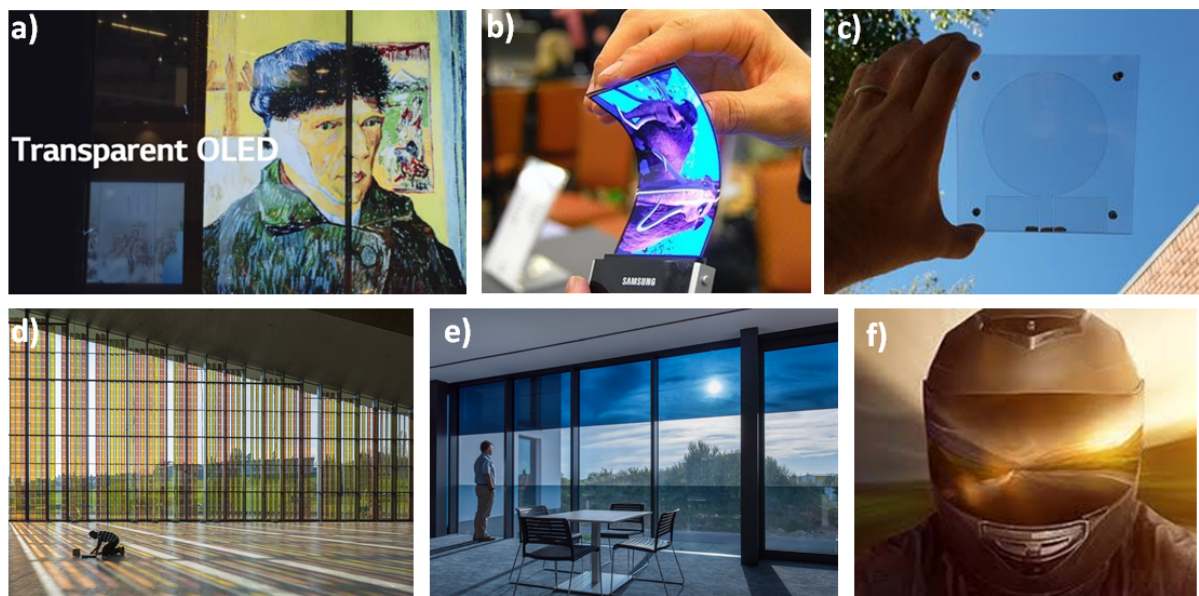


Figure 1: Exemples d'applications utilisant des électrodes transparentes. a) Écran TV OLED transparent de LG.^[28] b) Écran de smartphone OLED flexible de Samsung.^[29] c) Antenne transparente de Metamaterials.^[30] d) Façade de cellules solaires sensibilisées aux colorants par Solaronix, dans le centre de congrès SwissTech du campus de l'EPFL à Lausanne.^[31] e) Fenêtre intelligente avec film électrochromique par Sage Electrochromics.^[32] f) Un prototype de moto-visière par CEA Tech, avec dispositif de dégivrage-désembuage.^[33]

Bien que les propriétés de ces électrodes transparentes soient déjà remarquables, il reste des défis cruciaux à relever pour que cette technologie puisse être mature et parfaitement maîtrisée pour la mise en œuvre future des dispositifs. Poursuivant les travaux antérieurs au LMGP, les principaux objectifs de ma thèse de doctorat étaient : i/ l'investigation fondamentale des phénomènes physiques qui se déroulent à la fois à l'échelle des nanofils (échelle nanométrique) et des réseaux (échelle macroscopique), ii/ l'amélioration de leur stabilité et iii/ l'intégration dans les dispositifs. L'association de différentes techniques de caractérisation, comme les mesures électriques *in situ*, l'imagerie infrarouge (IR) et la microscopie électronique à balayage (MEB), a révélé des informations importantes pour les non-homogénéités et les instabilités des réseaux AgNW. De plus, la combinaison d'approches expérimentales et de simulation s'est

avérée importante pour mieux comprendre les mécanismes de défaillance et prédire les performances des TE et TH composés de réseaux de AgNW. Enfin, au cours de ma thèse, des pistes potentielles pour l'amélioration de la stabilité et de l'intégration dans les dispositifs ont été explorées, dans le cadre de plusieurs projets et collaborations avec des laboratoires et des partenaires industriels à Grenoble et ailleurs.

La présente thèse de doctorat comprend 6 chapitres. Le **chapitre 1** commence par une présentation générale sur le besoin de TCM émergents et le large éventail d'applications, puis présente une introduction de TE basés sur les réseaux de AgNW. Les principales techniques de synthèse des AgNW et de fabrication de TE sont présentées, suivies d'une description des propriétés physiques des réseaux et de leur optimisation (i.e. propriétés électriques, optiques et mécaniques), de leurs avantages et des problèmes d'instabilité. La stabilité est actuellement l'une des principales limites de l'intégration réussie des réseaux MNW dans les appareils. La **Figure 2** résume les principaux mécanismes de dégradation des réseaux MNW, tels que les contraintes électriques (a), thermiques (b), mécaniques (c) et environnementales (d). Il existe plusieurs approches développées par les chercheurs pour étudier les différentes instabilités en cours, du nanofil unique et les jonctions entre eux (échelle nanométrique) à la défaillance macroscopique d'un réseau entier.^[34-37] Dans des travaux antérieurs menés par l'équipe au LMGP, l'effet du recuit thermique sur les propriétés physiques a été attentivement étudié par des techniques macroscopiques et aussi des outils de nano-caractérisation, MEB et MET entre autres.^[38,39]

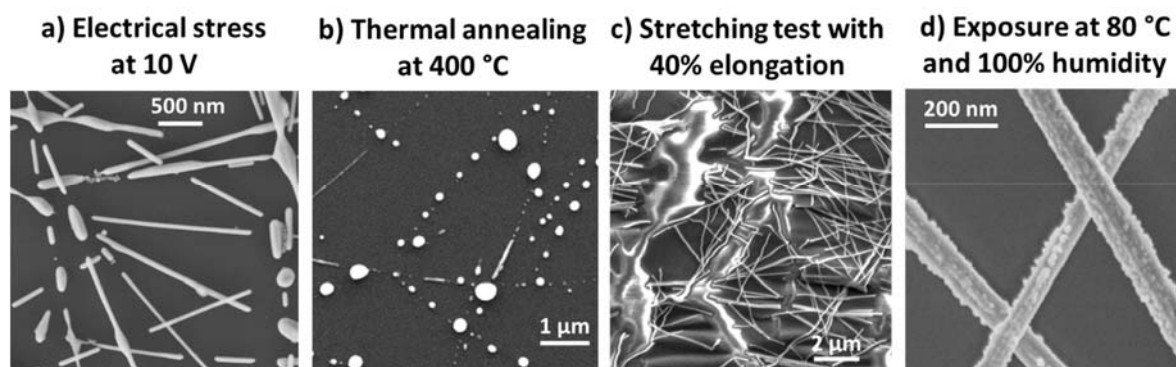


Figure 2: Images MEB de réseaux MNW montrant la dégradation due à différentes contraintes : a) contrainte électrique via une rampe de tension appliquée de 0,5 V / min. A 10 V les instabilités conduisent à une dégradation partielle des nanofils. b) AgNW sphéroïdisés après recuit thermique à 400 °C. c) AgNW, déposés sur PDMS, déformés et cassés à 40% d'allongement lors d'un test d'étirement réalisé *in situ* à l'intérieur d'un MEB. d) Contrainte environnementale, lorsque les CuNW (nanofils de cuivre) sont exposés à une température de 80 °C et à une humidité de 100% pendant 60 min.^[40]

Le **chapitre 2** se concentre plus spécifiquement sur la physique et les applications des TH. L'impact positif de la TH sur l'énergie, la santé ou les transports est important et, en parallèle, nous avons observé l'intérêt croissant de notre communauté scientifique pour approfondir l'étude des TH. Par conséquent, en particulier au cours des 5 dernières années, il y a une augmentation remarquable des publications rapportant les performances de chauffage des TCMs. C'est également le cas de notre équipe en LMGP et, ainsi, une partie importante de ma thèse est liée à l'étude et à l'optimisation de la fabrication et des propriétés des TH, et ainsi à leur implémentation dans les dispositifs. Pourtant, il n'y avait qu'un seul article de synthèse résumant les familles TCM et la gamme de dispositifs concernant la TH, publié par Gupta et al. en 2016.^[41] Pour toutes ces raisons, et en collaboration avec l'équipe scientifique de J.-P. Simonato au CEA-Liten (Grenoble, France) nous avons publié un article de revue intitulé «*Transparent Heaters: a Review*», publié dans *Advanced Functional Materials* par D.T. Papanastasiou, A. Schultheiss, D. Muñoz-Rojas, C. Celle, A. Carella, J.-P. Simonato et D. Bellet.^[1] Notre volonté a été dans un premier temps d'introduire la physique thermique du TH qui n'a pas été précédemment résumée, à partir de l'effet Joule (comme le montre la **Figure 3a**) puis des principales propriétés TH telles que la densité de puissance et la température en régime permanent (Figure 3b). De plus, nous voulions fournir une discussion critique sur les différents matériaux actifs (Figure 3c) et enfin, nous concentrer sur les défis futurs en termes de meilleure compréhension physique, de performances améliorées et d'intégration du TH dans les dispositifs industriels.

Préalablement à l'analyse approfondie des résultats expérimentaux et de simulation obtenus dans le cadre de cette thèse, des bases importantes concernant les étapes de fabrication des réseaux AgNW par spray coating, la caractérisation de leurs propriétés électriques, optiques et mécaniques, la caractérisation morphologique par microscopie électronique et les mesures de température, sont présentées au **chapitre 3**. Par ailleurs, la comparaison entre spray, rod et spin coating pour le dépôt des nanofils ultra-longs est présentée, sur la base de l'article de recherche intitulé «*Rapid synthesis of ultra-long silver nanowires for high performance transparent electrodes*», publié dans *Nanoscale Advances* par A. Madeira, DT Papanastasiou, T. Toupance, L. Servant, M. Tréguer-Delapierre, D. Bellet, IA Goldthorpe ; un travail réalisé en collaboration avec deux équipes scientifiques de l'ICMCB à Bordeaux et de l'Université de Waterloo au Canada.^[42] Enfin, les méthodes de simulation utilisées et développées au cours de ma thèse sont présentées et des résultats préliminaires tels que l'effet des longueurs et diamètres des nanofils sur les performances électriques sont présentés. Les résultats de telles simulations sont

comparés à ceux expérimentaux du dépôt de réseaux AgNW de différentes dimensions de nanofils. Les suspensions AgNW ont été aimablement fournies par l'équipe de J.-P. Simonato, ainsi que pour la plupart des AgNW que j'ai utilisés pour la fabrication et l'étude de TE au cours de ma thèse.

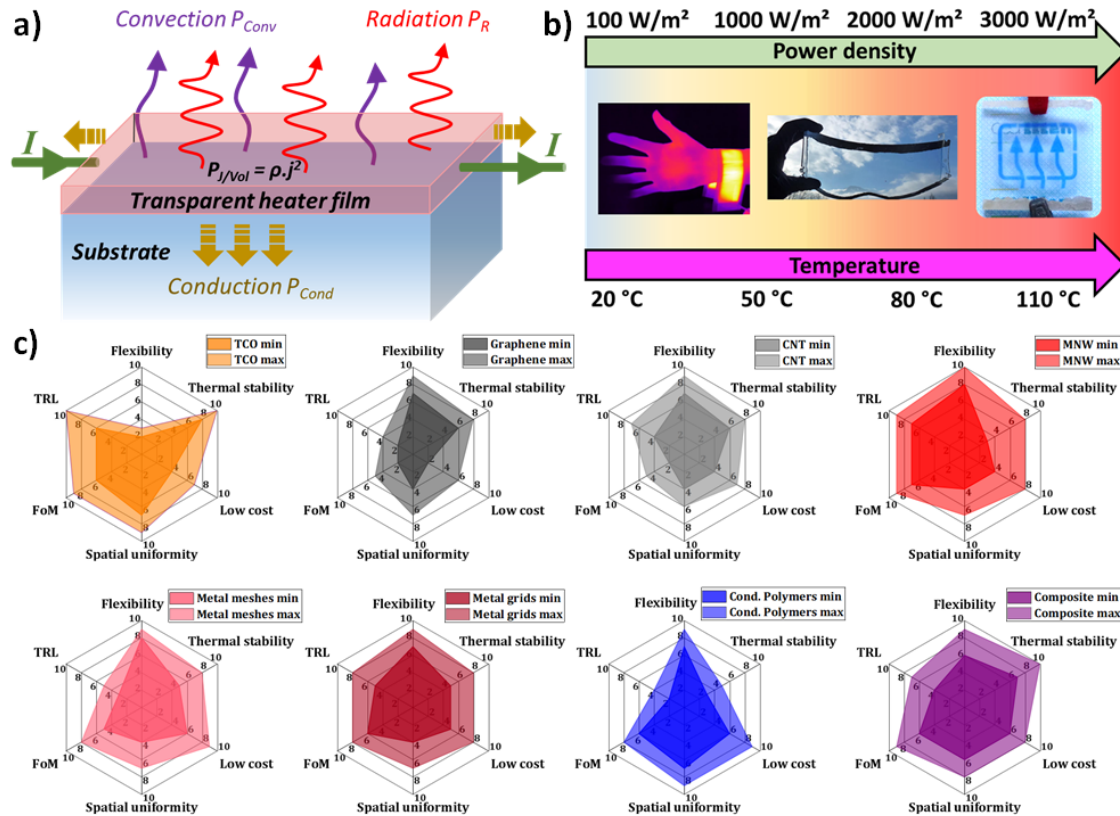


Figure 3: a) Représentation schématique d'un dispositif de chauffage transparent (TH): le TH est traversé par un courant électrique, générant de la chaleur grâce à l'effet Joule. Un état stationnaire est atteint une fois que cette chaleur générée est égale à la somme des pertes de chaleur indiquées avec différentes couleurs. b) Principaux domaines d'application des TH par rapport à la densité de puissance surfacique ou à la température requise. Les flèches associées représentent les températures maximales typiques en régime stationnaire pour les principales technologies TH. c) Comparaison des TH fabriqués avec les différentes technologies. Cette figure montre les tendances générales avec six critères (dans le sens des aiguilles d'une montre à partir du haut) : flexibilité, stabilité thermique, faible coût (du matériau et du procédé de fabrication), uniformité spatiale, valeur du mérite (FoM) et niveau de maturité technologique (TRL). En fonction de la synthèse et de l'utilisation des TH expérimentaux, une gamme de valeurs de mérite avec des valeurs minimales et maximales est proposée. Les notes pour tous les critères de chaque technologie TH ne sont que des indications générales, car les valeurs réelles dépendent grandement de l'application.^[1]

Le **chapitre 4** traite de la dégradation des réseaux de nanofils d'argent sous stresses électriques et thermiques par des approches expérimentales et de modélisation. À partir de mesures électriques lors d'une rampe de tension, avec enregistrement *in situ* de la distribution spatiale de la température par imagerie IR, nous avons observé la propagation de la défaillance, déclenchée par effet Joule.^[43,44] Pour expliquer davantage ce phénomène, au cours de ma thèse,

j'ai effectué des simulations électriques et thermiques dans COMSOL Multiphysics® sur des couches minces métalliques de géométrie simplifiée. Ainsi, nous avons pu vérifier que la présence d'un défaut microscopique peut introduire une forte augmentation locale de la densité de courant qui impacte également la distribution de température de surface même à basse tension appliquée (**Figure 4**). Cette étude a été menée dans le cadre du projet EARTH, entre LMGP et LEPMI-Bourget-du-Lac, financé par le labex CEMAM et est présentée en détail dans l'article intitulé «*Dynamic degradation of metallic nanowire networks under electrical stress: a comparison between experiments and simulations*» publié dans *Nanoscale Advances* par N. Charvin, J. Resende, DT Papanastasiou, D. Muñoz-Rojas, C. Jiménez, A. Nourdine, D. Bellet et L. Flandin.^[44]

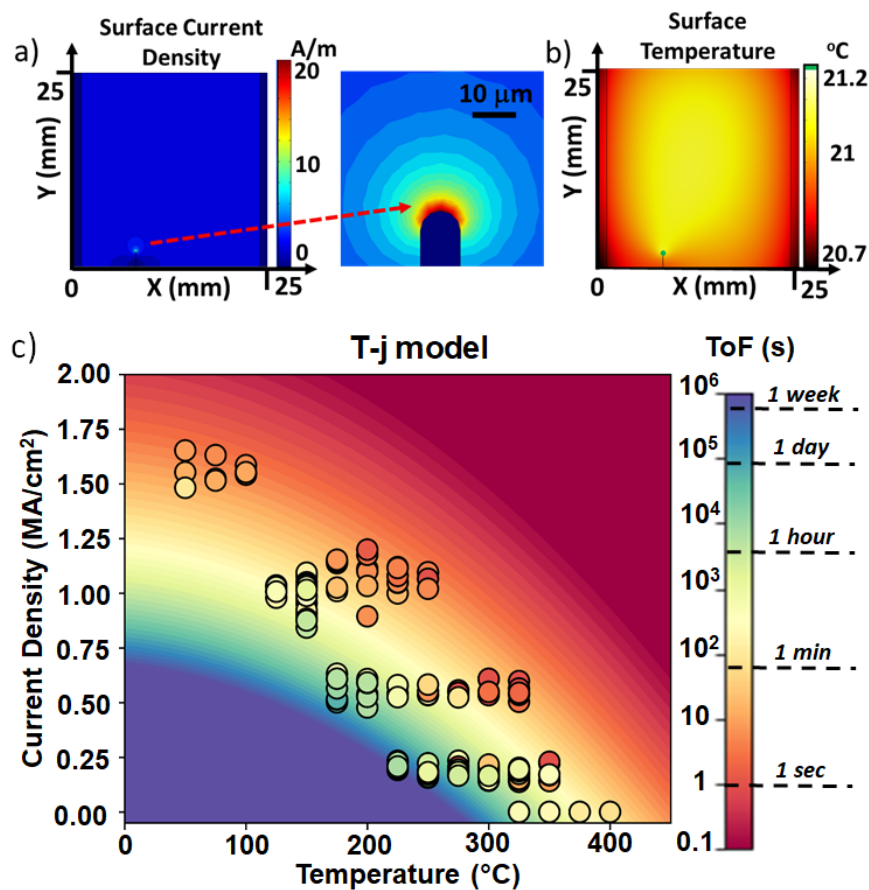


Figure 4: a) Simulation COMSOL de la densité de courant de surface sous une tension 1 V appliquée entre les électrodes verticales opposées. Échantillon entier (à gauche) et zoom (à droite) sur la zone d'encoche. La taille de l'échantillon de la couche mince d'Ag est de 25 x 25 mm² et la hauteur de l'encoche verticale en bas à gauche est de 2 mm. b) Simulation COMSOL de la distribution de la température de surface sous une tension de 1 V. c) Modèle *T-j* : diagramme densité-température du courant montrant les valeurs calculées et expérimentales du temps de défaillance (ToF) pour les réseaux AgNW. La carte de couleurs représente le temps de défaillance calculé et les exemples de durée sont notés dans l'échelle arc-en-ciel, c'est-à-dire 1 seconde, 1 minute, 1 heure, etc. Les petits cercles correspondent aux couples *T-I* expérimentaux et leur couleur intérieure correspond au *ToF* mesuré expérimentalement.

La deuxième partie du chapitre 4 est liée aux principaux résultats de l'expérience Température-Courant ($T-I$), qui a été menée afin d'explorer le temps de défaillance (ToF) des réseaux d'AgNW, visant à développer un modèle physique capable de prédire les limites de performance sous l'application de température et puissance électrique. Les résultats sont inclus dans l'article intitulé «*Endurance tests on silver nanowire networks under constant thermal and electrical stress*» à soumettre par J. Resende, DT Papanastasiou, D. Moritz, N. Fontanals, C. Jiménez et D. Bellet. Cette étude statistique que nous avons réalisée, concernent environ 200 échantillons, où nous avons appliqué plusieurs valeurs de température et de courant, en suivant l'évolution de la résistance et en mesurant le ToF pour chaque couple $T-I$.

La conclusion importante de l'expérience T-I est que la dégradation est principalement provoquée par des instabilités morphologiques induites thermiquement, soit directement liées aux températures imposées élevées (Plateau-Rayleigh), soit indirectement par le chauffage local induit par effet Joule (forte densité de courant locale). Ensuite, en utilisant cette approche, nous avons combiné la contribution électrique et thermique à la diffusion atomique activée thermiquement afin de calculer le ToF . Le modèle semi-empirique proposé offre une bonne première approximation des résultats expérimentaux (comme le montre la Figure 4c) et il fournit des informations utiles sur les limites des réseaux AgNW pour la mise en œuvre industrielle en tant que TE.

La défaillance des réseaux AgNW reste le principal défi à relever pour leur intégration réussie dans les dispositifs, pour lesquels la stabilité électrique est cruciale. Les rapports précédents traitent toujours de réseaux homogènes. Étant donné que les réseaux présentent des inhomogénéités aléatoires ou peuvent même être endommagés pendant la fabrication ou le fonctionnement du dispositif, l'étude de ce problème mérite plus d'attention. Ainsi, comme présenté au **chapitre 5**, nous avons étudié l'effet de la non-homogénéité de manière plus macroscopique, en combinant toujours des approches expérimentales et de simulations. Pour cette raison, nous avons intentionnellement conçu et fabriqué des réseaux avec des régions à motifs triangulaires en utilisant une approche de fabrication simple et peu coûteuse avec des masques imprimés en 3D. Ces masques sont schématisés dans l'encart de la **Figure 5**. Cette étude a également été menée dans le cadre du projet EARTH. L'article intitulé «*Effects of non-homogeneity and oxide coating on silver nanowire networks under electrical stress: comparison between experimental and modelling approaches*» est également soumis par les

auteurs suivants: DT Papanastasiou, N. Charvin, J. Résende, VH Nguyen, A. Sekkat, D. Muñoz-Rojas, C. Jiménez, L. Flandin et D. Bellet.

Dans un premier temps, nous avons étudié l'impact des non-homogénéités sur la distribution spatiale du potentiel électrique par cartographie à une pointe (1P). Ensuite, nous avons effectué des tests de stresses électriques en augmentant la tension appliquée comme présenté précédemment. En parallèle, nous avons étudié la position des points chauds et la propagation des fissures par imagerie IR *in situ*, et nous avons observé les différences entre les réseaux AgNW de référence et non-homogènes. Les expériences ont démontré que les variations de densité de réseau, à la fois positives et négatives, contrôlent principalement le début de la défaillance, comme le montrent les images IR de la Figure 5. En outre, elles ont révélé l'apparition d'un échauffement local plus élevé pour les réseaux non-homogènes, à une tension appliquée inférieure. Ce fait déclenche la dégradation du réseau. De plus, les données expérimentales ont été combinées et validées avec une modélisation physique d'échantillons de même taille, tant pour la distribution électrique que thermique. Pour cette dernière, la modélisation et les résultats expérimentaux sont comparés sur la Figure 5d-i. Les simulations ont également fourni la distribution spatiale de la densité de courant et une compréhension objective des résultats expérimentaux.

Une bonne stratégie pour améliorer la stabilité des réseaux de AgNW, est d'empêcher la diffusion des atomes d'argent qui conduit à des instabilités morphologiques des nanofils. Plusieurs études ont montré une amélioration de la stabilité en revêtant les réseaux d'une fine couche mince d'oxyde métallique, comme l'oxyde de zinc (ZnO),^[45,47,48] oxyde d'aluminium (Al₂O₃),^[49-52] oxyde de zinc dopé à l'aluminium (AZO),^[53-55] ou avec du graphène oxydé (GO).^[46,56] Au LMGP, l'équipe AgNW travaille toujours en étroite collaboration avec l'équipe SALD (Spatial Atomic Layer Deposition- dépôt par couche atomique spatiale), dirigée par Dr David Muñoz-Rojas, pour l'amélioration de la stabilité du réseau AgNW. Ceci est réalisé par l'encapsulation avec le dépôt d'une fine couche mince d'oxyde par la méthode SALD à pression atmosphérique (AP-SALD) développée au laboratoire.^[57] Tout en conservant les avantages de l'ALD (dépôt à basse température, contrôle de l'épaisseur, matériaux de haute qualité et conformité), l'AP-SALD peut être jusqu'à 2 ordres de grandeur plus rapide que l'ALD et cette technique est compatible avec la technologie roll-to-roll (R2R) à pression atmosphérique.^[58] Suite aux précédentes études de l'équipe sur le dépôt d'oxyde sur des réseaux AgNW homogènes,^[45,55,59] au cours de ma thèse nous avons étudié l'effet d'une fine couche de ZnO sur la stabilité des réseaux non-homogènes. À notre connaissance, cela n'a pas été étudié auparavant

et semble essentiel pour l'intégration des réseaux AgNW dans des dispositifs modernes actuels. Comme démontré par la cartographie 1P, la présence de ZnO se traduit par une distribution électrique plus homogène. Ainsi, les films minces transparents de ZnO empêchent non seulement la diffusion atomique de l'argent, comme déjà démontré, mais diminuent également la contrainte électrique très localisée grâce à l'homogénéisation de la distribution électrique qu'ils assurent.

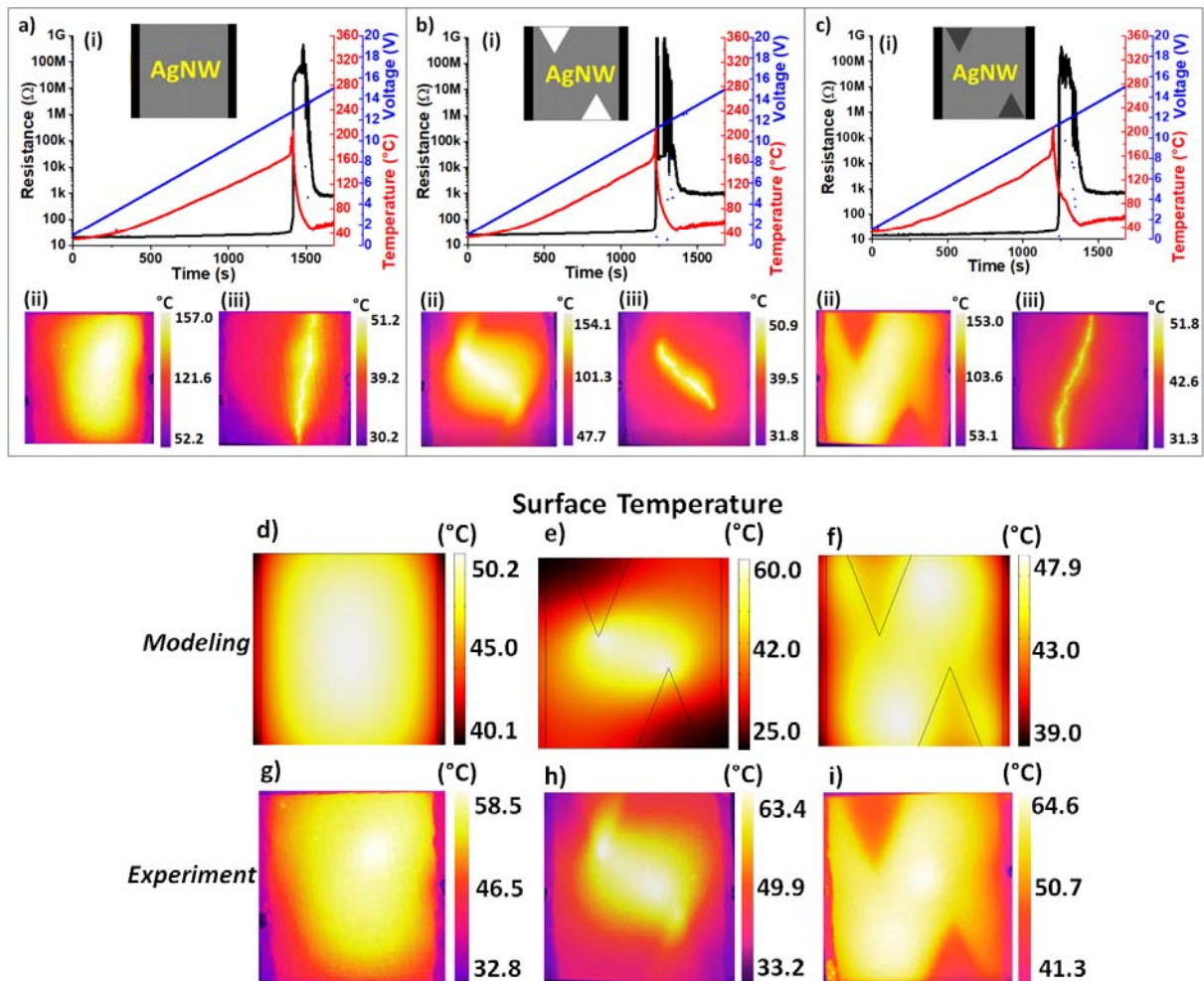


Figure 5: a-c) Résistance électrique (noir), tension (bleu) et température de surface maximale (mesurée à partir de l'imagerie IR et représentée en rouge) pendant la rampe de tension de 0,5 V/min appliquée à des réseaux AgNW non recouverts, et ce pour de trois configurations différentes de densité de réseau: a) homogène, b) triangles vides, c) triangles plus denses. Les schémas associés sont affichés dans l'encart. Dans chaque cas, les images IR de gauche (ii) ont été prises avant la propagation de l'instabilité du réseau, tandis que celles de droite (iii) ont été prises après la dégradation lorsque la résistance avait chuté à quelques k Ω . d-i) Distribution de la température de surface simulée et expérimentale pour les trois géométries de l'échantillon. d-f) Résultats de la modélisation lorsqu'une polarisation de 5 V est appliquée entre les contacts parallèles (côtés verticaux gauche et droit). g-i) Résultats expérimentaux pour la distribution spatiale de la température obtenue par imagerie IR à 5 volts, lors d'une rampe de tension de 0,5 V / min. La taille de tous les échantillons est de 25x25 mm².

Le dernier chapitre de ma thèse est lié à l'intégration des réseaux AgNW et d'autres nanomatériaux basés sur l'Ag dans des dispositifs, à travers plusieurs projets et collaborations sur lesquels j'ai eu la grande chance de travailler et d'élargir mes connaissances sur divers sujets. La première section du **chapitre 6** est liée aux TH, qui sont au cœur de nos recherches sur AgNW. Nous avons appliqué cette technologie sur des dispositifs biomédicaux de laboratoire sur puce (lab-on-chip), grâce à la collaboration avec le directeur du LMGP, Prof Franz Bruckert. Nous avons appliqué et étudié en profondeur ces TH sur des dispositifs au cours de ma thèse. Nous avons essayé de développer la technique PCR quantitative *in situ* (qPCR) pour l'amplification de l'ADN dans une puce microfluidique avec observation directe de la fluorescence par un microscope. La PCR est couramment utilisée pour la détection de maladies infectieuses, y compris celles par des bactéries ou des virus, comme la pandémie de coronavirus à laquelle nous sommes confrontés depuis Mars 2020.^[60-62] Comme présenté dans la section 6.1, nous avons intégré les réseaux AgNW sur des puces, comme le montre la photo de la **Figure 6a**, et appliqué des paliers de tension afin d'induire les cycles de chauffage et de refroidissement et obtenir les températures nécessaires pour le test PCR. L'imagerie IR (Figure 6b) et les thermocouples standards ont également été utilisés pour l'étalonnage du système et la vérification de la performance électrique stable du réseau AgNW. Grâce à la transparence optique du TH à base d'AgNW, le signal fluorescent n'est pas affecté et nous pouvons ainsi étudier sa variance *in situ*, lors de cycles thermiques successifs induits par la puissance. Un tel exemple est présenté sur la figure 6c.

Dans la deuxième section du chapitre 6, l'intégration des réseaux AgNW sur des collecteurs d'énergie flexibles est présentée. Dans le cadre du projet Institut Carnot Energies du Futur FREE en collaboration avec le Pr Alain Sylvestre de G2Elab et le Pr Skandar Basrour de TIMA à Grenoble, nous visons à élaborer des générateurs électrostatiques aux propriétés mécaniques supérieures (comme extensibilité), notamment dans le cadre du grappillage énergétique en vue de l'intégration dans l'internet des objets (IoT), mais aussi les vêtements intelligents et les véhicules hybrides.^[26,64] Pour cela, il est nécessaire de remplacer les contacts électriques traditionnels, comme les couches minces d'or ou les pâtes conductrices, par une technologie (semi) transparente et qui conserve sa conductivité électrique tout en étant sous contrainte mécanique. Les électrodes transparentes basées sur les réseaux AgNW constituent un candidat prometteur grâce à leur excellente stabilité en flexion et à leurs performances propices aux tests d'étirement.^[65-67] Au cours de ma thèse, nous avons optimisé les propriétés mécaniques des électrodes étirables à base d'AgNW et amélioré leur intégration dans les composites

AgNW/PDMS et les «sandwiches» avec des composants qui constituent le milieu diélectrique des dispositifs de récupération d'énergie.

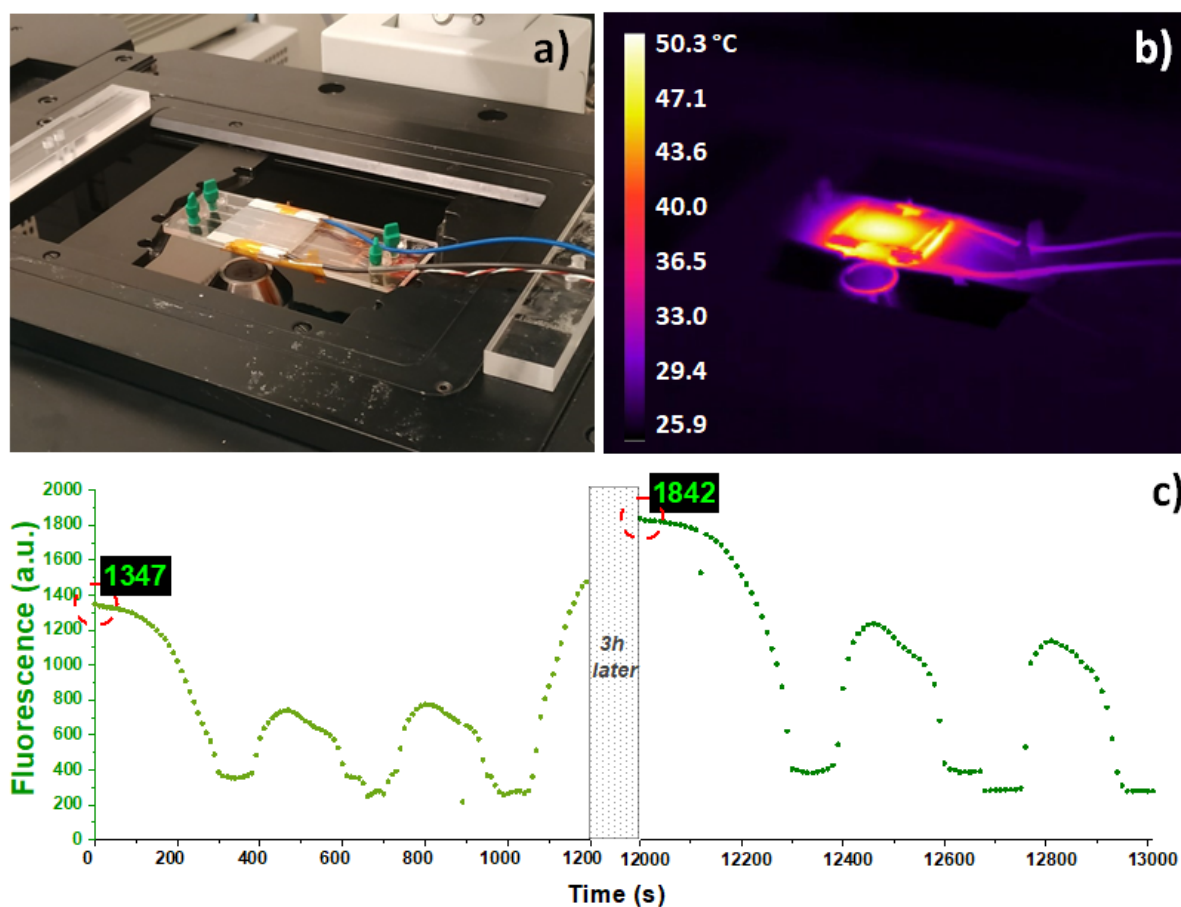


Figure 6: Dispositif « Lab-on-a-chip » pour les études de qPCR *in situ*, basé sur le TH constitué d'un réseau de AgNW. a) Photo de la puce TH-bio placée au-dessus du microscope pour les mesures de fluorescence du colorant de liaison à l'ADN. Le réseau AgNW est déposé sur du verre Corning 25x25 mm² et la puce plastique a une taille de 25x75 mm². Un thermocouple Pt100 est placé sous la puce pour mesurer et comparer la température avec les mesures de la caméra IR sur le côté supérieur du réseau TH-AgNW. b) Image IR de l'assemblage précédent, pendant le cycle thermique de l'ADN induit par la puissance électrique (effet Joule). c) Mesures de fluorescence *in situ* du colorant de liaison SYBR Green pendant quatre cycles d'amplification réalisés en utilisant un chauffage induit par le TH-AgNW/ZnO. Une petite augmentation de fluorescence peut être remarquée entre le premier et le second (à gauche). Le troisième et le quatrième cycle sont effectués après 3 heures (à droite). Le refroidissement de l'installation à température ambiante a révélé une amplification de 36% à partir de l'augmentation de la fluorescence à 1842.

Poursuivant l'intégration des AgNW dans les dispositifs, la section 6.3 comprend une brève présentation et une sélection des résultats des deux projets ANR, auxquels notre équipe participe, en collaboration avec des laboratoires et des partenaires industriels. Le premier, *PANASSE (Planar Assembly of NANowires for Sidewalls Emission)*, concerne la fabrication de cathodes froides à base de AgNW pour des sources de rayons-X compactes, à intégrer dans la future génération de scanners médicaux. *PANASSE* est une collaboration avec Thalès à

Palaiseau et le laboratoire IEMN à Lille, qui ont une grande expertise dans le développement de cathodes CNT et en nanocaractérisation, respectivement. Le deuxième projet, *MEANING (MEtAllic Nanowire networks: from fundamental aspects to INDUSTRIAL integration)*, est lié à l'intégration des réseaux AgNW dans le photovoltaïque organique flexible (OPV) émergeant, en collaboration avec des chercheurs en nanochimie du laboratoire ICMCB à Bordeaux et le partenaire industriel ARMOR à Nantes. Les résultats préliminaires sont liés à la caractérisation électrique réalisée en LMGP aux réseaux AgNW déposés dans de grands substrats plastiques par ARMOR.

La dernière partie du chapitre 6 est liée à l'étude d'une technologie différente des réseaux AgNW, celle des nanocomposites constitués de nanoparticules d'argent (AgNPs) sur des revêtements polymères, qui sont élaborées par le Dr Lavinia Balan et Marine Dabert (thèse de doctorat 2017-20) dans IS2M et CEMHTI. Dans le cadre de notre collaboration, nous avons réalisé la caractérisation électrique de ces matériaux hybrides au LMGP, en nous concentrant sur l'effet du recuit thermique. Ces nanocomposites peuvent fournir des propriétés électriques et optiques intéressantes, telles qu'une réflectivité élevée dans le NIR, en modifiant la nature du métal et leur synthèse. L'article intitulé «*Exploring the Effects of Thermal Recalling on the Optical and Electrical Properties of a Photo-generated Ag @ polymer Metallized Coating*» a également été soumis récemment par M. Dabert, DT Papanastasiou, L. Vidal, S. Hajjar-Garreau, D. Bellet, L. Balan.

References

- [1] D. T. Papanastasiou, A. Schultheiss, D. Muñoz-Rojas, C. Celle, A. Carella, J.-P. Simonato, D. Bellet, *Advanced Functional Materials* **2020**, *30*, 1910225.
- [2] T. Sanniccolo, M. Lagrange, A. Cabos, C. Celle, J.-P. Simonato, D. Bellet, *Small* **2016**, *12*, 6052.
- [3] K. Ellmer, *Nature Photonics* **2012**, *6*, 809.
- [4] A. Kumar, C. Zhou, *ACS Nano* **2010**, *4*, 11.
- [5] R. A. Afre, N. Sharma, M. Sharon, M. Sharon, *REVIEWS ON ADVANCED MATERIALS SCIENCE* **2018**, *53*, 79.
- [6] G. U. Kulkarni, S. Kiruthika, R. Gupta, K. Rao, *Current Opinion in Chemical Engineering* **2015**, *8*, 60.
- [7] D. Li, W.-Y. Lai, Y.-Z. Zhang, W. Huang, *Advanced Materials* **2018**, *30*, 1704738.
- [8] Y. Zhou, R. Azumi, *Sci Technol Adv Mater* **2016**, *17*, 493.
- [9] N. N. Rosli, M. A. Ibrahim, N. Ahmad Ludin, M. A. Mat Teridi, K. Sopian, *Renewable and Sustainable Energy Reviews* **2019**, *99*, 83.
- [10] Y. Xu, J. Liu, *Small* **2016**, *12*, 1400.
- [11] M. N. Gueye, A. Carella, R. Demadrille, J.-P. Simonato, *ACS Appl. Mater. Interfaces* **2017**, *9*, 27250.
- [12] M. N. Gueye, A. Carella, J. Faure-Vincent, R. Demadrille, J.-P. Simonato, *Progress in Materials Science* **2020**, *108*, 100616.
- [13] G. Xu, Y. Li, *Nano Select* **2020**, *1*, 169.

- [14] H. B. Lee, W.-Y. Jin, M. M. Ovhal, N. Kumar, J.-W. Kang, *J. Mater. Chem. C* **2019**, *7*, 1087.
- [15] D. Langley, G. Giusti, C. Mayousse, C. Celle, D. Bellet, J.-P. Simonato, *Nanotechnology* **2013**, *24*, 452001.
- [16] D. Bellet, M. Lagrange, T. Sannicolo, S. Aghazadehchors, V. H. Nguyen, D. P. Langley, D. Muñoz-Rojas, C. Jiménez, Y. Bréchet, N. D. Nguyen, *Materials* **2017**, *10*, 570.
- [17] M. Morales-Masis, S. De Wolf, R. Woods-Robinson, J. W. Ager, C. Ballif, *Adv. Electron. Mater.* **2017**, *3*, n/a.
- [18] M. Singh, S. Rana, *Materials Today Communications* **2020**, *24*, 101317.
- [19] H. Sohn, C. Park, J.-M. Oh, S. W. Kang, M.-J. Kim, *Materials* **2019**, *12*, 2526.
- [20] D. P. Langley, G. Giusti, M. Lagrange, R. Collins, C. Jiménez, Y. Bréchet, D. Bellet, *Solar Energy Materials and Solar Cells* **2014**, *125*, 318.
- [21] F. Guo, N. Li, V. V. Radmilović, V. R. Radmilović, M. Turbiez, E. Spiecker, K. Forberich, C. J. Brabec, *Energy Environ. Sci.* **2015**, *8*, 1690.
- [22] P. Aurang, D. Doganay, A. Bek, R. Turan, H. E. Unalan, *Solar Energy* **2017**, *141*, 110.
- [23] D. T. Papanastasiou, T. Sannicolo, J. Resende, V. H. Nguyen, C. Jimenez, D. Munoz-Rojas, N. D. Nguyen, D. Bellet, in *Advances toward the Development of Nanotechnology*, **2019**, p. 472.
- [24] C. Celle, C. Mayousse, E. Moreau, H. Basti, A. Carella, J.-P. Simonato, *Nano Research* **2012**, *5*, 427.
- [25] S. Zhang, S. Li, Z. Xia, K. Cai, *J. Mater. Chem. B* **2020**, *8*, 852.
- [26] S. Yao, P. Ren, R. Song, Y. Liu, Q. Huang, J. Dong, B. T. O'Connor, Y. Zhu, *Adv. Mater.* **2020**, *32*, 1902343.
- [27] H. Jeong, Y. Noh, S. H. Ko, D. Lee, *Composites Science and Technology* **2019**, *174*, 50.
- [28] "LG Transparent OLED," can be found under <https://www.lg-informationdisplay.com/ISE2019>, **n.d.**
- [29] "Samsung secures flexible display patent for foldable smartphones," can be found under <https://www.cbronline.com/uncategorised/samsung-secures-flexible-display-patent-for-foldable-smartphones/>, **n.d.**
- [30] "Transparent Antennas," can be found under <https://metamaterial.com/solutions/transparent-antennas-2/>, **n.d.**
- [31] "SwissTech Convention Center to the EPFL campus," can be found under <https://www.itsliquid.com/swisstech-convention-center.html>, **n.d.**
- [32] "SageGlass LightZone," can be found under <https://www.sageglass.com/en/products/sageglass-lightzone>, **n.d.**
- [33] "New developments in transparent heating polymer films," can be found under http://www.cea-tech.fr/cea-tech/english/Pages/ec_2017/transparent-heating-polymer-films-nanomaterials-processes.aspx, **n.d.**
- [34] F. N. Kholid, H. Huang, Y. Zhang, H. J. Fan, *Nanotechnology* **2016**, *27*, 025703.
- [35] N. M. Batra, A. Syed, P. M. F. J. Costa, *Nanoscale* **2019**, *11*, 3606.
- [36] M. Lagrange, T. Sannicolo, D. Muñoz-Rojas, B. G. Lohan, A. Khan, M. Anikin, C. Jiménez, F. Bruckert, Y. Bréchet, D. Bellet, *Nanotechnology* **2017**, *28*, 055709.
- [37] K. Maize, S. R. Das, S. Sadeque, A. M. S. Mohammed, A. Shakouri, D. B. Janes, M. A. Alam, *Applied Physics Letters* **2015**, *106*, 143104.
- [38] D. P. Langley, M. Lagrange, G. Giusti, C. Jiménez, Y. Bréchet, N. D. Nguyen, D. Bellet, *Nanoscale* **2014**, *6*, 13535.
- [39] M. Lagrange, D. P. Langley, G. Giusti, C. Jiménez, Y. Bréchet, D. Bellet, *Nanoscale* **2015**, *7*, 17410.
- [40] H. Zhai, R. Wang, X. Wang, Y. Cheng, L. Shi, J. Sun, *Nano Res.* **2016**, *9*, 3924.
- [41] R. Gupta, K. D. M. Rao, S. Kiruthika, G. U. Kulkarni, *ACS Appl. Mater. Interfaces* **2016**, *8*, 12559.
- [42] A. Madeira, D. T. Papanastasiou, T. Toupance, L. Servant, M. Tréguer-Delapierre, D. Bellet, I. A. Goldthorpe, *Nanoscale Adv.* **2020**, *2*, 3804.
- [43] T. Sannicolo, N. Charvin, L. Flandin, S. Kraus, D. T. Papanastasiou, C. Celle, J.-P. Simonato, D. Muñoz-Rojas, C. Jiménez, D. Bellet, *ACS Nano* **2018**, *12*, 4648.

- [44] N. Charvin, J. Resende, D. T. Papanastasiou, D. Muñoz-Rojas, C. Jiménez, A. Nourdine, D. Bellet, L. Flandin, *Nanoscale Adv.* **2021**, *3*, 675.
- [45] A. Khan, V. H. Nguyen, D. Muñoz-Rojas, S. Aghazadehchors, C. Jiménez, N. D. Nguyen, D. Bellet, *ACS Applied Materials & Interfaces* **2018**, *10*, 19208.
- [46] W. H. Chae, T. Sannicolo, J. C. Grossman, *ACS Appl. Mater. Interfaces* **2020**, acsami.0c03587.
- [47] A.-T. Pham, X.-Q. Nguyen, D.-H. Tran, V. Ngoc Phan, T.-T. Duong, D.-C. Nguyen, *Nanotechnology* **2016**, *27*, 335202.
- [48] M. Go, B. Hwang, S. Lim, *Materials and Manufacturing Processes* **2019**, *34*, 1605.
- [49] J.-M. Lee, Y.-H. Kim, H.-K. Kim, H.-J. Kim, C.-H. Hong, *Scientific Reports* **2020**, *10*, DOI 10.1038/s41598-020-61449-6.
- [50] S. Aghazadehchors, V. H. Nguyen, D. Muñoz-Rojas, C. Jiménez, L. Rapenne, N. D. Nguyen, D. Bellet, *Nanoscale* **2019**, *11*, 19969.
- [51] C. Celle, A. Cabos, T. Fontecave, B. Laguitton, A. Benayad, L. Guettaz, N. Pélissier, V. H. Nguyen, D. Bellet, D. Muñoz-Rojas, J.-P. Simonato, *Nanotechnology* **2018**, *29*, 085701.
- [52] B. Hwang, Y. An, H. Lee, E. Lee, S. Becker, Y.-H. Kim, H. Kim, *Scientific Reports* **2017**, *7*, DOI 10.1038/srep41336.
- [53] M. Göbelt, R. Keding, S. W. Schmitt, B. Hoffmann, S. Jäckle, M. Latzel, V. V. Radmilović, V. R. Radmilović, E. Spiecker, S. Christiansen, *Nano Energy* **2015**, *16*, 196.
- [54] H.-G. Cheong, J.-H. Kim, J.-H. Song, U. Jeong, J.-W. Park, *Thin Solid Films* **2015**, *589*, 633.
- [55] V. H. Nguyen, J. Resende, D. T. Papanastasiou, N. Fontanals, C. Jiménez, D. Muñoz-Rojas, D. Bellet, *Nanoscale* **2019**, *11*, 12097.
- [56] T. Sannicolo, W. H. Chae, J. Mwaura, V. Bulović, J. C. Grossman, *ACS Appl. Energy Mater.* **2021**, acsaem.0c02639.
- [57] D. Muñoz-Rojas, V. H. Nguyen, C. Masse de la Huerta, S. Aghazadehchors, C. Jiménez, D. Bellet, *Comptes Rendus Physique* **2017**, *18*, 391.
- [58] D. Muñoz-Rojas, J. MacManus-Driscoll, *Materials Horizons* **2014**, Doi:10.1039/c3mh00136a.
- [59] S. Aghazadehchors, V. H. Nguyen, D. Muñoz-Rojas, C. Jiménez, L. Rapenne, N. D. Nguyen, D. Bellet, *Nanoscale* **2019**, *11*, 19969.
- [60] WHO, "Coronavirus disease (COVID-19) pandemic," can be found under <https://www.who.int/emergencies/diseases/novel-coronavirus-2019>, **n.d.**
- [61] WHO, "Diagnostic detection of 2019-nCoV by real-time RT-PCR," can be found under https://www.who.int/docs/default-source/coronaviruse/protocol-v2-1.pdf?sfvrsn=a9ef618c_2, **n.d.**
- [62] Y. Wang, H. Kang, X. Liu, Z. Tong, *J Med Virol* **2020**, *92*, 538.
- [63] N. Sethuraman, S. S. Jeremiah, A. Ryo, *JAMA* **2020**, *323*, 2249.
- [64] J. Wang, H. Lou, J. Meng, Z. Peng, B. Wang, J. Wan, *Sensors and Actuators B: Chemical* **2020**, *305*, 127529.
- [65] Y. Zhang, P. He, M. Luo, X. Xu, G. Dai, J. Yang, *Nano Res.* **2020**, *13*, 919.
- [66] W. Zhou, S. Yao, H. Wang, Q. Du, Y. Ma, Y. Zhu, *ACS Nano* **2020**, *14*, 5798.
- [67] H.-W. Zhu, H.-L. Gao, H.-Y. Zhao, J. Ge, B.-C. Hu, J. Huang, S.-H. Yu, *Nano Res.* **2020**, *13*, 2879.

